SYNTHESIS OF 6-SUBSTITUTEDCHROMONE-2-CARBOXAMIDE DERIVATIVES AS CORROSION INHIBITORS FOR METALS IN ACIDIC MEDIUM

by

SIYABONGA SIHLE NYEMBE

Student Number: 17022203

A thesis submitted in fulfillment of the requirements for the degree of

Masters in Chemistry (MNMMSC)

Department of chemistry

Faculty of Science, Engineering, and Agriculture

University of Venda

Supervisor: Prof. L.C. MURULANA

Co-Supervisor: Prof. I.DI RAMAITE

Co-Supervisor: Prof. M.M KABANDA

December 2024

Plagiarism declaration

I, Sihle Siyabonga Nyembe, hereby declare that this dissertation for the degree of Master of Science in Chemistry at the University of Venda is my original work and has not been submitted for any degree at any other university or institution. This work is conducted under the supervision of Prof L.C Murulana, Prof. N.E Ramaite and Prof. M.M Kabanda as my co-supervisors. The dissertation does not contain any other persons' writing unless specifically acknowledged and referenced accordingly.

Full Names: Sihle Siyabonga Nyembe Date: 11/27/2024

Signature:

Dedication

This thesis is dedicated to my grandmother, **Ethel Sikhuthali Ngwenya,** for her never-ending support and encouraging me to stay in prayer and reading the Bible.

Table of Contents

Acknowledgements

I would like to thank God for being with me in this journey, his protection, guidance He bestowed on me throughout this study, and above all the gift of life.

I would like to express my deepest gratitude to my supervisor and mentor, Prof L.C. Murulana, for his guidance, supervision, and assistance and patience throughout this project. Thank you for your kindness. Thank you for your moral support, constructive criticism, and attentive reading of my writing for this project. Your expertise in research helped me navigate challenging situations. You excelled as a supervisor by providing unwavering support and ensuring the project's success. Thank you for ensuring I completed all project-related approaches successfully. You are a remarkable mentor and supervisor that every student would appreciate and wish to have.

I appreciate my co-supervisor, Prof I.D.I. Ramaite, for his expertise in organic chemistry. Your assistance in selecting and synthesizing the compounds used in this study was crucial to the project's success. Again, I would like to thank my second co-supervisor, Prof M.M. Kabanda for his expertise in Quantum Computational chemistry. Your assistance in studying the interaction between the synthesized compounds and the surfaces of the three metals. Through your assistance we managed to predict the compound’s ability to combat corrosion and link the corrosion activities to molecular properties.

I would like to thank the Corrosion Science Research Group (CorroSci) for their immense support and contribution. Thank you for making sure that I was able to run all the techniques required (such as Gravimetric analysis, Electrochemical analysis and Adsorption film analysis) for physical testing.

I would like to thank the University of Venda and the Department of Chemistry.

Finally, I would like to thank ABSA Scholarship and MQA bursary for their financial assistance.

It is my pleasure to also thank the following people for their immense support and contribution in this study: Ms N Maseko, Mr P Pandelani, Mr N Mabasa, Family and Friends.

Abstract

Corrosion is the gradual deterioration of a metal's properties as a result of its interaction with the surrounding environment. One method of controlling corrosion is to use corrosion inhibitors, substances added to a corrosive environment in trace quantities to reduce the rate of corrosion. In this study, five (5) non-toxic and inexpensive 6-substitutedchromone-2-carboxamides derivatives (Chromone-2-carboxamide, 6-bromochromone-2-carboxamide, 6-chlorochromone-2-carboxamide, 6-methoxychromone-2-carboxamide and 6-nitrochromone-2-carboxamide) were successful synthesized and evaluated as potential corrosion inhibitors in 1.5 M HCl for mild steel (MS) and zinc (Zn), and 1.0 M HCl for aluminium (Al) using experimental and computational techniques. All these inhibitors were first synthesized and then characterized by spectroscopic methods namely: Nuclear Magnetic Resonance (NMR) spectroscopy (^{1}H NMR and ^{13}C NMR), Mass Spectrometry and Fourier-Transform Infrared (FTIR) spectroscopy. The corrosion inhibition potentials of the corrosion were investigated using gravimetric analysis (GA), electrochemical analysis, theoretical studies, and surface morphology studies. Results from GA on MS showed an increase in percentage inhibition efficiency (%IE) as inhibitor concentration was increased, with NO_2-Chr-2-Carb showing the highest %IE (97.44%). The Langmuir adsorption isotherm was found to be the best-fit for all the corrosion inhibitors for all metal surfaces. All the synthesized compounds reduced the corrosion rate of three metals in the HCl solution. These corrosion inhibitors also exhibited mixed-type inhibitive action for the Al and MS, while physical adsorption was dominating on Zn. Spectra from FTIR showed that all corrosion inhibitors formed adsorption films on all metal surfaces, successfully inhibiting the corrosion process. Potentiodynamic Polarization (PDP) measurements revealed that these inhibitors reduced the rate of anodic and cathodic corrosion reactions, as shown by Tafel polarization measurements. Electrochemical Impedance spectroscopy (EIS) measurements revealed an increase in diameter of imperfect semicircles with increase in the concentration of inhibitors, suggesting increase in the surface coverage of adsorptive inhibitors on the metal surfaces, thus increase in charge transfer resistance. Spectroscopic studies for surface

analysis by SEM/EDS and wettability contact angle technique proved that the inhibitors induced a barrier for the corrosion process and created the hydrophobic surfaces. Quantum chemical calculations confirmed the importance of heteroatoms (O and N) in corrosion inhibition and gave a clear view on how the inhibitors adsorbed on the metal surfaces.

List of Abbreviations

Chr-2-Carb	Chromone-2-carboxamide
Br-Chr-2-Carb	6-bromochromone-2-carboxamide
Cl-Chr-2-Carb	6-chlorochromone-2-carboxamide
CH_3O-Chr-2-Carb	6-methoxychromone-2-carboxamide
NO_2-Chr-2-Carb	6-nitrochromone-2-carboxamide
%IE	Inhibition efficiency
ΔG^o_{ads}	Change in free energy of adsorption
ΔH^*_a	Enthalpy of activation
ΔS^*_a	Entropy of activation
AC	Alternating current
Al	Aluminium
BCC	Body-centred cubic
C_R	Corrosion rate
DC	Direct current
DFT	Density functional theory
DIIS	Iterative subspace direct inversion
DN	Double numeric
DND	Double-numerical +d
DNP	Double numeric with polarization functions
E_a	Activation energy
E_{corr}	Corrosion potential

EIS	Electrochemical impedance spectroscopy
E_{OCP}	Evolution of open-circuit potential
E_{OCP}	Open circuit potential
E_{pp}	Passivation potential
FCC	Face-centred cubic
$Fe(OH)_2$	Ferrous hydroxide
$Fe(OH)_3$	Ferric hydroxide
$FeCO_3$	Siderite or ferrous carbonate
FT-IR	Fourier-transform infrared spectroscopy
GDP	Gross domestic product
GGA	Generalized gradient approximation
GTO	Gaussian-type orbitals
H_2S	Hydrogen sulfide
H_2SO_4	Sulfuric acid
HCl	Hydrochloric acid
HF	Hartree-Fock
I	Electric current
I_{corr}	Corrosion current density
LC	Liquid chromatography
LC/MS	Liquid chromatography/mass spectrometry
LDA	Local density approximation
MS	Mild steel
O_2	Oxygen

OCP	Open-circuit potential
PBE	Perdew-Burke-Ernzerhof
PCM	Polarizable continuum model
PDP	Potentiodynamic polarization
Q_{ads}	Heat of adsorption
QM	Quantum mechanical
R	Resistance
R_{ct}	Charge transfer resistance:
RE	Reference electrode
R_L	Inductive resistance
RT	Retention time
SCE	Saturated calomel electrode
SCF	Self-consistent field
SEM/EDS	Scanning electron microscopy/energy dispersive X-ray spectroscopy
SHE	Standard hydrogen electrode
STO	Slater-type orbital
US	United States
V	Voltage
VCA	Video contact angle system
WE	Working electrode
Zn	Zinc
β_a	Anodic Tafel constant/slope
β_c	Cathodic Tafel constant/slope

List of figures

List of tables

List of schemes

List of Appendixes

CHAPTER 1: Introduction

The work represented in this dissertation is titled ***"SYNTHESIS OF 6-SUBSTITUTED CHROMONE-2-CARBOXAMIDE DERIVATIVES AND THEIR USE AS CORROSION INHIBITORS FOR METALS IN ACIDIC MEDIUM"*** *is broken down into four chapters.*

This chapter provides a basic overview of corrosion, the importance of corrosion management, and the use of organic compounds to control corrosion. It also explains why and how this research is being conducted as well as the significance of employing hydrochloric acid (HCl) as a corrosive solution (environment).

1.1. Introduction

Mild steel (MS) is widely used because of its outstanding physical properties, such as high tensile strength, high impact strength, good ductility, and weldability [1,2]. It has exceptional mechanical qualities, is affordable compared to other high-priced corrosion-resistant alloys, and has a simple manufacturing procedure [3,4]. Aluminium (Al) is a highly reactive metal that has high corrosion resistance. Al's corrosion resistance due to the formation of a barrier oxide film that is bonded strongly to its surface when exposed to moisture. However, it can be corroded if exposed to corrosive environment (acidic environment) [5]. Zinc (Zn) is the fourth most widely manufactured and used metal worldwide, following iron, aluminum, and copper. Its popularity stems from its anticorrosive characteristics and affordability. Zn is commonly used in galvanizing to form a thin layer that protects other metals against corrosion, including iron and copper [6]. MS, alloys, and other metals display low corrosion resistance in aggressive medium, due to this fact it becomes difficult to control their corrosion and becomes a critical industrial issue. Acid (e.g. HCl) is commonly used in industrial applications such as pipeline cleaning, oil well treatment, and gas processing [6,7]. Unfortunately, metals display a susceptibility response towards factors (such as air, humidity, salt, marine water, acids, alkalis, etc) that allows them to revert to a more stable oxidized state. This is commonly referred to as corrosion [8, 9]. Corrosion is caused by a redox reaction between the metal surface and the factors listed above. Regrettably, the corrosion of metals causes massive economic losses that have a negative impact on any nation's GDP growth [10]. Because metal-based structures are so common in our daily lives, corrosion control is critical. As a result, it is critical to establish some outstanding and environmentally friendly inhibitors because using corrosion inhibitors is the most efficient and practical method of overcoming corrosion when compared to other corrosion mitigating methods [11 – 13].

Considering the economic burden that is brought by corrosion around the world, researchers have discovered mitigation strategies that are helpful in preventing the high rate of corrosion. The mitigation strategies are classified as active and passive. The active technique involves the use of competitive chemical reactions to prevent the deterioration of metals, and it also involves the use of external cathodic protection with or without

coatings, sacrificial (more reactive) metals, and inhibitors. On the other hand, the passive technique involves material selection, organic and inorganic coatings, and metallic coatings. When a passive technique is used in boilers, oxygen and ionic species are removed and replaced by inhibitors [14, 15]. Below is a detailed explanation of how and why these prevention methods are used.

Corrosion can be controlled by using protective coatings. Metals are protected from corrosion by protective coatings. The very same protective coatings form a physical barrier between the coated metal surface and the surrounding environment. They impart some unique properties to the protected surface, such as hardness, electrical properties, oxidation resistance, and thermal insulating properties. Protective coatings are classified as inorganic, Organic, and metallic. Organic coatings (e.g. paints, varnishes, lacquers and enamels) are mostly preferred due to their simplicity in application, flexibility, toughness, adhesion, chemical resistance, and durability [16, 17].

According to the galvanic series, one metal is protected by connecting it to another metal that is more anodic. This method is known as a galvanic cathodic protection system. Without cathodic protection, one area of the structure has a higher negative potential than another, resulting in corrosion. If, on the other hand, a much less inert object (that is, one with a much higher negative potential, such as a magnesium anode) is placed adjacent to the structure to be protected, such as a pipeline and a metallic connection (insulated wire) is installed between the object and the structure, the object becomes the anode, and the entire structure becomes the cathode. A sacrificial (more reactive) metal, such as magnesium or zinc, is placed in contact with the corrosive environment and electrically connected to the structure to be protected.

An iron that has been zinc-coated (i.e. galvanized iron) is also protected, even if the surface has been scratched. This is due to zinc's increased reactivity. It begins by producing its own zinc oxide (ZnO) coating. Second, if the iron is exposed, the zinc will oxidize first (because it is more reactive), providing electrons to the iron and preventing corrosion. The following are the redox reactions [18]:

Anode: $Zn_{(s)} \rightarrow Zn^{2+}_{(aq)} + 2e^-$ (1)

Cathode: $Fe^{2+}_{(aq)} + 2e^- \rightarrow Fe_{(s)}$ (2)

Overall: $Zn_{(s)} + Fe^{2+}_{(aq)} \rightarrow Zn^{2+}_{(aq)} + Fe_{(s)}$ (3)

The zinc donates electrons to the iron, sacrificing itself to keep the iron from corroding. When the zinc is depleted, it must be replaced with another piece.

Corrosion inhibitors are chemical compounds that, when present in small concentrations, can reduce, or slow the corrosion of metals on an acidic environment. Corrosion inhibitors are a common and inexpensive method of preventing or controlling corrosion because they allow the use of less costly metals such as carbon steel in an aggressive environment [19]. The use of chemical inhibitors to slow down corrosion processes varies greatly. Organic inhibitors have been found to be the most effective in reducing the corrosion of metal when added to a corrosive environment, and are highly preferred as majority are non-toxic to the environment, as observed by a number of researchers. They bind to metal surfaces via chemisorption and physisorption. When a metal encounters an aqueous solution, most of the metal surface is covered with adsorbed water molecules. The use of a small amount of inhibitors is sufficient to inhibit the anodic and cathodic reactions when added to an abrasive medium. Organic compounds such as organic heterocyclic compounds, organic dyes, amino acids, green aromatic acids, etc., have been used as efficient inhibitors for mild steel (MS) in hydrochloric acid (HCl) medium. This gives a clear view that organic inhibitors are the most desirable and cost-effective way to reduce corrosion attacks on the metallic surface. Heterocyclic organic compounds with the pi system and heteroatoms such as oxygen (O), nitrogen (N), and sulfur (S) may be effective inhibitors of mild steel (MS) deterioration in the acid medium [20, 21]. Both the size and molecular weight of organic inhibitors also influence inhibition efficiency. The larger the molecule, the more effective the inhibition: $R_3N > R_2NH > RNH_2$, here R represents a hydrocarbon chain [22]. Figure 1.1 below displays organic compounds containing heteroatoms such as nitrogen, sulfur, oxygen and π (pi system), which may be good corrosion inhibitors [22]

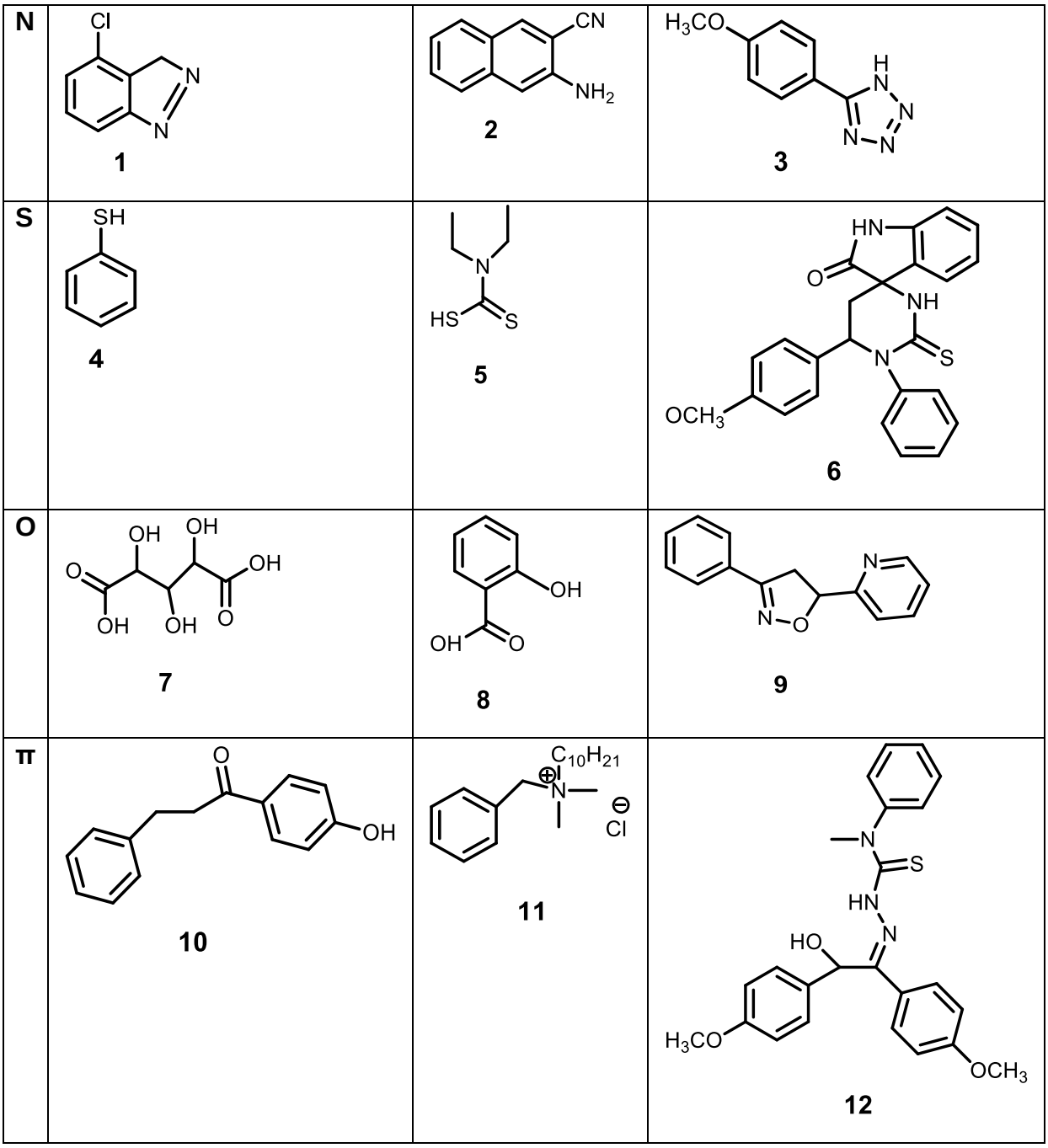

Figure 1.1: Examples of organic corrosion inhibitors with Nitrogen, sulfur, oxygen and π (pi system).

Corrosion inhibition mechanism: In the process of metal- corrosion inhibition mechanism, the inhibitors are first adsorbed on the metallic surface, which result to donor acceptor interactions. The chloride ions (Cl^-) from acidic medium (HCl) expedite the adsorption of the positive inhibitor complex on the metallic surface, through electrostatic interactions.

The adsorption of the inhibitor is typically a combination of physical and chemical adsorption, rather than being entirely physical or entirely chemical. Through physisorption, the inhibitor is attracted to the negatively charged metallic surface in the acidic medium. In the chemisorption process, heteroatoms (S, N, O, P) transfer their lone pair of electrons into the d-orbitals of the atoms of the metallic surface [23 – 25]. Figure 1.2 displays an example of the corrosion inhibition mechanism by (4-hydroxy-3-(phenyldiazenyl)-2H-chromen-2-one compound [24].

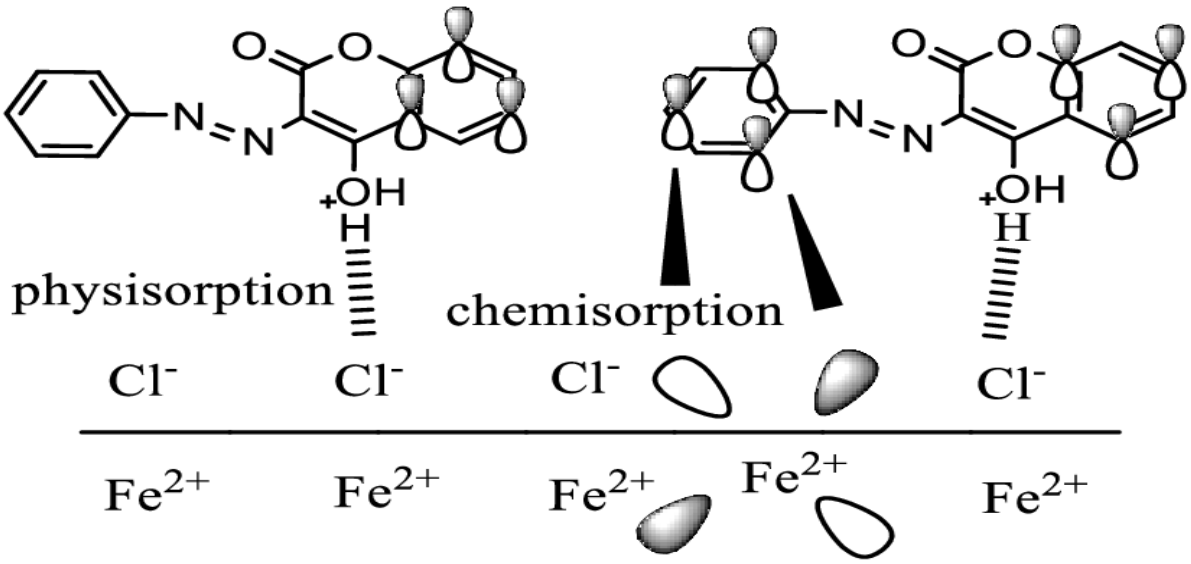

Figure 1.2: Schematic representation of the Corrosion inhibition mechanism (4-hydroxy-3-(phenyldiazenyl)-2H-chromen-2-one, as organic inhibitor).

1.2. Problem statement

Corrosion is one of the leading challenges the world is facing adding to the world's health and safety burden. Corrosion gradually deteriorates critical mineral resources, which are scarce together with those which are plentiful. The progressive depletion of limited resources due to corrosion causes huge economic losses and affects the ecosystem [26, 27]. Natural resources are progressively depleted, including metals and fuels used to manufacture them. Corroded equipment leads to health issues, as they contaminate

clean water and food, they also cause pollution due to escaping products from the corroded equipment [28].

Because corrosion cannot be avoided, it is critical that it be managed so that equipment can perform its required tasks effectively and efficiently. One method of controlling corrosion is to reduce the corrosion rate (corrosion inhibition). Given the global impact of corrosion, more research on corrosion inhibition must be conducted. Training and educational initiatives centered on the sensible use of corrosion inhibitors are required [29].

Several researchers have found the use of nano-technology as corrosion inhibitors underperforming, and fail to withstand harsh environment (corrosive environment). Nanoparticles perform best when work synergetic with organic inhibitors, but not much effective when working alone as corrosion inhibitors. Organic corrosion inhibitors were found to be the best candidates in protecting metals from harsh environment. To overcome the problem of underperforming corrosion protection methods, 6-substitutedchromone-2-carboxamides as novel organic inhibitors were chosen to be the best solution. The structures of these compounds possess characteristics (e.g. aromatic rings, heteroatoms and pi-electrons) of excellent inhibitor. Such characteristics can propel us to further test their potential to reduce the rate of corrosion.

1.3. Justification of the study

Corrosion is a major problem worldwide in all industries, companies, workplaces and at homes. It has a negative impact on safety, health, and environmental issues. There are many corrosion-related accidents which are reported every year. Some of the reported devastative corrosion accidents have claimed lives and incurred substantial economic losses. The effects of corrosion on the equipment and its surroundings should always be considered to avoid termination and contamination of metallic products. The cost of corrosion in developed countries is approximately 3 – 4 % of GDP. This has an impact on a country's economy and assets, including infrastructure, transportation, utilities, nuclear and military facilities, and manufacturing and production plants. Corrosion is an all-

encompassing foe that must be accepted as an unavoidable process. As products and manufacturing processes have become more complex, and the penalties for corrosion failures have become more costly, there has been a rise in awareness that adds to the preceding assertion by arguing that corrosion, like corruption, eats deeply into the fabric of a nation's economy in an irreversible way, making a recovery an unattainable mirage. Furthermore, it is estimated that corrosion accounts for 10% of global metal output. The economic cost of corrosion is classified into two ways, which are direct and indirect costs. The direct costs include expensive materials needed to prevent corrosion damage, the labour for corrosion management, equipment required for corrosion-related activities, loss of reliability, and loss of capital due to corrosion-induced deterioration. The National Association of Corrosion Engineers (NACE) has reported that the total of all these direct costs is calculated to be $137.9 billion per year. The indirect costs of corrosion involve plant downtime (loss of revenue), environmental contamination (product contamination), loss of equipment efficiency, over-design to make allowance for metal loss and delays that may arise from lawsuits and ill-will etc, user costs, and insurance costs. The sum of the direct costs is calculated, up to $276 billion, and contributes more than three pct to the U.S. Gross Domestic Product (GDP) [30, 31].

The global economic loss from corrosion is estimated to be greater than US$1.8 trillion, while the direct cost of corrosion in South Africa is estimated to be around R130 billion. The global economic loss from corrosion is estimated to be more than US$1.8 trillion, while the direct cost of corrosion in South Africa is estimated to be around R130 billion. Half of every ton of steel produced is simply used to replace corroded steel. This implies a significant carbon footprint, as each ton of steel produced generates 380 kg of carbon dioxide (CO_2). According to The World Bank's 2017 figures, South Africa's GDP was USD348.9 billion (approximately ZAR4 885 billion). Using NACE's 2016 figure of 3.4 % of global GDP as the annual cost of corrosion, this means that approximately ZAR166 billion is currently spent in South Africa to combat or prevent corrosion problems. Atmospheric corrosion of coated and uncoated metal surfaces is regarded as a significant contributor to this total [32, 33].

1.4. Aim and objectives of the study

The general goal of this research is to generate measurable and testable experimental data for the control of corrosion of three metals, zinc, mild steel, and aluminium, in contact with an aggressive environment (HCl), using organic synthesized inhibitors (6-substituted chromone-2-carboxamide derivatives).

The objectives of this study are to:

1. synthesize and characterize 6-substituted chromone-2-carboxamide derivatives using NMR, FTIR, and Mass Spectrometry.
2. To evaluate the inhibition efficiency of the organic synthesized inhibitors for mild steel, zinc and aluminium and the interaction of the three metals with the 6-substituted chromone-2-carboxamide derivatives by gravimetric weight loss analysis, electrochemical impedance spectroscopy (EIS) and potentiodynamic polarization (PDP).
3. identify the mechanism by which the 6-substituted chromone-2-carboxamide derivatives prevent corrosion using adsorption isotherms (whether the inhibition is physical, chemical or mixed type).
4. determine the functional groups of the 6-substituted chromone-2-carboxamide that are responsible for the adsorption on the metal surface and subsequently the inhibition of corrosion using FTIR.
5. evaluate the metal's surface exposed to the corrosive solution in the presence and absence of the inhibitor and state the elemental composition of the metals before and after exposure to the inhibitors using SEM/EDS.
6. To utilize quantum chemical/theoretical techniques e.g. density functional theory (DFT) in order to estimate molecular properties of the inhibitor as well as the binding energies between the inhibitor and the metal surface.

CHAPTER 2: Literature review

This chapter reviews the literature relevant to the current study. This summary covers the fundamental principles of corrosion, including theories, forms, and classification. It covers corrosion variables, repercussions, costs, and the underlying thermodynamics and kinetics. This chapter also provides an overview of metal corrosion and preventative measures, including the use of organic compounds as inhibitors. Moreover, this chapter covers the mechanism, definition, and characteristics of chromones that make them excellent corrosion inhibitors, including the synthesized 6-substitutedchromone-2-carboxamides. Furthermore, this chapter spotlights corrosion monitoring techniques, specifically those used in this study.

2.1. Corrosion description

Corrosion is defined as an electrochemical process in which metals and alloys undergo gradual deterioration. It is a natural dissolution of metallic materials that causes massive economic and safety losses. Corrosion can be caused by both natural and man-made activities. Corrosion destroys a metal's useful properties such as malleability, ductility, electrical conductivity, and surface appearance. The environment slowly and continuously corrodes metals or alloys. The most well-known example of corrosion is iron rusting when exposed to atmospheric conditions. Another example is the formation of a green film or basic carbonate [$CuCO_3$+$Cu(OH)_2$] on the surface of copper when exposed to moist CO_2 and oxygen-containing air. Metal deterioration is a huge waste of both resources and money, so it must be protected in the most cost-effective and practical way possible [34 – 36].

A process of corrosion is propelled by two coupled reactions that occur at the metal-aqueous interface, and the two coupled reactions are spontaneous. The first reaction involves chemical species from the aqueous environment removing electrons from the metal, while the second one involves metal surface atoms participating in replenishing the electron deficiency. Electronic current is generated at the metallic surface as a result of the exchange of electrons between the two coupled reactions. An influential factor is the imposition of an electric potential on the surface of the metal of a value sufficient to balance the supply and demand for electrons in the two coupled reactions. The metal's potential is much more important than simply balancing the complementary reactions that produce it because it is one of the primary factors determining what the reactions will be. The preferred reaction for iron at the potential it acquires in neutral aerated water is the dissolution of the metal as a soluble species that diffuses away into the solution, allowing the reaction to continue, that is, the iron corrodes. If the potential is reduced by removing dissolved oxygen, the reaction is slowed or stopped. Alternatively, by increasing the potential in the water, the preferred reaction can be altered to produce a solid product on the iron surface, providing effective corrosion protection. Increasing the water's alkalinity has a similar effect [37].

2.2. Theories of corrosion

2.2.1. Acid theory of corrosion

According to acid theory, the corrosion of a metal (iron) is caused by the availability of acids in its vicinity. This theory holds that iron is corroded by carbon dioxide, moisture, and oxygen in the atmosphere. Acidic corrosion is the progressive destruction and eroding of a material (for example, metal) caused by acidic contaminants in the environment. Acids can come from soil, advanced manufacturing air, water, or toxic substances that interact with the metals they interact with. The process of corrosion in most metals increases in the presence of acids when the metals come into contact with the acids. Corrosion in acid solutions is much faster than in neutral solutions, which is faster than in alkaline solutions. In acidic solutions (e.g. HCl) and concentrated alkali solutions, Hg is usually transformed from the metal's surface during corrosion. Unlike acidic and alkali solutions, in neutral solutions, the evolution of Hg is usually far less and may be insignificant. The availability of O_2 is also required for corrosion to occur in normal water. In acid, neutral, or slightly alkaline water, oxygen can cause significant corrosion. If other factors remain constant, the rate of corrosion in natural waters will be directly proportional to O_2 content. Oxygen also speeds up the deterioration of iron in moderately strong non-oxidizing acid solutions. The acidic theory of corrosion was developed through rust analysis, which provides the CO_2 ion test. Below is the representation of the balanced chemical reactions taking place in the corrosion of iron (Fe) in the presence of acids [38, 39]:

$$Fe_{(s)} + 2CO_2 + H_2O + \frac{1}{2}O_2 \rightarrow Fe\,(HCO_3)_2 \quad (4)$$

$$2Fe(HCO_3)_{2(s)} + H_2O_{(g)} \rightarrow 2Fe(OH)CO_{3(s)} + 2CO_{2(g)} + 2H_2O_{(g)} \quad (5)$$

$$2Fe(OH)CO_{3(s)} + 2H_2O_{(g)} \rightarrow 2Fe\,(OH)_{3(s)} + 2CO_{2\,(s)} \quad (6)$$

We observe that $Fe\,(HCO_3)_{2(s)}$, $Fe\,(OH)CO_3$ and $Fe\,(OH)_3$ are products of corrosion [40-42].

2.2.2. Extreme value theory of corrosion

Extreme value theory or extreme value analysis predicts the most likely maximum extent of corrosion, such as the deepest pit in the case of pitting corrosion. One intriguing application of this theory is its application to material strength in size effect analysis. It is extremely helpful in assessing the size effect and making reliable extrapolations possible, as described by Gumbel. The theory is thus well geared to localized corrosion since failure caused by localized corrosion typically occurs if each local site fails, such as when a single pit perforates the wall of a container structure. In this situation, if the most likely maximum pit depth after time (t) equals the wall thickness, then the anticipated lifetime is (t). This theory was first developed specific for the fields of hydrology and meteorology and is now used to interpolate a size factor that allows one to approximate the maximum pit depth in a large surface area in terms of the distribution of a small number of pit depth data from the sample size data. This theory makes use of EVAN computer program as well as the MVLUE method.

There are two possible ways to define extremes. One possible way is by selecting a proper threshold and then collecting every observation above that threshold, and other way is by sorting the data according to certain a priori sampling scheme, so that the one, two, or three, etc, largest value is selected (s). The manner that the extremes are interpreted and thus measured indicates the techniques suitable for analysis and simulation, as shown by an example in figure 2.1 [46]. The probabilities of the maxima in each small area deduced from the dispersion of the entire collection of pits are given by extreme value theory. The cumulative distribution of the maximum pit depths from the n smaller areas is represented in this formula: $F(d_{max}) = \exp\{-\exp[-b(d_{max} - U_{N})]\}$, where d_{max} maximum pit depths, b is a parameter that is inversely related to the distribution's width and U_N is a parameter comparable to the average maximum pit depth. This formula is used if the probability distribution for all pits in the entire sample decays exponentially at large depths [43-45].

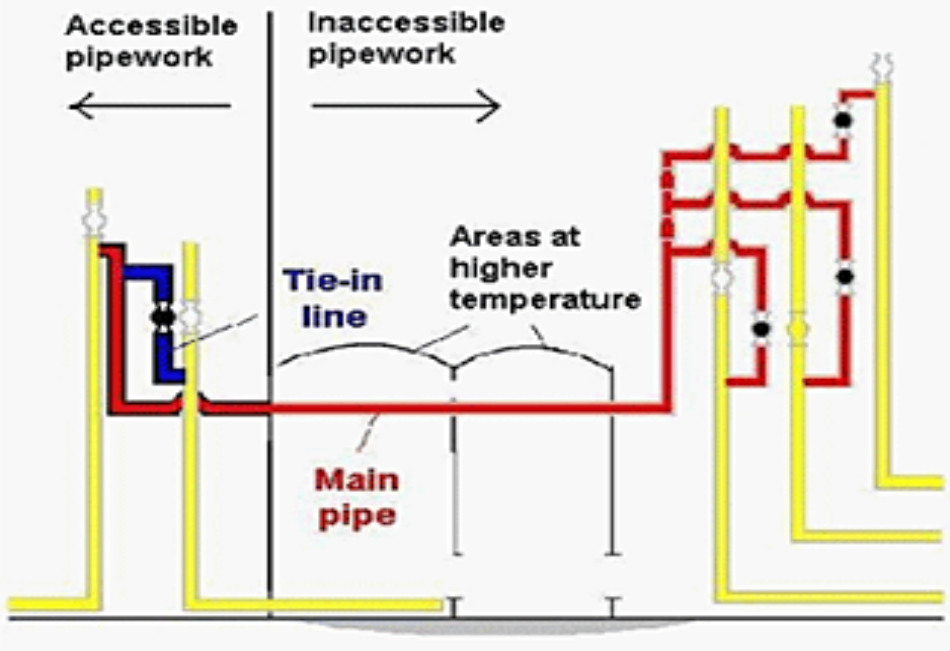

Figure 2.1: Examples of extreme value analysis and corrosion mapping.

2.3. Basic principles of corrosion

During the corrosion process, two reactions are involved (the anodic and cathodic reaction). Metal atoms are ionized and pass into solution leaving their electrons within the original metal surface in the anodic reaction, and the free electrons on the metal are taken up by chemical species such as O_2 and H_2O in the cathodic reaction. The anodic and cathodic reactions occur at equivalent rates at different parts of the metals or alloys. These two reactions result in the metal turning to its oxide state [47].

The chemical and electrochemical processes responsible for corrosion make corrosion a complex process. The process of corrosion can be explained in three steps involved in the electrochemical reaction as shown in Figure 2.2 [48]:

1) Ion is oxidized to Fe^{2+} ion and is lost on the metal of the anodic site due to the lower potential in the anodic site.
2) The initially produced Fe^{2+} ion leads to the release of the two electrons that migrate through electrically conductive metal, from anode to cathode.

3) On the cathodic site oxygen is reduced to water, to form OH^- on the surface of the metal, and the electric circuit is completed by the electrons that flow to the cathode.

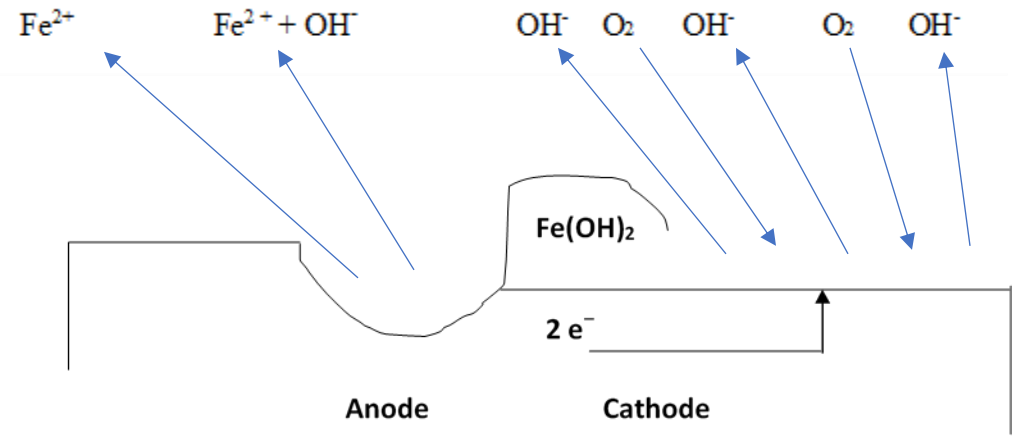

Figure 2.2: Electrochemical reaction to the corrosion process.

The reduction and oxidation reactions occur as follows:

Anodic reaction: $Fe_{(s)} \rightarrow Fe^{+2}_{(aq)} + 2e^-$ (7)

Cathodic reaction: $\frac{1}{2} O_{2(g)} + H_2O_{(l)} + 2e^- \rightarrow 2OH^-_{(aq)}$ (8)

The formation of ferrous hydroxide precipitates due to the diffusion of Fe^{+2} ions and OH^- ions when they meet is shown as follows:

$Fe^{+2}_{(aq)} + 2OH^-_{(aq)} \rightarrow Fe(OH)_{2(s)}$ (9)

The reduction of protons in acid solutions in the cathodic site. H^+ completes the electrical circuit as shown:

$2H^+_{(aq)} + 2e^- \rightarrow H_{2(g)}$ (10)

Cathodic reaction in neutral and alkaline electrolytes is as follows:

$$O_{2(g)} + 4e^- + 2H_2O_{(l)} \rightarrow 4OH^-(aq) \quad (11)$$

The formation of Ferric hydroxide due to enough O_2 available. Enough O_2 caused $Fe(OH)_2$ to be easily oxidized

$$4\ Fe(OH)_{2(s)} + O_2 + 2H_2O_{(l)} \rightarrow 4Fe(OH)_{3(s)} \quad (12)$$

The product known as yellow rust is actually related to $Fe(OH)_3.H_2O$.

Black anhydrous magnetite (Fe_3O_4) as a corrosion product is resulted due to the limited supply of O_2 [48-49].

2.4. Classification of corrosion

Corrosion is generally divided into two categories depending on the mechanism of corrosion: dry corrosion (chemical) and wet corrosion (electrochemical). The above categories are discussed briefly in the sub-headings below.

Dry corrosion (chemical): This form of corrosion occurs because of direct attack by atmospheric gases such as oxygen, carbon dioxide, chlorine, sulphur dioxide, hydrogen sulphide, and others on the surface of metal when the metal or surface is exposed to the atmosphere for an extended period. It usually occurs in the absence of moisture, unlike electrochemical corrosion. The extent of corrosion and protective values are determined by the following factors: chemical affinity between the environment and the metal, protective value of the film, nature of the film formed, and adhesion between the film and the metal surface. The degree of corrosion in nonferrous films is determined by the film's electronic and ionic conductivities [50].

Wet corrosion (electrochemical): This type of corrosion takes place when the metal comes into contact with moisture or is immersed in an aqueous medium. It is the process by which electrons move from one metal surface to another in an ion-friendly environment. It is usually more common and more severe than dry corrosion [51].

This research will investigate the corrosion process in the presence of moisture (electrochemical corrosion).

2.5. The corrosion cell

A corrosion cell is defined as a metallic surface condition in which there is a flow of electric current among two metal surfaces and it is made up of four main parts which are: anode, cathode, electrolyte, and electric linkage between anode and cathode for electron current to flow. The electrolyte is typically made up of ions that can conduct electrical currents all through the electrochemical reaction, which involves two-way traffic. The electrode is an electronic conductor through which electric charges flow in a unidirectional fashion through one-way traffic. The corrosion cell's key components include the anode site, cathode site, electrolyte, cathode reactant, and anode reactant. The anode is the electrode or region upon that metallic surface where oxidation occurs, whereas the cathode is the electrode or location on the metallic surface where reduction typically happens, as shown in Figure 2.3. The electron is taken up by the cathode electrode from the anodic zone. The cathode is the negative electrode that hosts the reduction half-reaction. Cations that are positively charged ions migrate to the cathodic region whereas the anions which are negatively charged ions migrate to the anodic region to complete the corrosion reaction. This occurs as a result of the generation of H_{2g} from H^+ ions, and the establishment of OH^- ions from dissolved O_2, which lead to the reduction of metal ions (M^+) to a lower valence state. A moisture electrolyte zone is required to form a galvanic cell on the metal itself or between two dissimilar metals if they are electrically joined in some way [52, 53]. The presence of a negative Gibbs free energy change in the electrochemical cell reaction indicates that the corrosion process occurs spontaneously, and corrosion is only possible. A positive Gibbs free energy indicates that the corrosion process occurred spontaneously [54]. Below is a diagram depicting the corrosion cell [53].

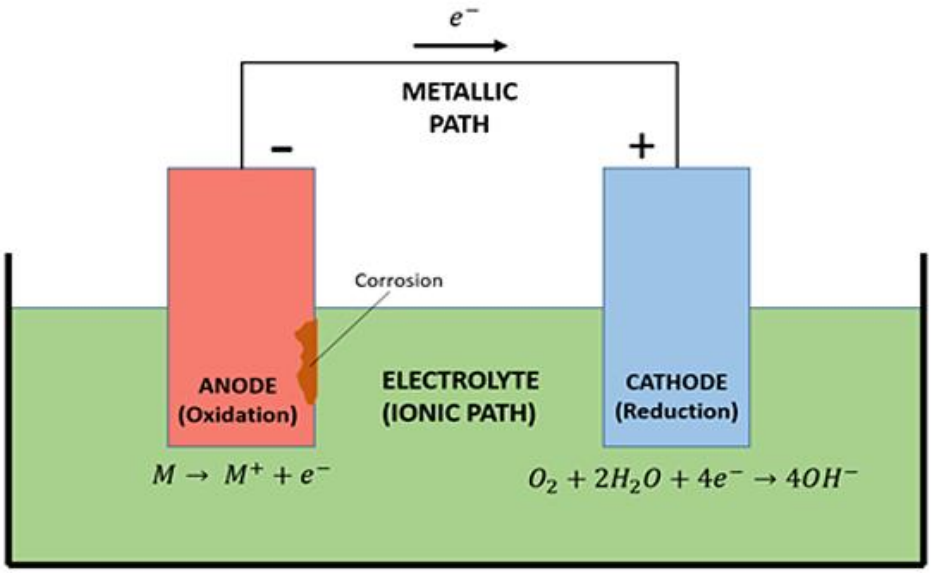

Figure 2.3: A schematic illustration of an electrochemical cell demonstrating corrosion principles.

2.6. Different types of corrosion

Corrosion can be classified based on how it appears on corroded metallic surfaces. The majority of corrosion types can be identified with the unaided eye, but in some cases, high magnifications are required. Corrosion can be classified based on the appearance of corrosion damage, the mechanism of attack, the industry sector, and the preventive methods used [55, 56]. Some forms of corrosion are; uniform corrosion, galvanic corrosion, pitting corrosion, crevice corrosion, stretch corrosion, intergranular corrosion, and erosion-corrosion. These forms of corrosion are briefly explained below:

Uniform/general corrosion: Uniform/general corrosion is the most common type of corrosion which spreads evenly across the metallic surface once it begins. The most effective illustrations of such a type of corrosive process are mostly the uniform deterioration of steel in acidic medium as well as the atmospheric corrosion of both ferrous and non-ferrous metals. Metallic surface corrosion (Zinc, ion) in acidic solutions (HCl, H_2SO_4) is a good example of uniform corrosion. Corrosion proceeds at the same rate throughout the area exposed to the environment and there are no clearly defined anode & cathode areas. The extent of the corrosion can be expressed by loss in weight per unit

area or by average penetration depth [57 – 59]. Figure 2.4 below gives a clear view of how uniform corrosion occurs [60].

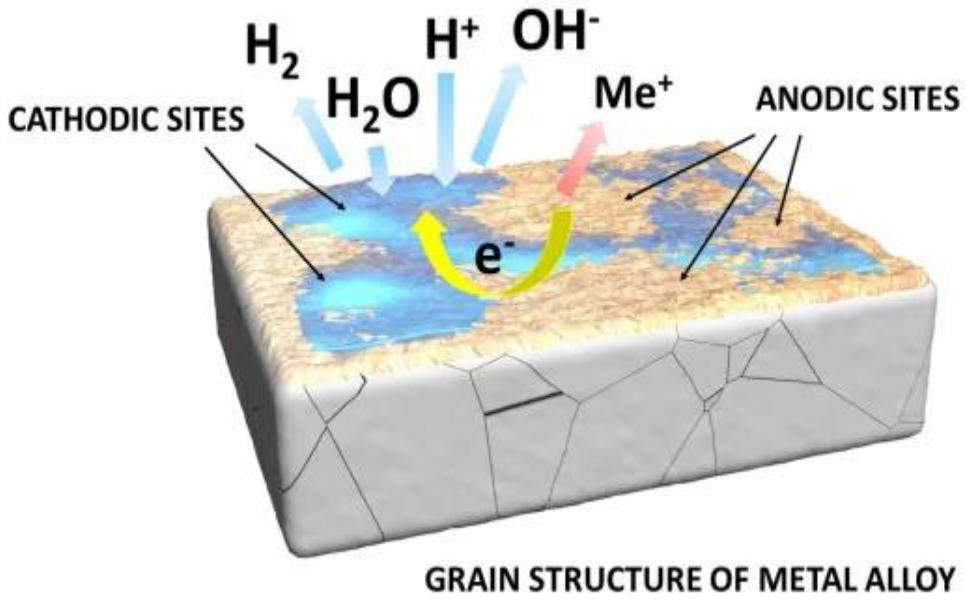

Figure 2.4: Diagram depicting the process occurring during Uniform corrosion.

Galvanic corrosion: This type of corrosion occurs as a result of a potential difference between two interconnected metals. Two different metals come into physical or electrical contact with each other while immersed in a common electrolyte, or when the same metal is exposed to varying concentrations of an electrolyte. The more reactive metal serves as the anode, while the less reactive metal serves as the cathode. The more negative a metal is, the more it acts as a cathode and increases corrosion. Galvanic corrosion, for instance, can happen once stainless or carbon steel comes into contact with alloying elements of magnesium or aluminium and speed up the corrosion of those metals. [61 – 63]. Figure 2.5 below displays how the galvanic corrosion mechanism occurs [64].

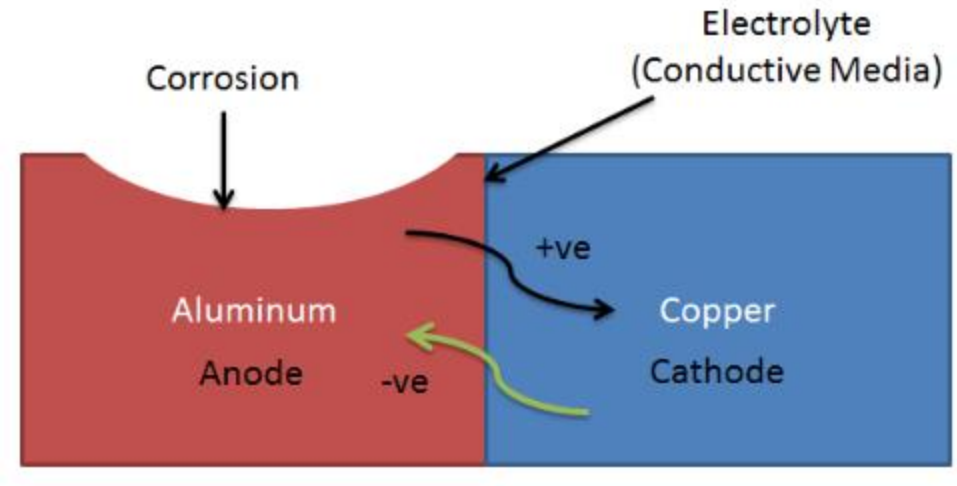

Figure 2.5: Diagram depicting the mechanism of Galvanic corrosion.

Pitting corrosion: This is a more localized type of corrosion that begins in pits/cracks or holes on the metallic surface. Pitting corrosion is a terribly dangerous type of corrosion because once it begins, it quickly spreads and damages the metallic surface. These issues are particularly dangerous because they are difficult to detect before a component or structure fails. Pitting is still one of the most common and destructive forms of corrosion in passivated alloys, but it can be avoided by controlling the alloy's environment [65, 66].

When an electrical and chemical failure reveals a small local site on a metallic surface to potentially harmful species like chloride ions, a pit is created. Environmental variation exists at the location of pitting compared to the entire metal surface. Surface pitting of steel occurs as a result of the reaction between chlorine and H_2S [67]. Figure 2.6 shows a structure that has undergone pitting corrosion, and the pitting corrosion process [68].

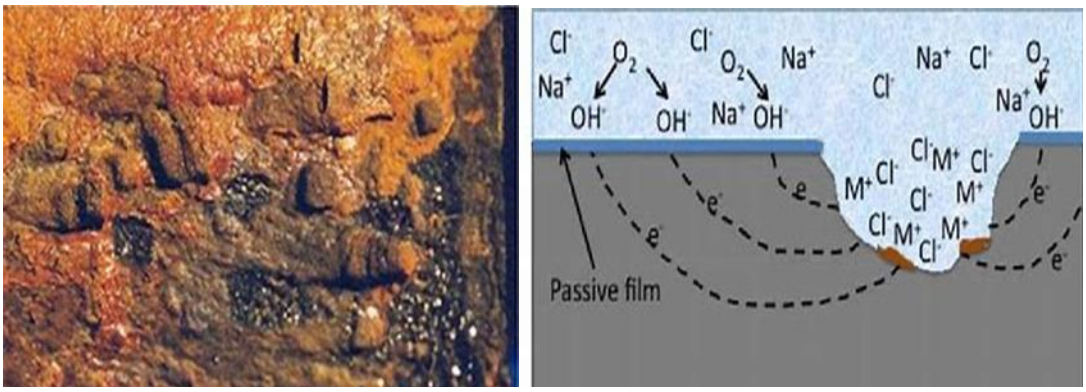

Figure 2.6: Diagram and schematic illustration portraying Pitting corrosion process.

Crevice corrosion: This type of corrosion occurs in confined spaces (crevices) where the working fluid's access to the environment is restricted. Crevice corrosion begins and spreads through crevices and other shielded areas of the metallic surface. Crevices include gaps and contact areas between parts, under gaskets or seals, inside cracks and seams, spaces filled with deposits, and under sludge piles. Crevice corrosion is influenced by the type of crevice (metal-metal, metal-nonmetal), the geometry of the crevice (size, surface finish), as well as metallurgical and environmental factors. A critical crevice corrosion temperature is frequently used to rank the resistance of a material to crevice corrosion [69 – 71]. Figure 2.7 below shows how metals are attacked by crevice corrosion and the process behind this type of corrosion [72].

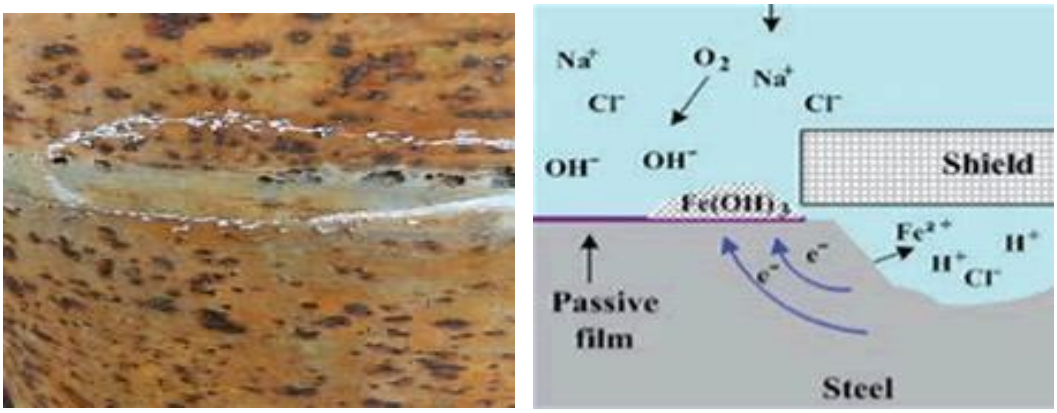

Figure 2.7: Diagram and schematic illustration depicting the process occurring during Crevice corrosion.

Intergranular corrosion: is a type of corrosion in which the material's crystallite boundaries are more susceptible to corrosion than their interiors. Anodic dissolution of alloying element-depleted regions, phase 2 precipitates, or regions with segregated alloying or impurity elements causes corrosion attack at grain boundaries. The remaining exposed surface typically serves as the cathode, and large cathodic areas aid in anodic dissolution, as displayed in Figure 2.8 [73 – 75].

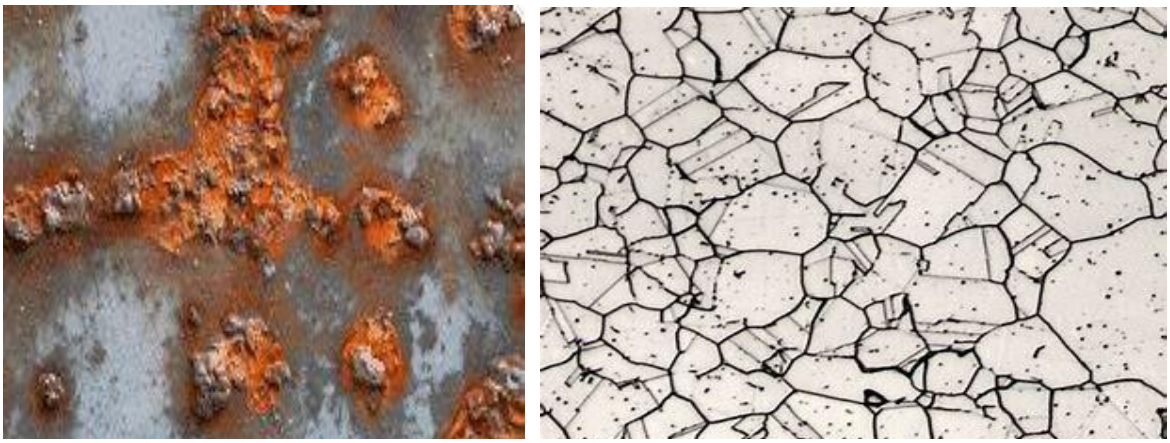

Figure 2.8: Diagrams portraying the grain boundary attack.

Selective leaching corrosion: The removal of one element from a solid alloy through corrosion is known as selective corrosion. The most common example is brass dezincification, which involves selectively leaching zinc from a copper-zinc brass alloy. This process results in a porous copper structure that is weakened. The selective removal of zinc can be done on a large scale or on a small scale. What Causes Dezincification? Brasses with more than 15% zinc undergo dezincification. Zinc is an element that is extremely reactive as evidenced by its galvanic series ranking, and it has a low standard electrode potential (-0.763) which is lower than copper's standard electrode potential (+0.337). This reactivity is caused by zinc's extremely weak atomic bond in comparison to other metals and the potential difference is the driving force behind dezincification. Simply put, zinc atoms are effortlessly given up to solutions with aggressive properties. The more active zinc is selectively removed from the brass during dezincification, having left behind a porous, more noble copper-rich reserve [76, 77]. Both parts of the alloy are initially dissolved by corrosion, however the more noble steel this case, copper—then precipitates from the solution at the surface. Due to galvanic effects, this causes the

parent alloy to dissolve more readily, which results in an additional copper deposition. Overall, a component's surface and subsurface areas are reduced to a spongy mass of material with significantly reduced mechanical strength, raising the possibility of collapse under typical working stresses [78]. Figure 2.9 shows metals that have undergone dezincification as a result of selective corrosion [78]

Figure 2.9: Dezincification as a result of selective corrosion.

2.7. Atmospheric interaction with the metallic surface

Most of the metal-critical infrastructures are exposed to some large extent to terrestrial air conditions and hence can undergo atmospheric corrosion. In extreme circumstances, the material can be utterly obliterated and transformed into oxide film (corrosion products). Over the last several years, the understanding of the effects of climatic conditions on metallic corrosion has greatly improved. This has resulted in the establishment and confirmation of atmospheric corrosion kinetics through a classical bi-logarithmic equation. The toxic effect of the atmosphere is impacted by a variety of atmospheric factors (such as climatic conditions, and air-chemical pollutants, all of which make a significant contribution to the metal corrosion process in different ways. Moisture

can form on the surface of the metal as a result of rain deposition, wet aerosols, and the wetting of hygroscopic salt on the surface [97 – 81].

2.7.1. Rain

Rain is one of the known climatic factors that contribute to the formation of moisture on a metallic surface, however, it may also possess direct or indirect effects [82]. Clear illustrations of direct effect are the dilution and washing away of corrosive contaminants deposited on the metal surface. If the process of dilution and washing away of the corrosive contaminants is extended, the corrosion rate decreases. Precipitation may also dissolve some metal corrosion products that are water-soluble (e.g., $ZnCO_3$ and OH). A new metal surface will be in relatively close contact with water from the raindrops, thus increasing the rate of corrosion. Rain washes away the chloride ions at the surface of the metal, in this way it accelerates them. This can make it hard for the corrosion inhibitors to be adsorbed in the corrosive surface of the metal, as it is made clear in the corrosion mechanism that the chloride ions make the corrosive surface to be negative so that it can be easy for the corrosion inhibitor to be adsorbed on the corrosive surface of the metal. In brief, we can conclude that rain can disturb the inhibition process. This result in an increase in the rate of corrosion with time [83 – 84]. This situation can be represented as shown in the equation below:

$$K= at^b [CI]^c (W/D)^d \quad (13)$$

where:

K= is mass loss

A, b, c and d= are constants

[CI]= chloride deposition rate

W= rainfall (mm)

D= rainy days

t= time of exposure

Acid rain is a broad term that refers to several ways in which acid is released from the atmosphere. Acid rain is thought to be caused by the washout of sulfur oxides, nitrogen oxides, and other components in the atmosphere. The primary sources of these oxides are coal-fired power generation, smelters (which produce SO_2), and industrial emissions (producing NOx). The above oxides might very well react with other chemicals to form abrasive substances that must be washed away. Acid rain is indeed a highly corrosive medium that contains H^+ as well as NH_4^+, Mg^{2+}, SO_4^{2-}, NO_3^-, Cl^-, and other elements, causing significant damage to the metallic surface [85 – 87]. Usually, acid rain-related deterioration is a slow process that takes centuries. However, in recent decades, it has been speeded up, particularly in large cities, near plants, airports, and so on, leading to a severe deterioration of critical infrastructure [88].

2.7.2. Wet aerosols

Aerosols in the atmosphere can be chemically or biologically oriented, and they can also seem like both chemical and biological particulates held in the atmosphere at moments. This type of aerosol is distinguished by specific sizes that can be in the nanometre range. Stetzenbach discovered that the transportation of aerosols is influenced by their physical properties (such as density, size, and shape) [89 – 91]. The extent of airflow, humidity levels, and temperature are all external factors (environmental factors) that influence aerosols. Its atmospheric transportation is distinctive because It is small enough for it to be held and carried long distances by the winds. Wet aerosol contains H^+ ions, of which the inclusion and concentration of the H+ ions are closely dependent on the relative proportion of H_2SO_4 and NH_3 in the atmosphere. The concentration of the H^+ ions determines the extent of degradation rate caused by aerosol accumulation, hence the extent of corrosion. The deposition of some aerosols (such as marine aerosols) is influenced by wind turbulence. Other factors affect aerosol deposition onto a metal object (e.g. wind speed, aerosol size, object shape, etc) [92 – 94].

2.7.3. The wetting of hygroscopic salt on the surface

As salt is hygroscopic in nature, it attracts water. Corrosion is caused by the presence of oxygen in the water in the presence of salt. It can be concluded without any doubt that water and salt speed up the process of corrosion. Corrosion is defined as a movement of electrons from one substance to another, hence salt in water enhances water's ability to transport electrons via oxidation reaction. Winds act as a strong factor in the deposition of salt droplets onto the metallic surface, from the atmosphere [95]. The hygroscopic salts play a key role in determining the rate of atmospheric corrosion, involving the period and frequency of wettability to which metallic surfaces are exposed, as well as the rate at which it evaporates. These variables also affect the hygroscopicity, and recrystallization of chloride ions, which may have an impact on high corrosion kinetics. The wetting of hygroscopic salt on the metallic surface can reduce the critical humidity level and impact the contaminant sorption, thus increasing the chances of corrosion occurring [96, 97].

2.8. Corrosion thermodynamics and kinetics

Knowledge of the Fundamental theory of thermodynamics and kinetics is key to determining the influence of corrosion on the phase structure and macrostructure of alloys, through interpreting the thermodynamic stabilities and corrosion kinetics (which involves corrosion rate) [98].

2.8.1. Kinetics of Corrosion

Corrosion kinetics plays a key role in determining the rate of corrosion of a metal as it reflects the speed of the corrosion cycle. Through the study of corrosion kinetics researchers noted that on the electrochemical theory of corrosion an assumption can be made that as the metal encounters water to which oxygen or any depolarizer (such as H_2O_2) are added, the role of the depolarizer is to take up electrons at the cathodic site of the metallic surface while the metal gives them up the via the anodic site. Hydrogen peroxide or hydroxyl ions are formed as a result of cathodic reduction of oxygen at the metallic surface [99 – 101].

Through kinetic considerations, corrosion as a heterogeneous process, the surface of a metal is covered by a thin layer of stagnant liquid (known as Nernst boundary layer), and reacting species diffuse before reaching the metal surface. Diffusion-controlled occurs when the rate of chemical reaction at the interface is greater than the rate of diffusion. When the rate of diffusion exceeds the rate of chemical reaction, the system is said to be chemically-controlled. Considering the relationship between the rate of the chemical reaction and the rate of diffusion two conditions arises (which are diffusion-controlled and chemically-controlled) [102 – 103].

2.8.2. Thermodynamics of corrosion

Corrosion reactions are considered electrochemical in nature due to the involvement of electron transfer [104]. Corrosion thermodynamics plays a vital role in assisting us in conceptualizing the energy shifts that arise during the corrosion reaction. Thermodynamics helps track the energy transfer in a metallic corrosion reaction. When a metal performs work oxidizes, and charged electrons are transferred or ionizes. Some metals (e.g. platinum and gold) can't corrode since they have low potential energy and capability to perform work. Corrosion is made more understandable and predictable by the following tools as explained below [105]:

Gibb's Free Energy

Gibb's free energy also known as free enthalpy is the best tool used in predicting if a corrosion reaction is thermodynamically possible. It is a key factor in the spontaneity of reduction-oxidation reaction in the concept of electrochemistry. A positive Gibb's free energy means that the reaction will not occur, negative Gibb's free energy indicates that the reaction is possible (spontaneous corrosion reaction may occur) and zero Gibb's free energy indicates that the reactions are in equilibrium. Below is the equation of Gibb's free energy and the parameters explained [107].

ΔG = -nFE (14)

where: ΔG is the Gibb's free energy

n is electron transferred in oxidation reaction (mol e^-)

F is Faraday's constant (96,500 J/V -mol e^-)

E is Standard emf potential (for cathode half-cell and for anode half-cell in volts)

Nernst Equation

In the study of corrosion, this equation plays a vital role in analyzing concentration cells, and in calculating metal potentials in varying metal ion oxidation/reduction conditions. It is also of paramount importance in construction of Pourbaix diagram. The Nernst equation can be shown as stated/displayed in the following equation [107 – 108]:

$$E_{cell} = E° + 2.3 \frac{RT}{nF} \log_{10} \frac{[oxid]}{[red]} \quad (15)$$

where: E_{cell} = the Cell potential under environmental conditions (volts)

E° = Standard reduction potential (volts)

R = Universal gas constant (8.3143 J/mol K)

T = Absolute temperature (degrees Kelvin)

n = electrons transferred in the reaction (mol e^-)

F = Faraday's constant (96,500 coulombs/mol e^-)

[oxid] = activity of oxidized species(M)

[red] = activity of reduced species(M)

Corrosion rates

Corrosion rate is defined as the rate at which a metal corrodes due to its interaction with the surrounding environment. It is also described as the percentage of corrosion loss in thickness annually. The rate of corrosion is best determined by the potential between the

anode and cathode, as well as the resistance of the corrosion cell. It is very useful when interpreting the corrosion process. The corrosion rate of metals is critical for evaluating repair methods in the laboratory, predicting service life and morphological evaluation of corroding frameworks, and controlling maintenance tasks on-site [109 – 110].

During the study of corrosion, it has been noted that the cathodic reaction is the slowest step (referred to as a rate-determining step) of the three steps taking place in metallic corrosion. This helps us to deduce the relationship between the resistance of the corrosion cell and the corrosion current, using this formula, $I = \frac{V}{R}$ where V is the potential difference (in volts), I is the corrosion current (in amphere) and R is the resistance of the corrosion [111 – 112]. The corrosion current is inversely proportional to the resistance and directly proportional to the potential difference. The rapid corroding of electrodes and easily passing of metallic ions into the solution, with a small V (potential) utilized between the electrodes result in a high current and thus a low Rp (polarization resistance. This directly relates to an increased corrosion rate.

The metallic corrosion rate can be calculated using gravimetric analysis (weight loss measurements) or (more practically) by reducing the cross-section of the reinforcement. These two methods produce an average corrosion rate, implying that measurement times of several years are involved. Neither of the two methods is non - destructive. As a result, measuring the polarization resistance Rp is the recommended method for determining the corrosion rate of steel in concrete. It should be noted that Rp measurements yield an instantaneous corrosion rate that is heavily influenced by environmental variations (such as climate change) [112 – 117].

2.9. Factors influencing corrosion rate

The rate of corrosion is influenced by two main factors. As a result, understanding these factors and the mechanisms by which they affect the corrosion rate is critical, because the rate of corrosion varies by atmosphere. The factors will be briefly discussed below as follows:

The nature of the metals: A more reactive metal forms ions faster than a less reactive metal. Metals that are more reactive corrode more quickly. When two different metals come into physical contact, the more reactive metal corrodes and donates its electrons to the less reactive metal [118]. This factor will be briefly discussed in the following sub-headings:

Position in galvanic series*:* The metal in the higher position in the series is more active and corrodes. Corrosion rate and extent are proportional to the difference in electrode potential between them. The rate and severity of corrosion are determined by the difference in their positions; the greater the difference, the faster the anodic metal corrodes [119].

Over voltage: When a metal with a high position in the galvanic series (for example, zinc) is immersed in H_2SO_4, it corrodes, forming a film and hydrogen gas. Because of the high overvoltage (0.70 V) of the zinc metal, which reduces the effective electrode potential to a small value, the initial rate of reaction is quite slow. However, if a few drops of copper sulphate ($CuSO_4$) are added, the corrosion rate of zinc is accelerated, because some copper deposits on the zinc metal, forming minute cathodes with a hydrogen over voltage of only 0.33 V; thus, lowering the over voltage of the corroding metal/alloy accelerates the corrosion rate. Because Zn has a higher voltage than hydrogen, its corrosion rate is very slow (Zn rod dipped in $ZnSO_4$). When $CuSO_4$ solution is added to H_2SO_4, however, Cu is deposited on the Zn rod and acts as a small cathode. Cu has a lower voltage value over hydrogen. As a result, the rate of corrosion of Zn in the presence of Cu increases. Thus, metals with lower overvoltage corrode more slowly, whereas metals with higher overvoltage corrode at a faster rate. For example, corrosion of a Zn rod dipped in H_2SO_4 is extremely slow. When a small amount of $CuSO_4$ solution is added to H_2SO_4, Cu is deposited on the Zn rod and acts as the cathode, and the rate of corrosion of the Zn rod is increased [120].

Purity of metal: Metal impurities generally cause heterogeneity and the formation of minute electrochemical cells, causing the anodic part to corrode. For example, corrosion occurs when Zn metal contains impurities such as Pb (or) Fe. The rate and extent of corrosion increase with the amount of impurities present [121].

Nature of the surface film: When metals are exposed to air, almost all of them develop a thin layer of metal oxide on their surfaces. The specific volume ratio is the ratio of the volume of metal oxide to the volume of metal. The lower the oxidation corrosion rate, the greater the specific volume ratio. For example, the specific volume ratios of Ni, Cr, and are 1.6, 2.0, and 3.6, respectively. As a result, the rate of oxidation corrosion is lowest for (w) tungsten [122].

Nature of the corrosion product: Based on solubility, if the corrosion product is soluble in the corroding medium, corrosion will proceed more quickly; otherwise, corrosion will be suppressed, as in the case of Pb in H_2SO_4. Considering volatility, if the corrosion product is volatile, it evaporates as soon as it forms, exposing the underlying metal surface to further attack. As a result, corrosion occurs quickly and continuously. Mo, for example, generates MoO_3 volatile oxide [123 – 125].

Nature of the corroding environment: Corrosion usually occurs as a result of the metal's tendency to return to its native state, the form in which it is found in nature. This necessitates the metal atoms giving up their valence electrons to the environment, as well as the presence of ions in the process. The newly formed ions can then combine with other ions from compounds to form new ions. When chemically active particles (NaCl, $(NH_4)_2SO_4$) are present in the environment, they absorb moisture and act as strong electrolytes. As a result, the rate of corrosion is high. If inactive charcoal is present, it absorbs sulphur gases and moisture, gradually increasing corrosion [126]. This factor will be further discussed in the following sub-headings:

Temperature: The corrosion rate increases with increasing temperature because the reaction and diffusion rate of ions in the corrosion medium increases [127].

Humidity: Because moisture serves as a medium for O_2 in air and acts as an electrolyte, the higher the humidity of the atmosphere, the greater the rate and extent of corrosion. For example, iron corrosion in dry air is slower than in moist air. Iron reacts with oxygen and water to form ferrous hydroxide, which then reacts with CO_2 in the atmosphere to form ferrous bicarbonate [128].

$$2Fe + O_2 + 2H_2O \text{ –--------> } 2Fe(OH)_2 \quad (16)$$

$Fe(OH)_2 + CO_2$ –-------> $Fe(HCO_3)_2$ (17)

Effect of pH: Acidic media are normally more corrosive than alkaline and neutral media. As a result, metals can be roughly classified based on the pH range in which they will be affected (or) resistant. However, atmospheric metals such as Al, Pb, and others are corroded in alkaline medium, and the corrosion rate of iron in O_2-free water is slow until the pH is below, at which point Zn is rapidly corroded in weakly acidic solutions [129]. Pourbaix diagram, also known as Electrode potential-pH (Pourbaix) diagram gives a clear view (a phase map) of the most stable compounds of a metal, its corrosion products, and associated ions in solution [12]. It employs thermodynamic considerations to define potentials in aqueous solutions that correspond to the equilibrium states of all possible reactions between a given element, its ions, and its solid and gaseous compounds as pH varies. Pourbaix diagram displays three areas: immunity, corrosion, and passivation, which reflect the metal's thermodynamic stability, its ions, and its oxides and hydroxides. Figure 2.10 shows a Pourbaix diagram for aluminium metal [129].

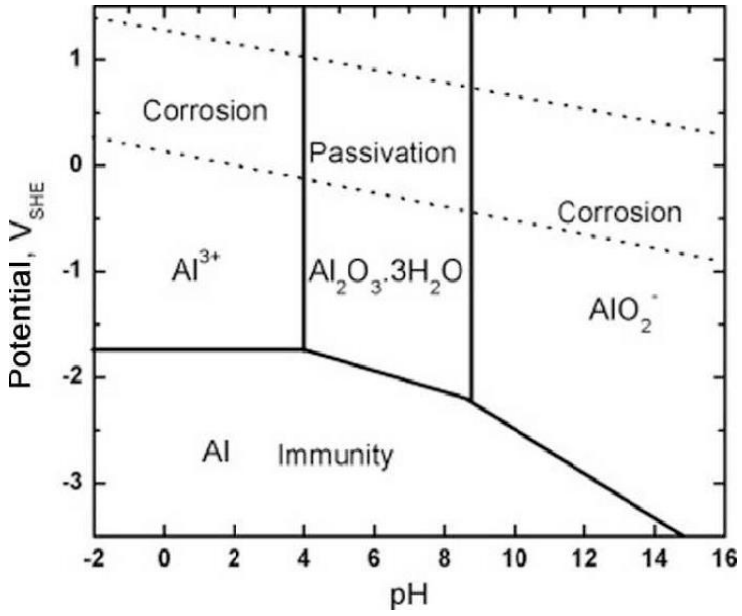

Figure 2.10: Pourbaix diagram for aluminium.

2.10. The effects and cost implications of corrosion

Corrosion has both direct and indirect effects on our daily lives. Corrosion reduces the useful service life of our possessions, and manufacturers and suppliers of goods and services incur corrosion costs, which they pass on to consumers. The impact of corrosion on our lives while traveling from home to work or school is far more serious. Corrosion of steel reinforcing bar (rebar) in concrete can occur out of sight and result in the failure of a section of highway, the collapse of electrical towers, and damage to buildings, parking structures, and bridges, among other things, resulting in significant repair costs and endangering public safety. For example, the collapse of the Silver Bridge over the Ohio River in Point Pleasant, OH in 1967 caused the deaths of 46 people and cost millions of dollars [130].

Corrosion is a major operational challenge in the whole world (industries, companies business sectors etc). Corrosion mechanisms have an impact on a wide range of materials, equipment, and infrastructure that operate in a variety of service conditions and environments. Every year, significant funds are spent on corrosion prevention, monitoring, and repair. Metal corrosion costs the United States (US) economy nearly $300 billion per year at current prices. Approximately one-third of these costs could be

avoided if corrosion-resistant materials were used more widely, and best corrosion-related technical practices were followed. These figures are based on a recent revision of the findings of the 1978 study Economic Effects of Metallic Corrosion in the United States. The research was carried out by Battelle Columbus Laboratories and the National Institute of Standards and Technology (NIST) and was published in April 1995 [131 – 132].

2.11. Chromones as potential corrosion inhibitors

Chromone is a compound with a benzopyran-4-one group, and its pKa indicates that it is an extremely weak basic molecule. Chromones are benzopyran derivatives with a keto group substituted on the pyran ring. The benzopyran ring system serves as the foundation for several important classes of bioactive natural products, including coumarin, chromones, and flavonoids. The most important heterocyclic compounds are chromone and its derivatives, which are a common and fundamental property of a variety of natural goods and therapeutic medicines. These heterocycles have a wide range of pharmacological properties, and structural changes provide a high degree of variability, which has proven valuable in the hunt for new corrosion inhibitors. Chromone derivatives depict a strong electron-donating tendency towards metallic ions, of which this characteristic makes them to form strong ligands in coordination compounds. These organic compounds display good characteristics of being the best corrosion inhibitors. More research still needs to be done to explore the chromone derivatives in corrosion science [133 – 135].

Chromone derivatives contain heteroatoms (such as O), aromatic rings as electron density rich centres which makes them to be good adsorptive centres. These compounds also contain π electrons (pi system) and electronegativity functional groups, which makes them to be good corrosion inhibitors. Figure 2.11 show some chromones which were tested and found to be good corrosion inhibitors [136].

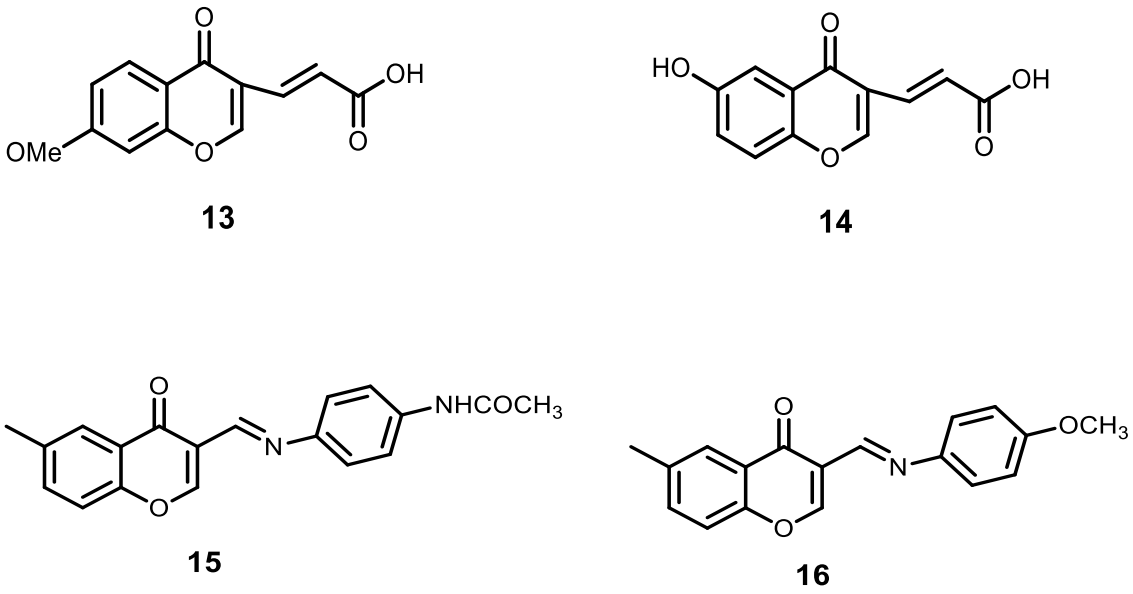

13 14 15 16

Figure 2.11: Chromones which were tested and found to be good corrosion inhibitors.

2.11.1. The chromone compounds utilized in this study

In this study, chromone-2-carboxamide derivatives will be synthesized and tested for their inhibition potential. These compounds are prepared from 5-substituted-2-hydroxyacetoacephonones (as starting materials), and then condensed the starting materials by diethyl oxalate in the presence of NaOEt to produce 6-substitutedchromone-2-carboxylates. The 6-substitutedchromone-2-carboxylates are then converted to carboxylic acids using HCl and AcOH with a ratio of 1:1. The carboxylic acids are further converted to acid chlorides using thionyl chloride which is a strong and good chlorinating agent. The acid chlorides are then converted to the target compounds which are the carboxamide derivatives using specific amines in the presence of DCM (dichloromethane). Figure 2.12 gives a clear view of the structure of 6-substitutedchromone-2-carboxamide derivatives.

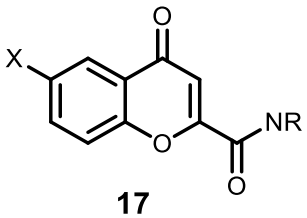

17

Figure 2.12: Structure of 6-substitutedchromone-2-carboxamide derivatives.

2.11.2. Nature and characteristics of chromones as better corrosion inhibitors

The physical and chemical properties of these compounds encourage us to explore them as corrosion inhibitors. Their structures display π electrons which can be able to interact with the surface of the metal (π system). The presence of these functional groups (-OCH_3, NO_2 and halide) with greater electron-donating properties, indicates that there are more chances of them being good and effective corrosion inhibitors. Also, the presence of the heteroatom (O) gives researchers confidence to test and use them as corrosion inhibitors. Figure 2.13 shows compounds which were synthesized and used as potential corrosion inhibitors.

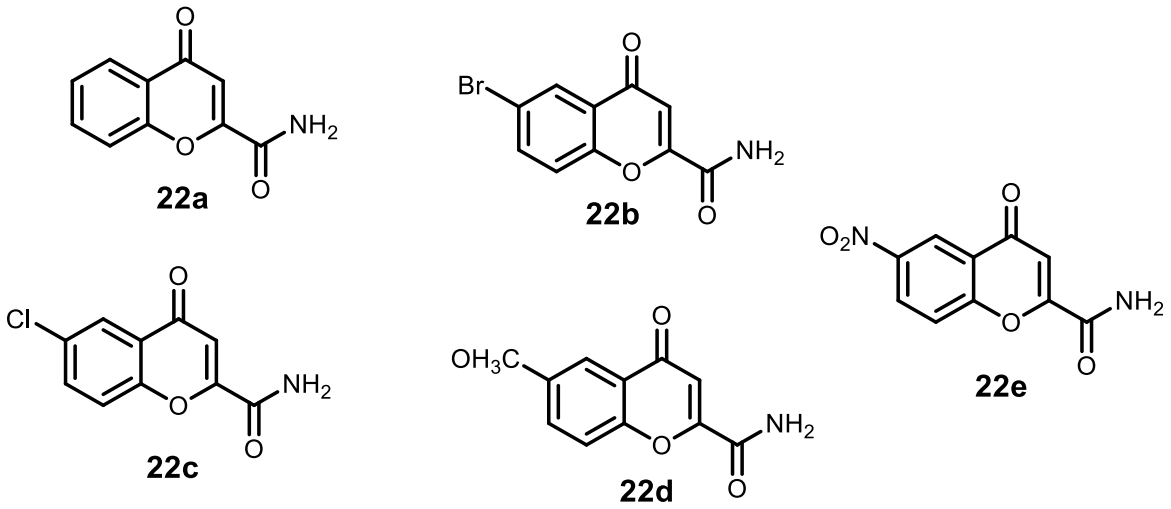

Figure 2.13: Compounds to be synthesized and used as potential corrosion inhibitors.

2.12. Techniques for corrosion monitoring

Corrosion monitoring is critical in any field that employs resources that deteriorate over time; however, it is extremely crucial in industries that deal with volatile materials, which often explode if improperly stored. The more metals ages as they are getting used, they become more prone to corrosion attack and much less resistant to harsh environmental conditions (e.g. temperatures and pressures). Corrosion monitoring plays a vital role in tracking/identifying the potential trouble spots in metals to prevent accidents and to ensure safety. Through corrosion monitoring, huge costs of damaged equipment is reduced as it helps sustain the quality of equipment.

Corrosion monitoring is performed with the aim to obtain three main important data/ information as listed below:

- The level and area of the corrosion.
- The corrosion rate (i.e., how fast it is spreading over time).
- The root cause(s) of the corrosion.

There are two main types of corrosion monitoring techniques: electrochemical and nonelectrochemical. Some of these techniques are classified as destructive and non-destructive methods as they are explained below:

2.12.1. Electrochemical methods

The corrosion principle in an aqueous phase that occurs independent of mechanical contact is primarily electrochemical in nature. Since the corrosion process involves electrical charge, electrochemical techniques play a vital role in studying the corrosion process. These electrochemical techniques are well-known for investigating corrosion occurrence due to their sensitivity, versatility, accuracy, quickest and can be used to investigate a wide range of corrosion-related occurrence. The data obtained from these techniques (electrochemical measurements) help us to determine a metal's proclivity for localized corrosion types (e.g. crevice, pitting and uniform corrosion) to investigate the passivation behaviour of a corrosive environment system. These techniques can be applied both in the line of work and in the research lab for extended study of corrosion mechanism. These techniques are also known as direct current (DC) techniques [137 – 138]. Corrosion coupons, polarization Resistance, electrochemical impedance spectroscopy (EIS) as well as electrochemical frequency (EFM) are some of the electrochemical techniques used. This study will focus more on the two main techniques (EIS and polarization techniques) which will be utilized in this study, and they are clearly explained below:

Electrochemical impedance spectroscopy (EIS): EIS has been discovered to be a quick and accurate technique in corrosion monitoring (investigating corrosion rates and localized corrosion occurrence). It is exceptionally good due to its ability to extract and give information about the corrosion mechanisms. This technique is widely applied in corrosion science (corrosion research). The fact that it could use extremely small amplitude signals without negatively affecting the qualities being analysed, makes it more significant than other techniques used. Another important feature of this technique is the ability to work in low or varying environments. It allows for the studies of the effects, efficiency, and significance of various components through an electrical system (electrical circuit known as circuitry. It has better resolution compared to other commonly used destructive techniques. It is a dominant technique for integrated data (electrochemical measurements), able to evaluate corrosion kinetics, evaluate diffusion coefficients and

kinetic parameters (e.g. rate constants), portraying corrosion mechanisms, and expounding the process of the reactions taking place on the electrolyte interface [139 – 140].

Electrochemical polarization techniques for corrosion monitoring: In the field of corrosion, polarization (also called overpotential or overvoltage) is defined as the shift of the potential away from the open circuit of a corroding system. Open Circuit Potential (OCP), also known as Open Circuit Voltage (OCV) is defined as the potential between two places when no current flows between them. The OCP is commonly used to determine whether a system operates as expected. In metal corrosion studies OCP of a metal is used to detect corrosion development on its surface (helps to determine the stability of materials in a corrosive medium). A constant OCP over time suggests that the system is stable. OCP reflects the electrochemical system's thermodynamic equilibrium, which occurs when oxidation and reduction rates are balanced. OCP measurements typically require high impedance circuits to prevent inaccuracies from leakage currents. Anodic polarization is the shift of the potential in a positive direction (greater than E_{corr}), while the shift of the potential in a negative direction (below E_{corr}) is referred to as cathodic polarization. When surfaces of two or more metals come into contact, that leads to the flow of current between the electrodes (from anode to cathode site) resulting in corrosion of both or all the metals. The directional flow of current is controlled by the potential difference created by the open circuit in between both the anode and cathode. The level of the current flow, on the other hand, is determined by the polarization measurement (polarization characteristics of the electrodes). Polarization techniques play a key role and are more helpful in determining the rate of the anodic and cathodic reaction separately or combined and to obtain the overall corrosion rate. These techniques provide quality measurement and monitoring of different types of corrosion, such as localized, general, crevice, and pitting corrosion. Electrochemical polarization techniques can be created by employing external electrochemical signals (e.g. potential). The concentration of aggressive ions is among the key factors influencing polarization. These corrosive species can be deposited at the anodic site and absorbed at the cathodic site, as the corrosion condition continues close to the electrodes. The polarization of the electrodes (cathode and anode) is inversely proportional to the corrosion current (the greater the

polarization the lower the corrosion current, even though the OCP different is greater [141 – 143].

2.12.2. Non-electrochemical methods

There are several non-electrochemical techniques discovered and used to study corrosion conditions (qualitative and quantitative measurement of corrosion level). Gravimetric analysis, surface analysis, which is also called surface potential measurement, FTIR spectroscopy, scanning electron microscopy (SEM), are all non-electrochemical techniques. Due to technological improvement, other techniques were added (e.g. field signature method (FSM), ultrasonic testing (UT), etc. In this research study, gravimetric analysis and surface analysis will be utilized.

Gravimetric/weight loss analysis: This technique has been established as the most ideal method for studying corrosion by monitoring the corrosion inhibition of various compounds in a variety of mediums. The gravimetric technique (weight loss) is the most used method of assessing inhibition. The gravimetric method is simple, dependable, precise, and accurate, and it yields expedient statistical results (quantitative data). This technique is employed as the baseline method of measurement in many corrosion monitoring systems, as it provides a simple and reliable measurement. For this reason, it has become the standard method of measurement in many corrosion monitoring programs. The main limitation of this technique is that it takes a long time. In recent times, chemists prefer other techniques over this one [144 – 145].

Surface Analysis: Surface analysis methods play a major role in studying and understanding the surface chemistry of metals and finding the efficacy of surface engineering, failure of materials due to corrosion, or in designing of new materials. This technique also involves elemental identification which helps to detect if there are any surface-active contaminants. Surface analysis methods have been extremely successful in illuminating nearly all aspects of the corrosion occurrence. This technique can be

performed simultaneously in the absence and presence of an inhibitor, aiding in the interpretation of the process of corrosion inhibition (inhibition mechanism) [146]. Surface analysis of metals is performed effectively and qualitatively by utilizing the following methods: Electron Dispersive Spectroscopy (EDS)/Scanning Electron Microscopy (SEM), and X-Ray Diffraction (XRD), which are commonly used and are exceptionally supportive for surface analysis. Due to technology, new instruments of surface analysis and methods that are more advanced and valuable are being designed.

Fourier transform infrared (FT-IR) Spectroscopy: FT-IR Spectroscopy has proven to be a very good and valuable tool for the confirmation of the functional groups of the inhibitors that interacted with the surface of the metal. It is used to confirm functional groups on corroded metals in the presence and absence of corrosion inhibitors. This technique is also exceptionally useful in identifying/determining the type of bond existing between the inhibitor and the surface of the metal. Researchers have discovered that this technique is very useful in analyzing the protective film formed on metallic surface. The first step in utilizing this technique is the scratching off the specimen's surfaces using a pointy knife and the resulting powder is then investigated [147 – 149].

Scanning electron microscopy (SEM): Like Electron Dispersive Spectroscopy (EDS), SEM is also a good and valuable tool for examining and analyzing metallic surface components of corrosion samples. This technique provides better significance of probable causes of corrosion activity. SEM is very significant in the evaluation of corrosion failures of different metals during service. When used coupled with EDS spectroscopy, they clearly show the major cracking modes together with the cause of the damage initiation and evolution. In addition to the determination of the number, size, and morphology of small particles, SEM is powerful and exceptionally capable due to its high magnification and high-resolution imaging [150 – 151].

Contact angle studies: The contact angle is the angle formed by a liquid when it comes into touch/contact with a solid. It is a measurement of how liquid spreads up on a solid

surface. Contact angle studies play a key role in metal corrosion studies, by being useful in measuring the wettabi lity of a metal surface. The greater the wetting ability (wettability), the narrower the contact angle or tension on the metal surface. A wetting liquid has a contact angle in relation to the solid that is less than 90°. On the other hand, a non-wetting liquid has a contact angle with the underlying solid that ranges between 90° and 180°. This angle is influenced by the solid and liquid's respective attributes, as well as the attraction and repellent forces that occur between liquid and solid, as well as the various phase contact characteristics (gas, liquid, and solid). Special forces (such as adhesion and cohesion), referred to as intermolecular forces, are very helpful in describing the interactions between the liquid and the metallic surface. This angle is influenced by the solid and liquid's respective attributes, as well as the attraction and repellent forces that occur between liquid and solid, as well as the various phase contact characteristics (gas, liquid, and solid). Both adhesion and cohesion effects, referred to as intermolecular forces, are very helpful in describing the interactions between the liquid and the metallic surface. The contact angle formed at the contact point between solid and liquid is determined by the resulting equilibrium of the cohesive forces of identical molecules (e.g. hydrogen bonds and Van der Waals forces, and the adhesive forces) between solid and liquid molecules (i.e. mechanical and electrostatic forces) [152 – 54].

Importance of Contact angle In Corrosion Science:

Knowing about contact angle is crucial in corrosion research studies for a variety of motives, including:

1. *Corrosion Defense:* A greater contact angle frequently suggests a lesser wettability, implying that the liquid is not spreading easily across the surface. This may result in the creation of a liquid layer that prevents direct interaction between the acidic substance and the metallic surface.
2. *Solid Surface Energy and Adhesion:* The contact angle is proportional to the metal surface energy. A smaller/lower contact angle indicates more wettability, which could lead to stronger binding of aggressive substances (corrosive medium) to the metal surface, thereby speeding up corrosion.

3. *Hydrophobic and Hydrophilic Surfaces:* This angle (contact angle) is used to determine whether a surface is hydrophobic (repellent to water) or hydrophilic (attractive to water). The corrosion inhibitors used can impact the contact angle and thus the ability of metal surfaces to repel corrosion.
4. *Self-Cleaning Surfaces:* When establishing self-cleaning surfaces, it is critical to have a deeper insight into the contact angle. Surfaces having a high contact angle make it easier to remove liquids and pollutants, which may minimize the chances (risk) of corrosion.
5. *Material Selection:* Corrosion research projects frequently include material selection for specific purposes. When analyzing the corrosion resistance of various materials and inhibitors, the contact angle may serve as an important metric.

2.13. Quantum chemical studies

Computational chemistry is a subfield of chemistry that employs computer simulation to help solve chemical problems. It employs theoretical chemistry methods embedded in computer programs to compute the structures and properties of molecules, and solids. It is important in the study of electrochemistry because it allows researchers to analyze the structure of corrosion inhibitors and how they interact with metal surfaces. Several methods are employed in computational chemistry; some of them are based on molecular mechanics approaches while others are based on quantum chemistry-based approaches. Molecular mechanics approaches find utilisability from their description of systems using Newtonian mechanics. Quantum chemistry-based approaches on the other hand find their applicability by describing the system as a wavefunction whose solution can be obtained by solving the Schrodinger equation [155 – 156].

2.13.1. The Schrödinger equation

The Schrödinger equation, commonly known as Schrödinger's wave equation, is a partial differential equation that describes the dynamics of quantum mechanical systems employing the wave function. It is also known as SchE as its abbreviated name, and it

has received its name after Erwin Schrödinger, who won a Nobel Prize in Physics with Paul Dirac in 1933. It is a linear partial differential equation that drives a quantum-mechanical system's wave function. The Schrödinger equation is known to be a cornerstone of the wave mechanics due to its contribution; it is a solution to the characterization of electrons, atoms, and molecules due to the lack of mathematical procedures. It is set on three aspects, which are Classical plane wave equation, Broglie's Hypothesis of matter-wave and Conservation of Energy [157 – 158].

The time-dependent Schrödinger equation illustrates how the wave function of a particle varies through time and space. Free particles are an easy situation/case to consider because their solution is a plane wave and their potential energy is zero (V = 0). The time-dependent Schrödinger wave equation form is dependent on the physical context of the system being portrayed because it depicts an evolving system over time. The Hamiltonian operator represents a system's entire energy, including kinetic and potential energy. A collection of all outcomes that can be achieved when the total energy of the system is measured is known as its spectrum (also known as the system's energy spectrum or its set of energy eigenvalues) [159 – 160]. The time-independent model of the Schrödinger wave equation is:

$$-\frac{\hbar^2}{2m}\frac{d^2\varphi(\mathrm{x})}{\mathrm{dx}^2}+V(x)\,\Psi(x)=\ \mathrm{E}\Psi(\mathrm{x}) \tag{18}$$

where Ψ is the state vector of the quantum system (is a wave function), $\hbar$ is Planck's constant

m is the mass of the system, **V(x)** is the potential energy of the particle at the point x and **E** is the total energy of the system

In its time-independent form, the Schrödinger wave equation defines the features of stationary states, which are wave functions that have produced standing waves. The time-dependent Schrödinger equation offers a general method of finding the energy eigenfunctions, which are wavefunctions that reflect time-independent stationary states, and also determining comparable energy levels and eigenvalues. The Schrödinger equation defines how particles behave in a quantum system. For many systems, it is however frequently challenging to precisely solve the Schrödinger equation. To solve the

Schrödinger equation, physicists established a number of approximation methods; some of these methods will be described in the subsections that follow.

2.13.2. The Born Oppenheimer approximation

According to the Born-Oppenheimer approximation, a concept in quantum mechanics it is feasible to distinguish between the motion of the nuclei and the motion of the electrons in a molecule. When representing the mobility of the electrons in a molecule, the approximation ignores the motion of the atomic nuclei. The Born-Oppenheimer approximation has a physical foundation in the fact that an atomic nucleus in a molecule has a mass more than 1000 times greater than an electron mass. As a result of this difference, the nuclei move significantly more slowly than the electrons. A mutual attractive force of Ze^2/r^2 is also exerted on an atomic nucleus and an electron due to their opposing charges. Both particles are accelerated by this force. The acceleration of the atomic nuclei is tiny compared to the acceleration of the electrons because the acceleration is inversely proportional to the mass (a = F/m); the discrepancy is greater than 2000. As a result, while the nuclei are stationary, the electrons are moving and reacting to forces very quickly. This solution (approximation) to the nuclear Schrödinger equation provides the vibrational wavefunctions and energies [161 – 162].

In the Born-Oppenheimer approximation, as the nuclear configuration changes, the electrons are compelled to remain in a specific eigenstate of the electronic Hamiltonian. To put it another way, the molecule's nuclei develop on a single potential energy surface and are bound together by its electrical arrangement. The Born-Oppenheimer approximation offers an unusual viewpoint on how molecules move by suggesting that we examine electronic dynamics on a time scale resembling nuclear dynamics. The dynamics of the molecule can be divided into a time-independent electronic problem connected to a time-dependent nuclear dynamics since electrons are substantially lighter than nuclei. This approximation is occasionally used synonymous of classical-nuclei approximation, in which the nuclei are considered as classical point particles. However, the nuclear kinetic operator does contribute to molecule energies, even under the Born-Oppenheimer approximation. It is frequently essential to accurately capture the dynamics

of the nuclei along a single potential energy surface, for instance, to characterize tunneling events [163 – 164].

2.13.3. The ab-initio approximation

The ab-initio approximation, commonly referred to as the "from first principles" approximation, is a computational strategy used in solid-state physics and quantum chemistry with the goal of calculating a system's properties using only fundamental physical principles and no outside data. In other words, it is a strategy that aims to resolve fundamental equations, such the Schrödinger equation, that control a system in quantum mechanics. The Latin phrase "ab initio" means "from the beginning" or "from first principles." The ab initio techniques attempt to solve the Schrödinger equation for the wavefunction of the system in order to characterize the electronic structure and characteristics of molecules, atoms, and materials [165].

The underlying notion behind the ab initio approximation is that one may accurately determine the electronic structure and other properties, like as energies, forces, and charge distributions, by solving the Schrödinger equation, which explains the behavior of electrons in a system. Building a mathematical representation of the system, choosing an appropriate basis set (a collection of functions to represent the electronic wavefunction), and using various approximation approaches to solve the Schrödinger equation are typical steps in the ab initio procedures. These techniques can range from fairly straightforward ones, like the Hartree-Fock method, to more complex ones that take into account electron correlation effects, such post-Hartree-Fock methods (including linked clusters, configuration interaction, and DFT) [166 – 167].

In-depth information about the electrical structure and characteristics of molecules and materials can be obtained using ab initio calculations, which are quite accurate. They take a lot of computer resources, though, and are computationally demanding. To make the calculations tractable for bigger systems, approximations and numerical approaches are used. Although ab initio methods aim to be as precise as possible, due to computational constraints and the level of theory used, they are still approximations. Nevertheless, they

have made major contributions to the fields of chemistry, materials science, and condensed matter physics by successfully predicting and understanding the features of a wide variety of systems [168].

2.13.4. Linear combination of atomic orbitals

Linear combination of atomic orbitals (LCAO) is a common method in quantum chemistry for obtaining molecular orbitals, which characterize the electronic structure of a molecule. By combining the atomic orbitals from different atoms, the LCAO approach creates molecular orbitals that cover the entire molecular system. For each atom in the molecule, atomic orbitals are first defined using the LCAO method. These atomic orbitals indicate the probability distribution of finding an electron in various regions around the atom and are often solutions to the Schrödinger equation for an isolated atom. Mathematical functions can be used to depict the atomic orbitals [169].

The atomic orbitals are linearly coupled with the proper coefficients to produce molecular orbitals. In a linear combination, atomic orbitals are added or subtracted with the proper phase factors and weights. As part of the quantum chemical calculation, a set of equations, such as the secular equations, are solved to provide the coefficients and phase factors. The distribution of electrons within the molecule is described by the consequent linear combinations of atomic orbitals, or molecular orbitals. The occupation of these orbitals by electrons defines the electronic structure and characteristics of the molecule. Molecular orbitals have a certain energy associated with them [170].

The molecular orbitals and their energies are described in both qualitative and quantitative terms using the LCAO approach. The LCAO method takes into account the overlapping and interaction of electron densities between various atoms in the molecule by combining atomic orbitals. In order to comprehend chemical bonding and reactivity, it is essential to be able to depict bonding, non-bonding, and antibonding orbitals.

Depending on the required precision and processing cost, the LCAO approach can be used at various levels of theory, such as the Hartree-Fock method or density functional theory (DFT). In order to better describe the electrical structure in practice, more complex

basis sets, such as contracted Gaussian functions, are frequently used as atomic orbitals. Obtaining molecular orbitals and describing the electronic structure of molecules can both be accomplished effectively using the LCAO methodology. It makes it possible to understand and anticipate chemical behavior by analyzing bonding patterns, electronic energies, and characteristics [171].

2.13.5. Basis sets

Basis sets are sets of mathematical functions used in quantum chemistry to approximate the wavefunctions of electrons in atoms, molecules, as well as solids. The electronic structure of the system under study is represented using these functions as a foundation. In quantum chemical calculations, basis sets are crucial because they affect the precision and effectiveness of the computations. The size, complexity, and required level of accuracy of the system under study all influence the basis set selection [172]. The following list includes several popular basis set types:

a) Slater-type orbitals (STOs) For a single electron in the field of a nucleus, these basis functions are Schrödinger's equation solutions. They can give precise descriptions of electron concentrations and are mathematically related to atomic orbitals. For larger systems, STOs may be computationally expensive [172]. Below is a mathematical formula for the STO.

$$x_{\zeta,n,l,m}(r,\theta,\varphi) = NY_{l,m}(\theta,\varphi)r^{n-1}e^{-\zeta r} \quad (19)$$

where: N is the normalization constant, Yl,m are the spherical functions, ζ is the orbital exponent and n the principal quantum number.

b) GTOs, or Gaussian-type orbitals:

The atomic nuclei serve as the center of these basic functions, which are mathematically expressed as Gaussian functions. Due to their high computing efficiency and capacity to

precisely characterize electron concentrations, GTOs have grown to be the most often used basis functions. In popular Gaussian basis sets like the 6-31G and 6-311G sets, they are frequently employed [172]. Below is a mathematical formula for the STO.

$$x_{\zeta,n,l,m}(r,\theta,\varphi) = NY_{l,m}(\theta,\varphi)r^{2n-2-1}e^{-\zeta r^2}, \quad (20)$$

$$x_{\zeta,l_x,l_y,l_z} = Nx^{l_x}y^{l_y}z^{l_z}e^{-\zeta r^2}, \quad (21)$$

The total of l_(x,) l_(y,) l_z determines the type of orbital.

GTOs are presented as a set of Gaussian functions. They have an electron density distribution that is Gaussian around the nucleus. STOs, on the other hand, are defined using Slater-type functions that decay exponentially with distance from the nucleus. GTOs have certain desirable mathematical qualities, such as being analytically integrable, which simplifies calculations involving them, while STOs are more physically precise than GTOs due to their exponential decay, although they are not as analytically handy. STO integrals can be more complex and computationally intensive. Electron repulsion integrals play an important role in quantum chemistry computations. Because of the analytical features of GTOs, these integrals can be computed more efficiently in GTO-based approaches. For STOs, evaluating electron repulsion integrals can be computationally more intensive and may require additional approximations [173].

c) Contracted Gaussian functions:

These basic functions are linear assemblages of GTOs with various exponents and contraction coefficients. Compared to individual GTOs, they offer a more adaptable and effective representation of the wavefunction. Examples are the basis sets from the Stuttgart-Dresden group (def2-XVP) and the correlation-consistent basis sets (cc-pVXZ) [173].

d) Plane waves

In solid-state physics, this kind of basis set is frequently employed to describe the electronic structure of periodic systems. Plane waves, which are suitable for systems with extended periodicity like crystals, are technically referred to as traveling waves [174]. Some known examples of plan wave basis sets are Kinetic Energy Cutoff, Simple cubic lattice, Monkhorst-Pack grid, Pseudopotential plane wave basis sets, and Augmented plane wave. Plane wave basis sets can differ to Gaussian basis sets in that plane wave basis sets represent electronic wavefunctions as a linear superposition of plane waves. Each plane wave has a wavevector and a specified energy. While Gaussian basis sets reflect the electron density around atomic centers using a combination of Gaussian-type orbitals. The electron density in these orbitals is distributed Gaussian [175].

Plane wave basis sets are useful for solid-state physics and DFT computations of crystals because they excel at modeling periodic systems and extended electronic structures. In quantum chemistry computations for molecules and finite systems where periodicity is not a significant issue, Gaussian basis sets are more typically used. The choice between the two is determined by the system's nature, the level of accuracy required, and the computational resources available [176].

It's crucial to remember that the basis set selection is merely one element of a quantum chemical calculation. The degree of theory (e.g., Hartree-Fock, density functional theory), how electron correlation is handled, and whether relativistic effects are included all have an effect on how accurate the conclusions are. Extrapolation methods and basis set improvements are frequently used to increase calculation accuracy while minimizing processing costs [176].

2.13.6. Hartree-Fock Method and Post Hartree-Fock Methods

The Hartree-Fock (HF) method is a computational method used in quantum chemistry to approximate a molecule's electronic structure. It calculates the ground-state electrical energy and molecule characteristics in an efficient manner. The HF technique proposes that each electron flows independently in a mean-field created by all the other electrons. The method entails solving a set of self-consistent field (SCF) equations iteratively to produce the electronic wave function that minimizes the system's total energy. The HF

technique represents the wave function as a single determinant known as the Hartree-Fock wave function. It is built by arranging electrons in a set of molecular orbitals predicted by solving the SCF equations. The HF method employs a variational approach to find the wave function with the lowest energy. While the HF technique is an ideal spot to start for electronic structure calculations, it has some limitations. It ignores electron correlation, which is the interaction of electrons outside of the mean field approximation. This causes errors, especially in systems with strong electron correlation. Post-Hartree-Fock approaches are used to improve on the HF method and account for electron correlation issues [177 – 178].

MP2 (Møller-Plesset second-order perturbation theory) is one of the most extensively utilized post-Hartree-Fock approaches. It considers electron correlation to be a disturbance in the HF wave function. The electronic energy is calculated using the MP2 method, which includes second-order factors that account for electron-electron interactions beyond the HF level. When compared to the HF technique alone, this perturbation theory provides a more precise explanation of electron correlation. The MP2 approach captures electrical correlation by expanding the wave function in terms of a sequence of corrections to the HF wave function. These corrections involve the two-electron integrals and are used to determine the correlation energy. The MP2 approach is relatively computationally demanding, but it provides a reasonable balance of accuracy and computational cost for many systems. It's worth mentioning that alternative post-Hartree-Fock approaches, including as coupled-cluster theory (CC), configuration interaction (CI), and density functional theory (DFT), provide varying degrees of accuracy and computing complexity. These strategies are used based on the system being studied specific requirements and characteristics [179 – 180].

2.13.7. The Density Functional theory method

Density functional theory (DFT) is defined as a computational quantum mechanical technique commonly used in the field of condensed matter physics, materials science, and quantum chemistry. It offers a useful and effective method for researching the electronic composition and characteristics of molecules, solids, and surfaces. Based on

the DFT principle, the Schrödinger equation can be solved using the electron probability density parameters rather than the wave function (ψ) in order to determine an object's energy, and in particular its ground-state energy. Functionals are used by the DFT approach to estimate the ground-state characteristics of a many-electron system [181].

A functional is the result of another functional. In other words, every characteristic of the ground state depends on the electron density. The precise density functional is not known, though. The electron correlation effects are taken into consideration by DFT, but they are mainly ignored by the HF technique. Compared to HF approaches, this leads to computations that are faster and slightly more complex [182].

The Hohenberg-Kohn theorem, which says that the ground-state electron density dictates in a unique way the ground-state wavefunction and energy of a system, is the basis of DFT. In contrast to conventional wavefunction-based techniques, the computational complexity in DFT is substantially lower since the electronic structure is defined by the electron density rather than the wavefunction [183]. The fundamental ideas behind DFT can be summed up as follows:

1. Electron density: The primary quantity of importance in DFT is the electron density, which depicts how electrons are distributed within a system. Calculations of many attributes, including total energy, electronic structure, and response qualities, all revolve around the electron density as the key variable [184].
2. Exchange-correlation functional: Analytically, it is unknown what the precise shape of the exchange-correlation energy functional is, which takes into account the effects of electron exchange and electron-electron correlation. The local density approximation (LDA), generalized gradient approximation (GGA), and hybrid functionals are some of the approximations that are utilized to approximate this functional [185].
3. Kohn-Sham equations: DFT projects the many-electron issue onto an extra set of hypotheticals, non-interacting particles known as Kohn-Sham orbitals. Although the effective potential in the Kohn-Sham equations depends on the electron density and the exchange-correlation functional, they are similar to the Schrödinger equation for non-interacting particles [182].

4. Self-consistent iteration: Iteratively maximizing the electron density and corresponding Kohn-Sham orbitals until convergence is reached requires the self-consistent solution of the Kohn-Sham equations. The input exchange-correlation functional is verified using this technique to guarantee that the estimated electron density is accurate [186].

DFT has a number of benefits, including the ability to be used with a variety of systems, such as molecules, solids, and surfaces. Numerous parameters, such as energy, forces, and response qualities, are satisfactorily predicted. Compared to conventional wavefunction-based techniques, DFT is computationally more effective, making it useful for analyzing bigger systems. It's crucial to remember that DFT has some restrictions as well. Calculation accuracy can be strongly impacted by the exchange-correlation functional used, and there is no universal functional that works effectively for all kinds of systems and features. Additionally, DFT has difficulty adequately modeling charge transfer, dispersion forces, and excited-state characteristics, as well as some strong correlation effects [187].

Due to its balance of accuracy and computing efficiency, DFT continues to be one of the most popular and adaptable techniques for researching the electrical structure and characteristics of materials, despite these drawbacks. To overcome the issues and broaden the applicability of DFT, researchers keep improving exchange-correlation functionals and applying cutting-edge methods like time-dependent DFT and hybrid functionals [188].

DFT has established itself as a cornerstone to link some conventional, empirical concepts in corrosion science with quantum mechanics. In the study of corrosion inhibition mechanisms, density functional theory is crucial. DFT is very useful in corrosion science in the designing of novel, effective organic corrosion inhibitors as it links a compound's electron structure to its reactivity. According to some quantum chemical parameters, density functional theory (DFT) is increasingly used to predict a material's potential ability to combat corrosion, including the energy of the highest occupied molecular orbital (E_{HOMO}), energy of the lowest unoccupied molecular orbital (E_{LUMO}), gap energy, chemical

hardness and softness, ionization potential, electron affinity, electronegativity, and fraction of electron transferred [189].

2.13.8. Molecular properties obtained from Quantum chemical studies and relevant for corrosion inhibitors

Several molecular properties have been linked to providing information on the ability of corrosion inhibitors to bind on the metal surfaces. Among the molecular properties include the atomic charges, highest occupied molecular orbital (HOMO) and the lowest unoccupied molecular orbital (LUMO), dipole moment, etc. We attempt to describe in the subsequent paragraphs how some of these molecular properties have been linked with contribution towards inhibitors ability to combat metal corrosion [190 – 191].

2.13.9. Atomic charges

The inhibitor's inhibitory action is normally determined by the adsorption of those molecules on the metal surface. According to the molecular structures, adsorption on the metal surface can occur in three ways. The first one is a neutral molecule through chemisorption, which involves the sharing of a lone pair electron between electronegative atoms and metal. The second is by intermolecular force, which is relevant to the inhibitors' dipole. The third route is via the aromatic ring's plane conjugating system (aromaticity), which donates electrons to the metal surface, accepts electrons from the metal surface, and the intercalation of the hyperconjugation system. Mulliken population modeling has been frequently utilized to model the activation centers for inhibitor adsorption on the metal surface, and it is generally employed to calculate the charge distribution throughout the entire skeleton of the molecule. The more negative the adsorbed center's atomic partial charges are, the more easily the atom donates its electron to the metal. The estimated Mulliken charges revealed that each inhibitor had more than one active center. Notably, the negative charge was discovered to be largely localized on the ring moiety as well as on the carbon atoms of the aliphatic hydrocarbon chain. This implies that inhibitors bind to the metallic surface via the ring moiety and the aliphatic hydrocarbon chain, which

are thought to be very active centers through which inhibitor compounds could adsorb on the meal surface, and thus N-substituted compounds have higher inhibition efficiency than the others [192].

2.13.10. Interaction and Binding energy

The energy required to interact (interaction energy) is describe as the amount of energy necessary for one mole of an inhibitory molecule to be adsorbed on the metallic surface. Organic compound corrosion inhibitors' binding energy is the amount of energy required to break the bond between the inhibitor and the metal surface. The binding energy can also be defined as the negative values of the interaction energy. A large binding energy implies that the inhibitor molecule can be strongly adsorbed over a metal surface. The interaction and binding energy for a simulated system in a vacuum can be calculated employing the equations below [193]:

$$E_{inter} = E_{Total} - (E_{surface} + E_{inh}) \quad (22)$$

In the presence of a solvent:

$$E_{inter} = E_{Total} - (E_{surface+solvent} + E_{inh}) \quad (23)$$

$$E_{binding} = -E_{inter} \quad (24)$$

The organic inhibitors are firstly adsorbed on the surface of the metal, allowing the heteroatoms and p-electrons to perfectly interact with the surface of the metal. Furthermore, the inhibitor molecules remove H_2O molecules from their adsorption sites and take their location, implying that increasing the inhibitor molecules in the solution will displace more H_2O molecules. More stable compounds cannot bind at all. The density functional theory (DFT) is used to calculate the binding energy of a molecule on a metal surface using the MedeA-VASP 5.4 program [194].

2.13.11. HOMO and LUMO

Some quantum chemical factors that govern electronic interaction are introduced into surface atoms and inhibitors. These energies are the highest occupied molecular orbital (HOMO) and the lowest unoccupied molecular orbital (LUMO). We are able to compute the electron affinity (I) and ionization potential (A) employing the HOMO and LUMO energies ($I= -E_{HOMO}$ and $A= -E_{LUMO}$). The E_{HOMO} and E_{LUMO} energies depict a molecule's ability to donate and accept electrons. According to literature, the ability of the inhibitor to give electrons increased as the E_{HOMO} value increased, whereas the ability of the inhibitor to absorb electrons increased as the E_{LUMO} value decreased. High values of E_{HOMO} indicate a molecule's ability to deliver electrons to a suitable acceptor via unoccupied molecular orbitals. The E_{LUMO}, on the other hand, shows a molecule's ability to receive electrons; lower values indicate a greater electron-accepting capacity [50].

The difference in energy between E_{LUMO} and E_{HOMO} is called the energy gape ($\Delta E= E_{LUMO} – E_{HOMO}$). That is the energy required to remove/eliminate an electron from the last orbital occupied, and is also an important parameter in describing a molecule's reactivity. Low ΔE enhances molecule adsorption and hence improves inhibition efficiency; as ΔE falls, the reactivity of the molecule increases, increasing the inhibition efficiency of the molecule. This parameter measures the stability of the generated complex on the metal surface. The lower the value of ΔE, the greater the stability of the produced compound [195].

2.13.12. Hardness (η), and softness (σ)

Softness is a chemistry term that describes the polarizability of an acid or base. The higher σ value, the softer the molecule and the greater the ability to transfer electrons to the metal. It is roughly described as the hardness reciprocal. The softer a species is, the larger and more neutral it is. In contrast, the smaller and more charged a species is, the harder it is. Metals are considered soft acids and inhibitor compounds are soft bases, according to the Hard and Soft Acids Bases (HSAB) concept. As a result, soft-soft interaction is the primary regulatory mechanism for inhibitor molecule adsorption. Softness is the inverse of hardness ($\sigma = 1/\eta$). The obtained values of η and σ are used to

calculate the fraction of the electron transferred ΔN, from the inhibitor to metallic surface. Chemical hardness (η) and softness (σ) reveal insight into a molecule's resistance to charge transfer and ability to receive electrons [196 – 197]. They are computed using the following equations:

$$\eta = -\frac{1}{2}(E_{HOMO}-E_{LUMO}) \quad (25)$$

$$\sigma = \frac{1}{\eta} \quad (26)$$

2.13.13. Back donation

A type of chemical bonding in which a ligand provides a pair of electrons to establish a sigma bond with an atom or ion, and the central atom donates electrons back by overlapping its d-orbitals with empty p- or d-orbitals on the ligand. This shows the molecules' proclivity to donate charges from electron-rich centers into unoccupied d-orbitals of the metal and their ability to absorb electrons back from occupied orbitals to form strong adsorbed coatings that protect the metal from corrosion attacks. [198 – 199].

2.13.14. Analysis of local reactive sites

Adsorption of inhibitor compounds on metallic surfaces through donor-acceptor interactions, has propelled researchers to investigate the presence of certain locations in all corrosion inhibitory compounds that are capable of interacting with metal surface atoms. In general, heteroatoms with a larger negative charge contribute more easily to donor-acceptor interactions. However, it is also necessary to study the real scenario to determine which skeletal element or regions the corrosion inhibitory molecules can deliver a significant number of charges by sequential centers and receive it at other centers. This electron donation and acceptance by the inhibitors' respective atoms is easily understood by analyzing Fukui indices (FIs) of individual atoms of the intended corrosion inhibitory compound. FIs allow us to investigate the locally reactive regions associated with these compounds' nucleophilic and electrophilic behavior. The maximum threshold value of f_k^+ and f_k^- can be used to study this behavior connected with distinct sites of inhibitor

compounds. The values of f_k^+ and f_k^- represent the changes in an inhibitor molecule's electron density when it takes and gives up electrons, respectively [200].

2.13.15. The fraction of electrons transferred (ΔN)

ΔN is predicted by the ability of an inhibitor molecule to transmit its electron to a metal surface, as well as its hardness and electronegativity. It has been documented in the academic research that the values of ΔN exhibit an inhibitory effect caused by electron donation. The fraction of electrons exchanged in the contact between the metal surface and the inhibitor molecule. If $\Delta N > 0$, an inhibitor can transmit its electron, and vice versa. Higher ΔN values implies that electrons get transferred from the inhibitor to the metal's free d orbital. With regard to Lukovits' research, if $\Delta N < 3.6$, the inhibition efficiency rose as the inhibitor's electron donating ability at the metal surface increased [201].

2.13.16. Dipole moment

Dipole moment which is expressed by the symbol μ is defined as the measure of polarity of a polar covalent bond. It is described as the product of atom charge and distance between two bound atoms. The total dipole moment, on the other hand, simply reflects a molecule's global polarity. The dipole moment of a whole molecule can be computed as the vector sum of all the individual bond dipole moments. The dipole moment in the form Debye is another essential electronic characteristic that arises from the non-uniform distribution of charges on the various atoms in the molecule; a large dipole moment probably promotes adsorption between chemical compound and metal surface. As dipole moment (μ) increases, the energy of deformability increases, making the molecule simpler to adsorb at the metal surface. Also, the volume of the inhibitor molecules rises as the μ increases. This increases the contact area between the molecule and the metal surface, boosting the inhibitors' potential to stop corrosion [202 – 203].

2.13.17. Selection of Appropriate Surface for Adsorption

2.13.17.1. Metals As Solids

In physics and materials science, a solid is matter with a specific shape and volume. A solid is hard, doesn't flow, and is difficult to compress since its constituent parts are tightly packed together. Liquids, in contrast, can vary their shape, whereas gases can alter both their shape and volume. Since solids have a defined shape and volume, it means they keep their shape and occupy up a certain amount of space. Depending on the makeup of the particles and how they are bound together, solids can have a variety of physical characteristics, including density, hardness, elasticity, and conductivity. Materials science also focuses on the behavior of solids under various conditions, such as temperature and pressure [204 – 205].

Solids can be categorized in a variety of ways. They can be categorized by the nature of their chemical bonds, as crystalline, polycrystalline, or amorphous, and by their composition. Metals falls under metallic Solids due to the nature of their chemical bonds. Metallic bonding holds the atoms in metals together. Metals conduct heat and electricity because the electrons are comparatively free to move. Solids made of metal are ductile, malleable, and opaque. Metals are also classified as crystalline Solids; A crystalline solid's particles are arranged in a clear lattice [206].

2.13.17.2. Using Crystal Structure to describe a Metal Surface (Solid State Chemistry)

In the realm of metals, surface is the outermost layer or border of a metal substance. It is the point of contact between the metal and its surroundings. Depending on the circumstances, the surface of a metal can be exposed to air, water, other materials, or even vacuum. A metal's surface can be chemically reactive, including oxidation or corrosion reactions with the surrounding environment. The reactivity of a metal is affected by elements such as its composition, exposure conditions, and protective surface treatments [206].

Based on surface treatments, metals can be surface treated to change their properties or improve specific surface features. Surface treatments include coating, plating, passivation, polishing, and etching. These treatments can improve corrosion resistance, improve aesthetics, provide wear resistance, or allow adherence to other materials. Looking at surface energy, the energy associated with a metal's surface is referred to as its surface energy. It has an effect on processes including wetting, adhesion, and interactions with liquids or other materials that come into contact with the surface [207].

Solids are made up of crystals, and crystals are made up of fundamental repeating unit known as the unit cells. The components of a solid can be arranged in one of two general ways: either they can aggregate in random patterns to form an amorphous solid (from the Greek ámorphos, meaning "shapeless"), or they can form a regular repeating three-dimensional structure called a crystal lattice [208]. This study focuses more on crystal lattice as we are dealing with metal corrosion (zinc, mild steel and aluminum).

2.13.17.3. Crystal Lattice (Crystals)

As mentioned above, crystals are made up of unit cells. Crystals contain distinct internal structures, which result in various flat surfaces, or faces. Figure 2.14 gives a clear vie on crystal lattice [209]. The faces connect at the substance's distinctive angles. Each structure produces a characteristic pattern when exposed to x-rays, which can be used to identify the material. The characteristic angles are independent of crystal size and reflect the regular repeating arrangement of the constituent atoms, molecules, or ions in space. Repulsive interactions, for example, cause an ionic crystal to break along fixed planes, producing new faces that connect at the same angles as those in the original crystal. In a covalent solid, such as a cut diamond, the angles at which the faces meet are likewise not arbitrary but are dictated by the arrangement of the carbon atoms in the crystal [209 – 210].

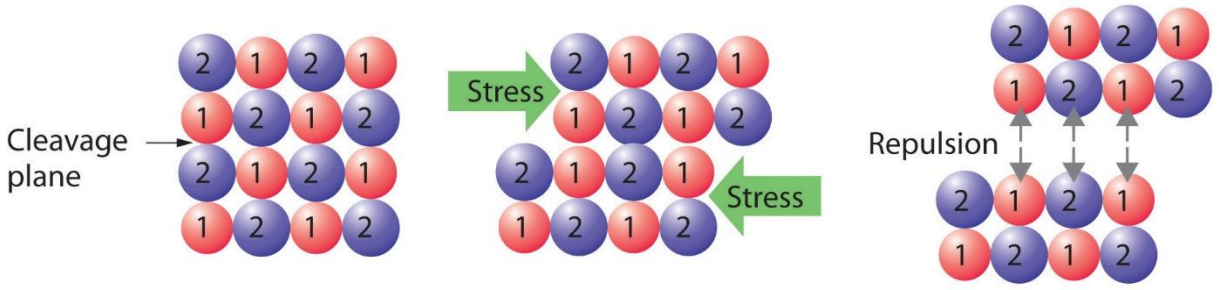

Figure 2.14: The ionic crystal deforms, causing one plane of atoms to glide along another. The layers divide as a result of the repulsive interactions between ions with similar charges.

Because all of the component atoms, molecules, or ions are the same distance from the same number and type of neighbors, crystals have relatively sharp, well-defined melting points; that is, the regularity of the crystalline lattice provides local environments that are the same. As a result, the intermolecular interactions that hold the solid together are consistent, and the same amount of thermal energy is required to break every contact at the same time [211].

2.13.17.4. Unit Cells

Unit cell is defined as the smallest repeating structure that represents the complete crystal lattice. It is a three-dimensional parallelepiped having fixed lengths along its edges and precise angles between the edges. The arrangement of atoms within the unit cell is reproduced throughout the crystal lattice. Depending on the crystal structure, the unit cell can have various shapes such as cubic, tetragonal, orthorhombic, hexagonal, and so on. Within the unit cell of each crystal structure, the atoms are arranged differently [212 – 213]. Figure 2.15 gives a clear view of the

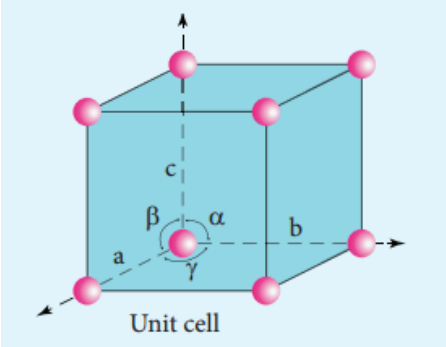

Figure 2.15: Crystal Lattice and Unit Cell.

There are three most common types of unity cells (which are primitive cubic, Body-centered Cubic and Face centered cubic unit cells) as shown in Figure 2.16. Each kind of unit cell correlates to a specific crystal structure and has an impact on the solid's overall characteristics and symmetry [215].

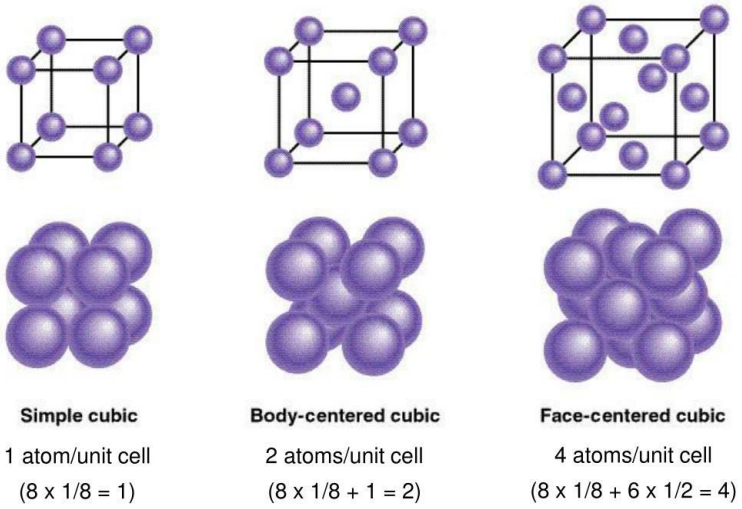

Figure 2.16: Types of unit cells.

1. Primitive Cubic Unit Cell

In a cubic crystal lattice, the primitive cubic unit cell is the most basic/simplest sort of unit cell. A cube with all edges of identical length (a) and all angles equal to 90 degrees is termed primordial or primitive cubic unit cell. It is the simplest and most symmetrical sort

of cubic unit cell. There is only one atom at each corner of the cube. The atom at each corner is shared by eight adjacent unit cells, with each unit cell contributing 1/8th of an atom to the final count. Each atom in this unit cell has a coordination number of six. This means that each atom has direct touch with six nearby atoms in the adjacent unit cells. A primitive cubic unit cell has a relatively poor packing efficiency of roughly 52.4%. This is due to the fact that the unit cell only contains 1/8th of each corner atom, leaving a substantial amount of free space [216].

Certain alkali metals, such as sodium (Na) and potassium (K), exhibit a primitive cubic unit cell in their solid state at higher temperatures. It should be noted that the primitive cubic unit cell is very rare in nature due to its low packing efficiency and is not as common as other forms of cubic unit cells such as the body-centered cubic (BCC) or face-centered cubic (FCC) unit cells. It does, however, serve as a crucial building element in comprehending crystal formations and their properties. Below is the structure of the simple cubic cell [217]:

2. Body-centered Cubic Unit Cell

Body-centered cubic (BCC) unit cells are a form of crystal lattice structure that is widespread in metals such as iron, chromium, and tungsten. It is one of three varieties of cubic unit cells, the others being simple cubic (SC) and face-centered cubic (FCC). Similar to the SC unit cell, the lattice points of the BCC unit cell are situated at the cube's eight corners. There is also an additional lattice point in the cube's center. The body-centered atom is named after its core lattice point. As a result, the cubic is known as a "body-centered" cubic. The coordination number of the BCC unit cell is 8, which means that each atom is directly surrounded by 8 surrounding atoms. The coordination number is the number of nearby atoms to which a central atom is bound. This kind of unit cell is identified by the following parameters: The distance between the corners of the cube (Edge length) and the distance between two opposite corners of the cube (Body diagonal). In a BCC unit cell, the interaction between the edge length (a) and the body diagonal (d) is given by: $d = \sqrt{(4a)}$ [218].

A BCC structure has a packing efficiency of roughly 68%, which means that the atoms occupy only 68% of the total volume, with the remaining 32% being unoccupied space. Because of its high density, strength, and ductility, the BCC crystal structure is an essential structure for many metallic materials. It also has distinct physical qualities that distinguish it from other crystal formations, such as greater melting temperatures and reduced electrical resistance. Overall, this kind of unit cell is a fundamental idea in solid-state physics and materials science, serving as a foundation for understanding the atomic organization and properties of a variety of metallic materials [218].

3. Face-centred Cubic Unit Cell (FCC)

Face-centered cubic (FCC) unit cell is another frequent crystal lattice form observed in numerous metallic materials. It is one of three varieties of cubic unit cells, the others being simple cubic (SC) and body-centered cubic (BCC) which already explained above. Similarly to the SC unit cell, the lattice points of this kind unit cell are situated at the cube's eight corners. However, in addition to the corner atoms, each face of the cube has an additional lattice point. These face-centered atoms are placed at the cube's midpoints on each face. The coordination number of ace-centered cubic unit cell is 12, which means that each atom is directly surrounded by 12 encompassing atoms. The coordination number is the number of nearby atoms to which a central atom is bound. This kind of unit cell is identified by the following parameters: The distance between the corners of the cube (Edge length) and The distance between two opposite face centers of the cube (Face diagonal). In an FCC unit cell, the correlation between the edge length (a) and the face diagonal (d) is given by: $d = \sqrt{(2a)}$ [219].

The packing efficiency of an FCC structure is roughly 74%, which means that the atoms occupy approximately 74% of the total volume, while the remaining 26% is unoccupied space. The FCC crystal structure is well-known for its dense packing, which results in great density and stability. It has outstanding mechanical qualities such as strong ductility, malleability, and deformation resistance. The FCC structure is used by several common metallic materials, including copper, aluminum, gold, and silver. To investigate the atomic setting and properties of metallic materials, the FCC unit cell is frequently utilized in

materials science, metallurgy, and solid-state physics. It is an essential building block in the study of crystal structures, crystallography, and many physical and mechanical properties of materials [220].

2.13.17.5. Unit Cells Contained by the Metals to be used In this Study

There are three metals which are utilized in this research project (Zinc, Aluminium and Mild Steel). Below are described and specified the type of unity cell each one contain:

Zinc

Zinc has a hexagonal close-packed (HCP) crystal structure. The HCP unit cell is made up of closely packed hexagonal layers of atoms that alternate in place. The unit cell has three axes, two of which are equal in length and lie on the hexagonal plane, and one of which is perpendicular to the hexagonal plane [221].

Aluminium

The crystal structure of aluminium is face-centered cubic (FCC). As previously stated, the FCC unit cell is made up of eight lattice points plus an extra lattice point in the center of each face [222].

Mild Steel

Mild steel is a low-carbon steel alloy whose crystal structure is determined by its composition and heat treatment. Mild steel also known as iron (Fe), has a body-centered cubic (BCC) crystal structure when annealed or unalloyed. The BCC unit cell has lattice points at each of the cube's eight corners and an additional lattice point in the center. It should be noted that mild steel can be subjected to a variety of heat treatments and alloying materials, which can modify its crystal structure and properties. These differences can lead to distinct sorts of unit cells or even more complex crystal formations [223].

2.13.17.6. Planes and Miller Indices In All Unit Cells

Miller indices are a method of describing crystallographic planes within a crystal lattice. They were invented in the nineteenth century by British mineralogist William Hallowes Miller. To comprehend Miller indices, we must first understand the concept of lattice planes within a unit cell. Miller indices can be used to describe the lattice planes in each unit cell. Miller indices are critical tools in crystallography, materials science, and solid-state physics. They enable the study and understanding of crystal structures and their properties by providing a succinct and standardized approach to define the orientation and symmetry of crystallographic planes within unit cells. As a result, its miller indices are described as [hkil], where h, k, i, and l are all integers. The following are some examples of the most frequent crystal formations. [224 – 225].

a) Primitive Cubic Unit Cell

Certain planes in the primitive cubic unit cell crystal structure are related with certain Miller indices. The primitive cubic unit cell, on the other hand, has a simple structure with only one atom at each corner of the cube and no additional lattice points or planes within the unit cell. As a result, unlike the face-centered cubic (FCC) and body-centered cubic (BCC) designs, the primitive cubic unit cell lacks specified shared planes. The primitive cubic unit cell has lattice points only at the cube's eight corners. As a result, the planes that cross through these corners establish the lattice planes within the unit cell. In a nutshell unlike the FCC and BCC structures, the primitive cubic unit cell lacks unique shared planes with different Miller indices. The planes within the primitive cubic unit cell are determined by the planes running through the cube's corners, and their Miller indices are (hkl), where h, k, and l can be any integer value [226 – 227].

b) Body-centered Cubic Unit Cell

Certain planes in the body-centered cubic (BCC) crystal structure are connected with distinct Miller indices. The (100) plane, which has Miller indices of (100), is one of the most prevalent planes in the BCC structure.

The (100) plane intersects the x-axis at a/2, where 'a' denotes the edge length of the BCC structure's unit cell. It does not cross the y and z axes. As a result, the Miller indices in the BCC structure for the (100) plane are (1, 0, 0).

The (110) plane intercepts the x,y, and z axes at a/2, a/2, and a/2, respectively, such that the miller indices are (1,1,1).

The (110) plane intersects the x,y, and z axes at a/2, a/2, and a/2, that produces miller indices of (1,1,1).

c) Face-centred Cubic Unit Cell (FCC)

The three most frequent planes in FCC crystals are (100), (110), and (111), with the following Miller indices:

The (100) plane intersects the x-axis at a/2 but not the y or z axes, resulting in miller indices of (1,0,0).

The plane (110) intersects the axes x, y, and z at a/2, a/2, and a/2, respectively, resulting in miller indices of (1,1,1).

The (111) plane intersects the x,y, and z axes at a/2, a/2, and a/2, resulting in miller indices of (1,1,1).

Hexagonal closed packed Unit Cells

The (1000) plane is perpendicular to the hexagonal axis and travels across the centers of the hexagonal faces in the HCP crystal structure. This plane's Miller indices are (1, 0, 0, 0).

The (1010) plane is perpendicular to the hexagonal axis and intersects the hexagonal faces at the edges' midpoints, resulting in miller indices of (1,0,1,0).

The (1120) is inclined to the hexagonal axis and intersects the hexagonal faces at the edges' centers, producing miller indices of (1,1,2,0).

CHAPTER 3: Experimental

This chapter describes the materials and methods used in this research. This study employed organic synthesis, weight loss technique (gravimetric analysis), potentiodynamic polarization (PDP) and electrochemical impedance spectroscopy (EIS), Wettability contact angle studies, Nuclear Magnetic Resonance (NMR), Fourier Transform Infrared Spectroscopy (FTIR), and computational analysis.

3. 1. Chemicals and Materials

Commercially available chemicals such as 5-substituted-2-hydroxyacetophenones, thionyl chloride, N,N-DMF, DCM, dichloroethane, HCl, NaOEt, diethyl oxalate, and other reagents and solvents used were purchased from Sigma Aldrich, Merck, and Rochelle chemicals. All the reagents and solvents were used without further purification. BÜCHI Melting Point B-540 was used to determine the melting points of the compounds. NMR spectra were recorded on a Bruker AMX 400, using $CDCl_3$ and DMSO-d_6 as NMR solvents. The 13C spectra were interpreted using DEPT spectra and the normal 13C spectra with the same frequencies. IR spectra were recorded on an FTIR Bruker Alpha spectrophotometer and were reported in wavenumber (cm^{-1}).

Chemical shifts(δ) were reported in parts per million (ppm). Two NMR solvents were used (CDCl3 and DMSO-d6. In CDCl3 1H shifts were located at (δ= 7.26 ppm) and in DMSO-d6 at (δ= 2.5 ppm). 13C shifts were observed in CDCl3 at (δ= 77.16) and in DMSO-d6 at (δ= 39.52 ppm). Splitting patterns were represented as follows: s for singlet, d for doublet, t for triplet, q for a quartet, bs for broad singlet, and m for multiplet. The coupling constants (J-values were reported in Hertz (Hz).

Glassware was washed and dried in the oven before and after every reaction. Some of the reactions were monitored by thin-layer chromatography (TLC) and were visualized under UV light (254-365 nm). Some of the synthesized compounds were purified by recrystallization using different solvents. All melting points were determined on a Buchi Melting Point B-540 apparatus using open capillary tubes and the melting points were uncorrected.

3.2. Organic Inhibitors utilized

Five 6-substitutedchromone-2-carboxamide derivatives including the parent (Chromone-2-carboxamide) were used as corrosion inhibitors. These compounds display good properties (e.g. anticorrosion, and non-toxicity). All the 6-substitutedchromone-2-carboxamide derivatives investigated in this study were synthesized by using materials (starting materials, reagents, and solvents) purchased from Sigma-Aldrich, and they were

purified by column chromatography in the presence of ethyl acetate and hexane using the ratio 70:30. Table 3.1 below displays their abbreviations, IUPAC names, and molecular structures.

Table 3.1: The abbreviations, IUPAC names, and molecular structures of the 6-substituted chromone-2-carboxamide derivatives compounds.

Abbreviation	IUPAC name	**Molecular structure**
Chr-2-Carb	Chromone-2-carboxamide	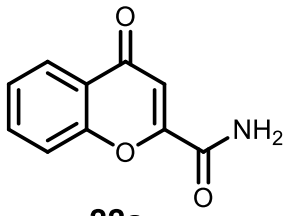 **22a**
Br-Chr-2-Carb	6-Bromochromone-2-carboxamide	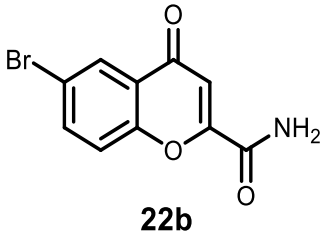 **22b**
Cl-Chr-2-Carb	6-Chlorochromone-2-carboxamide	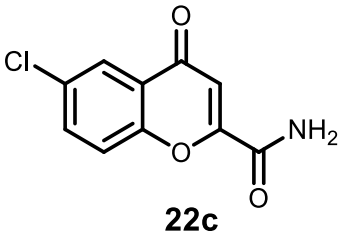 **22c**
CH_3O-Chr-2-Carb	6-Methoxychromone-2-carboxamide	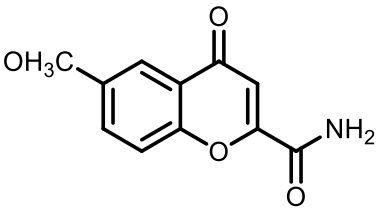 **22d**

NO_2-Chr-2-Carb	6-Nitrochromone-2-carboxamide	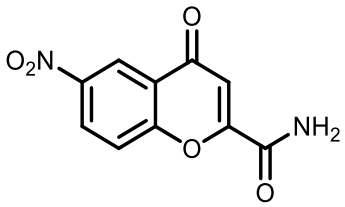 **22e**

3.3. Spectroscopic techniques (FTIR and NMR)

Spectroscopic techniques (such as carbon and proton NMR and as well as IR spectra) were used to confirm the structures of all the compounds synthesized (6-substitutedchromone-2-carboxamide derivatives). Bruker NMR was used for the analysis and approximately 30 – 50 mg of each sample of the synthesized compounds was dissolved in the effective NMR solvent inside a clean and dry NMR tube. The chemical shifts the ^{13}CNMR and ^{1}HNMR were then attributed to various carbons and hydrogens. The Bruker FTIR spectrum was used to locate the functional groups present in the structures of the compounds. The FT-IR instrument was also employed to examine the adsorption film formed on the surface of the metals (Zn, Al and MS) in the acid solutions with and without the synthesized inhibitors at a lower temperature of 303 K. A sharp tip of a spatula was used to carefully scratch off the films formed from the surface of the metals. Powders were then analysed using FT-IR. Below is figure 1 displaying the NMR and FT-IR instruments.

Figure 3.1: Spectroscopic instruments utilized (a) NMR and (b) FT-IR.

3.4. Metal Specimen

In this research project MS, Zn and Al coupons with dimensions of 3 cm width 2 cm breath and a tiny opening (hole) of 2 mm diameter which allowed them to be hanged on a glass rod for corrosion testing. The MS used in all the experimental procedures had the following chemical composition (wt %): (Mn= 0.37), (Ni= 0.039), (P= 0.02), (S= 0.03), (C= 0.21), (Fe= 99.32), and (Mo= 0.01). Al coupons with a 99 (wt %) were utilized as well. surfaces of all the specimens were gently polished using struers 200 mm silicon-carbide (SiC) emery paper attached to a LaboSystem instrument (Cleveland, United States). This chosen size of emery paper maintains a smooth surface of the specimens as compared to the other sizes such as 400 mm. The chosen size of emery paper reduces surface roughness, and promotes reliable measurements.

3.5. Solutions and Preparations

A strong solution of 1.5 M HCl as corrosive media was appropriately prepared by diluting an adequate quantity of analytical level 32 % HCl with excessively distilled water in a 1000 mL volumetric flask. Firstly, the inhibitor compounds were dissolved by a small amount of acetone and DCM (were dissolved overnight and stirred with a magnetic stirrer to ensure complete dissolution of the inhibitors). A stock solution of $1.5x10^{-3}$M of the organic inhibitors was prepared by adding distilled water to the mark. Solutions of five concentrations ($1x10^{-4}$M and $2x10^{-4}$M, $3x10^{-4}$M, $4x10^{-4,}$ and $5x10^{-4}$M) of the corrosion inhibitors were carefully prepared by weighing the inhibitors and adding distilled water to the 1000 mL volumetric flask mark.

3.6. Gravimetric Analysis

Gravimetric analysis is preferred since it is more precise and trustworthy. This approach is less expensive and produces more precise results. Its popularity stems primarily from its ease of use [6]. Weight loss measurements were performed by completely immersing each weighed metal specimen (zinc and mild steel) in the corrosive solution 1.5 M and aluminium on 1.0 M of HCl in the absence and presence of various concentrations of all

investigated corrosion inhibitors at temperatures of 303K, 313K, 323K, and 333K, respectively, which were maintained using thermostat water baths.

After 8 hours of exposure to acid medium, the metal specimens were rinsed with tap water and brushed with a smooth brush under flowing tap water to remove non-adherent corrosion products. The metals were reweighed after 10 minutes of being dried with acetone and a clean paper towel. All weight loss data was collated, recorded, and utilized to compute the corrosion rate (ρ), surface coverage (θ), and percentage inhibition efficiency (%IE) using the formulae (27), (28), and (29). The inhibition efficiency (% IE) was computed using the corrosion rate parameters outlined on equations 28 and 29:

$$\rho = \left(\frac{\Delta W}{St}\right) \tag{27}$$

where: ΔW represents the average weight loss of the metal coupons before and after immersion in the uninhibited and inhibited corrosive environments. S and t represent the surface area of the metal samples and the immersion period in hours, respectively.

$$\theta = \left(1 - \frac{\rho 1}{\rho 2}\right) \tag{28}$$

where: ρ1 is the corrosion rate of metal in the presence of inhibitor and ρ2 is the corrosion rate of metal in the absence of inhibitor.

$$\%IE = \left(1 - \frac{\rho 1}{\rho 2}\right) x100\% \tag{29}$$

where: ρ1 and ρ2 represent the corrosion rate of metal in the presence and in the absence of the inhibitor as highlighted above.

Figure 3.2: Complete system set up for the Gravimetric technique.

3.7. Electrochemical techniques:

As mentioned in the introduction above, corrosion is an electrochemical process. As a result, a variety of electrochemical approaches for corrosion monitoring have been devised and researched. Potentiodynamic Polarization (PDP) and Electrochemical Impedance Spectroscopy (EIS) are two electrochemical techniques that have been extensively researched for the corrosion process of zinc, aluminium, and mild steel, and are thus used in this work. The system and procedure are explained in the following subsection.

3.7.1. Potentiodynamic Polarization (PDP)

PDP tests were conducted at a potential range of -250 to +250 mV (SCE) with a scan rate of 1 $mV.s^{-1}$ to acquire Tafel curves. PDP measurements were performed on Al, zinc and MS specimens in both the presence and absence of inhibitors. The PDP method was used to calculate crucial electrochemical parameters, including corrosion current density (i_{corr}), corrosion potential (E_{corr}), and anodic and cathodic Tafel slopes. The inhibition efficiency (IE) for corrosion current density values were estimated using equation 30 shown below:

$$\%IE_{PDP}=\left(\frac{i^{\circ}_{corr}-i^{i}_{corr}}{i^{\circ}_{corr}}\right) \text{x } 100 \quad (30)$$

where: i°_{corr} and i^{i}_{corr} are the values of corrosion current density in the absence and presence of inhibitor, respectively.

3.7.2. Electrochemical Impedance Spectroscopy (EIS)

The electrochemical impedance curves were generated using a frequency response analyser (FRA) linked to a potentiostat at a frequency range of 100 kHz to 0.00001 kHz. Potentiodynamic settings were used with an amplitude of 5 mV peak to peak and an AC signal at Ecorr. The metal specimens used had a 6 cm^2 surface area and were exposed to an aggressive/acid solution. All measurements were taken in air conditions with no stirring. The Nyquist and Bode graphs from EIS data were explored to gain more insight on the dissolution of Al, Zn and MS. EIS was utilized to assess the deterioration of Al and MS in 1.0 M HCl. After obtaining electrochemical parameters, the % inhibition efficiency was calculated using the following equation:

$$\%IE_{EIS} = \left(1 - \frac{R^{\circ}ct}{Rct}\right) X\ 100 \quad (31)$$

where: R°_{ct} is the charge transfer resistance in the absence of the inhibitor and R_{ct} is the charge transfer resistance in the presence of the inhibitor.

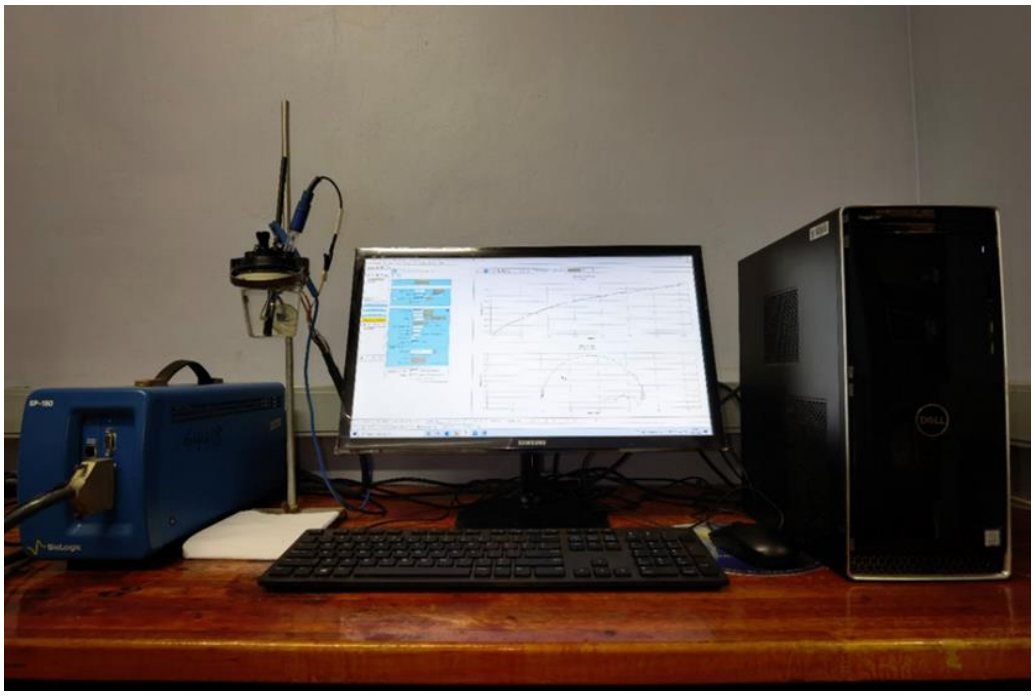

Figure 3.3: Set up for the electrochemical technique system.

3.8. Wettability study to determine the contact angle.

The wetting ability of Al, MS, and Zn sheets in the presence and absence of the synthesized inhibitors was evaluated by measuring the contact angle of water on the three metal surfaces. A video contact angle system, or VCA, is frequently used to estimate contact angles. These systems are typically costly; however, smartphones can serve as a better solution as an alternative [228 – 229]. To capture a photograph of the water droplet the following tools were used; a smartphone, pipette, macro lens, and lens mount. The data were examined using ImageJ version 1.53, an open-source image editor that calculates the contact angle straight from the image. Following its attachment to the lens mount, the macro lens was clipped over the smartphone's camera lens. In a well-lit environment, the sample was put flush against the edge of a workbench. The pipette was used for dispensing a one-microliter drop of clean and pure water near the sample's leading edge. The smartphone was put roughly 1-3 cm away from the droplet to snap a sharp shot with the maximum possible resolution. The study was carried out on a grayscale image (32-bit) with enough magnification to enable static contact angle

measurement. The inertia of the contact angle was measured employing the Drop Analysis-LBADSA plugin [228]. Before testing, the metal specimens were sanded with silicone paper, then rinsed with water and dried at room temperature. They were then submerged in corrosive solutions, both uninhibited and inhibited (800 ppm), for 7 hours. After a 7-hour soaking, the samples were scrubbed with a brush, washed with distilled water, dried, and placed in a desiccator until tested.

3.9. Scanning electron microscope/energy dispersive x-ray spectroscopy (SEM/EDS) analysis

A scanning electron microscopy (SEM) technique was used to analyze the surface morphology of Al, MS, and Zn prior to and after exposure to the acidic medium (1.5 M HCl on the MS and Zn, and 1 M HCl on Al) with and without the 6-substitutedchromone-2-carboxamides. Surface morphological changes of Al, MS, and Zn electrodes were analyzed using the Phenom Pro X SEM instrument with an EDS detector for elemental composition. Before SEM/EDX examination, samples underwent gravimetric analysis for 8 hours for the MS and Zn, and 6 hours for Al at 30°C. After the reaction period, samples were removed, cleaned with a stubble brush, washed with distilled water, and ethanol, and dehydrated with acetone. Photographs were taken of the samples that yielded more accurate results. To assess the impact of 6-substitutedchromone-2-carboxamides on surface morphology, untreated polished metal samples were analyzed and compared to samples exposed to an acidic medium (HCl) with and without varying concentrations of the synthesized inhibitors.

3.10. Computational analysis

Corrosion computational studies are crucial for understanding intramolecular interactions, particularly those between metals and inhibitors (metal-inhibitor). Density functional theory (DFT) was used to optimize the structures of the synthesised inhibitors and investigate their characteristics. The interaction energy values between the metal surface and inhibitor molecule (also referred to as binding energy values) were determined

utilizing Accelyrs Materials Studio. The 6-substitutedchromone-2-carboxamides display various active sites that can interact with the mild steel, zinc and aluminium atoms (111), for this purpose the density functional theory (DFT) calculations were carried out in vacuum utilizing $DMol_3$ module of Material Studio 2020 Software [230]. This software was used to generate a metal crystal structure of interest. Imported a metal crystal structure (crystallographic information file) and created a unit cell for the synthesized inhibitors to interact with the surfaces of the three metals (Iron, zinc and aluminium). The Becke exchange functional and the Lee-Yang Parr correlation functional (BLYP) together with generalized gradient approximation (GGA) functional was used to describe electronic exchange and correlation, along with a double numeric polarization (DNP) basis set, and the accuracy and efficacy of this level of theory have been confirmed by past research studies on the related system [231]. The convergence criteria and the global orbital cutoffs were set to “Medium”. The simulation was carried out using the forcite quench. On the energy tab, force field was set to COMPASS used to calculate energies and search for equilibrium configurations. The systems were optimized using tolerances of energy, gradient, and displacement convergence of 1×10^{-5} Ha, 2×10^{-5} Ha, and 5×10^{-3} Å, respectively. A DIIS (direct inversion in an iterative subspace) of size 6 and a thermal smearing value of 0.005 Ha were used to accelerate the convergence. However, a smearing value of 0.05 Ha was used in the iron system. Al (111), Zn (111) and Fe (110) surfaces were chosen due to their most stable planes with more active sites. The optimized cleaved surfaces of Al (111) and Zn (111) were expanded into supercells of size $5 \times 5 \times 1$, providing enough space (larger surface) for the metal-inhibitor interaction. However, a supercell of size $4 \times 4 \times 1$ was used on the Fe (111) system. To avoid periodic boundary conditions, a 20 Å vacuum layer was added above the solution layer in the z-direction. Furthermore, the geometry of all surface layers was confined to the bulk positions. K-points of $2 \times 2 \times 1$ were used to model the adsorption process. A parallel adsorption model for each system was used, constraining the two bottom layers of the slab while allowing full relaxation of the inhibitor and the top layer of the metals (upper half). The interaction energies were calculated by adding up the energy of optimized isolated compound ($E_{compound}$) with the energy of the isolated metal (Fe, Zn and

Al) surfaces (E_{surf}), and subtracting it to the total energy of the compound/metal surface adsorption systems ($E_{compound/surf}$) as shown in equation 32 below.

$$E_{ads} = E_{molecule+surface} - E_{molecule} - E_{surface} \quad (32)$$

3.11. Synthesis and characterization of inhibitors

In this synthetic work, five target compounds **22a-22d** (6-substitutedchromone-2-carboxamides) were successfully synthesized. The first step in synthesis of these target compounds was the conversion of the starting materials **18a-18d** (5-substituted-2-Hydroxacetophenones) into ethyl 6-substituted-chromone-2-carboxylates **19a-19d** as clearly presented below in section 4.1.1 below. The 6-substituted-chromone-2-carboxylates **19a-19d** were then converted to 6-substituted-chromone-2-carboxylic acids **20a-20d** as clearly explained in section 4.1.2 below. The 6-substituted-chromone-2-carboxylic acids **20a-20d** were used as starting material in producing the target compounds 6-substitutedchromone-2-carboxamides **22a-22d** via the 6-substitutedchromone-2-carbonyl chlorides **21a-21d** as clearly elaborated in section 4.1.3 below. A general reaction scheme for this synthetic work is presented below. All synthesized compounds were characterized by 1H and 13C NMR, and FT-IR spectroscopies.

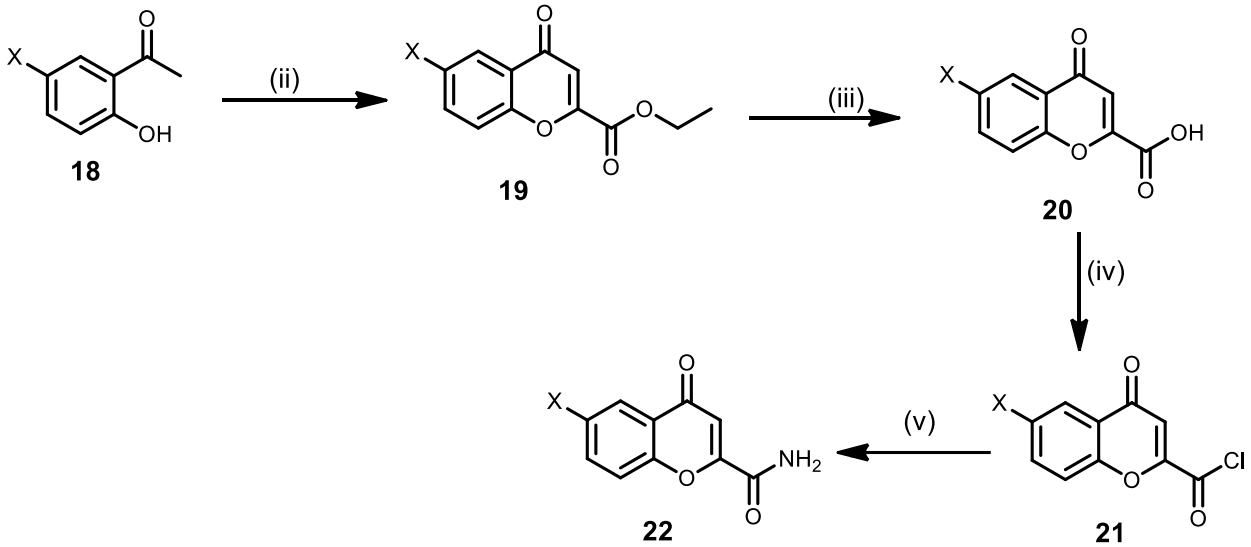

X	A	B	C	D	E

	H	Br	Cl	CH_3O	NO_2

Reagents and condition: (i) NaOEt-$(COOEt)_2$ (ii) AcOH-HCl (2;1), heat, 1.5 hr, (iii) DMF, $SOCl_2$, $ClCH_2CH_2Cl$ (v) DCM, Et_3N, aq.NH_4OH, 0 °C, r.t .

Scheme 1: Proposed Synthetic Scheme.

CHAPTER 4: Synthesis, Gravimetric analysis, and FT-IR spectroscopy Results and Discussions

This chapter provides a summary and discusses the results of the 6-substituted chromone-2-carboxamides synthesis. The substituted chromone-2-carboxamides were characterized utilizing NMR and FT-IR spectroscopy techniques. Gravimetric analysis was performed considering the impact of temperature and inhibitor concentration. Adsorption isotherms, thermodynamic parameters, and adsorption film formed were all employed to evaluate 6-substituted chromone-2-carboxamide as corrosion inhibitors.

4.1. Synthesis and characterization of inhibitors

4.1.1. Preparation of ethyl 6-substituted- chromone-2-carboxylates (19a – 19e)

The synthesis of ethyl 6-substituted-chromone-2-carboxylates **19a-19e** was carried out with the aid of the Kostanecki-Robinson reaction, which involves the condensation of the 5-substituted-2-Hydroxyacetophenones **18a-18e**. A mixture of diethyl oxalate and a corresponding 2-hydroxyacetophenone was added to a stirred ethanolic solution [generated in situ by adding sodium metal to dry ethanol] in a dried round bottom flask. The yellow mixture was boiled gently under reflux for 30 minutes and then allowed to cool to room temperature. The yellow sodium salt was filtered off, and washed with diethyl ether (3x 50 ml). The combined ethereal extracts were dried (anhyd. $MgSO_4$), filtered off, and evaporated. Work-up afforded the corresponding ethyl-chromone-2-carboxylates **19a-19e**. The assignment of protons in the ^1H NMR was done with the help of spectroscopic techniques and considering chemical shifts and multiplicities. The assignments of carbons were done using DEPT 135 and ^{13}C NMR. The carbon and proton NMRs were clear and corresponded with the number of carbons and protons in the carboxylate structures. In addition, the 1H NMR, ^{13}C NMR, and Dept NMR showed the existence of CH_2, CH_3, and =C-H in the two aromatic rings. The chemical shifts of the aromatic protons of the intermediates **19a-19e** were appearing at low field (7.00-8.25 ppm), while the C-3 protons of all the intermediates appeared around (6.00-6.90 ppm). Furthermore, the carbon and proton NMR, as well as the DEPT NMR confirmed the presence of the OCH_3 of the ethyl 6-methoxychromone-2-carboxylate **19d**. The preparation of the intermediates **19a-19e** was followed as shown in scheme 2. The spectral data of all the synthesized carboxylates **19a-19e** from the ^{13}CNMR is displayed in table 2 below.

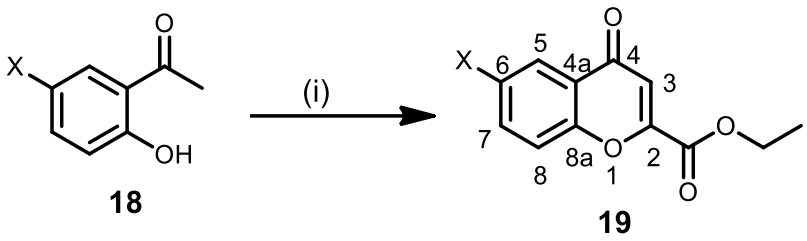

18 19

Reagents: (i) $(COOEt)_2$, NaOEt

Scheme 2: Synthesis of ethyl 6-substituted -chromone-2-carboxylates **19a-19e**.

Table 4.1: Percentage yields and melting points of the ethyl 6-substituted- chromone-2-carboxylates **19a-19e**.

19	X	% YIELD	M.P (°C)	Lit. M.P. (°C)
A	H	95	71-73	72-74[280]
B	Br	88	148.2-150	151 – 156[280]
C	Cl	88	107.2-108,1	1 41– 148[280]
D	OCH_3	97	102.105.3	100.4 –109[280]
E	NO_2	98	192.3	183 – 189[280]

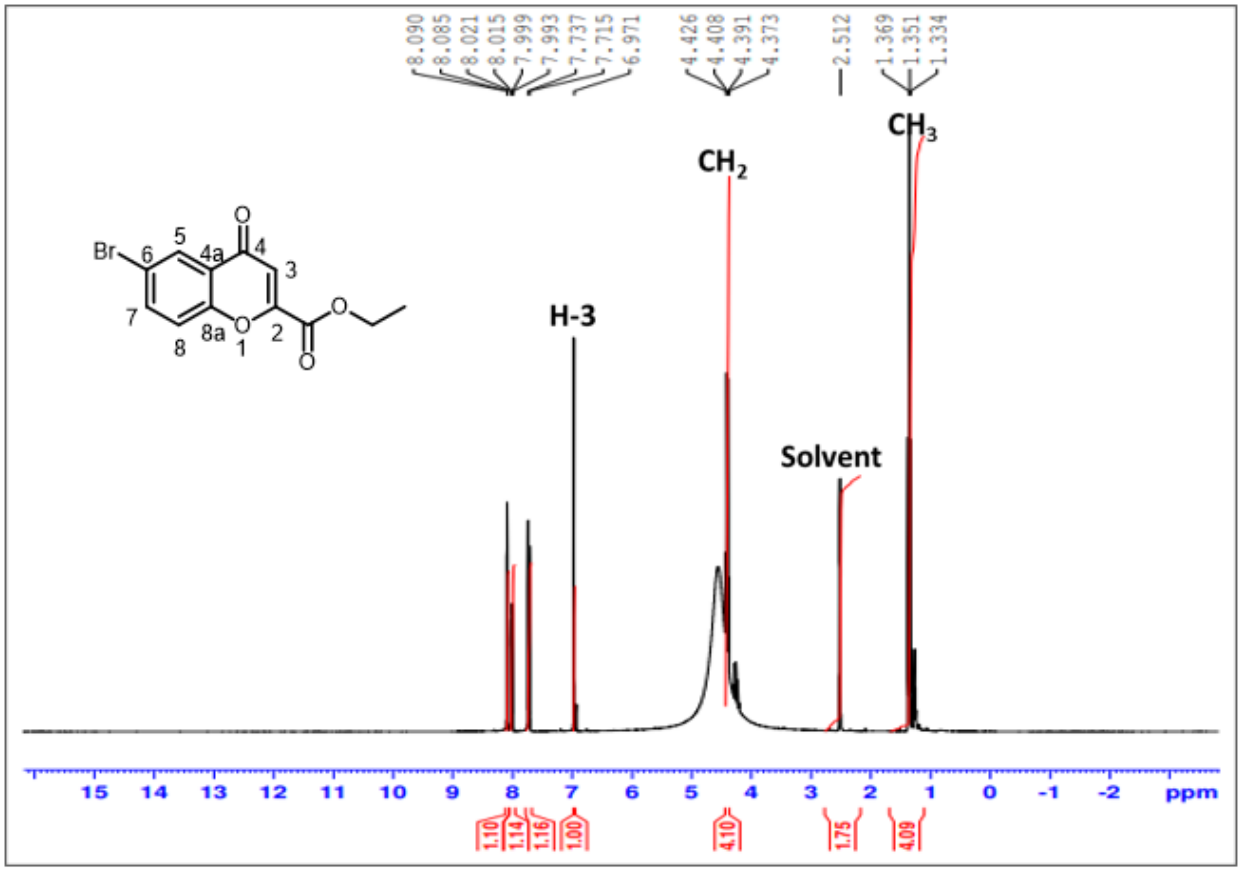

Figure 4.1: 400 MHz ^{1}H NMR spectrum of 6-bromochromone-2-carboxylates **19b** in DMSO-d_6.

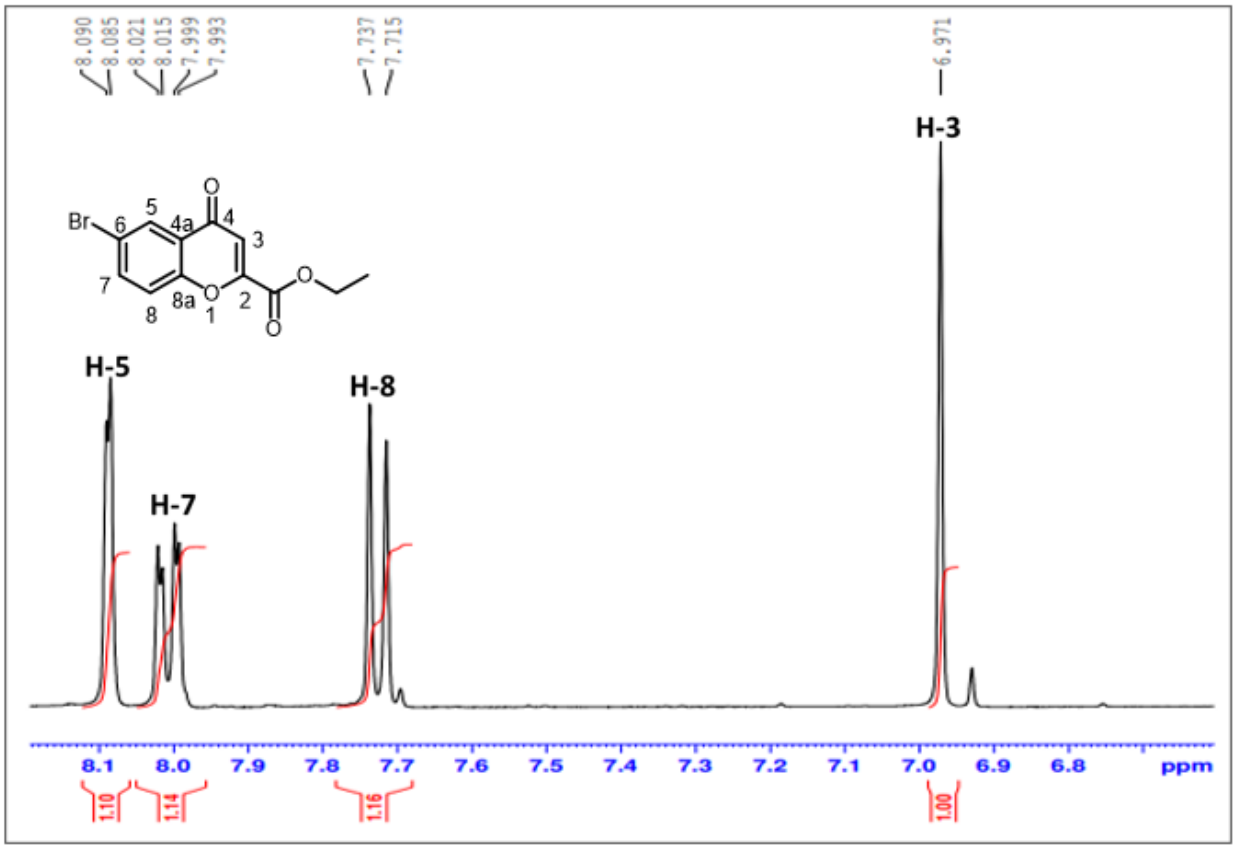

Figure 4.2: 400 MHz ^{1}H expansion NMR spectrum of 6-bromochromone-2-carboxylates **19b** in DMSO-d_6.

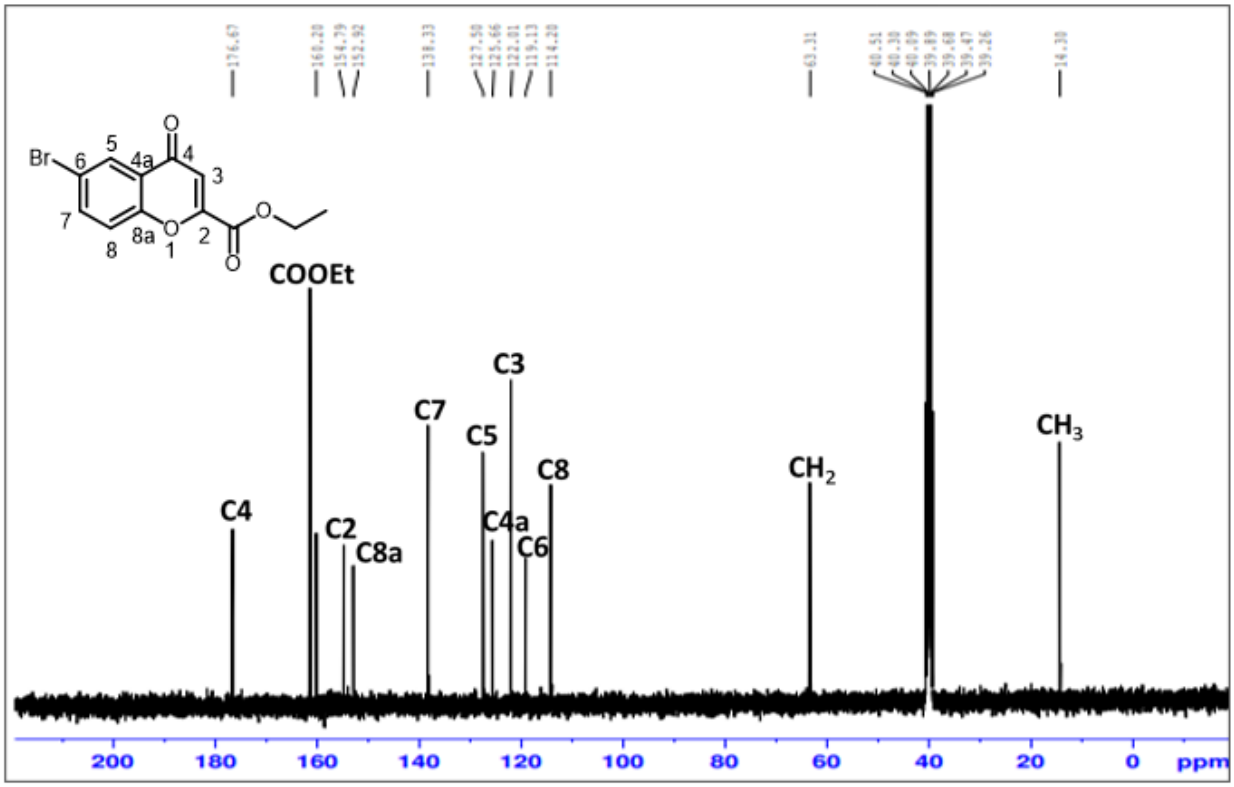

Figure 4.3: 100 MHz ^{13}C NMR spectrum of 6-bromochromone-2-carboxylates **19b** in DMSO-d_6.

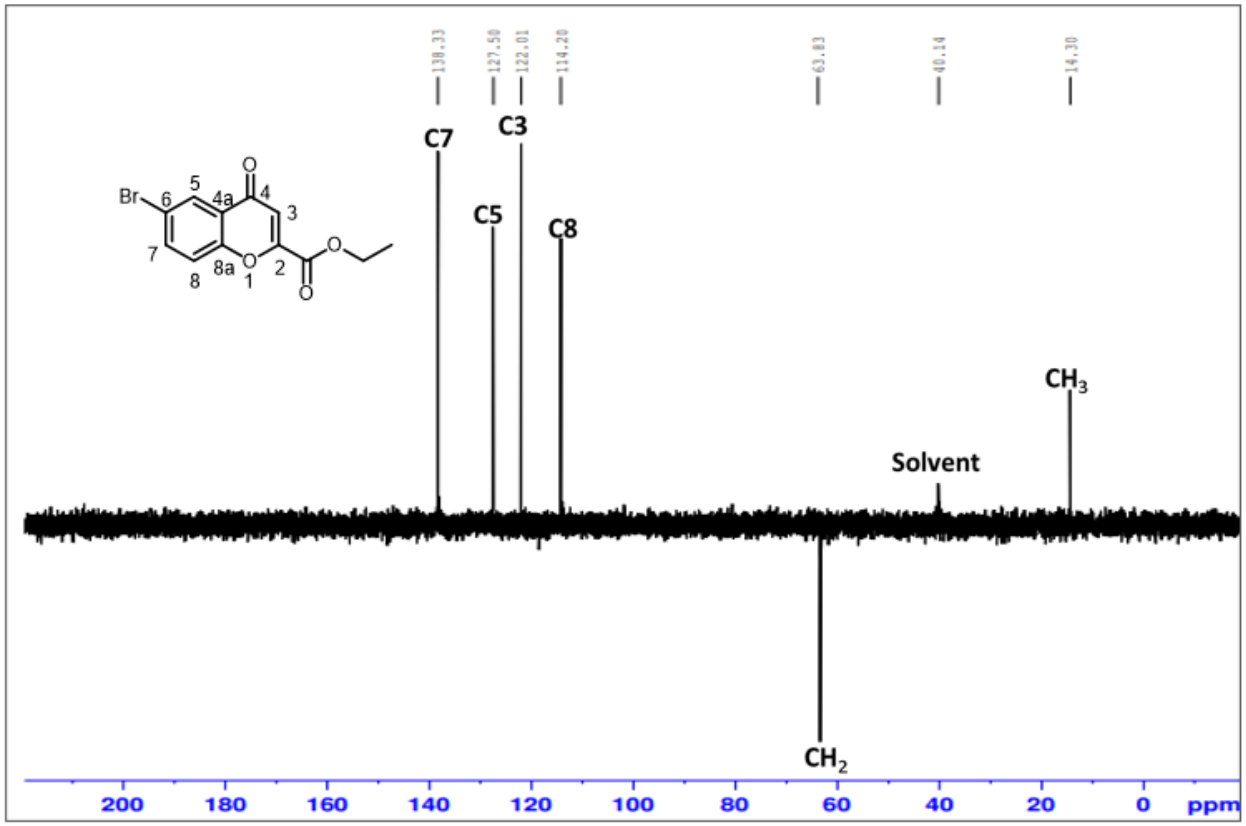

Figure 4.4: DEPT NMR spectrum of 6-bromochromone-2-carboxylates **19b** in DMSO-d_6.

Table 4.2: ^{13}C NMR chemical shift values (ppm) of ethyl 6-substitutedchromone-2-carboxylates **19a-19e** in DMSO-d_6 (at 100 MHz).

Nucleus	**a (X=H)**	**b (X=Br)**	**c (X=Cl)**	**D (X=OCH_3)**	**E (X=NO_2)**
COOEt	160.44	160.20	161.38	161.46	161.40
C-2	155.82	154.79	154.40	160.42	158.81
C-3	119.34	122.01	121.86	113.22	121.39
C-4	177.97	176.67	176.82	177.44	177.07
C4a	125.41	125.66	124.37	157.51	124.22
C-5	126.67	127.50	131.16	105.02	121.69
C-6	124.22	119.13	125.29	152.37	145.20

C-7	135.78	138.33	135.61	124.90	129.74
C-8	114.20	114.20	114.09	120.97	114.48
C-8a	152.69	152.92	152.92	150.52	153.29
CH_2	63.18	63.31	63.30	63.13	63.46
CH_3	14.33	14.30	14.30	14.31	14.31
OCH_3	-	-	-	56.25	-

4.1.2. Synthesis of 6-substituted-chromone-2-carboxylic acids (20a – 20e)

The carboxylic acids **20a-20e** were prepared from the intermediates **19a-19e** (ethyl 6-substituted-chromone-2-carboxylates) using AcOH and HCl (with ratio 2:1) and boiling the solution under reflux. All the products were then recrystallized from acetic acid. A reaction mixture of ethyl 6-substituted-chromone-2-carboxylates **19a-19e**, concentrated HCl (15 ml) and AcOH (30 ml) were boiled gently under reflux for 1.5 hr in a dried round bottom flask. The mixture was cooled at room temperature and the precipitate formed was filtered off to afford chromone-2-carboxylic acid. The protons in the 1H NMR were assigned considering chemical shifts, multiplicities, and taking proton integration into account. The carbons were assigned using ^{13}C NMR and DEPT 135 NMR. The proton and carbon NMR proved that indeed the reaction worked, clear peaks were observed. Dept NMR proved that the reaction was successful as there was a disappearance of CH_2 and CH_3 the no peak. Furthermore, the IR spectra of the synthesized 6-substituted-substituted-chromone-2-carboxylic acids **20a-20e** revealed the CO_2H around 1721.13-1733.48 cm^{-1}, and C=O stretching for C-4 at around 1621.37-1629.50. The 6-substituted-substituted-chromone-2-carboxylic acids **20a-20e** were prepared as shown in scheme 3 below.

The OH signal of the carboxylic acids **20a-20e** wasn't visible in the proton NMR spectra of the produced 6-substituted-chromone-2-carboxylic acids **20a-20e**, which could be attributed to the DMSO-d6 NMR solvent utilized. Both the proton and carbon NMR spectra confirmed the disappearance of CH_2 and CH_3 peaks. Both the carbon and proton NMR, as well as the DEPT NMR confirmed the presence of the methoxy (OCH_3) of the 6-

methoxychromone-2-carboxylic acid **20d**. The spectral data of all the synthesized carboxylates **19a-19e** from the ^{13}CNMR is displayed in table 2 below.

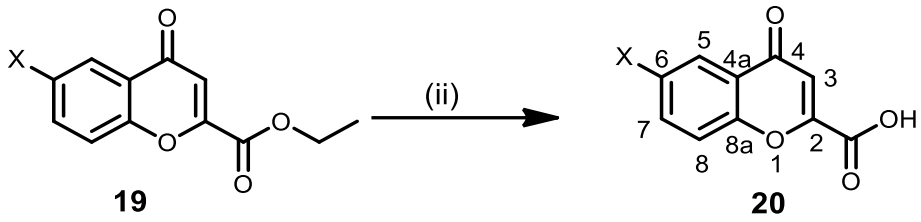

Reagents and conditions: (ii) AcOH-HCl (2; 1), 1.5 hr

Scheme 3: Synthesis of 6-substituted-chromone-2-carboxylic acids **20a-20e**.

Table 4.3: Percentage yields and melting points of the ethyl 6-substituted-chromone-2-carboxylic acids **20a-20e**.

20	X	% YIELD	M.P. (°C)	Lit. M.P. (°C)
a	H	87	267	285[281]
b	Br	91	265 – 268	263 – 267[281]
c	Cl	93	234 – 236	254 – 256[281]
d	OMe	86	272 – 274	293 – 294[281]
e	NO_2	75	228	–

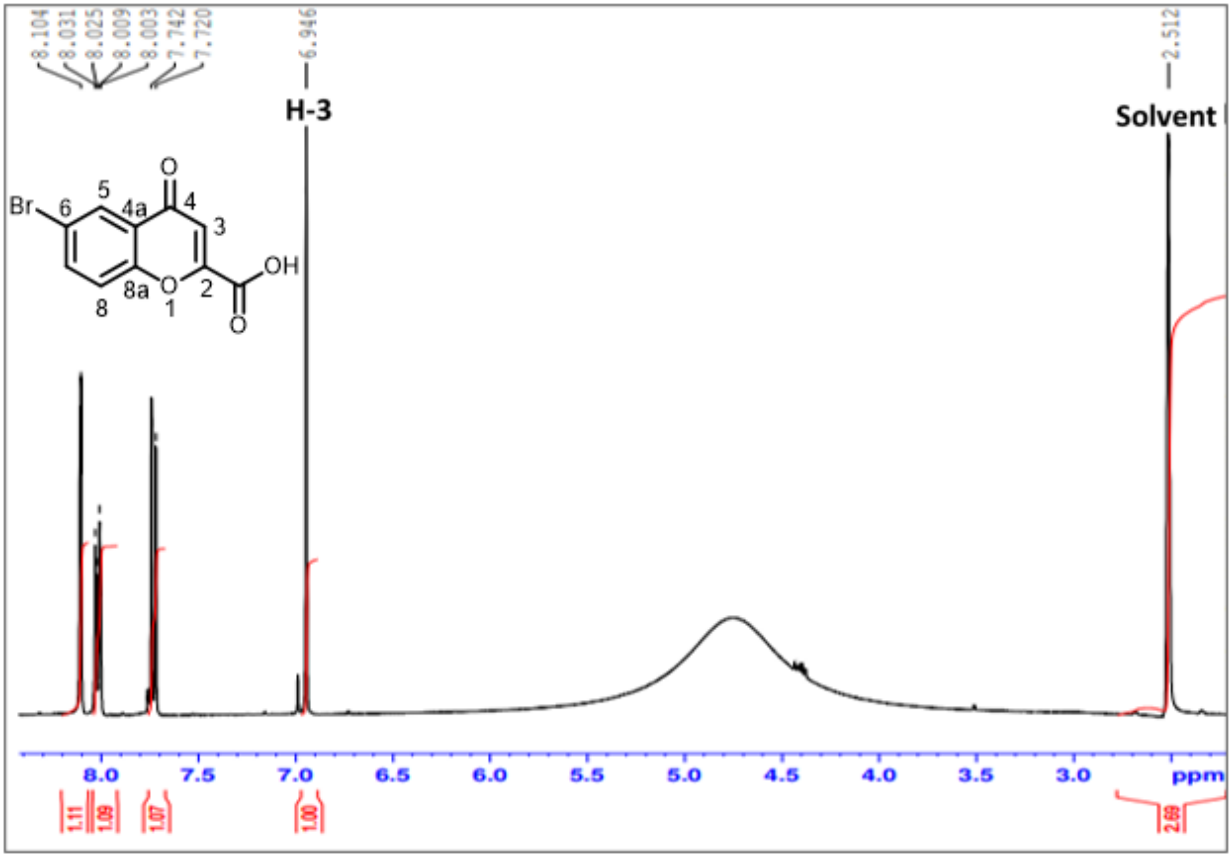

Figure 4.5: 400 MHz ^{1}H NMR spectrum of 6-bromochromone-2-carboxylic acid **20b** in DMSO-d_6.

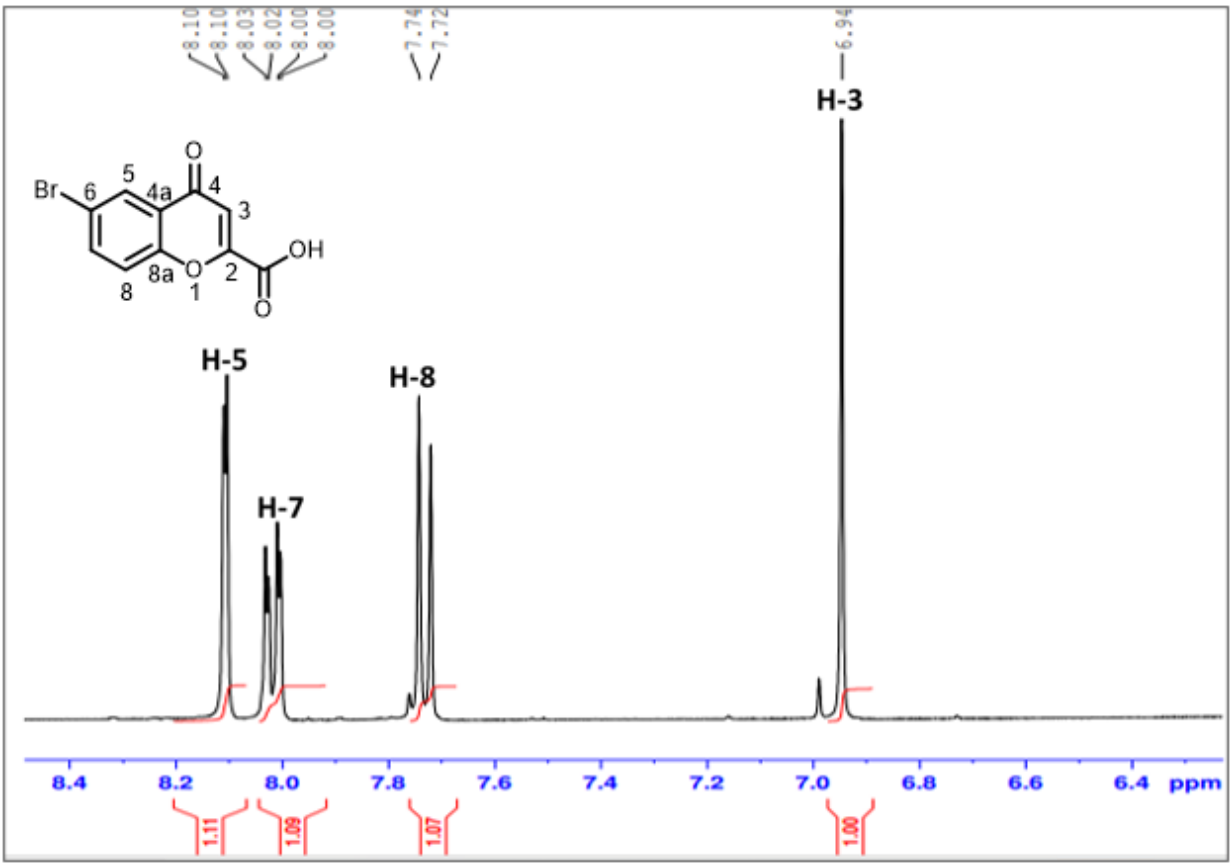

Figure 4.6: 400 MHz ^{1}H expansion NMR spectrum of 6-bromochromone-2-carboxylic acid **20b** in DMSO-d_6.

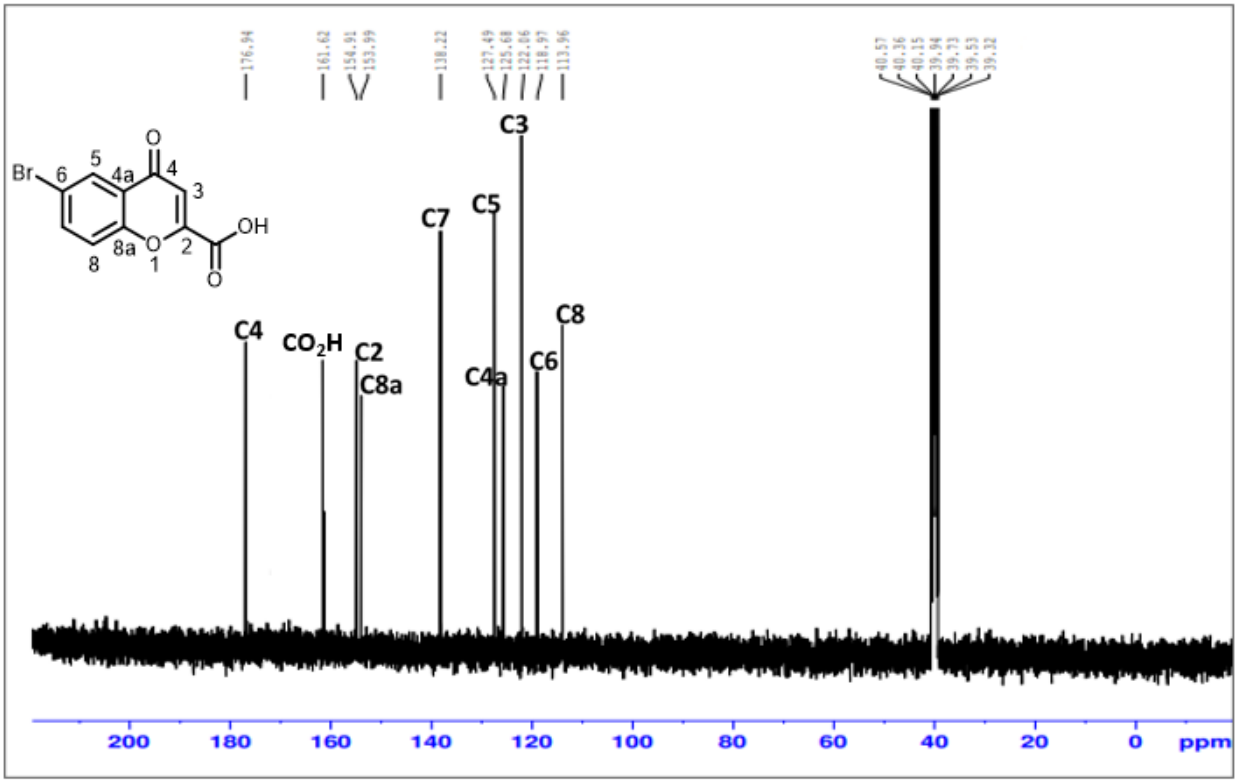

Figure 4.7: 100 MHz ^{13}C NMR spectrum of 6-bromochromone-2-carboxylic acid 20b in DMSO-d_6.

Table 4.4: ^{13}C NMR chemical shift values (ppm) of 6-substituted-chromone-2-carboxylic acids **20a-20e** in DMSO-d_6 (at 100 MHz).

Nucleus	**a (X=H)**	**B (X=Br)**	**C (X=Cl)**	**d (X=OMe)**	**E ($X=NO_2$)**
COOH	161.88	161.62	161.7	161.89	161.42
C-2	155.88	154.91	154.52	161.39	158.94
C-3	119.31	122.06	121.88	112.97	121.40
C-4	178.09	176.94	177.07	177.82	177.37
C-4a	125.36	125.68	124.36	157.44	124.69
C-5	126.50	127.49	131.01	104.98	124.19

C-6	124.15	118.97	125.30	153.45	145.13
C-7	135.63	138.22	135.48	124.88	129.63
C-8	113.92	113.96	113.84	121.01	114.17
C-8a	153.70	153.99	154.02	150.63	154.49
OCH_3	-	-	-	56.26	-

4.1.3. Synthesis of target compounds (6-substituted-chromone-2-carboxamides) 22a – 22e)

A stirred solution of 6-substitutedchromone-2-carboxylic acids **20a-20e** in dry 1.2-dichloroethane (12 ml) and dry N, N-dimethylformamide were treated with thionyl chloride (which is a good and strong chlorinating agent) at room temperature (rt) in a 100 ml dried round-bottom flask. The resulting mixture was heated under reflux for 2 hrs under inert conditions (using calcium chloride drying tube was used). The reaction mixture was homogenous upon completion and was monitored by TLC. The reaction mixture was allowed to cool to room temperature. The solvent was removed under vacuum using a rotary evaporator. A dry 1.2-dichloroethane was added and removed under vacuum. Work-up afforded 6-substitutedchromone-2-carbonyl chlorides **20a-20e**. Then the obtained 6-substitutedchromone-2-carbonyl chlorides **21a-21e** were slowly added to a stirred solution of ammonium hydroxide and dry dichloromethane in the presence of triethylamine. The solution was stirred at room temperature and TLC was used to monitor the reaction. After the TLC confirmed that the reaction is completed, the mixture was washed with water, 10 % Na_2CO_2 (10 g of Na_2CO_2 in 90 ml of water), and brine, saturated aqueous NaCl (100 ml). The resulted solvent was evaporated to get the desired crude chromone-2-carboxamides **22a-22e**. The product was then purified by flash silica gel chromatography (using 8 % hexane in ethyl acetate). The spectral data from ^{1}HNM and ^{13}CNMR obtained for the synthesised target compounds are listed in figure 4.1 – 4.6 below. The preparation of the target compounds **22a-22e** was followed as shown in scheme 4 below. The spectral data (chemical shift values) of all the synthesized carboxamides from the ^{13}CNMR is displayed in table 5 below.

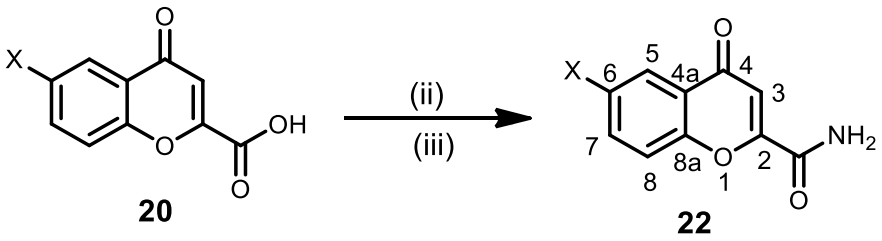

Reagents and conditions: (ii) DMF, $SOCl_2$, $ClCH_2CH_2Cl$, heat, 2 hr (iii) DCM, Et_3N, aq.NH_4OH, 0 °C, r.t

Scheme 4: Synthesis of 6-substituted-chromone-2-carboxamides **22a-22e**.

Table 4.5: Percentage yields and melting points of the ethyl 6-substituted-chromone-2-carboxamides **22a-22e**.

17	X	% YIELD	M.P. (°C)	Lit. M.P. (°C)
a	H	74	126.3	–
b	Br	68	213.2	–
c	Cl	84	278.6	–
d	Ome	89	263.9	–
e	NO_2	42	284.5	–

Characterization of the target compounds (22):

Spectroscopic techniques such as carbon and proton NMR and as well as IR spectra were used to confirm the structures of all the synthesized target compounds **22a-22e** as well as the structure of the synthesized intermediates. TLC was utilized in monitoring the reactions and in purifying the compounds, and it confirmed that reactions were successful completed. Figure 4.8 – 4.26 and below shows the assignment of the carbons and protons in the structures of the target compounds. Multiplicities were confirmed by the ^{1}HNMR spectra, and coupling constants were (J-values) were calculated from the peak intensities in order to deduce strength of the spin-spin splitting interaction and the distance between

the splitting of the aromatic protons. It has been noted that the NH_2 peak was not clear and not visible in the ^{1}HNMR of some of the target compounds. The disappearance of the NH_2 peak is due to the DMSO-d_6 NMR solvent used, which has a tendency to absorb or to alter the OH and NH_2 due to its hygroscopicity. Fortunately, the FTIR spectra confirmed the presence of the NH_2 peak around wavenumber 3300 cm^{-1} for all the synthesized target compounds **22a-22e**. Furthermore, the mass spectrometry has confirmed the masses of the target compounds. A singlet proton at around 6.7 – 7.0 ppm for the proton at carbon number three (**C3**) was appearing in all the ^{1}HNMR Spectra for the target compounds. Also, the solvent peaks were appearing at around 2.5 ppm on the ^{1}HNMR and around 40.0 ppm on the ^{13}CNMR for all the NMR spectra of the synthesized compounds. Spectroscopic data obtained from ^{13}CNMR is displayed in table 4.6 below showing the assignment of all the carbons of the synthesized compounds, including the carbon of the methoxy group (OCH_3)

4.1.3.1. Characterization of Chr-2-Carb (Chromone-2-carboxamide) 22a

Chromone-2-carboxamide **22a** compound was purified as brownish crystal product and characterized by spectroscopic techniques as highlighted above. On the first aromatic ring the ^{1}HNMR spectrum showed a doublet of a doublet around 8.0 ppm with two coupling constants of 1.6 Hz which is due to the proton at carbon five (**C5**), a triplet of doublets around 7.8 ppm with three coupling constants of 1.6 Hz, 1.2 Hz and 1.6 Hz which is due to proton on carbon six (**C6**), a doublet around 7.7 ppm with a coupling constant of 8.4 Hz which due to proton at carbon eight (**C8**) and a triplet around 7.5 ppm with a coupling constant of 8 Hz which is due to proton on carbon seven (**C7**). A water peak appeared at 4.725 ppm due to the DMSO-d_6 NMR solvent used.

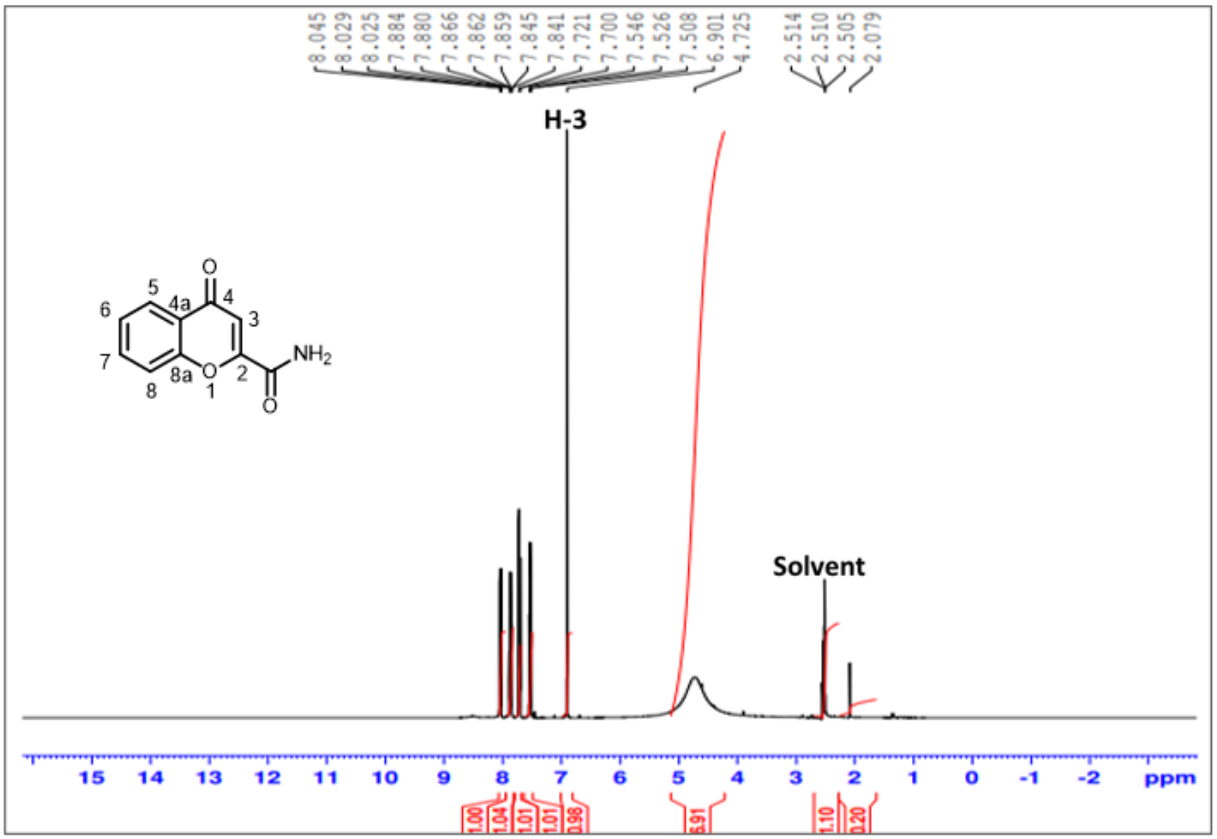

Figure 4.8: 400 MHz ^{1}H NMR spectrum of Chromone-2-carboxamide **22a** in DMSO-d$_6$.

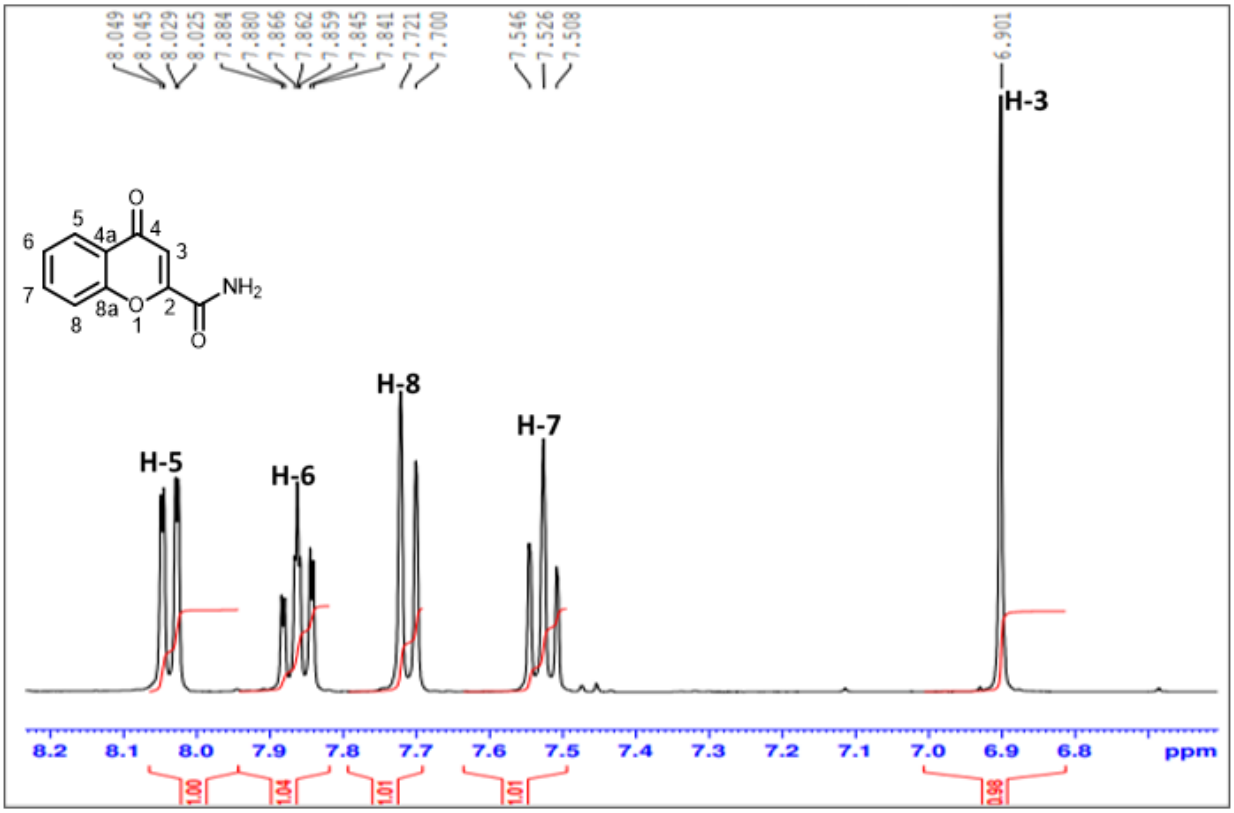

Figure 4.9: 400 MHz ^{1}H expansion NMR spectrum of Chromone-2-carboxamide **22a** in DMSO-d_6.

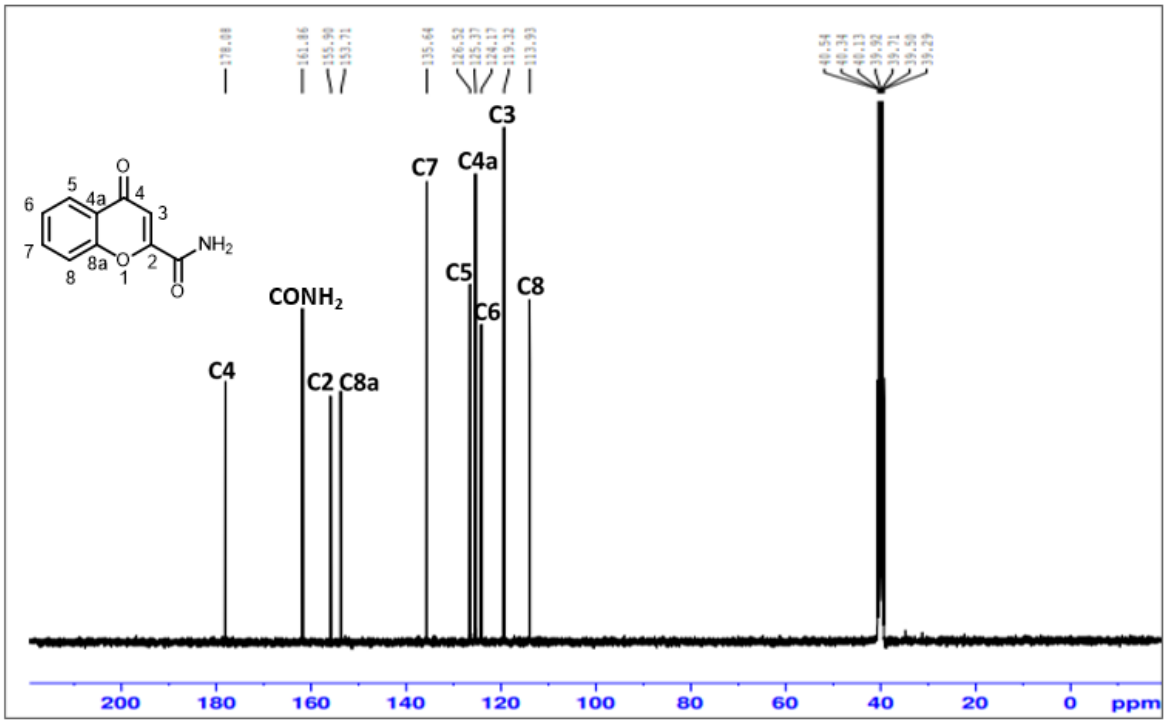

Figure 4.10: 100 MHz ^{13}C NMR spectrum of Chromone-2-carboxamide **22a** in DMSO-d_6.

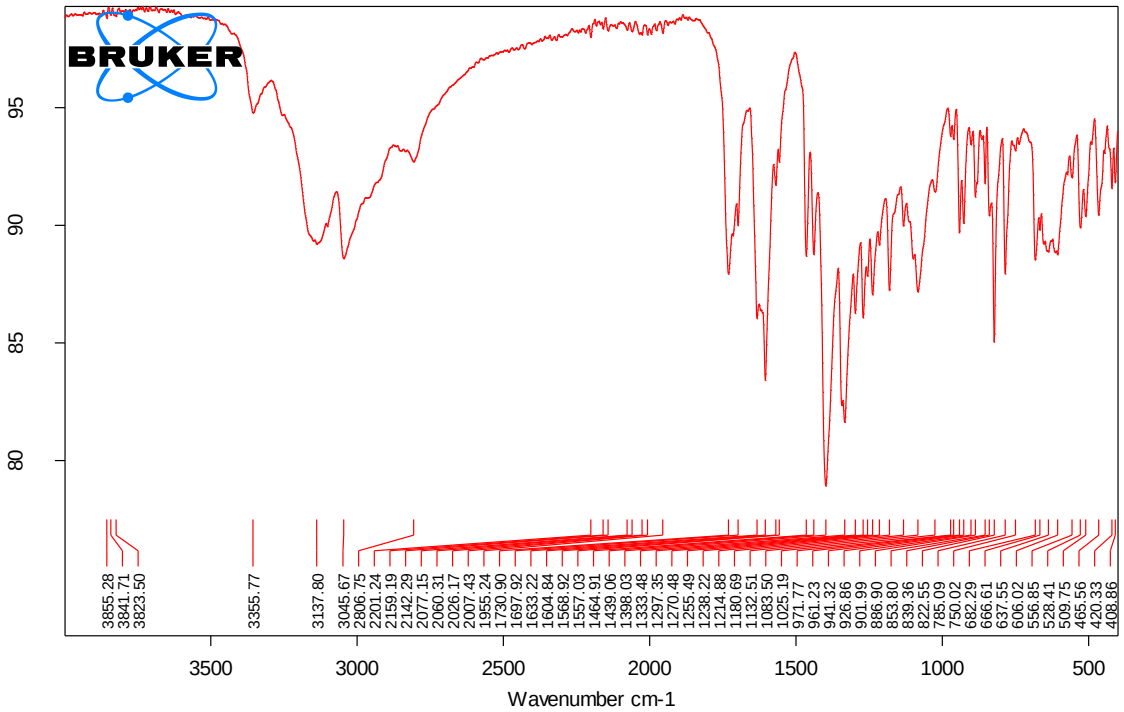

Figure 4.11: FT-IR spectrum of Chromone-2-carboxamide 22a.

4.1.3.2. Characterization of Br-Chr-2-Carb (6-bromochromone-2-carboxamide) 22b

6-bromochromone-2-carboxamide **22b** compound was purified as dark brown crystal product and characterized by spectroscopic techniques as highlighted above. As observed on figure 4.13, the 1HNMR spectrum confirmed a doublet around 8.1 ppm with a coupling constant of 2 Hz which is due to the proton at carbon five (**C5**), a doublet of doublet around 8.03 ppm with two coupling constants of 2.4 Hz which is due to proton on carbon seven (**C7**), a doublet around 7.7 ppm with a coupling constant of 8.8 Hz which is due to proton at carbon 8 (**C8**). A water peak appeared at 3.713 ppm due to the DMSO-d6 NMR solvent used.

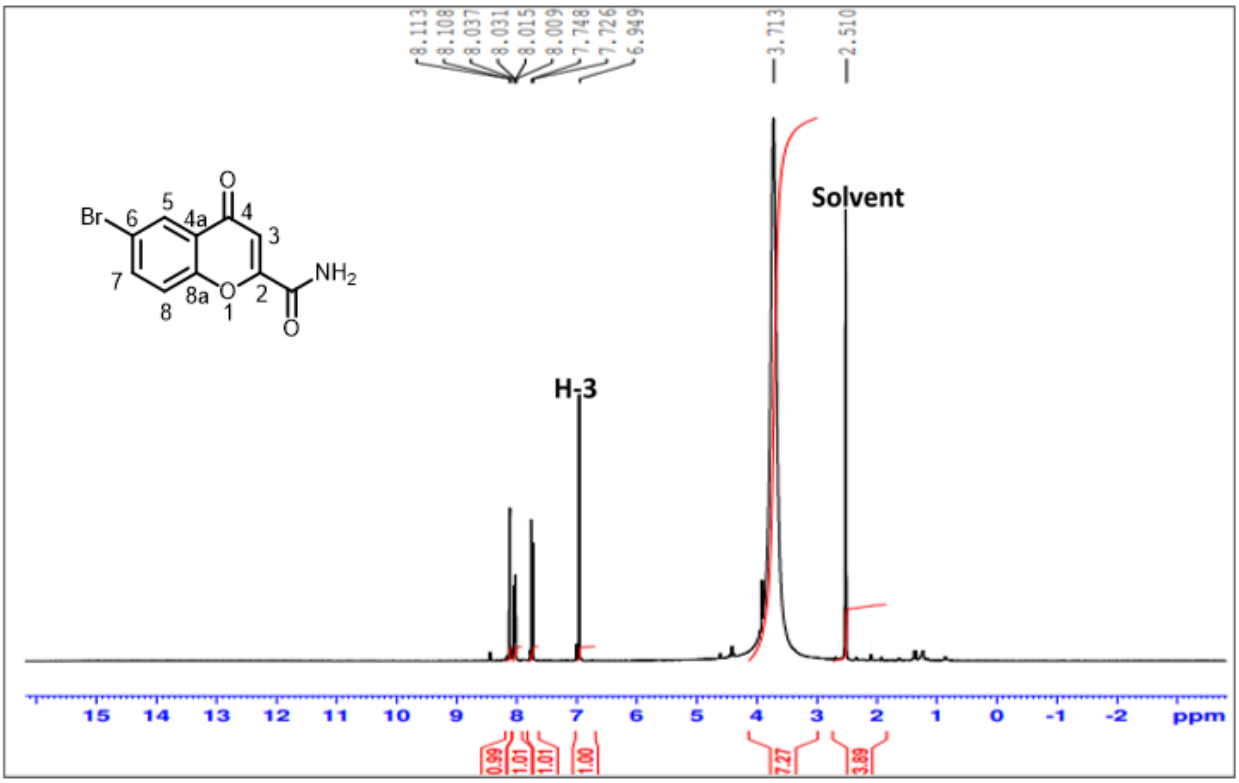

Figure 4.12: 400 MHz ^{1}H NMR spectrum of 6-bromochromone-2-carboxamide **22b** in DMSO-d_6.

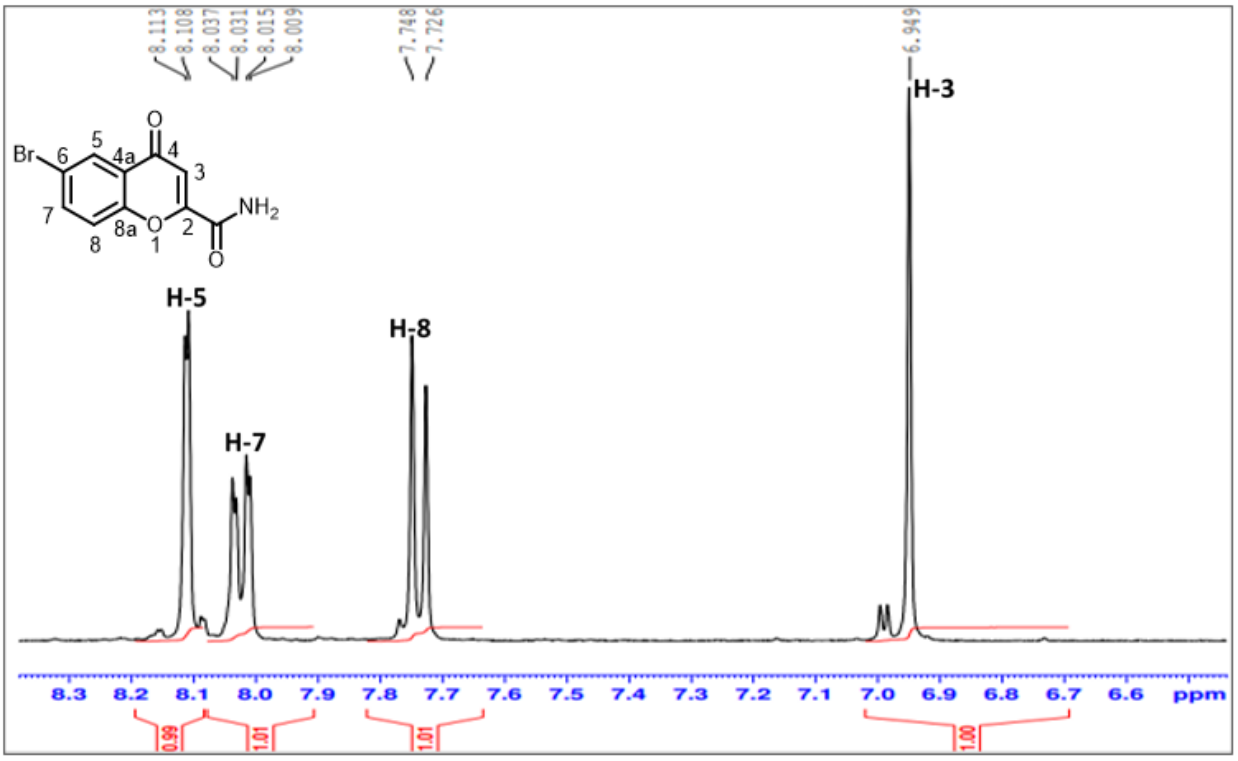

Figure 4.13: 400 MHz ^{1}H expansion NMR spectrum of 6-bromochromone-2-carboxamide **22b** in DMSO-d_6.

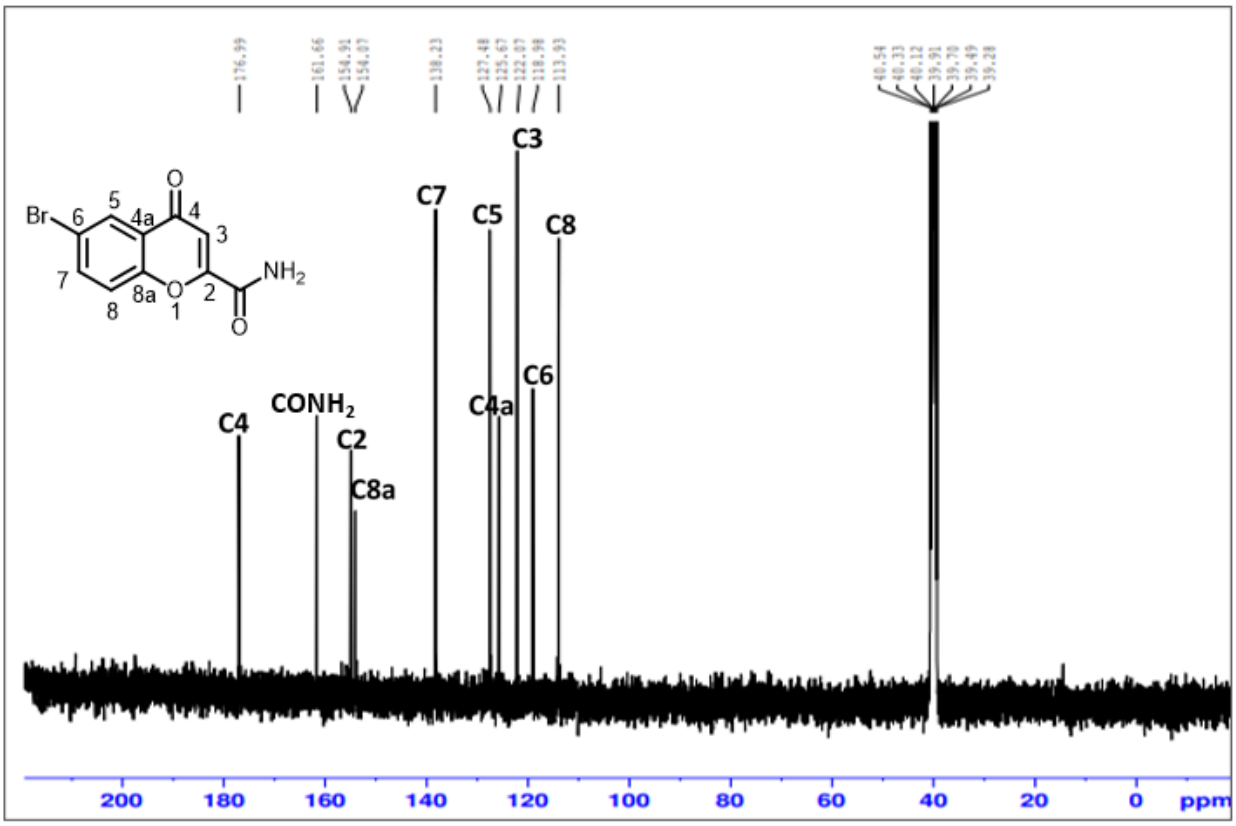

Figure 4.14: 100 MHz ^{13}C NMR spectrum of 6-bromochromone-2-carboxamide **22b** in DMSO-d6.

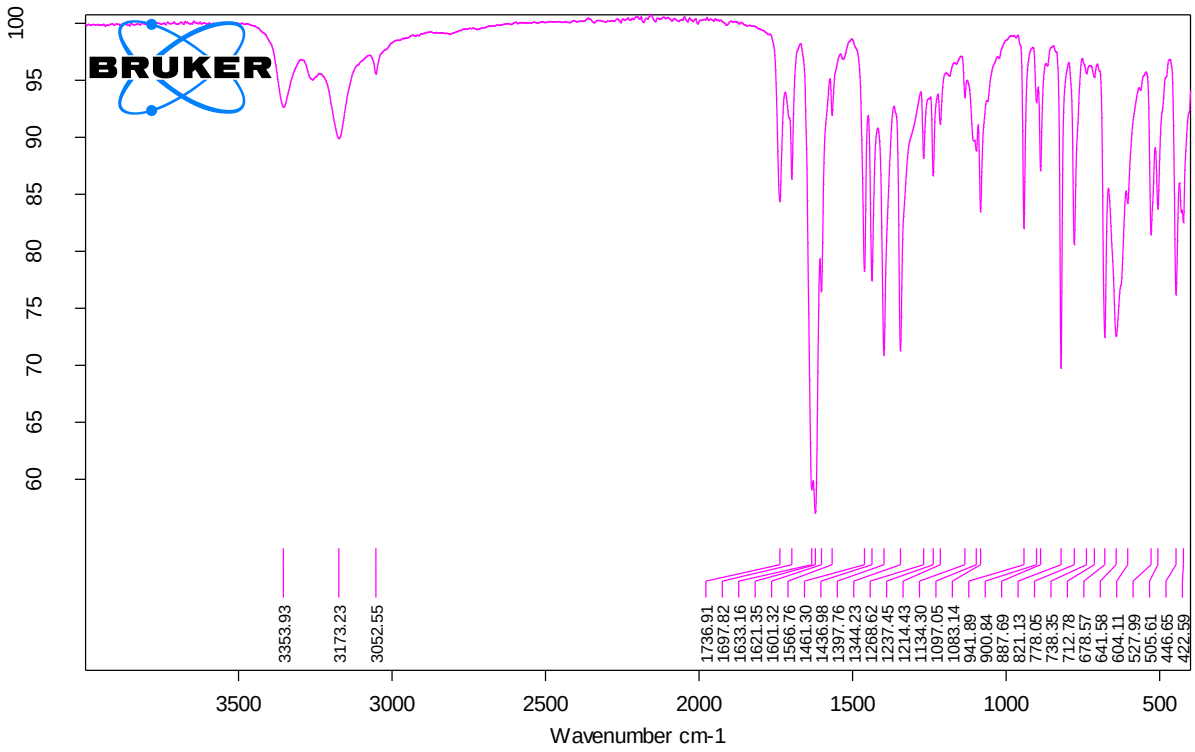

Figure 4.15: FT-IR spectrum of 6-bromochromone-2-carboxamide 22b.

4.1.3.3. Characterization of Cl-Chr-2-Carb (6-chlorochromone-2-carboxamide) 22c

6-chlorochromone-2-carboxamide **22c** compound was purified as yellowish crystal product and characterized by spectroscopic techniques as highlighted above. As observed on figure 4.16, the 1HNMR spectrum showed a doublet around 7.98 ppm with a coupling constant of 2 Hz which is due to the proton at carbon five (**C5**), a doublet of a doublet around 7.96 ppm with coupling constants of 2 Hz which is due to proton on carbon seven (**C7**). A doublet is observed around 7.789 ppm with a coupling constant of 8.8 Hz which is due to proton at carbon 8 (**C8**). A water peak appeared at 3.751 ppm due to the DMSO-d_6 NMR solvent used.

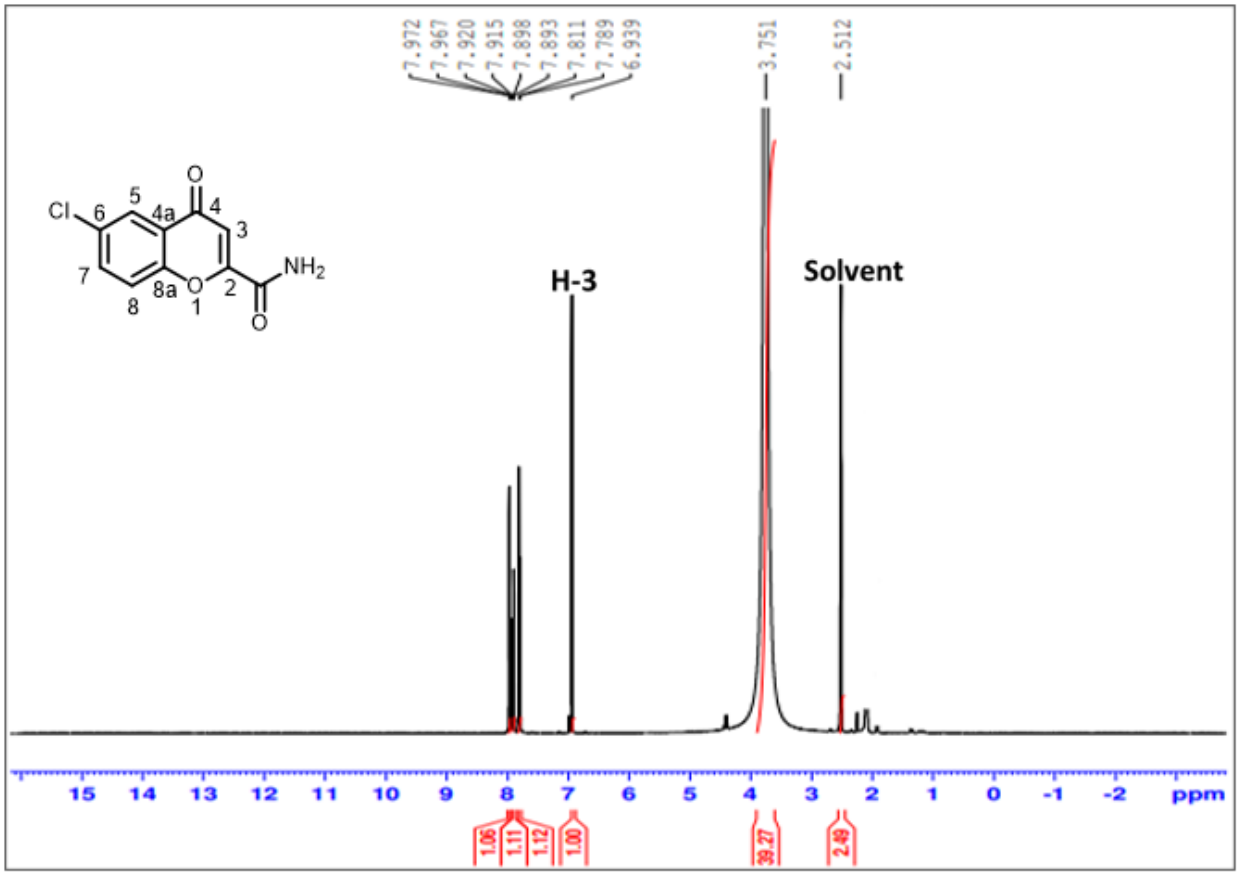

Figure 4.16: 400 MHz ^{1}H NMR spectrum of 6-chlorochromone-2-carboxamide **22c** in DMSO-d_6.

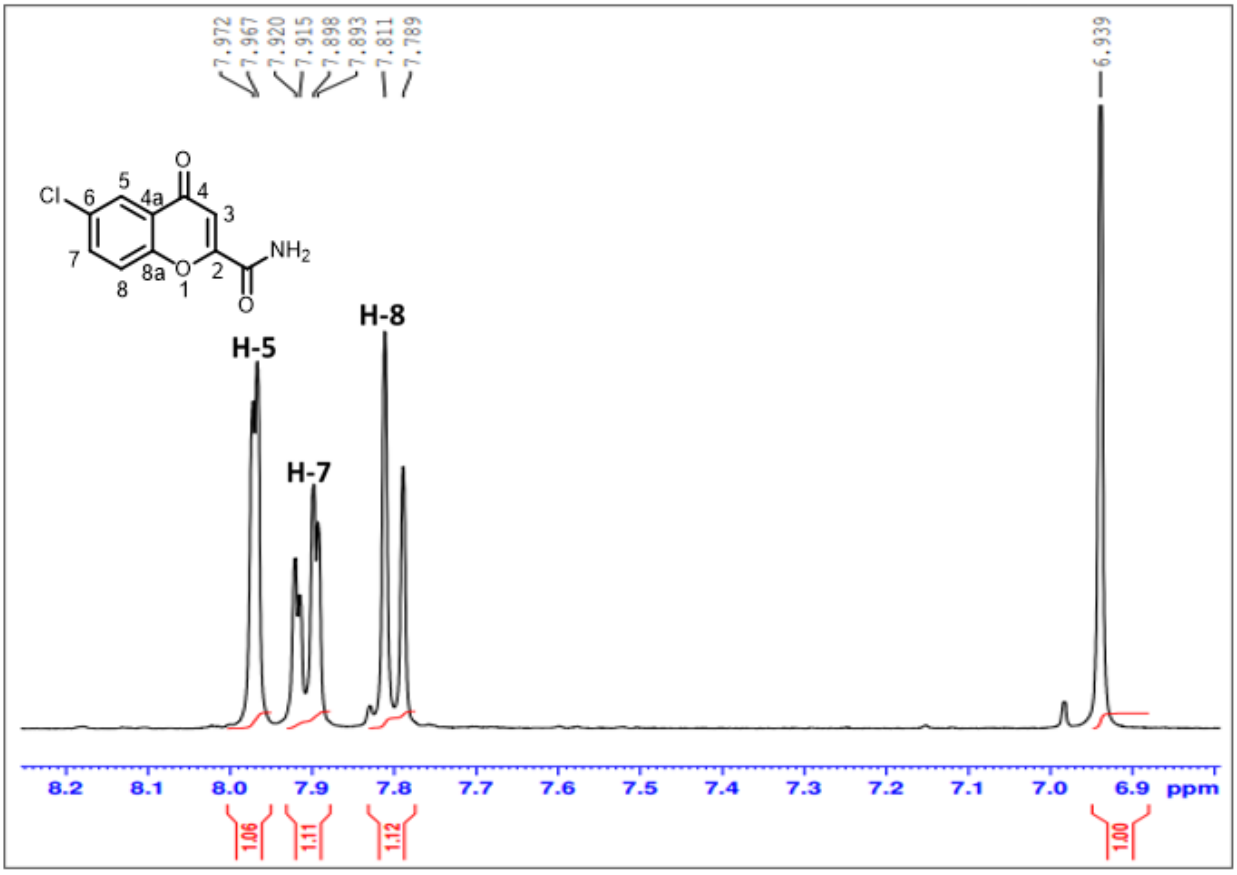

Figure 4.17: 400 MHz ^{1}H expansion NMR spectrum of 6-chlorochromone-2-carboxamide **22c** in DMSO-d_6.

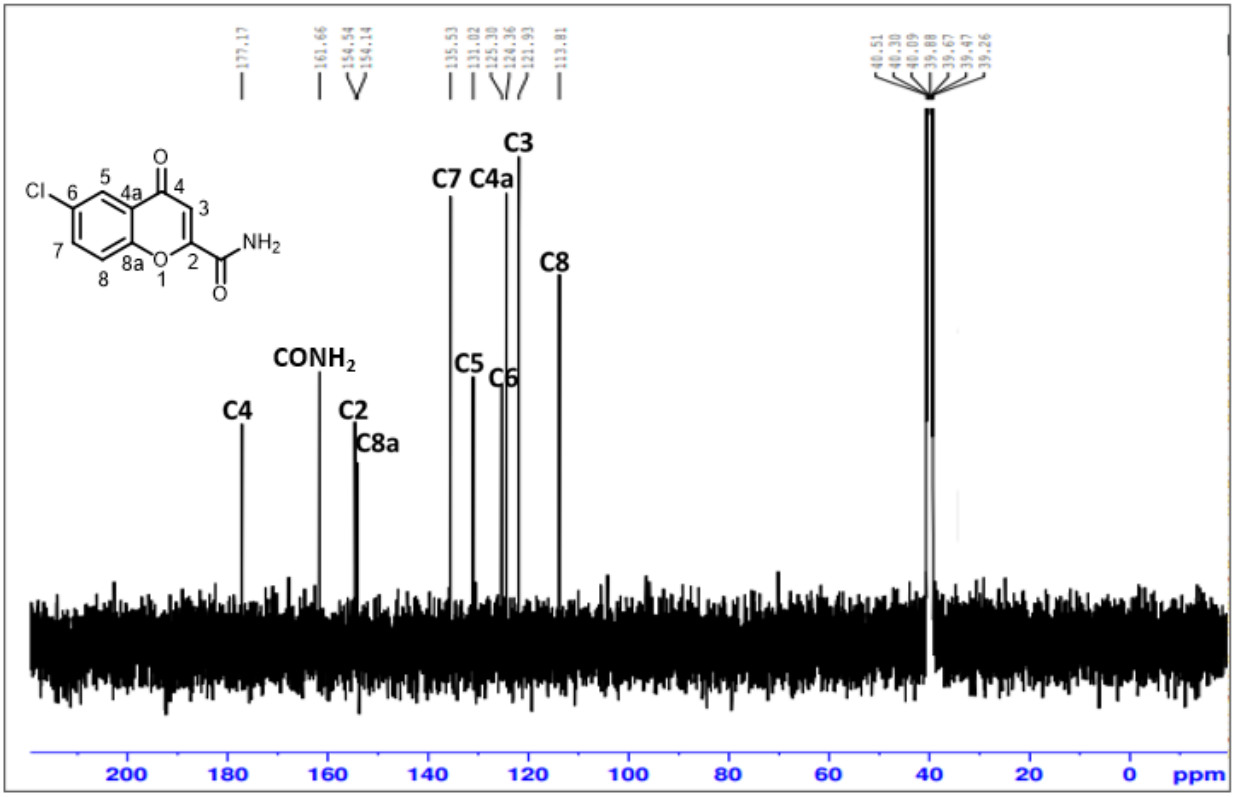

Figure 4.18: 100 MHz ^{13}C NMR spectrum of 6-chlorochromone-2-carboxamide **22c** in DMSO-$_{d6}$.

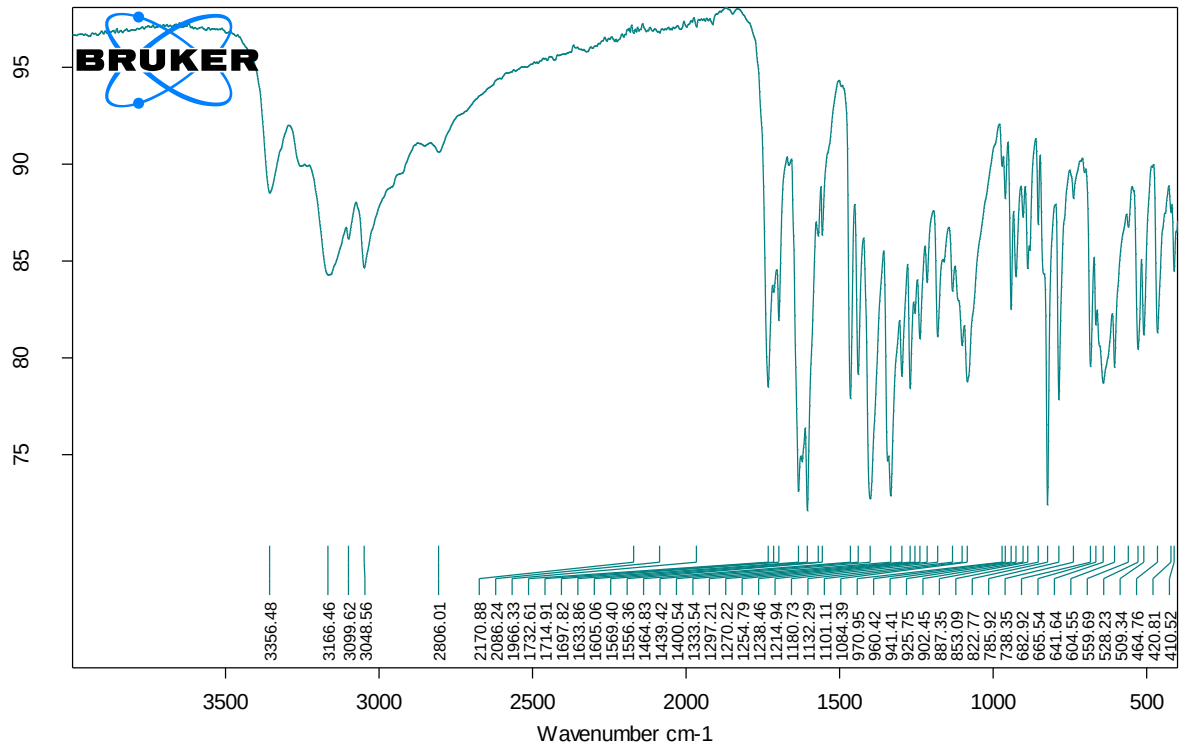

Figure 4.19: FT-IR spectrum of 6-chlorochromone-2-carboxamide 22c.

4.1.3.4. Characterization of CH_3O-Chr-2-Carb (6-methoxychromone-2-carboxamide) 22d

6-methoxychromone-2-carboxamide **22d** compound was purified as a green crystal product and characterized by spectroscopic techniques as highlighted above. As observed on figure 4.20, the 1HNMR spectrum showed a doublet at 7.686 and 7.709 ppm with a coupling constant of 9.2 Hz which is due to the proton at carbon 8 (**C8**), a doublet of doublet around 7.4 ppm with two coupling constants of 3.2 Hz which is due to proton on carbon seven (**C7**), a doublet at 7.396 and 7.404 ppm with a coupling constant of 3.2 Hz which is due to proton at carbon five (**C5**). A broad singlet water peak appeared around 5.9 ppm which is due to the DMSO-d_6 NMR solvent used. Furthermore, a singlet peak was observed at 7.947 ppm which is the NH_2 peak.

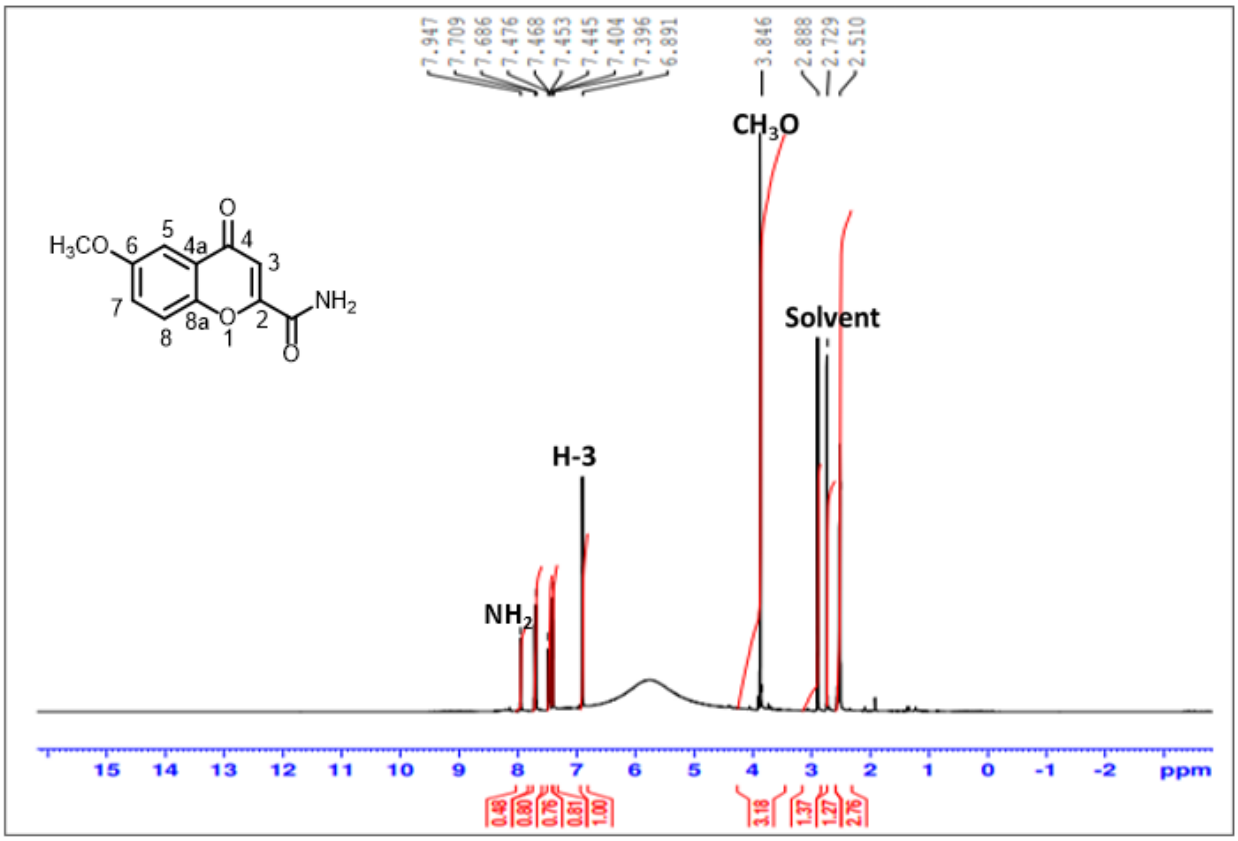

Figure 4.20: 400 MHz ^{1}H NMR spectrum of 6-methoxychromone-2-carboxamide **22d** in DMSO-d_6.

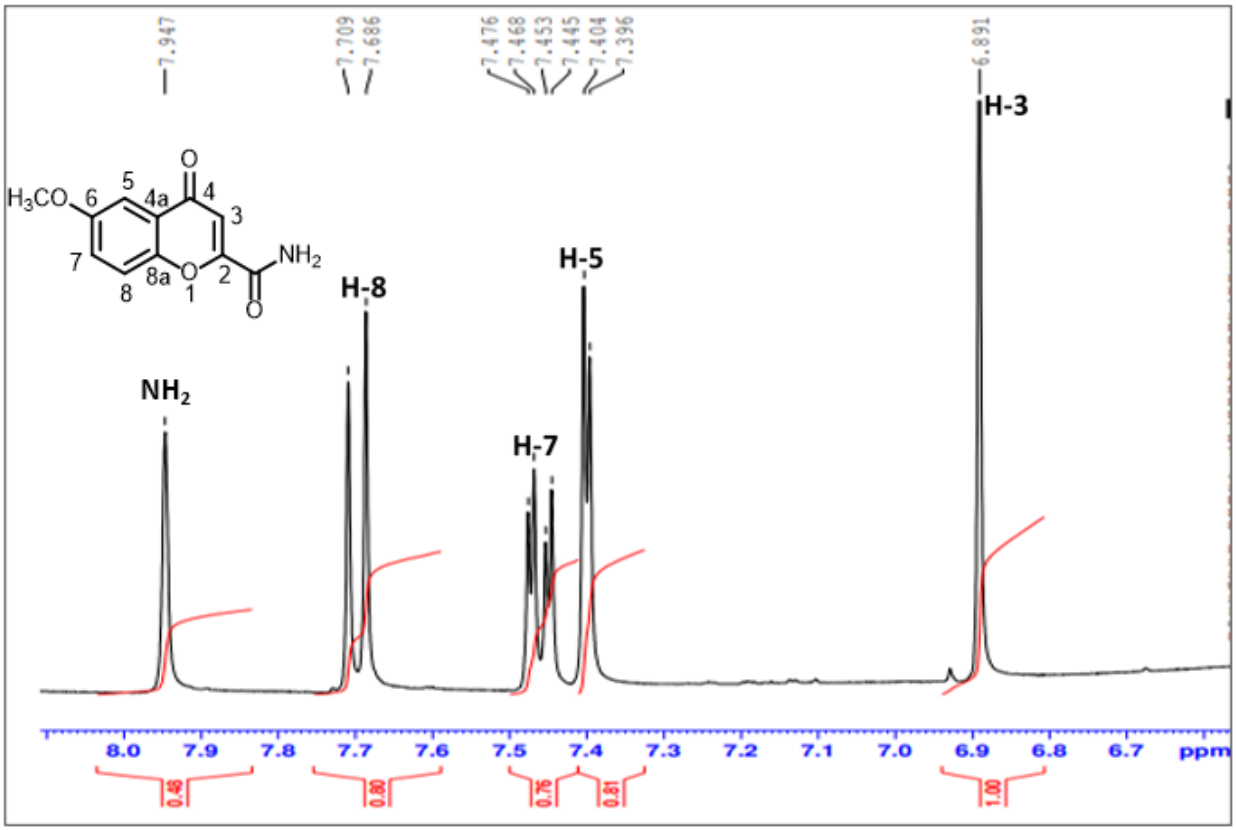

Figure 4.21: 400 MHz ^{1}H expansion NMR spectrum of 6-methoxychromone-2-carboxamide **22d** in DMSO-d_6.

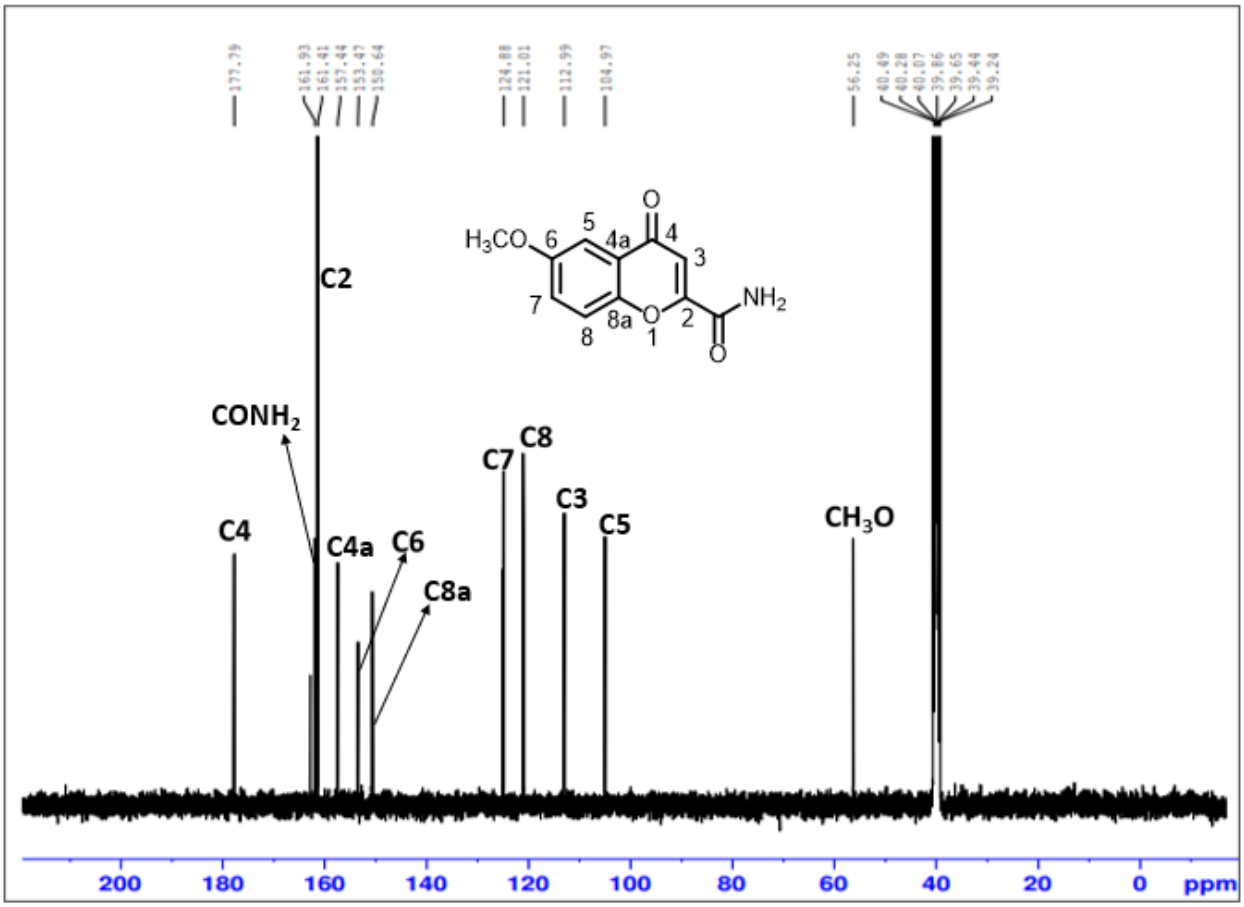

Figure 4.22: 100 MHz ^{13}C NMR spectrum of 6-methoxychromone-2-carboxamide **22d** in DMSO-d_6.

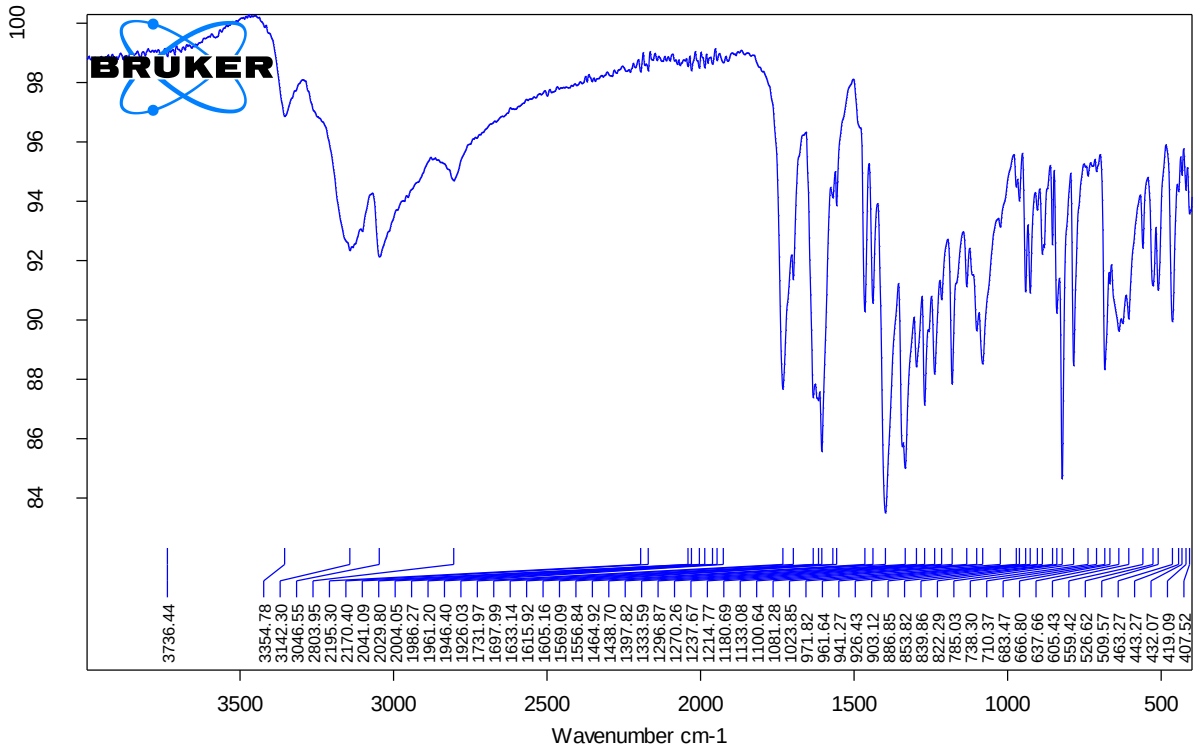

Figure 4.23: FT-IR spectrum of 6-methoxychromone-2-carboxamide 22d.

4.1.3.5. Characterization of NO_2-Chr-2-Carb (6-nitrochromone-2-carboxamide) 22e

The 6-nitrochromone-2-carboxamide **22e** compound was purified as a brown crystal product and characterized by spectroscopic techniques as mentioned above. As displayed in Figures 4.23 and 4.24, the ^{1}HNMR spectrum showed a doublet at 8.69 ppm with a coupling constant of 2.4 Hz which is due to the proton at carbon five (**C5**), a doublet of a doublet around 8.6 ppm with coupling constants of 2.8 Hz which is due to proton on carbon seven (**C7**). A doublet is observed at 7.9 ppm with a coupling constant of 9.2 Hz which is due to the proton at carbon 8 (**C8**). A water peak appeared at 4.152 ppm due to the DMSO-d_6 NMR solvent used.

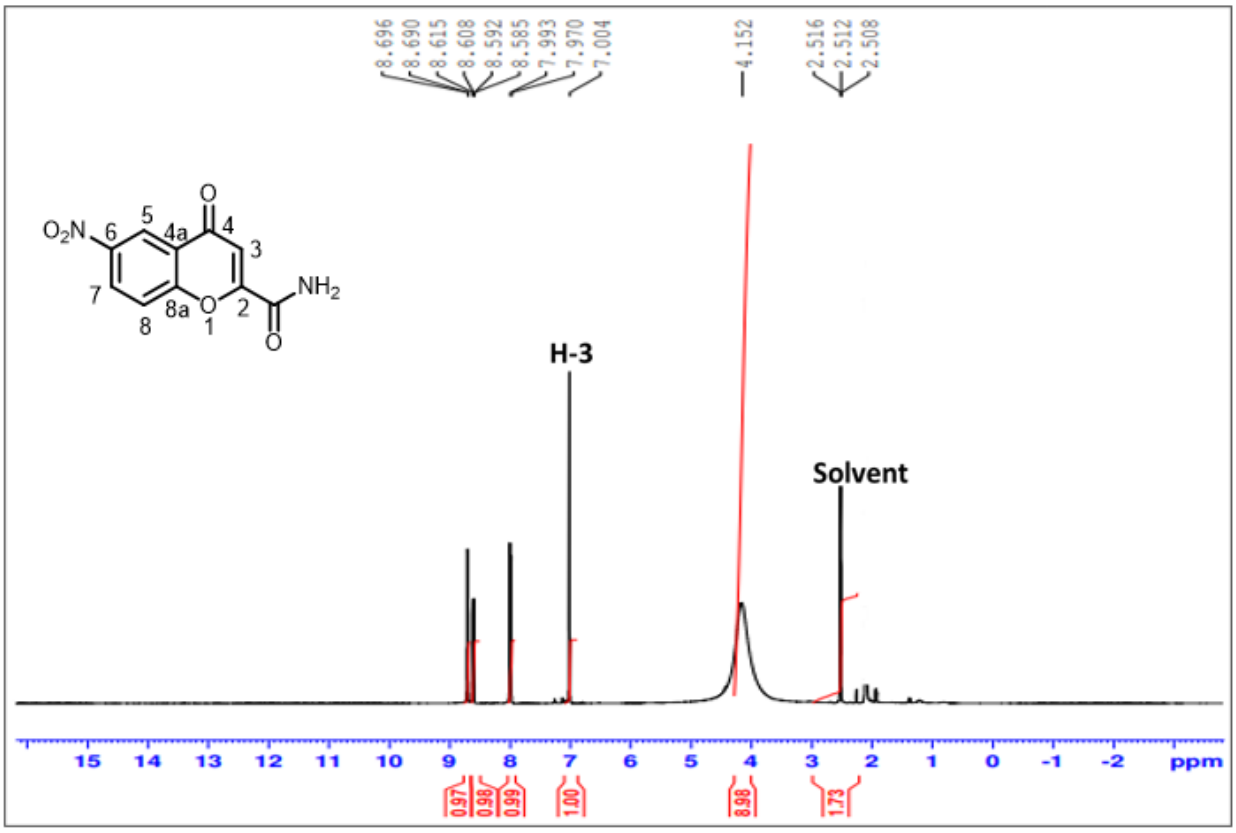

Figure 4.24: 400 MHz ^{1}H NMR spectrum of 6-nitrochromone-2-carboxamide **22e** in DMSO-d_6.

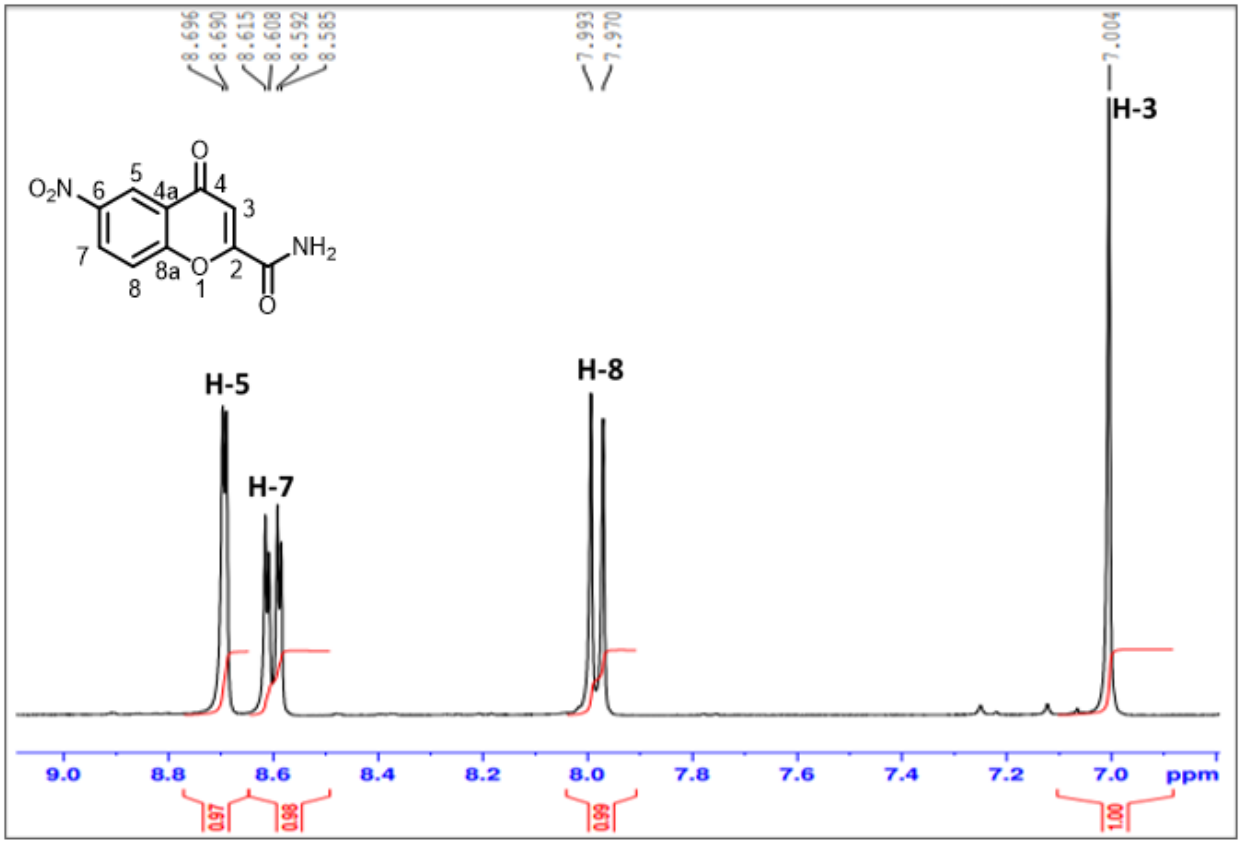

Figure 4.25: 400 MHz ^{1}H expansion NMR spectrum of 6-nitrochromone-2-carboxamide **22e** in DMSO-d_6.

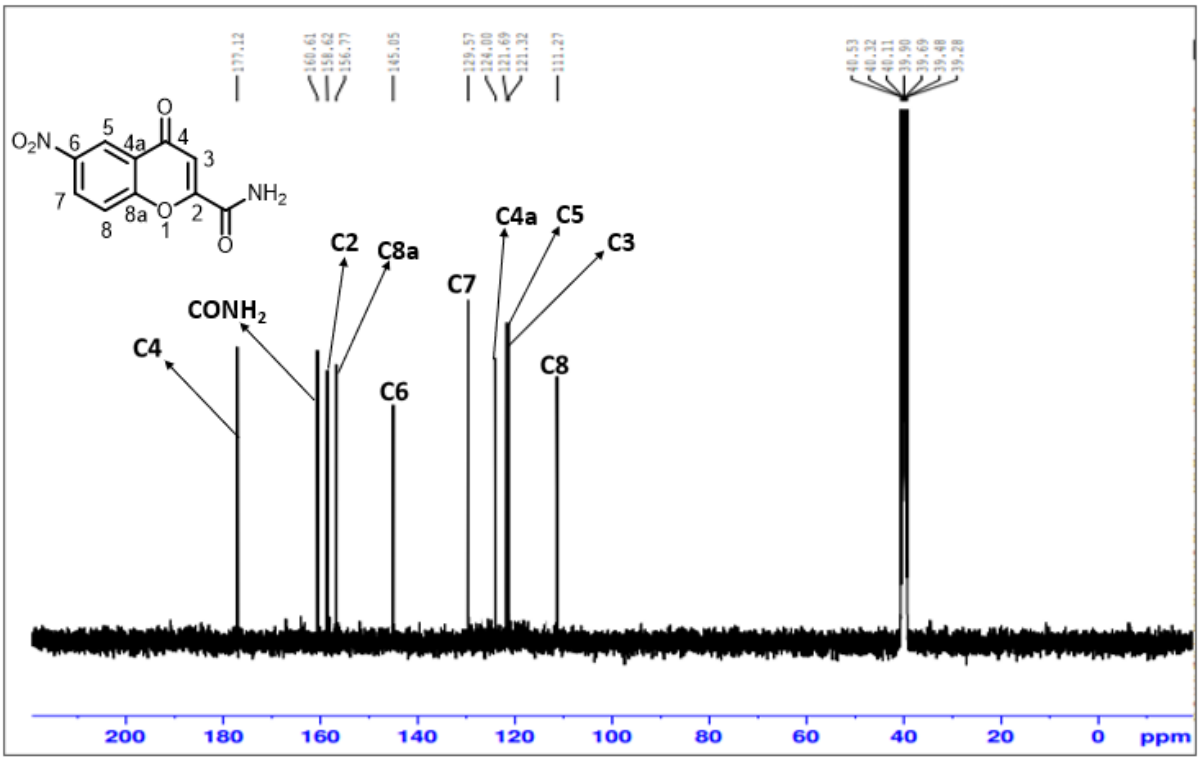

Figure 4.26: 100 MHz ^{13}C NMR spectrum of 6-nitrochromone-2-carboxamide **22e** in DMSO-d_6.

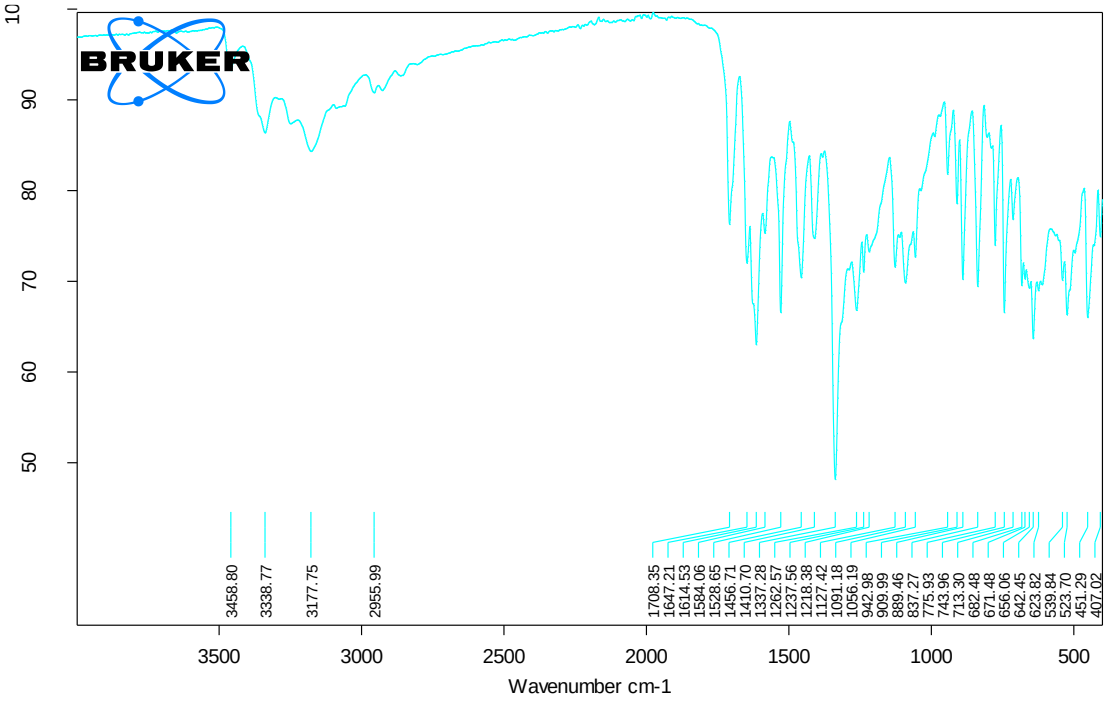

Figure 4.27: FT-IR spectrum of 6-nitrochromone-2-carboxamide 22e.

Table 4.6: ^{13}C NMR chemical shift values (ppm) of 6-substituted-chromone-2-carboxamides **22a-22e** in DMSO-d_6 (at 100 MHz).

Nucleus	a (X=H)	b (X=Br)	C (X=Cl)	d (X=OCH_3)	E (X=NO_2)
$CONH_2$	161.86	161.66	161.66	161.93	160.61
C-2	155.90	154.91	154.54	161.41	158.62
C-3	119.32	122.07	121.93	112.99	121.32
C-4	178.08	176.99	177.17	177.79	177.12
C-4a	125.37	125.67	157.44	124.88	124.57
C-5	126.52	127.48	131.02	104.97	121.69
C-6	124.17	118.98	125.30	153.47	145.05
C-7	135.64	138.23	124.88	157.44	129.57
C-8	113.93	113.93	113.81	121.01	111.27
C-8a	153.71	154.07	154.14	150.64	156.77
OCH_3	-	-	-	56.25	-

Table 4.7: Peaks identified from FTIR spectra of the synthesized 6-substituted chromone-2-carboxamides **22a-22e**.

Inhibitor	Functional Groups Peaks obtained from FTIR spectra (cm^{-1})				
	$CONH_2$	NH_2	Ar (C=C)	Ar (C-O)	=C-H
Chr-2-Carb **22a**	1730.90	3355.77	1568.92 – 1633.22	1697.92	3137.80
6-Br-2-Carb **22b**	1736.91	3353.93	1566.76 – 1633.16	1697.82	3173.23
6-Chl-2-Carb **22c**	1732.61	3356.48	1569.40 – 1633.86	1697.82	3166.46
6-Met-2-Carb **22d**	1731.97	3354.78	1569.09 – 1633.14	1697.99	3142.30
6-Nit-2-Carb **22e**	1708.35	3458.80	1584.06 – 1614.53	1647.21	3177.75

4.2. Mild steel

4.2.1. Gravimetric analysis (GA) in the absence and presence of corrosion inhibitors

In general, variation in temperature has a strong influence on the rate of corrosion of metals; that is, an increase in temperature increases the reaction rate due to an increase in corrosion rate [232]. The results for the corrosion test in blank and in the presence various concentrations of 6-Substituted chromone-2-carboxamide derivatives are graphically depicted in Figures 4.27 – 4.31 and Table 4.8. Figures 4.27 – 4.31 show the weight loss measurements of mild steel in the absence and presence of the five synthesized inhibitors under different temperatures. It is seen in Table 4.8 that the weight loss increases as the temperature increase, and it decreases as the increase in concentration of the 6-Substituted chromone-2-carboxamide derivatives. Such findings indicate that these compounds are effectively protecting the mild steel from the acid attack. It is evident from the weight loss data that theses inhibitors are more effective in the lower temperatures, and a similar trend is observed in all the five synthesized compounds interacting with the mild steel surface. The data on table 4.8 shows that indeed the 6-Substituted chromone-2-carboxamide derivatives created a barrier for the corrosion process on the mild steel surface.

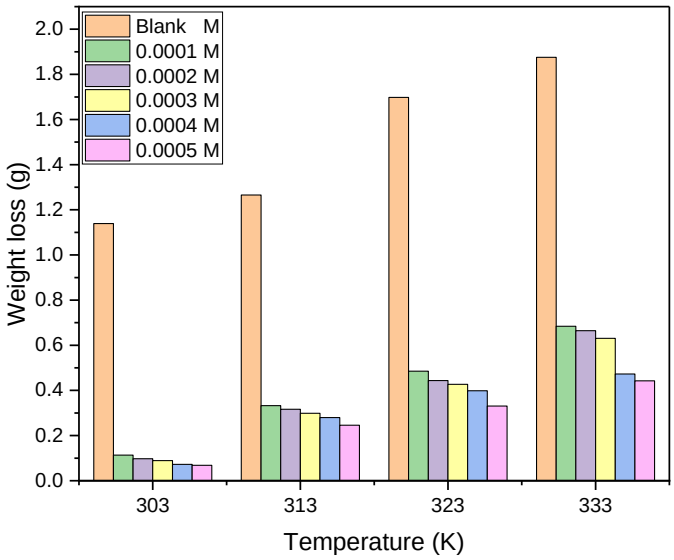

Figure 4.28: The graph showing the weight loss measurements of mild steel in the absence and presence of Chr-2-Carb in 1.5 M HCl.

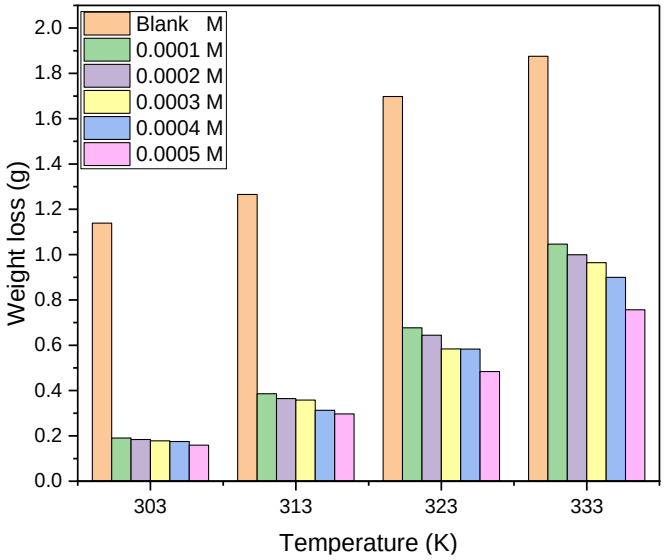

Figure 4.29: The graph showing the weight loss measurements of mild steel in the absence and presence of Br- Chr-2-Carb in 1.5 M HCl.

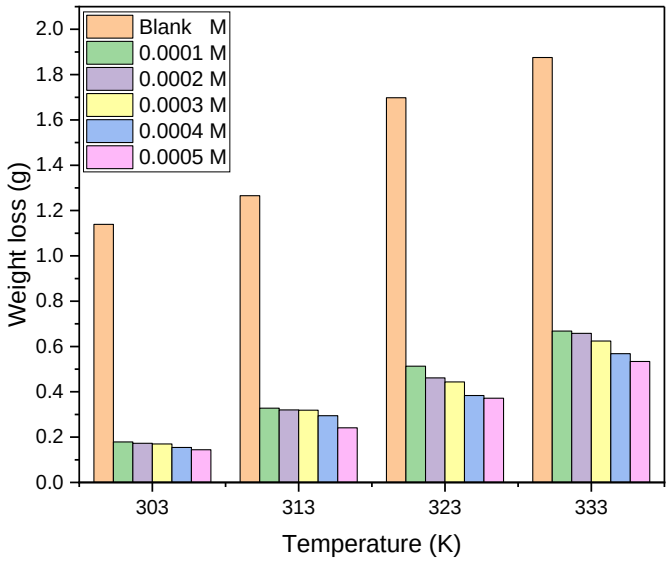

Figure 4.30: The graph showing the weight loss measurements of mild steel in the absence and presence of Cl- Chr-2-Carb in 1.5 M HCl.

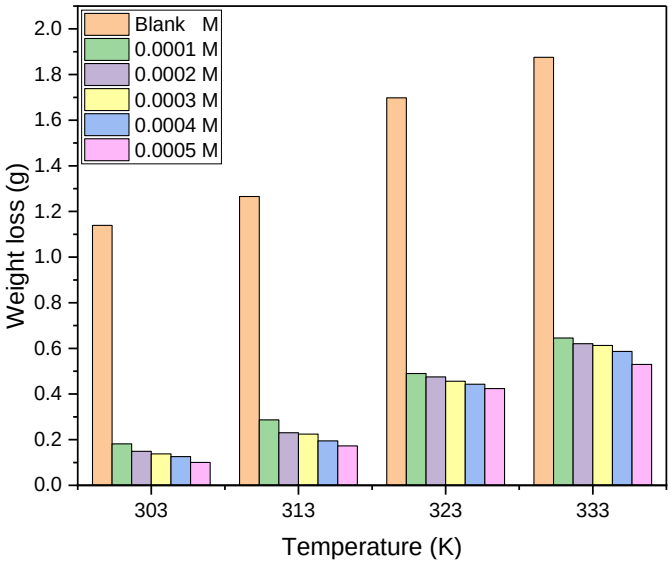

Figure 4.31: The graph showing the weight loss measurements of mild steel in the absence and presence of CH_3O-Chr-2-Carb in 1.5 M HCl.

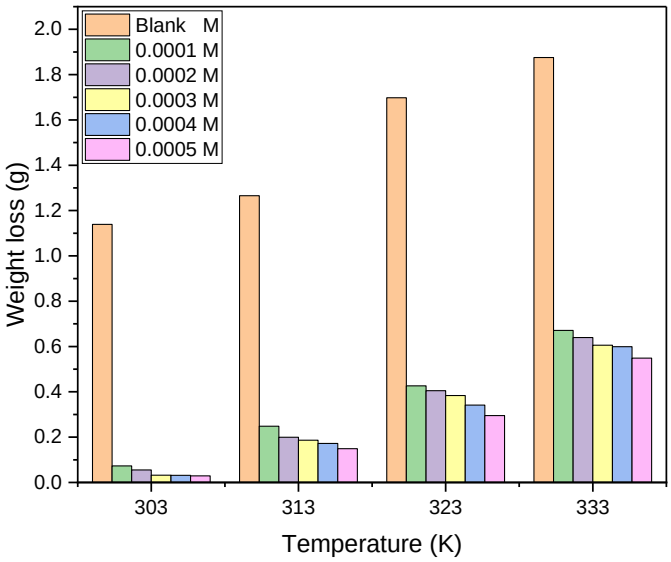

Figure 4.32: The graph showing the weight loss measurements of mild steel in the absence and Presence of NO_2-Chr-2-Carb in 1.5 M HCl.

Table 4.8: Weight loss measurements of mild steel in the absence and presence of 6-Substituted chromone-2-carboxamides in 1.5 M HCl

Inhibitor	Concentration ($x10^{-4}$ M)	Weight loss (g)			
		303 K	313 K	323 K	333 K
	0.0000	1.1391	1.2657	1.6978	1.8754
Chr-2-Carb	1.0	0.1133	0.3328	0.4851	0.6844
	2.0	0.0973	0.3164	0.4437	0.6643
	3.0	0.0892	0.2989	0.4271	0.6310
	4.0	0.0724	0.2798	0.3983	0.4727
	5.0	0.0683	0.2460	0.3308	0.4423
Br-Chr-2-Carb	1.0	0.1909	0.3861	0.6772	1.0463
	2.0	0.1839	0.3644	0.6446	0.9998

	3.0	0.1780	0.3583	0.5835	0.9645
	4.0	0.1754	0.3130	0.5831	0.9000
	5.0	0.1589	0.2971	0.4842	0.7567
Cl-Chr-2-Carb	1.0	0.1788	0.3280	0.5130	0.6681
	2.0	0.1731	0.3204	0.4615	0.6579
	3.0	0.1697	0.3189	0.4439	0.6243
	4.0	0.1544	0.2948	0.3836	0.5685
	5.0	0.1443	0.2412	0.3718	0.5342
CH_3O-Chr-2-Carb	1.0	0.1816	0.2871	0.4901	0.6455
	2.0	0.1492	0.2306	0.4753	0.6205
	3.0	0.1377	0.2245	0.4563	0.6130
	4.0	0.1262	0.1949	0.4431	0.5868
	5.0	0.1004	0.1731	0.4243	0.5296
NO_2-Chr-2-Carb	1.0	0.0728	0.2483	0.4262	0.6713
	2.0	0.0550	0.1997	0.4050	0.6397
	3.0	0.0319	0.1864	0.3837	0.6056
	4.0	0.0312	0.1724	0.3417	0.5990
	5.0	0.0292	0.1489	0.2953	0.5487

4.2.2. Corrosion rate and inhibition efficiency

The corrosion rate (C_R) and %IE on mild steel (MS) in the absence (blank) and presence of various concentrations of 6-substituted chromone-2-carboxamide derivatives in 1.5 M HCl solution and at various temperatures, 30 °C to 60 °C (303 to 333 K) are presented in Table 4.9. From the results mentioned in table 4.6 it has been noted that the addition of 6-Substituted chromone-2-carboxamide derivatives led to the decrease in the corrosion rate of MS while the percentage inhibitory efficiency (%IE) increases with the increase in the concentration of the inhibitors. The effect of temperatures (30 K to 60 K) and

concentrations (1.0×10^{-4} M to 5.0×10^{-4} M) on the corrosion inhibition of the 6-Substituted chromone-2-carboxamide is clearly shown in the same table. Moreover, figure 4.33 – 4.37 reveal that the %IE increases as the concentration of all five inhibitors are increased. Noticeable, figures reveal that, at the lowest concentration of the inhibitors (1.0×10^{-4} M) at lower temperature (303 K) the percentage inhibition efficiency (%IE) for Chr-2-Carb, Br-Chr-2-Carb, Cl-Chr-2-Carb, CH_3O-Chr-2-Carb and NO_2-Chr-2-Carb was obtained to be 90.00, 83.24, 84.30, 84.06 and 93.61% respectively. However, when the inhibitor concentration was raised to 5.0×10^{-5} M at the same lower temperature (303 K) the %IE for Chr-2-Carb, Br-Chr-2-Carb, Cl-Chr-2-Carb, CH_3O-Chr-2-Carb and NO_2-Chr-2-Carb attained the highest levels of performance of 94.00, 86.05, 87.33, 91.19 and 97.44%, indicating high inhibitive potential of these inhibitors. Noticeable, the %IE of NO_2-Chr-2-Carb is 97.44% at 303 K and drops to 70.74% at 333 K for the highest concentration of 5.0×10^{-5} M. This is noted for all of the inhibitors investigated. The inhibitors' protective characteristics are achievable as a result of the existence aromatic ring (aromaticity), pie-electrons and heteroatoms with positively charged MS surfaces). At all temperatures tested, the synthesized 6-Substituted chromone-2-carboxamides had the highest inhibitory efficacy at 5.010^{-4} M. The weight loss in the blank (uninhibited solution) was greater and observed to diminish at a faster rate as the temperature of the solution rose from 303 to 333 K.

At all temperatures tested, the C_R was much higher in the uninhibited solution. The maximum C_R was spotted at the solution's highest temperature (333 K), which also happened to be the temperature with the lowest %IE. fortunately, the corrosion rate was reduced promptly when the inhibitor was added to the acid solution. For example, at 303 K, the C_R of MS in the absence of the synthesized 6-Substituted chromone-2-carboxamides was 0.02373 $g.cm^{-2}.h^{-1}$. Table 4.6 clearly shows that at the same temperature (303 K), the corrosion rate decreased significantly after the addition of the 6-Substituted chromone-2-carboxamides, and this behavior is noticed across all temperatures studied. At 303 K, the C_R for 6-Nit-2-Carb fell considerably to 0.00151 $g.cm^{-2}.h^{-1}$ at the lowest inhibitor concentration and to 0.000608 $g.cm^{-2}.h^{-1}$ at the highest inhibitor concentration. In corrosive environment, elevated temperatures frequently accelerate the metal dissolution rate of reaction and

weakens the adsorption tendency of inhibitors on metallic surface [232]. This statement supports the findings of the study.

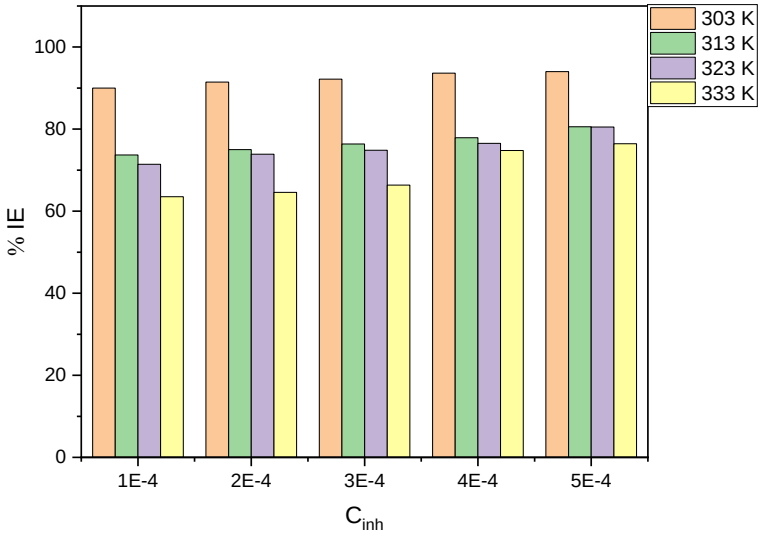

Figure 4.33: The graph of percentage inhibition efficiency with various concentrations of Chr-2-Carb at various temperatures in 1.5 M HCl.

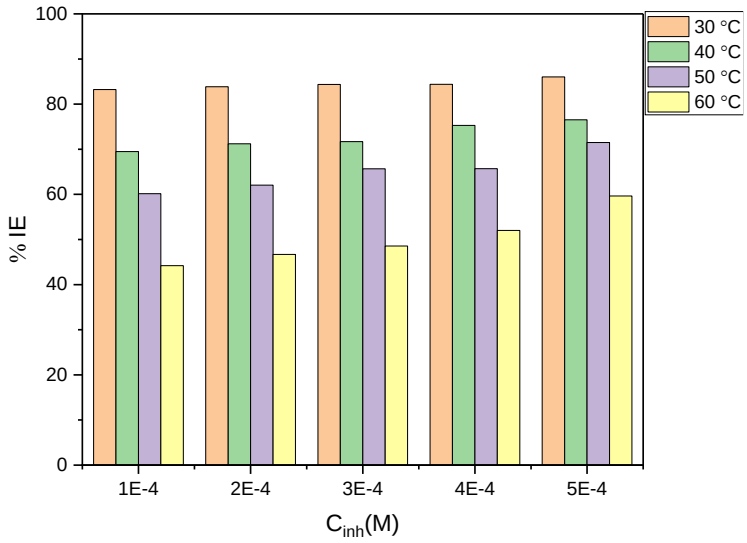

Figure 4.34: The graph of percentage inhibition efficiency with various concentrations of Br-Chr-2-Carb at various temperatures in 1.5 M HCl.

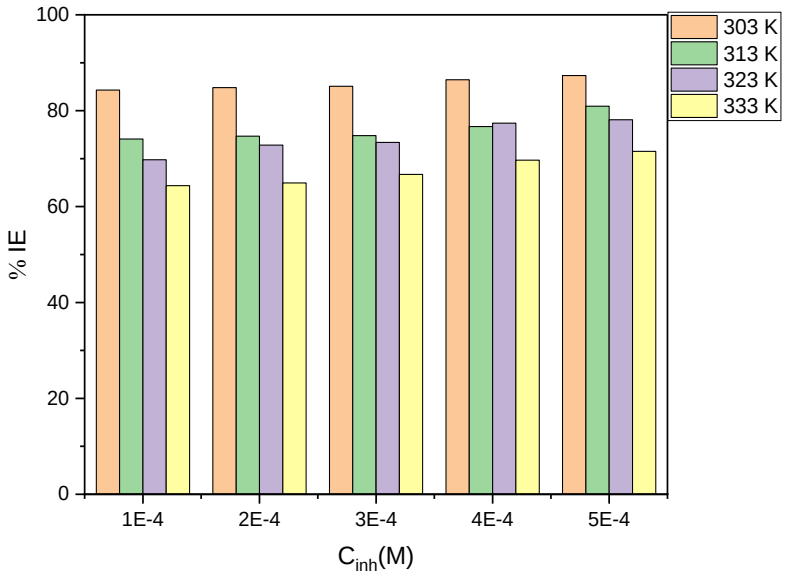

Figure 4.35: The graph of percentage inhibition efficiency with various concentrations of Cl-Chr-2-Carb at various temperatures in 1.5 M HCl.

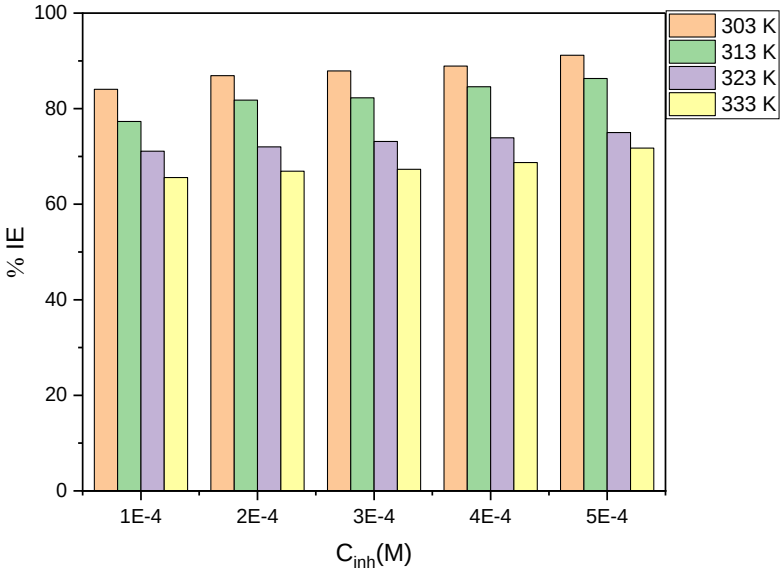

Figure 4.36: The graph of percentage inhibition efficiency with various concentrations of CH_3O-Chr-2-Carb at various temperatures in 1.5 M HCl.

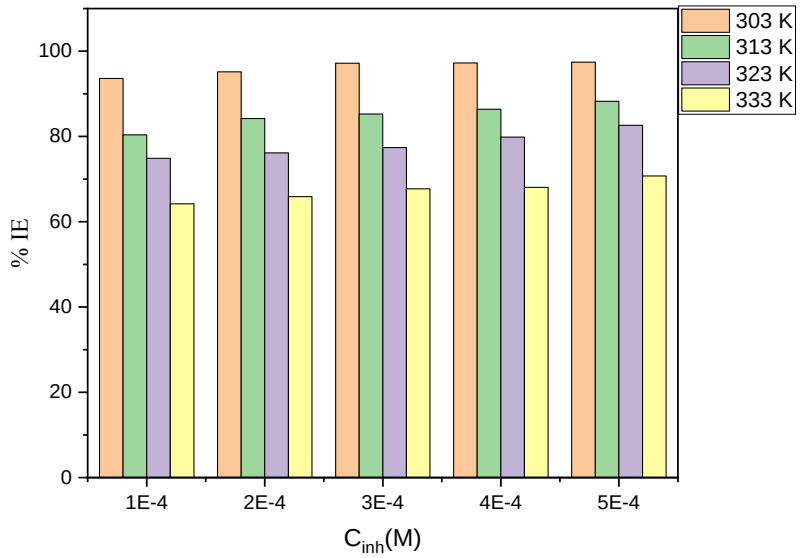

Figure 4.37: The graph of percentage inhibition efficiency with various concentrations of NO_2-Chr-2-Carb at various temperatures in 1.5 M HCl.

Table 4.9: The corrosion parameters for mild steel in 1.5 M HCl in the absence and presence of various concentrations of Chr-2-Carb obtained from weight loss measurements at 303 – 333 K.

Inhibitor	Temperature (K)	Inhibitor concentration ($x10^{-4}$ M)	Corrosion rate ($g.cm^{-2}.h^{-1}$)	Surface coverage (θ)	Inhibition efficiency (%)
	303	-	0.02373	-	-
		1.0	0.00236	0.9000	90.00
		2.0	0.00202	0.9146	91.46
		3.0	0.00186	0.9217	92.17
		4.0	0.00151	0.9364	93.64
		5.0	0.00142	0.9400	94.00
	313	-	0.02637	-	-
		1.0	0.00693	0.7371	73.71
		2.0	0.00659	0.7500	75.00
		3.0	0.00623	0.7638	76.38

Chr-2-Carb		4.0	0.00583	0.7789	77.89
		5.0	0.00513	0.8056	80.56
	323	-	0.03537	-	-
		1.0	0.01011	0.7143	71.43
		2.0	0.00924	0.7387	73.87
		3.0	0.00889	0.7484	74.84
		4.0	0.00829	0.7654	76.54
		5.0	0.00689	0.8052	80.52
	333	-	0.03907	-	-
		1.0	0.01426	0.6351	63.51
		2.0	0.01384	0.6458	64.58
		3.0	0.01314	0.6635	66.35
		4.0	0.00985	0.7479	74.79
		5.0	0.00921	0.7642	76.42

Table 4.10: The corrosion parameters for mild steel in 1.5 M HCl in the absence and presence of various concentrations of Br-Chr-2-Carb obtained from weight loss measurements at 303 – 333 K.

Inhibitor	**Temperature (K)**	**Inhibitor concentration ($x10^{-4}$ M)**	**Corrosion rate ($g.cm^{-2}.h^{-1}$)**	**Surface coverage (θ)**	**Inhibition efficiency (%)**
	303	-	0.02373	-	-
		1.0	0.00398	0.8324	83.24
		2.0	0.00383	0.8385	83.85
		3.0	0.00371	0.8437	84.37
		4.0	0.00370	0.8460	84.60
		5.0	0.00313	0.8605	86.05

Br-Chr-2-Carb					
	313	-	0.02637	-	-
		1.0	0.00804	0.6949	69.49
		2.0	0.00759	0.7120	71.20
		3.0	0.00746	0.7169	71.69
		4.0	0.00652	0.7527	75.27
		5.0	0.00619	0.7653	76.53
	323	-	0.03537	-	-
		1.0	0.01411	0.6014	60.14
		2.0	0.01343	0.6206	62.06
		3.0	0.01216	0.6566	65.66
		4.0	0.01215	0.6569	65.69
		5.0	0.01009	0.7150	71.50
	333	-	0.03907	-	-
		1.0	0.02179	0.4421	44.21
		2.0	0.02083	0.4669	46.69
		3.0	0.02009	0.4857	48.57
		4.0	0.01875	0.5201	52.01
		5.0	0.01576	0.5965	59.65

Table 4.11: The corrosion parameters for mild steel in 1.5 M HCl in the absence and presence of various concentrations of Cl-Chr-2-Carb obtained from weight loss measurements at 303 – 333 K.

Inhibitor	Temperature (K)	Inhibitor concentration ($x10^{-4}$ M)	Corrosion rate ($g.cm^{-2}.h^{-1}$)	Surface coverage (θ)	Inhibition efficiency (%)
Cl-Chr-2-Carb	303	-	0.02373	-	-
		1.0	0.00373	0.8430	84.30
		2.0	0.00361	0.8480	84.80
		3.0	0.00354	0.8510	85.10
		4.0	0.00322	0.8645	86.45
		5.0	0.00301	0.8733	87.33
	313	-	0.02637	-	-
		1.0	0.00683	0.7409	74.09
		2.0	0.00668	0.7469	74.69
		3.0	0.00664	0.7480	74.80
		4.0	0.00614	0.7671	76.71
		5.0	0.00503	0.8094	80.94
	323	-	0.03537	-	-
		1.0	0.01070	0.6978	69.78
		2.0	0.00961	0.7282	72.82
		3.0	0.00925	0.7339	73.39
		4.0	0.00799	0.7741	77.41
		5.0	0.00775	0.7810	78.10

	333	-	0.03907	-	-
		1.0	0.01392	0.6438	64.38
		2.0	0.01370	0.6492	64.92
		3.0	0.01300	0.6671	66.71
		4.0	0.01180	0.6967	69.67
		5.0	0.01110	0.7152	71.52

Table 4.12: The corrosion parameters for mild steel in 1.5 M HCl in the absence and presence of various concentrations of CH_3O-Chr-2-Carb obtained from weight loss measurements at 303 – 333 K.

Inhibitor	**Temperature (K)**	**Inhibitor concentration ($x10^{-4}$ M)**	**Corrosion rate ($g.cm^{-2}.h^{-1}$)**	**Surface coverage (θ)**	**Inhibition efficiency (%)**
CH_3O-Chr-2-Carb	303	-	0.02373	-	-
		1.0	0.00378	0.8406	84.06
		2.0	0.00311	0.8690	86.90
		3.0	0.00287	0.8791	87.91
		4.0	0.00269	0.8892	88.92
		5.0	0.00209	0.9119	91.19
	313	-	0.02637	-	-
		1.0	0.00598	0.7732	77.32
		2.0	0.00480	0.8178	81.78
		3.0	0.00468	0.8226	82.26
		4.0	0.00406	0.8460	84.60
		5.0	0.00361	0.8632	86.32
		-	0.03537	-	-
		1.0	0.01012	0.7111	71.11

	323	2.0	0.00990	0.7200	72.00
		3.0	0.00951	0.7312	73.12
		4.0	0.00923	0.7390	73.90
		5.0	0.00884	0.7500	75.00
	333	-	0.03907	-	-
		1.0	0.01344	0.6558	65.58
		2.0	0.01293	0.6691	66.91
		3.0	0.01277	0.6731	67.31
		4.0	0.01223	0.6871	68.71
		5.0	0.01103	71.76	71.76

Table 4.13: The corrosion parameters for mild steel in 1.5 M HCl in the absence and presence of various concentrations of NO_2-Chr-2-carb obtained from weight loss measurements at 303 – 333 K.

Inhibitor	**Temperature (K)**	**Inhibitor concentration ($x10^{-4}$ M)**	**Corrosion rate ($g.cm^{-2}.h^{-1}$)**	**Surface coverage (θ)**	**Inhibition efficiency (%)**
NO_2-Chr-2-Carb	303	-	0.02373	-	-
		1.0	0.00151	0.9361	93.61
		2.0	0.00115	0.9517	95.17
		3.0	0.000646	0.9719	97.19
		4.0	0.000650	0.9726	97.26
		5.0	0.000608	0.9744	97.44
	313	-	0.02637	-	-
		1.0	0.00517	0.8038	80.38
		2.0	0.00416	0.8422	84.22
		3.0	0.00388	0.8527	85.27

		4.0	0.00359	0.8638	86.38
		5.0	0.00310	0.8824	88.24
	323	-	0.03537	-	-
		1.0	0.00888	0.7489	74.89
		2.0	0.00844	0.7615	76.15
		3.0	0.00799	0.7740	77.40
		4.0	0.00712	0.7987	79.87
		5.0	0.00615	0.8261	82.61
	333	-	0.03907	-	-
		1.0	0.01399	0.6420	64.20
		2.0	0.01333	0.6589	65.89
		3.0	0.01262	0.6771	67.71
		4.0	0.01248	0.6806	68.06
		5.0	0.01143	0.7074	70.74

4.2.3. Thermodynamic parameters: adsorption Isotherms

Adsorption isotherms signify the type of interaction between 6-substituted chromone-2-carboxamide inhibitor molecules and the surfaces of the used metals (mild steel, zinc and aluminum) substrates. Adsorption Isotherms are used to demonstrate the corrosion inhibition process (how the inhibitor adsorbs) on the metal surface. Adsorption isotherms play a vital role in studying the mechanism of an electrochemical reaction. When the organic inhibitors adsorbed on the metal surface they replaced or substitute the water molecules absorbed in aqueous solution as shown in the equation below [233, 234].

$$Org_{(sol)} + {}_nH_2O_{(ads)} \longrightarrow Org_{(ads)} + {}_nH_2O_{(sol)} \quad (33)$$

where n is the size ratio which represent the number of water molecules replaced by one molecule of the synthesized organic inhibitor.

Various adsorption isothermal principles such as Langmuir, Frumkin, and Temkin-Parsons were employed (fitted) in this work. The Langmuir adsorption isotherm emerged to be the best fit, with the best regression coefficient values (R^2 value) near unity. The regression coefficient values found through utilizing Langmuir adsorption isotherm in this research work are displayed in Table 4.14 below. Due to the fact that Langmuir adsorption isotherm is based on the notion that each metal site has the responsibility to hold one adsorbed species, one adsorbed H_2O molecule is replaced by one molecule of the inhibitor substance on the metal's surface. Langmuir adsorption isotherm is represented by the following equation below:

$$\frac{C_{inh}}{\theta} = \frac{1}{K_{ads}} + C_{inh}. \quad (34)$$

where C_{ihn} is the inhibitor concentration, θ is the surface coverage and K_{ads} equilibrium constant of adsorption.

From the Langmuir adsorption isotherm plots below, the values of equilibrium constant (K_{ads}) were calculated from the intercepts and the standard Gibb's free energy ($\Delta G°$) values were then calculated from the K_{ads} values utilizing equation (35).

$$\Delta G°_{ads} = -RT\ln(K_{ads}) \quad (35)$$

R denotes gas constant, T is absolute temperature, 55.5 denotes the molar concentration of water in the solution, $\Delta G°_{ads}$ represents the standard Gibb's free energy of adsorption and K_{ads} denotes the equilibrium constant of adsorption of the inhibitor on the metal.

The calculated values of K_{ads} and $\Delta G°_{ads}$ for mild steel in 1.5 M HCl in the presence of the studied 6-substituted chromone-2-carboxamides are listed in Table 4.24. The equilibrium constant of adsorption (K_{ads}) denotes the degree of interaction between the inhibitor molecules and the metal's surface. Furthermore, the literature reveals that high K_{ads} values indicate stronger binding power [235, 236]. The high values of K_{ads} found in this study indicate that the 6-substituted chromone-2-carboxamides inhibitors adsorb strongly on the mild steel surface. At the lower temperature (303 K) the K_{ads} values were higher (decreasing with the increase in temperature) signifying that the inhibitors were adsorb strongly on the MS surface in lower temperatures.

The $\Delta G°_{ads}$ values reflect a kind of adsorption that occurs on the metal surface. It helps researchers to deduce the type of interaction occurring between the inhibitors and the metal surface (physisorption, chemisorption or mixed-type adsorption). According to the literature, values of $\Delta G°_{ads}$ around -20 kJ/mol or lower are related to physical adsorption (physisorption) involving weak van Der Waals interaction, while values of $\Delta G°_{ads}$ around -40 kJ/mol or more negative are connected with chemical adsorption (chemisorption) with chemical bonding [237]. Furthermore, the literature states that a rise in $\Delta G°_{ads}$ values with increasing temperature indicates exothermic adsorption, while a decrease in $\Delta G°_{ads}$ values with increasing temperature indicates endothermic adsorption. In this study, the $\Delta G°_{ads}$ values decreased with a rise in temperature signifying endothermic adsorption.

$\Delta G°_{ads}$ values between -20 and -40 kJ/mol signify mixed-type of adsorption [238]. In this research project, the values of $\Delta G°_{ads}$ were found to be negative for all of the investigated inhibitors, signifying that the inhibition processes were spontaneous. In this study, the $\Delta G°_{ads}$ values were found to be between -20 and -40 kJ/mol indicating a mixed-type of adsorption with physisorption dominating.

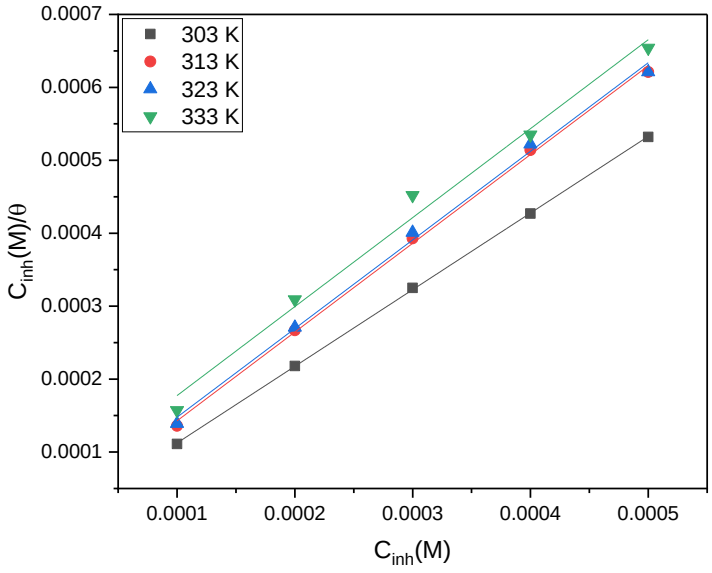

Figure 4.38: Langmuir adsorption isotherm for the adsorption of Chr-2-Carb on MS metal in 1.5 M HCl at 303, 313, 323 and 333K.

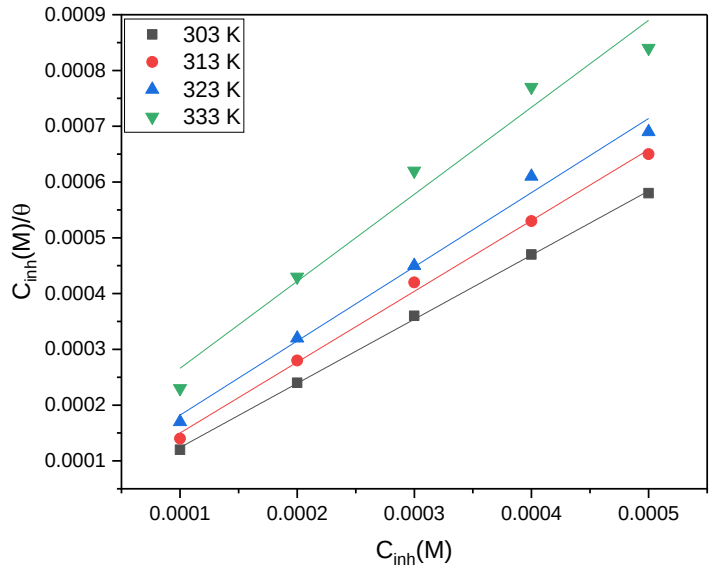

Figure 4.39: Langmuir adsorption isotherm for the adsorption of Br-Chr-2-Carb on MS metal in 1.5 M HCl at 303, 313, 323 and 333K.

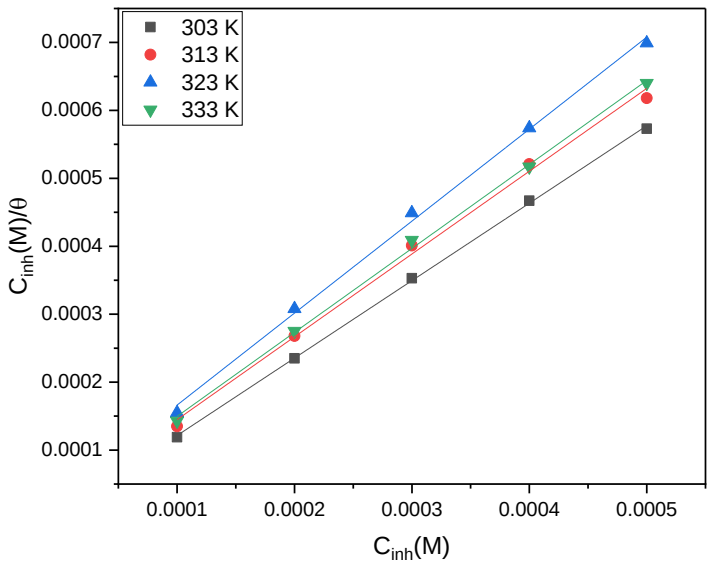

Figure 4.40: Langmuir adsorption isotherm for the adsorption of Cl-Chr-2-Carb on MS metal in 1.5 M HCl at 303, 313, 323 and 333K.

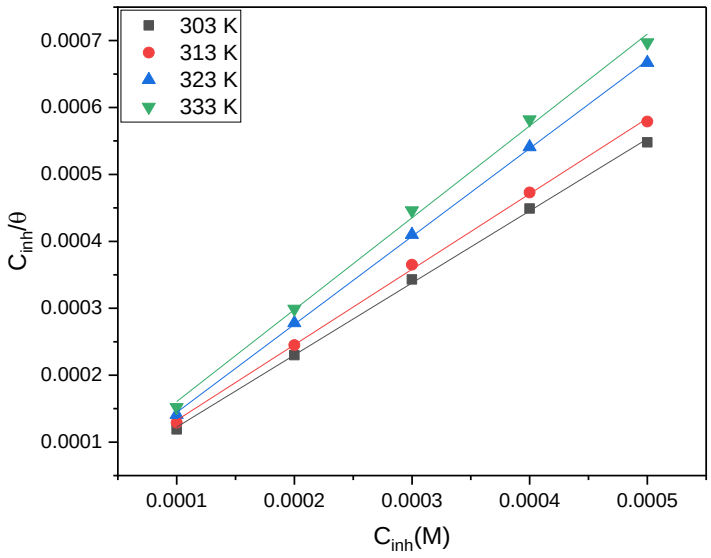

Figure 4.41: Langmuir adsorption isotherm for the adsorption of CH_3O-Chr-2-Carb on MS metal in 1.5 M HCl at 303, 313, 323 and 333K.

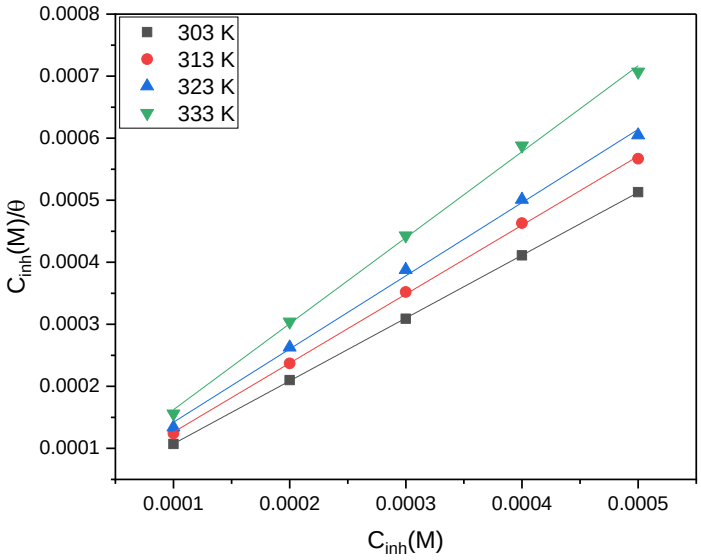

Figure 4.42: Langmuir adsorption isotherm for the adsorption of NO_2-Chr-2-Carb on MS metal in 1.5 M HCl at 303, 313, 323 and 333K.

Table 4.14: Adsorption parameters from Langmuir Adsorption Isotherm plot for Chr-2-Carb, Br-Chr-2-Carb, Cl-Chr-2-Carb, CH3O-Chr-2-Carb and NO2-Chr-2-Carb in 1.5 M.

Inhibitor	Temperature (K)	R^2	Slope	Intercept	K_{ads} ($L.mol^{-1}$)	$\Delta G°ads$ ($kJ.mol^{-1}$)
Chr-2-carb	303	0.99989	1.051	0.0000073	136.9863	22.5131
	313	0.99859	1.217	0.0000211	47.3934	20.4939
	323	0.99701	1.215	0.0000263	38.0228	20.5569
	333	0.98907	1.220	0.0000554	18.0505	19.1307
Br-Chr-2-carb	303	0.99470	1.150	0.000009	111.1111	21.9856
	313	0.99734	1.270	0.000023	43.4783	20.2696
	323	0.99109	1.330	0.000049	20.4082	18.8861
	333	0.97235	1.560	0.000110	9.0909	17.2316
Cl-Chr-2-carb	303	0.99961	1.140	0.0000074	135.1351	22.4788
	313	0.99618	1.219	0.0000229	43.6681	20.2809
	323	0.99788	1.354	0.0000308	32.4675	20.1328

	333	0.99854	1.236	0.0000260	38.4615	21.2219
CH_3O-Chr-2-carb	303	0.99933	1.077	0.0000147	68.0272	20.7496
	313	0.99932	1.128	0.0000198	50.5050	20.6593
	323	0.99978	1.315	0.0000129	77.5194	22.4700
	333	0.99764	1.373	0.0000233	42.9185	21.5288
NO_2-Chr-2-carb	303	0.99997	1.013	0.0000061	163.9344	22.9655
	313	0.99954	1.112	0.0000150	66.6667	21.3819
	323	0.99800	1.180	0.0000242	41.3223	20.7805
	333	0.99868	1.386	0.0000238	42.0168	21.4699

4.2.4. Effects of temperature and kinetic parameters

Temperature has an impact on MS corrosion in acidic media, giving us a better interpretation of the inhibitive mechanism of the corrosion process. As a result, temperature changes can be used to better understand the type of adsorption of the examined 6-substituted chromone-2-carboxamide on the MS surface. The Arrhenius equation is frequently used to describe the dependence of metal corrosion rates on ambient temperature. As reported in the literature, in an acidic environment (acidic solution), the rate of metal corrosion rises significantly with temperature as a result of a decrease in the hydrogen evolution overpotential [235]. Arrhenius equation is frequently used to describe the dependence of metal corrosion rates on ambient temperature. From the Arrhenius equation, the activation energy (Ea) of metal corrosion is determined through an Arrhenius-type plot based on the equation below.

$$\log C_R = \log A - \frac{E_a}{2.303RT} \quad (36)$$

where E_A is the activation energy of MS corrosion in the absence and presence of various concentrations of the inhibitors, C_R is the corrosion rate in $g.cm^{-2}.h^{-1}$, A is the Arrhenius pre-exponential factor, T is the absolute temperature, and R is the universal gas constant. The resultant values of Ea for MS in 1.5 M HCl in the absence and inclusion of inhibitors

were derived/calculated from the slope of log CR against 1/T plots (figures 4.43-4.47) and are shown in Table 4.15.

Based on the results of this study, table 4.15 clearly shows that E_a values for inhibited solutions were higher than those for uninhibited solutions, implying that dissolution of MS is slower attributed to the initiation of the metal-inhibitor complex (inhibitor-Fe complex). This signifies physical adsorption of the synthesized inhibitors [239]. The observed higher E_a values of the inhibited systems is due to the increased in thickness of the double layer on the MS surface after the adsorption of the synthesized inhibitors. A rise in E_a values with increasing inhibitor compound concentrations shows that inhibitors generate an energy impediment (energy barrier) for the corrosion process that increases with increasing inhibitor concentration. This further emphasizes the electrostatic character of the inhibitor binding on the MS surface [240 – 241].

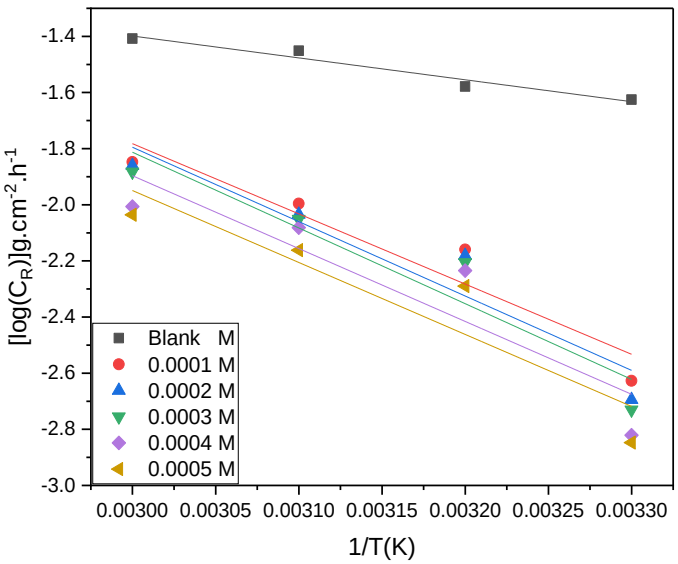

Figure 4.43: Arrhenius plots for MS corrosion in 1.5 M HCl solution in the absence and presence of different concentrations of Chr-2-Carb.

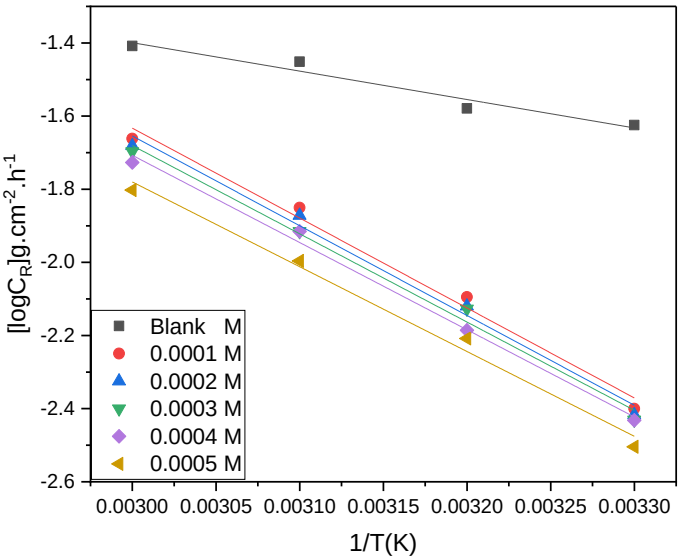

Figure 4.44: Arrhenius plots for MS corrosion in 1.5 M HCl solution in the absence and presence of different concentrations of Br-Chr-2-Carb.

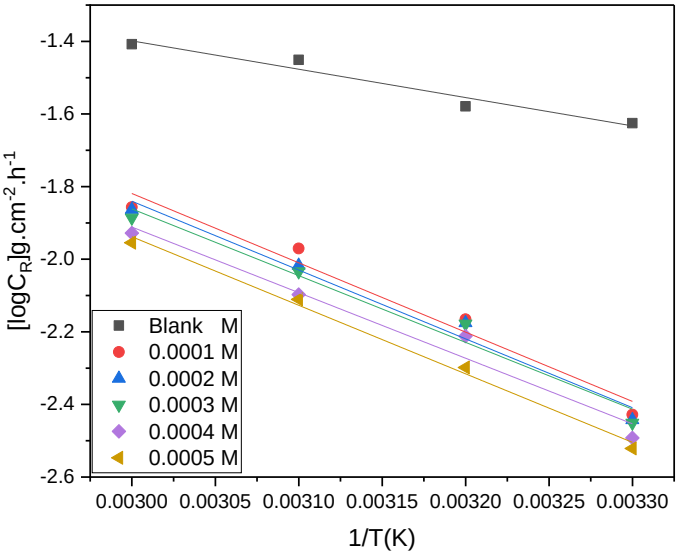

Figure 4.45: Arrhenius plots for MS corrosion in 1.5 M HCl solution in the absence and presence of different concentrations of Cl-Chr-2-Carb.

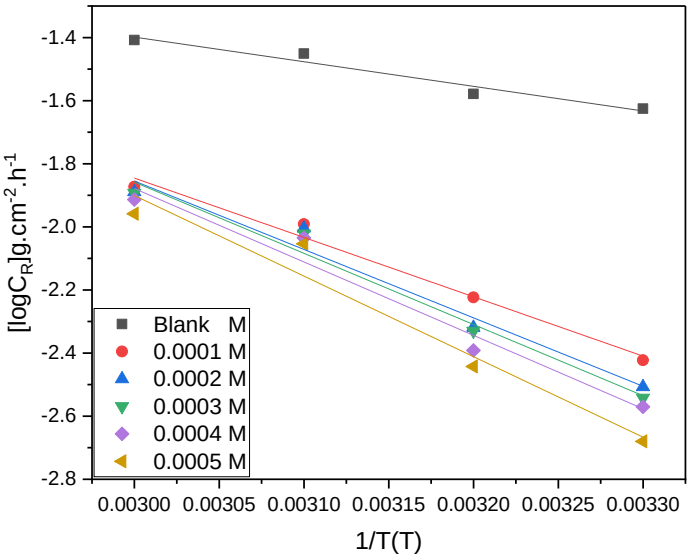

Figure 4.46: Arrhenius plots for MS corrosion in 1.5 M HCl solution in the absence and presence of different concentrations of CH_3O-Chr-2-Carb.

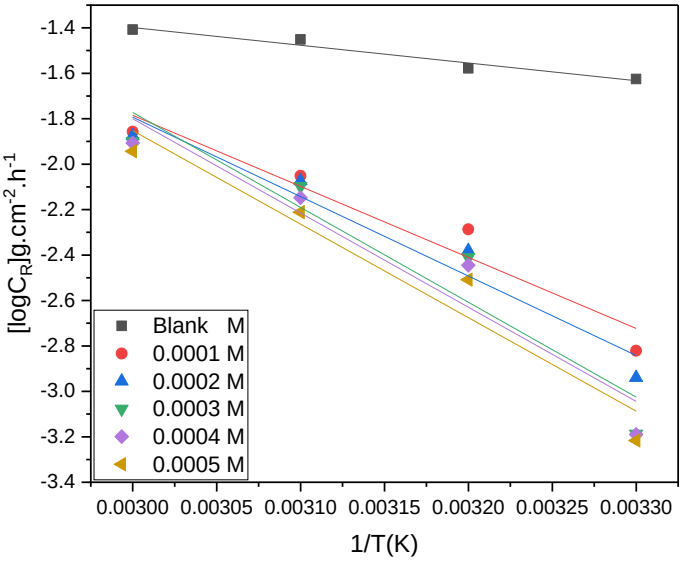

Figure 4.47: Arrhenius plots for MS corrosion in 1.5 M HCl solution in the absence and presence of different concentrations of NO_2-Chr-2-Carb.

Thermodynamic parameters such as enthalpy of activation (ΔH^*_a) and entropy of activation (ΔS^*_a) can provide more information on the effect of temperature on the corrosion rate of MS in 1.5 M HCl. The transition-state equation below relates corrosion rate and temperature to these factors (parameters). Figures 4.48 - 4.52 display a plot of

log(CR/T) against (1/T) with the best fitted data with a slope (-ΔH*/2.303R) and an intercept [log(R/Nh)+(S*/2.303R)] which were used to compute the values of the standard enthalpy (ΔH*) and entropy of activation (ΔS*) in the absence and presence of the studied 6-substituted chromone-2-carboxamides. Table 4.15 clearly demonstrate their results. Equation 4.5 was utilized in the calculations for enthalpy of activation (H*) and entropy of activation (ΔS*) [242, 243].

$$\log\left(\frac{C_R}{T}\right) = \left[\log\left(\frac{R}{Nh}\right) + \left(\frac{\Delta S_a^*}{2.303R}\right)\right] + \left(\frac{-\Delta H_a^*}{2.303R}\right)\left(\frac{1}{T}\right) \quad (37)$$

where h represents Planck's constant and N denote Avogadro number, 2.303 is a conversion factor from natural log to log10, and T is the absolute temperature.

Literature has reported that positive activation enthalpies depict endothermic character of the steel dissolution process (endothermic reaction), implying that MS dissolution is difficult [244]. Results on table 4.15 shows that the blank has a lower ΔH_a^* values as opposed to those of the five synthesized and tested corrosion inhibitors. This shows that there was an adsorption process between the inhibitor molecules and the surface of MS. Furthermore, a significant quantity of energy was required to transfer from the reactants and generate the corrosion products, confirming inhibitor adsorption and a decrease in the MS rusting. It has been demonstrated in the literature that ΔH_a^* values less than 41.86 kJ.mol^{-1} is related with physisorption, while values around 100 kJ.mol^{-1} or greater are associated with chemisorption [245]. The data shown in Table 4.15 reveal that ΔH_a^* values are slightly smaller than activation energies and are between 41.86 kJ.mol^{-1} and 100 kJ.mol^{-1} and some less than 41.86 kJ.mol^{-1}.

Results of this on table shows that ΔH_a^* values in the presence of Chromone-2-carboxamide (Chr-2-Carb) are ranging from 45.2666 kJ.mol^{-1} to 49.0196 kJ.mol^{-1} signifying a mixed-type of adsorption on the MS surface. Since ΔH_a^* values between 41.86 kJ.mol^{-1} and 100 kJ.mol^{-1} depict a mixed-type of adsorption. ΔH_a^* values in the presence of 6-Bromochromone-2-carboxamide (Br-Chr-2-carb) reflect a mixed type of adsorption with values ranging from 41.7624 kJ.mol^{-1} to 44.4738 kJ.mol^{-1}. In the presence of 6-Chlorochromone-2-carboxamide (Cl-Chr-2-carb) the ΔH_a^* values are below 41.86 kJ.mol^{-1} ranging from 31.9719 kJ.mol^{-1} to 33.9575 kJ.mol^{-1} associated with physical

adsorption of the Cl-Chr-2-carb on the MS surface. The ΔH_a^* values in the presence of 6-Methoxychromone-2-carboxamide are between 33.3946 kJ.mol^{-1} and 48.8837 kJ.mol^{-1} showing a mixed type of adsorption with physical adsorption dominating. While in the presence of 6-Nitrochromone-2-carboxamide (NO_2-Chr-2-carb) the enthalpy of activation values is between 57.2534 kJ.mol^{-1} and 77.3399 kJ.mol^{-1} indicating mixed-type of adsorption on the MS surface. The results on table 4:15 show dominating of physical adsorption of the synthesized inhibitors on the MS surface.

Larger negative values of ΔS^* signifies that the activated complex in the rate-determining stage reflects inhibitor attachment rather than dissolution. This shows that the adsorption of inhibitor molecules on the MS surface reduces system disorder as it moves from reactants to active complex [246]. The increase in ΔS^* values caused by inhibitor molecule adsorption on the MS surface from the acid solution can be interpreted as a quasi-substitution process between organic molecules in the aqueous phase and water molecules on the electrode surface. Literature has revealed that the adsorption of the inhibitor molecules is believed to follow desorptions of water molecules from the electrode surface in such a process, resulting in a drop in MS's electrical capacity [247, 248]. Higher ΔS^* values were obtained in this study.

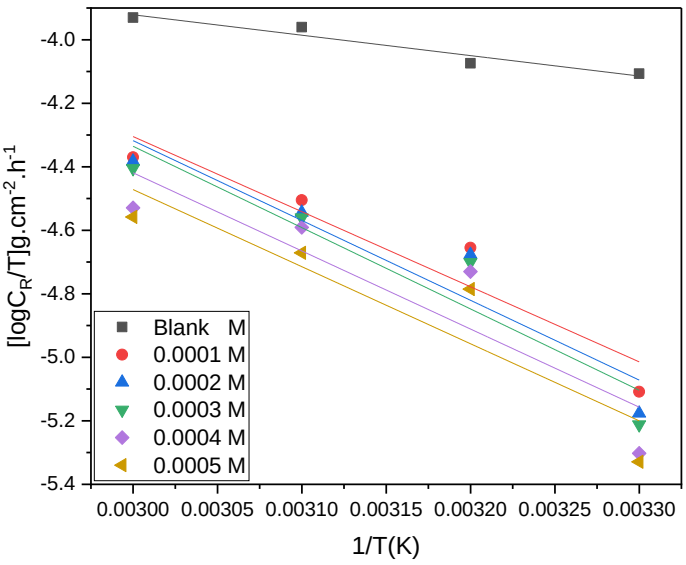

Figure 4.48: Transition state plots for MS corrosion in 1.5 M HCl solution in the absence and presence of different concentrations of Chr-2-Carb.

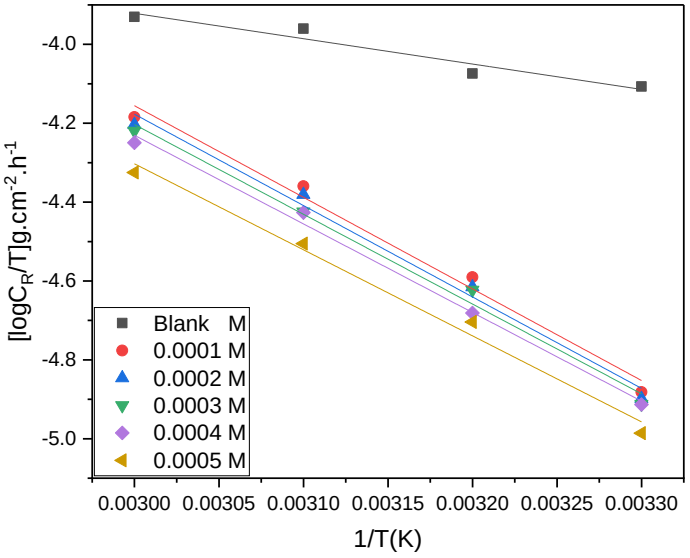

Figure 4.49: Transition state plots for MS corrosion in 1.5 M HCl solution in the absence and presence of different concentrations of Br-Chr-2-carb.

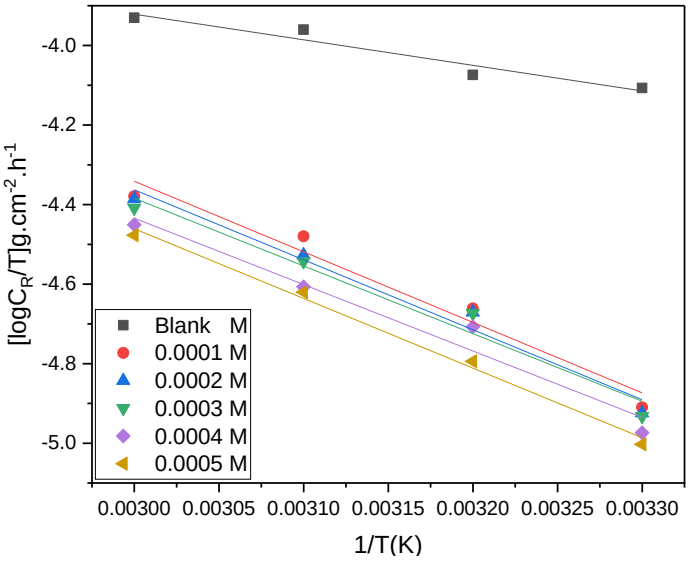

Figure 4.50: Transition state plots for MS corrosion in 1.5 M HCl solution in the absence and presence of different concentrations of Cl-Chr-2-Carb.

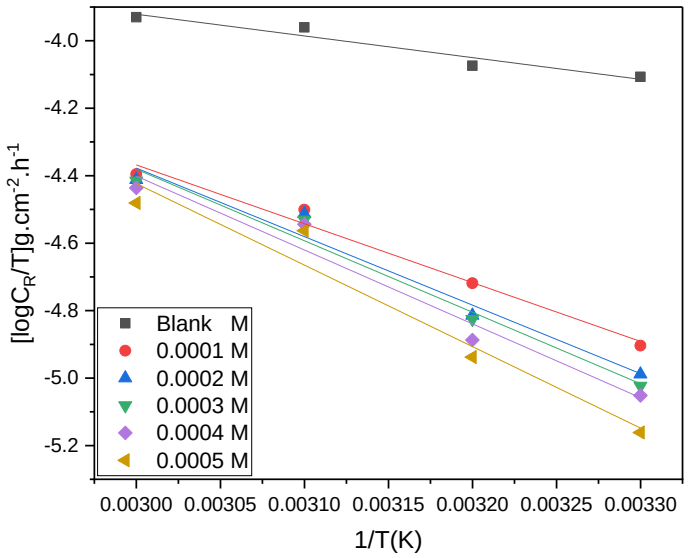

Figure 4.51: Transition state plots for MS corrosion in 1.5 M HCl solution in the absence and presence of different concentrations of CH_3O-Chr-2-Carb.

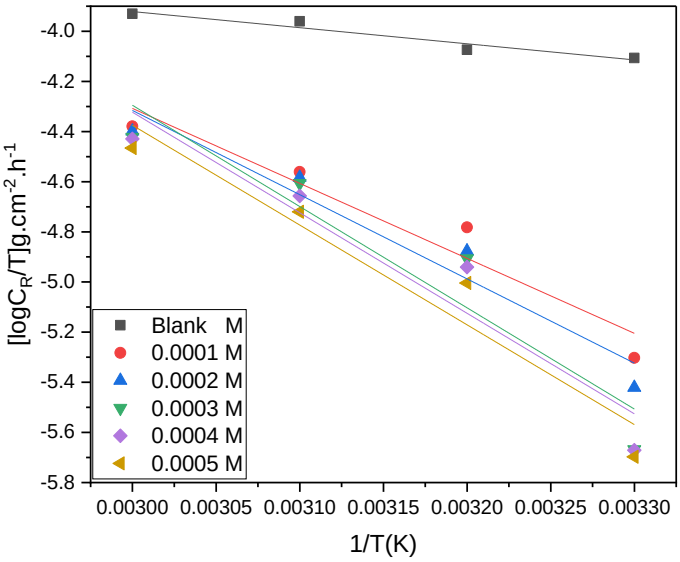

Figure 4.52: Transition state plots for MS corrosion in 1.5 M HCl solution in the absence and presence of different concentrations of NO_2-Chr-2-Carb.

Table 4.15: Arrhenius and transition parameters for MS in 1.5 M HCl in the absence and presence of various concentrations of the studied 6-substituted chromone-2-carboxamides.

Inhibitor	Concentration of inhibitors (x10^{-4} M)	Ea (kJ.mol^{-1})	ΔH* (kJ.mol^{-1})	ΔS* (J.mol^{-1} .K^{1})
Blank	-	14.9357	12.3104	-214.1170
Chr-2-Carb	1.0	47.8899	45.2666	-174.3587
	2.0	50.7429	48.1197	-170.7536
	3.0	51.6429	49.0196	-169.7242
	4.0	49.7089	47.0857	-172.4911
	5.0	49.0922	46.4729	-174.1849
Br-Chr-2-Carb	1.0	47.0857	44.4738	-174.1700
	2.0	46.9899	44.3666	-174,4801

	3.0	46.2048	43.5815	-175.7239
	4.0	45.6706	43.007	-176.7018
	5.0	44.3953	41.7624	-178.9134
Cl-Chr-2-Carb	1.0	36.5541	33.9575	-189.4163
	2.0	36.2956	33.6799	-189.9567
	3.0	35.2003	32,5904	-191,5523
	4.0	34.5876	31.9719	-192,7745
	5.0	36,1481	33.5363	-190.9578
CH_3O-Chr-2-Carb	1.0	36.0122	33.3946	-190.3716
	2.0	41.5097	38.8921	-183.2885
	3.0	43.1966	40.5848	-181.1118
	4.0	44.5485	41.9309	-174.5279
	5.0	48.8837	46.2584	-174.0752
NO_2-Chr-2-Carb	1.0	59.8767	57.2534	-158.7749
	2.0	66.9425	64.3191	-149.6298
	3.0	79.9633	77.3399	-132.5152
	4.0	79.4079	76.7847	-133,4655
	5.0	78.8144	76.1911	-134.6570

4.2.5. Adsorption film analysis

This technique was utilized in order to identify or locate the adsorbed functional groups of the synthesized organic compounds upon the metal surface, FTIR was used with a wavenumber ranging from 4000 to 400 cm^{-1}. Figures 4.53 – 4.57 help us to easily compare the FT-IR spectra of the synthesized 6-substituted chromone-2-carboxamides to the adsorption film formed in the presence of the inhibitors after the mild steel corrosion. 6-substituted chromone-2-carboxamides contain heteroatoms which contribute more on the formation of the adsorption film (heteroatom such as O and N)

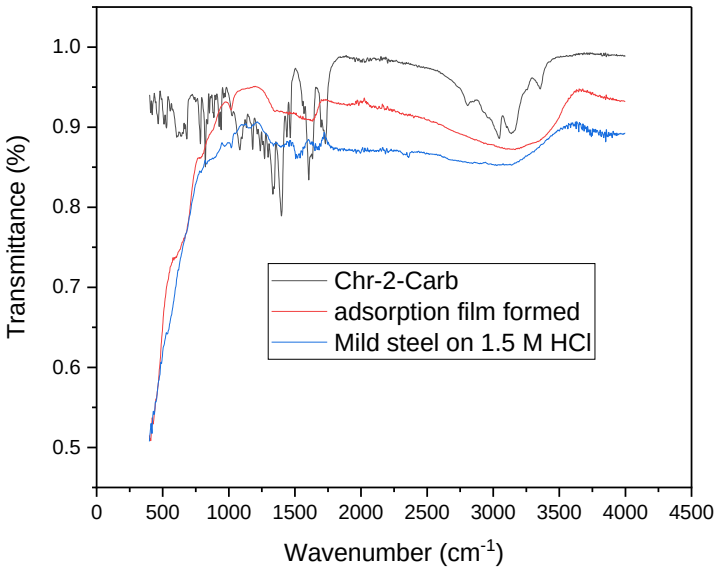

Figure 4.53: FT-IR spectra comparison of the frequencies for the pure compound and adsorption films formed on the mild steel in 1.5 M HCl by Chr-2-Carb corrosion inhibitor.

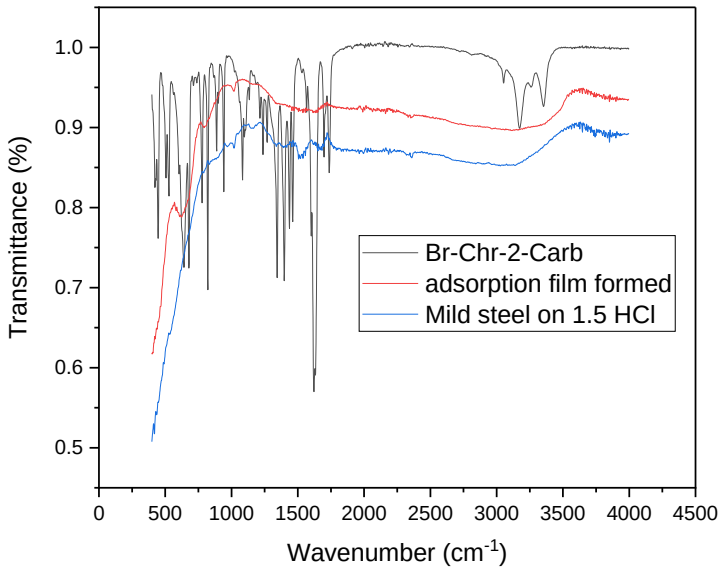

Figure 4.54: FT-IR spectra comparison of the frequencies for the pure compound and adsorption films formed on the mild steel in 1.5 M HCl by Br-Chr-2-Carb corrosion inhibitor.

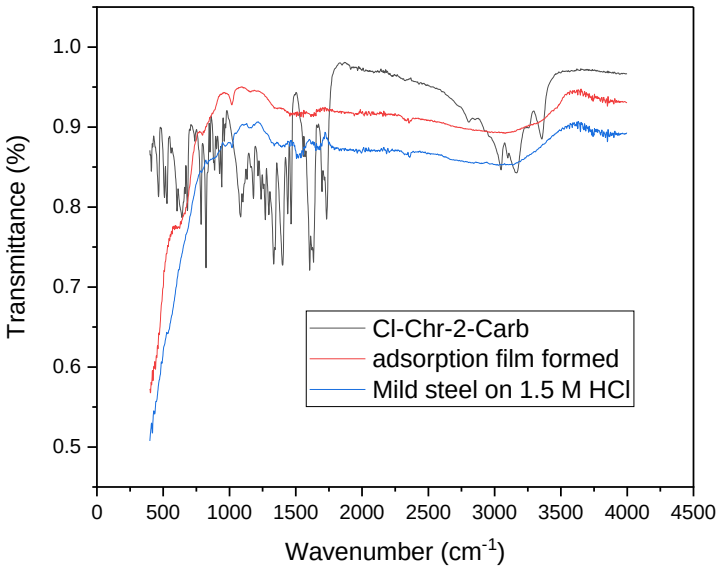

Figure 4.55: FT-IR spectra comparison of the frequencies for the pure compound and adsorption films formed on the mild steel in 1.5 M HCl by Cl-Chr-2-Carb corrosion inhibitor.

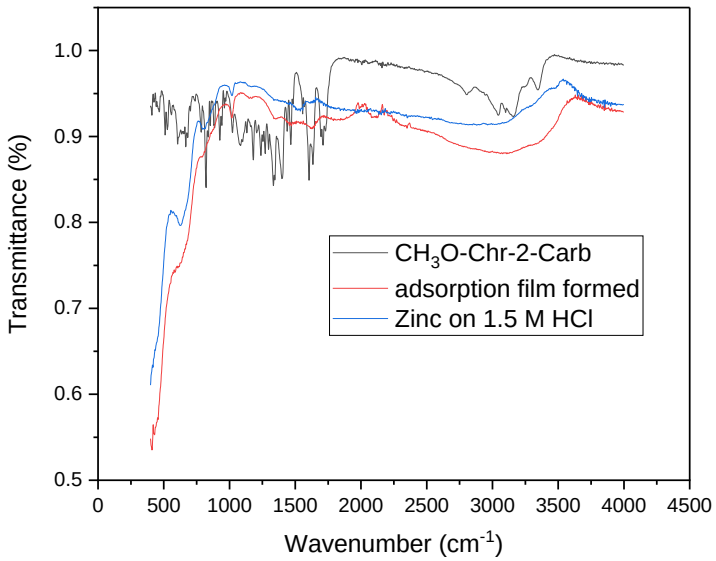

Figure 4.56: FT-IR spectra comparison of the frequencies for the pure compound and adsorption films formed on the mild steel in 1.5 M HCl CH_3O-Chr-2-Carb corrosion inhibitor.

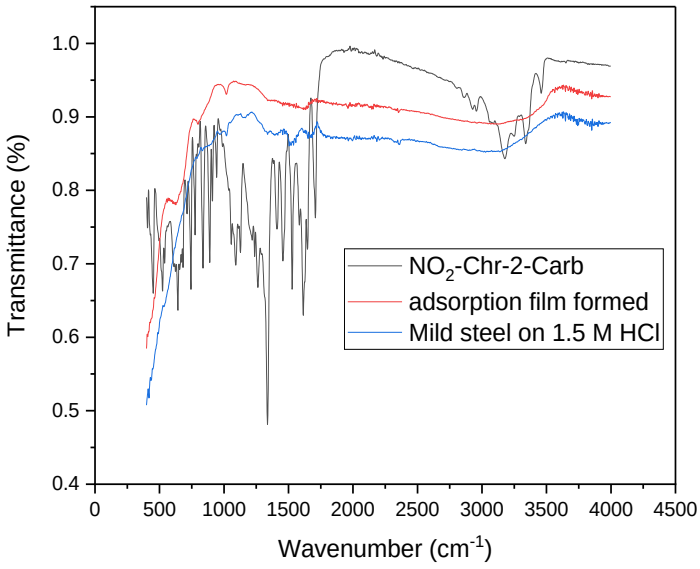

Figure 4.57: FT-IR spectra comparison of the frequencies for the pure compound and adsorption films formed on the mild steel in 1.5 M HCl NO_2-Chr-2-Carb corrosion inhibitor.

The figures displayed above shows that some of the functional groups that were observed in the synthesized compounds disappeared. The disappeared functional groups play a key role in the complex formation with the mild steel surface, believed to be preventing the dissolution process. The scratched FT-IR spectra (adsorption film formed) shows the intensity of the peaks decreased which means that a coordinate bond was formed through the functional groups of these peaks with the mild steel ($Fe2^+$), forming the Fe2+- inhibitor complex on the mild steel surface, controlling the dissolution process. All the above figures clearly shows that the aromatic C-O peak [Ar (C-O)] disappeared in the spectra of the adsorption film as displayed in table 4.16. It is also noted that the carbonyl carbon (C=O) peaks which were appearing around 1700 cm^{-1} on the spectra of the synthesized compounds shifted to around 1600 cm^{-1} wavenumber on the adsorption film spectra. Ar (C=C) peaks observed around 1560 cm^{-1} with 1584.06 cm^{-1} corresponding to NO_2-Chr-2-Carb seemed to have shifted to around 1556 cm^{-1} with 1539.19 in the presence of Br-Chr-2-Carb on the adsorption film spectra. The aromatic C-H (=C-H) stretching observed around 3137 cm^{-1} to 3177.75 on the spectra of the synthesized compounds shifted to around 3000 cm^{-1} and 3100 cm^{-1} on the adsorption film spectra. Furthermore, the NH_2

peak disappeared in the spectra of the adsorption film and new bonds appeared around 3600 cm^{-1} and 3800 cm^{-1} of the adsorption film spectra.

Table 4.16: Peaks identified from FTIR spectra of the synthesized 6-substituted chromone-2-carboxamides and adsorption film formed on the Mild steel in 1.5 M HCl.

Inhibitor-Mild steel	Functional Groups Peaks obtained from FTIR spectra (cm^{-1})				
	C=O	NH_2	Ar (C=C)	Ar (C-O)	=C-H
Chr-2-Carb	1614.36	-	1556.71	-	3046.21
Br-Chr-2-Carb	1633.16	-	1539.19	-	3117.48
Cl-Chr-2-Carb	1614.60	-	1556.83	-	3071.68
CH_3O-Chr-2-Carb	1633.71	-	1556.40	-	3099.54
NO_2-Chr-2-Carb	1633.69	-	1556.23	-	3100.08

4.3. Zinc

4.3.1. Gravimetric analysis (GA) and the effect of inhibitor concentration

GA measurements of zinc specimen was performed in an inhibited and uninhibited HCl solutions at four temperatures of 303 – 333 K. The potential of the 6-substituted chromone-2-carboxamides to reduce zinc corrosion was investigated in different concentrations of 1.0×10^{-4}, 2.0×10^{-4}, 3.0×10^{-4}, 4.0×10^{-4}, and 5.0×10^{-4} M in 1.5 M HCl. The results for the zinc corrosion test in blank and in the presence of various concentrations of 6-Substituted chromone-2-carboxamide derivatives are graphically depicted in the Figure 4.58 – 4.62 and Table 4.17 below.

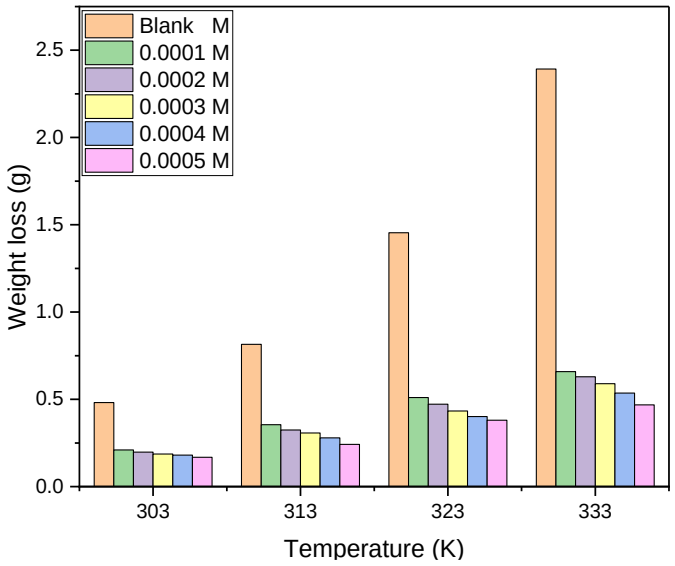

Figure 4.58: The graph showing the weight loss measurements of zinc in the absence and presence of Chr-2-Carb in 1.5 M HCl.

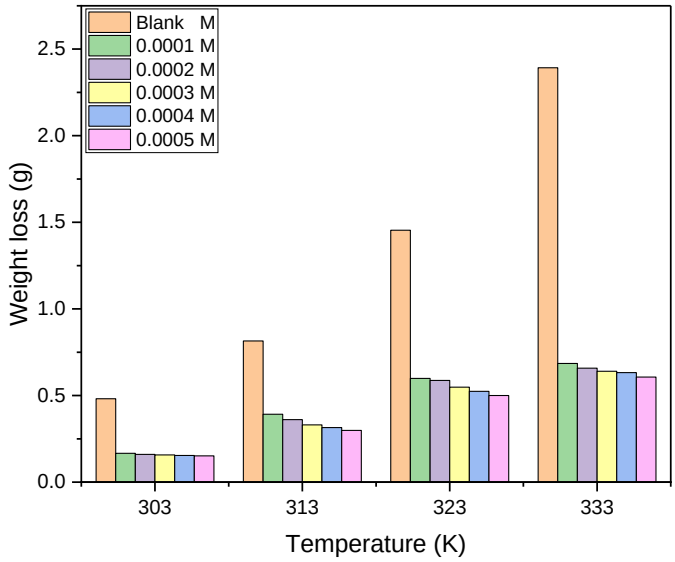

Figure 4.59: The graph showing the weight loss measurements of zinc in the absence and presence of Br-Chr-2-Carb in 1.5 M HCl.

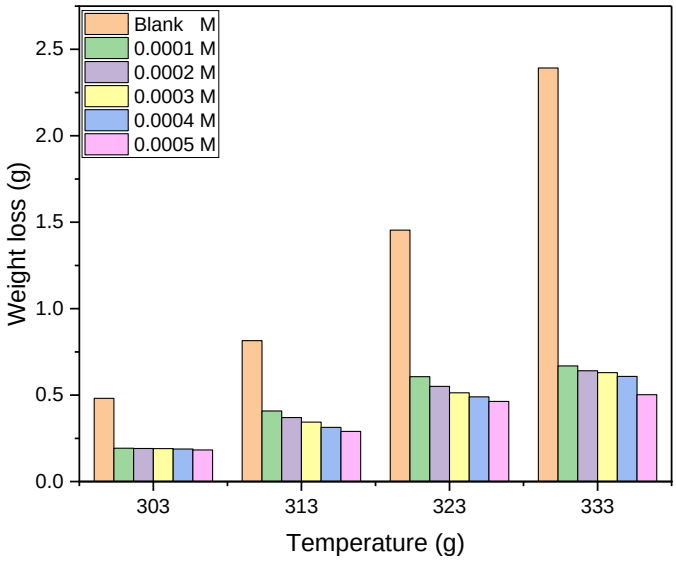

Figure 4.60: The graph showing the weight loss measurements of zinc in the absence and presence of Cl-Chr-2-Carb in 1.5 M HCl.

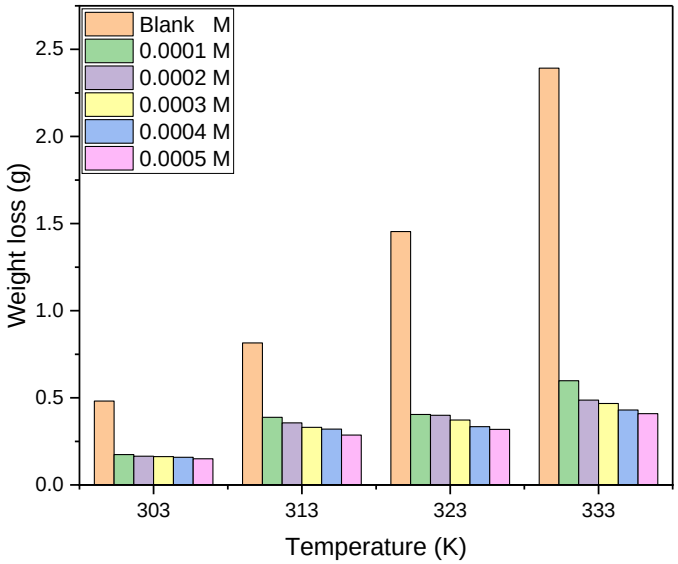

Figure 4.61: The graph showing the weight loss measurements of zinc in the absence and presence of CH_3O-Chr-2-Carb in 1.5 M HCl.

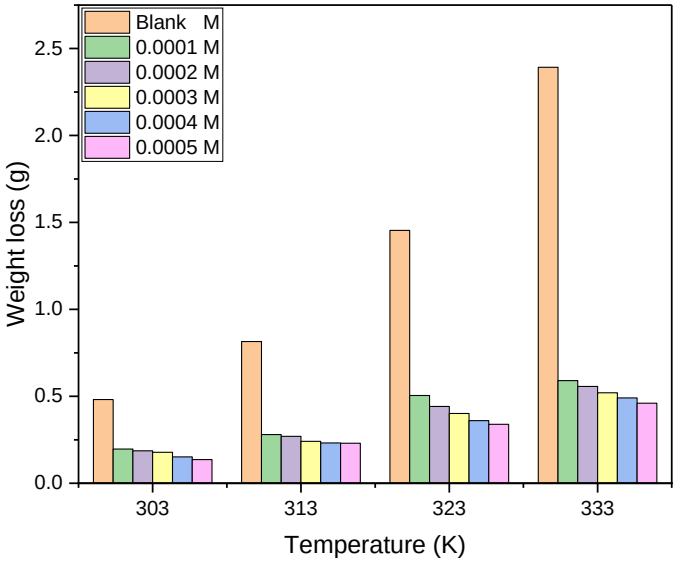

Figure 4.62: The graph showing the weight loss measurements of zinc in the absence and presence of NO_2-Chr-2-Carb in 1.5 M HCl.

Table 4.17: Weight loss measurements of zinc in the absence and presence of 6-Substituted chromone-2-carboxamides in 1.5 M HCl.

Inhibitor	Concentration ($x10^{-4}$ M)	Weight loss (g)			
		303 K	313 K	323 K	333 K
	0.0000	0.4815	0.8150	1.4540	2.3926
Chr-2-Carb	1.0	0.2102	0.3545	0.5104	0.6588
	2.0	0.1977	0.3240	0.4720	0.6295
	3.0	0.1868	0.3073	0.4330	0.5893
	4.0	0.1805	0.2793	0.4011	0.5361
	5.0	0.1683	0.2421	0.3802	0.4682
Br-Chr-2-Carb	1.0	0.1664	0.3920	0.5985	0.6854
	2.0	0.1605	0.3611	0.5873	0.6581

	3.0	0.1569	0.3307	0.5485	0.6402
	4.0	0.1537	0.3149	0.5242	0.6324
	5.0	0.1518	0.2986	0.5002	0.6064
Cl-Chr-2-Carb	1.0	0.1927	0.4082	0.6066	0.6685
	2.0	0.1914	0.3703	0.5503	0.6409
	3.0	0.1902	0.3436	0.5131	0.6298
	4.0	0.1879	0.3134	0.4902	0.6084
	5.0	0.1831	0.2904	0.4637	0.5026
CH_3O-Chr-2-Carb	1.0	0.1740	0.3878	0.4041	0.5982
	2.0	0.1650	0.3562	0.4001	0.4869
	3.0	0.1628	0.3309	0.3726	0.4672
	4.0	0.1583	0.3201	0.3348	0.4302
	5.0	0.1501	0.2864	0.3186	0.4092
NO_2-Chr-2-Carb	1.0	0.1965	0.2803	0.5044	0.5901
	2.0	0.1869	0.2701	0.4421	0.5568
	3.0	0.1797	0.2409	0.4010	0.5203
	4.0	0.1518	0.2316	0.3601	0.4908
	5.0	0.1361	0.2300	0.3392	0.4603

The results reported in the figures above show that the mass loss of zinc dropped dramatically as the concentration of the tested 6-substituted chromone-2-carboxamides increased. The results presented in the table above show that the weight loss readings for zinc were much lower in the presence of the inhibitors than in the blank solution (uninhibited solution). As illustrated in Table 4.17, the weight loss of zinc for the blank test was 0.2558 g, 0.3832 g, 0.6913 g, and 1.1077 g at temperatures of 303 K, 313 K, 323 K, and 333 K, respectively, as compared to tests conducted in the presence of the synthesized inhibitors 6-substituted chromone-2-carboxamides, where the mass loss of

zinc has decreased dramatically. For instance, the weight loss in the presence of 1.0×10^{-4} M Chr-2-Carb was found to be 0.2102 g 0.3545 g, 0.5104 g, 0.6588 g at the four temperatures 303 K, 313 K, 323 K, and 333 K, respectively. A comparable behavior was noted in all of the 6-substituted chromone-2-carboxamides concentrations examined. These findings correlate with the proven fact that increasing the quantity of inhibitor minimizes zinc weight loss, and as a result the rate of zinc corrosion is reduced.

4.3.2. Corrosion rate and inhibition efficiency

The corrosion rate (C_R) of zinc metal, percentage inhibition efficiency (% IE), and as well as the surface coverage (θ) were computed from the weight loss measurement of zinc in 1.5 M HCl in the absence and presence of various concentrations of the 6-substituted chromone-2-carboxamides at temperature 303 – 333 K. The values are displayed in Tables (4.18 – 4.22) and Figures 4.63 – 4.67.

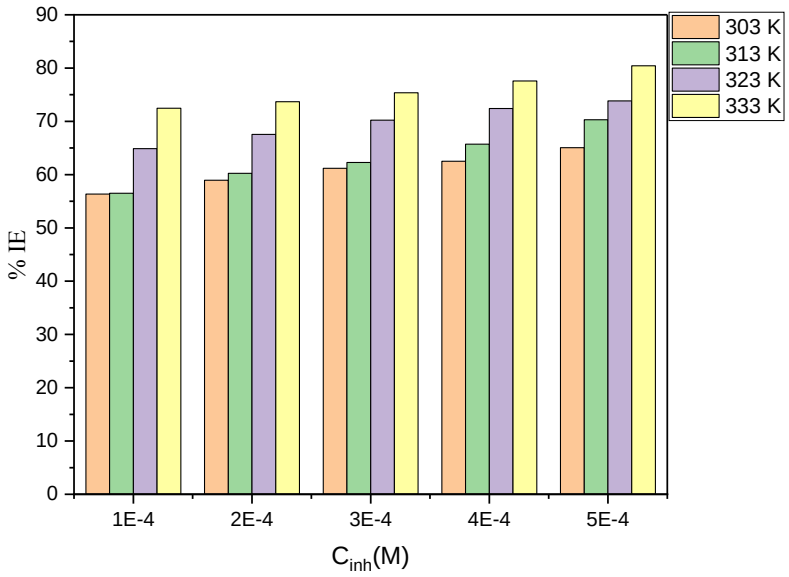

Figure 4.63: The variation of percentage inhibition efficiency with various concentration of Chr-2-Carb at various temperatures in 1.5 M HCl.

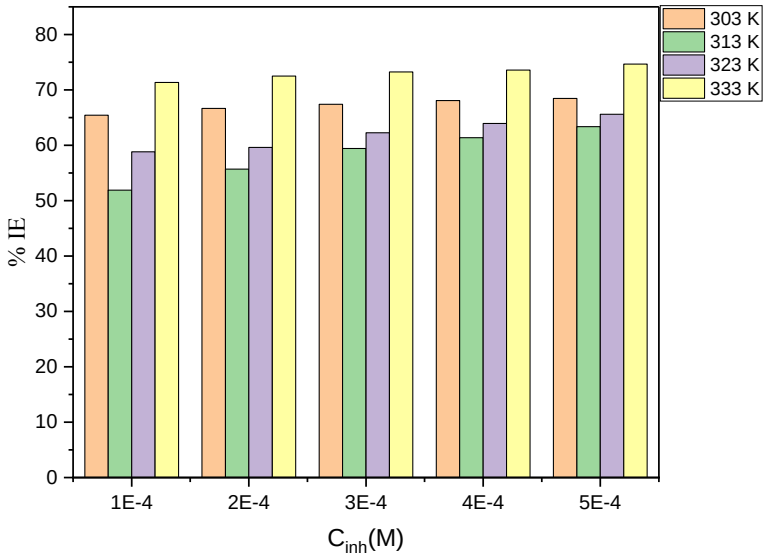

Figure 4.64: The variation of percentage inhibition efficiency with various concentration of Br-Chr-2-Carb at various temperatures in 1.5 M HCl.

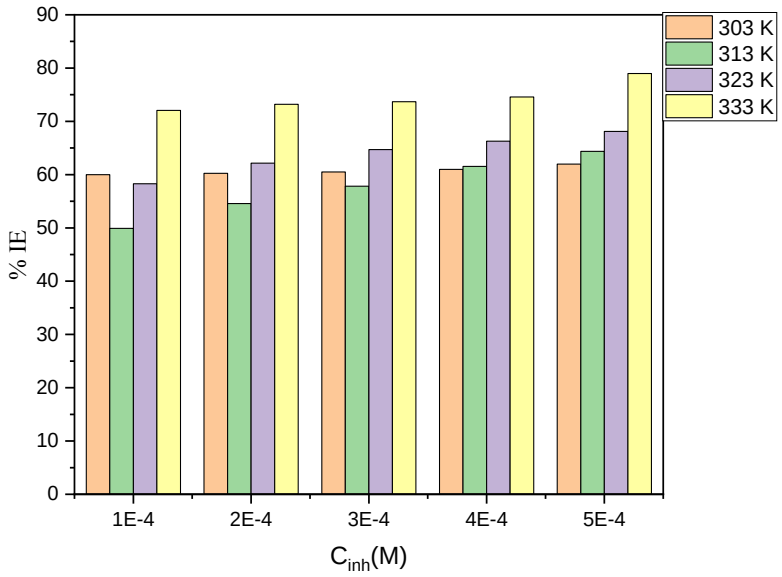

Figure 4.65: The variation of percentage inhibition efficiency with various concentration of Cl-Chr-2-Carb at various temperatures in 1.5 M HCl.

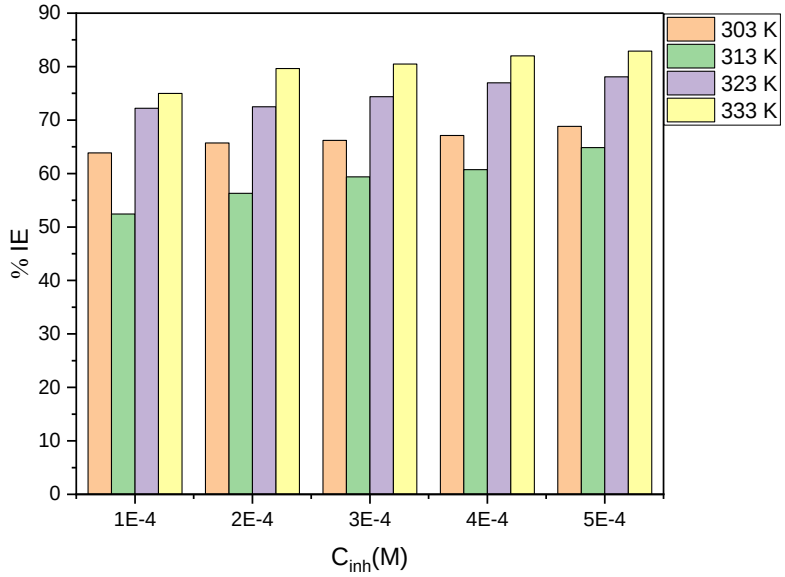

Figure 4.66: The variation of percentage inhibition efficiency with various concentration of CH_3O-Chr-2-Carb at various temperatures in 1.5 M HCl.

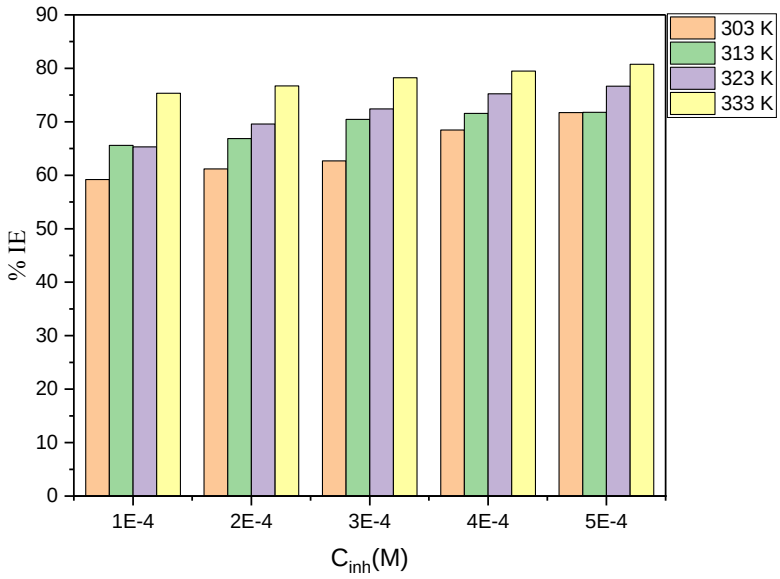

Figure 4.67: The variation of percentage inhibition efficiency with various concentration of NO_2-Chr-2-Carb at various temperatures in 1.5 M HCl.

Table 4.18: The corrosion parameters for zinc in 1.5 M HCl in the absence and presence of various concentrations of Chr-2-Carb obtained from weight loss measurements at 303 – 333 K.

Inhibitor	Temperature (K)	Inhibitor concentration (x10^{-4} M)	Corrosion rate (g.cm^{-2}.h^{-1})	Surface coverage (θ)	Inhibition efficiency (%)
	303	-	0.0100	-	-
		1.0	0.00438	0.5634	56.34
		2.0	0.00412	0.5894	58.94
		3.0	0.00389	0.6120	61.20
		4.0	0.00376	0.6251	62.51
		5.0	0.00351	0.6505	65.05
		-	0.0169	-	-
		1.0	0.00739	0.5650	56.50

Chr-2-Carb	313	2.0	0.00675	0.6024	60.24
		3.0	0.00640	0.6229	62.29
		4.0	0.00582	0.6573	65.73
		5.0	0.00504	0.7029	70.29
	323	-	0.0303	-	-
		1.0	0.0106	0.6489	64.89
		2.0	0.00983	0.6754	67.54
		3.0	0.00902	0.7022	70.22
		4.0	0.00836	0.7241	72.41
		5.0	0.00792	0.7385	73.85
	333	-	0.0498	-	-
		1.0	0.0137	0.7247	72.47
		2.0	0.0131	0.7369	73.69
		3.0	0.0123	0.7537	75.37
		4.0	0.0111	0.7759	77.59
		5.0	0.00975	0.8043	80.43

Table 4.19: The corrosion parameters for zinc in 1.5 M HCl in the absence and presence of various concentrations of Br-Chr-2-Carb obtained from weight loss measurements at 303 – 333 K.

Inhibitor	**Temperature (K)**	**Inhibitor concentration (x10^{-4} M)**	**Corrosion rate (g.cm^{-2}.h^{-1})**	**Surface coverage (θ)**	**Inhibition efficiency (%)**
	303	-	0.0100	-	-
		1.0	0.00347	0.6544	65.44
		2.0	0.00334	0.6667	66.67
		3.0	0.00327	0.6741	67.41

Br-Chr-2-Carb		4.0	0.00320	0.6807	68.07
		5.0	0.00316	0.6846	68.46
	313	-	0.0169	-	-
		1.0	0.00817	0.5190	51.90
		2.0	0.00752	0.5569	55.69
		3.0	0.00689	0.5942	59.42
		4.0	0.00656	0.6136	61.36
		5.0	0.00622	0.6336	63.36
	323	-	0.0303	-	-
		1.0	0.0125	0.5883	58.83
		2.0	0.0122	0.5961	59.61
		3.0	0.0114	0.6227	62.27
		4.0	0.0109	0.6394	63.94
		5.0	0.0104	0.6559	65.59
	333	-	0.0498	-	-
		1.0	0.0143	0.7135	71.35
		2.0	0.0137	0.7249	72.49
		3.0	0.0133	0.7324	73.24
		4.0	0.0131	0.7357	73.57
		5.0	0.0126	0.7466	74.66

Table 4.20: The corrosion parameters for zinc in 1.5 M HCl in the absence and presence of various concentrations of Cl-Chr-2-Carb obtained from weight loss measurements at 303 – 333 K.

Inhibitor	Temperature (K)	Inhibitor concentration ($x10^{-4}$ M)	Corrosion rate ($g.cm^{-2}.h^{-1}$)	Surface coverage (θ)	Inhibition efficiency (%)
Cl-Chr-2-Carb	303	-	0.0100	-	-
		1.0	0.00401	0.5998	59.98
		2.0	0.00399	0.6025	60.25
		3.0	0.00396	0.6049	60.49
		4.0	0.00391	0.6098	60.98
		5.0	0.00381	0.6197	61.97
	313	-	0.0169	-	-
		1.0	0.00850	0.4991	49.91
		2.0	0.00771	0.5456	54.56
		3.0	0.00716	0.5784	57.84
		4.0	0.00653	0.6154	61.54
		5.0	0.00605	0.6437	64.37
	323	-	0.0303	-	-
		1.0	0.0126	0.5828	58.28
		2.0	0.0115	0.6215	62.15
		3.0	0.0107	0.6471	64.71
		4.0	0.0102	0.6629	66.29
		5.0	0.00966	0.6812	68.12
	333	-	0.0498	-	-
		1.0	0.0139	0.7205	72.05
		2.0	0.0134	0.7321	73.21

		3.0	0.0131	0.7368	73.68
		4.0	0.0127	0.7457	74.57
		5.0	0.0105	0.7899	78.99

Table 4.21: The corrosion parameters for zinc in 1.5 M HCl in the absence and presence of various concentrations of CH_3O-Chr-2-Carb obtained from weight loss measurements at 303 – 333 K.

Inhibitor	**Temperature (K)**	**Inhibitor concentration ($x10^{-4}$ M)**	**Corrosion rate ($g.cm^{-2}.h^{-1}$)**	**Surface coverage (θ)**	**Inhibition efficiency (%)**
CH_3O-Chr-2-Carb	303	-	0.0100	-	-
		1.0	0.00363	0.6386	63.86
		2.0	0.00344	0.6573	65.73
		3.0	0.00339	0.6619	66.19
		4.0	0.00329	0.6712	67.12
		5.0	0.00313	0.6883	68.83
	313	-	0.0169	-	-
		1.0	0.00808	0.5242	52.42
		2.0	0.00742	0.5629	56.29
		3.0	0.00689	0.5939	59.39
		4.0	0.00669	0.6072	60.72
		5.0	0.00597	0.6486	64.86
	323	-	0.0303	-	-
		1.0	0.00842	0.7221	72.21
		2.0	0.00833	0.7248	72.48
		3.0	0.00776	0.7437	74.37
		4.0	0.00698	0.7697	76.97

		5.0	0.00664	0.7809	78.09
	333	-	0.0498	-	-
		1.0	0.0125	0.7499	74.99
		2.0	0.0101	0.7965	79.65
		3.0	0.00973	0.8047	80.47
		4.0	0.00896	0.8201	82.01
		5.0	0.00853	0.8289	82.89

Table 4.22: The corrosion parameters for zinc in 1.5 M HCl in the absence and presence of various concentrations of NO2-Chr-2-Carb obtained from weight loss measurements at 303 – 333 K.

Inhibitor	**Temperature (K)**	**Inhibitor concentration ($x10^{-4}$ M)**	**Corrosion rate ($g.cm^{-2}.h^{-1}$)**	**Surface coverage (θ)**	**Inhibition efficiency (%)**
	303	-	0.0100	-	-
		1.0	0.00409	0.5919	59.19
		2.0	0.00389	0.6118	61.18
		3.0	0.00374	0.6268	62.68
		4.0	0.00316	0.6847	68.47
		5.0	0.001361	0.7173	71.73
	313	-	0.0169	-	-
		1.0	0.00584	0.6560	65.60
		2.0	0.00563	0.6686	66.86
		3.0	0.00502	0.7044	70.44
		4.0	0.00483	0.7158	71.58
		5.0	0.00479	0.7178	71.78

NO_2-Chr-2-Carb	323	-	0.0303	-	-
		1.0	0.0105	0.6530	65.30
		2.0	0.00921	0.6959	69.59
		3.0	0.00835	0.7242	72.42
		4.0	0.00750	0.7523	75.23
		5.0	0.00707	0.7667	76.67
	333	-	0.0498	-	-
		1.0	0.0122	0.7534	75.34
		2.0	0.0116	0.7672	76.72
		3.0	0.0108	0.7825	78.25
		4.0	0.0102	0.7949	79.49
		5.0	0.00959	0.8076	80.76

The tables above disclose that the corrosion rate of zinc in blank solution was comparatively high at all temperatures explored. The corrosion rate, however, decreased right after the five 6-substituted chromone-2-carboxamides were added to the corrosive medium. Tables 4.18 – 4.22 show that increasing the concentration of the synthesized inhibitors enhanced the percentage inhibition efficiency at all temperatures. Furthermore, the inhibitory efficiency values of these molecules are seen to rise with corrosive medium temperature. Increases in inhibitor concentration have been linked to lower corrosion rates and higher inhibition efficiency values [238]. Tables 4.18 – 4.22, on the other hand, reveal no consistent trend in inhibition efficiency values as 6-substituted chromone-2-carboxamides concentration and temperature were raised. Despite the fact that the tests were performed in triplicate, no clear trend was identified. This discovery can be related to the fact that corrosion is an extremely intricate process due to factors that contribute to the inhibition mechanism such as electron exchange and inhibitor desorption, among others. The maximum inhibitory efficiency obtained in 1.5 M HCl was 82.89% at the CH_3O-Chr-2-Carb concentration of $5.0x10^{-4}$ M and a temperature of 333 K. The lowest inhibition efficiency was 49.91% at a Cl-Chr-2-Carb concentration of $1.0x10^{-1}$ M at a

temperature of 313 K. Despite the fact that there was no regular trend in the values of the 6-substituted chromone-2-carboxamides inhibition efficiency, it can be seen in Table 4.30 that inhibition efficiency values rose with increasing temperature. In this present study, it has been observed that corrosion rate of zinc was decreasing with the increasing concentration of the 6-substituted chromone-2-carboxamides. The corrosion rate was high in the uninhibited solution at all the temperatures (303, 313, 323 and 333 K) studied, were 0.0100, 0.0169, 0.0303 and 0.0498 $g.cm^{-2}.h^{-1}$ respectively. The results show that adding an inhibitor to the solution reduces the rate of zinc corrosion, and this is true at all temperatures and for all inhibitors tested. Several authors have seen and reported similar outcomes [238].

4.3.3. Thermodynamic parameters: adsorption Isotherms

Significant aspects regarding the interaction between the inhibitor molecule and zinc metal surface can be obtained from the adsorption isotherms. The experimental data were fitted adjusted to a number of adsorption isotherms to provide light on the kind and strength of adsorption. Amongst the tested known isotherms Langmuir isotherm provided a best fit which is presented graphically in Figure 4.68 to figure 4.72. The Langmuir isotherm can be represented as shown by equation (4.2) in section 4.2.3 above. This isotherm appears to be the most adequate for describing the adsorption of the 6-substituted chromone-2-carboxamides studied on the zinc surface. This is confirmed by the slope and coefficient values linear regression close to the unit (close to 1). From the Langmuir adsorption isotherm plots below, the values of equilibrium constant (K_{ads}) were calculated from the intercepts and the standard Gibb's free energy ($\Delta G°$) values were then calculated from the K_{ads} values utilizing equation (4.3) which clearly explained in section 4.2.3 of this study.

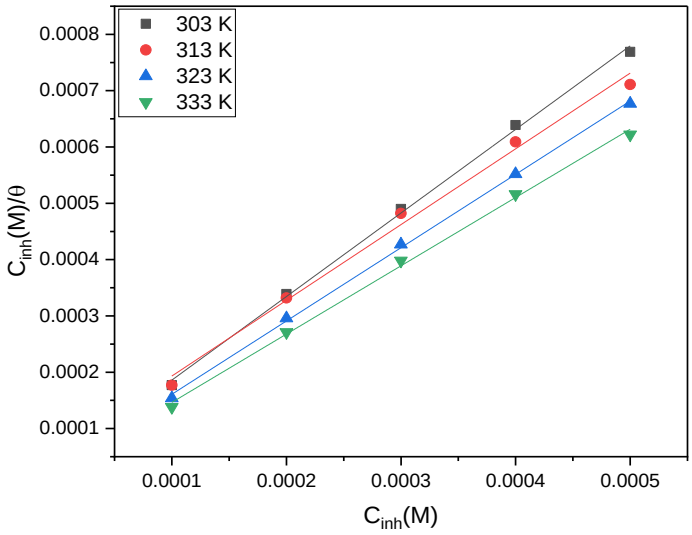

Figure 4.68: Langmuir adsorption isotherm for the adsorption of Chr-2-Carb on zinc metal in 1.5 M HCl at 303, 313, 323 and 333K.

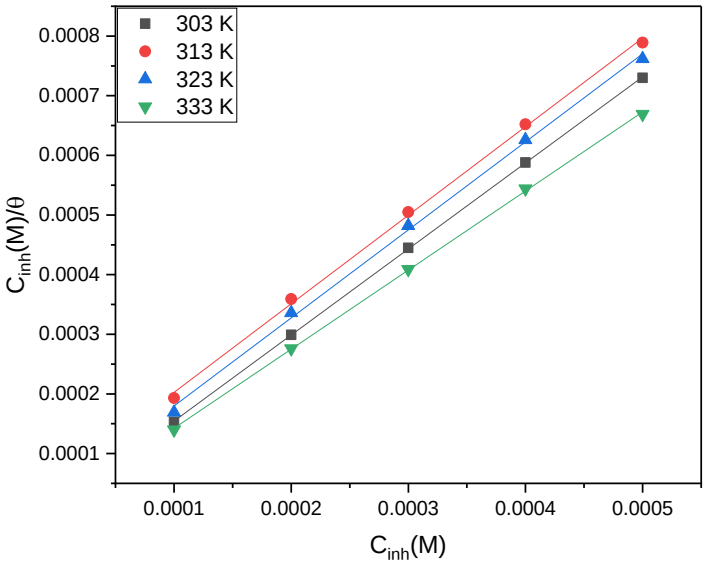

Figure 4.69: Langmuir adsorption isotherm for the adsorption of Br-Chr-2-Carb on zinc metal in 1.5 M HCl at 303, 313, 323 and 333K.

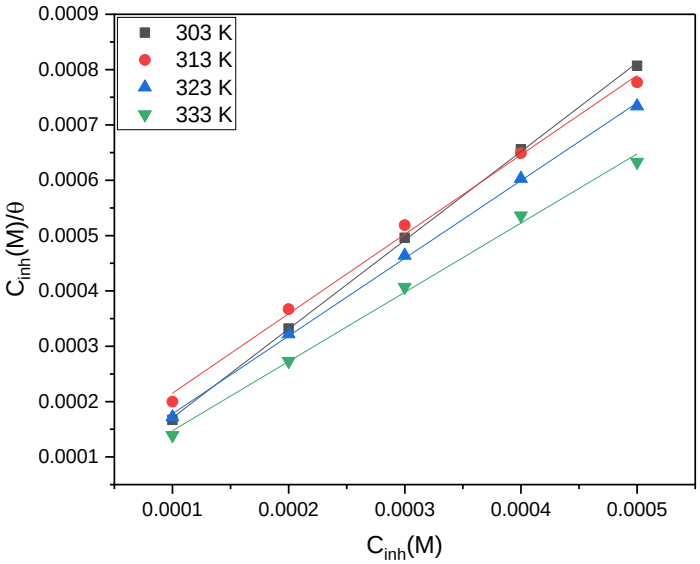

Figure 4.70: Langmuir adsorption isotherm for the adsorption of Cl-Chr-2-Carb on zinc metal in 1.5 M HCl at 303, 313, 323 and 333K.

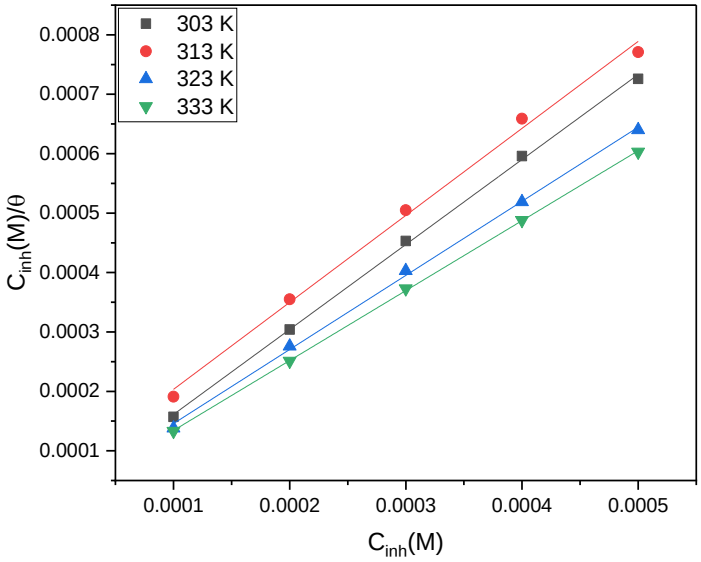

Figure 4.71: Langmuir adsorption isotherm for the adsorption of CH_3O-Chr-2-Carb on zinc metal in 1.5 M HCl at 303, 313, 323 and 333K.

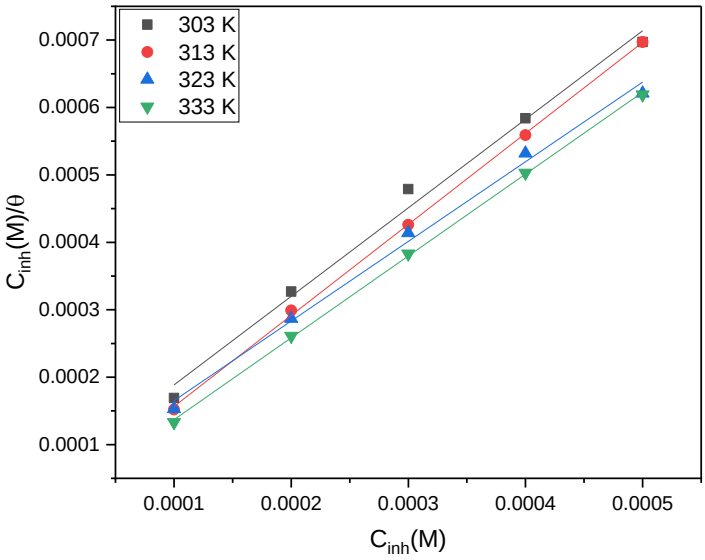

Figure 4.72: Langmuir adsorption isotherm for the adsorption of NO2-Chr-2-Carb on zinc metal in 1.5 M HCl at 303, 313, 323 and 333K.

Table 4.23: Adsorption parameters from Langmuir Adsorption Isotherm plot for Chr-2-Carb, Br-Chr-2-Carb, Cl-Chr-2-Carb, CH_3O-Chr-2-Carb and NO_2-Chr-2-Carb in 1.0 M.

Inhibitor	Temperature (K)	R^2	Slope	Intercept	K_{ads} ($L.mol^{-1}$)	$\Delta G°_{ads}$ ($kJ.mol^{-1}$)
Chr-2-Carb	303	0.99852	1.484	0.0000376	26.5957	18.3836
	313	0.99323	1.345	0.0000587	17.0358	17.8311
	323	0.99901	1.302	0.0000306	32.6797	20.1503
	333	0.99740	1.213	0.0000251	39.8406	21.3227
Br-Chr-2-Carb	303	0.99996	1.443	0.0000101	99.0099	21.6952
	313	0.99884	1.485	0.0000541	18.4843	18.0434
	323	0.99854	1.476	0.0000322	31.0559	20.0134
	333	0.99975	1.326	0.0000098	102.0408	23.9267
	303	0.99969	1.604	0.0000104	96.1538	21.6214

Cl-Chr-2-Carb	313	0.99642	1.436	0.0000716	13.9665	17.3141
	323	0.99938	1.405	0.0000375	26.6665	19.6042
	333	0.99647	1.251	0.0000223	44.8431	21.6502
CH_3O-Chr-2-Carb	303	0.99933	1.430	0.0000182	54.9451	20.2116
	313	0.99604	1.464	0.0000570	17.5439	17.9076
	323	0.99888	1.247	0.0000211	47.3934	21.8034
	333	0.99987	1.177	0.0000165	60.6060	22.4842
NO_2-Chr-2-Carb	303	0.99142	1.313	0.0000573	17.45201	17.3223
	313	0.99954	1.350	0.0000216	46.2963	20.4329
	323	0.99463	1.181	0.0000471	21.2314	18.9992
	333	0.99967	1.214	0.0000156	64.1026	22.6395

4.3.4. Effects of temperature and kinetic parameters

The rate of corrosion is greatly influenced by temperature. The interactions between the zinc electrode and the corrodent acidic medium can be drastically influenced by temperature changes and either the presence or absence of corrosion inhibitors. The impact of temperature on inhibitor adsorption on the metallic surface is particularly complex because many alterations are capable of occurring on the metal surface, such as fast etching, inhibitor detachment (desorption), and the inhibitor breakdown or simply reconfiguration. As observed from section 4.3.1, temperature has an impact on zinc metal corrosion in an acidic environment. It became clear that increasing the temperature of the acidic medium decreased the rate of zinc corrosion. As a result, temperature changes can be used to gain a greater insight into the type of adsorption of the examined 6-substituted chromone-2-carboxamides on the zinc surface. The equation developed by Arrhenius is frequently used to shed light on the dependence of metal corrosion rates on ambient temperature [249].

The previous section (4.2.4) demonstrated the form of Arrhenius equation [Equation (36)] used to calculate the activation energy (E_a) of zinc corrosion. The E_a values of zinc corrosion in the uninhibited system and presence of various concentrations of the examined 6-substituted chromone-2-carboxamides were calculated utilizing the graph of log C_R against 1/T Figures (4.73 - 4.77) and are reported in Table 4.24.

Based on the results of this study, Table 4.24 clearly shows that E_a values for the uninhibited solutions (blank) were higher than those for inhibited solutions. This is due to an increase in adsorption of preferred 6-substituted chromone-2-carboxamides inhibitor molecules on the zinc surface as the temperature of the corrosive environment rises. This signifies chemical adsorption of the synthesized inhibitors on the zinc metal. A comparable type of behavior has been observed in the literature [238]. A more detailed inspection at Table 4.24, the values of the E_a are higher at low concentration of the inhibitors ($1.0x10^{-4}$) indicating physisorption in the first stage.

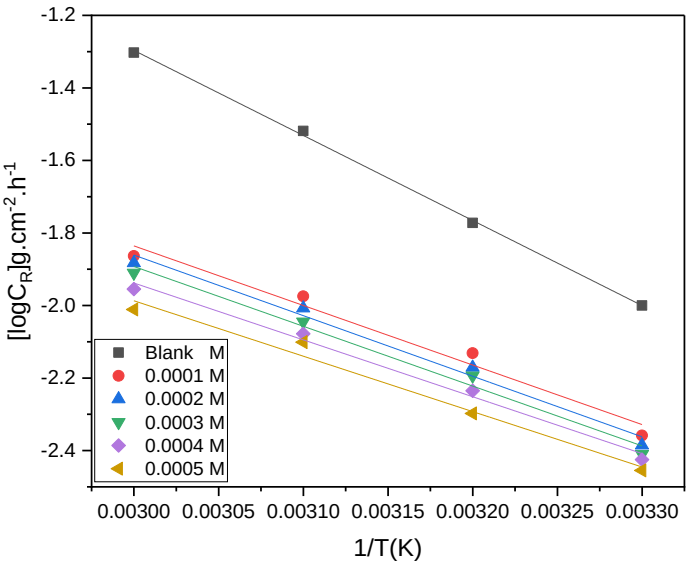

Figure 4.73: Arrhenius plots for zinc corrosion in 1.5 M HCl solution in the absence and presence of different concentrations of Chr-2-Carb.

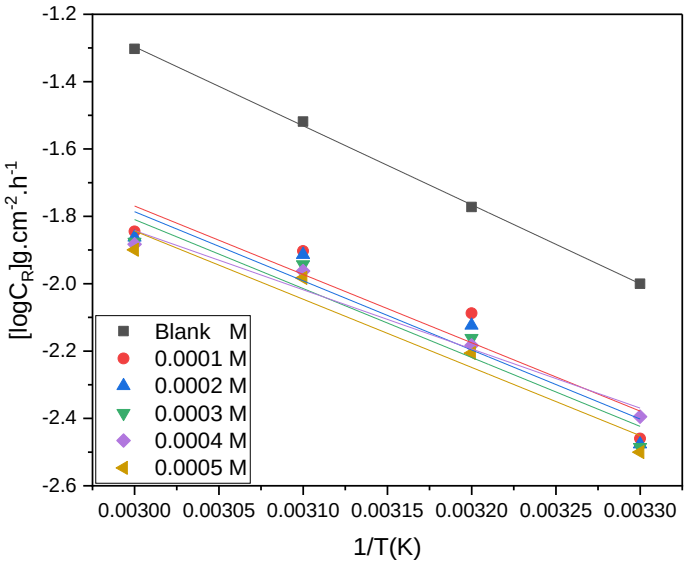

Figure 4.74: Arrhenius plots for zinc corrosion in 1.5 M HCl solution in the absence and presence of different concentrations of Br-Chr-2-Carb.

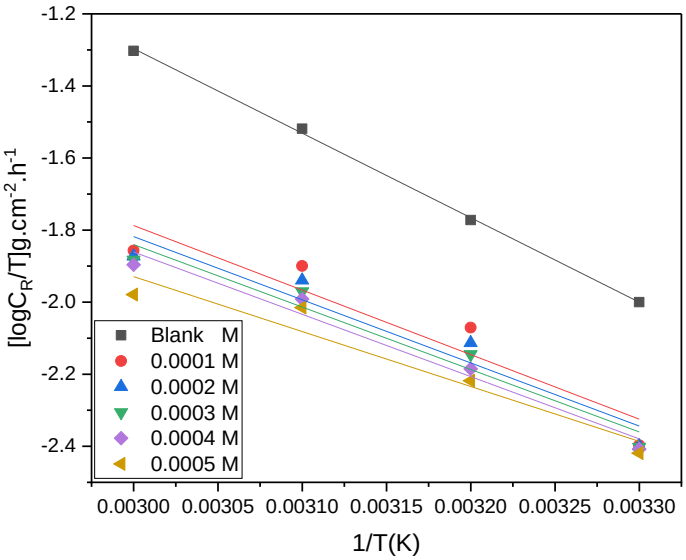

Figure 4.75: Arrhenius plots for zinc corrosion in 1.5 M HCl solution in the absence and presence of different concentrations of Cl-Chr-2-Carb.

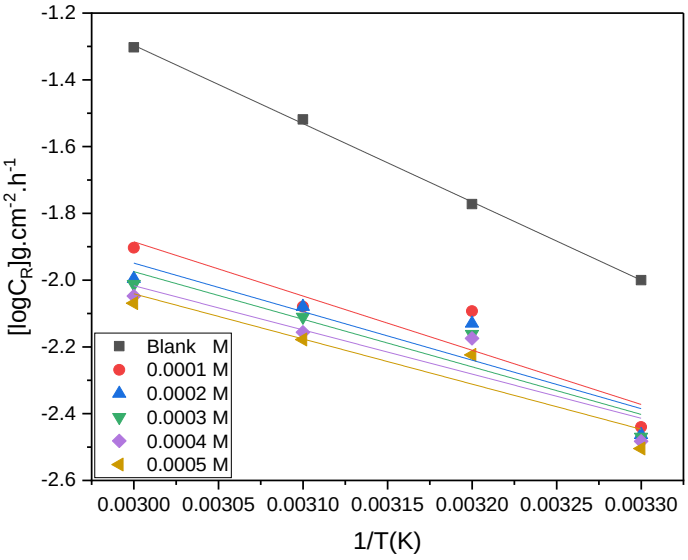

Figure 4.76: Arrhenius plots for zinc corrosion in 1.5 M HCl solution in the absence and presence of different concentrations of CH_3O-Chr-2-Carb.

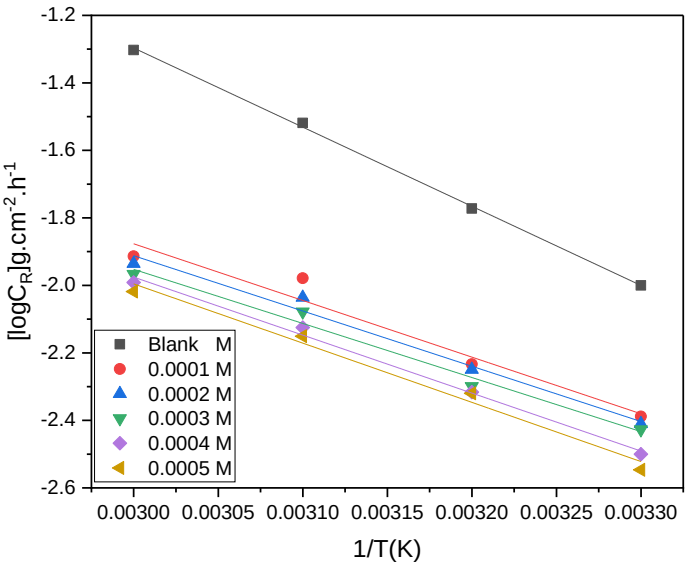

Figure 4.77: Arrhenius plots for zinc corrosion in 1.5 M HCl solution in the absence and presence of different concentrations of NO_2-Chr-2-Carb.

The thermodynamic parameters enthalpy of activation (ΔH^*_a) and entropy of activation (ΔS^*_a) can provide further insight into the effect of temperature on the extent of corrosion of zinc in 1.5 M HCl. The transition-state equation (47) relates CR and temperature to these factors. Figures 4.78 - 4.82 show the graphs of log(CR/T) against (1/T) with the best fitted data having a slope (-H*/2.303R) and an intercept [log(R/Nh)+(S*/2.303R)] which were used for calculating the resultant values of the standard enthalpy (ΔH^*_a) and entropy of activation (ΔS^*_a) in both the absence and the presence of the studied 6-substituted chromone-2-carboxamides [242, 243].

The interaction of the zinc metal and the 6-sub (adsorption process) is depicted in two ways: endothermic or exothermic. Furthermore, endothermic process absorbs heat and it entirely suggests chemisorption, while exothermic process gives of heat and may either suggest physisorption or chemisorption which are clearly defined earlier in this chapter. Results displayed in table 4.24 shows positive enthalpy values, indicating endothermic adsorption of the 6-substituted chromone-2-carboxamides on the zinc surface. This means that the zinc dissolution is delayed due to the existence of the examined 6-substituted chromone-2-carboxamides. Ogoko et al. discovered similar results.

Through literature review publications, it has been noted that moreover, tables 4.24 shows that the activation energy and enthalpy of activation values are slightly closer to each other (a difference of than 3), and the enthalpy of activation values were slightly lower than the activation energy values. Similar findings were also reported in different research publications. values around 40.86 kJ/mol imply physisorption kind of behavior, while values of roughly 100.00 kJ/mol convey chemisorption behavior. From this current research project, the ΔH^*_a values ranges from 22.7309 kJ/mol to 36.7666 kJ/mol, showing that the 6-substituted chromone-2-carboxamides adsorbed physical on the zinc surface. Moreover, table 4.24 shows that the E_a and ΔH^*_a values are slightly close (less than 3 kJ/mol), and the enthalpy of activation values were slightly lower than the activation energy values. Similar findings were also reported in different research publications.

As highlighted in section 4.2.4 above, larger negative values of ΔS^* signifies that the activated complex in the rate-determining stage reflects inhibitor attachment rather than dissolution. Higher ΔS^* values were obtained in this study, as displayed in table 4.24. This shows that the adsorption of inhibitor molecules on the zinc surface reduces system disorder as it moves from reactants to active complex [338]. The increase in ΔS^* values caused by inhibitor molecule adsorption on the MS surface from the acid solution can be interpreted as a quasi-substitution process between organic molecules in the aqueous phase and water molecules on the electrode surface. Literature has revealed that the adsorption of inhibitor molecules is believed to follow desorptions of water molecules from the electrode surface in such a process, resulting in a drop in zinc's electrical capacity.

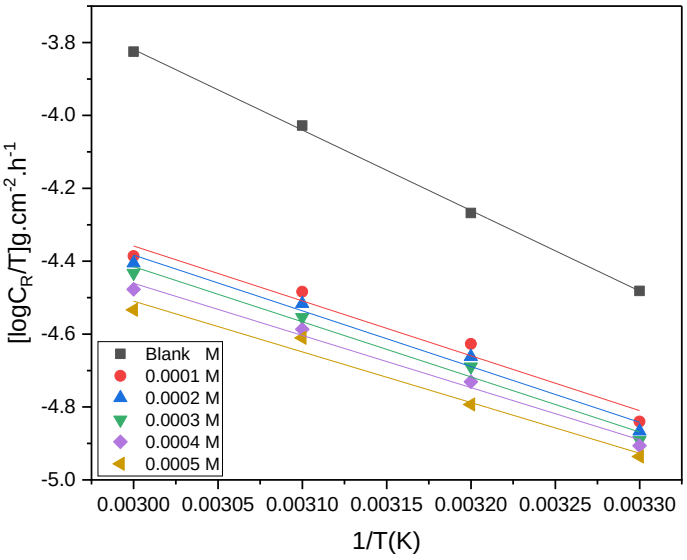

Figure 4.78: Transition state plots for zinc corrosion in 1.5 M HCl solution in the absence and presence of different concentrations Chr-2-Carb.

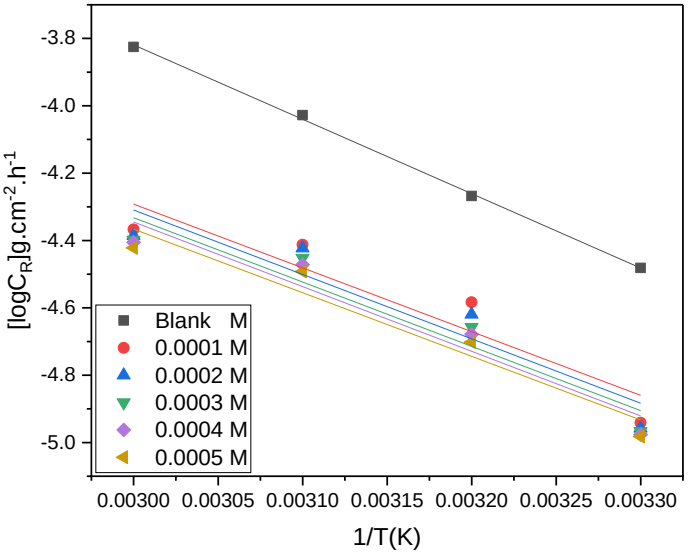

Figure 4.79: Transition state plots for zinc corrosion in 1.5 M HCl solution in the absence and presence of different concentrations Br-Chr-2-Carb.

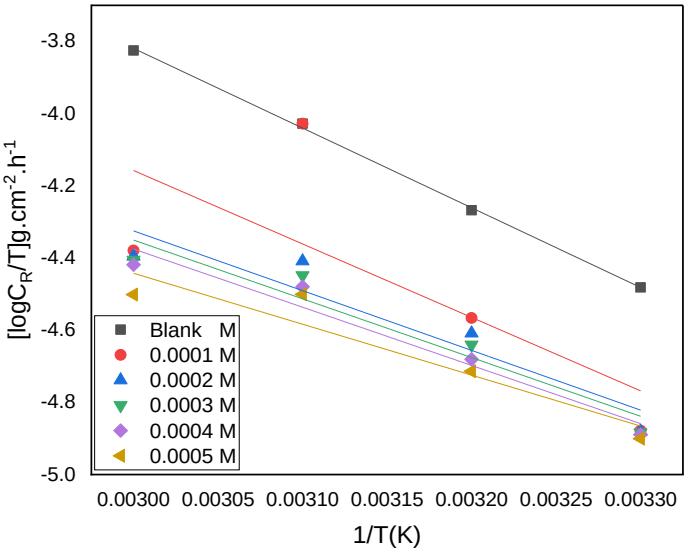

Figure 4.80: Transition state plots for zinc corrosion in 1.5 M HCl solution in the absence and presence of different concentrations Cl-Chr-2-Carb.

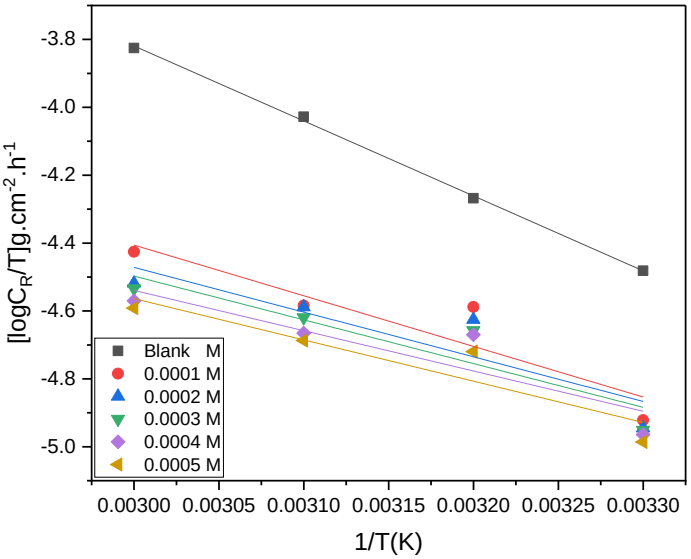

Figure 4.81: Transition state plots for zinc corrosion in 1.5 M HCl solution in the absence and presence of different concentrations CH_3O-Chr-2-Carb.

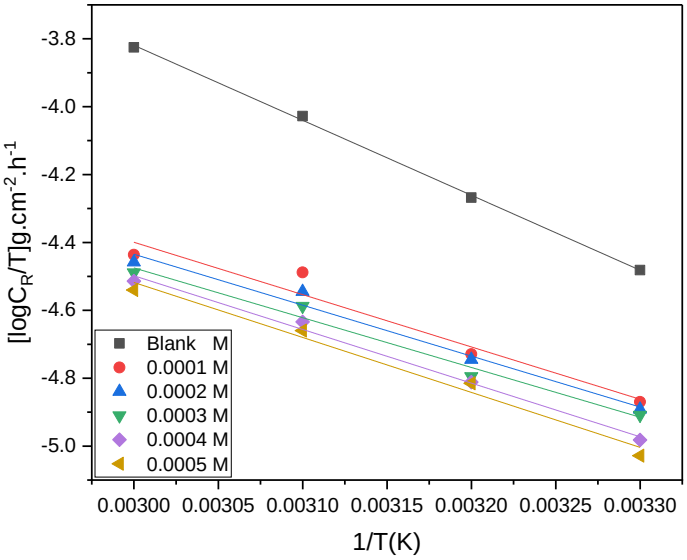

Figure 4.82: Transition state plots for zinc corrosion in 1.5 M HCl solution in the absence and presence of different concentrations NO_2-Chr-2-Carb.

Table 4.24: Arrhenius and transition parameters for zinc in 1.5 M HCl in the absence and presence of various concentrations of the studied 6-substituted chromone-2-carboxamides.

Inhibitor	Concentration of inhibitors ($x10^{-4}$ M)	E_a ($kJ.mol^{-1}$)	ΔH^* ($kJ.mol^{-1}$)	ΔS^* ($J.mol^{-1}.K^{1}$)
Blank	-	44.9027	42.2794	-174.2224
Chr-2-Carb	1.0	31.4415	28.8296	-196.2363
	2.0	31.9777	29.2835	-195.8524
	3.0	31.5755	28.9618	-196.5356
	4.0	30.0054	27.4012	-198.9476
	5.0	29.2394	26.6295	-200.3613
Br-Chr-2-Carb	1.0	38.8653	36.2477	-186.0223
	2.0	39.2961	36.6211	-185.6814

	3.0	39.1946	36.5713	-185.9358
	4.0	39.3899	36.7666	-185.7866
	5.0	38.7829	36.1635	-186.7491
Cl-Chr-2-Carb	1.0	34.2946	31.6713	-192.1339
	2.0	33.5516	30.9359	-193.3484
	3.0	33.1897	30.5683	-194.0101
	4.0	33.0883	30.4859	-194.2883
	5.0	29.1819	26.5625	-195.1411
CH_3O-Chr-2-Carb	1.0	31.0968	28.5731	-196.9669
	2.0	27.8225	25.2164	-201.8859
	3.0	27.2863	24.6764	-202.8019
	4.0	25.3332	22.7309	-205.6866
	5.0	25.8855	23.2805	-205.1725
NO_2-Chr-2-Carb	1.0	32.1481	29.5248	-195.6700
	2.0	31.3572	28.7397	-196.9891
	3.0	30.6851	28.0733	-196.9163
	4.0	32.8776	30.2830	-195.5058
	5.0	33.5978	31.0087	-194.7250

4.3.5. Adsorption film analysis

The FTIR spectra of the 6-substituted chromone-2-carboxamides were compared to the adsorption film spectra formed after scratching from the zinc metal surface after weight loss measurements. These spectra are shown in Figures (4.83 – 4.87).

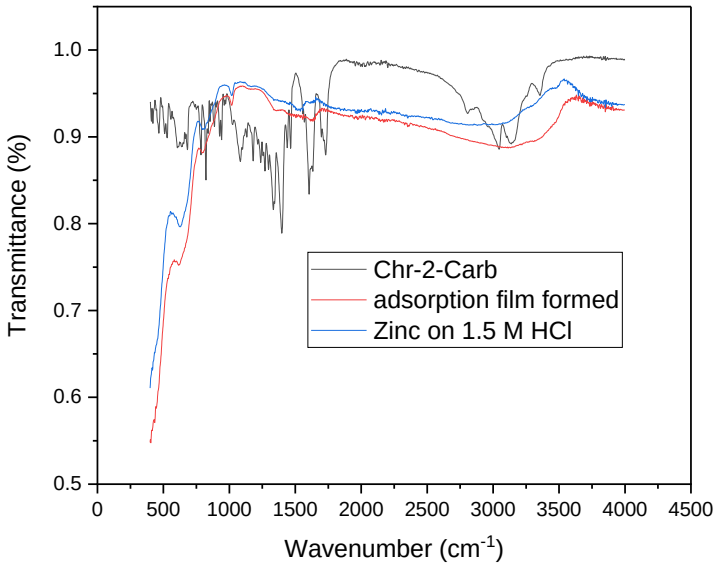

Figure 4.83: FT-IR spectra comparison of the frequencies for the pure compound and adsorption films formed on the Zinc in 1.5 M HCl by Chr-2-Carb corrosion inhibitor.

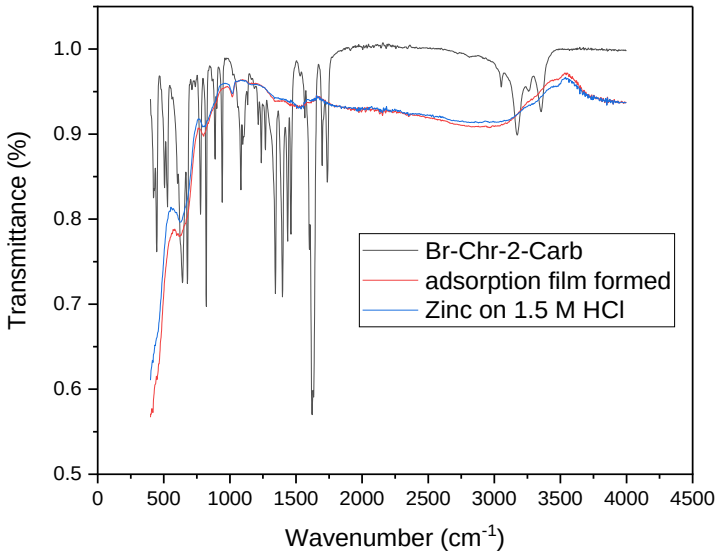

Figure 4.84: FT-IR spectra comparison of the frequencies for the pure compound and adsorption films formed on the Zinc in 1.5 M HCl by Br-Chr-2-Carb corrosion inhibitor.

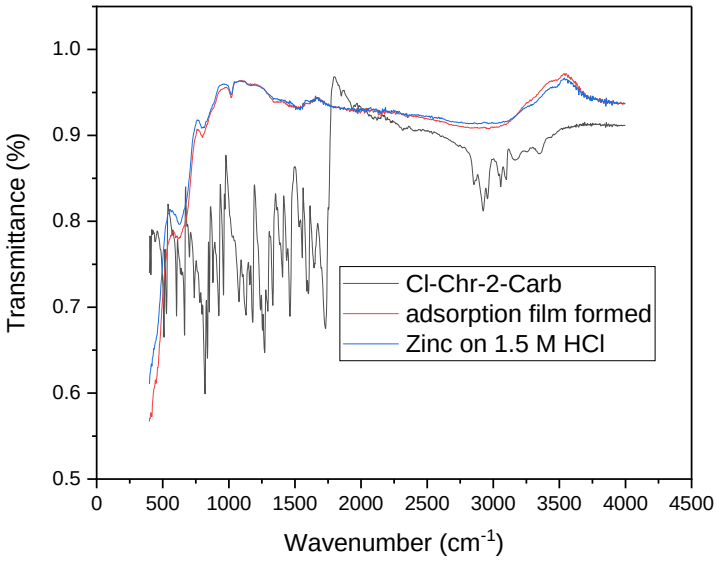

Figure 4.85: FT-IR spectra comparison of the frequencies for the pure compound and adsorption films formed on the Zinc in 1.5 M HCl by Cl-Chr-2-Carb corrosion inhibitor.

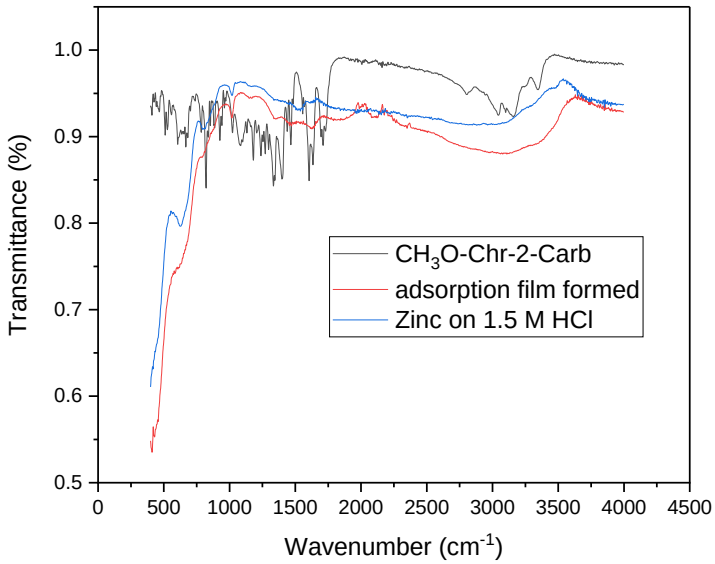

Figure 4.86: FT-IR spectra comparison of the frequencies for the pure compound and adsorption films formed on the Zinc in 1.5 M HCl CH_3O-Chr-2-Carb corrosion inhibitor.

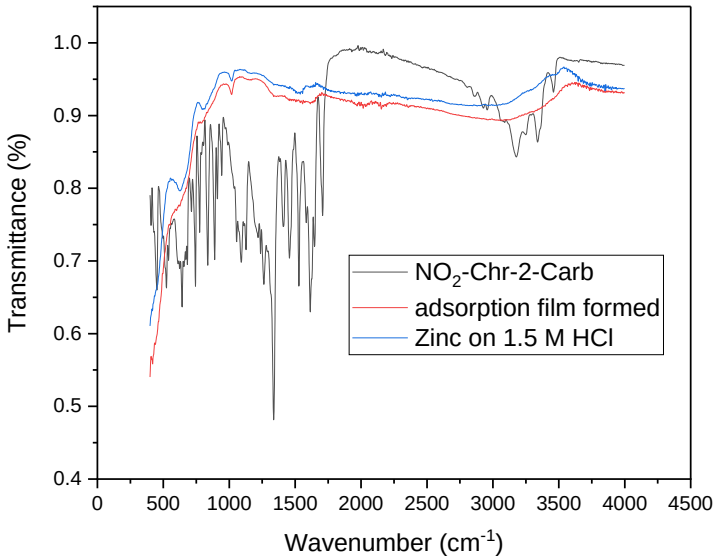

Figure 4.87: FT-IR spectra comparison of the frequencies for the pure compound and adsorption films formed on the Zinc in 1.5 M HCl NO_2-Chr-2-Carb corrosion inhibitor.

All the above figures clearly shows that the aromatic C-O peak [Ar (C-O)] disappeared in the spectra of the adsorption film as displayed in table 4.25, same observations as in the mild steel in section 4.2.5. It is also noted that the carbonyl carbon (C=O) peaks which were appearing around 1700 cm^{-1} on the spectra of the synthesized compounds shifted to around 1600 cm^{-1} wavenumber on the adsorption film spectra, while in the presence of 6-Br-2-Carb and NO_2-Chr-2-Carb there was no C=O) peaks formed on the adsorption film spectra. Ar (C=C) peaks at 1538.56 cm^{-1}, 1556.50 $cm^{-1}$and 1558.91 cm^{-1} corresponding to Br-Chr-2-Carb, Cl-Chr-2-Carb and NO_2-Chr-2-Carb respectively were observed on the adsorption film formed spectra, and no Ar (C=C) peaks appeared in the presence of Chr-2-Carb and CH_3O-Chr-2-Carb on the adsorption film spectra. The aromatic C-H (=C-H) stretching observed around 3137 cm^{-1} to 3177.75 on the spectra of the synthesized compounds shifted to around 2961.58 cm^{-1} – 3114.21 cm^{-1} and the highest wavenumber 3141.57 cm^{-1} in the presence of Cl-Chr-2-Carb on the adsorption film spectra. Furthermore, the NH_2 peak disappeared in the spectra of the adsorption film and new bonds appeared around 3600 cm^{-1} and 3800 cm^{-1} of the adsorption film spectra.

Table 4.25: Peaks identified from FTIR spectra of the synthesized 6-substituted chromone-2-carboxamides and adsorption film formed on the Zinc in 1.5 M HCl.

Inhibitor-Zinc	Functional Groups, Peaks obtained from FTIR spectra (cm^{-1})				
	$CONH_2$	NH_2	Ar (C=C)	Ar (C-O)	=C-H
Chr-2-Carb	1633.68	-	-	-	3114.21
Br-Chr-2-Carb	-	-	1538.56	-	2961.58
Cl-Chr-2-Carb	1633.80	-	1556.50	-	3141.57
CH_3O-Chr-2-Carb	1633.03	-	-	-	3109.21
NO_2-Chr-2-Carb	-	-	1558.91	-	3045.23

4.4. Aluminium

4.4.1. Gravimetric Analysis (GA) and the effect of inhibitor concentration

GA measurements of aluminium specimen were performed in inhibited and uninhibited HCl solutions at four temperatures of 303 – 333 K. The weight loss technique was first carried out by immersing the metal specimen in 1.5 M HCl solution at temperatures ranging from 303 to 333 K for 8 hours. All the metal specimens were consumed into powder due to the high acid concentration (1.5 M HCl) and longer period (8 hours). With this regard, the weight-loss process was repeated, but this time in 1.0 M HCl solution at temperatures ranging from 303 to 333 K for 6 hours. The potential of the 6-substituted chromone-2-carboxamides to reduce aluminium corrosion was investigated in different concentrations of 1.0×10^{-4}, 2.0×10^{-4}, 3.0×10^{-4}, 4.0×10^{-4}, and 5.0×10^{-4} M in 1.5 M HCl. The results for the Al corrosion test in blank and in the presence of various concentrations of 6-Sub6-substitutedmone-2-carboxamide derivatives are graphically depicted in Figures 4.88 – 4.92 and Table 4.26 below.

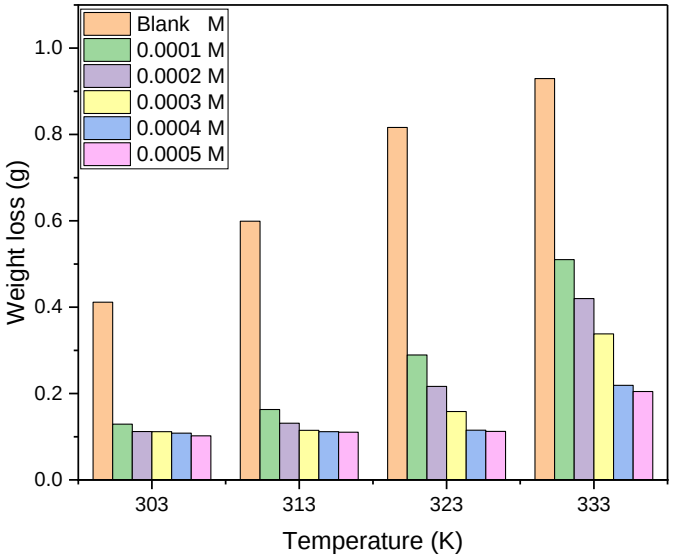

Figure 4.88: The graph showing the weight loss measurements of aluminium in the absence and presence of Chr-2-Carb in 1.0 M HCl.

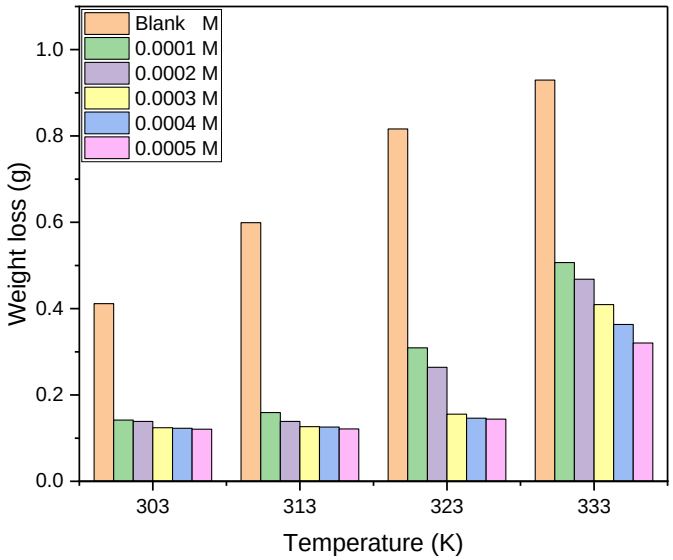

Figure 4.89: The graph showing the weight loss measurements of aluminium in the absence and presence of Br-Chr-2-Carb in 1.0 M HCl.

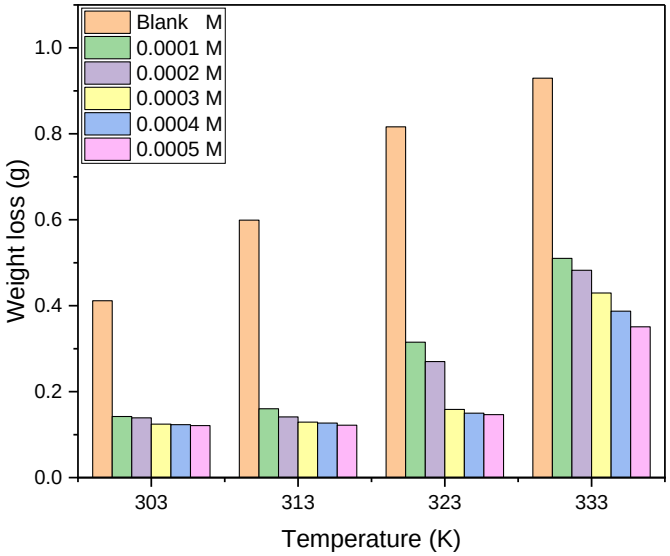

Figure 4.90: The graph showing the weight loss measurements of aluminium in the absence and presence of Cl-Chr-2-Carb in 1.0 M HCl.

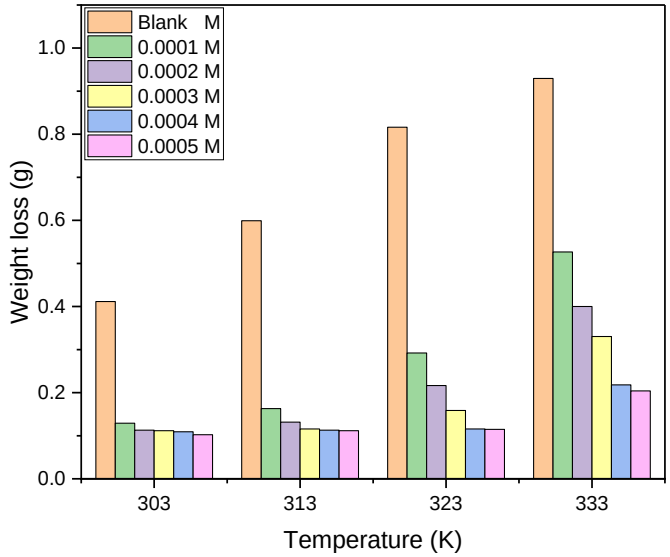

Figure 4.91: The graph showing the weight loss measurements of aluminium in the absence and presence of CH_3O-Chr-2-Carb in 1.0 M HCl.

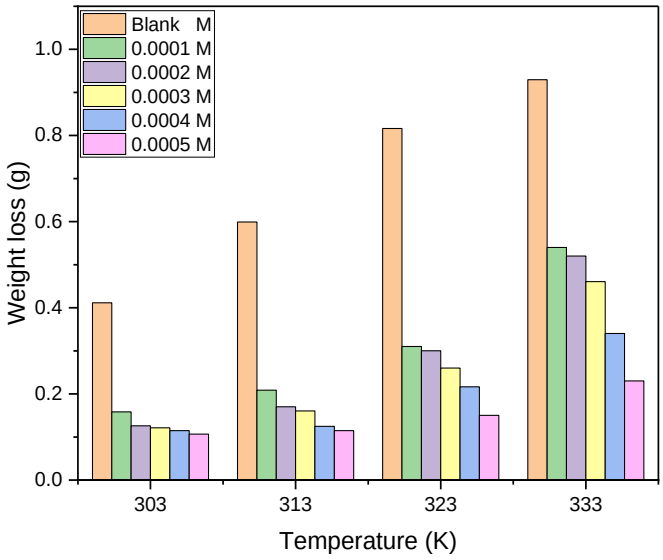

Figure 4.92: The graph showing the weight loss measurements of aluminium in the absence and presence of NO_2-Chr-2-Carb in 1.0 M HCl.

Table 4.26: Weight loss measurements of aluminium in the absence and presence of 6-Substituted chromone-2-carboxamides in 1.0 M HCl.

Inhibitor	**Concentration (x10^{-4} M)**	**Weight loss (g)**			
		303 K	313 K	323 K	333 K
	0.0000	0.4116	0.5991	0.8162	0.9294
Chr-2-Carb	1.0	0.1290	0.1631	0.2892	0.5101
	2.0	0.1121	0.1313	0.2166	0.4201
	3.0	0.1117	0.1149	0.1584	0.3381
	4.0	0.1084	0.1116	0.1152	0.2189
	5.0	0.1020	0.1103	0.1124	0.2046
Br-Chr-2-Carb	1.0	0.1419	0.1592	0.3091	0.5068
	2.0	0.1387	0.1386	0.2642	0.4681
	3.0	0.1242	0.1265	0.1554	0.4094
	4.0	0.1228	0.1258	0.1462	0.3635

	5.0	0.1208	0.1212	0.1441	0.3203
Cl-Chr-2-Carb	1.0	0.1421	0.1601	0.3152	0.5102
	2.0	0.1391	0.1411	0.2701	0.4824
	3.0	0.1244	0.1291	0.1587	0.4296
	4.0	0.1231	0.1269	0.1498	0.3872
	5.0	0.1210	0.1218	0.1465	03508
CH_3O-Chr-2-Carb	1.0	0.1292	0.1629	0.2921	0.5268
	2.0	0.1129	0.1315	0.2165	0.4001
	3.0	0.1118	0.1158	0.1586	0.3303
	4.0	0.1092	0.1128	0.1558	0.2182
	5.0	0.1023	0.1116	0.1149	0.2041
NO_2-Chr-2-Carb	1.0	0.1582	0.2087	0.3102	0.5401
	2.0	0.1258	0.1702	0.3001	0.5201
	3.0	0.1214	0.1606	0.2602	0.4607
	4.0	0.1148	0.1246	0.2164	0.3402
	5.0	0.1068	0.1184	0.1504	0.2301

Noticeable from the figures and the table above, the mass loss of aluminium dropped dramatically as the concentration of the tested 6-substituted chromone-2-carboxamides increased. The results presented in the table above show that the weight loss readings for aluminium were much lower in the presence of the inhibitors than in the blank solution (uninhibited solution). As illustrated in Table 4.26, the weight loss of aluminium for the blank test was 0.4116 g, 0. 5991 g, 0.8162 g, and 0.9294 g at temperatures of 303 K, 313 K, 323 K, and 333 K, respectively, as compared to tests conducted in the presence of the synthesized inhibitors 6-substituted chromone-2-carboxamides, where the mass loss of Al has decreased dramatically. For instance, the weight loss in the presence of 1.0×10^{-4} M Chr-2-Carb was found to be 0.1290 g 0.1631 g, 0.2892 g, 0.5101 g at the four

temperatures 303 K, 313 K, 323 K, and 333 K, respectively. A comparable behavior was noted in all of the 6-substituted chromone-2-carboxamides concentrations examined. These findings correlate with the proven fact that increasing the quantity of inhibitor minimizes Al weight loss, and as a result the rate of Al corrosion is reduced.

4.4.2. Corrosion rate, inhibition efficiency and surface coverage

The corrosion rate (C_R) of aluminium, percentage inhibition efficiency (% IE), and as well as the surface coverage (θ) were computed from the weight loss measurement of zinc in 1.5 M HCl in the absence and presence of various concentrations of the 6-substituted chromone-2-carboxamides at temperature 303 – 333 K. The values are displayed in Tables 4.27 – 4.31 and Figures 4.93 – 4.97.

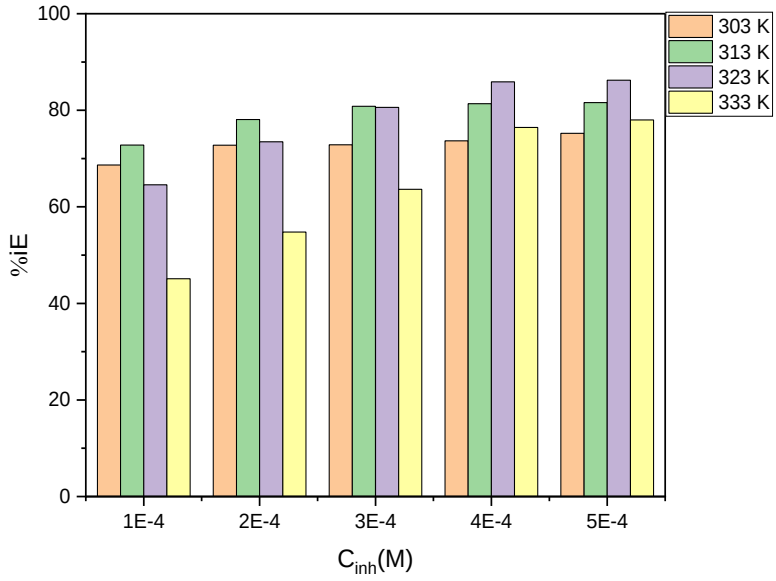

Figure 4.93: The variation of percentage inhibition efficiency with various concentration of Chr-2-Carb at various temperatures in 1.0 M HCl.

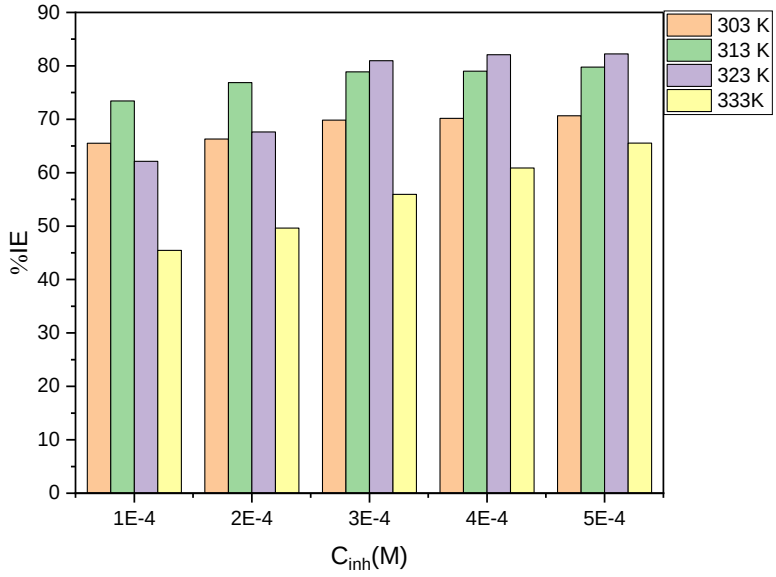

Figure 4.94: The variation of percentage inhibition efficiency with various concentration of Br-Chr-2-Carb at various temperatures in 1.0 M HCl.

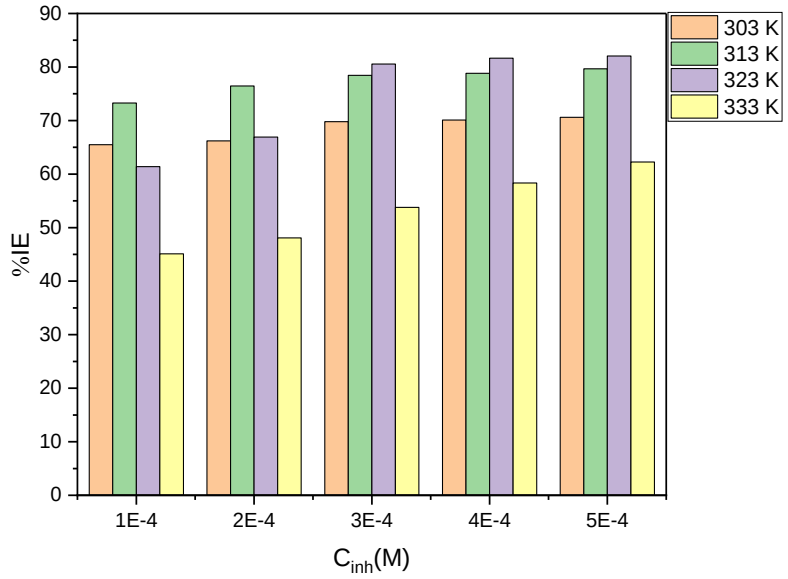

Figure 4.95: The variation of percentage inhibition efficiency with various concentration of Cl-Chr-2-Carb at various temperatures in 1.0 M HCl.

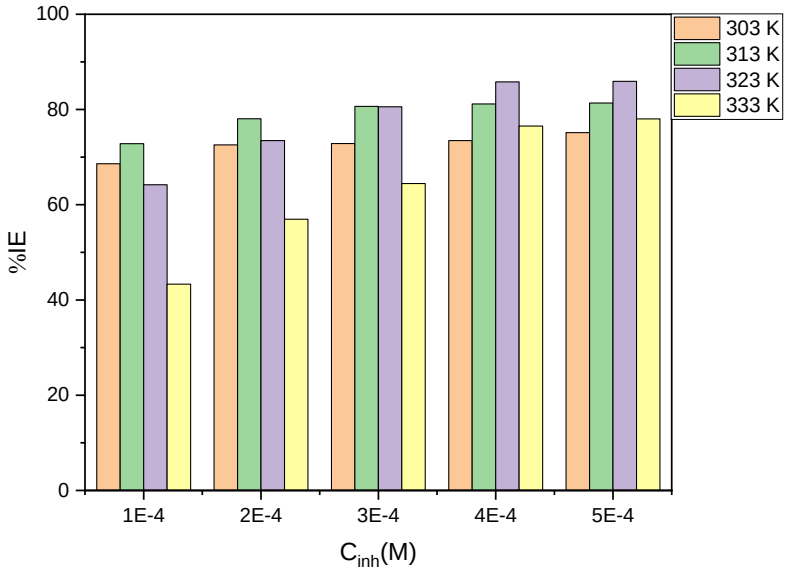

Figure 4.96: The variation of percentage inhibition efficiency with various concentration of CH3O-Chr-2-Carb at various temperatures in 1.0 M HCl.

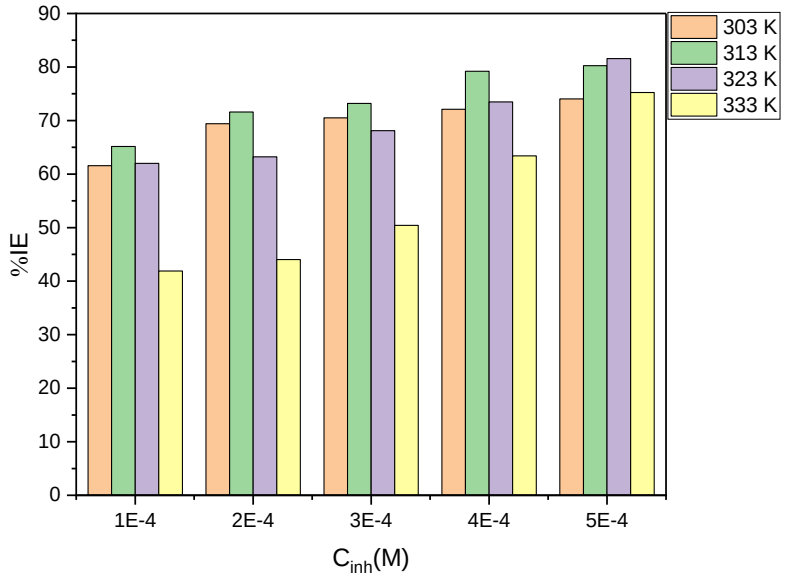

Figure 4.97: The variation of percentage inhibition efficiency with various concentration of NO_2-Chr-2-Carb at various temperatures in 1.0 M HCl.

Table 4.27: The corrosion parameters for aluminium in 1.0 M HCl in the absence and presence of various concentrations of Chr-2-Carb obtained from weight loss measurements at 303 – 333 K.

Inhibitor	Temperature (K)	Inhibitor concentration (x10^{-4} M)	Corrosion rate (g.cm^{-2}.h^{-1})	Surface coverage (θ)	Inhibition efficiency (%)
	303	-	0.01143	-	-
		1.0	0.00358	0.6866	68.66
		2.0	0.00311	0.7276	72.76
		3.0	0.00310	0.7286	72.86
		4.0	0.00301	0.7366	73.66
		5.0	0.00283	0.7522	75.22
		-	0.01664	-	-
		1.0	0.00453	0.7278	72.78

Chr-2-Carb	313	2.0	0.00365	0.7808	78.08
		3.0	0.00319	0.8082	80.82
		4.0	0.00310	0.8137	81.82
		5.0	0.00306	0.8159	81.59
	323	-	0.02267	-	-
		1.0	0.00803	0.6457	64.57
		2.0	0.00602	0.7346	73.46
		3.0	0.00440	0.8059	80.59
		4.0	0.00320	0.8589	85.89
		5.0	0.00312	0.8623	86.23
	333	-	0.02582	-	-
		1.0	0.01417	0.4512	45.12
		2.0	0.01167	0.5479	54.79
		3.0	0.00939	0.6362	63.62
		4.0	0.00608	0.7645	76.45
		5.0	0.00568	0.7799	77.99

Table 4.28: The corrosion parameters for aluminium in 1.0 M HCl in the absence and presence of various concentrations of Br-Chr-2-Carb obtained from weight loss measurements at 303 – 333 K.

Inhibitor	**Temperature (K)**	**Inhibitor concentration ($x10^{-4}$ M)**	**Corrosion rate ($g.cm^{-2}.h^{-1}$)**	**Surface coverage (θ)**	**Inhibition efficiency (%)**
	303	-	0.01143	-	-
		1.0	0.00394	0.6552	65.52
		2.0	0.00385	0.6630	66.30
		3.0	0.00345	0.6983	69.83

Br-Chr-2-Carb		4.0	0.00341	0.7017	70.17
		5.0	0.00336	0.7065	70.65
	313	-	0.01664	-	-
		1.0	0.00442	0.7343	73.43
		2.0	0.00385	0.7687	76.87
		3.0	0.00351	0.7888	78.88
		4.0	0.00349	0.7900	79.00
		5.0	0.00337	0.7977	79.77
	323	-	0.02267	-	-
		1.0	0.00859	0.6213	62.13
		2.0	0.00734	0.6763	67.63
		3.0	0.00432	0.8096	80.96
		4.0	0.00406	0.8209	82.09
		5.0	0.00400	0.8223	82.23
	333	-	0.02582	-	-
		1.0	0.01408	0.4547	45.47
		2.0	0.01300	0.4963	49.63
		3.0	0.01137	0.5595	55.95
		4.0	0.01009	0.6089	60.89
		5.0	0.00889	0.6554	65.54

Table 4.29: The corrosion parameters for aluminium in 1.0 M HCl in the absence and presence of various concentrations of Cl-Chr-2-Carb obtained from weight loss measurements at 303 – 333 K.

Inhibitor	Temperature (K)	Inhibitor concentration ($x10^{-4}$ M)	Corrosion rate ($g.cm^{-2}.h^{-1}$)	Surface coverage (θ)	Inhibition efficiency (%)
Cl-Chr-2-Carb	303	-	0.01143	-	-
		1.0	0.00395	0.6548	65.48
		2.0	0.00386	0.6621	66.21
		3.0	0.00346	0.6978	69.78
		4.0	0.00342	0.7009	70.09
		5.0	0.00336	0.7060	70.60
	313	-	0.01664	-	-
		1.0	0.00447	0.7328	73.28
		2.0	0.00392	0.7645	76.45
		3.0	0.00359	0.7845	78.45
		4.0	0.00353	0.7882	78.82
		5.0	0.00338	0.7967	79.67
	323	-	0.02267	-	-
		1.0	0.00876	0.6138	61.38
		2.0	0.00750	0.6691	66.91
		3.0	0.00441	0.8056	80.56
		4.0	0.00416	0.8165	81.65
		5.0	0.00407	0.8205	82.05
	333	-	0.02582	-	-
		1.0	0.01417	0.4510	45.10
		2.0	0.01340	0.4809	48.09

		3.0	0.01193	0.5378	53.78
		4.0	0.01076	0.5834	58.34
		5.0	0.00974	0.6226	62.26

Table 4.30: The corrosion parameters for aluminium in 1.0 M HCl in the absence and presence of various concentrations of CH_3O-Chr-2-Carb obtained from weight loss measurements at 303 – 333 K.

Inhibitor	Temperature (K)	Inhibitor concentration ($x10^{-4}$ M)	Corrosion rate ($g.cm^{-2}.h^{-1}$)	Surface coverage (θ)	Inhibition efficiency (%)
CH_3O-Chr-2-Carb	303	-	0.01143	-	-
		1.0	0.00359	0.6861	68.61
		2.0	0.00314	0.7257	72.57
		3.0	0.00311	0.7284	72.84
		4.0	0.00303	0.7347	73.47
		5.0	0.00284	0.7515	75.15
	313	-	0.01664	-	-
		1.0	0.00453	0.7281	72.81
		2.0	0.00365	0.7805	78.05
		3.0	0.00322	0.8067	80.67
		4.0	0.00313	0.8117	81.17
		5.0	0.00310	0.8137	81.37
	323	-	0.02267	-	-
		1.0	0.00811	0.6421	64.21
		2.0	0.00601	0.7347	73.47
		3.0	0.00441	0.8057	80.57
		4.0	0.00321	0.8581	85.81

		5.0	0.00318	0.8592	85.92
	333	-	0.02582	-	-
		1.0	0.01463	0.4332	43.32
		2.0	0.01111	0.5695	56.95
		3.0	0.00918	0.6446	64.46
		4.0	0.00606	0.7652	76.52
		5.0	0.00567	0.7804	78.04

Table 4.31: The corrosion parameters for aluminium in 1.0 M HCl in the absence and presence of various concentrations of NO_2-Chr-2-Carb obtained from weight loss measurements at 303 – 333 K.

Inhibitor	**Temperature (K)**	**Inhibitor concentration ($x10^{-4}$ M)**	**Corrosion rate ($g.cm^{-2}.h^{-1}$)**	**Surface coverage (θ)**	**Inhibition efficiency (%)**
	303	-	0.01143	-	-
		1.0	0.00439	0.6141	61.41
		2.0	0.00349	0.6941	69.41
		3.0	0.00337	0.7051	70.51
		4.0	0.00319	0.7211	72.11
		5.0	0.00297	0.7405	74.05
	313	-	0.01664	-	-
		1.0	0.00579	0.6516	65.16
		2.0	0.00473	0.7159	71.59
		3.0	0.00461	0.7319	73.19
		4.0	0.00346	0.7920	79.20
		5.0	0.00329	0.8024	80.24

NO_2-Chr-2-Carb	323	-	0.02267	-	-
		1.0	0.00862	0.6199	61.99
		2.0	0.00834	0.6323	63.23
		3.0	0.00723	0.6812	68.12
		4.0	0.00601	0.7349	73.49
		5.0	0.00423	0.8157	81.57
	333	-	0.02582	-	-
		1.0	0.01750	0.4189	41.89
		2.0	0.01445	0.4404	44.04
		3.0	0.01279	0.5043	50.43
		4.0	0.00945	0.6339	63.39
		5.0	0.00639	0.7524	75.24

The results displayed above disclose that the corrosion rate of Al in blank solution was comparatively high at all temperatures explored and increases with increasing temperature. The corrosion rate, however, decreased right after the five 6-substituted chromone-2-carboxamides were added to the acid solution. Tables 4.27 – 4.31 show that increasing the concentration of the synthesized inhibitors enhanced the percentage inhibition efficiency at all temperatures. Furthermore, the inhibitory efficiency values of these molecules are seen to rise with corrosive medium temperature. Noticeably, the percentage inhibition efficiency started decreasing at the highest temperature (333 K) and this indicates that the inhibitors were going desorption process as the particles of the synthesized inhibitors were aggregating. The minimum inhibitory efficiency obtained in 1.0 M HCl was 41.89 % at the 6-Nit-2-Carb concentration of $1.0x10^{-4}$ M and a temperature of 333 K. The highest inhibition efficiency was 86.23 % at a Chr-2-Carb concentration of $5.0x10^{-1}$ M at a temperature of 323 K. Despite the fact that there was no regular trend in the values of Chr-2-Carb inhibition efficiency, it can be seen in Table 4.30 that inhibition efficiency values decreased with increasing temperature from 323 K to 333K. The Increase in inhibitor concentration has been linked to lower corrosion rates and higher

inhibition efficiency values as explained in section 4.3.2 of this study. Tables 4.27 – 4.31, on the other hand, reveal no consistent trend in inhibition efficiency values as 6-substituted chromone-2-carboxamides concentration and temperature were raised. Despite the fact that the tests were performed in triplicate, no clear trend was identified. This discovery can be related to the fact that corrosion is an extremely intricate process due to factors that contribute to the inhibition mechanism such as electron exchange and inhibitor desorption, among others. In this present study, it has been observed that corrosion rate of Al was decreasing with the increasing concentration of the 6-substituted chromone-2-carboxamides. The corrosion rate was high in the uninhibited solution at all the temperatures (303, 313, 323 and 333 K) studied, were 0.01143, 0.01664, 0.02267 and 0.02582 $g.cm^{-2}.h^{-1}$ respectively. The results show that adding an inhibitor to the solution reduces the rate of Al corrosion, and this is true at all temperatures and for all inhibitors tested. Several authors have seen and reported similar outcomes [238].

4.4.3. Thermodynamic parameters: adsorption Isotherms

Significant aspects regarding the interaction between the inhibitor molecule and metal surface can be obtained from the adsorption isotherms. The experimental data were fitted adjusted to a number of adsorption isotherms to provide light on the kind and strength of adsorption. Amongst the tested known isotherms Langmuir isotherm provided a best fit which is presented graphically in Figures 4.98 - 4.102. The Langmuir isotherm can be represented as shown by equation (4.2) in section 4.2.3 above. This isotherm appears to be the most adequate for describing the adsorption of the 6-substituted chromone-2-carboxamides studied on the Al surface. This is confirmed by the slope and coefficient values linear regression close to the unit (close to 1). From the Langmuir adsorption isotherm plots below, the values of equilibrium constant (K_{ads}) were calculated from the intercepts and the standard Gibb's free energy ($\Delta G°$) values were then calculated from the K_{ads} values utilizing equation (4.3) which clearly explained in section 4.2.3 of this study.

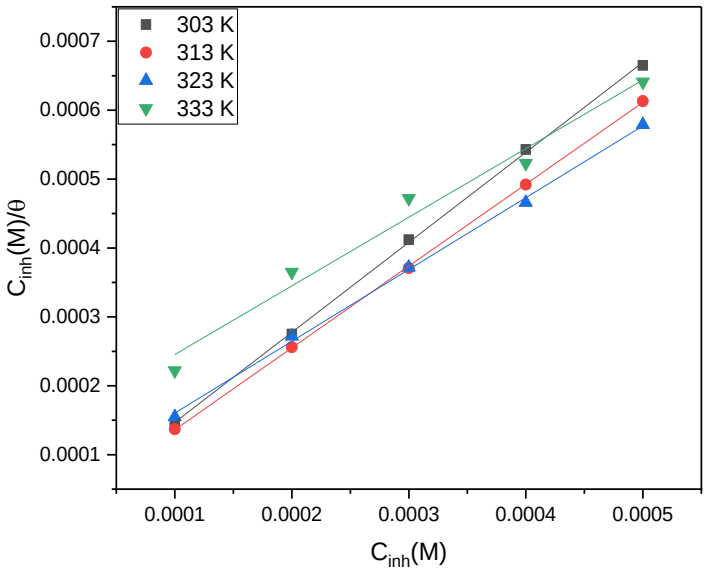

Figure 4.98: Langmuir adsorption isotherm for the adsorption of Chr-2-Carb on Al metal in 1.0 M HCl at 303, 313, 323 and 333K.

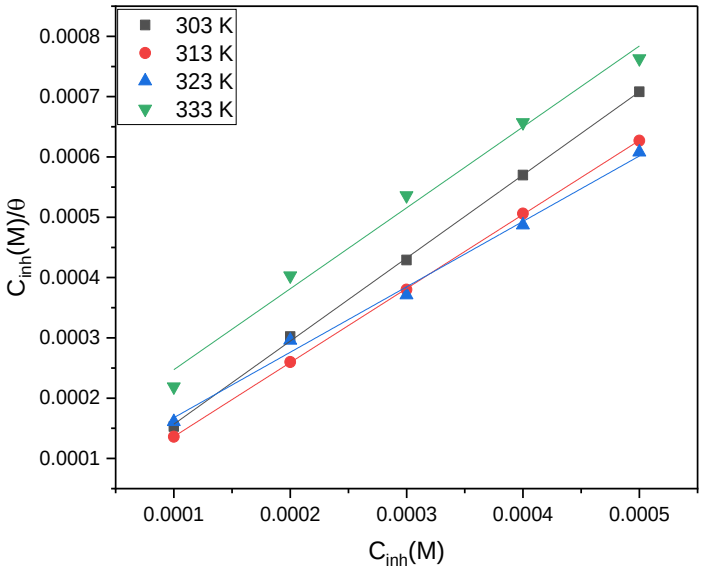

Figure 4.99: Langmuir adsorption isotherm for the adsorption of Br-Chr-2-Carb on Al metal in 1.0 M HCl at 303, 313, 323 and 333K.

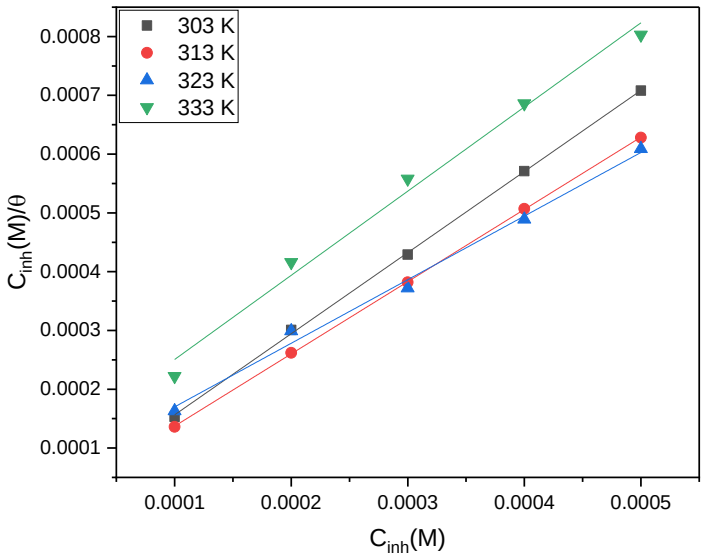

Figure 4.100: Langmuir adsorption isotherm for the adsorption of Cl-Chr-2-Carb on Al metal in 1.0 M HCl at 303, 313, 323 and 333K.

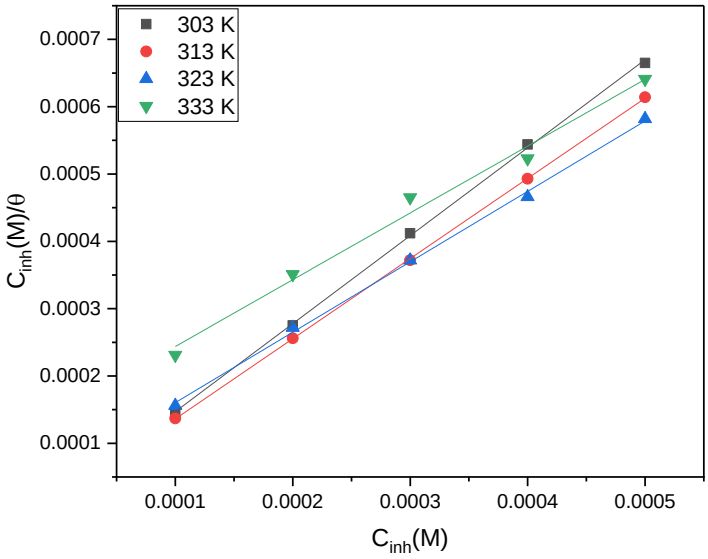

Figure 4.101: Langmuir adsorption isotherm for the adsorption of CH_3O-Chr-2-Carb on Al metal in 1.0 M HCl at 303, 313, 323 and 333K.

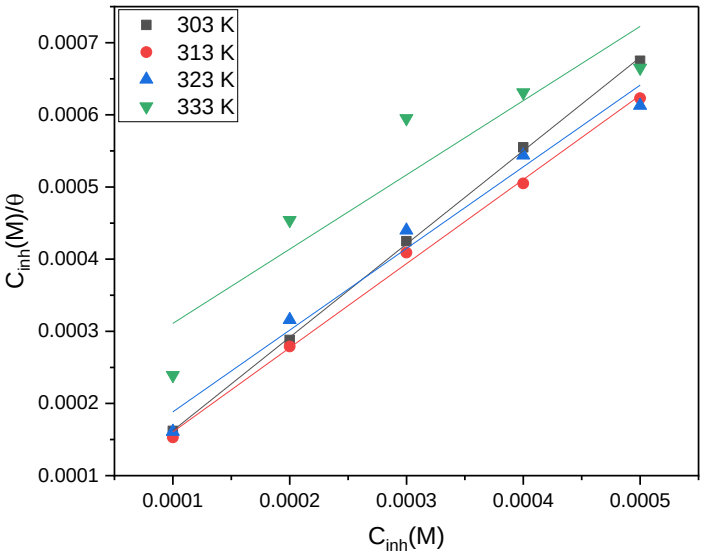

Figure 4.102: Langmuir adsorption isotherm for the adsorption of NO_2-Chr-2-Carb on Al metal in 1.0 M HCl at 303, 313, 323 and 333K.

Table 4.32: Adsorption parameters from Langmuir Adsorption Isotherm plot for Chr-2-Carb, Br-Chr-2-Carb, Cl-Chr-2-Carb, CH_3O-Chr-2-Carb and NO_2-Chr-2-Carb in 1.0 M.

Inhibitor	Temperature (K)	R^2	Slope	Intercept	K_{ads} ($L.mol^{-1}$)	$\Delta G°ads$ ($kJ.mol^{-1}$)
Chr-2-Carb	303	0.99965	1.306	0.0000164	60.9756	21.1496
	313	0.99991	1.188	0.0000174	57.4712	20.9956
	323	0.99865	1.042	0.0000562	17.7936	18.5177
	333	0.97873	0.996	0.000145	6.8587	6.8587
Br-Chr-2-Carb	303	0.99957	1.378	0.0000190	52.6316	20.1032
	313	0.99996	1.228	0.0000134	74.6269	21.6754
	323	0.99407	1.085	0.0000591	16.9205	18.3826
	333	0.98809	1.342	0.000113	8.8496	17.1571
Cl-Chr-2-Carb	303	0.99965	1.380	0.0000184	54.3478	20.1840
	313	0.99995	1.229	0.0000143	69.9301	21.5062
	323	0.99356	1.082	0.0000618	16.1812	18.2626

	333	0.98938	1.432	0.0000107	9.33109	17.2978
CH_3O-Chr-2-Carb	303	0.99960	1.307	0.0000163	61.3497	20.4893
	313	0.99994	1.191	0.0000171	58.4795	21.0409
	323	0.99862	1.046	0.0000358	17.9211	18.5369
	333	0.98908	0.992	0.000145	6.9156	16.4744
NO_2-Chr-2-Carb	303	0.99956	1.293	0.0000331	30.2115	18.7048
	313	0.99753	1.166	0.0000440	22.7273	18.5813
	323	0.97978	1.132	0.0000752	13.2979	17.7356
	333	0.86622	1.029	0.000208	4.8054	15.4665

Table 4.32 clearly displayed the computed K_{ads} and $\Delta G°_{ads}$ values for aluminium in 1.0 M HCl in the presence of the studied 6-substituted chromone-2-carboxamides. As explained in section 4.2.3 above, the equilibrium constant of adsorption (K_{ads}) denotes the degree of interaction between the inhibitor molecules and the Al surface. Furthermore, literature reveals that high K_{ads} values indicate stronger binding power as highlighted in section 4.2.3 of this study [236]. The high values of K_{ads} found in this study indicate that the 6-substituted chromone-2-carboxamides inhibitors adsorb strongly on the mild steel surface. At temperatures 303 K and 313 K the K_{ads} values were higher, signifying that the inhibitors were adsorb strongly on the Al surface in lower temperatures. It has been noted that the K_{ads} values were decreasing drastically from 313 to 333 K, weak binding of the inhibitors as the desorption process was taking place. It is also observed from table 4.32 above that the equilibrium constant (K_{ads}) values were increasing from temperature 303 K to 313 K in the presence of Br-Chr-2-Carb and Cl-Chr-2-Carb inhibitors. While in the presence of the other three inhibitors (Chr-2-Carb, CH_3O-Chr-2-Carb and NO_2-Chr-2-Carb) the K_{ads} values were decreasing with increasing temperature (303 to 333 K). A similar condition is observed from the $\Delta G°_{ads}$ values, where the $\Delta G°_{ads}$ values were increasing from temperature 303 K to 313 K in the presence of Br-Chr-2-Carb and Cl-Chr-2-Carb inhibitors. In the presence of the other three synthesized inhibitors (Chr-2-

Carb, CH_3O-Chr-2-Carb and NO_2-Chr-2-Carb) the $\Delta G°_{ads}$ values were decreasing with increasing temperature.

The $\Delta G°_{ads}$ values reflect a kind of adsorption that occurs on the metal surface. It helps researchers to deduce the type of interaction occurring between the inhibitors and the metal surface (physisorption, chemisorption or mixed-type adsorption). According to literature, values of $\Delta G°_{ads}$ around -20 kJ/mol or lower are related with physical adsorption (physisorption) involving weak Van Der Waals interaction, while values of $\Delta G°_{ads}$ around -40 kJ/mol or more negative are connected with chemical adsorption (chemisorption) with chemical bonding [237]. Furthermore, literature states that a rise in $\Delta G°_{ads}$ values with increasing temperature indicates exothermic adsorption, while a decrease in $\Delta G°_{ads}$ values with increasing temperature indicates endothermic adsorption. In this study the $\Delta G°_{ads}$ values were decreasing with a rise in temperature signifying endothermic adsorption.

$\Delta G°_{ads}$ values between -20 kJ/mol and -40 kJ/mol signifies mixed-type of adsorption [238]. In this research project, the values of $\Delta G°_{ads}$ were found to be negative for all of the investigated inhibitors, signifying that the inhibition processes were spontaneous. In this study the $\Delta G°_{ads}$ values were found to be between -20 and -40 kJ/mol, and some slightly less than -20 kJ/mol indicating a mixed-type of adsorption with physisorption dominating. Furthermore, all the $\Delta G°_{ads}$ values were less than -20 kJ/mol in the presence of NO_2-Chr-2-Carb, suggesting physical adsorption of the NO_2-Chr-2-Carb on the Al surface.

4.4.4. Thermodynamic activation and kinetic parameters

The rate of corrosion is greatly influenced by temperature, as an increase in temperature leads to an increase in aluminium corrosion rate. The interactions between the zinc electrode and the corrodent acidic medium can be drastically influenced by temperature changes and either the presence or absence of corrosion inhibitors. As displayed in the table below, temperature has an impact on aluminium metal corrosion in an acidic environment. It became clear that increasing the temperature of the acidic medium led to the increase in the rate of Al corrosion. As a result, temperature changes

can be used to gain a greater insight into the type of adsorption of the examined 6-substituted chromone-2-carboxamides on the Al surface. Several parameters have been discovered which are directly and indirectly related to the rate of corrosion of a metal. For instance, activation energy (E_a) is one of them. The E_a of aluminium metal corrosion is defined as the minimum amount of energy required to produce corrosion product on the aluminium metal surface. Several studies reveal that the high steel dissolutions are associated with low activation values higher values signify low dissolutions. The determination of activation parameters and impact of temperature for aluminium corrosion can be studied by utilizing Arrhenius equation.

The previous section (4.2.4) demonstrated the form of Arrhenius equation [Equation (36)] used to calculate the activation energy (E_a) of Al corrosion. The E_a values of Al corrosion in the uninhibited system and presence of various concentrations of the examined 6-substituted chromone-2-carboxamides were calculated utilizing the graph of log C_R against 1/T (Figure 4.103 - 4.107) and are reported in Tables 4.33.

Based on the results of this study, table 4.33 clearly shows that E_a values for the uninhibited solutions (blank) were lower than those for inhibited solutions, of which this observation is associated with physical adsorption. This is due to an increase in adsorption of preferred 6-substituted chromone-2-carboxamides inhibitor molecules on the Al surface as the temperature of the corrosive environment rises. However, Table 4.32 shows that in the highest concentrations of $4x10^{-4}$ M and $5x10^{-4}$ M Chr-2-Carb and CH_3O-Chr-2-Carb, as well as in $5x10^{-4}$ M of NO_2-Chr-2-Carb the E_a values were less than that of the blank. This signifies chemical adsorption of the synthesized inhibitors on the Al metal. A comparable type of behavior has been observed in the literature [238]. A more detailed inspection at Tables 4.33, the values of the E_a are higher at low concentration of the inhibitors ($1.0x10^{-4}$) indicating physisorption in the first stage. It is also noticed that the E_a value was less (37.8102 $kJ.mol^{-1}$) at $1x10^{-4}$ M NO_2-Chr-2-Carb than that of $2x10^{-4}$ M NO_2-Chr-2-Carb (40.1655 $kJ.mol^{-1}$), deviating from the trend.

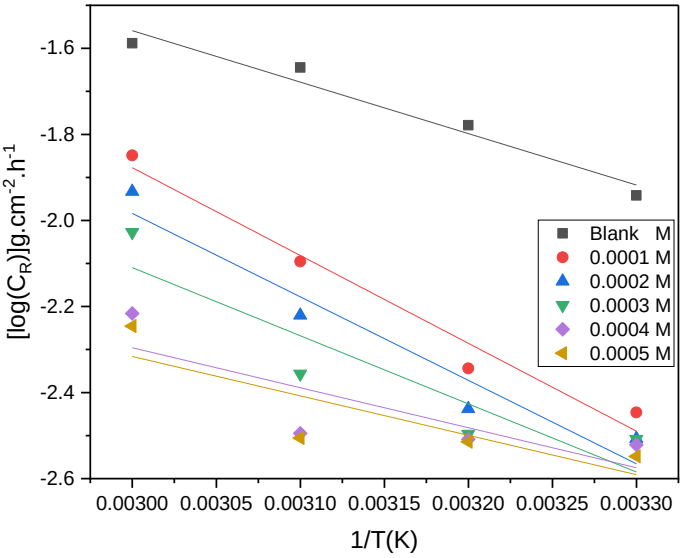

Figure 4.103: Arrhenius plots for aluminium corrosion in 1.0 M HCl solution in the absence and presence of different concentrations of Chr-2-Carb.

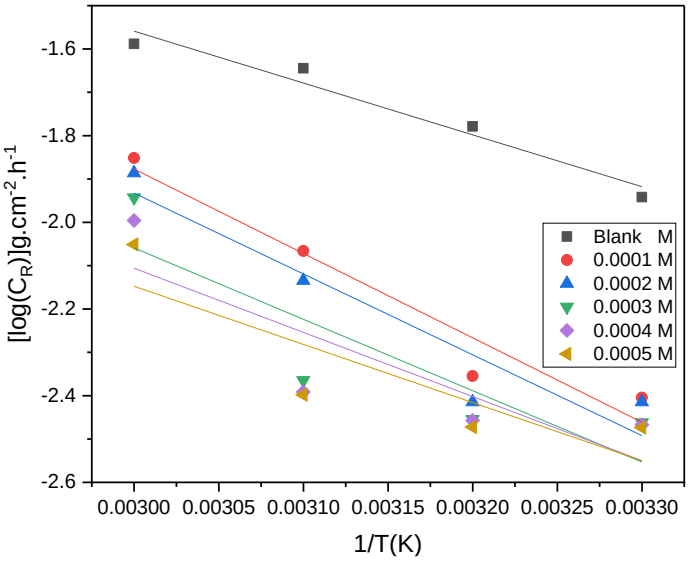

Figure 4.104: Arrhenius plots for aluminium corrosion in 1.0 M HCl solution in the absence and presence of different concentrations of Br-Chr-2-Carb.

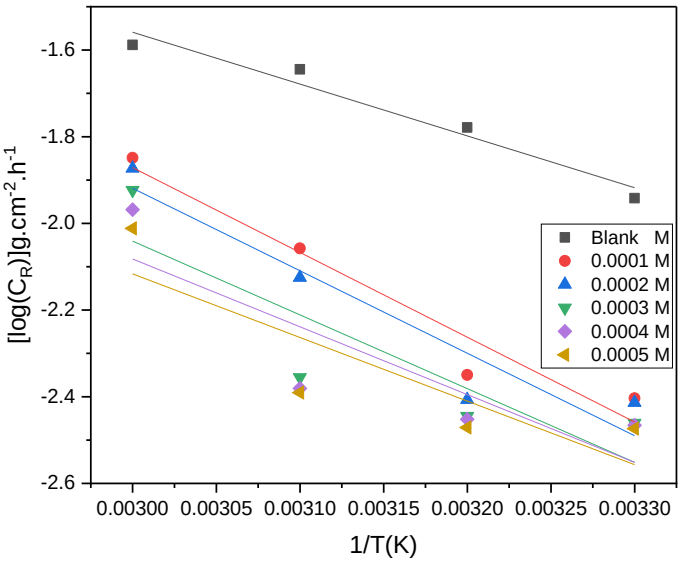

Figure 4.105: Arrhenius plots for aluminium corrosion in 1.0 M HCl solution in the absence and presence of different concentrations of Cl-Chr-2-Carb.

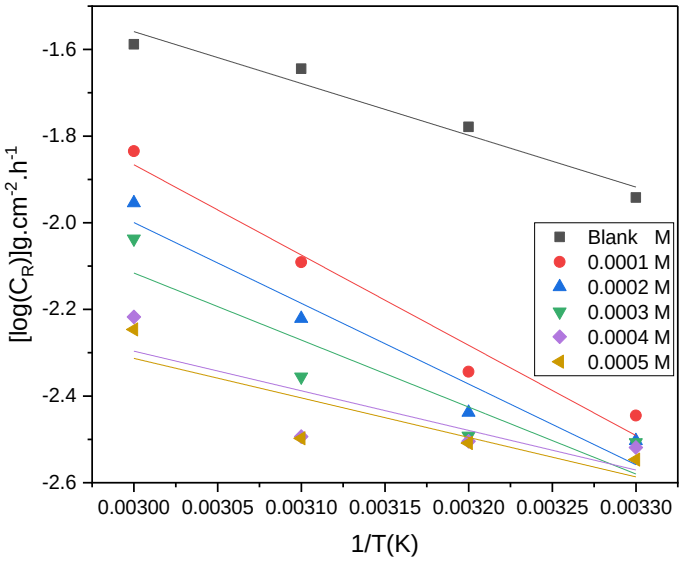

Figure 4.106: Arrhenius plots for aluminium corrosion in 1.0 M HCl solution in the absence and presence of different concentrations of CH_3O-Chr-2-Carb.

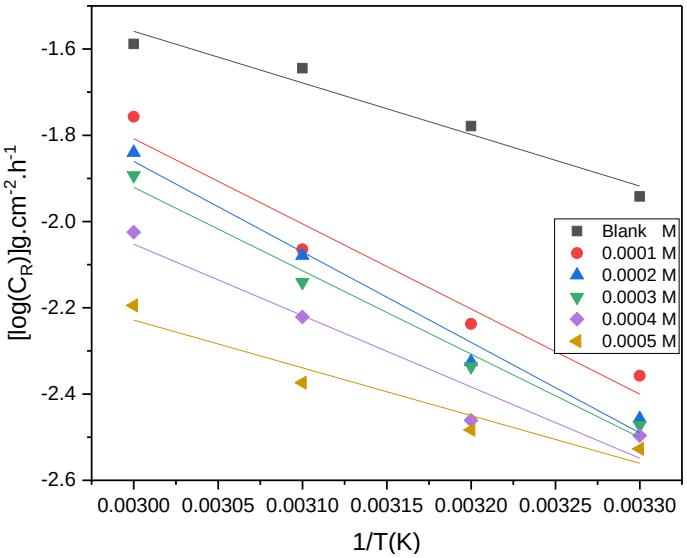

Figure 4.107: Arrhenius plots for aluminium corrosion in 1.0 M HCl solution in the absence and presence of different concentrations of NO_2-Chr-2-Carb.

Further detailed information based on the impact of temperature on the aluminium corrosion and inhibition efficiency was deduced from the enthalpy of activation and entropy of activation as they are regarded as activation parameters. These parameters are obtained through a transition-state plot, and a transition state equation is utilized in the calculations of these parameters. The transition state equation is displayed and clearly explained in section 4.2.4 equation (37) above. The transition state plots for the Al corrosion in 1.0 M are graphically presented in Figures 4.108 –4.112 and the calculated Arrhenius and transition parameters for aluminium are displayed in Table 4.33 below.

Results displayed in Table 4.33 show positive enthalpy values, indicating endothermic adsorption of the 6-substituted chromone-2-carboxamides on the aluminium surface. This is an indication that aluminium dissolution is delayed due to the existence of the examined 6-substituted chromone-2-carboxamides. Ogoko et al. discovered similar results. Table 4.33 shows that the activation energy and enthalpy of activation values are slightly close (less than 3), and the enthalpy of activation values were slightly lower than the activation energy values. Similar findings were also reported in different research publications. Furthermore, Table 4.33 shows that the E_a and ΔH^*_a values are slightly close (less than 3 kJ/mol difference), and the enthalpy of activation values were slightly lower than the

activation energy values. Similar findings were also reported in different research publications. It is also noted that at the highest concentrations of $4x10^{-4}$ M and $5x10^{-4}$ M Chr-2-Carb and CH_3O-Chr-2-Carb, as well as in $5x10^{-4}$ M of NO_2-Chr-2-Carb the ΔH^*_a values were less than that of the blank, and in same trend with the E_a values. This signifies the chemical adsorption of the synthesized inhibitors on the Al metal. Negative ΔS^* values indicate that the damage on the aluminium surface has decreased, and on the other hand positive ΔS^* values is an indication that the chaosness of the process has increased. As highlighted in section 4.2.4 above, larger negative values of ΔS^* signify that the activated complex in the rate-determining stage reflects inhibitor attachment rather than dissolution. Higher ΔS^* values were obtained in this study, as displayed in Table 4.32. This shows that the adsorption of inhibitor molecules on the Al surface reduces system disorder as it moves from reactants to active complex [338]. The increase in ΔS^* values caused by inhibitor molecule adsorption on the MS surface from the acid solution can be interpreted as a quasi-substitution process between organic molecules in the aqueous phase and water molecules on the electrode surface. Literature has revealed that the adsorption of inhibitor molecules is believed to follow the desorption of water molecules from the electrode surface in such a process, resulting in a drop in Al's electrical capacity.

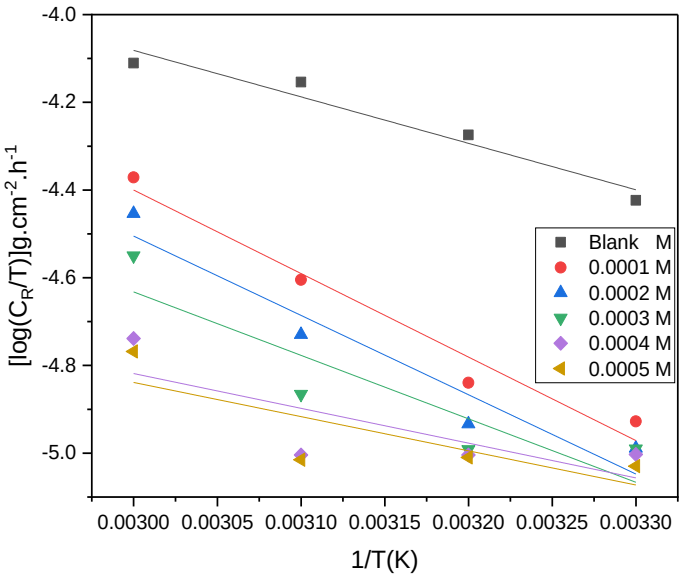

Figure 4.108: Transition state plots for aluminium corrosion in 1.0 M HCl solution in the absence and presence of different concentrations of Chr-2-Carb.

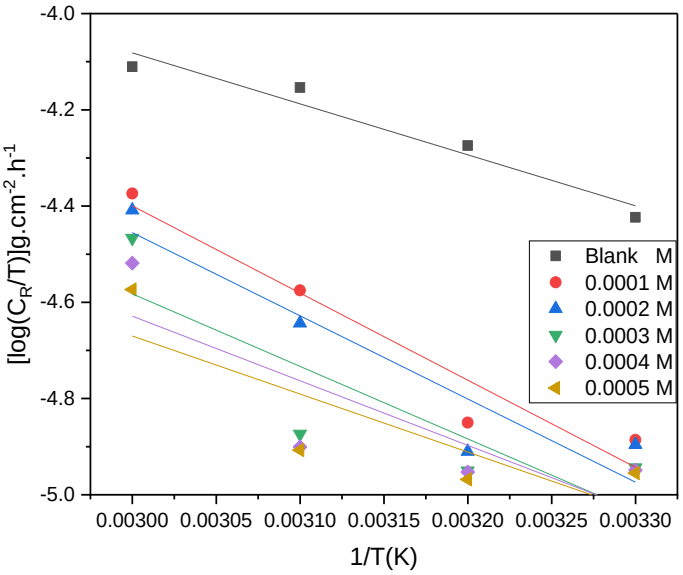

Figure 4.109: Transition state plots for aluminium corrosion in 1.0 M HCl solution in the absence and presence of different concentrations of Br-Chr-2-Carb.

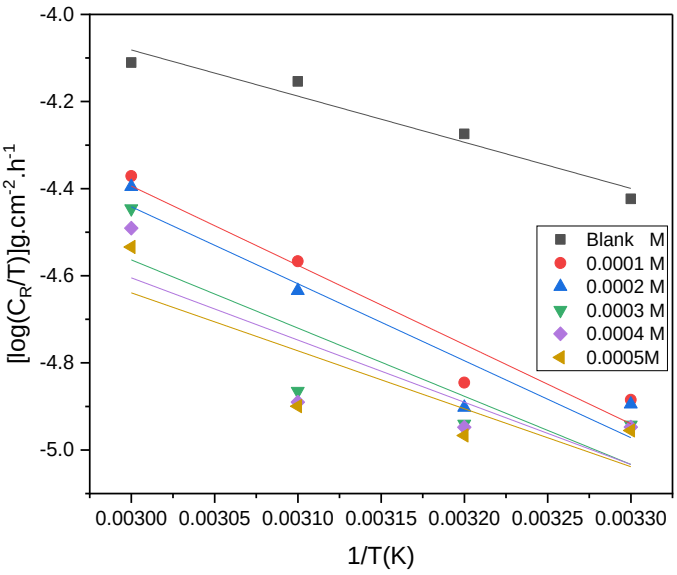

Figure 4.110: Transition state plots for aluminium corrosion in 1.0 M HCl solution in the absence and presence of different concentrations of Cl-Chr-2-Carb.

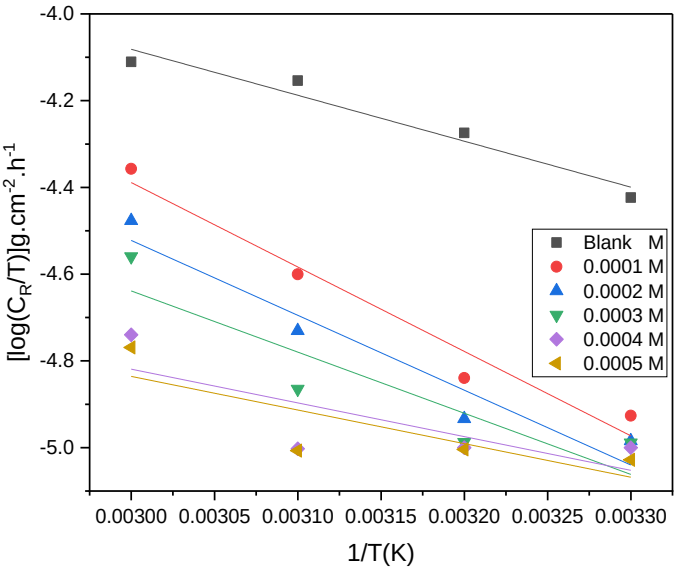

Figure 4.111: Arrhenius plots for aluminium corrosion in 1.0 M HCl solution in the absence and presence of different concentrations of CH_3O-Chr-2-Carb.

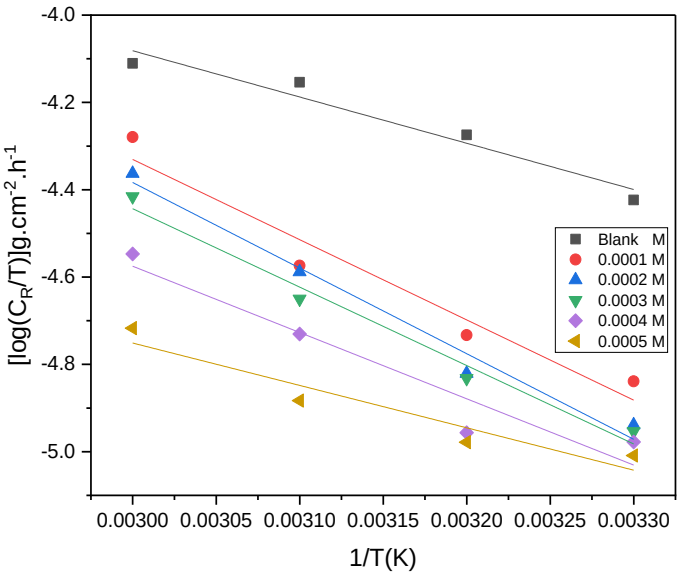

Figure 4.112: Transition state plots for aluminium corrosion in 1.0 M HCl solution in the absence and presence of different concentrations of NO_2-Chr-2-Carb.

Table 4.33: Arrhenius and transition parameters for aluminium in 1.0 M HCl in the absence and presence of various concentrations of the studied 6-substituted chromone-2-carboxamides.

Inhibitor	**Concentration of inhibitors (x10^{-4} M)**	**E_a (kJ.mol^{-1})**	**ΔH^* (kJ.mol^{-1})**	**ΔS^* (J.mol^{-1} .K^{1})**
Blank	-	22.9014	20.2838	-205.068
Chr-2-Carb	1.0	39.0836	36.4660	-186.6359
	2.0	37.1477	34.6335	-189.8962
	3.0	30.3232	27.7076	-199.9766
	4.0	17.8003	15.1903	-217.8297
	5.0	17.5398	14.9280	-218.3400
Br-Chr-2-Carb	1.0	37.2989	34.6756	-188.9652
	2.0	35.7192	33.1036	-191.4748

	3.0	31.5468	28.8603	-198.0606
	4.0	28.3433	25.7028	-202.5593
	5.0	25.7029	23.0852	-206.3119
Cl-Chr-2-Carb	1.0	37.4656	34.8422	-188.7013
	2.0	36.4449	33.8350	-190.4091
	3.0	32.5866	29.9747	-196.4515
	4.0	29.9556	27.3457	-200.2190
	5.0	28.1020	25.4787	-202.9374
CH_3O-Chr-2-Carb	1.0	39.8916	37.2722	-185.4927
	2.0	35.6733	33.0576	-192.0922
	3.0	29.6128	27.0029	-200.9469
	4.0	17.5073	14.8897	-218.2260
	5.0	17.4613	14.8380	-218.4322
NO_2-Chr-2-Carb	1.0	37.8102	35.1888	-187.7224
	2.0	40.1655	37.5441	-185.0933
	3.0	37.0194	34.3961	-189.6930
	4.0	31.6827	29.0729	-197.7227
	5.0	21.2009	18.5892	-212.8422

4.4.5. Adsorption film analysis

The FTIR spectra of the 6-substituted chromone-2-carboxamides were compared to the adsorption film spectra formed after scratching from the zinc metal surface after weight loss measurements process. These spectra are shown in Figures 4.113 – 4.117.

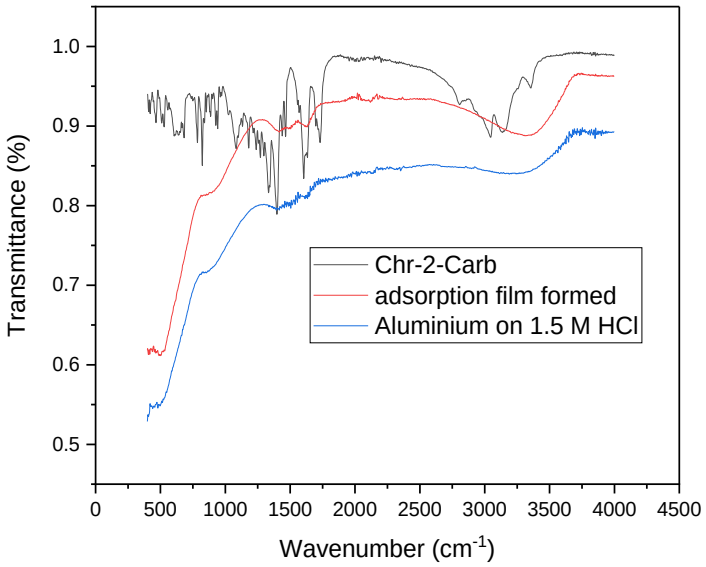

Figure 4.113: FT-IR spectra comparison of the frequencies for the pure compound and adsorption films formed on the Aluminium in 1.5 M HCl by Chr-2-Carb corrosion inhibitor.

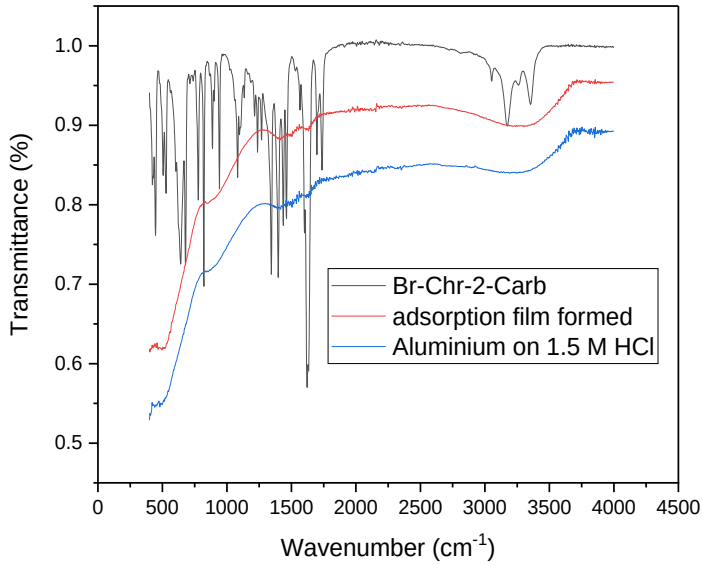

Figure 4.114: FT-IR spectra comparison of the frequencies for the pure compound and adsorption films formed on the Aluminium in 1.5 M HCl by Br-Chr-2-Carb corrosion inhibitor.

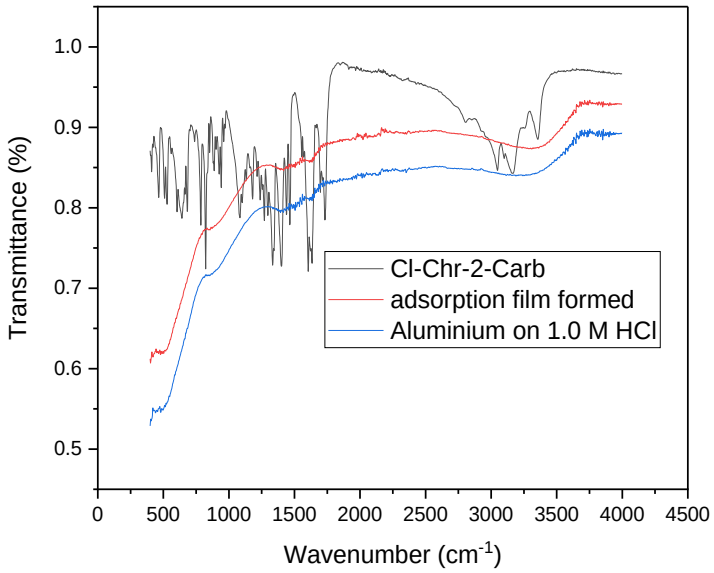

Figure 4.115: FT-IR spectra comparison of the frequencies for the pure compound and adsorption films formed on the Aluminium in 1.5 M HCl by Cl-Chr-2-Carb corrosion inhibitor.

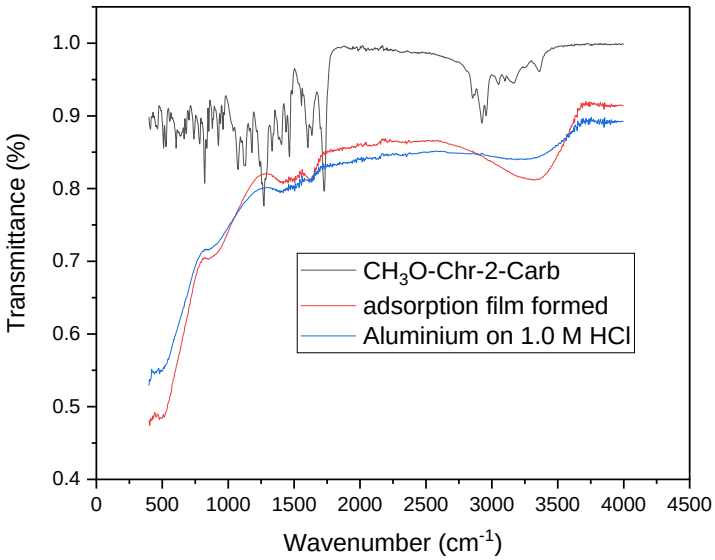

Figure 4.116: FT-IR spectra comparison of the frequencies for the pure compound and adsorption films formed on the Aluminium in 1.5 M HCl CH_3O-Chr-2-Carb corrosion inhibitor.

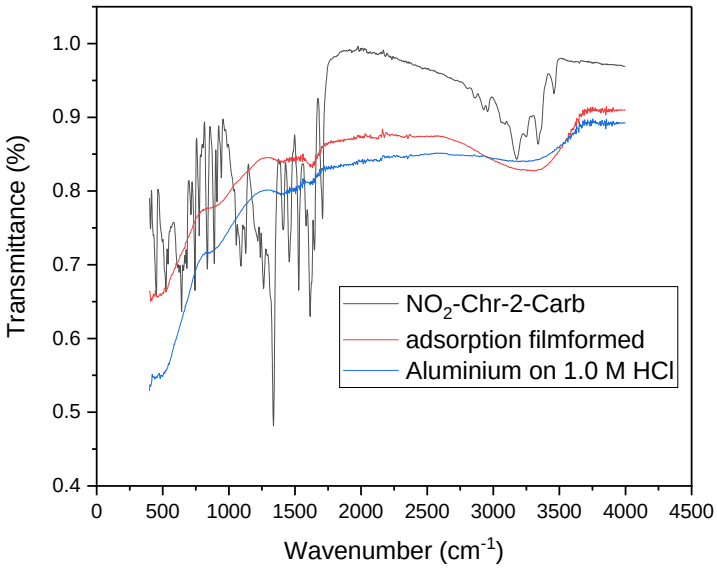

Figure 4.117: FT-IR spectra comparison of the frequencies for the pure compound and adsorption films formed on the Aluminium in 1.5 M HCl NO_2-Chr-2-Carb corrosion inhibitor.

All the above figures clearly show that the aromatic C-O peak [Ar (C-O)] disappeared in the spectra of the adsorption film as displayed in Table 4.34, same observations as in the mild steel and zinc in sections 4.2.5 and 4.3.5 of this study. Noticeably, the carbonyl carbon (C=O) peaks which were appearing around 1700 cm^{-1} on the spectra of the synthesized compounds shifted to around 1600 cm^{-1} wavenumber on the adsorption film spectra. Aromatic (C=C) peaks at 1556.15 cm^{-1}, 1504.92 $cm^{-1}$and 1556.40 cm^{-1} corresponding to Cl-Chr-2-Carb, CH_3O-Chr-2-Carb and NO_2-Chr-2-Carb respectively were observed on the adsorption film formed spectra, however in the presence of Chr-2-Carb and Br-Chr-2-Carb frequencies lowered to around 1400 cm^{-1} (1415.97 and 1416.50 respectively). The aromatic C-H (=C-H) stretching which were observed around 3100 cm^{-1} in the spectra of the synthesized compounds disappeared in the adsorption film formed spectra and new bonds occurred at around wavenumber 2000 cm^{-1} to 2300 cm^{-1}. Furthermore, the NH_2 peaks were observed around wavenumber 3350 cm^{-1} (on the presence of Chr-2-Carb, Br-Chr-2-Carb, Cl-Chr-2-Carb and CH_3O-Chr-2-Carb respectively) and 3338.77 cm^{-1} (on the presence of 6-Nit-2-Carb) some shifted to around 3300 cm^{-1} on the resulted adsorption film spectra formed. However, no NH_2 peaks

observed corresponding to Br-Chr-2-Carb and CH_3O-Chr-2-Carb on the adsorption spectra, and new bonds appeared around 3600 cm^{-1} and 3800 cm^{-1} of the adsorption film spectra.

Table 4.34: Peaks identified from FTIR spectra of the synthesized 6-substituted chromone-2-carboxamides and adsorption film formed on the Aluminium in 1.5 M HCl.

Inhibitor-Aluminium	**Functional Groups Peaks obtained from FTIR spectra (cm^{-1})**				
	C=O	NH_2	Ar (C=C)	Ar (C-O)	=C-H
Chr-2-Carb	1622.38	3311.03	1415.97	-	-
Br-Chr-2-Carb	1633.41	-	1416.50	-	-
Cl-Chr-2-Carb	1633.58	3307.79	1556.15	-	-
CH_3O-Chr-2-Carb	1633.61	-	1504.92	-	-
NO_2-Chr-2-Carbp	1694.36	3307.67	1556.40	-	-

CHAPTER 5: Electrochemical measurement results and discussions

This chapter discusses the electrochemical techniques that were utilized to evaluate the inhibitors' corrosion resistance, degradation, and inhibition mechanisms.

5.1. Electrochemical measurements

5.1.1. Open circuit potential (OCP) studies for mild steel

Figures 5.1 – 5.5 below show open circuit potential (OCP) and its evolution with time in the acidic medium before and after adding different amounts/concentrations of 6-substitutedchromone-2-carboxamides after 30 minutes of immersion at 298 K. From the figures displayed below it is evident that the presence of 6-substitutedchromone-2-carboxamides investigated led to a slight displacement of E_{corr} to negative potentials compared to the blank solution. In addition, the figures show that the OCP is stable for the corrosive medium (HCl) with and without the 6-substitutedchromone-2-carboxamides, indicating that the corroding specimens have reached steady state and the experiments may begin [250 – 252].

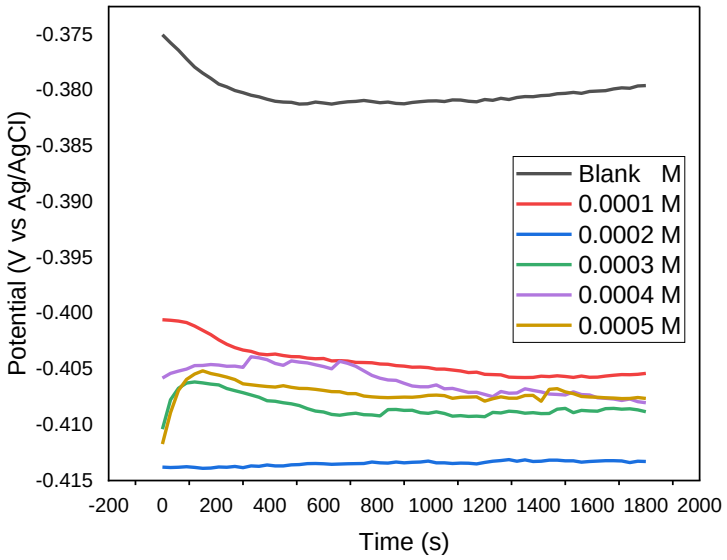

Figure 5.1: Open circuit potential (OCP) of mild steel and its evolution with time in 1.5 HCl before and after adding various concentrations of Chr-2-Carb at 298 K.

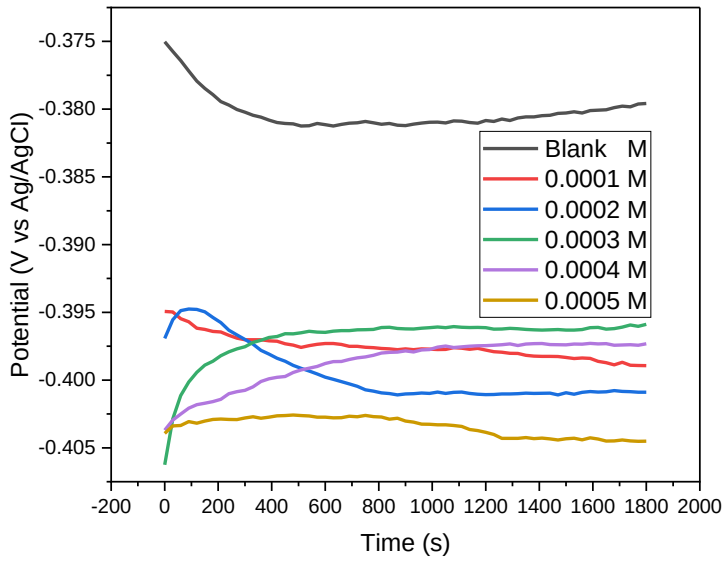

Figure 5.2: Open circuit potential (OCP) of mild steel and its evolution with time in 1.5 HCl before and after adding various concentrations of Br-Chr-2-carb at 298 K.

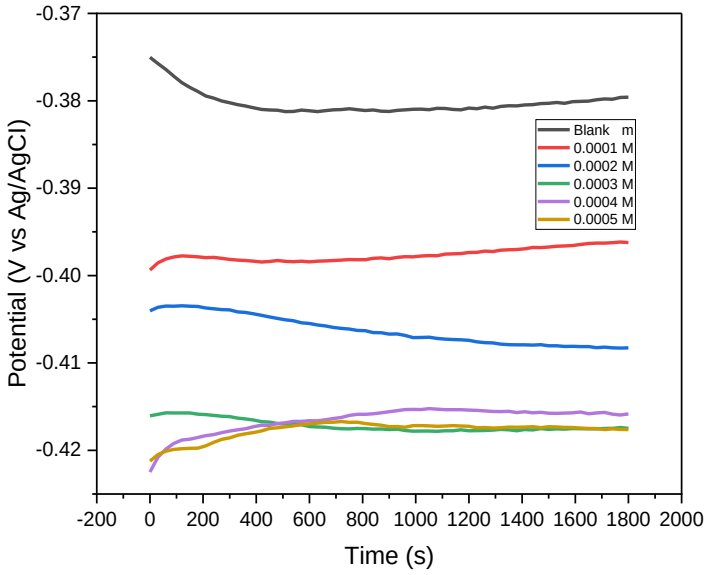

Figure 5.3: Open circuit potential (OCP) of mild steel and its evolution with time in 1.5 HCl before and after adding various concentrations of Cl-Chr-2-Carb at 298 K.

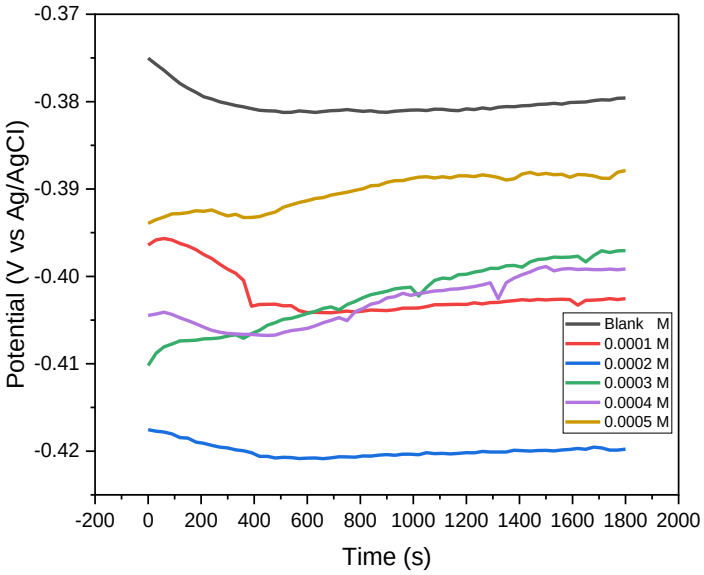

Figure 5.4: Open circuit potential (OCP) of mild steel and its evolution with time in 1.5 HCl before and after adding various concentrations of CH_3O-Chr-2-Carb at 298 K.

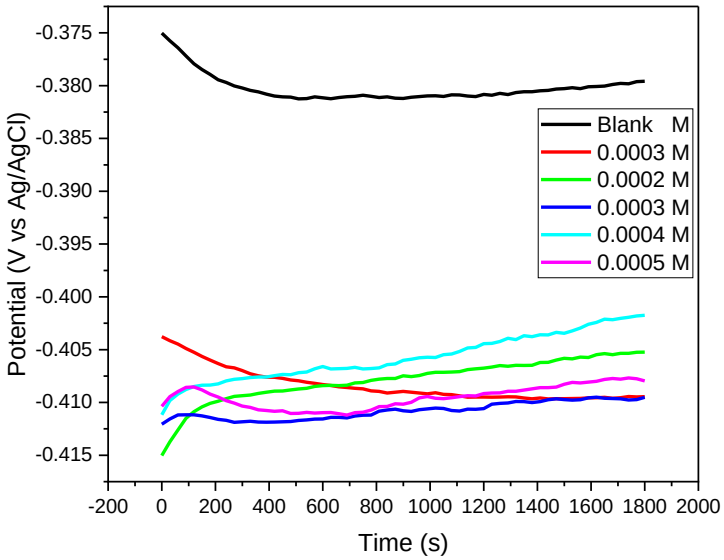

Figure 5.5: Open circuit potential (OCP) of mild steel and its evolution with time in 1.5 HCl before and after adding various concentrations of NO2-Chr-2-Carb at 298 K.

5.1.2. Potentiodynamic polarization (PDP) results for mild steel

It is essential to emphasize that corrosion of mild steel is the product of simultaneously anodic and cathodic half-reactions [253]. To gain a better understanding of this mechanism, PDP measurements were conducted at room temperature (303 K) in 1.5 M HCl in the absence and presence of the examined 6-substituted chromone-2-carboxamides, as displayed in Figures 5.6 – 5.10. These figures show that the introduction of the examined inhibitors influenced both the anodic and cathodic half-reactions of mild steel corrosion in the HCl. It is noted that both half-reactions were affected by the addition of all five synthesized inhibitors. Potentiodynamic parameters, including corrosion current density (i_{corr}), corrosion potential (E_{corr}), polarization resistance (R_P), and anodic (b_a) and cathodic (b_c) Tafel slopes, were effectively analyzed from both anodic and cathodic areas of the Tafel plots. These parameters are shown in Table 5.1. The potentiodynamic polarization inhibition efficiency (%IE_{PDP}) was then estimated using the determined i_{corr} value from equation (38) below.

$$IE_{PDP}(\%) = \frac{I_{corr} - I_{corr(inh)}}{I_{corr}} \times 100 \quad (38)$$

where I_{corr} and $I_{corr(inh)}$ are the corrosion current densities in the absence and presence of the synthesized inhibitors. Figures 5.6 – 5.10 together with Table 5.1 show that the introduction of the 6-substitutedchromone-2-carboxamides significantly reduced the corrosion current densities for both anodic and cathodic half-reactions, which signifies that both the anodic dissolution of mild steel and cathodic reduction of the hydrogen ions were inhibited.

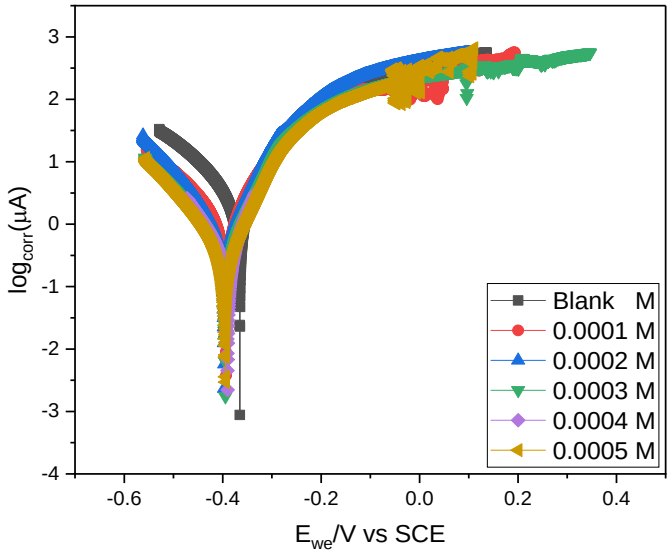

Figure 5.6: Tafel plots for mild steel in 1.5 M HCl in the absence and presence of various concentrations of Chr-2-carb at 303 K.

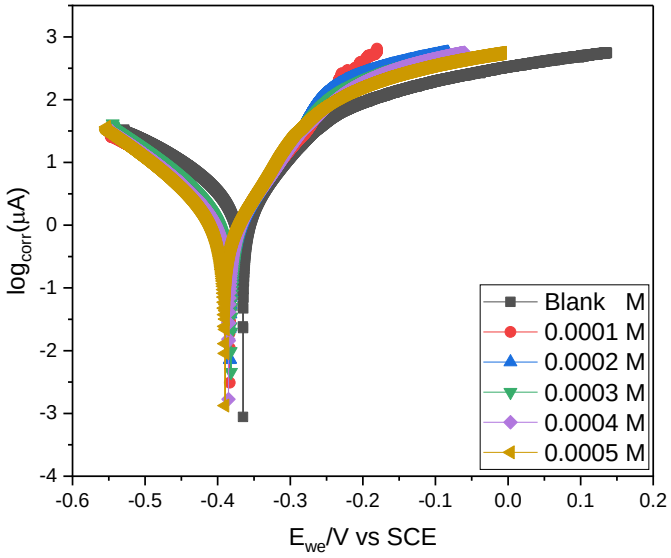

Figure 5.7: Tafel plots for mild steel in 1.5 M HCl in the absence and presence of various concentrations of Br-Chr-2-carb at 303 K.

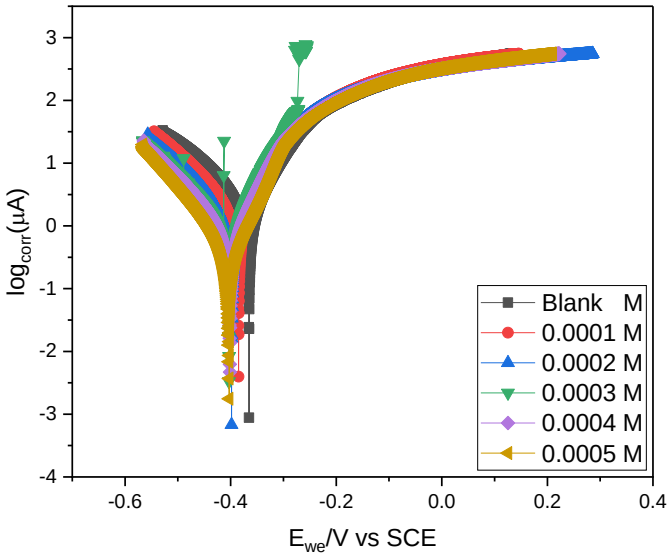

Figure 5.8: Tafel plots for mild steel in 1.5 M HCl in the absence and presence of various concentrations of Cl-Chr-2-carb at 303 K.

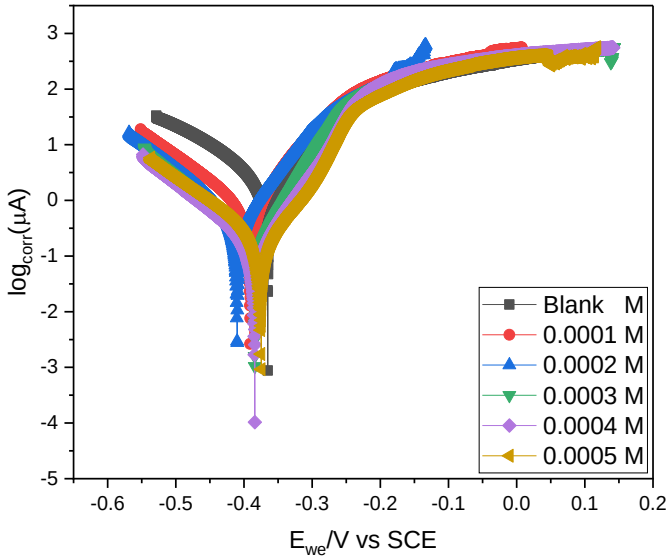

Figure 5.9: Tafel plots for mild steel in 1.5 M HCl in the absence and presence of various concentrations of CH3O-Chr-2-carb at 303 K.

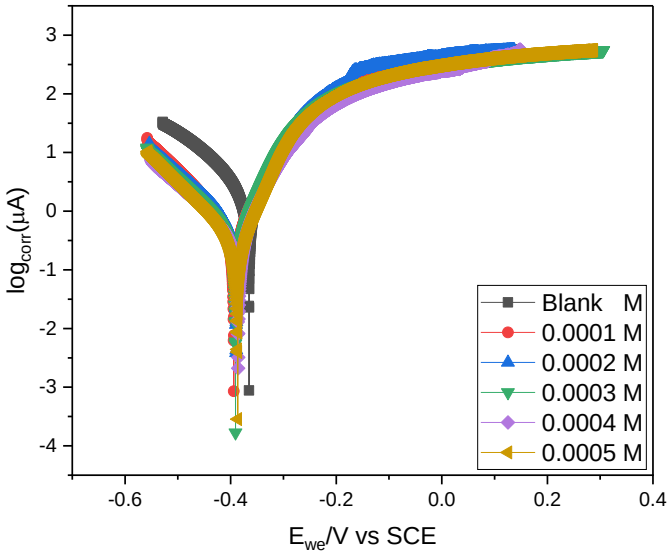

Figure 5.10: Tafel plots for mild steel in 1.5 M HCl in the absence and presence of various concentrations of NO_2-Chr-2-carb at 303 K.

Table 5.1: Potentiodynamic Polarization (PDP) parameters such as corrosion current density (i_{corr}), corrosion potential (E_{corr}), anodic (βa) and cathodic (βc) Tafel slopes for MS corrosion in 1.5 M HCl in with and without different concentrations of 6-substitutedchromone-2-carboxamides.

Inhibitor	Conc. (x10^{-4} M)	C_R (mpy)	E_{corr} (mV vs SCE)	β_a (mV.dec^{-1})	β_c (mV.dec^{-1})	I_{corr} (μA.cm^{-2})	% IE_{PDP}	IE_{WL} (%)
Chr-2-carb	**Blank**		-365.077	120.7	173.2	3491.580	–	–
	1.0		-417.684	101.4	132.8	1217.155	65.14	90.00
	2.0		-397.039	94.5	123.6	1042.076	70.15	91.46
	3.0		-394.49	92.6	137.4	609.012	82.56	92.17
	4.0		-387.314	59.7	107.9	411.991	88.20	93.64
	5.0		-389.858	58.4	92.0	246,167	92.95	94.00
	1.0		-383.225	73.9	117.8	923.987	73.54	83.24
	2.0		-372.899	57.4	109.0	864.827	75.23	83.85

Br-Chr-2-carb	3.0		-377.371	57.1	84.4	723.793	79.27	84.37
	4.0		-384.533	58.5	69.4	620.945	82.22	84.60
	5.0		-388.317	54.3	69.4	520.687	85.09	86.05
Cl-Chr-2-carb	1.0		-390.874	87.9	126.9	1107.257	68.29	84.30
	2.0		-401.252	92.8	131.0	1103.124	68.41	84.80
	3.0		-401.109	68.0	120.0	1170.53	70.55	85.10
	4.0		-398.583	64.9	105.5	704.268	79.83	86.45
	5.0		-388.639	51.9	104.3	339.515	90.28	87.33
CH_3O-Chr-2-carb	1.0		-422.089	107.0	117.0	1105.761	68.33	84.06
	2.0		-433.884	105.6	112.5	959.820	72.51	86.90
	3.0		-420.425	88.4	101.6	436.129	87.51	87.91
	4.0		-387.488	63.4	104.9	164.64	95.28	88.92
	5.0		-382.811	43.6	102.8	105.967	96.97	91.19
NO_2-Chr-2-carb	1.0		-426.554	111.0	116.0	1071.198	69.32	93.61
	2.0		-401.739	78.4	125.7	751.263	78.48	95.17
	3.0		-395.418	62.4	114.4	441.371	87.36	97.19
	4.0		-385.086	56.8	116.9	299.793	91.41	97.26
	5.0		-383.026	48.2	99.3	223.322	93.60	97.44

As presented in Table 5.1, a small difference in the values of E_{corr} for the inhibited system and the blank system is noted. The slight disparity in E_{corr} values is caused by the minimal number of alloying elements in MS, which are known to considerably impact the kinetics of iron dissolution. It is clearly observed that the E_{corr} values for the inhibited system shifted essentially towards the cathodic region relative to that of the blank system as shown in Figures 5.6 – 5.10. The maximum shift in E_{corr} value relative to the E_{corr} value of the blank is 68.807 mV. According to literature, an inhibitor is regarded as anodic or cathodic type when the displacement in E_{corr} is greater than 85 mV [254]. This study

depicts some mixed-type inhibitors, indicating that they inhibit both the anodic and cathodic half-reactions. Furthermore, a slight change in the values of βa and βc in the presence of the inhibitors when compared with the blank signifies that the 6-substitutedchromone-2-carboxamides have adsorbed on the mild steel surface without affecting the mechanism of the MS corrosion in the acid medium. Literature has indicated that the higher values of βc as compared to the values of βa signifies predominant cathodic reactions, making the inhibitors to be more effective on the cathodic site [255]. It is clear from Table 5.1 that the current densities (i_{corr}) decreases as the concentration of the inhibitors increases, suggesting that the inhibitors did bind on the MS surface and the binding effect increases and become more stable due to the presence of more particles of the 6-substitutedchromone-2-carboxamides at higher concentrations.

5.1.3. Electrochemical impedance spectroscopy (EIS) results for mild steel

EIS plays a key role in helping on deeper understanding of the kinetics of the corrosion process together with the mechanism of inhibition. In this research project, EIS was of useful in the investigation of the behavior of mild steel corrosion in 1.5 M HCl in the absence and presence of different concentrations of the investigated 6-substitutedchromone-2-carboxamides at 303 K. As highlighted in section 5.1.1, this technique was conducted at the OCP after 1800 seconds of mild steel immersion until a steady corrosion potential (E_{corr}) for all the working electrodes was established. Figures 5.11 – 5.15 show the obtained Nyquist plots, and corresponding Bode plots are presented in the appendix. The Nyquist plots are represented by the imperfect semicircles capacitive loops which are indicative of a charge transfer process that controls the corrosion of mild steel in the acidic environment. These figures show that the diameter of these imperfect semicircles increases with increase in the concentration of the inhibitors. This can be due to the increase in the surface coverage of adsorptive 6-substitutedchromone-2-carboxamides on mild steel surface. The Nyquist plots in the absence and presence of 6-substitutedchromone-2-carboxamides are essentially identical, showing that these inhibitors do not affect the corrosion mechanism of the mild steel specimen. This is in

agreement with the results from PDP. The observed increase in Nyquist diameter with 6-substitutedchromone-2-carboxamides concentrations reflected an increase in R_{ct} values showing that the inhibitors adsorbed on metal surfaces.

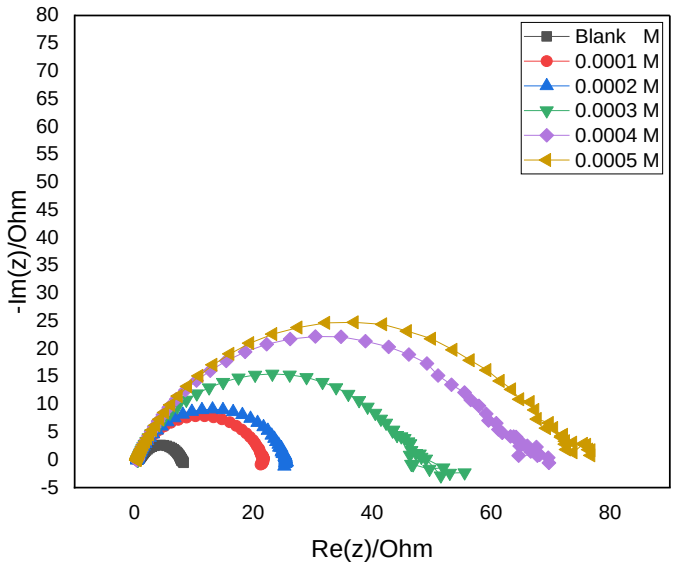

Figure 5.11: Nyquist plot of mild steel in 1.5 M HCl in the presence and absence of various concentrations of Chr-2-carb.

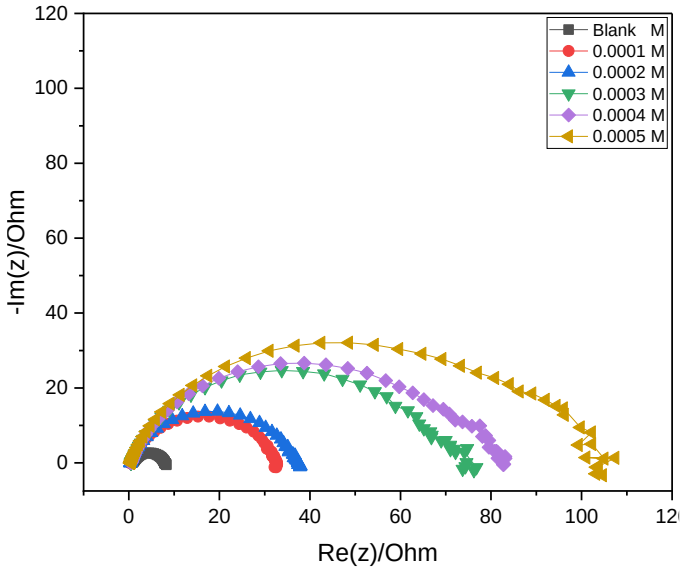

Figure 5.12: Nyquist plot of mild steel in 1.5 M HCl in the presence and absence of various concentrations of Br-Chr-2-carb.

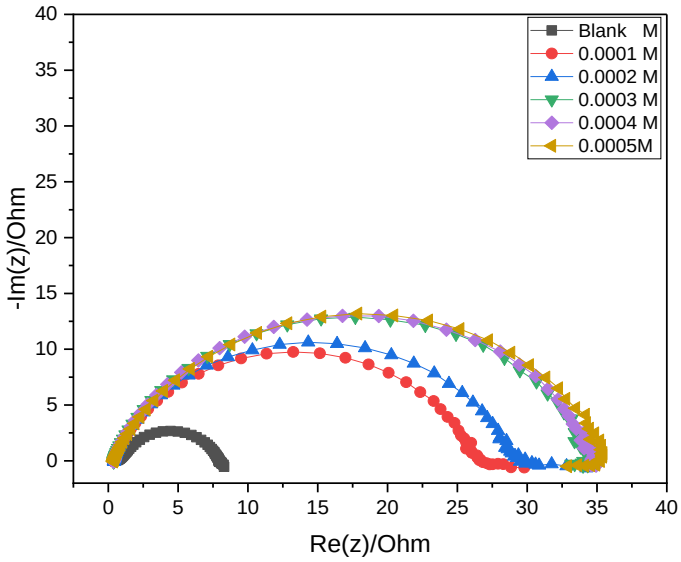

Figure 5.13: Nyquist plot of mild steel in 1.5 M HCl in the presence and absence of various concentrations of Cl-Chr-2-carb.

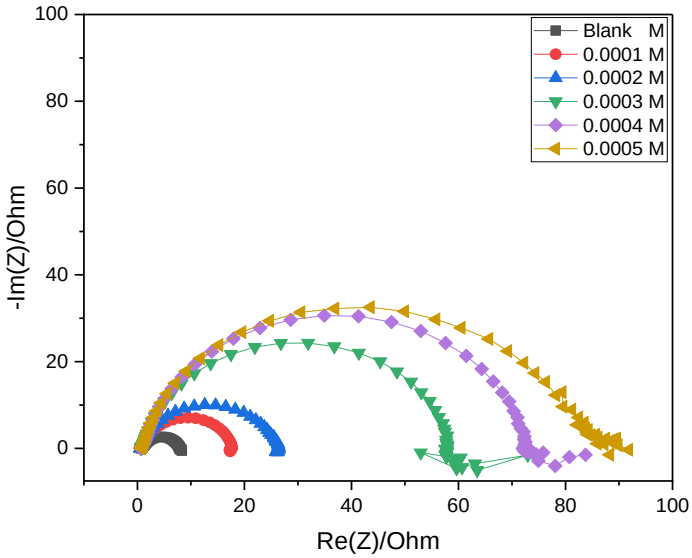

Figure 5.14: Nyquist plot of mild steel in 1.5 M HCl in the presence and absence of various concentrations of CH_3O-Chr-2-carb.

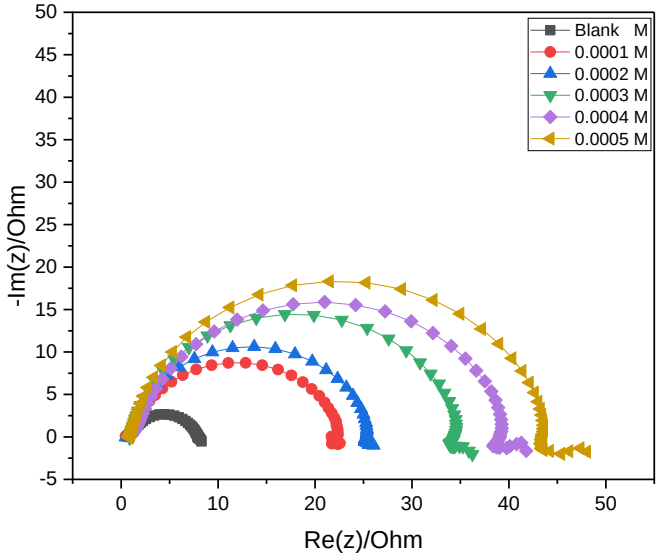

Figure 5.15: Nyquist plot of mild steel in 1.5 M HCl in the presence and absence of various concentrations of NO_2-Chr-2-carb.

Table 5.2: Electrochemical impedance spectroscopy (EIS) parameters such as the resistance of charge transfer (R_{ct}), constant phase element (Y_o), solution resistance (R_s) and the CPE exponent (n) for MS corrosion in 1.5 M HCl in absence and presence of different concentrations of 6-substitutedchromone-2-carboxamides.

Inhibitor	**Conc. ($x10^{-4}$ M)**	**R_{ct} (Ω)**	**Q_2 ($F.s^{(a-1)}$)**	**Rs (Ω)**	**n**	**(%) IE_{EIS}**	**(%) IE_{WL}**
Chr-2-carb	**Blank**	7.321	0.9954e-3	0.7303	0.7598	–	–
	1.0	25.22	0.885e-3	0.4765	0.7895	70.97	90.00
	2.0	26.23	0.2673e-3	1.035	0.8523	72.09	91.46
	3.0	46.63	0.8663e-3	0.5891	0.7788	84.29	92.17
	4.0	64.17	0.7777e-3	0.4377	0.7853	88.59	93.64
	5.0	72.55	0.78886e-3	0.4552	0.7730	89.91	94.00
	1.0	31.35	0.2955e-3	0.6019	0.7729	76.65	83.24

Br-Chr-2-carb	2.0	36.63	0.8333e-3	0.3439	0.8283	80.01	83.85
	3.0	60.48	0.3129e-3	1.088	0.7687	87.89	84.37
	4.0	71.55	0.8593e-3	0.4436	0.7891	89.76	84.60
	5.0	78.73	0.8484e-3	0.4369	0.7873	90.70	86.05
Cl-Chr-2-carb	1.0	26.05	0.6746e-3	0.7902	0.7701	71.89	84.30
	2.0	31.66	1.67e-3	0.7285	0.8338	76.88	84.80
	3.0	34.68	1.809e-3	0.5598	0.6725	78.89	85.10
	4.0	34.70	0.7479e-3	0.3864	0.8217	78.90	86.45
	5.0	85.86	0.1003	0.4433	0.808	91.47	87.33
CH_3O-Chr-2-carb	1.0	32.11	0.8464e-3	0.3998	0.7990	77.20	84.06
	2.0	58.90	0.2245e-3	0.7490	0.8528	87.57	86.90
	3.0	76.35	0.3828e-3	0.6321	0.7702	90.41	87.91
	4.0	84.68	0.291e-3	0.8266	0.8516	91.35	88.92
	5.0	104.3	0.4009e-3	0.5217	0.8394	92.98	91.19
NO_2-Chr-2-carb	1.0	35.53	0.610e-3	0.4200	0.8235	79.39	93.61
	2.0	42.36	0.7866e-e	0.5576	0.7866	82.72	95.17
	3.0	46.78	0.596e3	0.4478	0.8198	84.35	97.19
	4.0	51.66	0.6966e-3	0.3970	0.7991	85.83	97.26
	5.0	54.38	0.9502e-3	0.4916	0.7661	86.54	97.44

The results presented in Table 5.2 revealed that the charge transfer resistance for the blank solution was relatively low due to the high conductivity of the HCl solution. Other researchers observed similar R_{ct} values for blank solutions [256]. The data in Table 5 show that the value of R_{ct} increases with the addition of inhibitors when compared to the blank solution; this increase is due to the formation of a protective film at the metal/solution interface. The corrosion of MS in acidic medium is likely caused by the

charge transfer process [257]. This could be due to a number of factors such as frequency dispersion, distribution of surface-active sites, metal surface inhomogeneity, grain boundaries, roughness and etc. The electrochemical impedance parameters obtained from the Nyquist plots and the %IEEIS are displayed in Table 5.2. The charge transfer resistance equation (39) below was used to calculate $\%IE_{EIS}$.

$$IE_{EIS}(\%) = \left(1 - \frac{R_{ct}^{\circ}}{R_{ct}}\right) \times 100 \quad (39)$$

where R_{ct} and R_{ct}° are are the resistances of charge transfer in the presence and absence of the synthesized inhibitors, respectively. The R_{ct} is directly proportional to the (meaning the R_{ct} increases with the increase in the inhibition efficiency). As displayed in table 5.2 above, the efficiency increased to reach a maximum of 92.98 % for MS at the optimum concentration of CH_3O-Chr-2-carb.

To analyze Nyquist impedance plots, experimental data was fitted to a simple electrical equivalent circuit shown in figure 5.16 that includes components such as the resistance of charge transfer (Rct), constant phase element (Yo), solution resistance (Rs) and the CPE exponent (n) for MS.

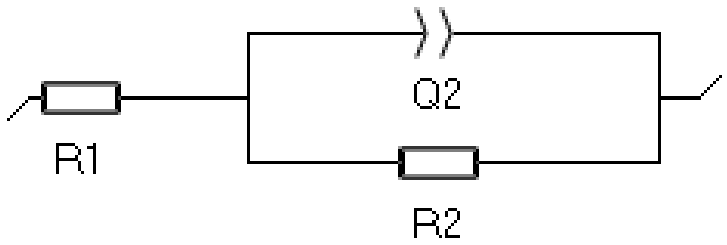

Figure 5.16: Equivalent circuit used to fit the impedance spectra obtained for mild steel and zinc corrosion in 1.5 HCl in the presence and absence of 6-substitutedchromone-2-carboxamides.

5.2. Electrochemical measurement for zinc

5.2.1. Open circuit potential (OCP) measurements for zinc

Figures 5.17 – 5.21 show the OCP/time evolution of the zinc metal in 1.5 M HCl solution with and without the synthesized 6-substituted chromone-2-carboxamides inhibitors. The

significance of this is to see the difference in OCP during this time frame and to understand how long it takes (waiting period) for stability before electrochemical experiments. This study discovered that the stability in the OCP begins at 800 s, giving us confidence to conclude that 1800 s is an adequate waiting period for the system to attain a stable OCP.

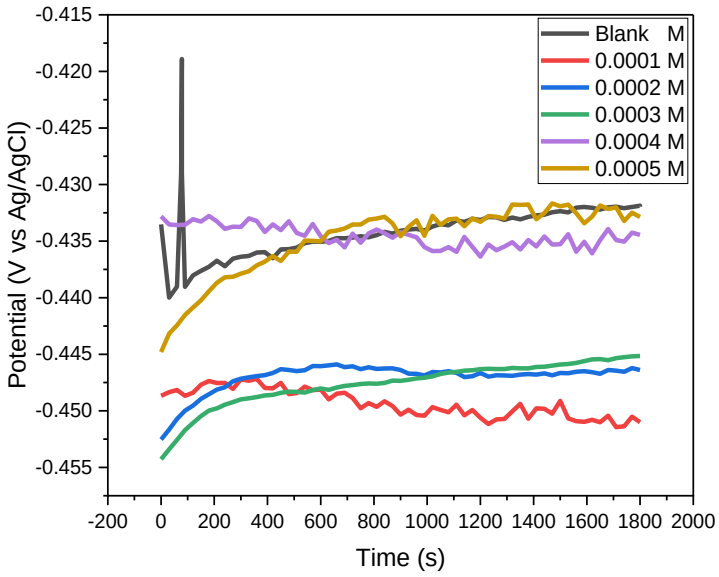

Figure 5.17: Open circuit potential (OCP) of zinc and its evolution with time in 1.5 HCl before and after adding various concentrations of Chr-2-Carb at 298 K.

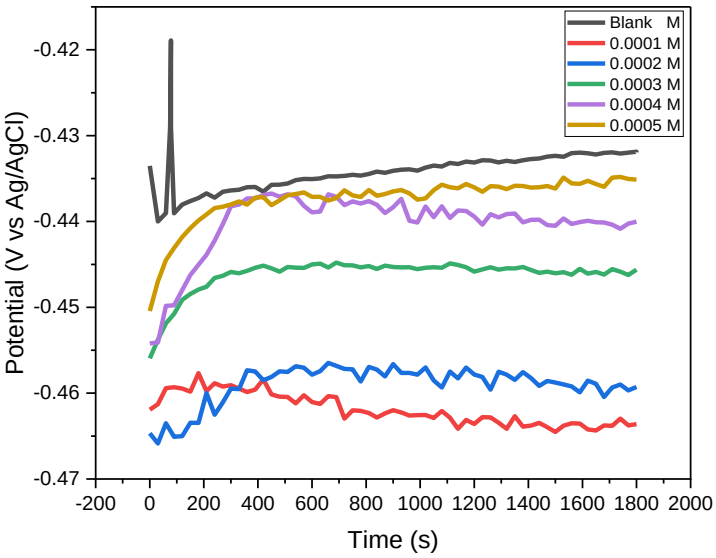

Figure 5.18: Open circuit potential (OCP) of zinc and its evolution with time in 1.5 HCl before and after adding various concentrations of Br-Chr-2-carb at 298 K.

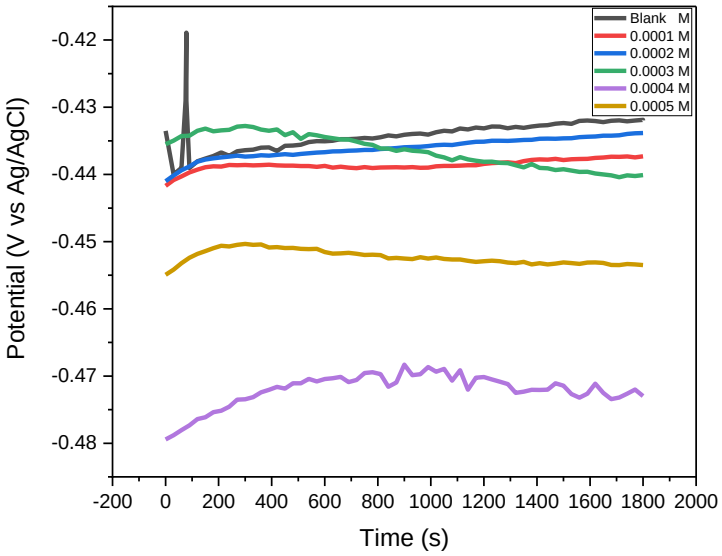

Figure 5.19: Open circuit potential (OCP) of zinc and its evolution with time in 1.5 HCl before and after adding various concentrations of Cl-Chr-2-Carb at 298 K.

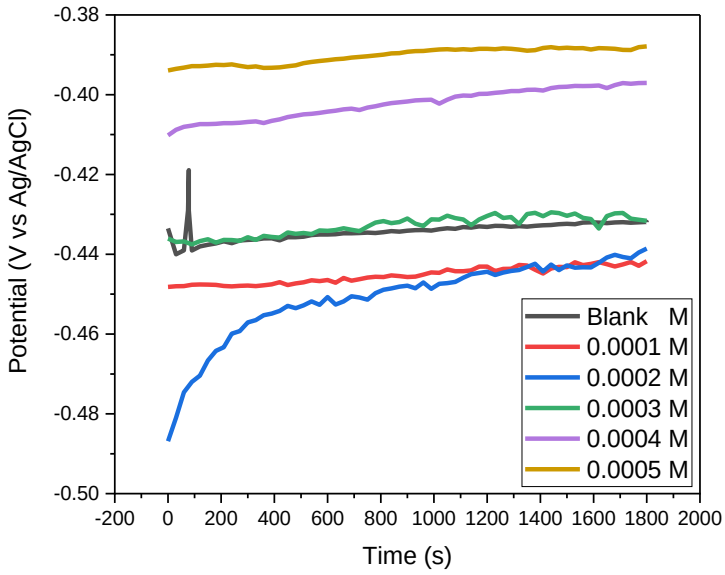

Figure 5.20: Open circuit potential (OCP) of zinc and its evolution with time in 1.5 HCl before and after adding various concentrations of CH_3O-Chr-2-Carb at 298 K.

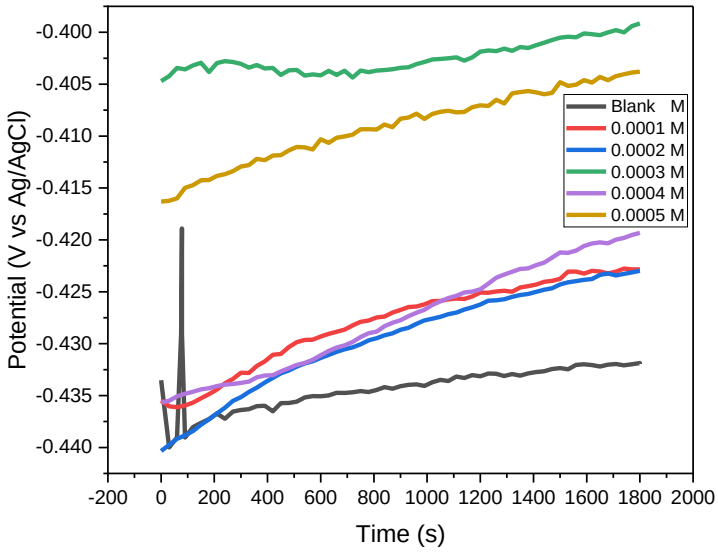

Figure 5.21: Open circuit potential (OCP) of zinc and its evolution with time in 1.5 HCl before and after adding various concentrations of NO2-Chr-2-Carb at 298 K.

5.2.2. Potentiodynamic polarization (PDP) results for zinc

As highlighted in the section above, also zinc corrosion is the product of simultaneously anodic and cathodic half-reactions. Same as in the previous section, PDP measurements were conducted at room temperature (303 K) in 1.5 M HCl in the absence and presence of the examined 6-substitutedchromone-2-carboxamides, as displayed in Figures (5.22 – 5.26). These figures show that the introduction of the examined inhibitors influenced both the anodic and cathodic half-reactions of zinc corrosion in the HCl. Potentiodynamic parameters, including corrosion current density (i_{corr}), corrosion potential (E_{corr}), polarization resistance (RP), and anodic (ba) and cathodic (bc) Tafel slopes, were effectively analyzed from both anodic and cathodic areas of the Tafel plots. The potentiodynamic polarization inhibition efficiency (%IE_{PDP}) was then estimated using the determined i_{corr} value from the equation (38) above. The parameters (corrosion current density (i_{corr}), corrosion potential (E_{corr}), polarization resistance (RP), and anodic (ba) and cathodic (bc) Tafel slopes) obtained from the Tafel plots extrapolation including the %IE_{PDP} are presented in table 5.3 below. CH_3O-Chr-2-carb exhibited largely cathodic

inhibition as compared to the other for inhibitors. It clearly observed from table 5.3 that the Tafel slops of both the cathode and anode differ with concentration of the synthesized inhibitors. This signifies that the 6-substitutedchromone-2-carboxamides affect both the anodic and cathodic half reactions [258]. In addition, the results reveals that the i_{corr} lessens with the raise in concentration of the synthesized inhibitors which led to an increase in inhibition efficiency. It is clearly observed that electron donating (-OCH_3) and electron withdrawing (-Cl, -Br and NO_2) substituents contributed in the increase in the inhibition efficiency of the 6-substitutedchromone-2-carboxamides, including the non-substituted one (Chr-2-carb). The results of this study revealed that the inhibition efficiencies of the CH_3O-Chr-2-carb are greater as compared to the ones for the other inhibitors. Such observations may be due to the increased molecular size of CH_3O-Chr-2-carb. In addition, the inhibitor with an electron withdrawing group (NO_2) substituent showed to be effective and this may be due to the two Oxygen atoms of the nitro group as highlighted in the previous sections of this study. It can be concluded that both the methoxy and the nitro groups enhance the inhibition efficiency by using some of their electrons in additions to the ones of the chromone-2-carboxamide molecule to interact with the zinc metal [259].

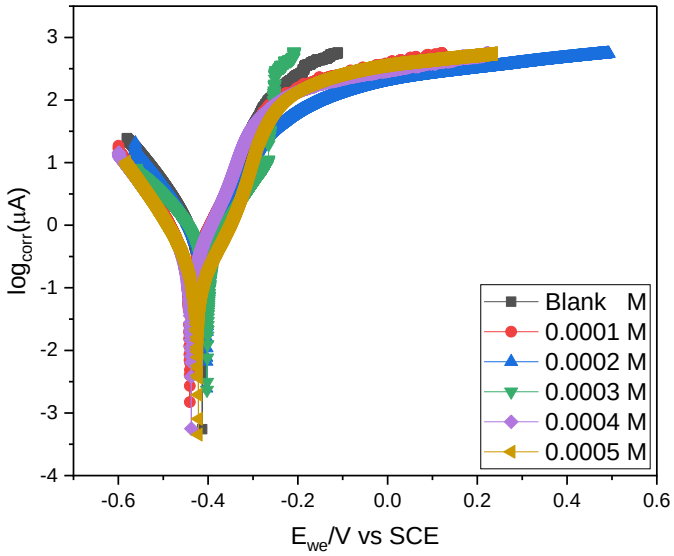

Figure 5.22: Tafel plots for zinc in 1.5 M HCl in the absence and presence of various concentrations of Chr-2-carb at 303 K.

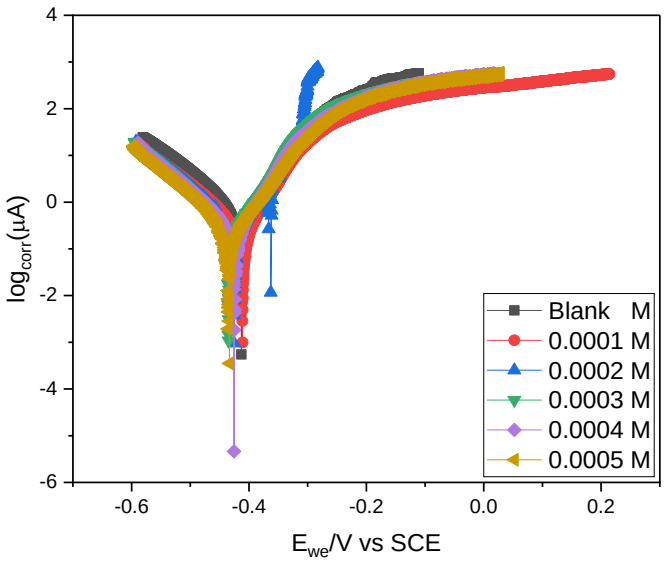

Figure 5.23: Tafel plots for zinc in 1.5 M HCl in the absence and presence of various concentrations of Br-Chr-2-carb at 303 K.

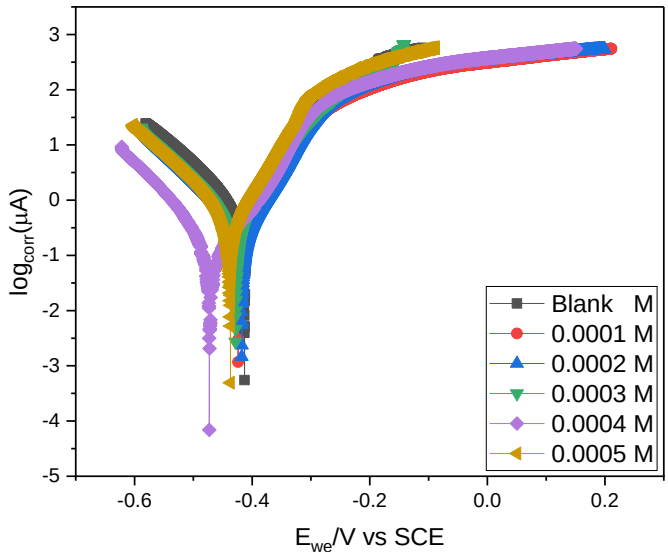

Figure 5.24: Tafel plots for zinc in 1.5 M HCl in the absence and presence of various concentrations of Cl-Chr-2-carb at 303 K.

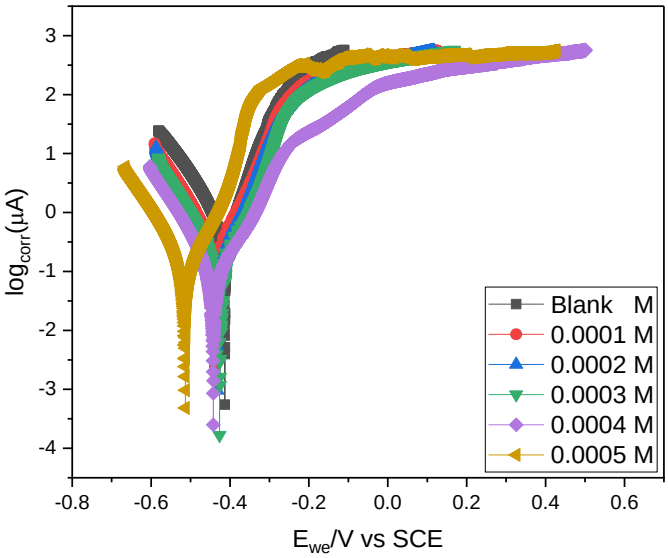

Figure 5.25: Tafel plots for zinc in 1.5 M HCl in the absence and presence of various concentrations of CH_3O-Chr-2-carb at 303 K.

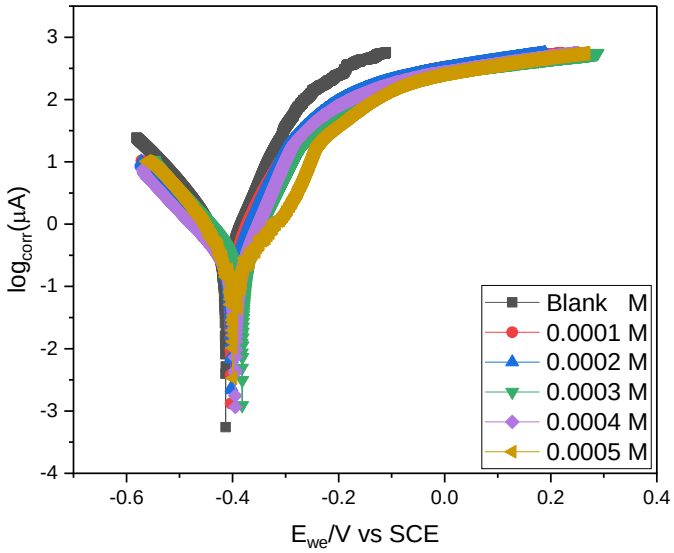

Figure 5.26: Tafel plots for zinc in 1.5 M HCl in the absence and presence of various concentrations of NO_2-Chr-2-carb at 303 K.

Table 5.3: Potentiodynamic Polarization (PDP) parameters such as corrosion current density (i_{corr}), corrosion potential (E_{corr}), anodic (βa) and cathodic (βc) Tafel slopes for zinc corrosion in 1.5 M HCl in with and without different concentrations of 6-substitutedchromone-2-carboxamides.

Inhibitor	Conc. ($x10^{-4}$ M)	C_R (mpy)	E_{corr} (mV vs SCE)	β_a ($mV.dec^{-1}$)	β_c ($mV.dec^{-1}$)	I_{corr} ($\mu A.cm^{-2}$)	% IE_{PDP}	IE_{WL} (%)
Chr-2-carb	**Blank**		-413.060	78.9	102.4	616.156		
	1.0		-440.715	76.4	91.0	307.150	50.15	56.34
	2.0		-394.536	76.3	90.4	287.923	53.27	58.94
	3.0		-4.00.313	76.0	83.8	272.044	55.85	61.20
	4.0		-433.670	57.2	92.4	197.437	67.96	62.51
	5.0		-421.703	63.0	61.1	97.363	84.19	65.05
Br-Chr-2-carb	1.0		-411.372	68.9	95.7	301.050	51.14	65.44
	2.0		-408.907	47.4	76.2	271.828	55.88	66.67
	3.0		-432.800	57.6	62.0	172.550	71.99	67.41
	4.0		-416.022	39.4	53.5	121.298	80.31	68.07

	5.0		-414.234	29.13	13.0	105.040	82.95	68.46
Cl-Chr-2-carb	1.0		-413.322	57.9	97.9	300.605	51.21	59.98
	2.0		-405.550	53.7	99.4	247.893	59.77	60.25
	3.0		-424.957	49.2	65.4	214.144	65.25	60.49
	4.0		-464.150	79.6	75.6	105.287	82.91	60.98
	5.0		-436.163	19.9	23.8	88.737	85.59	61.97
CH_3O-Chr-2-carb	1.0		-436.643	63.6	69.2	106.105	82.78	63.86
	2.0		-425.911	45.0	69.8	99.111	83.91	65.73
	3.0		-426.516	61.2	70.6	58.878	90.44	66.19
	4.0		-509.982	38.6	48.4	46.297	92.49	67.12
	5.0		-471.737	42.0	51.0	39.883	93.53	68.83
NO_2-Chr-2-carb	1.0		-402.891	49.6	79.7	242.266	60.68	59.19
	2.0		-400.904	51.4	94.9	232.390	62.28	61.18
	3.0		-382.281	55.6	81.6	184.599	70.04	62.68
	4.0		-392.288	41.4	79.0	109.225	82.27	68.47
	5.0		-398.672	48.3	33.6	67.323	89.07	71.73

5.2.3. Electrochemical impedance spectroscopy (EIS) results for zinc

EIS plays a key role in helping get a deeper understanding of the kinetics of the corrosion process together with the mechanism of inhibition. As noted in the previous section on mild steel corrosion, EIS became useful in the investigation of the behavior of zinc corrosion in 1.5 M HCl in the absence and presence of different concentrations of the investigated 6-substituted chromone-2-carboxamides at 303 K. As mentioned, this technique was conducted at the OCP after 1800 seconds of zinc immersion until a steady corrosion potential (E_{corr}) for all the working electrodes was established. Figures 5.27 – 5.31 show the obtained Nyquist plots and corresponding Bode plots. The Nyquist plots and corresponding Bode plots are represented by the imperfect semicircles capacitive loops which are indicative of a charge transfer process that controls the corrosion of zinc in acidic medium. These figures show that the diameter of these imperfect semicircles increases with an increase in the concentration of the inhibitors. This can be attributed to the increase in the surface coverage of adsorptive quinoxaline molecules on the zinc surface. As observed from the figures below, the Nyquist and Bode plots present a single depressed capacitive arc and a single peak respectively suggesting that the dissolution of the zinc metal is administered by a single charge transfer procedure [260, 261]. The observed depressed capacitive loop in the Nyquist plots semicircle denotes electrodes that are solid, and the dispersion of frequency is due to the roughness of the metal surface of the electrode [262]. Same as observed in the mild system, also in the zinc system the Nyquist plots in the absence and presence of 6-substitutedchromone-2-carboxamides are essentially identical, showing that these inhibitors do not affect the corrosion mechanism of the zinc specimen.

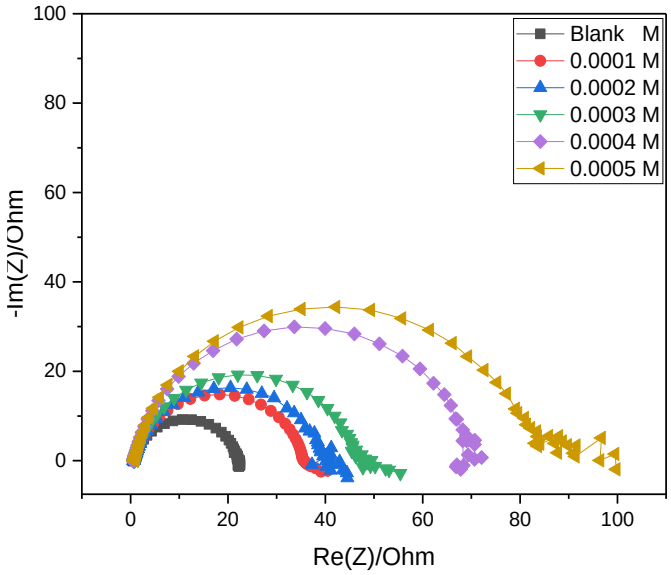

Figure 5.27: Nyquist plot of zinc in 1.5 M HCl in the presence and absence of various concentrations of Chr-2-carb.

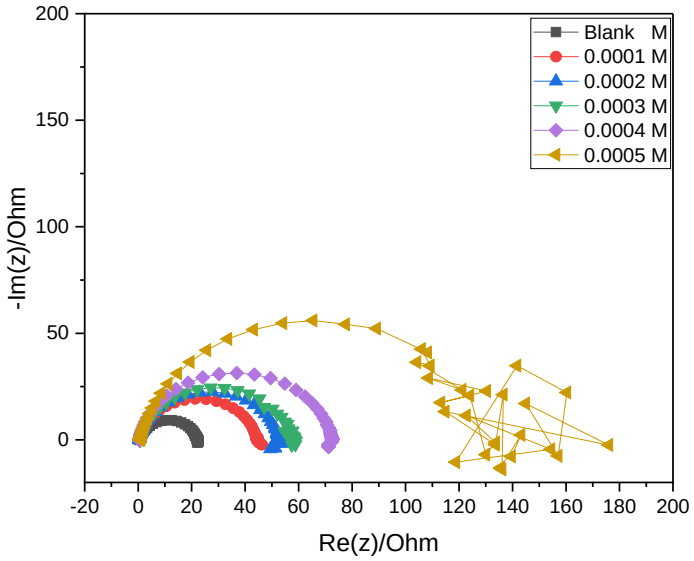

Figure 5.28: Nyquist plot of zinc in 1.0 M HCl in the presence and absence of various concentrations of Br-Chr-2-carb.

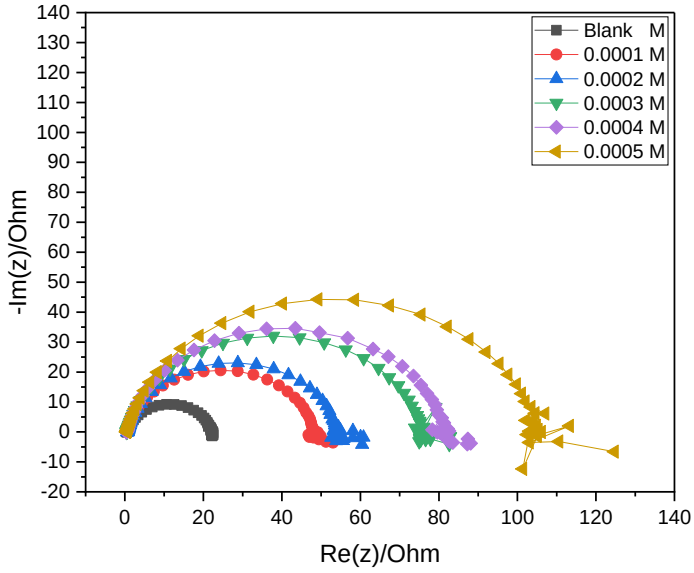

Figure 5.29: Nyquist plot of zinc in 1.0 M HCl in the presence and absence of various concentrations of Cl-Chr-2-carb.

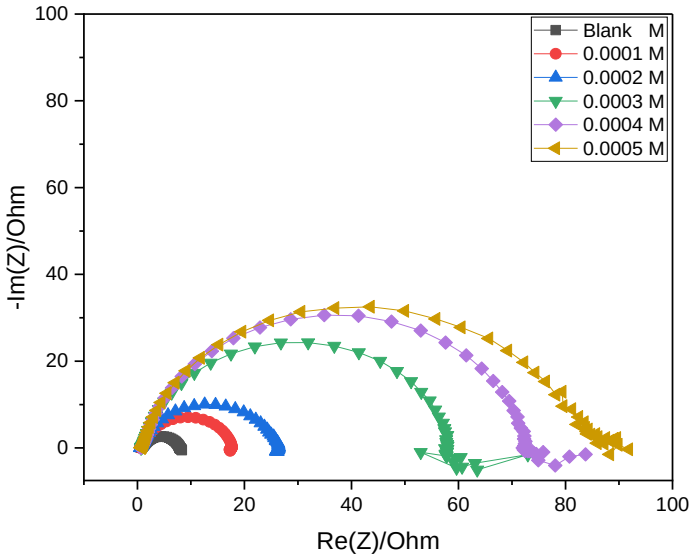

Figure 5.30: Nyquist plot of zinc in 1.0 M HCl in the presence and absence of various concentrations of CH_3O-Chr-2-carb.

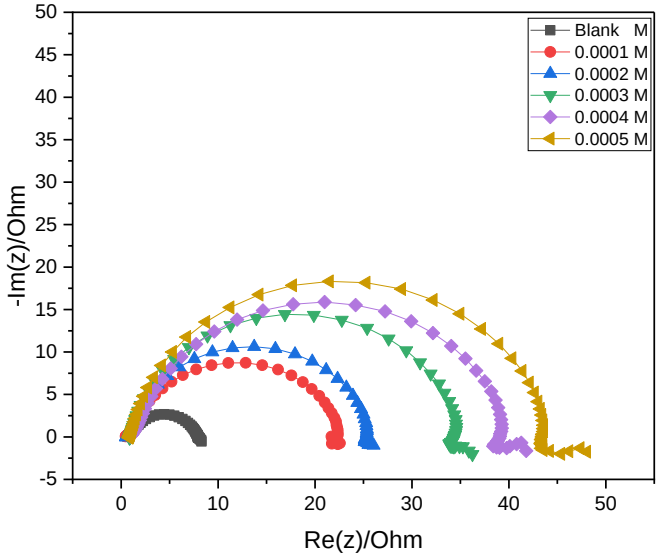

Figure 5.31: Nyquist plot of zinc in 1.0 M HCl in the presence and absence of various concentrations of NO_2-Chr-2-carb.

Table 5.4: Electrochemical impedance spectroscopy (EIS) parameters such as the resistance of charge transfer (R_{ct}), constant phase element (Y_o), solution resistance (R_s) and the CPE exponent (n) for zinc corrosion in 1.0 M HCl in absence and presence of different concentrations of 6-substitutedchromone-2-carboxamides.

Inhibitor	Conc. (x10^{-4} M)	Rct (Ω)	Q_2 ($F.s^{(a-1)}$)	Rs (Ω)	n	% IE_{EIS}	(%) IE_{WL}
Chr-2-carb	**Blank**	21.94	0.5835e-3	0.5392	0.8508	–	–
	1.0	46.61	0.2151e-3	0.8964	0.8715	52.93	56.34
	2.0	47.88	0.4525e-3	0.8256	0.7162	54.18	58.94
	3.0	53.76	0.8504e-3	0.4915	0.7797	59.19	61.20
	4.0	69.81	0.3313e-3	0.5429	0.8818	68.57	62.51
	5.0	89.60	0.4729e-3	0.7550	0.7980	75.51	65.05
Br-Chr-2-carb	1.0	47.76	0.825e-3	0.4719	0.7793	54.06	65.44
	2.0	48.54	0.7855e-3	0.5306	0.7786	54.80	66.67
	3.0	49.08	0.8516e-3	0.2884	0.7837	55.29	67.41

	4.0	54.27	0.8162e-3	0.2772	0.7835	59.57	68.07
	5.0	141.6	0.6324e-3	0.7576	0.7757	84.51	68.46
Cl-Chr-2-carb	1.0	48.18	0.2982e-3	0.5718	0.8862	54.46	59.98
	2.0	62.60	0.6918e-3	0.3557	0.7912	64.95	60.25
	3.0	76.69	0.248e-3	0.4589	0.8741	71.39	60.49
	4.0	85.41	0.5826e-3	0.3965	0.7712	74.31	60.98
	5.0	92.36	0.6779e3	0.3569	0.7897	76.25	61.97
CH_3O-Chr-2-carb	1.0	46.92	0.3552e-3	0.7465	0.8559	53.24	63.86
	2.0	58.67	0.5004e-3	0.5080	0.7753	62.60	65.73
	3.0	106.0	0.4776e-3	0.5331	0.7709	79.30	66.19
	4.0	135.7	0.2167e-3	0.6551	0.8016	83.83	67.12
	5.0	167.1	0.2109e-3	0.02031	0.8224	86.87	68.83
NO_2-Chr-2-carb	1.0	43.37	0.6837e-3	1.014	0.7787	49.41	59.19
	2.0	48.35	0.3765e-3	0.7709	0.8535	54.62	61.18
	3.0	52.4	0.52455e-3	0.7573	0.8013	58.13	62.68
	4.0	75.42	0.3247e-3	0.9232	0.8535	70.91	68.47
	5.0	80.18	0.5335e-3	0.7672	0.8170	72.64	71.73

The outcomes shown in Table 5.4 revealed that the charge transfer resistance for the blank solution was relatively low due to the high conductivity of the HCl solution which is a similar observation noted on the mild steel system. The data shown in Table 5.4 reveals that the value of R_{ct} increases with the addition of inhibitors when compared to the blank solution; this increase is due to the formation of a protective film at the metal/solution interface as highlighted earlier. Like mild steel corrosion, the corrosion of zinc in acidic medium is also likely caused by the charge transfer process. This could be due to a number of factors such as frequency dispersion, distribution of surface-active sites, metal

surface inhomogeneity, grain boundaries, roughness etc. The electrochemical impedance parameters obtained from the Nyquist plots and the %IEEIS are displayed in Table 5.4 above. The charge transfer resistance equation (39) above in the previous section was used to calculate $\%IE_{EIS}$.

As displayed in Table 5.4 above, efficiency increased to reach a maximum of 86.87 % for zinc at the optimum concentration of CH_3O-Chr-2-carb.

Same as in the mild steel system, experimental data was fitted to a simple electrical equivalent circuit shown in figure 5.16 to analyze Nyquist impedance plots, that includes components such as the resistance of charge transfer (R_{ct}), constant phase element (Y_o), solution resistance (R_s) and the CPE exponent (n) for MS.

5.3. Electrochemical measurement for aluminium

5.3.1. Open circuit potential (OCP) studies for aluminium

Figures 5.32 – 5.36 show the OCP/time evolution of the aluminium metal in 1.0 M HCl solution with and without the synthesized 6-substituted chromone-2-carboxamides inhibitors. The purpose of this is to see the difference in OCP during this time frame and to understand how long it takes (waiting period) for stability before electrochemical experiments as explained in the previous section. This study discovered that the stability in the OCP begins at 1800 s, giving us the confidence to conclude that 1800 s is an adequate waiting period for the system to attain a stable OCP.

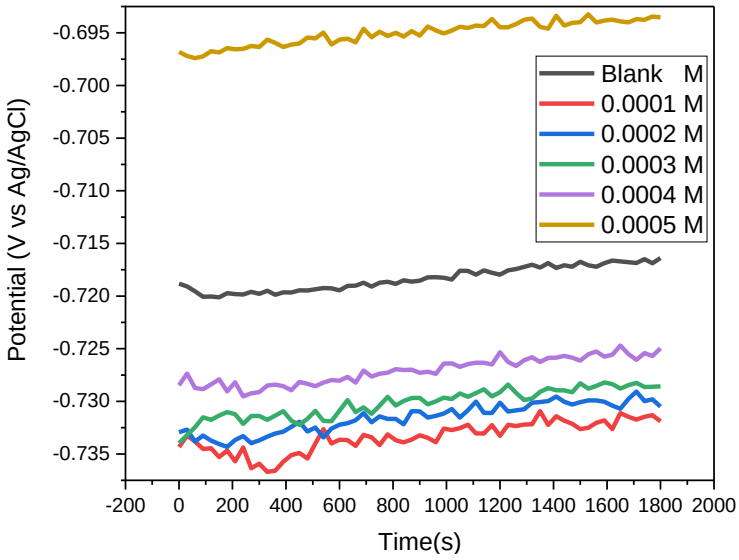

Figure 5.32: Open circuit potential (OCP) of aluminium and its evolution with time in 1.0 HCl before and after adding various concentrations of Chr-2-Carb at 298 K.

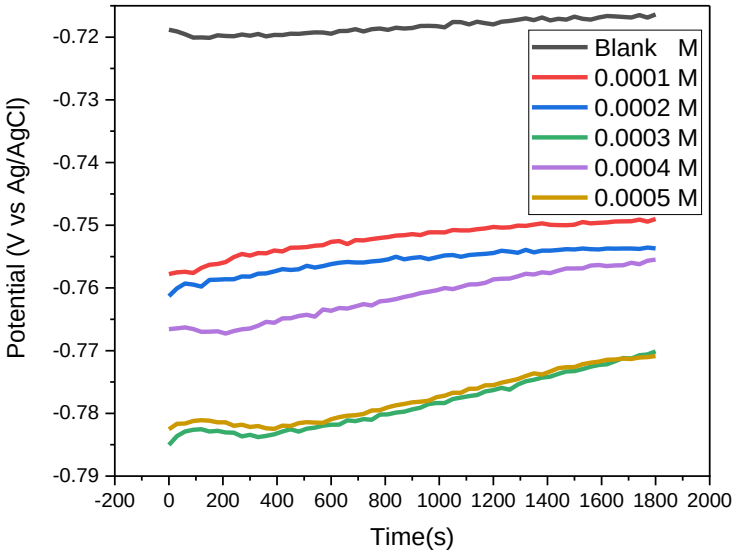

Figure 5.33: Open circuit potential (OCP) of aluminium and its evolution with time in 1.0 HCl before and after adding various concentrations of Br-Chr-2-carb at 298 K.

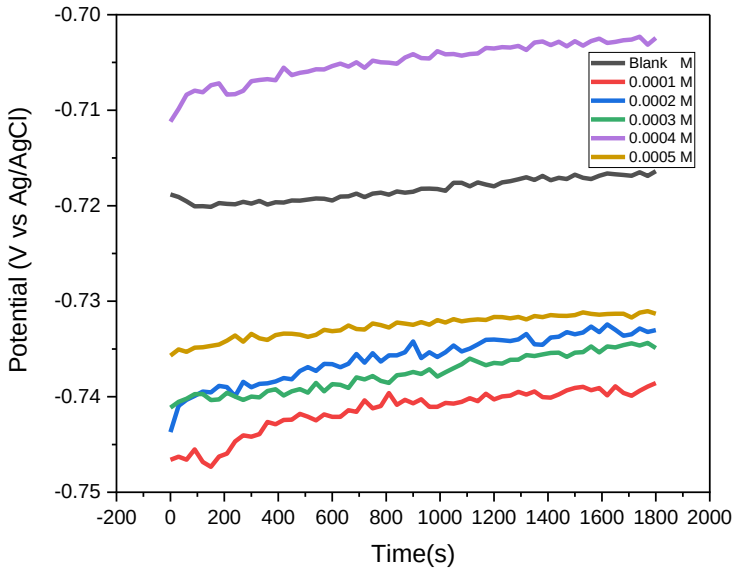

Figure 5.34: Open circuit potential (OCP) of aluminium and its evolution with time in 1.0 HCl before and after adding various concentrations of Cl-Chr-2-Carb at 298 K.

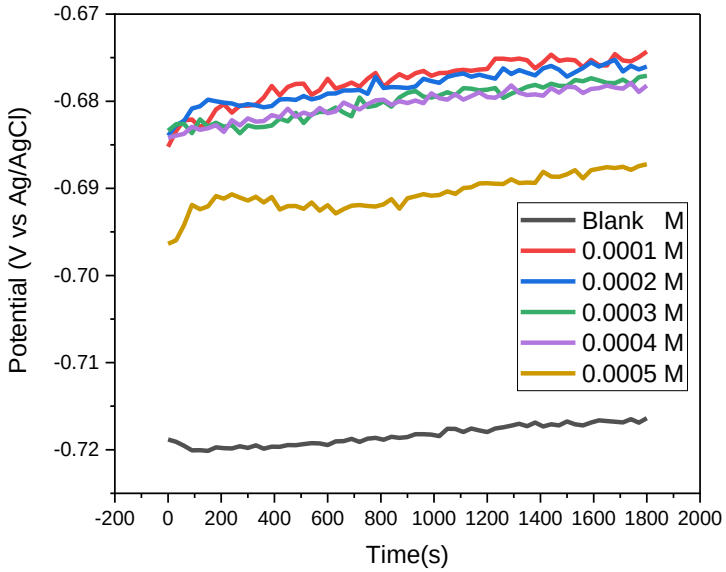

Figure 5.35: Open circuit potential (OCP) of aluminium and its evolution with time in 1.0 HCl before and after adding various concentrations of CH_3O-Chr-2-Carb at 298 K.

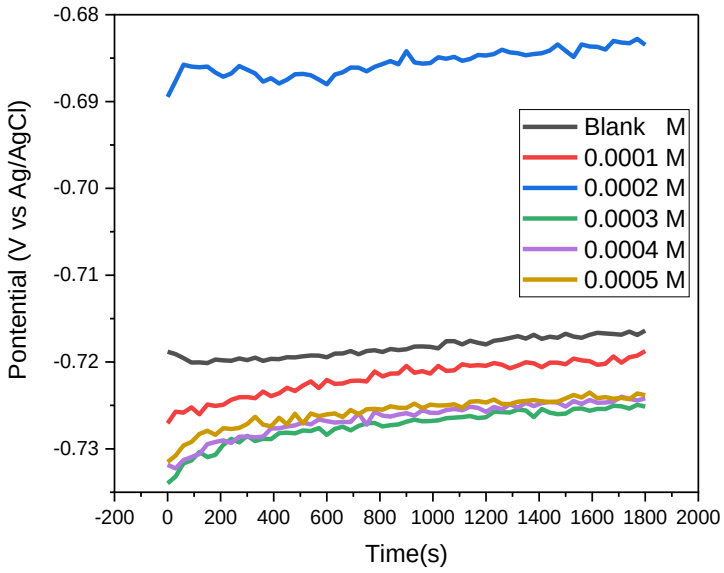

Figure 5.36: Open circuit potential (OCP) of aluminium and its evolution with time in 1.0 HCl before and after adding various concentrations of NO2-Chr-2-Carb at 298 K.

5.3.2. Potentiodynamic polarization (PDP) results for aluminium

As highlighted, the corrosion of aluminium is the product of simultaneously anodic and cathodic half-reaction. To better understand this mechanism, PDP measurements were conducted at room temperature (303 K) in 1.0 M HCl in the absence and presence of the examined 6-substituted chromone-2-carboxamides, as displayed in Figures 5.37 – 5.41. These figures show that the introduction of the examined inhibitors influenced both the anodic and cathodic half-reactions of aluminium corrosion in the HCl. Potentiodynamic parameters, including corrosion current density (i_{corr}), corrosion potential (E_{corr}), polarization resistance (R_P), and anodic (ba) and cathodic (bc) Tafel slopes, were effectively analyzed from both anodic and cathodic areas of the Tafel plots. Table 4.11 displays electrochemical variables such as I_{corr}, E_{corr}, βa, βc, and $\%IE_{PDP}$. The potentiodynamic polarization inhibition efficiency ($\%IE_{PDP}$) was then estimated using the determined i_{corr} value from equation (38).

The results obtained, the Tafel extrapolation plots indicate that adding the inhibitors led to decreased of current densities in both anodic and cathodic site compared to the blank. The decrease was slightly more pronounced with higher concentrations of the 6-

substituted chromone-2-carboxamides. All three inhibitors investigated have a minor cathodic effect, confirming their main cathodic character. The inhibitors' behavior indicates that they prevent the acidic attacks on the aluminium surface more in the cathodic site, the parallel impact of Tafel lines increases, indicating activation control of hydrogen evolution. According to the literature [263], hydrogen discharge happens by charge transfer at the metal contact. According to research findings, an anodic or cathodic inhibitor is identified when the displacement in E_{corr} exceeds ±85 mV, which corresponds to the corrosion potential of the blank [264]. The study found that using 6-substituted chromone-2-carboxamides resulted in a maximum change in E_{corr} values of less than 85 mV. These inhibitors are mixed-type, meaning they are neither anodic nor cathodic but they protect both the anodic and cathodic sites. Table 5.5 shows varying shifts for βa and βc compared to blank.

The addition of three inhibitors to the 1.0 M HCl solution resulted in a modest positive change in corrosion potential. It is worthily concluded that the inhibitors affect both anodic and cathodic reactions. The graphs show that hydrogen evolution has a greater influence than the Al dissolution [265]. The electrochemical parameters displayed in Table 5.5 indicate that increasing the concentration of inhibitors decreases i_{corr} values while increasing the percentage of IE_{PDP}, which culminates at the highest concentration of the five synthesized inhibitors. The behavior of these inhibitors indicates that they adsorb on the Al surface and become stable with increasing concentration due to the availability of more particles of the inhibitors at higher concentrations.

In the presence of Chr-2-carb, Cl-Chr-2-carb and CH_3O-Chr-2-carb trans-passive regions were observed, resulting in pitting corrosion. However, the extent of the trans-passive area was minimal, suggesting that these inhibitors reduced the extent of the damage inflicted by pitting. It is clearly observed that in the presence of the Br-Chr-2-carb and NO_2-Chr-2-carb there's no trans-passive area especially in the highest concentration ($5x10^{-4}$ M).

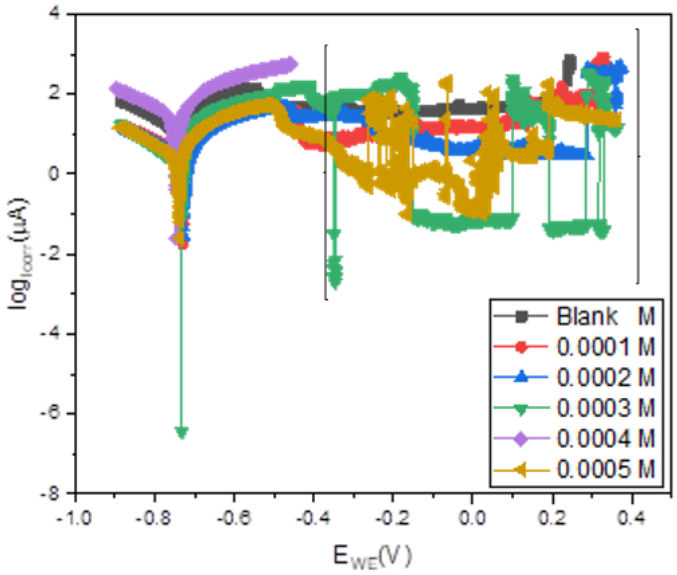

Figure 5.37: Tafel plots for aluminium in 1.0 M HCl in the absence and presence of various concentrations of Chr-2-carb at 303 K.

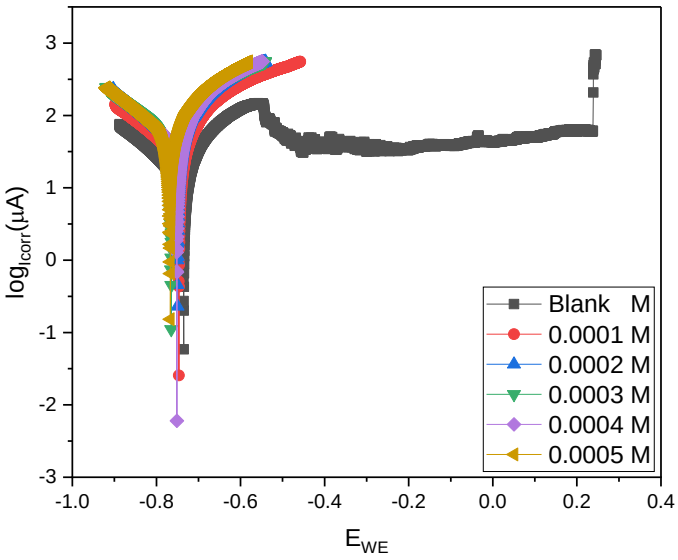

Figure 5.38: Tafel plots for aluminium in 1.0 M HCl in the absence and presence of various concentrations of Br-Chr-2-carb at 303 K.

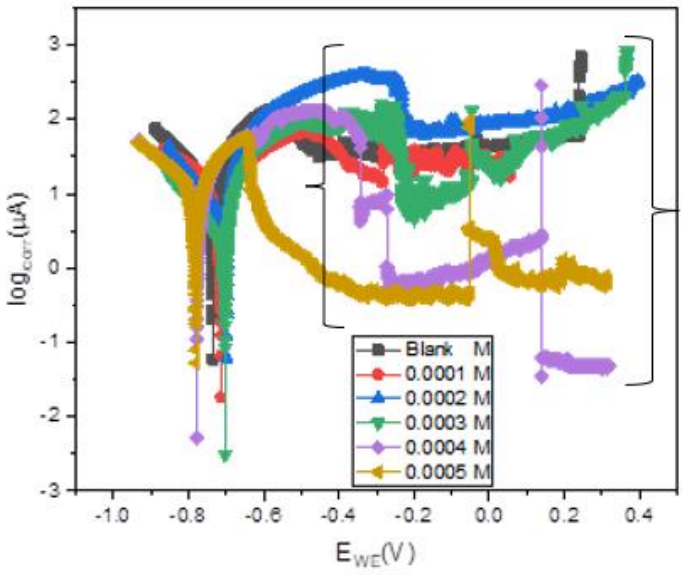

Figure 5.39: Tafel plots for aluminium in 1.0 M HCl in the absence and presence of various concentrations of Cl-Chr-2-carb at 303 K.

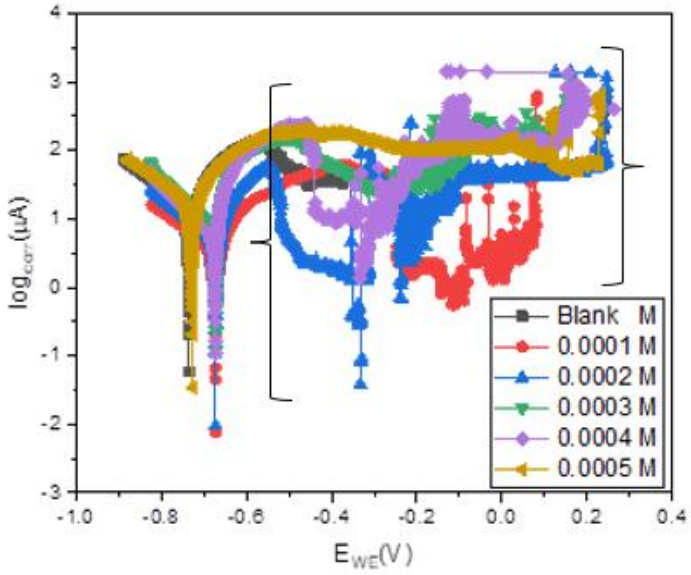

Figure 5.40: Tafel plots for aluminium in 1.0 M HCl in the absence and presence of various concentrations of CH_3O-Chr-2-carb at 303 K.

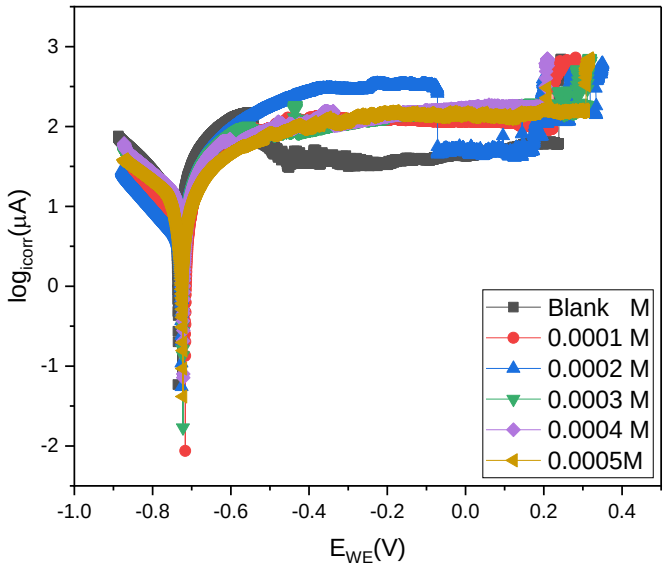

Figure 5.41: Tafel plots for aluminium in 1.0 M HCl in the absence and presence of various concentrations of NO_2-Chr-2-carb at 303 K.

Table 5.5: Potentiodynamic polarization (PDP) parameters such as corrosion potential (E_{corr}), corrosion current density (i_{corr}) and anodic and cathodic Tafel slopes (βa and βc) for Al corrosion in 1.0 M HCl in with and without different concentrations of 6-substitutedchromone-2-carboxamides.

Inhibitor	Conc. (x10^{-4} M)	E_{corr} (mV vs SCE)	β_a (mV.dec^{-1})	β_c (mV.dec^{-1})	I_{corr} (μA.cm^{-2})	% IE_{PDP}	IE_{WL} (%)
Chr-2-carb	**Blank**	-366.783	72.6	109.3	0.00352	–	–
	1.0	-409.920	24.7	63.7	0.000665	81.11	68.66
	2.0	-371.842	17.8	67,0	0.000504	85.68	72.76
	3.0	-408.565	24.7	61.1	0.000496	85.91	72.86
	4.0	-363.197	18.0	67.2	0.000450	87.22	73.66
	5.0	-373.707	20.6	54.8	0.000361	89.74	75.22
Br-Chr-2-carb	1.0	-399.249	40.4	60.1	0.000726	79.38	65.52
	2.0	-402.123	30.3	74.2	0.000624	82.27	66.30
	3.0	-387.625	18.4	58.7	0.000502	85.74	69.83

	4.0	-383.576	17.6	42.8	0.000291	91.73	70.17
	5.0	-384.775	48.6	61.2	0.000128	96.36	70.65
Cl-Chr-2-carb	1.0	-404.237	15.0	54.3	0.000565	83.95	65.48
	2.0	-375.743	16.3	59.8	0.000489	86.11	66.21
	3.0	-370.540	15.9	71.2	0.000329	90.65	69.78
	4.0	-369.950	50.2	57.3	0.000225	93.61	70.09
	5.0	-379.820	18.4	55.7	0.000164	95.34	70.60
CH_3O-Chr-2-carb	1.0	-402.291	28.7	46.3	0.000535	84.80	68.61
	2.0	-416.865	23.2	58.3	0.000484	86.25	72.57
	3.0	-410.567	23.8	52.7	0.000412	88.29	72.84
	4.0	-399.909	22.8	60.6	0.000322	90.85	73.47
	5.0	-401.311	24.0	51.8	0.000130	96.31	75.15
NO_2-Chr-2-carb	1.0	-403.331	23.4	58.3	0.000510	85.51	61.41
	2.0	-399.904	22.8	60.6	0.000421	88.04	69.41
	3.0	-385.04	22.5	72.8	0.000358	89.82	70.51
	4.0	-425.748	39.2	72.8	0.000208	94.09	72.11
	5.0	-423.490	48.0	77.8	0.000126	96.42	74.05

5.3.3. Electrochemical impedance spectroscopy (EIS) results for aluminium

Electrochemical impedance spectroscopy (EIS) is a well-known quantitative tool for studying corrosion and adsorption. In this study, EIS was used to analyze the corrosion behavior of Al in 1.0 M HCl with and without the synthesized inhibitors after 30 minutes of immersion at 303K. The impendence spectra obtained are shown as Nyquist and their corresponding Bode plots (Figures 5.43 – 5.47). Table 5.6 presents the EIS parameters obtained from these data. Inhibitors have little effect on the anodic and cathodic

processes of Al dissolution, as the form of the curves is constant in both cases. It is clear from the below figures that the diameter of the blank is much smaller than that of the inhibited system. Same as observed in the mild steel and zinc systems above, the diameter of the semi-circle was increasing with increasing concentration of the inhibitors. In addition, a shift in Nyquist plots origin in some of the concentrations of the inhibitors has been noted. This behavior was caused by the creation of an adsorption film layer on the Al surface. As inhibitor concentration increased, more particles of the inhibitors were able to cover the entire surface. The Increased in the inhibitor concertation stabilized the adsorption process and reduce Al passivation, which resulted in a shift in some of the semicircle loops. The imperfect semicircles and smaller arch for the blank suggest that Al corrosion is primarily controlled by charge transfer. This suggests that the inhibitors prevent corrosion by adsorbing on the metal surface, rather than altering its electrochemical process. The synthesized Inhibitors has reduced the Faradaic processes on bare Al surfaces as concentration increases. Similar results were observed by other researchers [234].

As displayed in the figures below, the Nyquist diagrams show a capacitive loop at high frequencies and an inductive loop at low frequencies. The high-frequency capacitive loop represents the charge transfer resistance of the aluminium corrosion process and double-layer behaviour. The inductive loop's behaviour can be traced to a variety of processes [266]. The induction loop could be caused by the stability of the adsorbed intermediate complex on the electrode surface, which may include both reactive products and inhibitor molecules [266,267].

Figure 5.47 depicts the equivalent circuit model utilized to fit the impendence spectra, other researchers used a similar circuit on the aluminium system [234]. Here R_1 denotes electrolyte resistance (R_s), Q_1 is the constant phase element (CPE), R_2 is the charge transfer resistance (R_{ct}), and R3 and L3 are inductive elements. To account for system inhomogeneities, a constant phase element was utilized instead of double-layer capacitance (C_{dl}). The observed imperfect semicircle loop at higher frequencies implies Al surface inhomogeneity caused by structural or interfacial factors, comparable to the ones obtained on the processes of adsorption of the inhibitors. Equation (39) was used

to compute the percentage inhibition efficiency EIS (%IE_{EIS}) at various inhibitor concentrations.

Table 5.5 below shows that increasing charge transfer resistance leads to an increase in %IE_{EIS}, which is proportional to inhibitor concentration. Increased inhibitor concertation leads to a decrease in capacity due to the creation of an adsorption film layer on the Al surface. This could be owing to thicker electrical double layers or decreased local dielectric constants. The synthesized inhibitors adsorb at the metal/solution contact, dislodging water molecules from the aluminium surface.

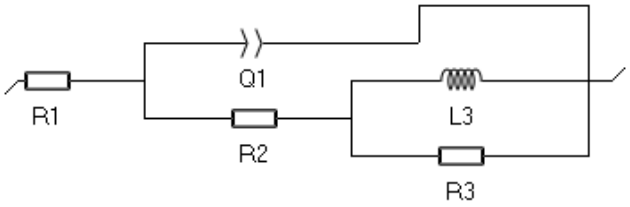

Figure 5.42: Equivalent circuit used to fit the impedance spectra obtained for Al corrosion in 1.0 M HCl in the absence and presence of 6-substituted chromone-2-carboxamides.

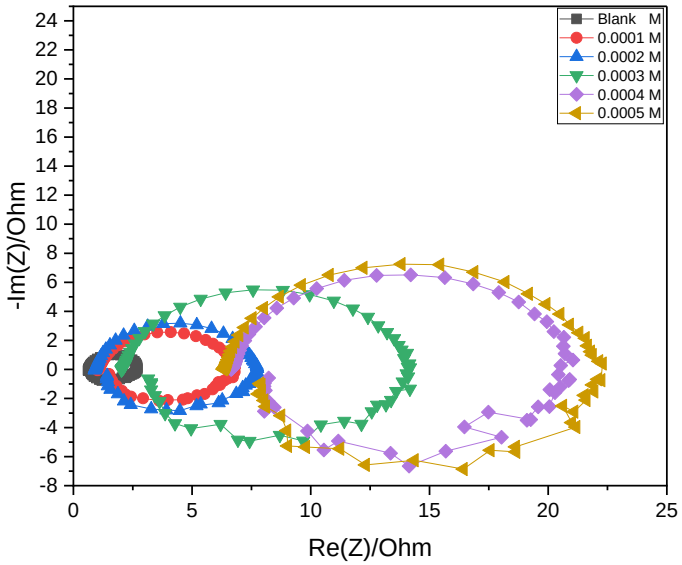

Figure 5.43: Nyquist plot of aluminium in 1.0 M HCl in the presence and absence of various concentrations of Chr-2-carb.

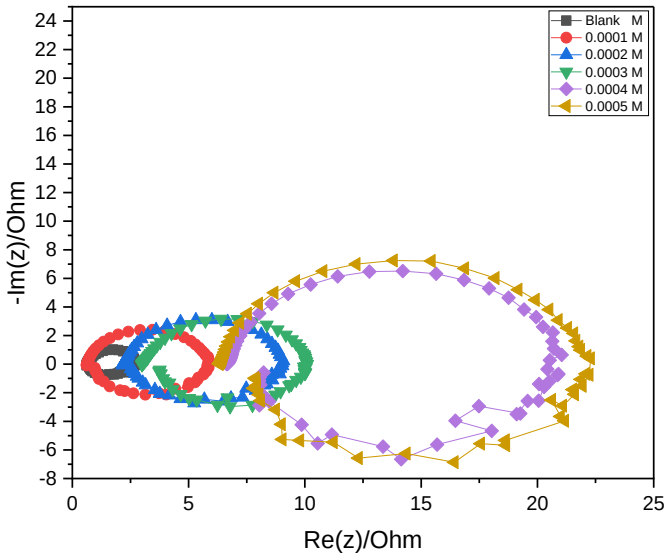

Figure 5.44: Nyquist plot of aluminium in 1.0 M HCl in the presence and absence of various concentrations of Br-Chr-2-carb.

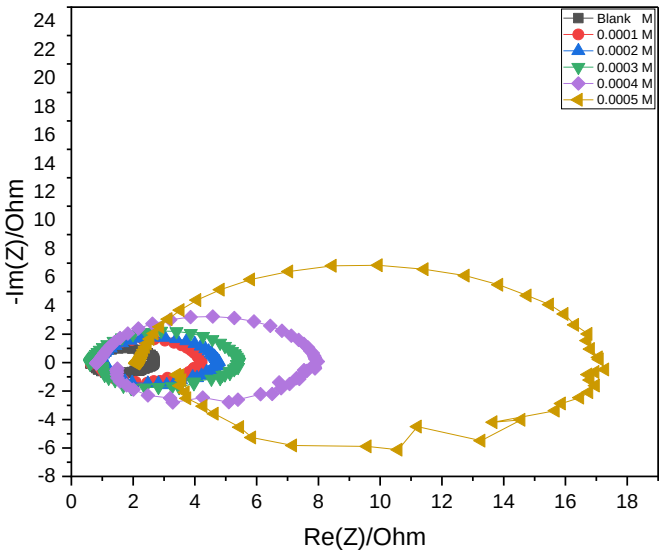

Figure 5.45: Nyquist plot of aluminium in 1.0 M HCl in the presence and absence of various concentrations of Cl-Chr-2-carb.

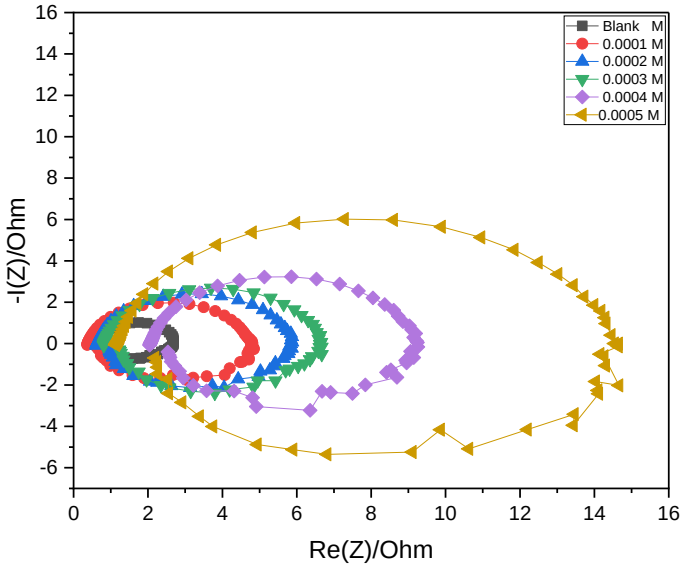

Figure 5.46: Nyquist plot of aluminium in 1.0 M HCl in the presence and absence of various concentrations of CH_3 O-Chr-2-carb.

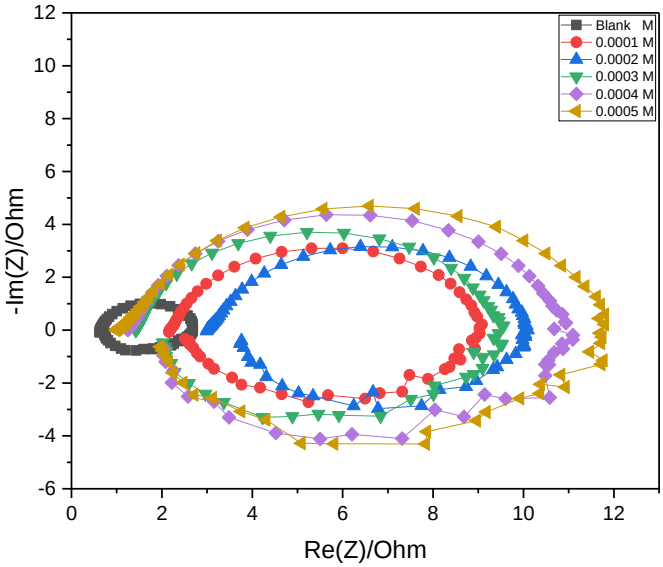

Figure 5.47: Nyquist plot of aluminium in 1.0 M HCl in the presence and absence of various concentrations of NO_2-Chr-2-carb.

Table 5.6: Electrochemical impedance (EIS) parameters such as the resistance of charge transfer (R_{ct}), constant phase element (Q_1), solution resistance (R_s) and the CPE exponent (n) for Al corrosion in 1.0 M HCl in absence and presence of different concentrations of 6-substitutedchromone-2-carboxamides at 303 K.

Inhibitor	Conc. ($x10^{-4}$ M)	R_{ct} (Ω)	Q_1 ($F.s^{(a-1)}$)	R_s (Ω)	L_3 (H)	R_3 (Ω)	n	% IE_{EIS}	(%) IE_{WL}
Chr-2-carb	**Blank**	0.1711	0.1666e-3	1.268	2.726	6.837	0.9867	–	–
	1.0	1.2940	0.2158e-3	0.9977	3.380	2.549	0.9775	86.78	68.66
	2.0	2.182	0.1469e-3	1.888	2.149	8.830	0.9776	92.16	72.76
	3.0	3.127	0.1435e-3	2.021	2.483	4.546	0.9717	94.53	72.86
	4.0	3.337	0.1284e-3	6.345	2.765	10.130	0.9371	94.87	73.66
	5.0	5.295	0.1791e-3	10.730	1.626	15.27	0.9368	96.77	75.22
Br-Chr-2-carb	1.0	0.7237	0.1576e-3	2.261	2.333	3.252	0.9561	76.36	65.52
	2.0	0.9948	0.1136e-3	3.344	3.583	5.492	0.9689	82.34	66.30
	3.0	1.098	85.78e-6	1.685	2.453	6.895	0.9674	84.42	69.83
	4.0	1.378	90.35e-6	2.927	2.368	5.519	0.9911	87.58	70.17
	5.0	4.116	0.1062e-3	26.28	1.784	4.510	0.9357	95.84	70.65
Cl-Chr-2-carb	1.0	0.5228	0.2517e-3	0.6222	1.831	3.245	0.9820	67.27	65.48
	2.0	0.8860	0.1427e-3	0.3203	4.993	2.428	0.9954	80.69	66.21
	3.0	1.018	0.174e-3	0.8718	2.347	5.264	0.9895	83.19	69.78
	4.0	3.490	0.275e-3	42.13	2.232	6.389	0.9427	95.09	70.09
	5.0	9.467	0.4123e-3	0.7178	5.311	3.832	0.995	98.19	70.60
	1.0	0.7265	88.69e-6	0.3551	2.840	2.781	0.9781	76.45	68.61
	2.0	1.406	0.121e-3	0.1438	3.856	3.720	0.9927	87.83	72.57
	3.0	1.907	0.3448e-3	4.753	2.727	4.425	0.9204	91.03	72.84

CH_3O-Chr-2-carb	4.0	2.155	79.93e-3	0.2150	11.99	11.26	0.9997	92.06	73.47
	5.0	3.754	0.2897e-3	33.760	2.194	5.003	0.9273	95.44	75.15
NO_2-Chr-2-carb	1.0	0.6527	0.276e-3	2.260	2.735	5.723	0.9553	73.79	61.41
	2.0	1.458	0.1061e-3	1.343	2.078	6.957	0.9779	88.26	69.41
	3.0	1.857	97.77e-6	0.103	10.3	8.589	0.9991	90.79	70.51
	4.0	2.119	57.73e-3	0.2032	5.130	6.701	0.9970	91.93	72.11
	5.0	2.950	66.22e-6	0.2088	3.223	8.004	0.9877	94.69	74.05

CHAPTER 6: Surface morphology analysis by SEM/ EDS and contact angle wettability

Surface research of the 6-substituted chromone-2-carboxamides protective coating on metal surfaces was carried out utilizing SEM/ EDS and contact angle Wettability techniques.

6.1. SEM/ EDS measurements

Scanning electron microscope (SEM) and energy dispersive X-ray spectroscopy (EDS) were utilized in order to complement the findings obtained from the other techniques such as gravimetric (weight loss), contact angle studies, FTIR analysis, and electrochemical (PPD, EIS) measurements. SEM has been very helpful in this study for the confirmation of the formation of adsorption film on the surface of the three-metal specimen. On the other hand, an energy dispersive Spectroscope (EDS) was utilized to determine the elements present on the surface of the metal specimen.

6.1.1. The SEM images and EDS spectra of Mild Steel

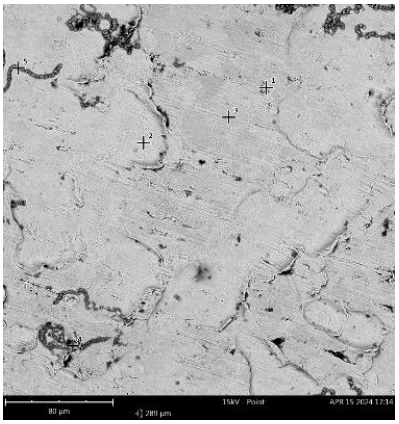

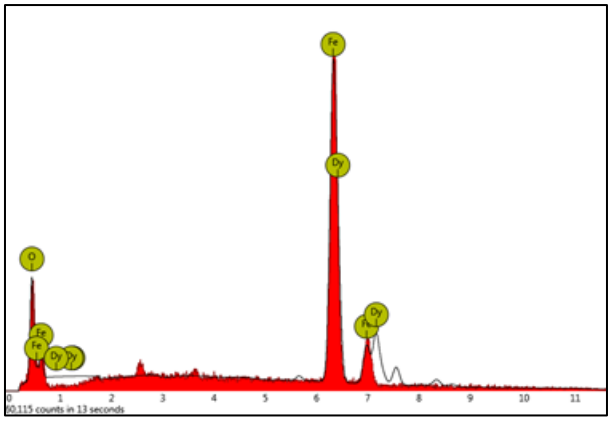

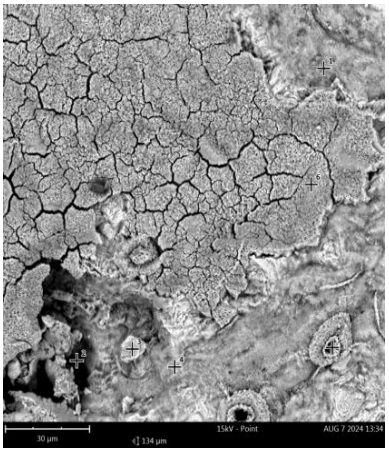

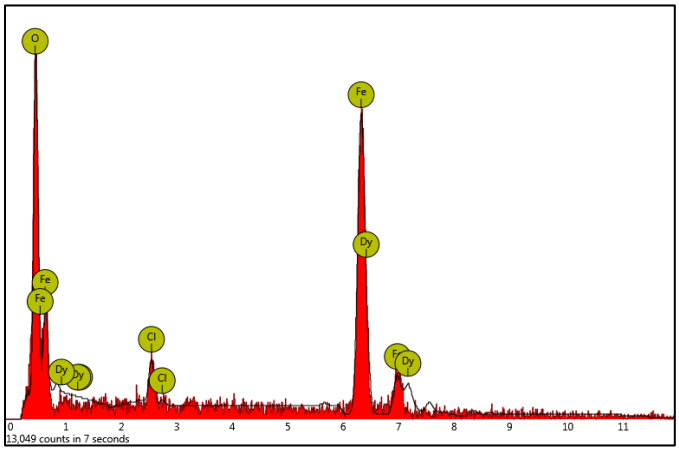

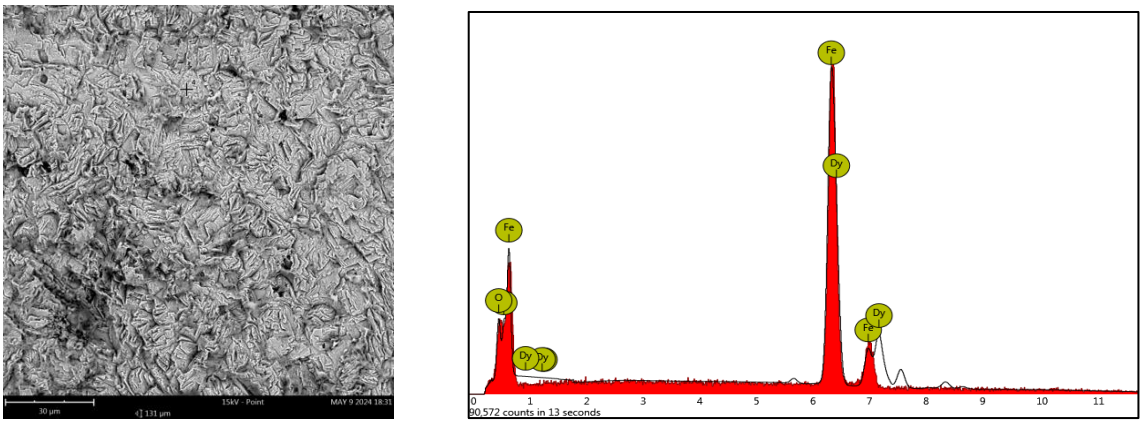

Figure 6.1: Scanning electron micrographs and EDS spectra of (a) freshly polished mild steel (b) mild steel in 1.5 M HCl (c) mild steel in 1.5 M HCl containing Chr-2-Carb.

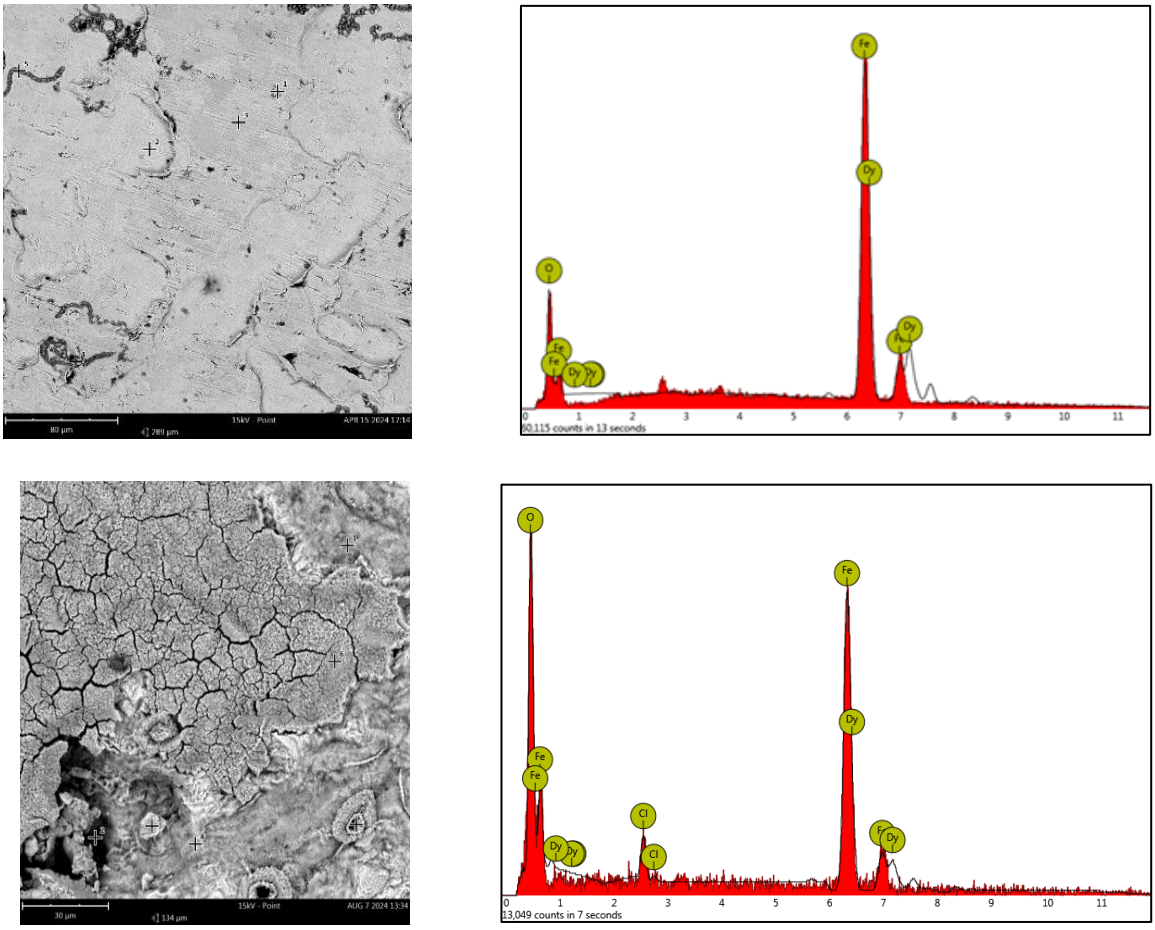

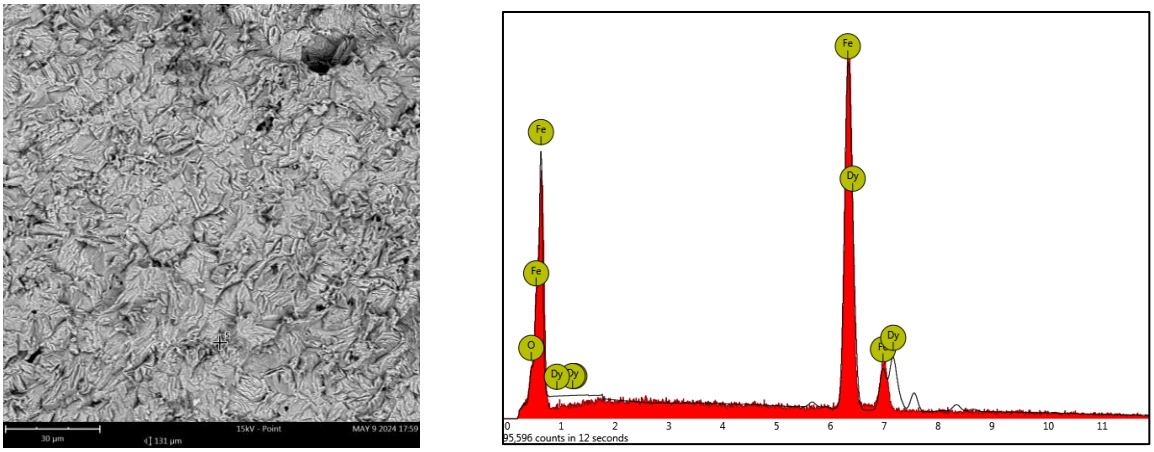

Figure 6.2: Scanning electron micrographs and EDS spectra of (a) freshly polished mild steel (b) mild steel in 1.5 M HCl (c) mild steel in 1.5 M HCl containing Br-Chr-2-Carb.

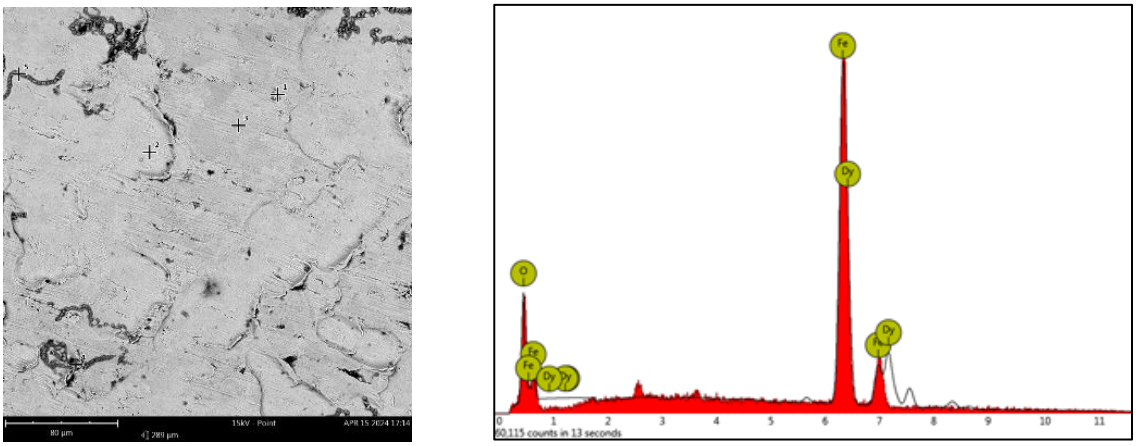

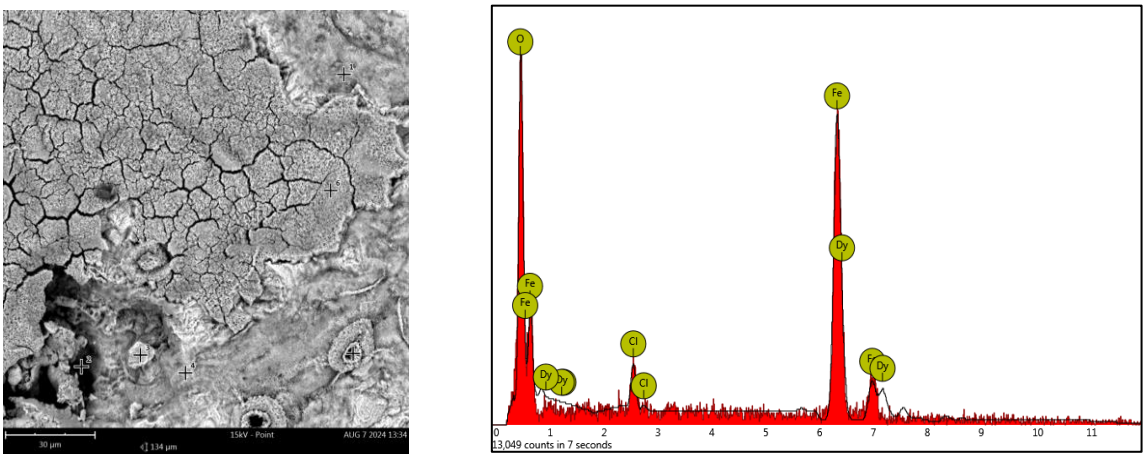

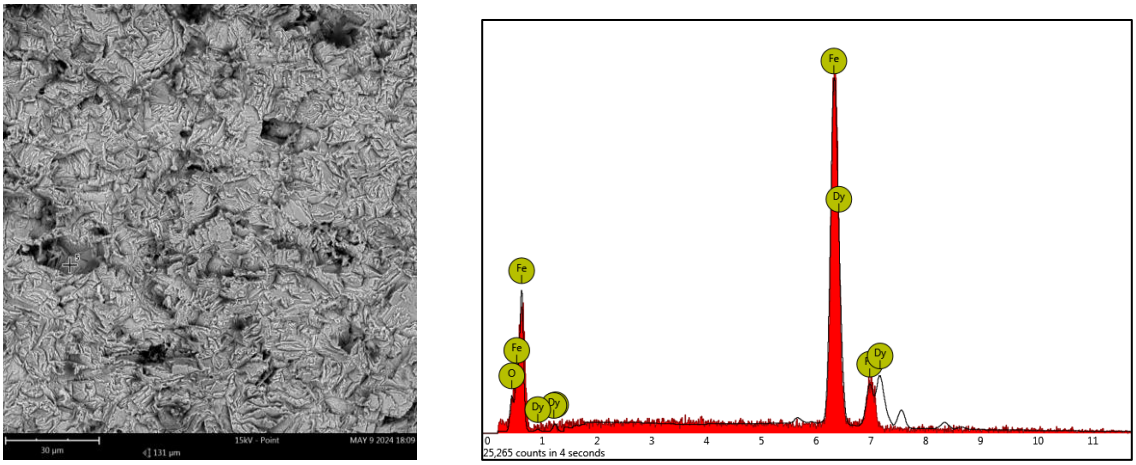

Figure 6.3: Scanning electron micrographs and EDS spectra (a) freshly polished mild steel (b) mild steel in 1.5 M HCl (c) mild steel in 1.5 M HCl containing Cl-Chr-2-Carb.

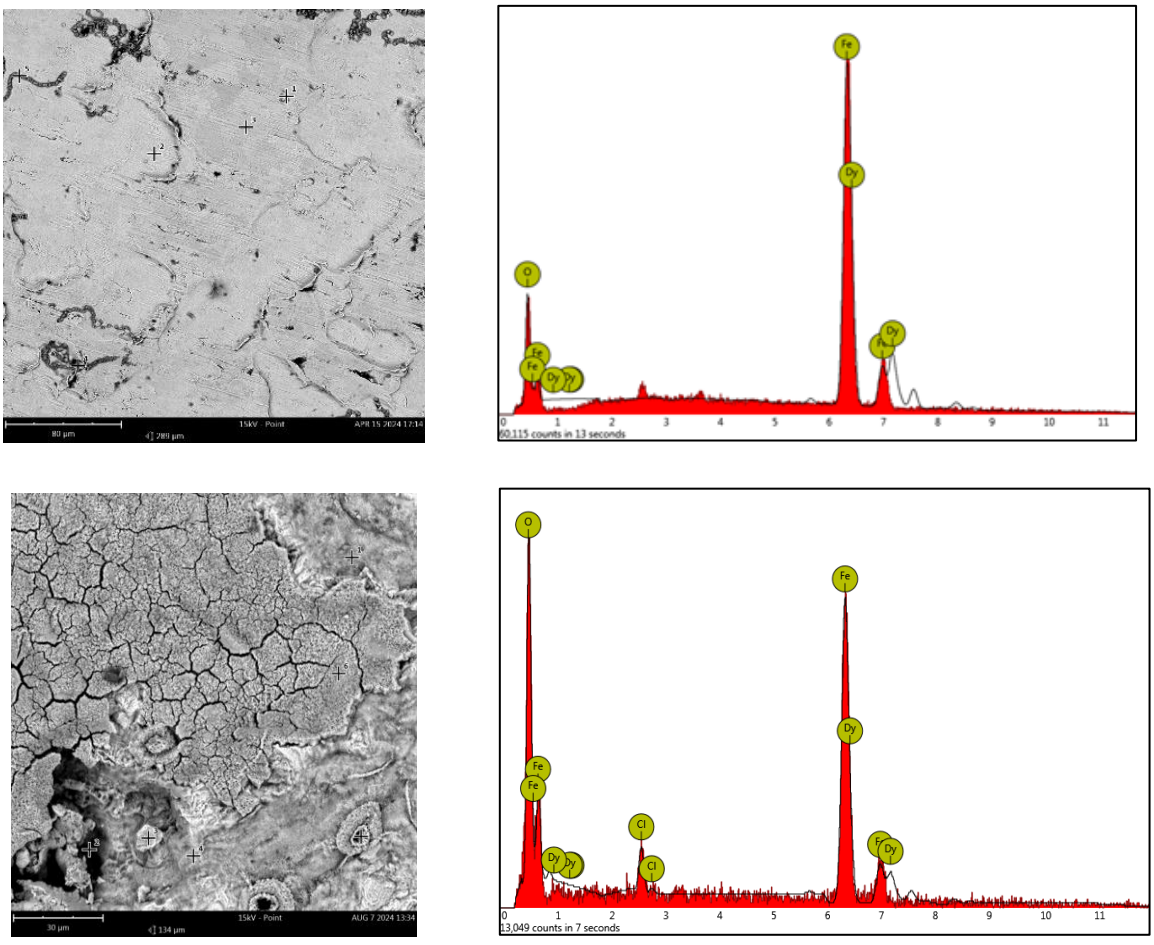

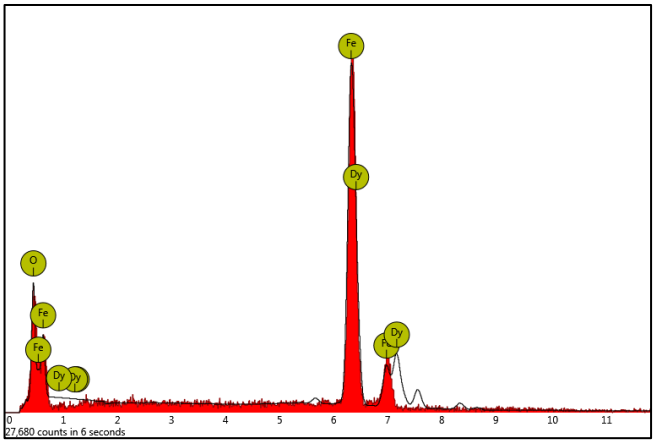

Figure 6.4: Scanning electron micrographs and EDS of (a) freshly polished mild steel (b) mild steel in 1.5 M HCl (c) mild steel in 1.5 M HCl containing CH3O-Chr-2-Carb.

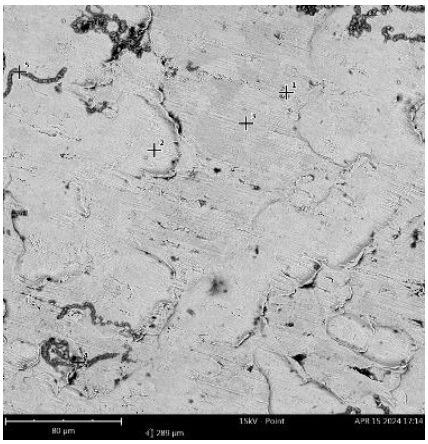

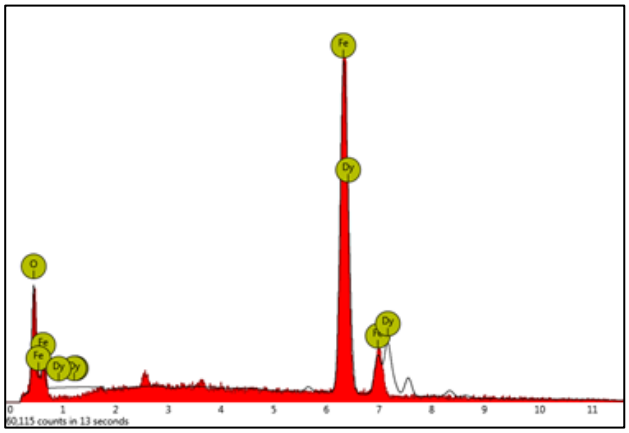

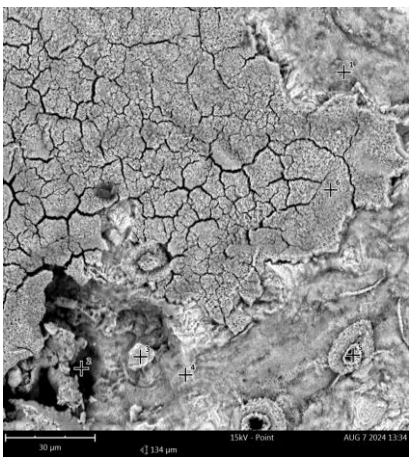

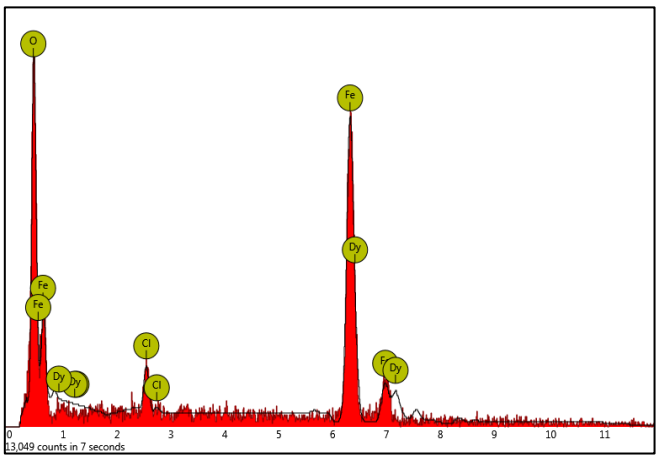

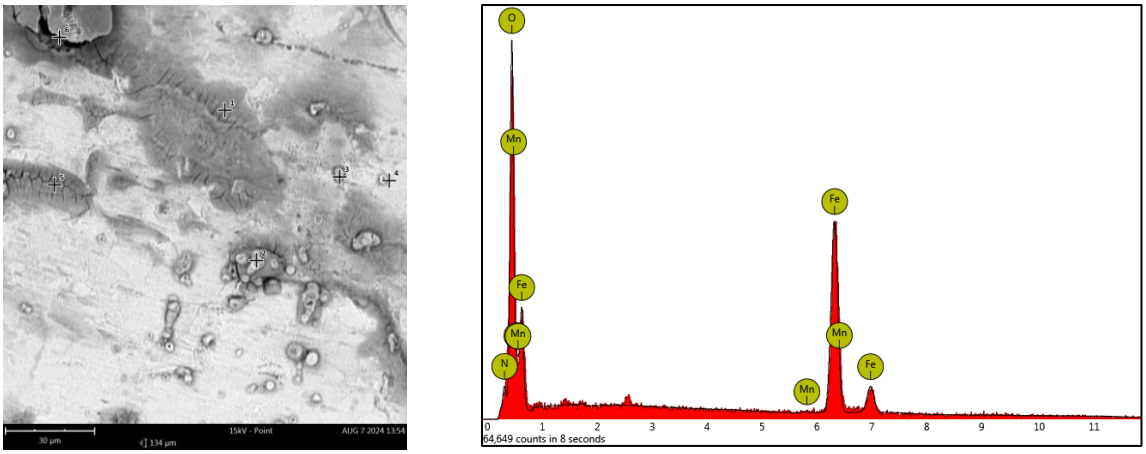

Figure 6.5: Scanning electron micrographs and EDS spectra of (a) freshly polished mild steel (b) mild steel in 1.5 M HCl (c) mild steel in 1.5 M HCl containing NO_2-Chr-2-Carb.

SEM played a vital role in this research project by helping us to study the images taken in order to study the surface morphology of freshly polished mild steel, mild steel in absence and presence of the synthesized inhibitors. The images were taken at different magnification ranges to have a full view of the surfaces of the metal specimen. From the results above the SEM images in Figure 6.1 clearly show that in the absence of Chr-2-Carb inhibitor, the mild steel surface became porous and rough, indicating that the mild steel surface was severely corroded by the HCl. However, in the presence of the five synthesized inhibitors, the surface is protected by the formation of a protective film that covers the entire metal surface as shown in Figures 6.1 – 6.5. It is observed that the presence of the five synthesized inhibitors leads to the formation of a stiffly stuck surface which has some irregular cracks that may be due to the drying up of the hydrated inhibitors. Similar observations have been reported by other researchers [268]. Stiffly stuck surface refers to a surface where corrosion inhibitors or protective coatings have adhered rigidly, creating a strong barrier against corrosive environment. This rigid adhesion prevents the detachment of the protective layer, ensuring long-term protection against corrosion. Overall, a stiffly stuck surface enhances the effectiveness and longevity of corrosion inhibitors, making them more reliable in harsh environments. Irregular cracks can significantly undermine corrosion protection by increasing permeability, reducing adhesion, and promoting localized corrosion. These can caused them to significantly

affect the effectiveness and long-term stability of corrosion protection. Furthermore, the inhibitors resulted in a decrease in the contact between mild steel and the aggressive medium (HCl) through the formation of the adsorption film. Moreover, the chemical analysis of the composition surface electrode by EDS revealed a high percentage of elemental iron which may be the result of the iron oxidation due to the HCl medium, suggesting that the HCl eaten the mild steel. As presented in Figures 6.6 and Table 6.1, the EDS spectra the EDS spectra of the Al immersed in the uninhibited system revealed the presence of Chlorine atoms, indicating that indeed the acidic medium has strongly interacted with the Al specimen. In addition, EDS also revealed that oxygen content is high in the blank system as compared to the pure metal and the metals immersed in the inhibited system and such observations signify the high oxidation process due to corrosion. Results from Table 6.1 show that in the presence of the 6-substituted chromone-2-carboxamides, the oxygen content has decreased, signifying that these inhibitors were able to control the mild steel corrosion. The presence of the oxygen content in the EDS spectra of the MS immersed in the inhibited system may be due to the oxygen heteroatoms of the 6-substitutedchromone-2-carboxamides inhibitors, showing the significant role played by the oxygen atoms as confirmed by the computational analysis study. Figure 6.5 shows the EDS spectrum of MS immersed in the inhibited system containing NO_2-Chr-2-Carb inhibitor showing the presence of nitrogen content in the surface, which may be due to the N of the N of the NO_2 and NH_2 groups. This observation confirms the formation of the adsorption film on the mild steel surface. Moreover, metals such as Dysprosium, Cobalt, Manganese and Antimony were observed in the EDS spectra as shown in Figures 6.1 – 6.5 above and Table 6.1 below, and these elements may be regarded to be responsible for inhibiting corrosion.

Table 6.1: Table showing the atomic number, element symbol, element name, concentration percentage and certainty of different regions on the mild steel metal surface.

Metal	Region	Atomic number	Element symbol	Element name	Concentration percentage (%)	Certainty
Mild steel metal	1	26	Fe	Iron	48.5	0.1
		66	Dy	Dysprosium	35.2	0.1
		8	O	Oxygen	16.4	1.9
	2	26	Fe	Iron	41.3	0.2
		66	Dy	Dysprosium	30.3	0.1
		8	O	Oxygen	28.5	1.2
Mild steel In HCl	1	26	Fe	Iron	29.5	0.4
		66	Dy	Dysprosium	14.2	0.1
		8	O	Oxygen	55.5	1.9
		17	Cl	Clorine	0.8	0.9
	2	26	Fe	Iron	27.7	0.4
		66	Dy	Dysprosium	14.1	0.1
		8	O	Oxygen	56.9	1.6
		17	Cl	Clorine	2.1	0.7
	3	26	Fe	Iron	28.0	0.1
		66	Dy	Dysprosium	22.0	0.1
		8	O	Oxygen	49.1	1.4
		17	Cl	Clorine	1.9	0.7
Mild steel In Chr-2-Carb	1	26	Fe	Iron	45.5	0.1
		66	Dy	Dysprosium	37.2	0.1
		8	O	Oxygen	17.3	1.8
	2	26	Fe	Iron	43.4	0.2
		66	Dy	Dysprosium	37.9	0.2
		8	O	Oxygen	18.7	1.6
	3	26	Fe	Iron	44.9	0.1
		66	Dy	Dysprosium	38.3	0.1
		8	O	Oxygen	16.8	1.7
		26	Fe	Iron	50.7	0.1

Mild steel In Br-Chr-2-Carb	1	66	Dy	Dysprosium	38.0	0.1
		8	O	Oxygen	11.3	1.8
	2	26	Fe	Iron	55.7	0.2
		66	Dy	Dysprosium	45.0	0.2
	3	26	Fe	Iron	49.3	0.1
		66	Dy	Dysprosium	36.7	0.1
		8	O	Oxygen	14.0	1.2
	4	26	Fe	Iron	47.2	0.1
		66	Dy	Dysprosium	32.1	0.1
		8	O	Oxygen	19.7	1.9
		27	Co	Cobalt	1.0	3.9
Mild steel In Cl-Chr-2-Carb	1	26	Fe	Iron	45.1	0.1
		66	Dy	Dysprosium	32.9	0.1
		8	O	Oxygen	21.1	2.1
		27	Co	Cobalt	0.9	4.9
	2	26	Fe	Iron	58.3	0.1
		66	Dy	Dysprosium	41.7	0.1
	3	26	Fe	Iron	52.1	0.1
		66	Dy	Dysprosium	36.9	0.1
		8	O	Oxygen	11.0	2.0
	4	26	Fe	Iron	45.1	0.1
		66	Dy	Dysprosium	34.3	0.1
		8	O	Oxygen	19.5	1.5
		27	Co	Cobalt	1.2	4.7
Mild steel In CH_3O-Chr-2-Carb	1	26	Fe	Iron	46.7	0.1
		66	Dy	Dysprosium	32.7	0.1
		8	O	Oxygen	20.6	1.8
	2	26	Fe	Iron	42.1	0.1
		66	Dy	Dysprosium	31.6	0.1
		8	O	Oxygen	26.4	1.6
	3	26	Fe	Iron	27.0	0.1
		66	Dy	Dysprosium	19.9	0.1
		8	O	Oxygen	53.2	1.6
	1	26	Fe	Iron	61.7	0.3
		8	O	Oxygen	32.9	1.4
		7	N	Nitrogen	5.1	1.0

Mild steel In NO_2-Chr-2-Carb		25	Mn	Manganese	0.3	0.2
	2	26	Fe	Iron	29.9	0.1
		66	Dy	Dysprosium	44.6	1.7
		8	O	Oxygen	25.2	0.1
		51	Sb	Antimony	0.3	1.2
	3	26	Fe	Iron	39.6	0.3
		66	Dy	Dysprosium	36.2	0.0
		8	O	Oxygen	21.8	1.3
		7	N	Nitrogen	3.4	1.0
	4	26	Fe	Iron	48.8	0.1
		66	Dy	Dysprosium	34.3	0.1
		8	O	Oxygen	17.0	1.6
	5	26	Fe	Iron	51.4	0.1
		66	Dy	Dysprosium	34.1	0.1
		8	O	Oxygen	14.5	1.4

6.1.2. The SEM images and EDS spectra of Zinc

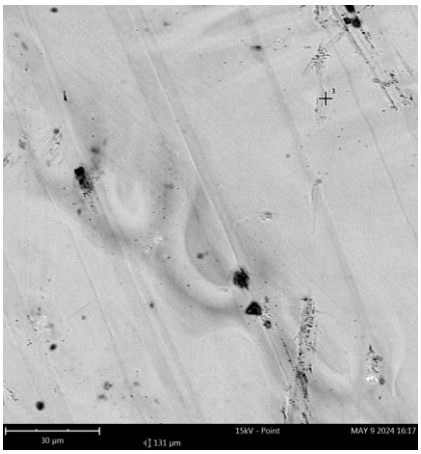

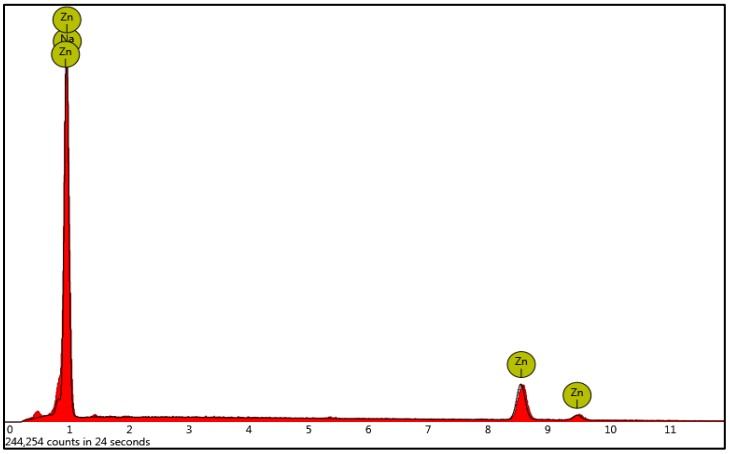

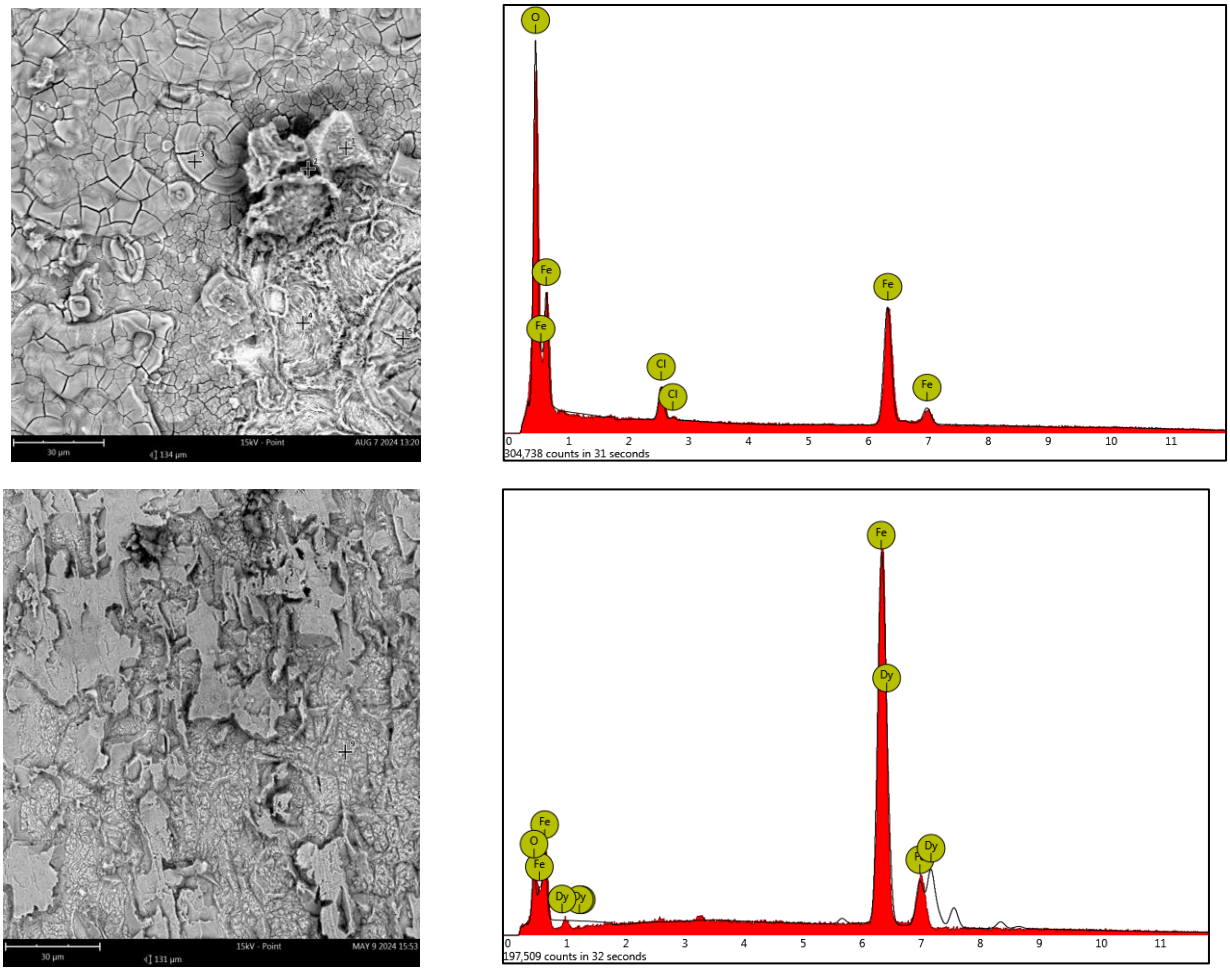

Figure 6.6: Scanning electron micrographs and EDS spectra of (a) freshly polished zinc (b) zinc 1.5 M HCl (c) zinc in 1.5 M HCl containing Chr-2-Carb.

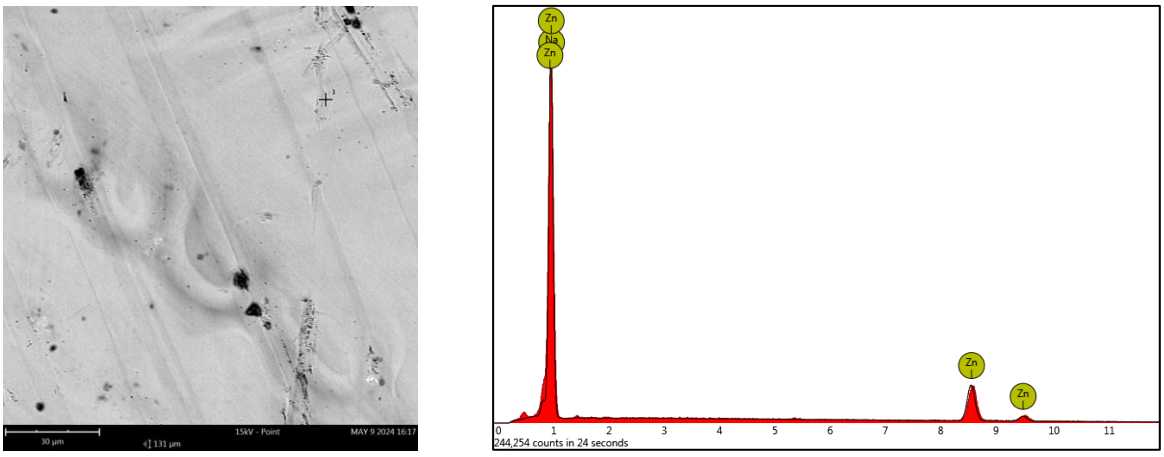

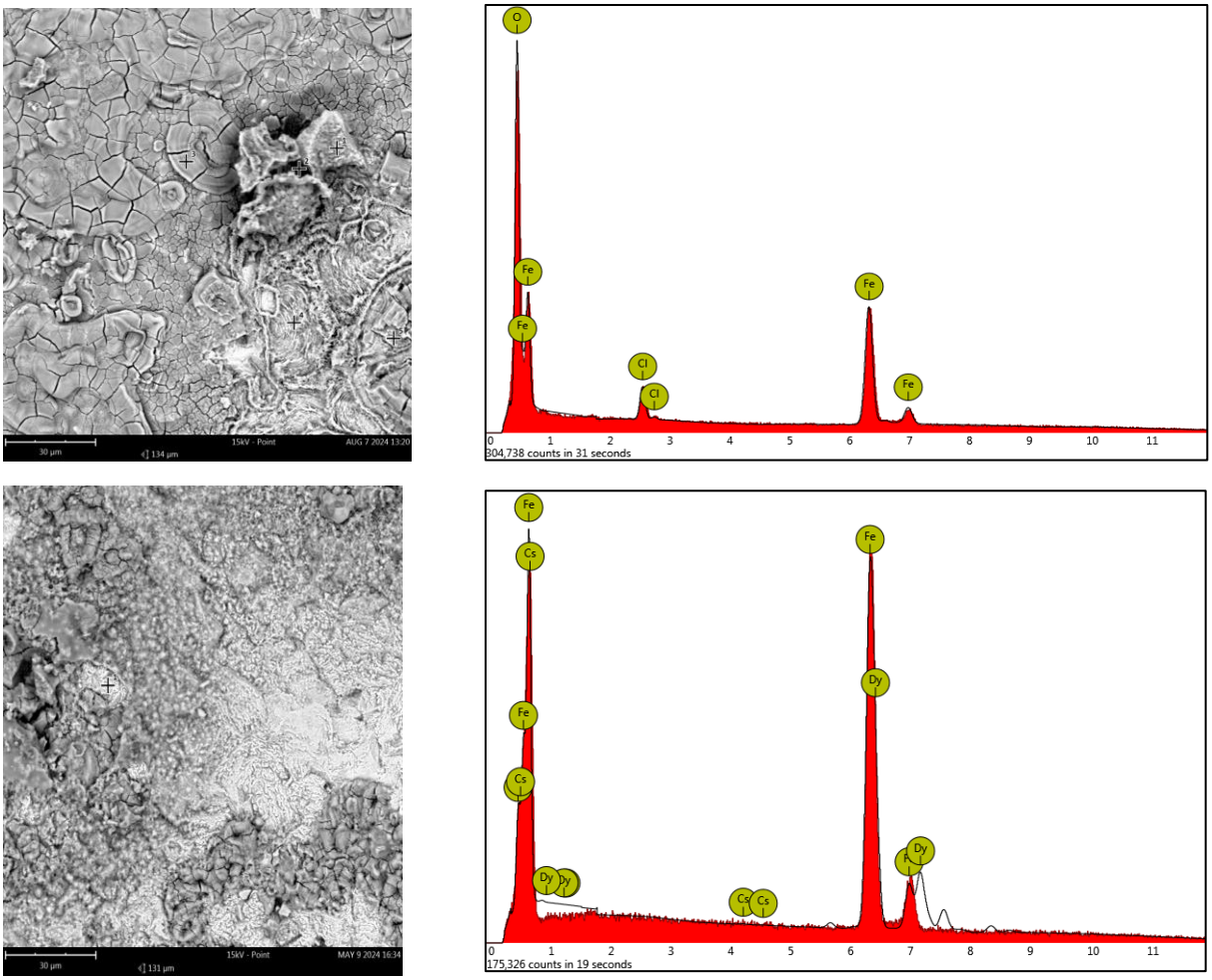

Figure 6.7: Scanning electron micrographs and EDS spectra of (a) freshly polished zinc (b) zinc 1.5 M HCl (c) zinc in 1.5 M HCl containing Br-Chr-2-Carb.

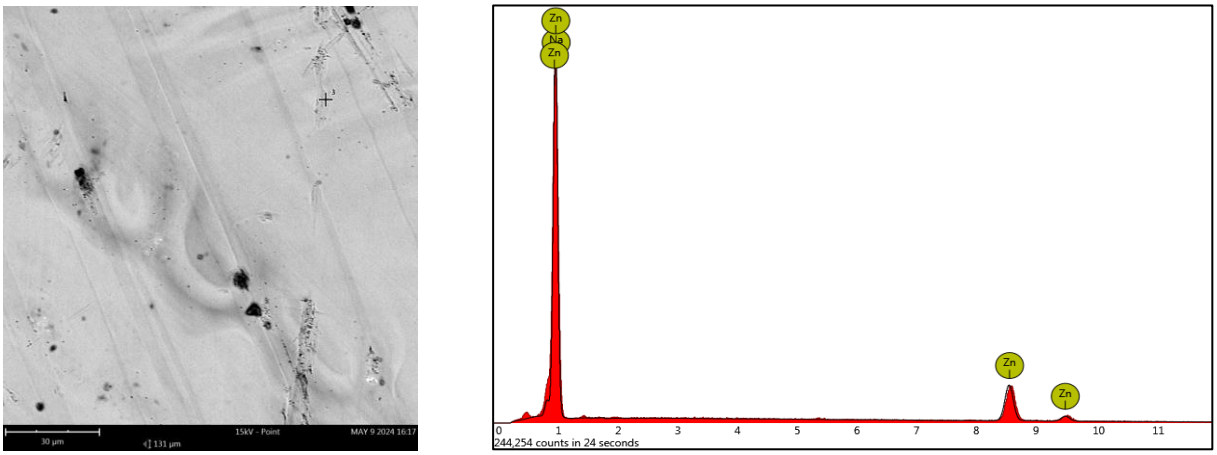

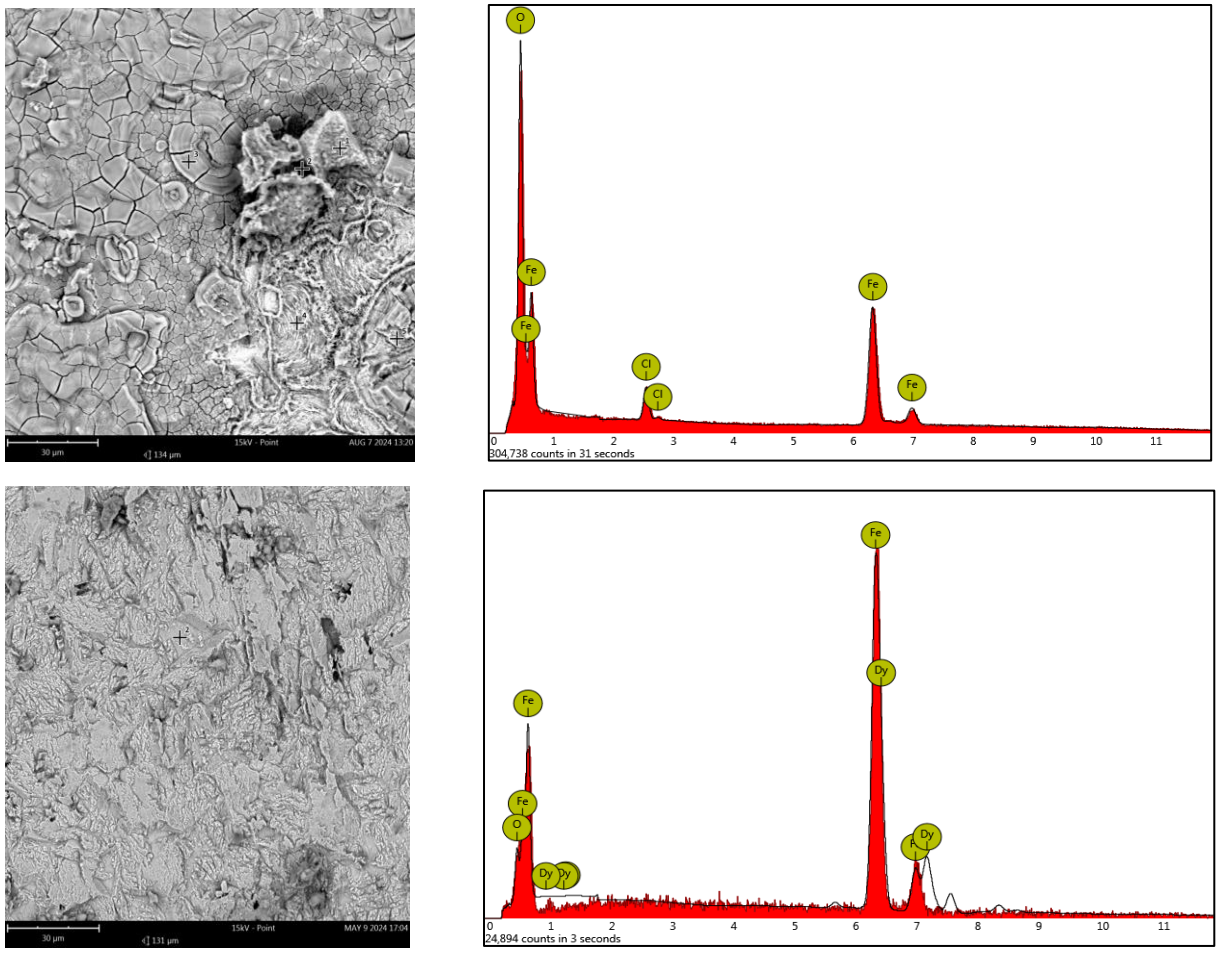

Figure 6.8: Scanning electron micrographs and EDS spectra of (a) freshly polished zinc (b) zinc 1.5 M HCl (c) zinc in 1.5 M HCl containing Cl-Chr-2-Carb.

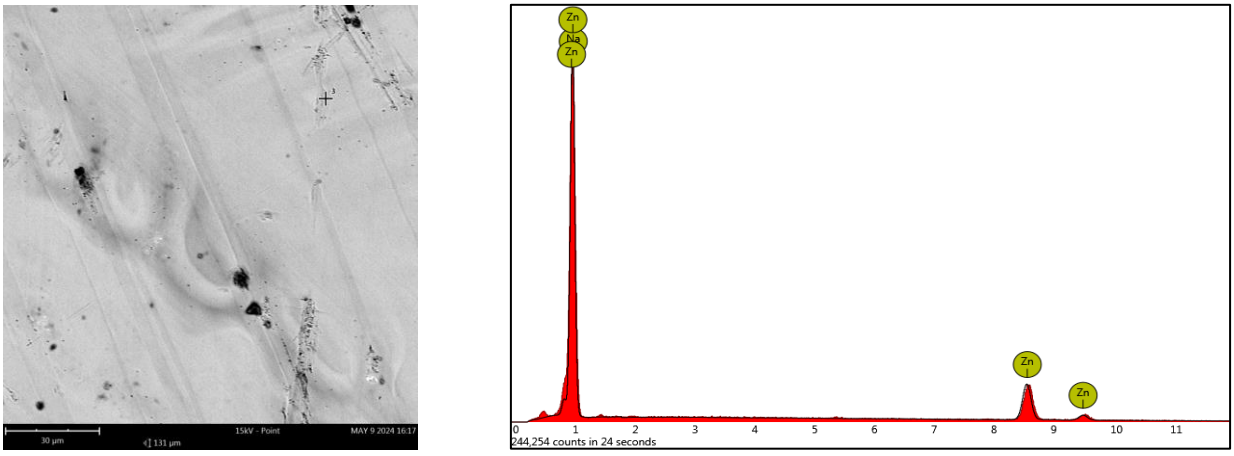

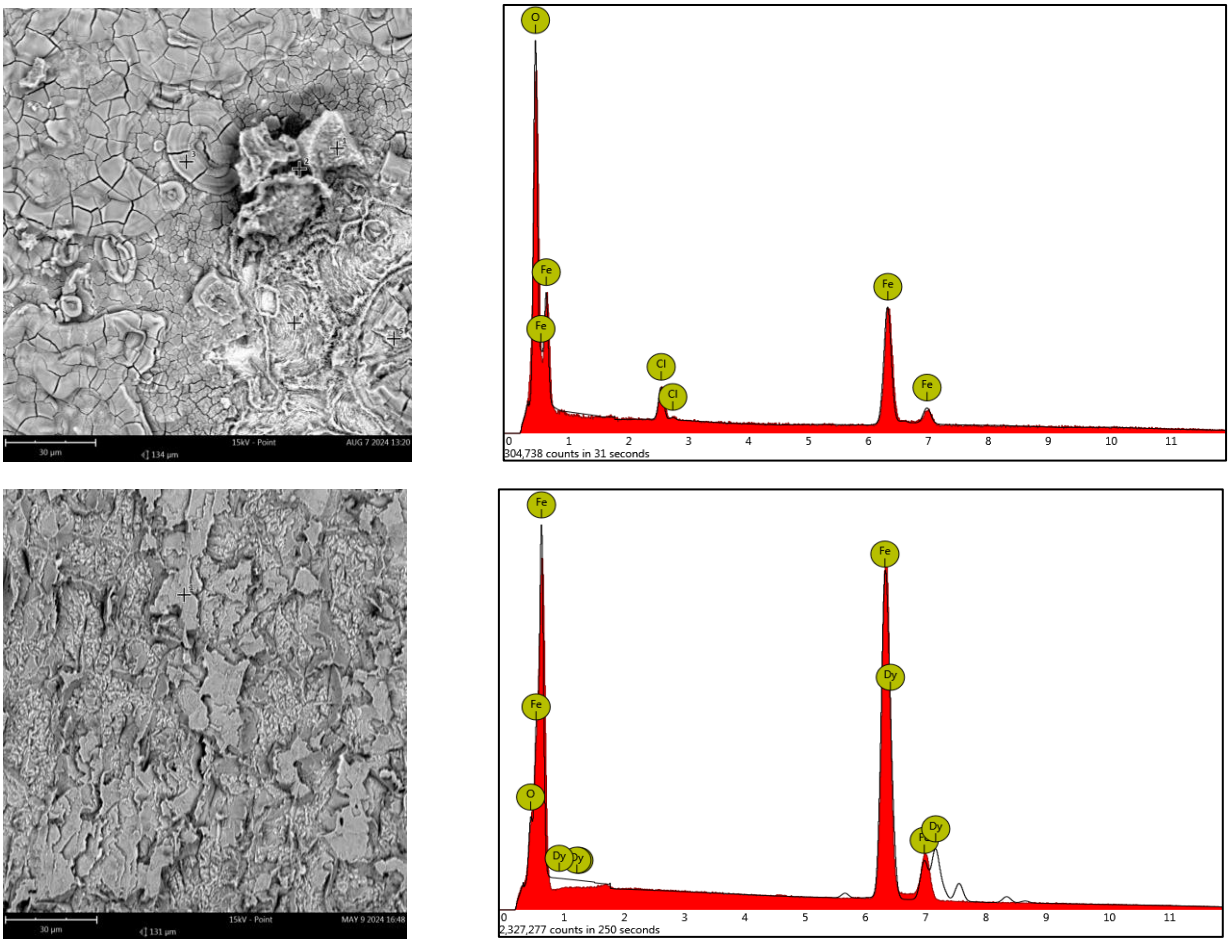

Figure 6.9: Scanning electron micrographs and EDS spectra of (a) freshly polished zinc (b) zinc 1.5 M HCl (c) zinc in 1.5 M HCl containing CH_3O-Chr-2-Carb.

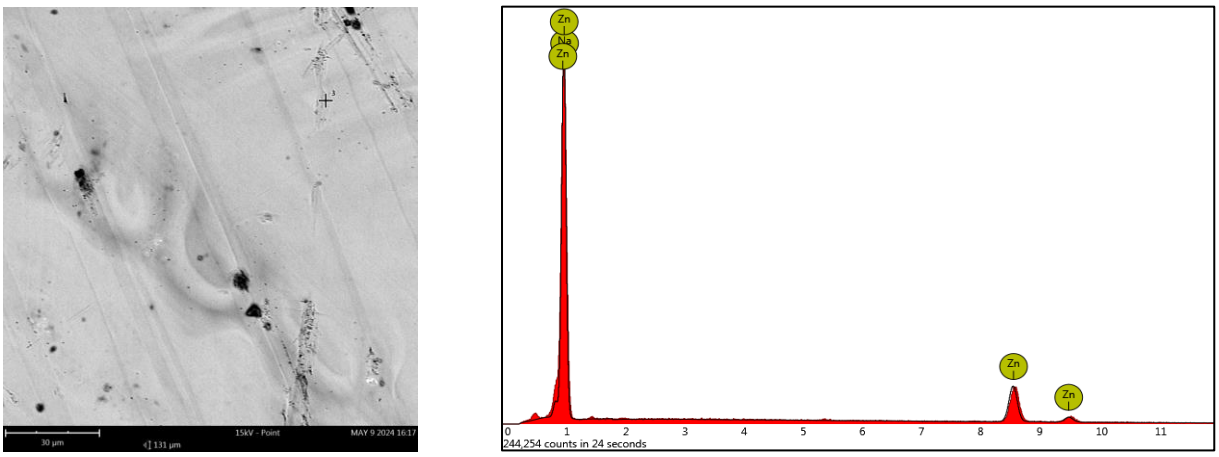

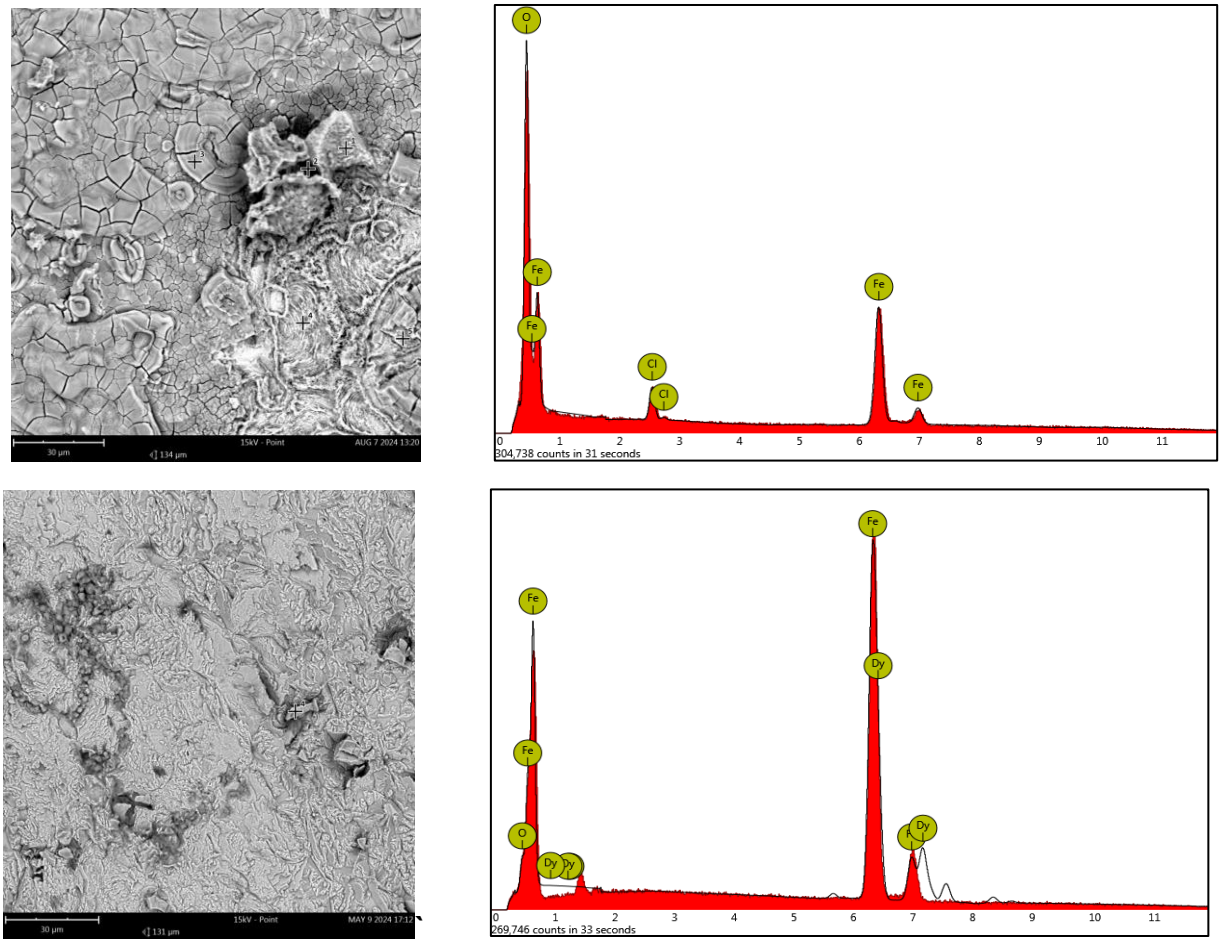

Figure 6.10: Scanning electron micrographs and EDS spectra of (a) freshly polished zinc (b) zinc 1.5 M HCl (c) zinc in 1.5 M HCl containing NO_2-Chr-2-Carb.

SEM also played a significant role in this study by making it easier for us to study the surface morphology of freshly polished zinc metal, zinc in the absence and presence of the synthesized inhibitors. From the results above, the SEM images in Figures 6.6 – 6.10 clearly shows that in the absence of the 6-substitutedchromone-2-carboxamides, the zinc surface is highly damaged with pitted areas. The results reveal pitting corrosion of the zinc specimen. By comparing the SEM images, it became clear that in the presence of the five synthesized inhibitors the surface of the zinc specimen is protected by the formation of a protective film which covers the entire metal surfaces as shown in figures 6.6 – 6.10. Noticeably, the inhibitors resulted in a decrease in the contact between mild steel and the aggressive medium (HCl) through the formation of the adsorption film. It is

noted that the surface becomes smoother after the addition of the 6-substitutedchromone-2-carboxamides, suggesting that these inhibitors have controlled the zinc corrosion.

EDS analysis was utilized to identify element present on the zinc samples. Figures 6.6 – 6.10 show the EDS spectra obtained on the zinc surface in the presence and absence of 6 substitutedchromone-2-carboxamides. The corrosive blank solution produces zinc oxide through corrosion reactions. The EDS spectrum of the blank shows the presence of high oxygen peak and high oxygen content as presented in Table 6.2 below. In addition, the EDS spectrum of the blank chlorine content in all the spots which is due to the HCl medium which has interacted more with the zinc specimen. Furthermore, EDS spectra of the zinc in the inhibited system revealed presence of Oxygen content which may be due to oxygen heteroatoms of the 6-substitutedchromone-2-carboxamides as the computational analysis study revealed the role of these oxygen heteroatoms in the adsorption of the 6-substitutedchromone-2-carboxamides on the zinc surface. Moreover, metals such as Sodium, Rhodium, Dysprosium and Cobalt were observed in the EDS spectra of the pure Al and the one for Al immersed in the inhibited system and these elements may be regarded to be responsible for inhibiting corrosion.

Table 6.2: Table showing the atomic number, element symbol, element name, concentration percentage and certainty of different regions on the zinc metal surface.

Metal	Region	Atomic number	Element symbol	Element name	Concentration percentage (%)	Certainty
Zinc metal	1	11	Na	Sodium	78.4	0.5
		30	Zn	Zinc	21.6	0.7
	2	11	Na	Sodium	78.6	0.5
		30	Zn	Zinc	21.4	0.6
	3	11	Na	Sodium	78.1	0.5
		30	Zn	Zinc	21.8	0.6
	1	26	Fe	Iron	38.3	0.1
		66	Dy	Dysprosium	7.8	1.3
		8	O	Oxygen	53.3	0.1

Zinc metal In HCl		17	Cl	Chlorine	0.7	1.0
	2	26	Fe	Iron	36.2	0.1
		66	Dy	Dysprosium	11.2	1.6
		8	O	Oxygen	51.5	0.1
		17	Cl	Chlorine	1.1	0.9
	3	26	Fe	Iron	37.0	0.1
		66	Dy	Dysprosium	52.5	0.1
		8	O	Oxygen	7.7	1.9
		17	Cl	Chlorine	2.7	0.6
	4	26	Fe	Iron	23.9	0.1
		66	Dy	Dysprosium	27.3	0.1
		8	O	Oxygen	32.4	1.4
		17	Cl	Chlorine	3.3	0.4
		45	Rh	Rhodium	3.1	0.2
Zinc In Chr-2-Carb	1	26	Fe	Iron	40.7	0.1
		66	Dy	Dysprosium	29.9	0.1
		8	O	Oxygen	29.4	1.7
	2	26	Fe	Iron	49.1	0.1
		66	Dy	Dysprosium	36.3	0.1
		8	O	Oxygen	14.6	1.8
	3	26	Fe	Iron	45.7	0.1
		66	Dy	Dysprosium	32.8	0.1
		8	O	Oxygen	21.5	1.9
	4	26	Fe	Iron	48.1	0.1
		66	Dy	Dysprosium	35.9	0.1
		8	O	Oxygen	15.9	1.6
Zinc In Br-Chr-2-Carb	1	26	Fe	Iron	43.4	0.1
		66	Dy	Dysprosium	31.9	0.1
		8	O	Oxygen	24.6	0.1
		55	Cs	Cesium		1.2
	2	8	O	Oxygen	32.5	0.5
		26	Fe	Iron	67.5	1.9
	3	26	Fe	Iron	42.7	0.1
		66	Dy	Dysprosium	31.0	0.1
		8	O	Oxygen	25.7	1.5
		27	Co	Cobalt	0.6	3.2
		26	Fe	Iron	63.5	0.1
		66	Dy	Dysprosium	20.4	0.1

Zinc In Cl-Chr-2-Carb	1	8	O	Oxygen	16.1	1.5
	2	26	Fe	Iron	52.0	0.1
		66	Dy	Dysprosium	39.2	0.1
		8	O	Oxygen	8.8	1.5
	3	26	Fe	Iron	48.7	0.1
		66	Dy	Dysprosium	36.4	0.1
		8	O	Oxygen	14.9	1.9
	4	26	Fe	Iron	49.5	0.1
		66	Dy	Dysprosium	38.6	0.1
		8	O	Oxygen	11.9	2.1
Zinc In CH_3O-Chr-2-Carb	1	26	Fe	Iron	47.3	0.1
		66	Dy	Dysprosium	36.2	0.1
		8	O	Oxygen	16.4	1.9
	2	26	Fe	Iron	52.9	0.1
		66	Dy	Dysprosium	45.9	0.2
		27	Co	Cobalt	1.2	3.6
	3	26	Fe	Iron	45.8	0.1
		66	Dy	Dysprosium	34.9	0.1
		8	O	Oxygen	19.3	1.9
Zinc In NO_2-Chr-2-Carb	1	26	Fe	Iron	56.0	0.1
		66	Dy	Dysprosium	44.0	0.1
	2	26	Fe	Iron	52.1	0.1
		66	Dy	Dysprosium	37.0	0.1
		8	O	Oxygen	10.9	1.9
	3	26	Fe	Iron	38.2	0.1
		66	Dy	Dysprosium	28.3	0.1
		8	O	Oxygen	33.5	1.7
	4	26	Fe	Iron	47.4	0.1
		66	Dy	Dysprosium	34.8	0.1
		8	O	Oxygen	17.9	2.4

6.1.3. The SEM images and EDS spectra of Aluminium

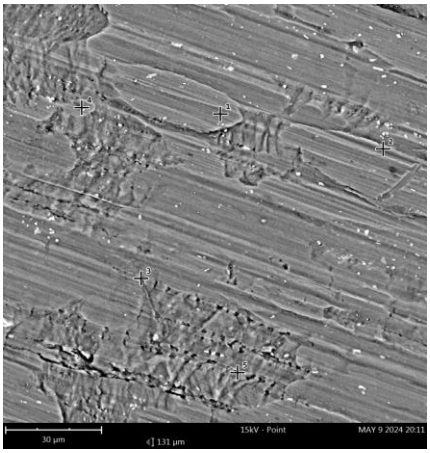

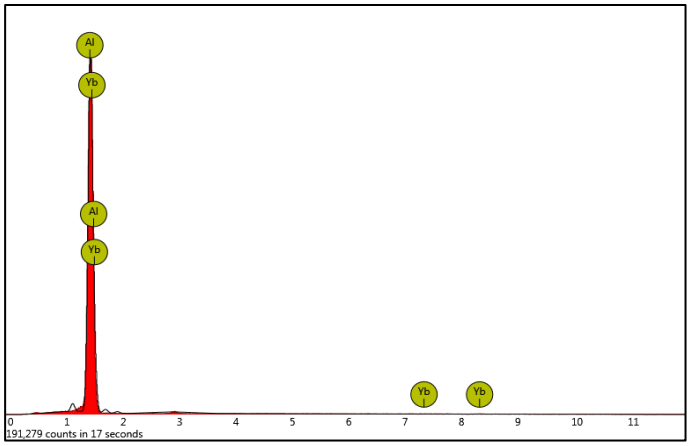

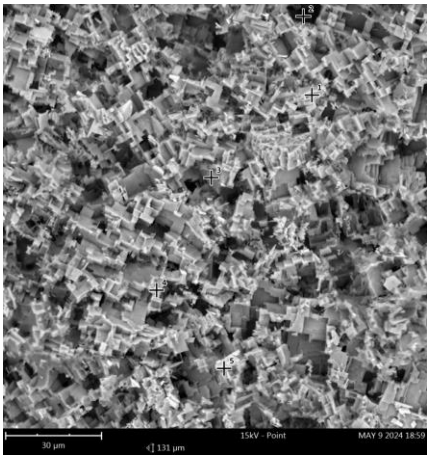

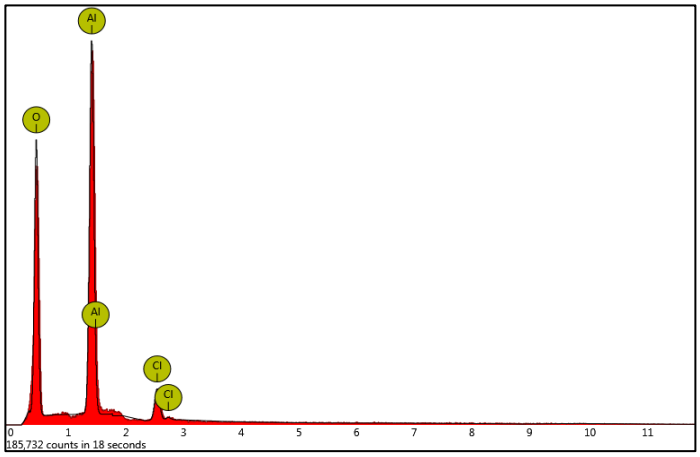

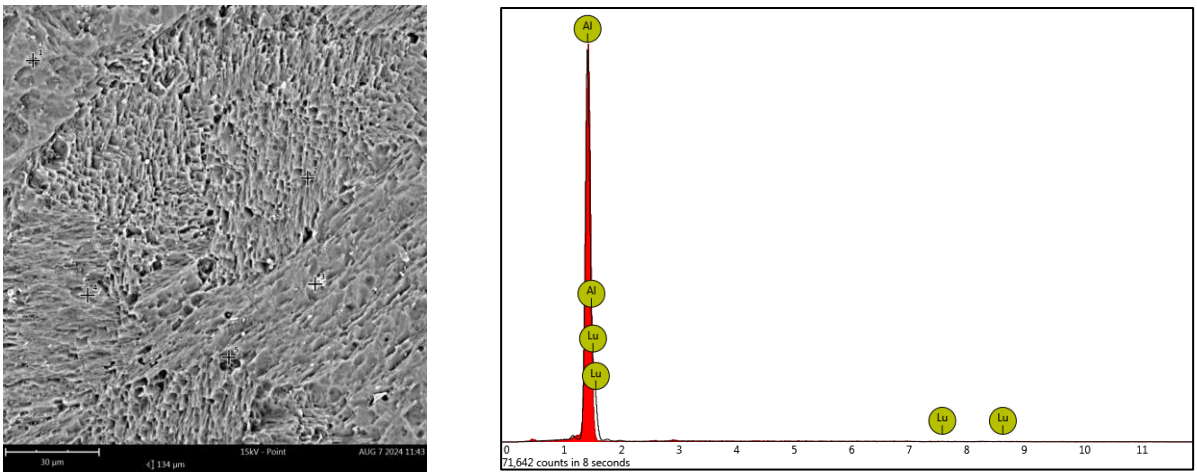

Figure 6.11: Scanning electron micrographs and EDS spectra of (a) freshly polished aluminium (b) aluminium 1.0 M HCl (c) aluminium in 1.0 M HCl containing Chr-2-Carb.

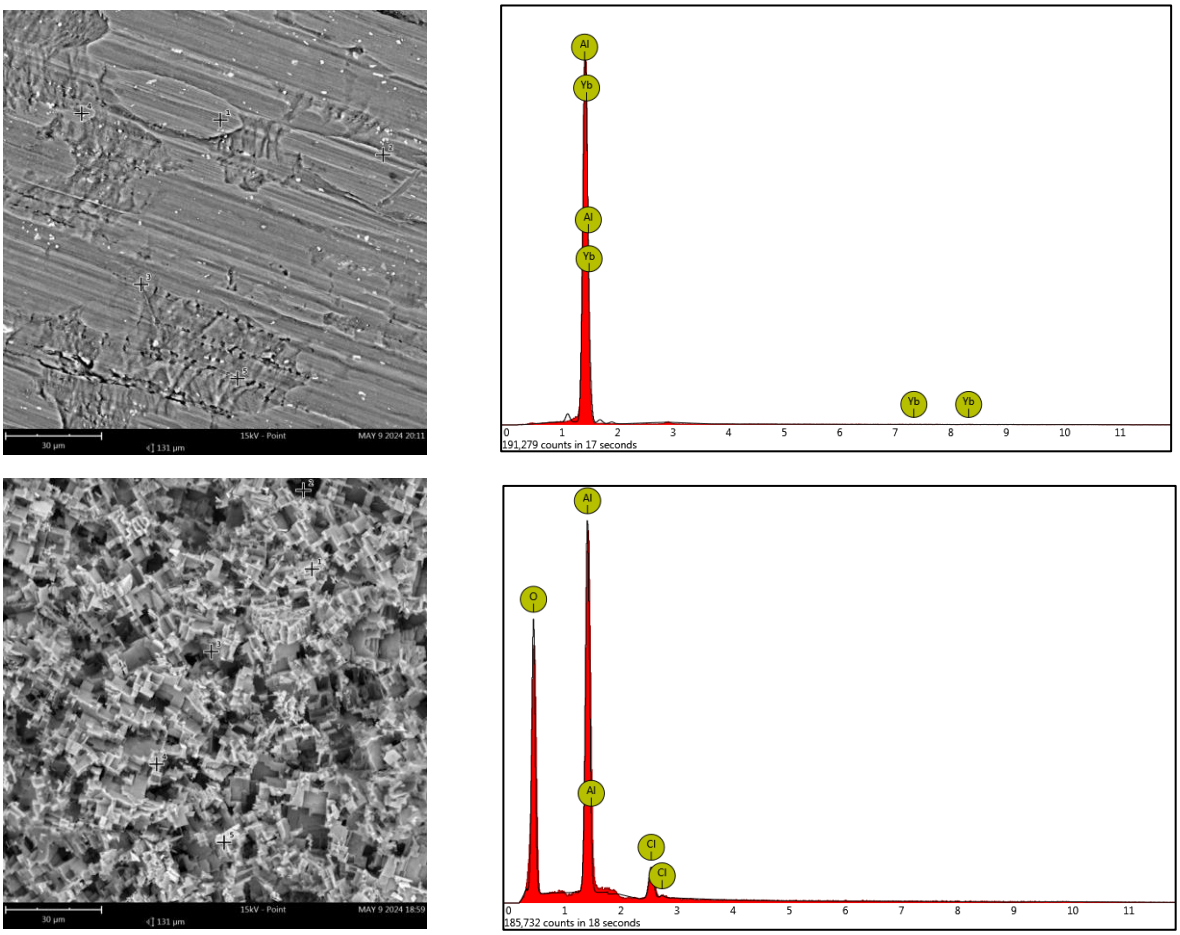

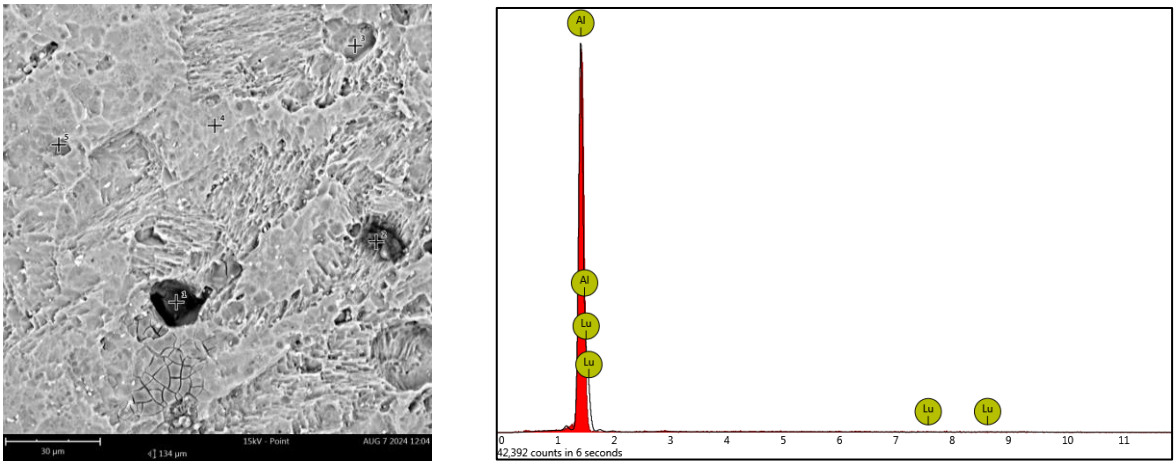

Figure 6.12: Scanning electron micrographs and EDS spectra of (a) freshly polished aluminium (b) aluminium 1.0 M HCl (c) aluminium in 1.0 M HCl containing Br-Chr-2-Carb.

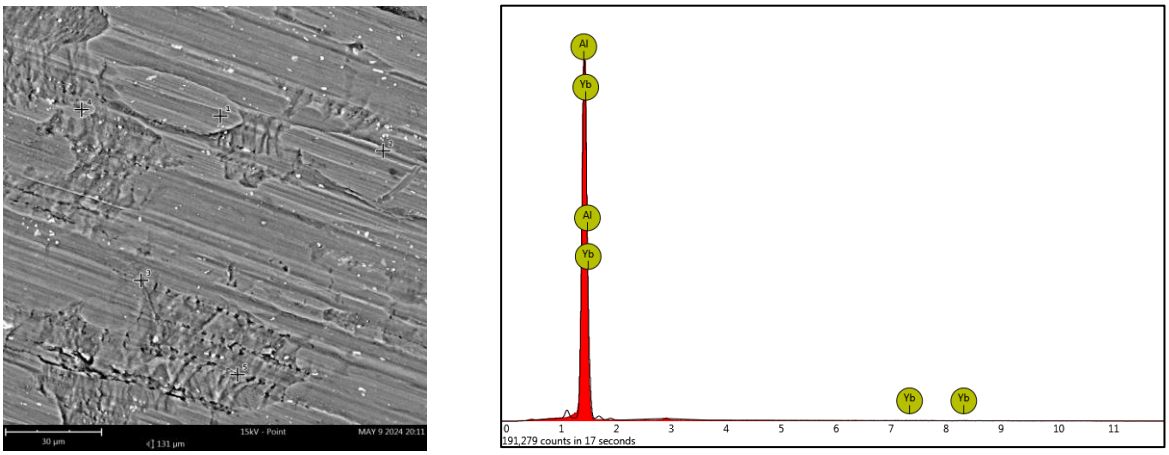

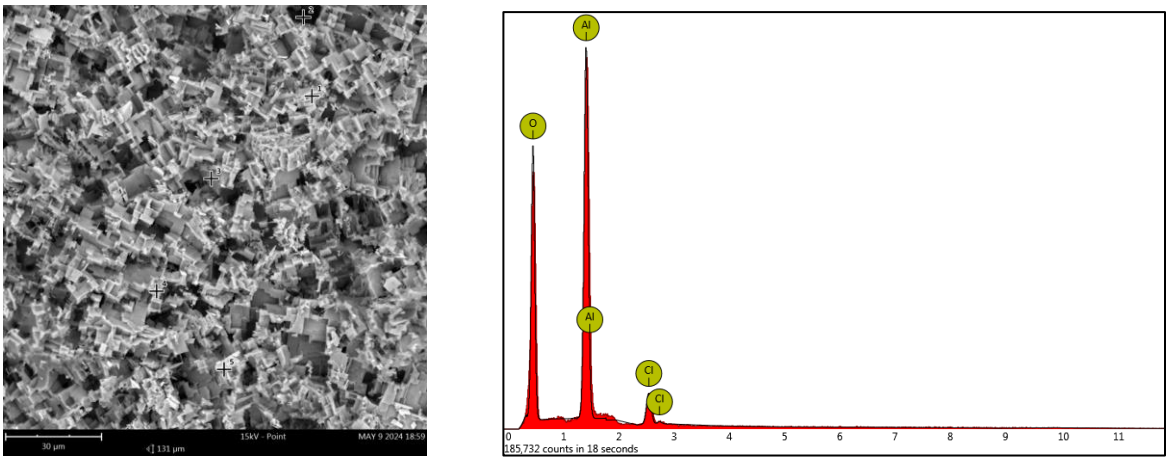

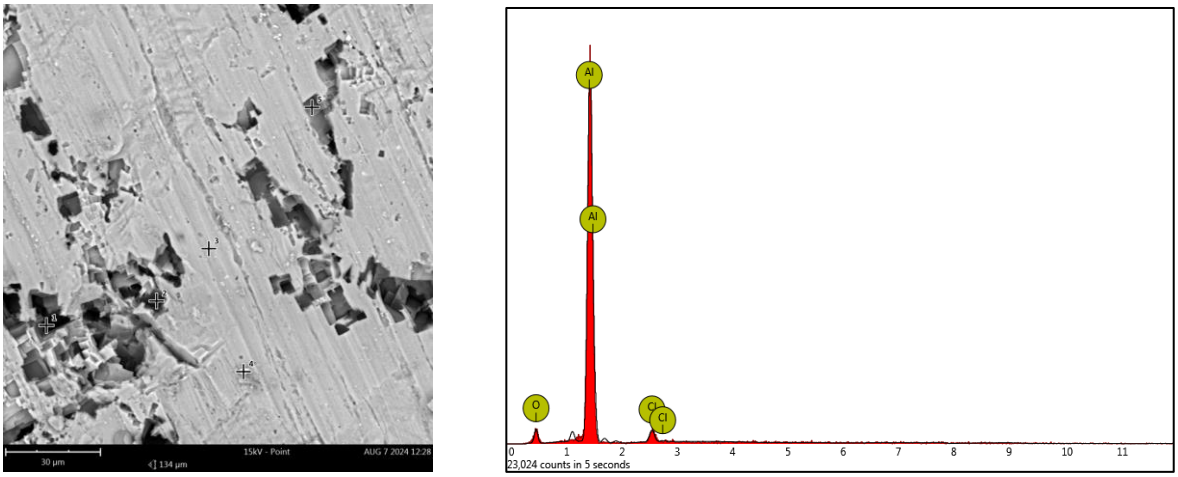

Figure 6.13: Scanning electron micrographs and EDS spectra of (a) freshly polished aluminium (b) aluminium 1.0 M HCl (c) aluminium in 1.0 M HCl containing Cl-Chr-2-Carb.

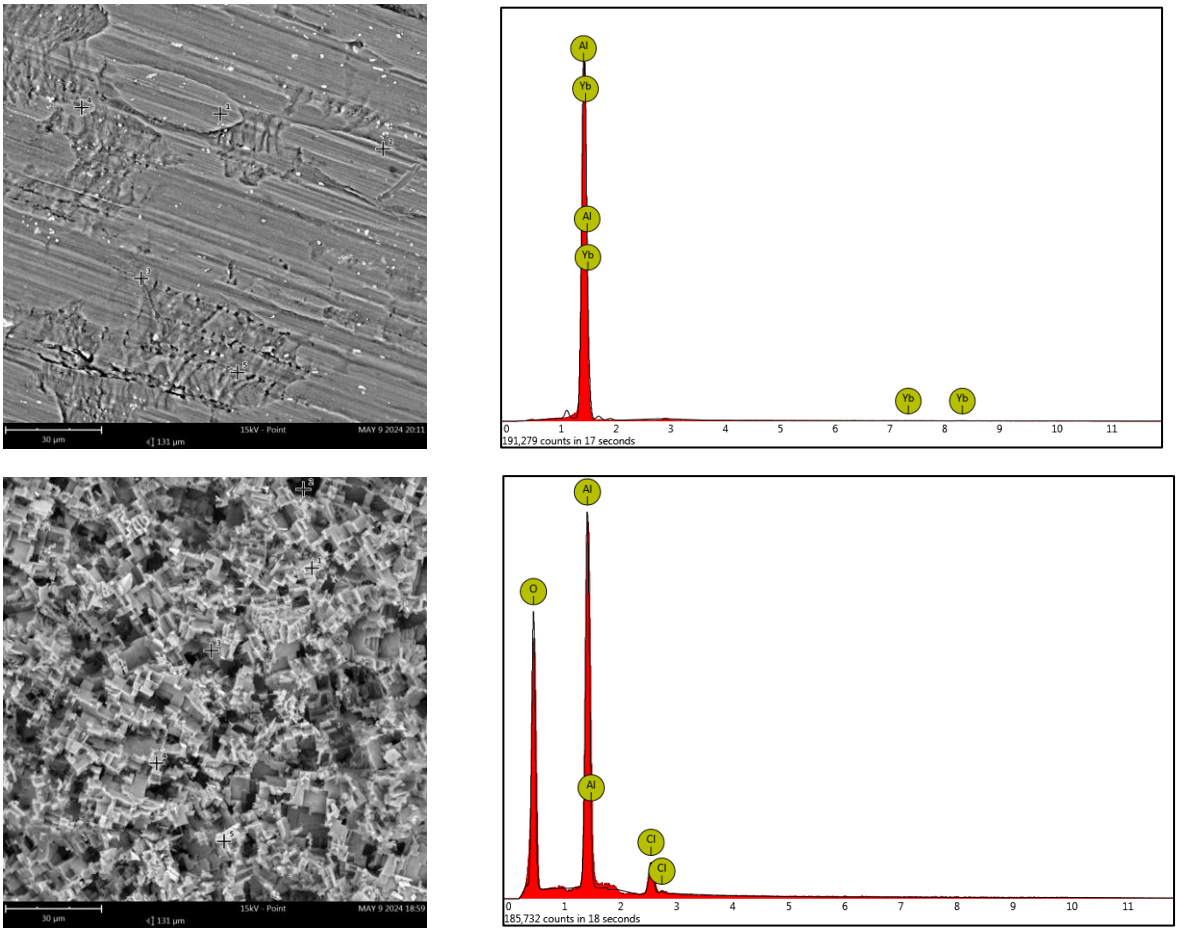

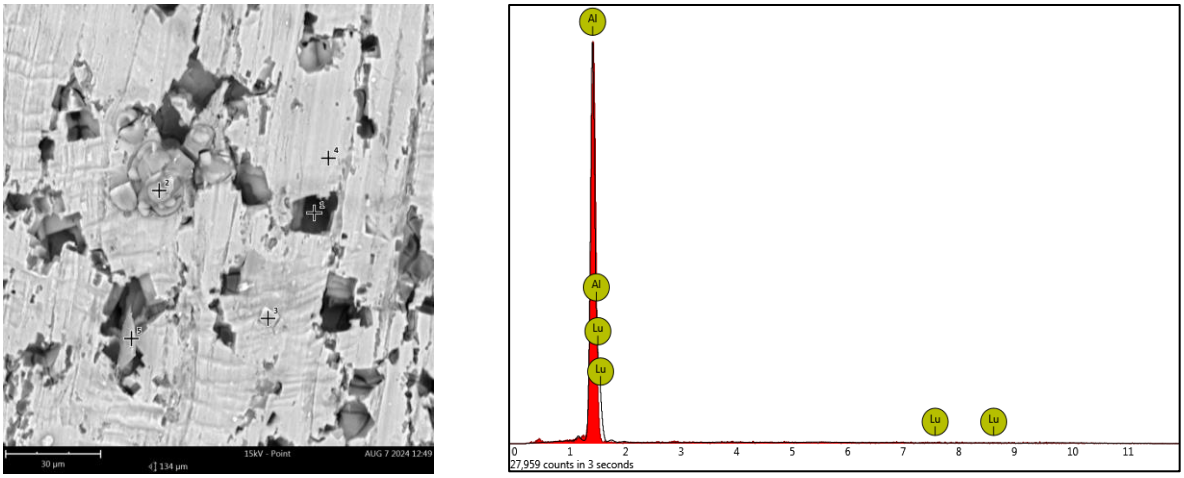

Figure 6.14: Scanning electron micrographs and EDS spectra of (a) freshly polished aluminium (b) aluminium 1.0 M HCl (c) aluminium in 1.0 M HCl containing CH_3O-Chr-2-Carb.

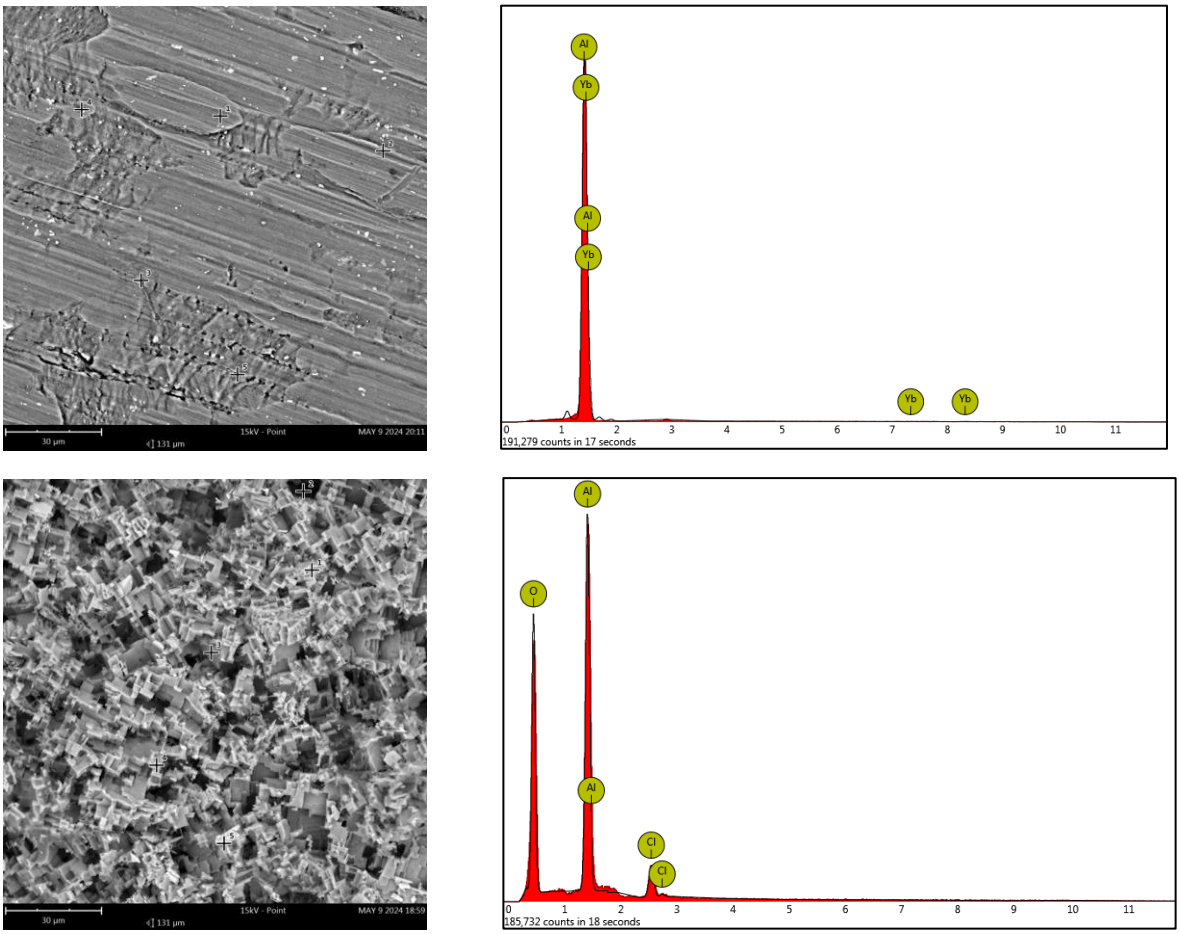

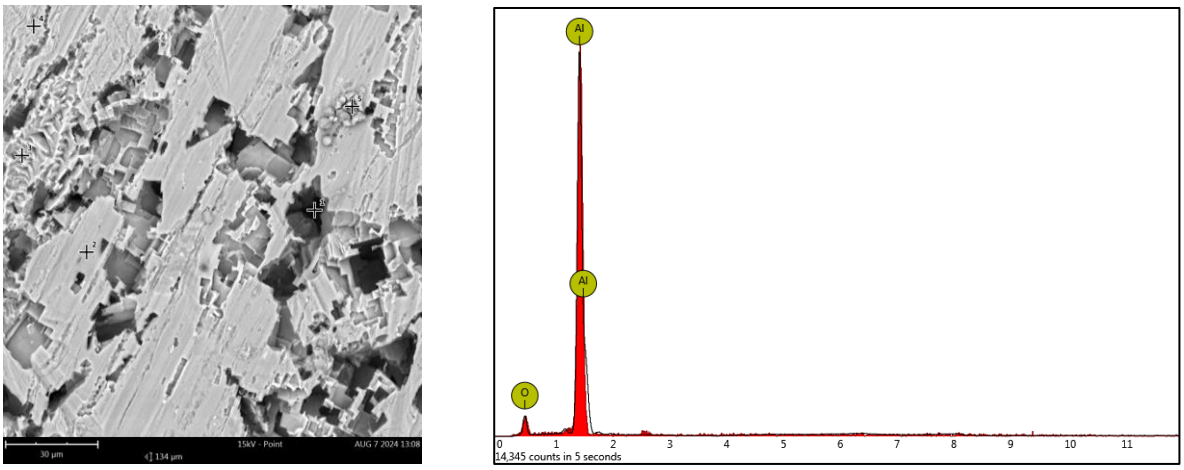

Figure 6.15: Scanning electron micrographs and EDS spectra of (a) freshly polished aluminium (b) aluminium 1.0 M HCl (c) aluminium in 1.0 M HCl containing NO_2-Chr-2-Carb.

Figures 6.11 – 6.15 show the morphology surface SEM images of Al in 1 M HCl in the absence and presence of the 6-substituted chromone-2-carboxamides at the highest concentration of $5x10^{-4}$ M. The SEM image of the Al immersed in HCl alone shows uniform roughness, indicating that the metal is highly damaged by the HCl. However, SEM confirmed the formation of adsorption film on the surface of the Al metals immersed in the inhibited solutions, and the surfaces were smoother as compared to the surface of the Al metal immersed in the HCl alone (Blank). The results revealed the Al submerged in the corrosive environment (1 M HCl) with the 6-substituted chromone-2-carboxamides, its entire surface becomes smooth and lustrous. Additionally, the adsorption of the synthesized inhibitors on the entire surface effectively protects aluminium [270]. SEM morphological maps demonstrate that the 6-substituted chromone-2-carboxamides exhibit excellent corrosion prevention potential.

EDS analysis technique has been utilized to obtain information on the composition of the surface of the aluminium sample in the absence and presence of the 6-substituted chromone-2-carboxamides in a 1 M HCl medium. The results of the EDS spectra are presented in Figures 6.11 – 6. 15. As presented in Figures 6.11 – 6. 15 and Table 6.3, the EDX analysis revealed low Al content (37.6%) and high oxygen content (58.1%) in the

absence of the 6-substitutedchromone-2-carboxamides. The low Al content is due to the highly damaged Al surface by the HCl medium, and the high oxygen content is due to the oxidation of the Al causing the Al metal specimen to revert to its oxide state and has lost its useful properties. Furthermore, the EDS spectra of the Al immersed in the uninhibited system revealed the presence of chlorine atoms (4.3%), indicating that indeed the acidic medium has strongly interacted with the Al specimen. Moreover, the EDS results show aluminium to be the dominant element in all the spectra of the aluminium metals immersed in the inhibited system. In addition, metals such as lutetium and ytterbium were observed in the EDS spectra of the pure Al and the one for Al immersed in the inhibited system and these elements may be regarded to be responsible for inhibiting corrosion. The chemical analysis of the composition surface electrode revealed chlorine content (5.3%) in the EDS spectrum of the Al immersed in the inhibited system with Cl-Chr-2-Carb, suggesting that the Chlorine substituent was part of the adsorption film formed on the surface of the Al surface. Noticeably, the EDS outcomes revealed oxygen content (19.9%) in the EDS spectra of the inhibited Al with NO_2-Chr-2-Carb. This revealed oxygen content is due to the two oxygen atoms of the nitro group, and this confirmed the significant role played by the oxygen atoms of the nitro group as revealed by the computational analysis study. The EDS spectra of the Al in the inhibited system with Cl-Chr-2-Carb and CH_3O-Chr-2-Carb also revealed the presence of Oxygen content which may be due to oxygen heteroatoms of these inhibitors.

Table 6.3: Table showing the atomic number, element symbol, element name, concentration percentage and certainty of different regions on the aluminium metal surface.

Metal	Region	Atomic number	Element symbol	Element name	Concentration percentage (%)	Certainty
Aluminium metal	1	13	Al	Aluminium	99.6	0.3
		70	Yb	Ytterbium	0.4	1.2
	2	13	Al	Aluminium	99.4	0.3
		70	Yb	Ytterbium	0.6	1.3
	3	13	Al	Aluminium	100	0.3

	4	13	Al	Aluminium	100	0.3
Aluminium In HCl	1	13	Al	Aluminium	37.6	0.3
		8	O	Oxygen	58.1	1.2
		17	Cl	Clorine	4.3	0.5
	2	13	Al	Aluminium	72.9	0.3
		8	O	Oxygen	27.1	1.2
	3	13	Al	Aluminium	78.8	0.3
		8	O	Oxygen	21.2	1.2
Aluminium In Chr-2-Carb	1	13	Al	Aluminium	93.8	0.3
		71	Lu	Lutetium	6.2	1.4
	2	13	Al	Aluminium	100	0.3
	3	13	Al	Aluminium	100	0.3
	4	13	Al	Aluminium	100	0.3
Aluminium In Br-Chr-2-Carb	1	13	Al	Aluminium	100	0.3
	2	13	Al	Aluminium	100	0.3
	3	13	Al	Aluminium	91.5	0.3
		71	Lu	Lutetium	8.5	1.9
	4	13	Al	Aluminium	91.5	0.3
Aluminium In Cl-Chr-2-Carb	1	13	Al	Aluminium	100	0.3
	2	13	Al	Aluminium	80.4	0.4
		17	Cl	Clorine	5.3	0.6
		8	O	Oxygen	14.4	0.6
Aluminium In CH_3O-Chr-2-Carb	1	13	Al	Aluminium	80.1	0.4
		8	O	Oxygen	19.9	1.0
	2	13	Al	Aluminium	79.3	0.3
		8	O	Oxygen	20.7	1.1
	3	13	Al	Aluminium	100	0.3
	4	13	Al	Aluminium	100	0.3
Aluminium In NO_2-Chr-2-Carb	1	13	Al	Aluminium	100	0.4
	2	13	Al	Aluminium	95.4	0.3
		70	Yb	Ytterbium	4.6	1.2
	3	13	Al	Aluminium	100	0.3
	4	13	Al	Aluminium	82.8	0.4
		8	O	Oxygen	17.2	1.5

6.2. Contact angle wettability

Contact angle measurement results obtained for the untreated metals, metals immersed in the aggressive environment (molar HCl medium), and the metals immersed in the inhibited acid medium for 8 hours for mild steel and zinc and 6 hours for aluminium at room temperature are displayed in Figures 6.16 – 6.30. As indicated earlier, literature has revealed that surfaces with h < 90 are hydrophilic, while the surfaces with h > 90 are hydrophobic [271, 272]. The contact angles measured over the three metal surfaces in the case of the blank solution were smaller as compared to the ones in the inhibited acid medium. The contact angles increased in the presence of the synthesized 6-substituted chromone-2-carboxamides. This increase can be attributed to the adsorption of the investigated inhibitors, which resulted in the formation of a barrier film on the surfaces of the metals.

6.2.1. Contact angle measurement results on mild steel

These results were attained for mild steel that was submerged in 1.5 M HCl medium for 8 hours at 303 K and contained the highest concentration (0.0005 M) of the inhibitors under investigation. The results are depicted in Figures 6.16 - 6.20.

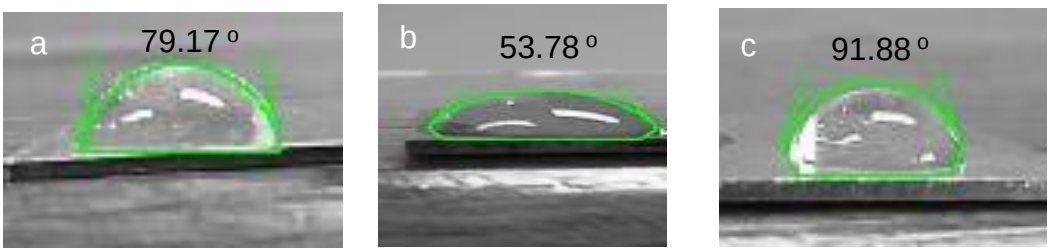

Figure 6.16: Measurements of the contact angles between (a) polished untreated mild steel substrate, (b) mild steel metal submerged in 1.5 M HCl medium only (Blank) for 8 hours, and (c) mild steel immersed in 1.5 M HCl with the highest concentration (0.0005 M) of Chr-2-Carb for 8 hours.

93.01 o

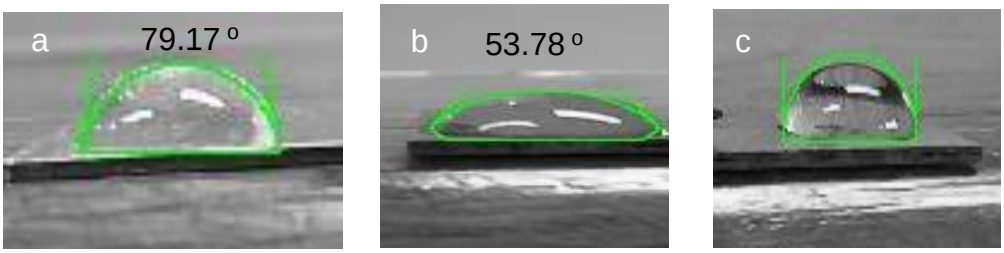

Figure 6.17: Measurements of the contact angles between (a) polished untreated mild steel substrate, (b) mild steel metal submerged in 1.5 M HCl medium only (Blank) for 8 hours, and (c) mild steel immersed in 1.5 M HCl with the highest concentration (0.0005 M) of Br-Chr-2-carb for 8 hours.

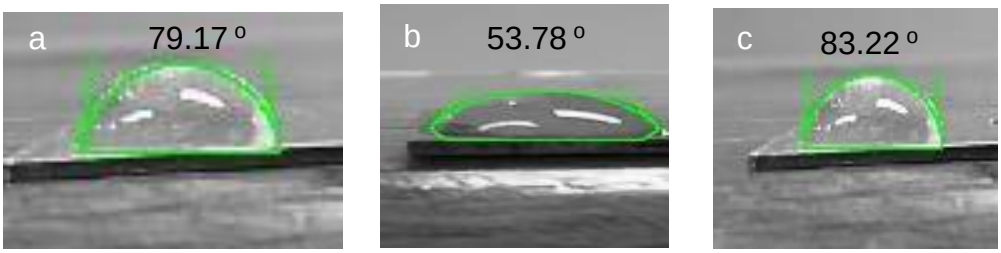

Figure 6.18: Measurements of the contact angles between (a) polished untreated mild steel substrate, (b) mild steel metal submerged in 1.5 M HCl medium only (Blank) for 8 hours, and (c) mild steel immersed in 1.5 M HCl with the highest concentration (0.0005 M) of Cl-Chr-2-carb for 8 hours.

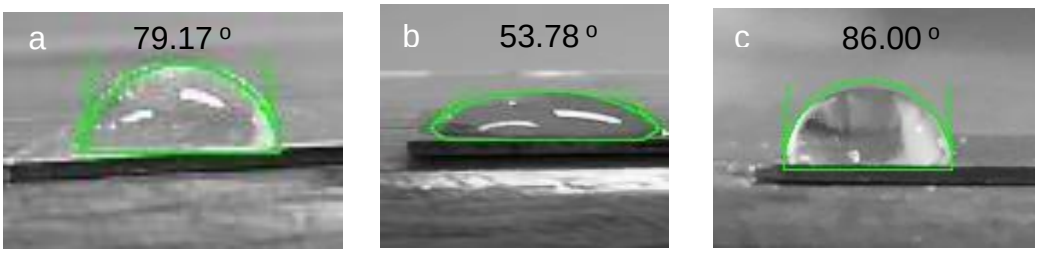

Figure 6.19: Measurements of the contact angles between (a) polished untreated mild steel substrate, (b) mild steel metal submerged in 1.5 M HCl medium only (Blank) for 8 hours, and (c) mild steel immersed in 1.5 M HCl with the highest concentration (0.0005 M) of CH_3O-Chr-2-carb for 8 hours.

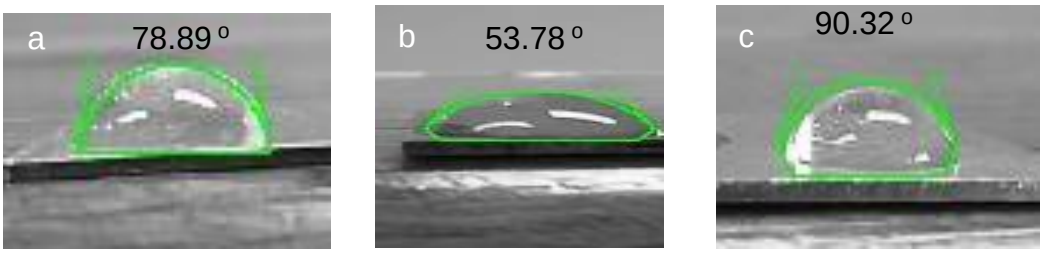

Figure 6.20: Measurements of the contact angles between (a) polished untreated mild steel substrate, (b) mild steel metal submerged in 1.5 M HCl medium only (Blank) for 8 hours, and (c) mild steel immersed in 1.5 M HCl with the highest concentration (0.0005 M) of NO_2-Chr-2-carb for 8 hours.

The contact angles measured for the mild steel immersed in 1.5 M HCl with the highest concentration (0.0005 M) of the aforementioned inhibitors for 8 hours were 91.88 º, 93.01 º, 83.22 º, 86.00 º and 90.32 º respectively. These inhibitors (Chr-2-Carb, Br-Chr-2-carb, and NO_2-Chr-2-carb) seemed to have created hydrophobic surfaces on the mild steel since their contact angles are above 90 º. The contact angles for Cl-Chr-2-carb and CH_3O-Chr-2-carb are getting closer, indicating that they were trying or close to create a hydrophobic surface on the MS metal. It is also observed that the contact angle for the MS metal in the blank was lower (53.78 º) showing that the HCl solution has created a more hydrophilic surface in the MS surface and thus increasing the mild steel corrosion.

6.2.2. Contact angle measurement results on zinc

For zinc metal in the solution of 1.5 M HCl and the synthesized inhibitors, the contact angles measured were 89.71°, 87.85°, 84.50°, 85.46 and 91.23, respectively. Such observed behavior demonstrates how the zinc metal surface was transformed from hydrophilic to being more water-repellent by the adsorption of the 6-substituted chromone-2-carboxamide derivatives inhibitors, lowering the zinc surface wettability [273]. This indicates that the synthesized 6-substituted chromone-2-carboxamide derivatives can have the ability to create a barrier layer for the metal corrosion process. Furthermore, the difference between the contact angle of the untreated zinc metal (79.24 ^{o}) and the contact angles in the presence of the inhibitors is huge and this shows that the inhibitors contributed to controlling the zinc corrosion. It is also observed that the contact angle for the zinc metal in the blank was lower (53.30 ^{o}) signifying that the HCl solution has created a more hydrophilic surface in the zinc surface and thus increasing the zinc corrosion. The results are depicted in Figures 6.21 - 6.25.

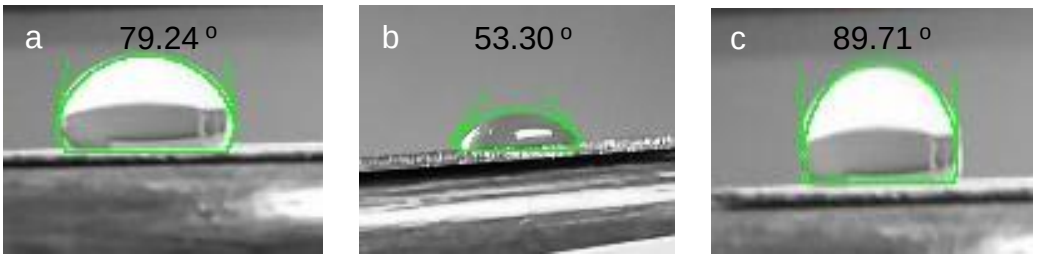

Figure 6.21: Measurements of the contact angles between (a) polished untreated zinc substrate, (b) zinc metal submerged in 1.5 M HCl medium only (Blank) for 8 hours, and (c) zinc immersed in 1.5 M HCl with the highest concentration (0.0005 M) of Chr-2-Carb for 8 hours.

53.30 ^{o}

Figure 6.22: Measurements of the contact angles between (a) polished untreated zinc substrate, (b) zinc metal submerged in 1.5 M HCl medium only (Blank) for 8 hours, and (c) zinc immersed in 1.5 M HCl with the highest concentration (0.0005 M) of Br-Chr-2-carb for 8 hours.

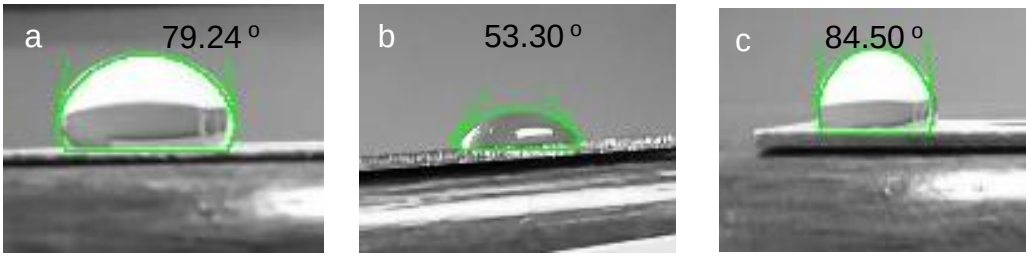

Figure 6.23: Measurements of the contact angles between (a) polished untreated zinc substrate, (b) zinc metal submerged in 1.5 M HCl medium only (Blank) for 8 hours, and (c) zinc immersed in 1.5 M HCl with the highest concentration (0.0005 M) of Cl-Chr-2-carb for 8 hours.

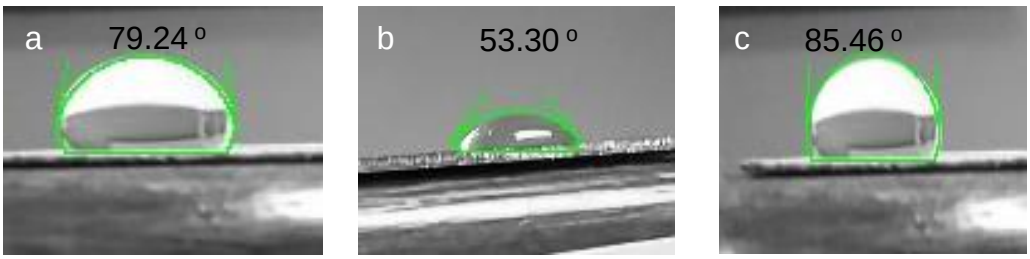

Figure 6.24: Measurements of the contact angles between (a) polished untreated zinc substrate, (b) zinc metal submerged in 1.5 M HCl medium only (Blank) for 8 hours, and

(c) zinc immersed in 1.5 M HCl with the highest concentration (0.0005 M) of CH_3O-Chr-2-carb for 8 hours.

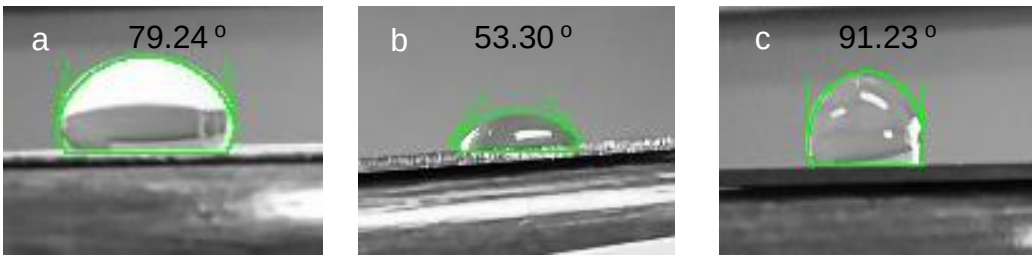

Figure 6.25: Measurements of the contact angles between (a) polished untreated zinc substrate, (b) zinc metal submerged in 1.5 M HCl medium only (Blank) for 8 hours, and (c) zinc immersed in 1.5 M HCl with the highest concentration (0.0005 M) of NO_2-Chr-2-carb for 8 hours.

6.2.3. Contact angle measurement results on aluminium

For aluminium in the presence of Br-Chr-2-carb, Cl-Chr-2-carb and CH_3O-Chr-2-carb in HCl as shown in Figures 6.27, 6.28 and 6.29, the contact angles observed where < 90° (86.89 º, 84.72 º and 88.92 º) signifying that the introduction of the aforementioned inhibitors failed to fully create hydrophobic surface on the aluminium surface. However, the contact angles in the presence of Chr-2-Carb, NO_2-Chr-2-carb in HCl the contact angles observed to be above 90° (90.89 º and 96.35 º) as shown in Figures 6.26 and 6.30, signifying that the adsorption of the two inhibitors on the Al surface has created a hydrophobic surface on the aluminum surface. In addition, the contact angles for the untreated aluminium metal were lower (82.54 º) than the ones for aluminum in the inhibited solution indicating that the inhibitors contributed to controlling the corrosion of aluminum metal. Furthermore, it is also observed that the contact angle for the aluminum metal in the blank was too low (48.89 º) signifying that the HCl solution has created a

more hydrophilic surface in the aluminum surface and thus increasing the aluminum corrosion.

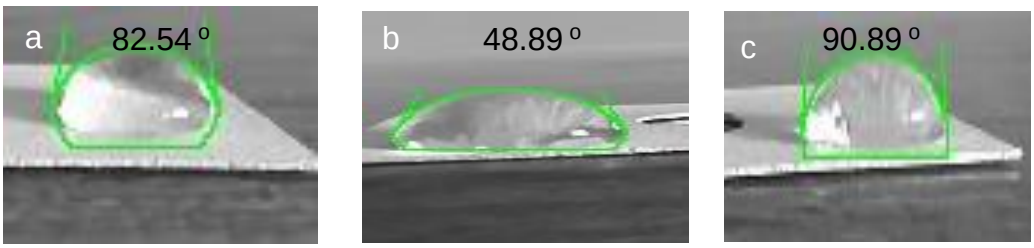

Figure 6.26: Measurements of the contact angles between (a) polished untreated aluminium substrate, (b) aluminium submerged in 1.5 M HCl medium only (Blank) for 8 hours, and (c) aluminium immersed in 1.5 M HCl with the highest concentration (0.0005 M) of Chr-2-Carb for 6 hours.

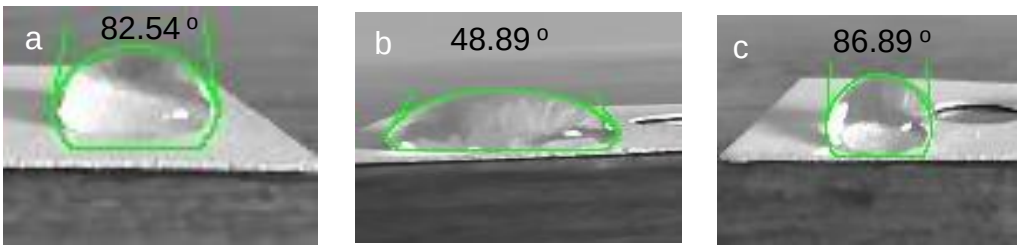

Figure 6.27: Measurements of the contact angles between (a) polished untreated aluminium substrate, (b) aluminium metal submerged in 1.5 M HCl medium only (Blank) for 8 hours, and (c) aluminium immersed in 1.5 M HCl with the highest concentration (0.0005 M) of Br-Chr-2-carb for 6 hours.

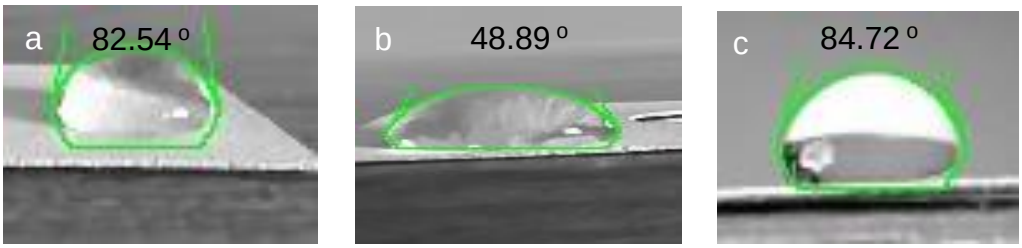

Figure 6.28: Measurements of the contact angles between (a) polished untreated aluminium substrate, (b) aluminium submerged in 1.5 M HCl medium only (Blank) for 8 hours, and (c) aluminium immersed in 1.5 M HCl with the highest concentration (0.0005 M) of Cl-Chr-2-carb for 6 hours.

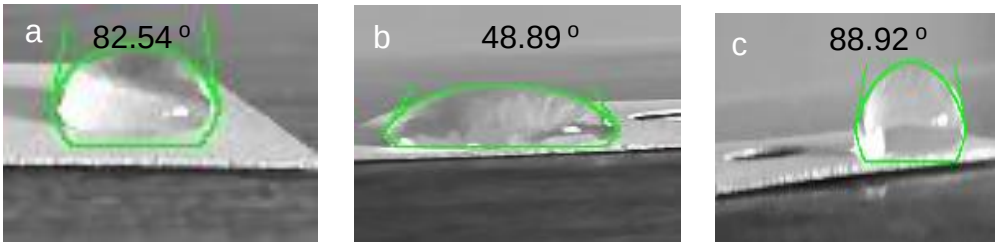

Figure 6.29: Measurements of the contact angles between (a) polished untreated aluminium substrate, (b) aluminium submerged in 1.5 M HCl medium only (Blank) for 8 hours, and (c) aluminium immersed in 1.5 M HCl with the highest concentration (0.0005 M) of CH_3O-Chr-2-carb for 6 hours.

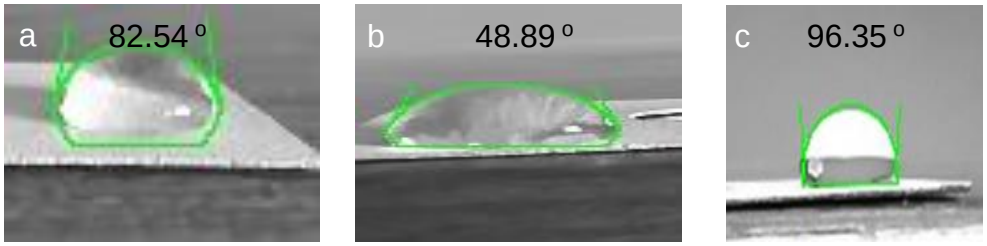

Figure 6.30: Measurements of the contact angles between (a) polished untreated aluminium substrate, (b) aluminium metal submerged in 1.5 M HCl medium only (Blank) for 8 hours, and (c) aluminium immersed in 1.5 M HCl with the highest concentration (0.0005 M) of NO_2-Chr-2-carb for 6 hours.

CHAPTER 7: Theoretical analysis: Computational Results

Quantum computational studies were performed to further study the electronic composition and characteristics of the 6-substitutedchromone-2-carboxamides and the metals.

7.1 Introduction

This chapter presents the theoretical results on the interaction between the inhibitors and the metal surfaces. Firstly, the Al···inhibitor interaction results are presented and compared among themselves, and then the results on Fe···inhibitor interaction results are presented. Finally, the zinc-inhibitor interaction results are presented among themselves. A comparison across results on different surfaces are then presented together to determine the preferred binding surface for the studied inhibitors.

The results in each case are presented by providing the structures of the interacting species, the bond distances between the inhibitor and the metal surface, the relative energies for cases in which more than one possible biding sites was possible as well as the binding energy for the metal···inhibitor surface interactions. The results have been analyzed and discussed following periodic format (started from by Al, followed with Fe and ended with Zinc), having in mind that Al and Zn don't have d-orbitals.

7.2. Interaction of different inhibitors with the Al (11) surface.

After the optimization of the Chr-2-Carb compound and the Al separately, adsorption locator was utilized and it revealed eleven interaction sites for the equilibrium adsorption configuration of Chr-2-Carb on the aluminium surface (111). The resulted energies and interaction sites involving Chr-2-Carb and the aluminum surface (adsorption geometries) are presented in table 7.1 and figure 7.1. Researchers have discovered that a binding energy of around 13 kcal/mol and above depicts chemical adsorption of a compound to the metal surface [274]. The results presented in table 7.1 reveals binding energies which are all greater than 13 kcal/mol, signifying chemisorption behavior. In this regard, it is noted that configuration (a) resulted in the highest binding energy of -55.477 kcal/mol due to the three bonds formed with the Al surface (Al ···O, Al ···N, and Al ···C), with the oxygen, nitrogen and carbon atoms close to the Al surface. The bond Al···O, Al ··· N, and Al ···C distances observed are 1.853 Å, 2.221 Å and 2.403 Å respectively. The bond distances observed are in perfect agreement with literature values. For instance, the Al···O bond

distances (ranging from 1.85 to 1.90 Å) are in good agreement with the literature value of 1.86 Å [275, 276]. The observed bond distances being smaller than the sum of ionic radii signifies that chemisorption process is taking place.

Table 7.1: Interaction energies between the Al surface and Chr-2-Carb inhibitor.

configuration	Relative energy (kcal/mol)	Interaction energy (kcal/mol)	Binding energy (kcal/mol)
(Al··· Chr-2-Carb)-a	0.000	-55.477	55.477
(Al··· Chr-2-Carb)-b	7.974	-47.503	47.503
(Al··· Chr-2-Carb)-c	16.174	-39.304	39.304
(Al··· Chr-2-Carb)-d	17.017	-38.461	38.461
(Al··· Chr-2-Carb)-e	18.677	-36.801	36.801
(Al··· Chr-2-Carb)-f	19.127	-36.351	36.351
(Al··· Chr-2-Carb)-g	30.457	-25.021	25.021
(Al··· Chr-2-Carb)-h	30.736	-24.742	24.742
(Al··· Chr-2-Carb)-i	31.047	-24.432	24.432
(Al··· Chr-2-Carb)-j	31.881	-23.597	23.597
(Al··· Chr-2-Carb)-k	41.797	-13.681	13.681

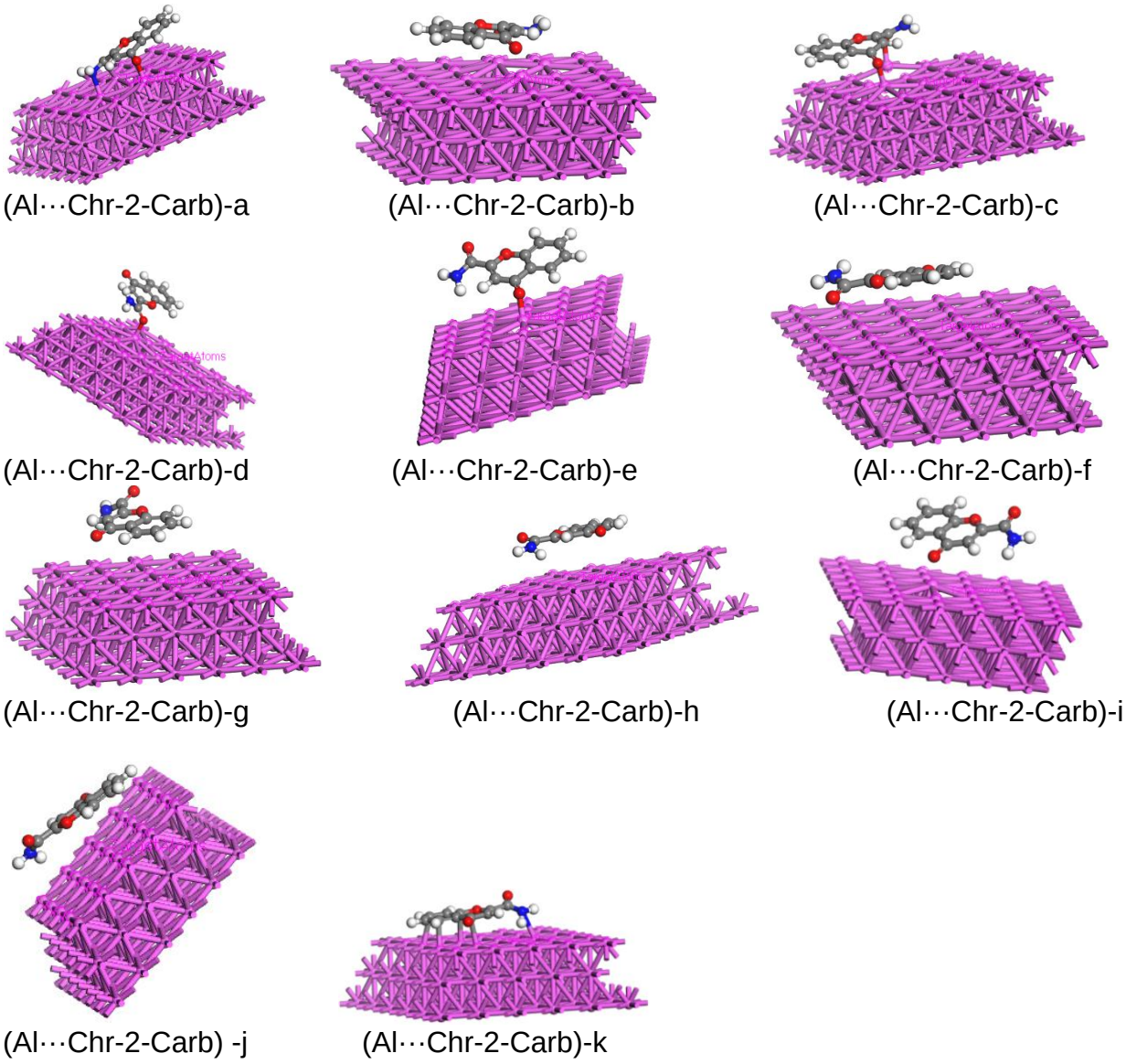

Figure 7.1: Interaction sites involving Chr-2-Carb and the aluminum surface. The aluminum surface is prepared in three layers and expanded in 5 x 5 along the x and y axis.

Two possible equilibrium reactions sites were identified upon interaction of Br-Chr-2-Carb on the aluminium surface. The arrangement of the Br-Chr-2-Carb on the aluminium surface are presented in Figure 7.2. The highest binding energy values (-64.657 and -45.920 kJ/mol) are greater than 13 kcal/mol, signifying chemisorption behavior by the Br-

Chr-2-Carb molecule. Configuration (a) resulted in the formation of three bonds between the Br-Chr-2-Carb and the Al surface (two Al ··· O and Al ··· N), of which contributed significantly in the transferring of electrons between the Br-Chr-2-Carb and the outermost electrons of Al(111) via electron donor acceptor interactions. The Al — O bond distance of the carbonyl oxygen ($CONH_2$) obtained is 1.863 Å, while the aromatic carbonyl oxygen [Ar(C=O)] obtained bond distance is 1.879 Å. Both the Al — O bond distances are ranging from 1.85 to 1.90 Å which is a good agreement with the literature value of 1.86 Å. Furthermore, Al — N bond distance obtained is 2.209 Å, suggesting that this configuration substantially favors the formation of chemical bonding. On the other hand, configuration (a) resulted in Br-Chr-2-Carb adsorbed in a horizontal orientation (lying flat), suggesting a strong interaction between the two aromatic rings and the Al surface (aromaticity) which provided a better surface coverage with highest energy (-64.657 kcal/mol) compared to configuration (b) where there's a bond formation.

Table 7.2: Interaction energies between the Al surface and Br-Chr-2-Carb inhibitor.

Configuration	Relative energy (kcal/mol)	Interaction energy (kcal/mol)	Binding energy (kcal/mol)
(Al···Br-Chr-2-Carb)-a	0.000	-64.657	64.657
(Al···Br-Chr-2-Carb)-b	18.737	-45.920	45.920

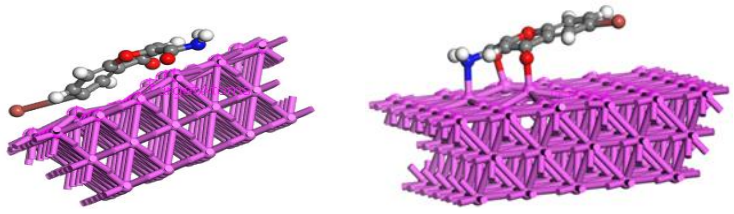

(Al···Br-Chr-2-Carb)-a (Al···Br-Chr-2-Carb)-b

Figure 7.2: Interaction sites involving Br-Chr-2-Carb and the aluminum surface. The aluminum surface is prepared in three layers and expanded in 5 x 5 along the x and y axis.

Three possible interaction sites for the equilibrium adsorption configuration of Cl-Chr-2-Carb on the aluminium surface. All the Interaction energies are displayed in table 7.3, and stable configurations are reported in Fig 7.3. The Cl-Chr-2-Carb adsorbs in a horizontal orientation on the Al(111), suggesting a strong interacting between the two aromatic rings and the Al surface (aromaticity) which provided a better surface coverage with high interaction energy values (-58.598, -53.170 and -33.796 kcal/mol). All these interaction energy values obtained are greater than 13 kcal/mol. It has been noted that configuration (a) shows that the N interacted closely with the Al(111) surface, which resulted to the highest interaction energy (-58.598 kcal/mol) as compared to configuration (b) and (c). Configuration (b) shows that the aromatic carbonyl oxygen [Ar(C=O)] interacted closely with the Al(111), which resulted to the highest interaction energy (-53.170) as compared to configuration (c). On the other hand, configuration (c) shows the Al ···O bond distance of the carbonyl oxygen ($CONH_2$) being close to the Al(111) which contributed to the strong interaction.

Table 7.3: Interaction energies between the Al surface and Cl-Chr-2-Carb.

configuration	Relative energy (kcal/mol)	Interaction energy (kcal/mol)	Binding energy (kcal/mol)
(Al···Cl-Chr-2-Carb)-a	0.000	-58.598	58.598
(Al···Cl-Chr-2-Carb)-b	5.428	-53.170	53.170
(Al···Cl-Chr-2-Carb)-c	24.802	-33.796	33.796

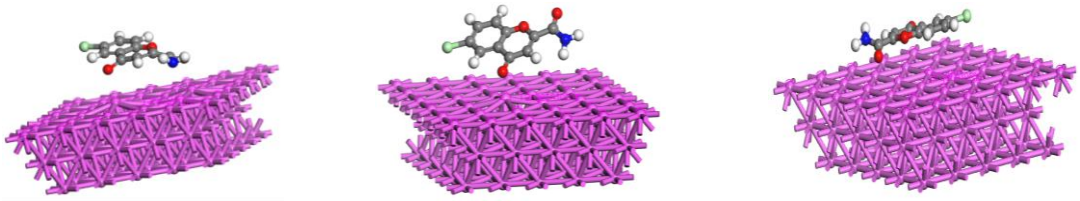

(Al···Cl-Chr-2-Carb)-a (Al···Cl-Chr-2-Carb)-b (Al···Cl-Chr-2-Carb)-c

Figure 7.3: Interaction sites involving Cl-Chr-2-Carb and the aluminum surface. The aluminum surface is prepared in three layers and expanded in 5 x 5 along the x and y axis.

Five different interaction sites for the equilibrium adsorption CH_3O-Chr-2-Carb on the aluminium surface. The results presented in table 7.4 reveal three binding energy values which are less than 13 kcal/mol for configuration (b), (c), (d) and (e), signifying a physical adsorption process. Only configuration (a) has higher binding energy than 13 kcal/mol, suggesting chemical adsorption process. These observations reveal mixed-type of adsorption of CH_3O-Chr-2-Carb on the Al(111) which is in good agreement with the experimental results (corrosion activities) which also depicted mixed-type of adsorption. All the configurations resulted in Al ··· O bond formation with bond distances (ranging from 1.86 to 1.90 Å) which are in good agreement with the literature value of 1.86 Å, as indicated earlier [275, 276]. Furthermore, configuration (a) resulted in two Al ···O bond formation which has led to the chemical adsorption of 6-methoxychromone-2-carboxamide on the Al(111) surface.

Table 7.4: Interaction energies between the Al surface and CH_3O-Chr-2-Carb inhibitor.

configuration	Relative energy (kcal/mol)	Interaction energy (kcal/mol)	Binding energy (kcal/mol)
(Al···CH_3O-Chr-2-Carb)-a	0.000	-28.754	28.754
(Al···CH_3O-Chr-2-Carb)-b	15.261	-13.493	13.493
(Al···CH_3O-Chr-2-Carb)-c	16.132	-12.622	12.622
(Al···CH_3O-Chr-2-Carb)-d	20.988	-7.766	7.766
(Al···CH_3O-Chr-2-Carb)-e	23.098	-5.656	5.656

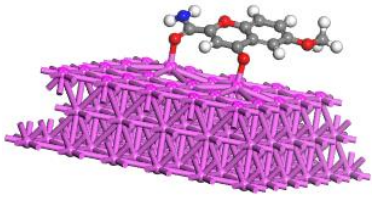

(Al···CH_3O-Chr-2-Carb)-a

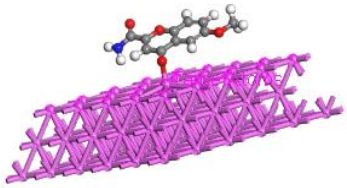

(Al···CH_3O-Chr-2-Carb)-b

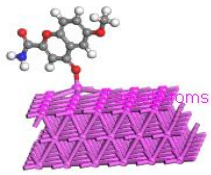

(Al··· CH_3O-Chr-2-Carb)-c

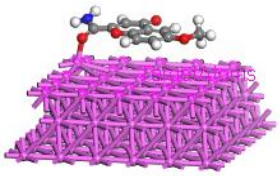

(Al···CH_3O-Chr-2-Carb)-d

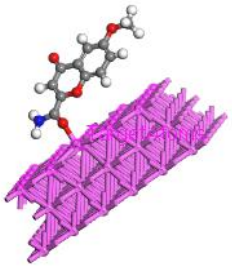

(Al···CH_3O-Chr-2-Carb)-e

Figure 7.4: Interaction sites involving CH_3O-Chr-2-Carb and the Al surface. The Al surface is prepared in three layers and expanded in 5 x 5 along the x and y axis.

The eleven possible interaction sites for the equilibrium adsorption configuration of NO_2-Chr-2-Carb on the aluminium surface are shown in Figure 7.5. The results presented in table 5.5 reveals binding energy values which are greater than 13 kcal/mol for all configuration (a) – (k) in figure 7.5, signifying a chemical adsorption process. Figure 7.5 clearly shows that the oxygen atoms of the nitro group (NO_2) contributed significantly on the chemical adsorption of the NO_2-Chr-2-Carb on the Al surface, which led to the highest interaction energy values as compared with interaction energy values observed on the other four synthesized compounds with Al(111) surface. Table 7.5 shows that the adsorption of NO_2-Chr-2-Carb on the Al(111) has a highest interaction energy of -75.405 kcal/mol, signifying strongest chemical bonding. It is noted that configuration (a) resulted to three Al ···O bond distances of the carbonyl oxygen ($CONH_2$), aromatic carbonyl oxygen [Ar(C=O)] and of the nitro group (NH_2) being close to the Al(111) contributed to the strongest interaction of NO_2-Chr-2-Carb/Al(111) system which led to the highest interaction energy of -75.405 kcal/mol as highlighted earlier. The relative energy values suggest that only the first two configurations are significantly stable. Most of over configurations, although they have very high binding energy at different binding sites, are

not stable enough to be considered possible to exist. The bond distances for the three oxygen atoms which resulted to the highest energy are 1.861 Å, 1.875 Å and 1.900 Å respectively. In some configurations (b), (c), (d), (e), (f), (h), (i) and (j) is observed that both oxygen atoms of the nitro group were binding on the Al surface simultaneously, which contributed to the highest interaction energy values. In addition, only configuration (e) resulted in the formation of NO_2-Chr-2-Carb /Al(111) system in which the Al ···N bond distance is 2.228 Å.

Table 7.5: Interaction energies between the Al surface and NO_2-Chr-2-Carb inhibitor.

Configuration	Relative energy (kcal/mol)	Interaction energy (kcal/mol)	Binding energy (kcal/mol)
(Al···NO_2-Chr-2-Carb)-a	0.000	-75.405	75.405
(Al···NO_2-Chr-2-Carb)-b	1.309	-74.096	74.096
(Al···NO_2-Chr-2-Carb)-c	6.396	-69.009	69.009
(Al···NO_2-Chr-2-Carb)-d	6.852	-68.553	68.553
(Al···NO_2-Chr-2-Carb)-e	12.668	-62.737	62.737
(Al···NO_2-Chr-2-Carb)-f	13.599	-61.806	61.806
(Al···NO_2-Chr-2-Carb)-g	14.799	-60.606	60.606
(Al···NO_2-Chr-2-Carb)-h	19.320	-56.085	56.085
(Al···NO_2-Chr-2-Carb)-i	27.031	-48.374	48.374
(Al···NO_2-Chr-2-Carb)-j	32.324	-43.081	43.081
(Al···NO_2-Chr-2-Carb)-k	37.072	-38.333	38.333

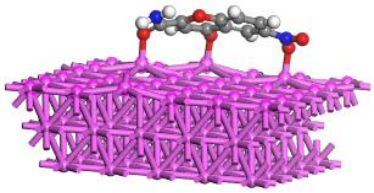

(Al···NO_2-Chr-2-Carb)-a

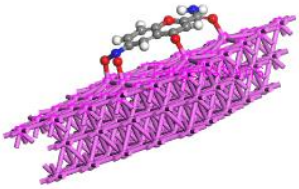

(Al···NO_2-Chr-2-Carb)-b

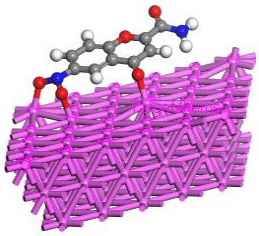

(Al···NO_2-Chr-2-Carb)-c

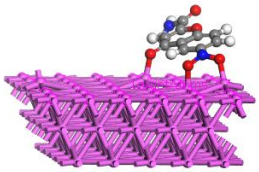

(Al···NO_2-Chr-2-Carb)-d

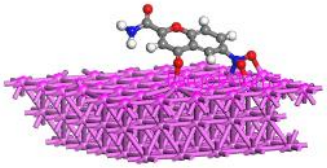

(Al···NO_2-Chr-2-Carb)-e

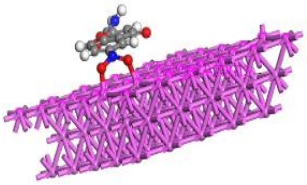

(Al···NO_2-Chr-2-Carb)-f

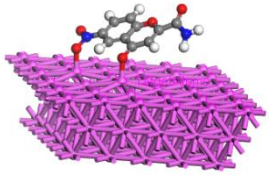

(Al···NO_2-Chr-2-Carb)-g

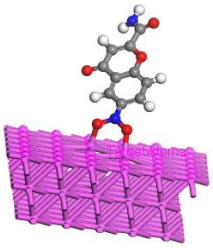

(Al···NO_2-Chr-2-Carb)-h

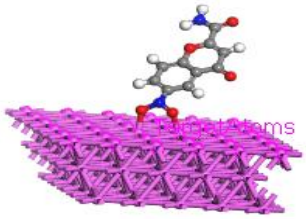

(Al···NO_2-Chr-2-Carb)-i

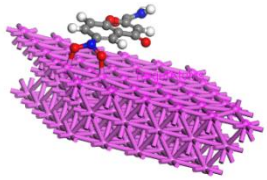

(Al···NO_2-Chr-2-Carb)-j

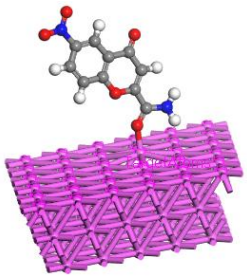

(Al···NO_2-Chr-2-Carb)-g

Figure 7.5: Interaction sites involving NO2-Chr-2-Carb and the aluminum surface. The aluminum surface is prepared in three layers and expanded in 5 x 5 along the x and y axis.

7.3. Interaction of different inhibitors with the Fe(111) surface.

The energies and Interaction sites involving Chr-2-Carb and the Iron surface (adsorption geometries) are presented in table 7.6 and figure 7.6 respectively. The results presented in table 7.6 suggest that the binding energies are significantly high so that it can be considered that Chr-2-Carb interact through chemical adsorption. However, the relative energy values suggest that only one position is stable enough. The Carbonyl group atoms of the chromone-2-carboxamide formed bonds with Fe (111) atoms, and the aromatic carbon atoms coordinate with the Fe(111) surface. Noticeably, configurations (d) and (e) in figure 7.6 show that the nitrogen atom also formed a bond with the Fe(111) surface. Other atoms stand parallel to the iron surface without forming bonds. To analyze the bonds between Chr-2-Carb atoms and the Fe(111) surface we compare the bond length to the sum of the covalent radii of the iron and inhibitor atoms. The Fe ··· O bond distances are ranging from 1.977 to 2.054 Å which are within sum of covalent range of iron and oxygen atoms [278]. The Fe···C bond distances were ranging from 2.252 to 2.545 Å, which suggests a covalent bonding. Furthermore, the Fe···N bond distances on configuration (d) and (e) are 2.158 Å and 2.187 Å respectively, which suggest chemical bonding. Literature revealed that bond lengths less than 3.5 Å signifies chemisorption type of adsorption [278]. Configuration (a) resulted to a higher interaction energy (-288.551 kcal/mol) due to the fact that most of the atoms form bonds with the Fe (111) surface, while configuration (f) gave a lower interaction energy because only one bond formed (Fe···O).

Table 7.6: Interaction energies between the Fe surface and Chr-2-Carb inhibitor.

Configuration	Relative energy (kcal/mol)	Interaction energy (kcal/mol)	Binding energy (kcal/mol)
(Fe···Chr-2-Carb)–a	0.000	-288.551	288.551
(Fe···Chr-2-Carb)–b	81.967	-206.584	206.584
(Fe···Chr-2-Carb)–c	83.853	-204.698	204.698
(Fe···Chr-2-Carb)–d	83.922	-204.629	204.629
(Fe···Chr-2-Carb)–e	85.917	-202.634	202.634
(Fe···Chr-2-Carb)–f	95.737	-192.814	192.814

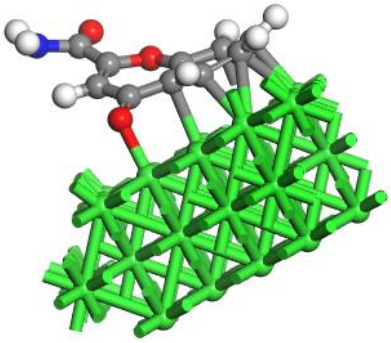

(Fe···Chr-2-Carb)–a

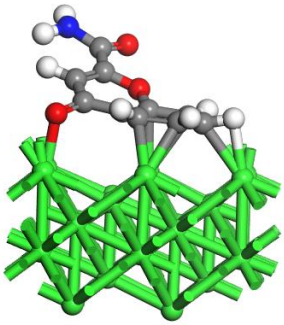

(Fe···Chr-2-Carb)–b

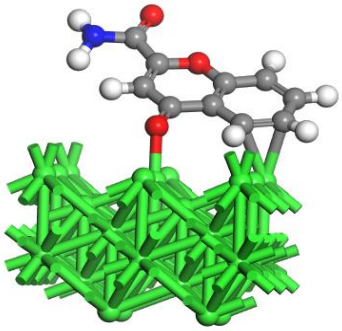

(Fe···Chr-2-Carb)–c

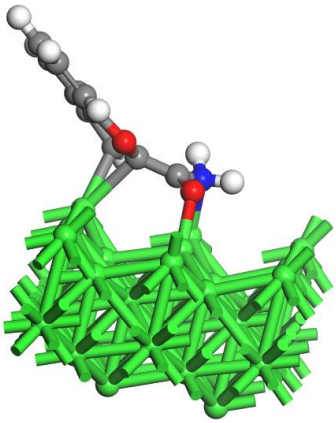

(Fe···Chr-2-Carb)–d

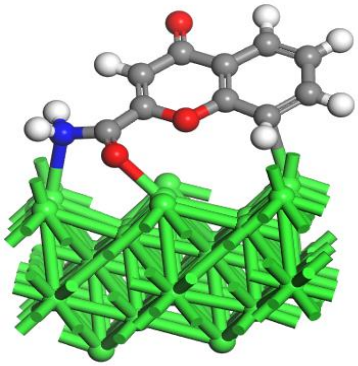

(Fe···Chr-2-Carb)–e

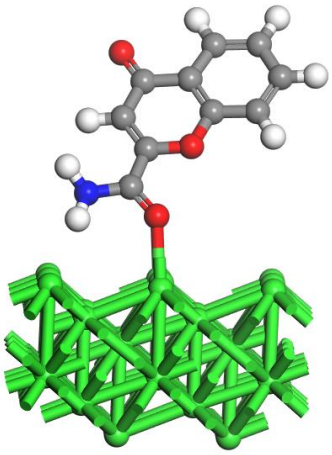

(Fe···Chr-2-Carb)–f

Figure 7.6: Interaction sites involving Chr-2-Carb and the Fe (111) surface. The Fe (111) surface is prepared in three layers and expanded in 5 x 5 along the x and y axis.

A variety of interaction (binding) sites of the Br-Chr-2-Carb on the Fe (111) surface were investigated. The energies and structures for the Br-Chr-2-Carb···Fe(111) in table 7.7 and figure 7.7 respectively. The results suggest that in terms of relative energy structures a-c can be considered to be possible stable arrangements for the Br-Chr-2-Carb···Fe(111) species. The interaction energies at all possible binding sites are indicative of chemical adsorption type. The carbonyl group atoms of the 6-bromochromone-2-carboxamide

formed bonds with Fe (111) atoms, and the aromatic carbon atoms coordinate with the Fe(111) surface. The Fe···O bond distances are ranging from 1.946 to 1.983 Å which are within sum of covalent range of iron and oxygen atoms [275, 276]. The Fe ··· C bond distances were ranging from 2.269 to 2.468 Å, which suggest a covalent bonding. Furthermore, the Fe ··· N bond distance on configuration (d) is 2.202 Å which suggest chemical bonding. As indicated earlier, literature revealed that bond lengths less than 3.5 Å signifies chemisorption type of adsorption. Configuration (a) resulted to a higher interaction energy (-239.995 kcal/mol) compared to the other configurations, suggesting a strong bonding of the oxygen with the Fe (111) surface.

Table 7.7: Interaction energies between the Fe surface and Br-Chr-2-Carb inhibitor.

Configuration	Relative energy (kcal/mol)	Interaction energy (kcal/mol)	Binding energy (kcal/mol)
(Fe··· Br-Chr-2-Carb)-a	0.000	-239.995	239.995
(Fe··· Br-Chr-2-Carb)-b	5.673	-234.322	234.322
(Fe··· Br-Chr-2-Carb)-c	5.741	-234.254	234.254
(Fe··· Br-Chr-2-Carb)-d	5.921	-234.074	234.074
(Fe··· Br-Chr-2-Carb)-e	6.406	-233.589	233.589
(Fe··· Br-Chr-2-Carb)-f	11.270	-228.725	228.725

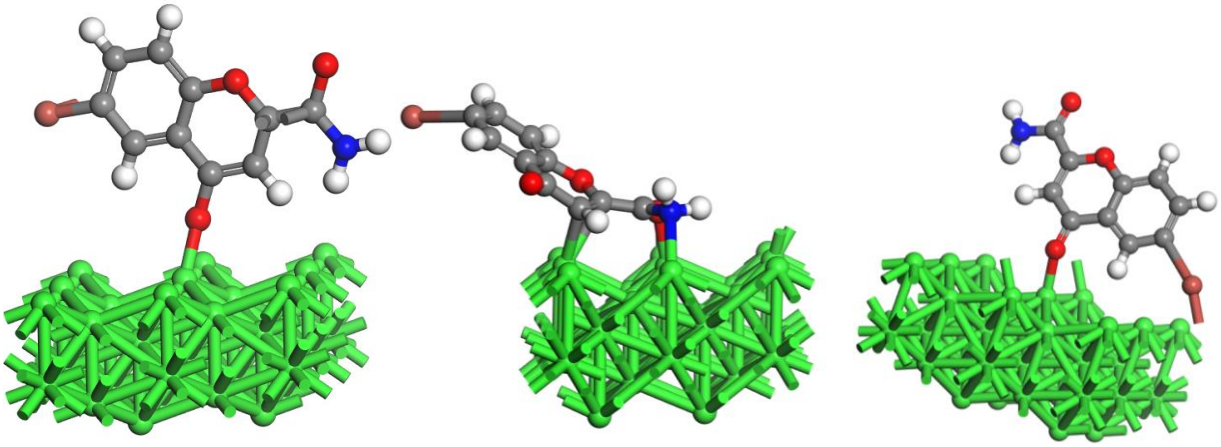

(Fe···Br-Chr-2-Carb)-a (Fe···Br-Chr-2-Carb)-b (Fe···Br-Chr-2-Carb)-c

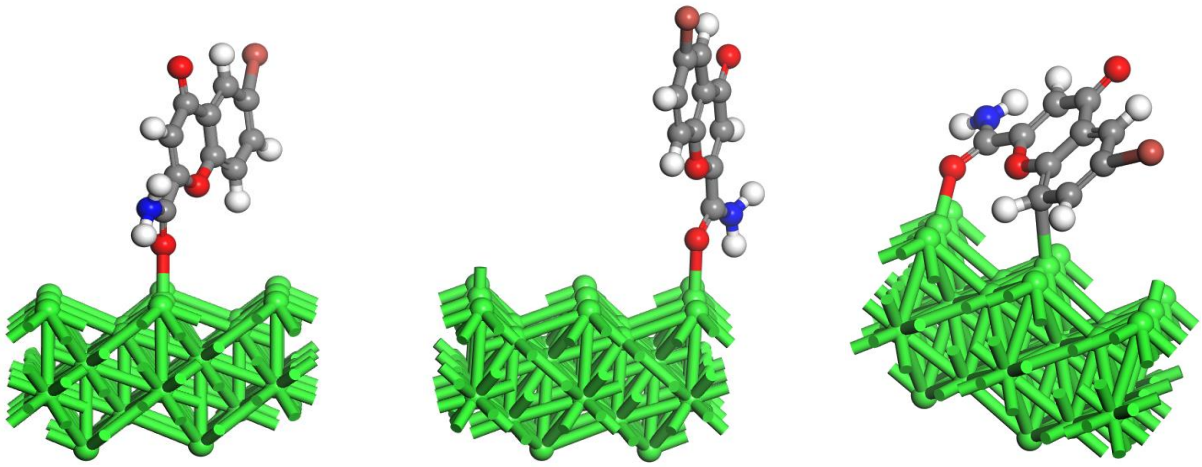

(Fe···Br-Chr-2-Carb)-d (Fe···Br-Chr-2-Carb)-e (Fe···Br-Chr-2-Carb)-f

Figure 7.7: Interaction sites involving Br-Chr-2-Carb and the Fe(111) surface. The Fe(111) surface is prepared in three layers and expanded in 2 x 2 along the x and y axis.

The structures of the Cl-Chr-2-Carb···Fe(111) species along are shown in figure 7.8 while the energies are presented in Table 7.8. About five different configurations were obtained of which only *a* and *b* geometries can be considered to be stable. Cl-Chr-2-Carb tends to interact with the Fe surface through the use of its heteroatoms and the aromatic ring. For instance, in configurations (a), and (b) the nitrogen atom interacts with the Fe(111) surface. The Fe···O bond distances are ranging from 1.587 to 2.070 Å which are

within sum of covalent range of iron and oxygen atoms [275, 276]. The Fe···C bond distances were ranging from 2.062 to 2.502 Å, which suggest a covalent bonding. Furthermore, the Fe···N bond distance on configurations (a), and (b) are 2.222 and 2.329 Å respectively which suggest chemical bonding. As mentioned earlier, bond lengths less than 3.5 Å signifies chemisorption type of adsorption [279]. Configuration (a) resulted to a little higher interaction energy (-245.913 kcal/mol) compared to the other configurations suggesting that both the oxygen and nitrogen atoms interacted strong with the Fe (111) surface, while configuration (e) gave a lowest interaction energy (-224.509 kcal/mol) because only one bond (Fe···O) formed.

Table 7.8: Interaction energies between the Fe surface and Cl-Chr-2-Carb inhibitor.

Configuration	Relative energy (kcal/mol)	Interaction energy (kcal/mol)	Binding energy (kcal/mol)
(Fe···Cl-Chr-2-Carb)-a	0.000	-245.913	245.913
(Fe···Cl-Chr-2-Carb)-b	3.301	-242.612	242.612
(Fe···Cl-Chr-2-Carb)-c	16.231	-229.682	229.682
(Fe···Cl-Chr-2-Carb)-d	20.651	-225.262	225.262
(Fe···Cl-Chr-2-Carb)-e	21.404	-224.509	224.509

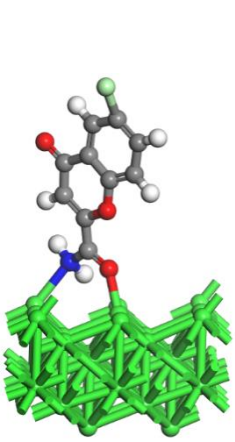

(Fe···Cl-Chr-2-Carb)-a

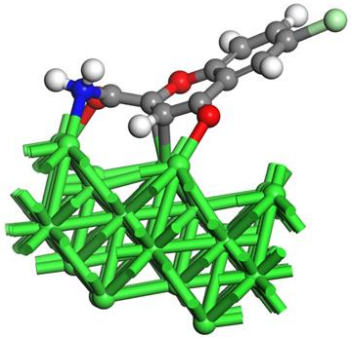

(Fe···Cl-Chr-2-Carb)-b

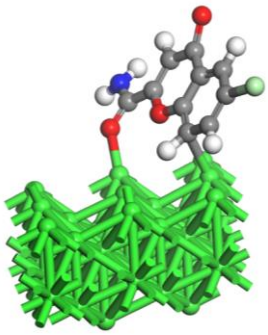

(Fe···Cl-Chr-2-Carb)-c

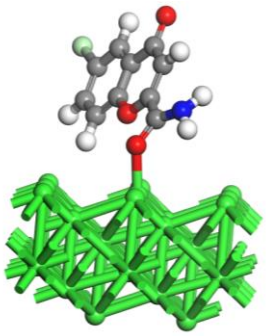

(Fe···Cl-Chr-2-Carb)-d

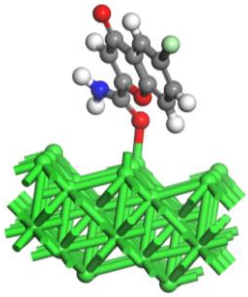

(Fe···Cl-Chr-2-Carb)-f

Figure 7.8: Interaction sites involving Cl-Chr-2-Carb and the Fe(111) surface. The Fe(111) surface is prepared in three layers and expanded in 2 x 2 along the x and y axis.

Six different binding sites were identified for the interaction involving CH_3O-Chr-2-Carb and the Fe(111) surface. The corresponding energies and Interaction sites presented in table 7.9 and figure 7.9 respectively. Only the first three configurations (a – c) while later configuration are considered to be not stable because their energies are significantly high with respect to the lowest energy configuration. All the binding sites appear to give very high binding energy values so that each binding site is likely to result in chemical bonding. The Fe···O bond distances range between 1.994 and 2.090 Å, and these values are within

the sum of covalent range of iron and oxygen atoms. The Fe···C bond distances were ranging from 2.293 to 2.353 Å, which suggest a covalent bonding. Furthermore, the Fe···N bond distance on configuration (d) is 2.202 Å which suggest chemical bonding. Literature revealed that bond lengths less than 3.5 Å signifies chemisorption type of adsorption as highlighted above.

Table 7.9: Interaction energies between the Fe surface and CH_3O-Chr-2-Carb inhibitor.

Configuration	Relative energy (kcal/mol)	Interaction energy (kcal/mol)	Binding energy (kcal/mol)
(Fe···CH_3O-Chr-2-Carb)-a	0.000	-268.269	268.269
(Fe···CH_3O-Chr-2-Carb)-b	5.902	-262.367	262.367
(Fe···CH_3O-Chr-2-Carb)-c	5.947	-262.322	262.322
(Fe···CH_3O-Chr-2-Carb)-d	21.607	-246.662	246.662
(Fe···CH_3O-Chr-2-Carb)-e	37.453	-230.816	230.816
(Fe···CH_3O-Chr-2-Carb)-f	93.945	-174.324	174.324

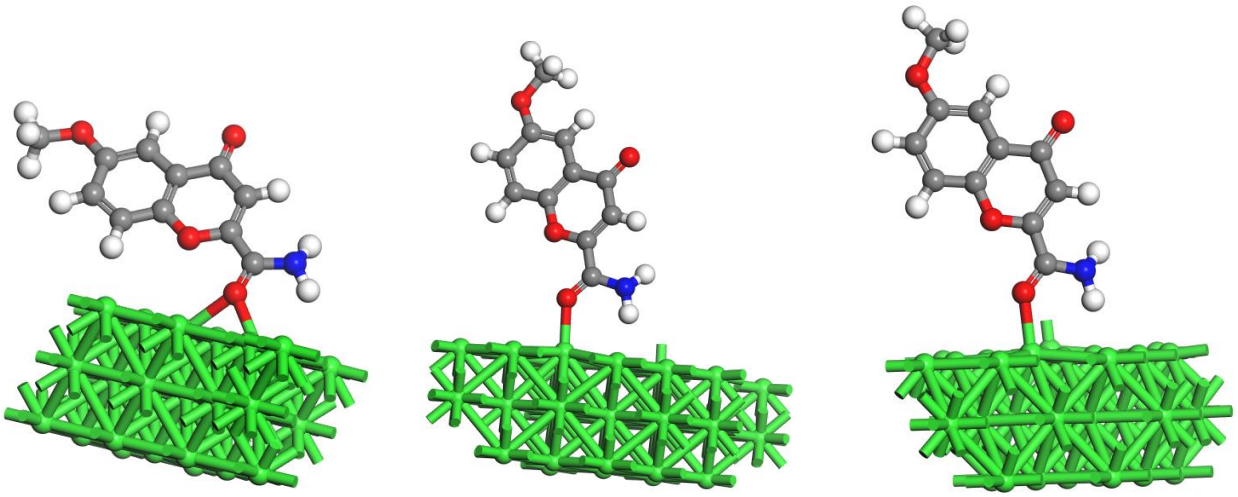

(Fe···CH_3O-Chr-2-Carb)- a (Fe···CH_3O-Chr-2-Carb)- b (Fe···CH_3O-Chr-2-Carb)- c

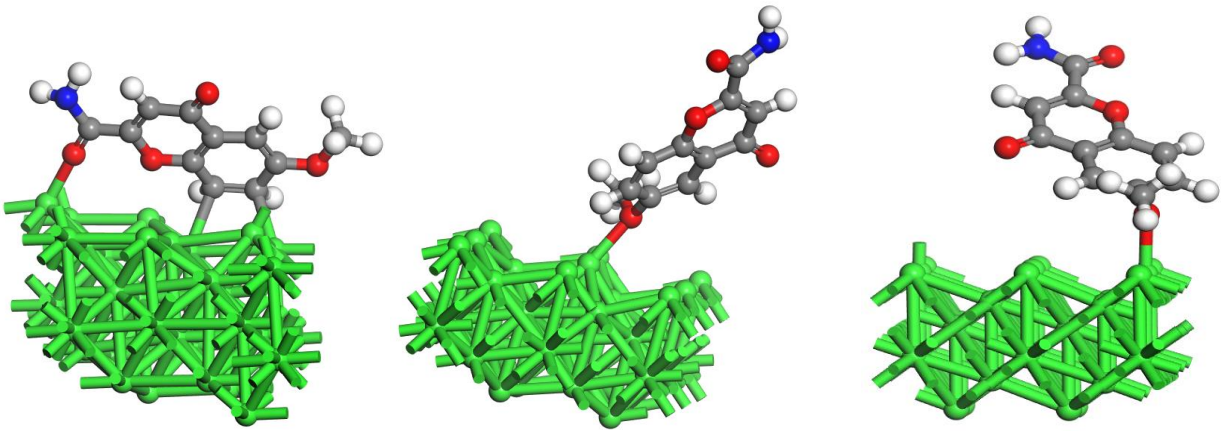

(Fe···CH_3O-Chr-2-Carb)- d (Fe···CH_3O-Chr-2-Carb)- e (Fe···CH_3O-Chr-2-Carb)- f

Figure 7.9: Interaction sites involving CH_3O-Chr-2-Carb and the Fe(111) surface. The Fe(111) surface is prepared in three layers and expanded in 2 x 2 along the x and y axis.

Seven different binding sites were investigated for the interaction between NO_2-Chr-2-Carb and the Fe (111) surface. The interaction energies and relative energies values for the interacting species are reported in Table 7.10 while the structures are presented in Figure 7.10. The outcome of the investigation suggests that only one species is stable. All the other species, despite having good binding energy values, are not stable enough

with respect to the lowest energy structure. In other words, the NO_2-Chr-2-Carb species is likely to interact with the Fe(111) surface through the configuration, in which the molecule binds on the surface through the use of its chromone ring and the carbonyl O atom of the amide group.

Table 7.10: Interaction energies between the Fe surface and NO_2-Chr-2-Carb.

configuration	Relative energy (kcal/mol)	Interaction energy (kcal/mol)	Binding energy (kcal/mol)
(Fe···NO_2-Chr-2-Carb)-a	0.000	-311.349	311.349
(Fe···NO_2-Chr-2-Carb)-b	23.848	-287.501	287.501
(Fe···NO_2-Chr-2-Carb)-c	48.532	-262.817	262.817
(Fe···NO_2-Chr-2-Carb)-d	62.823	-248.526	248.526
(Fe···NO_2-Chr-2-Carb)-e	63.388	-247.961	247.961
(Fe···NO_2-Chr-2-Carb)-f	68.607	-242.742	242.742
(Fe···NO_2-Chr-2-Carb)-g	70.055	-241.294	241.294

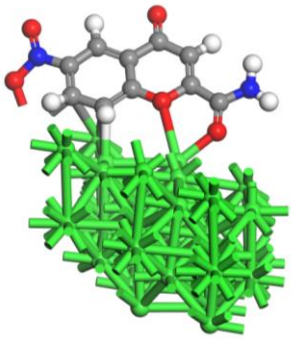

(Fe···NO_2-Chr-2-Carb)-a

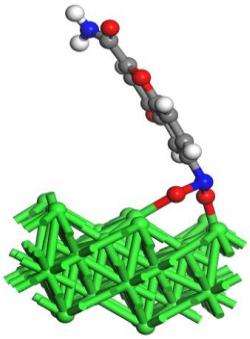

(Fe···NO_2-Chr-2-Carb)-b

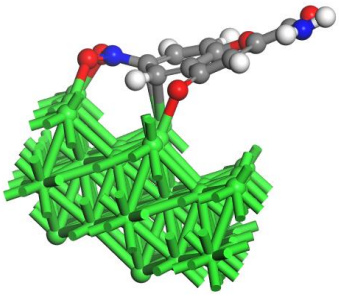

(Fe···NO_2-Chr-2-Carb)-c

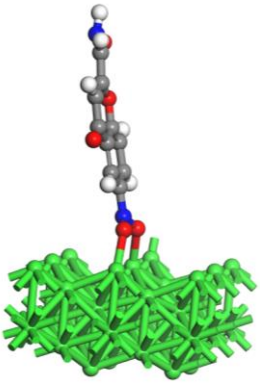

(Fe···NO_2-Chr-2-Carb)-d

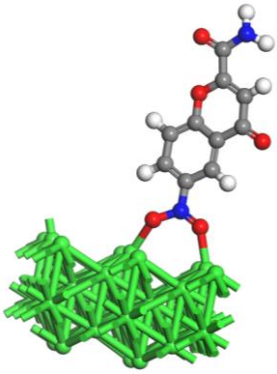

(Fe···NO_2-Chr-2-Carb)-e

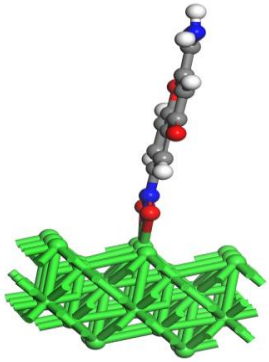

(Fe···NO_2-Chr-2-Carb)-f

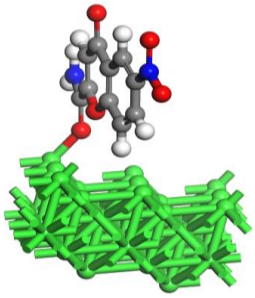

(Fe···NO_2-Chr-2-Carb)-g

Figure 7.10: Interaction sites involving NO_2-Chr-2-Carb and the Fe (111) surface. The Fe (111) surface is prepared in three layers and expanded in 2 x 2 along the x and y axis.

7.4. Interaction of different inhibitors with the Zn(111) surface

The interaction of Chr-2-Carb with Zn surface gave only one stable arrangement; it is shown in figure 7.11 configuration (a). The binding energy is significantly low as shown in table 7.11 below, signifying that Chr-2-Carb inhibitor adsorbed physically on the Zn (1 1 1) surface. This is in agreement with the experimental results, physical adsorption was dominant. The configuration (a) on figure 7.11 shows that the chromone-2-carboxamide prefers to adsorb in a horizontal orientation on the surface without a bond formation.

Two possible binding sites (stable arrangement) were obtained from the interaction between Br-Chr-2-Carb and the Zn(111) surface. The results presented in table 7.11 reveals binding energy values which are less than 13 kcal/mol (which are -10.287 and -8.918 kcal/mol respectively) for both the configurations (b) and (c) in figure 7.11, signifying an electrostatic force of attraction (physical adsorption process. This observation is in good agreement with the experimental result obtained in the lab, where it is observed that physical adsorption was dominant. Figure 7.11 shows that Br-Chr-2-Carb prefers to adsorb in a horizontal orientation and forming an Zn — O bond.

Two possible binding sites were obtained from the interaction between Cl-Chr-2-Carb and the Zn surface. The results presented in table 7.11 shows binding energy values which are greater than 13 kcal/mol (which are -21.392 and -27.017 kcal/mol respectively) for both the configurations (d) and (e) in figure 7.11, signifying chemical adsorption of the Cl-Chr-2-Carb. The observations through experimental results obtained in the lab revealed mixed-type of adsorption with physical adsorption being dominant. Figure 7.11 shows that Cl-Chr-2-Carb prefers to adsorb in a horizontal orientation and forming an Zn — O bond.

Only one possible binding obtained from the interaction between CH_3O-Chr-2-Carb and the Zn(111) surface. The results presented in table 7.11 below show that the interaction energy value is far away greater than 13 kcal/mol (-4986.955 kcal/mol), signifying a strong interaction between the CH_3O-Chr-2-Carb inhibitor and the Zn (1 1 1) surface. This interaction took more than two months to converge (finished successfully). The

configuration (f) in Figure 7.11 shows that the CH_3O-Chr-2-Carb prefers to adsorb in a horizontal orientation on the surface without any bond formation.

Only one possible binding site was obtained from the interaction between NO_2-Chr-2-Carb and the Zn(111) surface. It is clear from the results displayed in Table 7.11 below that the interaction energy value is way too less than 13 kcal/mol (-4.318 kcal/mol), signifying that the NO_2-Chr-2-Carb inhibitor adsorbed physically on the Zn (1 1 1) surface. This is in perfect agreement with the experimental results, physical adsorption was dominant, and the interaction was too weak. The configuration (e) in Figure 7.11 shows that the NO_2-Chr-2-Carb prefers to adsorb in a horizontal orientation on the Zn surface without a bond formation. Furthermore, the result presents that the interaction is due to the aromatic rings of the NO_2-Chr-2-Carb (aromaticity) through van der Waals forces of attraction.

Table 7.11: Interaction energies between the zinc surface and Chr-2-Carb, Br-Chr-2-Carb, Cl-Chr-2-Carb, CH_3O-Chr-2-Carb and NO_2-Chr-2-Carb inhibitors.

structure	Relative energy (kcal/mol)	Interaction energy (kcal/mol)	Binding energy (kcal/mol)
(Zn···Chr-2-Carb)–a	-	-7.775	7.775
(Zn···Br-Chr-2-Carb)–b	0,000	-10.287	10.287
(Zn···Br-Chr-2-Carb)–c	1,37	-8.918	8.918
(Zn···Cl-Chr-2-Carb)–d	0,000	-27.017	27.017
(Zn···Cl-Chr-2-Carb)–e	5,625	-21.392	21.392
(Zn···CH_3O-Chr-2-Carb)–f	-	-4986.955	4986.955
(Zn···NO_2-Chr-2-Carb)–g	-	-4.318	4.318

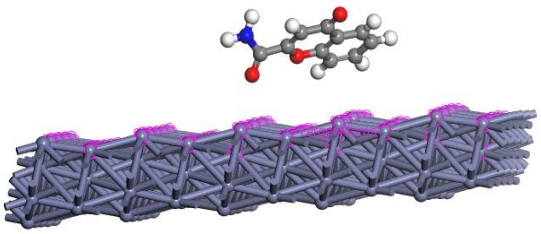

(Zn···Chr-2-Carb)–a

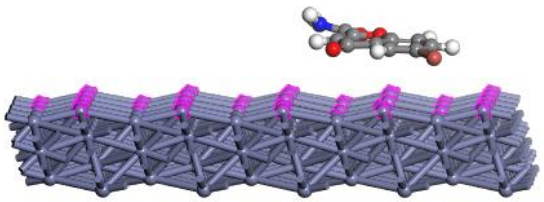

(Zn···Br-Chr-2-Carb)–b

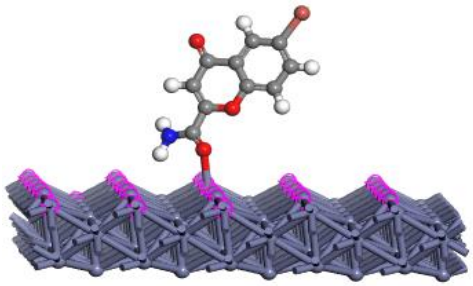

(Zn···Br-Chr-2-Carb)–c

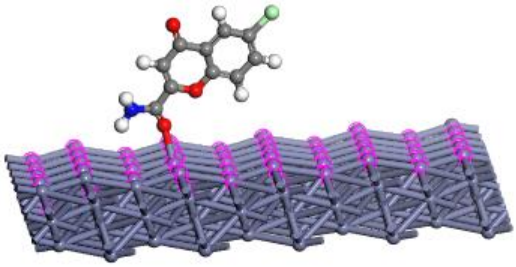

(Zn···Cl-Chr-2-Carb)–d

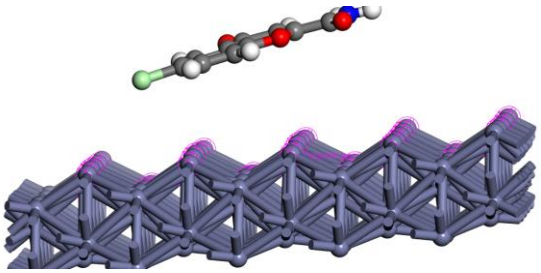

(Zn···Cl-Chr-2-Carb)–e

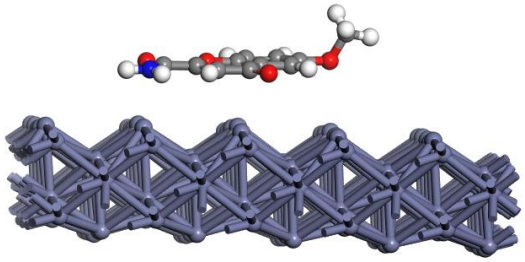

(Zn··· CH_3O-Chr-2-Carb)–f

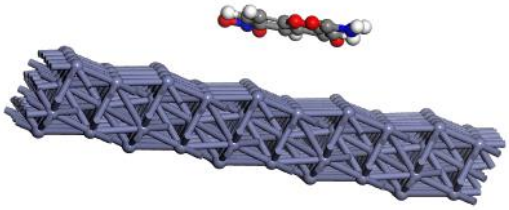

(Zn··· NO_2-Chr-2-Carb)–g

Figure 7.11: Interaction sites involving the five synthesized inhibitors (Chr-2-Carb, Br-Chr-2-Carb, Cl-Chr-2-Carb, CH_3O-Chr-2-Carb and NO_2-Chr-2-Carb) with the zinc surface. The Zn(111) surface is prepared in three layers and expanded in 5 x 5 along the x and y axis.

CHAPTER 8: Conclusions, recommendations and future studies

The final chapter summarizes and concludes the research's aims and goals. The five synthesized inhibitor compounds effectively inhibited Al, Zn and MS corrosion in the acidic medium (HCl). The inhibitors' adsorption mechanism on both metals was discovered to be mixed-type adsorption. The anodic and cathodic reactions were both suppressed to similar degrees.

8.1. Conclusions

The aim of this research project was accomplished. The 6-substitutedchromone-2-carboxamides (Chr-2-Carb, Br-Chr-2-Carb, Cl-Chr-2-Carb, CH_3O-Chr-2-Carb and NO_2-Chr-2-Carb) were successfully synthesized and characterized. These inhibitors were characterized by Fourier Transform Infrared spectrometry (FT-IR) and Nuclear Magnetic Resonance (^{1}H-NMR and ^{13}C-NMR) spectroscopy and gave the correct number of peaks in the appropriate chemical shifts. The synthesized 6-substituted chromone-2-carboxamides compounds were tested for their potential to inhibit Al, MS and Zn corrosions in an acidic environment (HCl solution) in various concentrations. The measurement of the inhibitory performance of the five inhibitors was carried out using gravimetric, FT-IR, wettability contact angle, SEM/EDS, and electrochemical techniques [such as Potentiodynamic polarization (PDP) and electrochemical impendence spectroscopy (EIS)] and computational analysis technique.

The synthesized 6-substituted chromone-2-carboxamide derivatives showed good to excellent inhibitory activity against Al, MS and Zn corrosion. Amongst the tested inhibitors, the CH_3O-Chr-2-Carb and NO_2-Chr-2-Carb exhibited higher %IE compared to the other three inhibitors (Chr-2-Carb, Br-Chr-2-Carb and Cl-Chr-2-Carb). The higher %IE of the CH_3O-Chr-2-Carb and NO_2-Chr-2-Carb is because of the presence of the methoxy and nitro groups which contain heteroatoms (Oxygen and Nitrogen) which play an important role in the adsorption of these compounds on the metal surfaces. Gravimetric analysis showed that corrosion rates decrease upon increasing inhibitor concentrations and rise in temperature of the solution. The inhibitors had the highest %IE at the lowest temperature (303 K) and maximal concentrations of the inhibitors for all the metals (Al, MS and Zn).

The temperature studies facilitated the assessment of the thermodynamic and kinetic parameters linked to the corrosion and corrosion inhibition of aluminum (Al) and mild steel (MS). The experiments demonstrated that the adsorption mechanism of the synthesized 6-substituted chromone-2-carboxamides is a combination of both physisorption and chemisorption, sometimes known as mixed-type adsorption, with physical adsorption having a dominant effect. Kinetic experiments demonstrated that the introduction of

these inhibitors into the solution increased the energy (activation energy) needed to generate corrosion products. This can be attributed to the creation of a protective coating on the surface of the two metals. Considering surface coverage values obtained from gravimetric analysis, the results showed that in all the tested isotherms Langmuir adsorption isotherm was the best fit which suggests that the adsorption of these inhibitors on the metal surfaces obeyed Langmuir adsorption isotherm. The regression coefficient for Langmuir was determined to be very close to unity (one). The adsorption process was determined to be spontaneous for all the evaluated metals, as evidenced by the negative values obtained for ΔG°_{ads}.

FTIR spectra confirmed the disappearance of some functional groups, suggesting complex formation between the inhibitors the metal. This observation was also seen through the decreased in intensity peaks of the adsorption spectra which means that a coordinate bond was formed through the functional groups of these peaks with the metals, forming the metal- inhibitor complex on the metal surfaces, controlling the dissolution process. The FTIR spectra also revealed the O atoms on the aromatic rings (C=O), and N atom in the C-N and N-H functional groups of the examined 6-substitutedchromone-2-carboxamide to be the most preferred sites for interaction with the three metals (MS, Zn and Al). Th FTIR spectra of the adsorption film also confirmed that these inhibitors has created a barrier for the corrosion process on the metals, thus they decreased the contact between the metals and the acidic medium.

Potentiodynamic Polarization (PDP) study revealed that these inhibitors affect both anodic and cathodic reactions for all the metals used, with Al exhibiting higher cathodic polarization. The polarization investigation yielded corrosion parameters (i_{corr}, E_{corr}, βa and βc). The parameters show that the 6-substitutedchromone-2-carboxamides are mixed type corrosion inhibitors that primarily block Al, MS and Zn through charge transfer. Increasing the concentration of inhibitors resulted in higher R_P values, indicating that corrosion is predominantly inhibited by the creation of a protective coating/film. Trans-passive regions were observed, resulting in pitting corrosion on the Al metal.

EIS data presented an imperfect semicircle loop for MS and Zn, indicating that the inhibitors effectively inhibited the MS and Al corrosion. Al has a stronger tendency to

produce oxide films than both MS and Zn, resulting in a more prominent passive zone on Nyquist plots. EIS data indicate that increasing the concentration of inhibitors reduces corrosion rate and increases %IE, and thus the charge transfer resistance was increased. The constant phase element exponent (n) values were close to unity for all the metals (Al, MS and Zn) indicating a pseudo-capacitive behavior of the electrode. All the five synthesized inhibitors showed mixed-type adsorption behavior.

Spectroscopic studies for surface analysis revealed interactions between Zn, Al, and MS with the 6-substitutedchromone-2-carboxamides, leading to the development of inhibitor-metal complexes. Water contact angle investigations confirmed the formation of an adsorption film on MS, Zn, and Al surfaces. The wettability contact angle technique also showed that these inhibitors created the hydrophobic surface on the three evaluated metals. SEM results clearly showed that in the absence of 6-substitutedchromone-2-carboxamides, the Zn, Al, and MS surfaces became porous and rough indicating that the metals were severely corroded by the HCl. The use of these inhibitors resulted in a decrease in the contact between the metals and the aggressive medium (HCl) through the formation of the adsorption film. The chemical analysis of the composition surface electrode by EDS revealed the elements detected on the metal surfaces. The EDS spectra of the metals immersed on uninhibited system revealed high oxygen content, suggesting increased oxidation of the metals. The HCl medium caused the metals to revert to their oxide states and thus led to the increased oxygen content.

Quantum chemical computations were conducted on gas phase and protonated versions of the synthesized compounds. The results of this technique revealed that these inhibitors will be effective in terms of the prevention of the corrosion of Al and MS metals. On the other hand, it showed poor interactions between the synthesized inhibitors and the zinc surface. Moreover, the DFT results showed a strong interaction between the inhibitors and the mild steel surface, signifying that these inhibitors strongly adsorbed on the mild steel surface. These observations are in agreement with the gravimetric analysis results. The binding energies computed in this research study are in good agreement with experimental data and according to the binding energies presented in the tables. NO_2-Chr-2-Carb inhibitor was shown to be most effective among the other evaluated inhibitors

against the corrosion of mild steel. DFT calculations revealed that both the oxygen atoms and the nitrogen atom of the nitro group of the NO_2-Chr-2-Carb compound formed a bond with the Al (111) and Fe(111) surfaces, suggesting that these heteroatoms contributed to the effectiveness of this inhibitor. The results and discussions of this technique will aid in the development of new chromone compounds for future research. In addition, the results and discussions of this technique will aid in the development of new chromone compounds for future research.

8.2. Recommendations and future studies

This research project discovered that chromone derivatives as organic inhibitors can prevent metal corrosion in harsh environments (acidic environments). This study suggests that chromone derivatives are effective metal defenders. Therefore, future studies should consider evaluating the chromone derivatives used in this study in a high-temperature environment of above 60°C. Additionally, future studies should evaluate these compounds in various corrosive mediums to assess their inhibitory potential. Quantum mechanical simulations of adsorbent-adsorbate interactions are recommended for corrosion prevention research due to their ability to accurately describe bond formation and breakdown processes. Quantum chemistry research could identify optimal molecule geometry suitable for high inhibitory efficiency. Further research could examine how shifting the testing solution affects inhibition efficiency.

References

1. Khan, M., M.W. Dewan, and M.Z. Sarkar, *Effects of welding technique, filler metal and post-weld heat treatment on stainless steel and mild steel dissimilar welding joint.* Journal of Manufacturing Processes, 2021. **64**: p. 1307-1321.
2. Ahamad, I. and M. Quraishi, *Bis (benzimidazol-2-yl) disulphide: an efficient water soluble inhibitor for corrosion of mild steel in acid media.* Corrosion science, 2009. **51**(9): p. 2006-2013.
3. Chugh, B., et al., *Comparative investigation of corrosion-mitigating behavior of thiadiazole-derived bis-schiff bases for mild steel in acid medium: experimental, theoretical, and surface study.* ACS omega, 2020. **5**(23): p. 13503-13520.
4. Olasunkanmi, L.O., et al., *Some quinoxalin-6-yl derivatives as corrosion inhibitors for mild steel in hydrochloric acid: experimental and theoretical studies.* The Journal of Physical Chemistry C, 2015. **119**(28): p. 16004-16019.
5. Vargel, C., *Corrosion of aluminium*. 2020: Elsevier.
6. Masuku, G., et al., *Quinoxaline derivatives as corrosion inhibitors of zinc in 1.0 M hydrochloric and sulphuric acid solutions: Adsorption, electrochemical, spectroscopic, and computational studies*. Journal of Molecular Liquids, 2023. **386**: p. 122458.
7. Cruz, J., et al., *Experimental and theoretical study of 1-(2-ethylamino)-2-methylimidazoline as an inhibitor of carbon steel corrosion in acid media.* Journal of Electroanalytical chemistry, 2004. **566**(1): p. 111-121.
8. Revie, R.W., *Corrosion and corrosion control: an introduction to corrosion science and engineering*. 2008: John Wiley & Sons.
9. Umoren, S. and M. Solomon, *Recent developments on the use of polymers as corrosion inhibitors-a review.* The Open Materials Science Journal, 2014. **8**(1).
10. Prabhu, R., et al., *Quinol-2-thione compounds as corrosion inhibitors for mild steel in acid solution.* Materials Chemistry and Physics, 2008. **108**(2-3): p. 283-289.
11. Lgaz, H., et al., *Corrosion inhibition of mild steel in hydrochloric acid by 5, 5', 5''-(nitrilotris (methylene)) tris-(8-quinolinol): Experimental, theoretical and molecular dynamic studies.* Moroccan Journal of Chemistry, 2016. **4**(2): p. J. Chem. 4 N° 2 (2016) 592-612.
12. Newaz, K.M.S., et al., *Application of Natural Product Extracts as Green Corrosion Inhibitors for Metals and Alloys in Acid Pickling Processes-A review.* International Journal of Electrochemical Science, 2015. **10**(8): p. 6120-6134.

13. Khan, G., et al., *Electrochemical investigation on the corrosion inhibition of mild steel by Quinazoline Schiff base compounds in hydrochloric acid solution.* Journal of colloid and interface science, 2017. **502**: p. 134-145.
14. Islam, N., *Corrosion And Its Effect: A Critical Appraisal.* Journal of Survey in Fisheries Sciences, 2022: p. 396-408.
15. Gerhardus, H.K., et al., *Corrosion costs and preventive strategies in the United States.* Materials Performance, 2002: p. 3-9.
16. Lopata, S.L., *Evolution of steel protection: A personal view*. 1984: ASTM International.
17. Selvaraj, R., M. Selvaraj, and S. Iyer, *Studies on the evaluation of the performance of organic coatings used for the prevention of corrosion of steel rebars in concrete structures.* Progress in organic coatings, 2009. **64**(4): p. 454-459.
18. Peabody, A., *Peabody's control of pipeline corrosion.* 2001.
19. Muralidharan, S. and S. Iyer, *Pyrrole and its derivaties as inhibitors for the corrosion of mild steel in acidic solutions.* JOURNAL-ELECTROCHEMICAL SOCIETY OF INDIA, 1999. **48**(2): p. 113-120.
20. Rbaa, M., et al., *8-Hydroxyquinoline based chitosan derived carbohydrate polymer as biodegradable and sustainable acid corrosion inhibitor for mild steel: Experimental and computational analyses.* International journal of biological macromolecules, 2020. **155**: p. 645-655.
21. Peme, T., et al., *Adsorption and corrosion inhibition studies of some selected dyes as corrosion inhibitors for mild steel in acidic medium: gravimetric, electrochemical, quantum chemical studies and synergistic effect with iodide ions.* Molecules, 2015. **20**(9): p. 16004-16029.
22. Malik, M.A., et al., *Anti-corrosion ability of surfactants: a review.* International journal of electrochemical science, 2011. **6**(6): p. 1927-1948.
23. Verma, C.B., M. Quraishi, and A. Singh, *2-Aminobenzene-1, 3-dicarbonitriles as green corrosion inhibitor for mild steel in 1 M HCl: Electrochemical, thermodynamic, surface and quantum chemical investigation.* Journal of the Taiwan Institute of Chemical Engineers, 2015. **49**: p. 229-239.
24. Deng, S., X. Li, and X. Xie, *Hydroxymethyl urea and 1, 3-bis (hydroxymethyl) urea as corrosion inhibitors for steel in HCl solution.* Corrosion Science, 2014. **80**: p. 276-289.
25. Verma, C., M. Quraishi, and A. Singh, *A thermodynamical, electrochemical, theoretical and surface investigation of diheteroaryl thioethers as effective corrosion inhibitors for mild steel in 1 M HCl.* Journal of the Taiwan Institute of Chemical Engineers, 2016. **58**: p. 127-140.
26. Kesavan, D., M. Gopiraman, and N. Sulochana, *Green inhibitors for corrosion of metals: a review.* Chem. Sci. Rev. Lett, 2012. **1**(1): p. 1-8.
27. Olsson, C.A., et al., *An XPS study of the adsorption of organic inhibitors on mild steel surfaces.* Corrosion Science, 2000. **42**(7): p. 1197-1211.

28. Farmer, J., et al., *Corrosion resistance of thermally sprayed high-boron iron-based amorphous-metal coatings: Fe49. 7Cr17. 7Mn1. 9Mo7. 4W1. 6B15. 2C3. 8Si2. 4.* Journal of materials research, 2007. **22**(8): p. 2297-2311.
29. Smith, L., *Control of corrosion in oil and gas production tubing.* British Corrosion Journal, 1999. **34**(4): p. 247-253.
30. Nešić, S., *Key issues related to modelling of internal corrosion of oil and gas pipelines–A review.* Corrosion science, 2007. **49**(12): p. 4308-4338.
31. Hansson, C.M., *The impact of corrosion on society.* Metallurgical and Materials Transactions A, 2011. **42**: p. 2952-2962.
32. Leitch, J. *Corrosivity profile of Southern Africa using ISO 9223 methodology*. in *14th International Corrosion Congress*. 1999.
33. Yang, L.J., *Risk Analysis and Mitigation Strategies for Preventing Corrosion during Industrial Power Failure.*
34. Abdallah, M., E. Helal, and A. Fouda, *Aminopyrimidine derivatives as inhibitors for corrosion of 1018 carbon steel in nitric acid solution.* Corrosion science, 2006. **48**(7): p. 1639-1654.
35. Soares da Silva, R.d.C.F., et al., *Application of Pseudomonas cepacia CCT 6659 Biosurfactant as a Metal Corrosion Inhibitor in a Constructed Accelerated Corrosion Chamber (ACC).* Fermentation, 2024. **10**(12): p. 602.
36. Cwalina, B., *Biodeterioration of concrete, brick and other mineral-based building materials.* Understanding biocorrosion, 2014: p. 281-312.
37. Pyun, S.-I., *Strategies of metal corrosion protection.* ChemTexts, 2020. **7**(1): p. 2.
38. Seechurn, Y., J.A. Wharton, and B.Y. Surnam, *Mechanistic modelling of atmospheric corrosion of carbon steel in Port-Louis by electrochemical characterisation of rust layers.* Materials Chemistry and Physics, 2022. **291**: p. 126694.
39. Seechurn, Y., J.A. Wharton, and B.Y. Surnam, *Mechanistic modelling of atmospheric corrosion of carbon steel in Port-Louis by electrochemical characterisation of rust layers.* Materials Chemistry and Physics, 2022. **291**: p. 126694.
40. Tang, S., et al., *Analysis of internal corrosion of supercritical CO2 pipeline.* Corrosion Reviews, 2021. **39**(3): p. 219-241.
41. Savoye, S., et al., *Experimental investigations on iron corrosion products formed in bicarbonate/carbonate-containing solutions at 90 C.* Corrosion Science, 2001. **43**(11): p. 2049-2064.
42. Dong, J., T. Nishimura, and T. Kodama, *Corrosion behavior of carbon steel in bicarbonate (HCO3) solutions.* MRS Online Proceedings Library (OPL), 2002. **713**: p. JJ11. 8.
43. Eliyan, F.F. and A. Alfantazi. *Corrosion Mechanisms of Iron and Pipeline Steels in Bicarbonate and Carbonate Solutions—A Review*. in *Proceedings of the Conference of EUROCORR*. 2013.

44. Seneviratne, S., et al., *Changes in climate extremes and their impacts on the natural physical environment.* 2012.
45. Zhang, X., et al., *Indices for monitoring changes in extremes based on daily temperature and precipitation data.* Wiley Interdisciplinary Reviews: Climate Change, 2011. **2**(6): p. 851-870.
46. Sofiani, F.M., et al., *A hybrid probabilistic-deterministic framework for prediction of characteristic size of corrosion pits in low-carbon steel following long-term seawater exposure.* Corrosion Science, 2024. **232**: p. 112039.
47. Benstock, D. and F. Cegla, *Extreme value analysis (EVA) of inspection data and its uncertainties.* Ndt & E international, 2017. **87**: p. 68-77.
48. Perez, N., *Electrochemical corrosion*, in *Materials Science: Theory and Engineering*. 2024, Springer. p. 835-898.
49. Sato, N., *Basics of corrosion chemistry.* Green Corrosion Chemistry and Engineering, 2012. **1**.
50. Pourbaix, M., *Lectures on electrochemical corrosion*. 2012: Springer Science & Business Media.
51. Guma, T., Y.D. AkuSY, and M. Dauda, *Effects of environmental and metallurgical factors on corrosion of steel-a review.* International Journal of Innovative Research in Advanced Engineering, 2014. **1**(11): p. 94-105.
52. Gong, K., M. Wu, and G. Liu, *Comparative study on corrosion behaviour of rusted X100 steel in dry/wet cycle and immersion environments.* Construction and Building Materials, 2020. **235**: p. 117440.
53. Quadri, T.W., et al., *Fundamentals of corrosion chemistry*, in *Environmentally Sustainable Corrosion Inhibitors*. 2022, Elsevier. p. 25-45.
54. Berradja, A., *Electrochemical techniques for corrosion and tribocorrosion monitoring: fundamentals of electrolytic corrosion.* Corrosion inhibitors, 2019: p. 1-24.
55. Wang, H., *Corrosion Theory and Corrosion Characterization Techniques*, in *Corrosion in CO2 Capture, Transportation, Geological Utilization and Storage: Causes and Mitigation Strategies*. 2023, Springer. p. 9-30.
56. Zehra, S., M. Mobin, and J. Aslam, *An overview of the corrosion chemistry.* Environmentally Sustainable Corrosion Inhibitors, 2022: p. 3-23.
57. Verma, C.B., M. Quraishi, and A. Singh, *2-Aminobenzene-1, 3-dicarbonitriles as green corrosion inhibitor for mild steel in 1 M HCl: Electrochemical, thermodynamic, surface and quantum chemical investigation.* Journal of the Taiwan Institute of Chemical Engineers, 2015. **49**: p. 229-239.
58. Deng, S., X. Li, and X. Xie, *Hydroxymethyl urea and 1, 3-bis (hydroxymethyl) urea as corrosion inhibitors for steel in HCl solution.* Corrosion Science, 2014. **80**: p. 276-289.
59. Verma, C., M. Quraishi, and A. Singh, *A thermodynamical, electrochemical, theoretical and surface investigation of diheteroaryl thioethers as effective*

corrosion inhibitors for mild steel in 1 M HCl. Journal of the Taiwan Institute of Chemical Engineers, 2016. **58**: p. 127-140.
60. Rivera-Tarazona, L.K., Z.T. Campbell, and T.H. Ware, *Stimuli-responsive engineered living materials.* Soft Matter, 2021. **17**(4): p. 785-809.
61. Li, M., et al., *New concepts in electrolytes.* Chemical reviews, 2020. **120**(14): p. 6783-6819.
62. Ikeuba, A.I., et al., *A review of the electrochemical and galvanic corrosion behavior of important intermetallic compounds in the context of aluminum alloys.* RSC advances, 2024. **14**(43): p. 31921-31953.
63. Smith, L., *Control of corrosion in oil and gas production tubing.* British Corrosion Journal, 1999. **34**(4): p. 247-253.
64. Nešić, S., *Key issues related to modelling of internal corrosion of oil and gas pipelines–A review.* Corrosion science, 2007. **49**(12): p. 4308-4338.
65. Hansson, C.M., *The impact of corrosion on society.* Metallurgical and Materials Transactions A, 2011. **42**: p. 2952-2962.
66. Akpanyung, K. and R. Loto. *Pitting corrosion evaluation: a review*. in *Journal of Physics: Conference Series*. 2019. IOP Publishing.
67. Aghuy, A.A., et al., *Effect of grain size on pitting corrosion of 304L austenitic stainless steel.* Corrosion Science, 2015. **94**: p. 368-376.
68. Omran, B.A., et al., *Basic corrosion fundamentals, aspects and currently applied strategies for corrosion mitigation.* A New Era for Microbial Corrosion Mitigation Using Nanotechnology: Biocorrosion and Nanotechnology, 2020: p. 1-45.
69. Ali, M., et al., *Corrosion-related failures in heat exchangers.* Corrosion Reviews, 2021. **39**(6): p. 519-546.
70. Thanikachalam, V., *The Corrosion and Erosion of Centrifugal Pumps in a Marine Environment: Causes, Effects and Mitigation.* International Journal of Advances in Engineering Research, 2017. **13**(6): p. 34-52.
71. Hussain, M.I., et al., *Corrosion resistance of nanostructured metals and alloys*, in *Corrosion Protection at the Nanoscale*. 2020, Elsevier. p. 63-87.
72. Chauhan, D.S., et al., *A review on corrosion inhibitors for high-pressure supercritical CO2 environment: Challenges and opportunities.* Journal of Petroleum Science and Engineering, 2022. **215**: p. 110695.
73. Thompson, N.G., M. Yunovich, and D. Dunmire, *Cost of corrosion and corrosion maintenance strategies.* Corrosion Reviews, 2007. **25**(3-4): p. 247-262.
74. Hendrikx, J.L.H.M., *The zinc electrode: its behaviour in the nickel oxide-zinc accumulator.* 1984.
75. Vilche, J., et al., *A survey of argentinean atmospheric corrosion: II—Copper samples.* Corrosion science, 1997. **39**(4): p. 655-679.
76. Deyá, C. and P.S. Carrizo, *Corrosion on Ancient Metals*, in *Reverse Engineering of Ancient Metals*. 2022, Springer. p. 123-146.

77. Shifler, D.A., *Localized Corrosion.* LaQue's Handbook of Marine Corrosion, 2022: p. 63-121.
78. Pujar, M., U.K. Mudali, and S.S. Singh, *Electrochemical noise studies of the effect of nitrogen on pitting corrosion resistance of high nitrogen austenitic stainless steels.* Corrosion science, 2011. **53**(12): p. 4178-4186.
79. Vajo, J., et al., *Application of extreme value analysis to crevice corrosion.* Corrosion Science, 2003. **45**(3): p. 497-509.
80. Marsh, G., et al., *An assessment of carbon steel overpacks for radioactive waste disposal*. 1986, Commission of the European Communities.
81. Cardoso, M., S. Amaral, and E. Martini, *Temperature effect in the corrosion resistance of Ni–Fe–Cr alloy in chloride medium.* Corrosion Science, 2008. **50**(9): p. 2429-2436.
82. Schindelholz, E. and R.G. Kelly, *Wetting phenomena and time of wetness in atmospheric corrosion: a review.* Corrosion reviews, 2012. **30**(5-6): p. 135-170.
83. Brits, A.G. and A. Brits, *The effect of water quality and chemical composition on the corrosion of mild steel pipelines*. 1998: Water Research Commission.
84. Boyd, C.E., *Water quality: an introduction*. 2019: Springer Nature.
85. Wang, M.-H.S., L.K. Wang, and N.K. Shammas, *Glossary of acid rain management and environmental protection*, in *Handbook of environment and waste management: Acid rain and greenhouse gas pollution control*. 2020, World Scientific. p. 719-749.
86. Wu, Q., et al., *Behavior of sulfur oxides in nonferrous metal smelters and implications on future control and emission estimation.* Environmental Science & Technology, 2019. **53**(15): p. 8796-8804.
87. Azevedo, M.S., *Mécanismes de corrosion de l'acier revêtu d'alliage à base de ZnMgAl en tests accélérés et en environnement naturel*. 2014, Université Pierre et Marie Curie-Paris VI.
88. Gautam, K. and E. Van Der Hoek, *Literature study on environmental impact of floods.* Netherlands: Delft Cluster, 2003.
89. Estillore, A.D., J.V. Trueblood, and V.H. Grassian, *Atmospheric chemistry of bioaerosols: heterogeneous and multiphase reactions with atmospheric oxidants and other trace gases.* Chemical science, 2016. **7**(11): p. 6604-6616.
90. Ilori, M.O., O.S. Obayori, and L.B. Salam, *Aeromicrobiology*. 2023: Elsevier.
91. Durant, J., et al., *Air quality and human health.* Environmental Tracking for Public Health Surveillance, 2012: p. 129.
92. Wendisch, M. and J.-L. Brenguier, *Airborne measurements for environmental research: methods and instruments*. 2013: John Wiley & Sons.
93. Tilgner, A., et al., *Acidity and the multiphase chemistry of atmospheric aqueous particles and clouds.* Atmospheric Chemistry and Physics, 2021. **21**(17): p. 13483-13536.

94. Arenas-Díaz, F., et al., *Dust and aerosols in the Atacama Desert.* Earth-Science Reviews, 2022. **226**: p. 103925.
95. Wei, C., et al., *Corrosion protection of ships*, in *Handbook of Environmental Degradation of Materials*. 2018, Elsevier. p. 533-557.
96. Kucera, V. and E. Mattsson, *Atmospheric corrosion*, in *Corrosion mechanisms*. 2020, CRC Press. p. 211-284.
97. Shan, H., et al., *Hygroscopic salt-embedded composite materials for sorption-based atmospheric water harvesting.* Nature Reviews Materials, 2024: p. 1-23.
98. oto, A.O., A.S. Salgado, and E.B. Niño, *Thermodynamic analysis of high entropy alloys and their mechanical behavior in high and low-temperature conditions with a microstructural approach-a review.* Intermetallics, 2020. **124**: p. 106850.
99. Badiea, A. and K. Mohana, *Corrosion mechanism of low-carbon steel in industrial water and adsorption thermodynamics in the presence of some plant extracts.* Journal of Materials Engineering and Performance, 2009. **18**: p. 1264-1271.
100. Groysman, A., *Corrosion in systems for storage and transportation of petroleum products and biofuels: identification, monitoring and solutions*. 2014: Springer Science & Business Media.
101. Perry, S.C., et al., *Electrochemical synthesis of hydrogen peroxide from water and oxygen.* Nature Reviews Chemistry, 2019. **3**(7): p. 442-458.
102. Rector, B.K., *The Effect of Solution Parameters on the Interfacial Chemical Dynamics of Early-Stage Corrosion*. 2023, The University of Western Ontario (Canada).
103. Korsmeyer, R.W., *Diffusion controlled systems: hydrogels.* Polymers for controlled drug delivery, 2023: p. 15-37.
104. Gulikers, J., *Theoretical considerations on the supposed linear relationship between concrete resistivity and corrosion rate of steel reinforcement.* Materials and Corrosion, 2005. **56**(6): p. 393-403.
105. Pillai, R., S.S. Raiman, and B.A. Pint, *First steps toward predicting corrosion behavior of structural materials in molten salts.* Journal of nuclear materials, 2021. **546**: p. 152755.
106. Bhatt, M.D. and J.Y. Lee, *Advancement of platinum (Pt)-free (non-Pt precious metals) and/or metal-free (non-precious-metals) electrocatalysts in energy applications: A review and perspectives.* Energy & Fuels, 2020. **34**(6): p. 6634-6695.
107. GHOSH, K., *FOUNDATIONS OF CORROSION SCIENCE AND ENGINEERING*. 2024: PHI Learning Pvt. Ltd.
108. Ghali, E., *Corrosion resistance of aluminum and magnesium alloys: understanding, performance, and testing*. 2010: John Wiley & Sons.
109. Vanaei, H., A. Eslami, and A. Egbewande, *A review on pipeline corrosion, in-line inspection (ILI), and corrosion growth rate models.* International Journal of Pressure Vessels and Piping, 2017. **149**: p. 43-54.

110. Amaya-Gómez, R., et al., *Statistical soil characterization of an underground corroded pipeline using in-line inspections.* Metals, 2021. **11**(2): p. 292.
111. Zhang, Z., et al., *Electrochemical noise comparative study of pitting corrosion of 316L stainless steel fabricated by selective laser melting and wrought.* Journal of Electroanalytical Chemistry, 2021. **894**: p. 115351.
112. Olasunkanmi, L.O., *Corrosion: Favoured, yet undesirable-Its kinetics and thermodynamics*. Corrosion-Fundamentals and Protection Mechanisms, 2022: p. 15-33.
113. Sammut, S., E. Gatt, and R.P. Borg, *Microscale miniaturisation of chloride ion detection sensors for long-term embedding in reinforced concrete structures.* Structural Control and Health Monitoring, 2021. **28**(12): p. e2834.
114. Reddy, M.S.B., et al., *Sensors in advancing the capabilities of corrosion detection: A review.* Sensors and Actuators A: Physical, 2021. **332**: p. 113086.
115. Andrade Perdrix, C. and M.C. Alonso, *Test methods for on-site corrosion rate measurement of steel reinforcement in concrete by means of the polarization resistance method.* 2004.
116. Scully, J.R., *Polarization resistance method for determination of instantaneous corrosion rates.* Corrosion, 2000. **56**(02).
117. Groysman, A., *Corrosion monitoring.* Corrosion Reviews, 2009. **27**(4-5): p. 205-343.
118. Shreir, L.L., *Corrosion: metal/environment reactions*. 2013: Newnes.
119. Pedeferri, P. and P. Pedeferri, *Galvanic corrosion.* Corrosion Science and Engineering, 2018: p. 183-206.
120. Arya, C. and P. Vassie, *Influence of cathode-to-anode area ratio and separation distance on galvanic corrosion currents of steel in concrete containing chlorides.* Cement and Concrete Research, 1995. **25**(5): p. 989-998.
121. Carter, V., *Metallic coatings for corrosion control: corrosion control series*. 2013: Newnes.
122. Korotcenkov, G., *Gas response control through structural and chemical modification of metal oxide films: state of the art and approaches.* Sensors and Actuators B: Chemical, 2005. **107**(1): p. 209-232.
123. Verma, C., et al., *Principles and theories of green chemistry for corrosion science and engineering: design and application.* Green Chemistry, 2024. **26**(8): p. 4270-4357.
124. Wu, X., et al., *Current Status and Future Trends of High-Temperature Gas Environment Corrosion on Metal Coatings in Solid Waste Incinerators.* Process Safety and Environmental Protection, 2024.
125. Fu, T., et al., *Oxidation protection of high-temperature coatings on the surface of Mo-based alloys—A Review.* Coatings, 2022. **12**(2): p. 141.

126. Ameur-Boudabbous, I., et al., *Transverse approach between tunnel environment and corrosion: Particulate matter in the Grand Mare tunnel.* Journal of the Air & Waste Management Association, 2014. **64**(2): p. 198-218.
127. WANG, Z.-y., et al., *Corrosion behavior on aluminum alloy LY12 in simulated atmospheric corrosion process.* Transactions of Nonferrous Metals Society of China, 2007. **17**(2): p. 326-334.
128. Koushik, B.G., et al., *Review on modelling of corrosion under droplet electrolyte for predicting atmospheric corrosion rate.* Journal of Materials Science & Technology, 2021. **62**: p. 254-267.
129. Fousova, M., V. Valesova, and D. Vojtech, *Corrosion of 3D-printed AlSi9Cu3Fe alloy*. Manufacturing Technology, 2019. **19**(1): p. 29-36
130. Bullard, S.G., B.J. Gromek, and M. Fout, *The Silver Bridge Disaster of 1967*. 2012: Arcadia Publishing.
131. Vukasovich, M., *A glossary of corrosion-related terms used in science and industry*. 1995: SAE.
132. Fragoza-Mar, L., et al., *Corrosion inhibitor activity of 1, 3-diketone malonates for mild steel in aqueous hydrochloric acid solution.* Corrosion Science, 2012. **61**: p. 171-184.
133. Kim, Y.-W., *Novel 2-substituted isoflavones: A privileged structure approach to new agents for hormone-dependent breast cancer*. 2003: The Ohio State University.
134. Zeb, A. and Zeb, *Phenolic Antioxidants in Foods: Chemistry, Biochemistry and Analysis*. 2021: Springer.
135. Adly, O.M. and H.F. El-Shafiy, *New metal complexes derived from S-benzyldithiocarbazate (SBDTC) and chromone-3-carboxaldehyde: synthesis, characterization, antimicrobial, antitumor activity and DFT calculations.* Journal of Coordination Chemistry, 2019. **72**(2): p. 218-238.
136. Kumar, R., et al., *Experimental and theoretical approach to exploit the corrosion inhibition activity of 3-formyl chromone derivatives on mild steel in 1 m H2SO4.* Corrosion Reviews, 2017. **35**(2): p. 95-110.
137. López-Ortega, A., J. Arana, and R. Bayón, *Tribocorrosion of passive materials: a review on test procedures and standards.* International Journal of Corrosion, 2018. **2018**(1): p. 7345346.
138. Rosenfeld, I., *New data on the mechanisms of metals protection with inhibitors.* Corrosion (Houston);(United States), 1981. **37**(7).
139. Walker, J., et al., *Magnesium biomaterials for orthopedic application: a review from a biological perspective.* Journal of Biomedical Materials Research Part B: Applied Biomaterials, 2014. **102**(6): p. 1316-1331.
140. Adlani, L., et al., *Performance of a new pyrazole derivative in 1 M HCl on the corrosion of carbon steel: experimental, quantum chemical and molecular*

dynamics simulation studies. Journal of Dispersion Science and Technology, 2024: p. 1-14.

141. Ghamsarizade, R., B. Ramezanzadeh, and H.E. Mohammadloo, *Corrosion measurements in coatings and paintings, in Electrochemical and Analytical Techniques for Sustainable Corrosion Monitoring*. 2023, Elsevier. p. 217-264.

142. Tan, Y., *Experimental methods designed for measuring corrosion in highly resistive and inhomogeneous media.* Corrosion science, 2011. **53**(4): p. 1145-1155.

143. Marco, I. and O. Van der Biest, *Polarization measurements from a rotating disc electrode for characterization of magnesium corrosion.* Corrosion Science, 2016. **102**: p. 384-393.

144. Jmiai, A., et al., *A new trend in corrosion protection of copper in acidic medium by using Jujube shell extract as an effective green and environmentally safe corrosion inhibitor: Experimental, quantum chemistry approach and Monte Carlo simulation study.* Journal of Molecular Liquids, 2021. **322**: p. 114509.

145. Demo, J., et al. *Development of a wireless miniaturized smart sensor network for aircraft corrosion monitoring*. in *2010 IEEE Aerospace Conference*. 2010. IEEE.

146. Bauer, J.C., *Nanoparticles as reactive precursors: Synthesis of alloys, intermetallic compounds and multi-metal oxides through low-temperature annealing and conversion chemistry*. 2009: Texas A&M University.

147. Vengatesh, G. and M. Sundaravadivelu, *Non-toxic bisacodyl as an effective corrosion inhibitor for mild steel in 1 M HCl: Thermodynamic, electrochemical, SEM, EDX, AFM, FT-IR, DFT and molecular dynamics simulation studies.* Journal of Molecular Liquids, 2019. **287**: p. 110906.

148. Holmberg, K. and A. Matthews, *Coatings tribology: properties, mechanisms, techniques and applications in surface engineering*. 2009: Elsevier.

149. Izadi, M., T. Shahrabi, and B. Ramezanzadeh, *Active corrosion protection performance of an epoxy coating applied on the mild steel modified with an eco-friendly sol-gel film impregnated with green corrosion inhibitor loaded nanocontainers.* Applied Surface Science, 2018. **440**: p. 491-505.

150. Yang, L., *Techniques for corrosion monitoring*. 2020: Woodhead Publishing.

151. Inkson, B.J., *Scanning electron microscopy (SEM) and transmission electron microscopy (TEM) for materials characterization*, in *Materials characterization using nondestructive evaluation (NDE) methods*. 2016, Elsevier. p. 17-43.

152. Gateman, S.M., et al., *Measuring changes in wettability and surface area during micro droplet corrosion measurements.* Electrochimica Acta, 2021. **399**: p. 139402.

153. Beketov, G. and O. Shynkarenko, *SURFACE WETTING AND CONTACT ANGLE: BASICS AND CHARACTERISATION.* Chemistry, Physics & Technology of Surface/Khimiya, Fizyka ta Tekhnologiya Poverhni, 2022. **13**(1).
154. Faghihnejad, A. and H. Zeng, *Fundamentals of surface adhesion, friction, and lubrication.* Polymer Adhesion, Friction, and Lubrication, 2013: p. 1-57.
155. Gece, G., *The use of quantum chemical methods in corrosion inhibitor studies.* Corrosion science, 2008. **50**(11): p. 2981-2992.
156. Engkvist, O., et al., *Computational prediction of chemical reactions: current status and outlook.* Drug discovery today, 2018. **23**(6): p. 1203-1218.
157. Reed, B.C., *Schrödinger's Equation*, in *Quantum Mechanics: An Enhanced Primer*. 2022, Springer. p. 35-56.
158. Fleisch, D.A., *A student's guide to the Schrödinger equation*. 2020: Cambridge University Press.
159. Cazorla, C. and J. Boronat, *Simulation and understanding of atomic and molecular quantum crystals.* Reviews of Modern Physics, 2017. **89**(3): p. 035003.
160. Hanc, J. *The time-independent Schrödinger equation in the frame of Feynman's version of quantum mechanics*. in *Proceedings of the 11th Workshop on Multimedia in Physics Teaching and Learning, Szeged, Hungary*. 2006.
161. Accorinti, H.L. and J.C.M. González, *Models and idealizations in quantum chemistry: The case of the born-oppenheimer approximation.* Philosophical Perspectives in Quantum Chemistry, 2022: p. 107-124.
162. Michaud, A., *Demystifying the Lorentz Force Equation.* Journal of Modern Physics, 2022. **13**(5): p. 776-838.
163. Takatsuka, K., et al., *Chemical Theory Beyond the Born-Oppenheimer Paradigm: Nonadiabatic Electronic and Nuclear Dynamics in Chemical Reactions*. 2014: World Scientific.
164. Takatsuka, K. and T. Yonehara, *Exploring dynamical electron theory beyond the Born–Oppenheimer framework: from chemical reactivity to non-adiabatically coupled electronic and nuclear wavepackets on-the-fly under laser field.* Physical Chemistry Chemical Physics, 2011. **13**(11): p. 4987-5016.
165. Ohno, K., K. Esfarjani, and Y. Kawazoe, *Computational materials science: from ab initio to Monte Carlo methods*. 2018: Springer.
166. Parrish, R.M., et al., *Psi4 1.1: An open-source electronic structure program emphasizing automation, advanced libraries, and interoperability.* Journal of chemical theory and computation, 2017. **13**(7): p. 3185-3197.
167. Louie, S.G., et al., *Discovering and understanding materials through computation.* Nature Materials, 2021. **20**(6): p. 728-735.
168. Schütt, K.T., et al., *Unifying machine learning and quantum chemistry with a deep neural network for molecular wavefunctions.* Nature communications, 2019. **10**(1): p. 5024.
169. Mayer, I., *Atomic orbitals from molecular wave functions: The effective minimal basis.* The Journal of Physical Chemistry, 1996. **100**(15): p. 6249-6257.

170. Wieduwilt, E.K., et al., *A step toward the quantification of noncovalent interactions in large biological systems: The independent gradient model-extremely localized molecular orbital approach.* Journal of Chemical Information and Modeling, 2021. **61**(2): p. 795-809.
171. Bannwarth, C., et al., *Extended tight-binding quantum chemistry methods.* Wiley Interdisciplinary Reviews: Computational Molecular Science, 2021. **11**(2): p. e1493.
172. Al-Mahayni, H., et al., *Experimental methods in chemical engineering: Density functional theory.* The Canadian Journal of Chemical Engineering, 2021. **99**(9): p. 1885-1911.
173. Sebens, C.T., *Electron charge density: A clue from quantum chemistry for quantum foundations.* Foundations of Physics, 2021. **51**(4): p. 75.
174. Gupta, A.K., et al., *Equivariant Neural Networks Utilizing Molecular Clusters for Accurate Molecular Crystal Lattice Energy Predictions.* ACS omega, 2024. **9**(38): p. 40269-40282.
175. Wind, P., et al., *MRChem multiresolution analysis code for molecular electronic structure calculations: performance and scaling properties.* Journal of Chemical Theory and Computation, 2022. **19**(1): p. 137-146.
176. Fathurrahman, F., et al., *PWDFT. jl: A Julia package for electronic structure calculation using density functional theory and plane wave basis.* Computer Physics Communications, 2020. **256**: p. 107372.
177. Kohanoff, J., *Electronic structure calculations for solids and molecules: theory and computational methods*. 2006: Cambridge university press.
178. Burton, H., *Holomorphic Hartree-Fock Theory: Moving Beyond the Coulson-Fischer Point*. 2020.
179. Corzo, H.H., et al., *Using projection operators with maximum overlap methods to simplify challenging self-consistent field optimization.* Journal of Computational Chemistry, 2022. **43**(6): p. 382-390.
180. Townsend, J. and K.D. Vogiatzis, *Data-driven acceleration of the coupled-cluster singles and doubles iterative solver.* The journal of physical chemistry letters, 2019. **10**(14): p. 4129-4135.
181. Ambroise, M.A., *The Algebraic Diagrammatic Construction Method for High Performance Computing Environments Using An Atomic Orbital Representation*. 2021.
182. Li, W., Z. Ni, and S. Li, *Cluster-in-molecule local correlation method for post-Hartree–Fock calculations of large systems.* Molecular Physics, 2016. **114**(9): p. 1447-1460.
183. Andreussi, O. and G. Fisicaro, *Continuum embeddings in condensed-matter simulations.* International Journal of Quantum Chemistry, 2019. **119**(1): p. e25725.

184. Huix-Rotllant, M., N. Ferré, and M. Barbatti, *Time-dependent density functional theory.* Quantum Chemistry and Dynamics of Excited States: Methods and Applications, 2020: p. 13-46.
185. Davidson, M.L., S. Grabowsky, and D. Jayatilaka, *X-ray constrained wavefunctions based on Hirshfeld atoms. I. Method and review.* Acta Crystallographica Section B: Structural Science, Crystal Engineering and Materials, 2022. **78**(3): p. 312-332.
186. Tsirelson, V.G. and R.P. Ozerov, *Electron density and bonding in crystals: Principles, theory and X-ray diffraction experiments in solid state physics and chemistry*. 2020: CRC Press.
187. Moldabekov, Z., et al., *Ab initio static exchange–correlation kernel across Jacob's ladder without functional derivatives.* Journal of Chemical Theory and Computation, 2023. **19**(4): p. 1286-1299.
188. Liu, X., *Theoretical Investigations into Thermal and Electrocatalytic Conversion of Carbon Dioxide*. 2018: Stanford University.
189. Zhu, Y. and J.M. Herbert, *Self-consistent predictor/corrector algorithms for stable and efficient integration of the time-dependent Kohn-Sham equation.* The Journal of chemical physics, 2018. **148**(4).
190. Han, Y., et al., *Machine learning accelerates quantum mechanics predictions of molecular crystals.* Physics Reports, 2021. **934**: p. 1-71.
191. Prentice, J.C., et al., *The ONETEP linear-scaling density functional theory program.* The Journal of chemical physics, 2020. **152**(17).
192. Verma, D.K., *Density functional theory (DFT) as a powerful tool for designing corrosion inhibitors in aqueous phase.* Advanced engineering testing, 2018. **87**.
193. Saha, S.K., et al., *Molecular level insights for the corrosion inhibition effectiveness of three amine derivatives on the carbon steel surface in the adverse medium: a combined density functional theory and molecular dynamics simulation study.* Surfaces and interfaces, 2018. **10**: p. 65-73.
194. Qadr, H.M. and D.M. Mamand, *Molecular structure and density functional theory investigation corrosion inhibitors of some oxadiazoles.* Journal of Bio-and Tribo-Corrosion, 2021. **7**(4): p. 140.
195. Awad, M.K., M.R. Mustafa, and M.M.A. Elnga, *Computational simulation of the molecular structure of some triazoles as inhibitors for the corrosion of metal surface.* Journal of molecular structure: theochem, 2010. **959**(1-3): p. 66-74.
196. Merimi, I., et al., *Adsorption and inhibition mechanism of (Z)-4-((4-methoxybenzylidene) amino)-5-methyl-2, 4-dihydro-3H-1, 2, 4-triazole-3-thione on carbon steel corrosion in HCl: Experimental and theoretical insights.* Journal of Molecular Structure, 2021. **1231**: p. 129901.

197. Li, N., et al., *In situ electrochemical atomic force microscopy and auger electro spectroscopy study on the passive film structure of 2024-T3 aluminum alloy combined with a density functional theory calculation.* Advanced Engineering Materials, 2019. **21**(12): p. 1900386.
198. Kumer, A., M.N. Sarker, and S. Paul, *The simulating study of HOMO, LUMO, thermo physical and quantitative structure of activity relationship (QSAR) of some anticancer active ionic liquids.* Eurasian Journal of Environmental Research, 2019. **3**(1): p. 1-10.
199. Saha, S.K., et al., *Novel Schiff-base molecules as efficient corrosion inhibitors for mild steel surface in 1 M HCl medium: experimental and theoretical approach.* Physical Chemistry Chemical Physics, 2016. **18**(27): p. 17898-17911.
200. Verma, D.K., et al., *Computational modeling: theoretical predictive tools for designing of potential organic corrosion inhibitors.* Journal of Molecular Structure, 2021. **1236**: p. 130294.
201. Elmsellem, H., et al., *Anti-corrosive Properties and Quantum Chemical Study of (E)-4-Methoxy-N-(Methoxybenzylidene) Aniline and (E)-N-(4-Methoxybenzylidene)-4-Nitroaniline Coating on Mild Steel in Molar Hydrochloric.* International Journal of Electrochemical Science, 2014. **9**(9): p. 5328-5351.
202. Cortés-Guzmán, F. and R.F. Bader, *Complementarity of QTAIM and MO theory in the study of bonding in donor–acceptor complexes.* Coordination Chemistry Reviews, 2005. **249**(5-6): p. 633-662.
203. Abdulazeez, I., M. Khaled, and A.A. Al-Saadi, *Impact of electron-withdrawing and electron-donating substituents on the corrosion inhibitive properties of benzimidazole derivatives: a quantum chemical study.* Journal of Molecular Structure, 2019. **1196**: p. 348-355.
204. Murmu, M., et al., *Density functional theory, Monte Carlo simulation and non-covalent interaction study for exploring the adsorption and corrosion inhibiting property of double azomethine functionalised organic molecules.* Journal of Adhesion Science and Technology, 2022. **36**(23-24): p. 2732-2760.
205. Kumara, A.M., et al., *In-situ synthesis of hydrophobic SiO 2-PMMA composite for surface protective coatings: Experimental and quantum chemical analysis.* Polymer, 2015. **77**(44): p. 79-86.
206. Targema, M., N.O. Obi-Egbedi, and M.D. Adeoye, *Molecular structure and solvent effects on the dipole moments and polarizabilities of some aniline derivatives.* Computational and theoretical Chemistry, 2013. **1012**: p. 47-53.
207. HUSSAIN, S., et al., *MATERIALS CHEMISTRY: PROPERTIES AND APPLICATIONS.* CHEMISTRY: THE MODERN APPROACH, 2024: p. 29.
208. Abdou, R., *MAAE 4917-Crystals.* 2021.
209. Kumar, C.S., M.M. Singh, and R. Krishna, *Advanced Materials Characterization: Basic Principles, Novel Applications, and Future Directions*. 2023: CRC Press.

210. Zhang, G.G. and D. Zhou, *Crystalline and amorphous solids*, in *Developing solid oral dosage forms*. 2017, Elsevier. p. 23-57.
211. West, A.R., *Solid state chemistry and its applications*. 2022: John Wiley & Sons.
212. Glusker, J.P. and K.N. Trueblood, *Crystal Structure Analysis: A Primer, IUCr Texts on Crystallography*. 2010, Oxford University Press.
213. Müller, U. and G. de la Flor, *Symmetry relationships between crystal structures: applications of crystallographic group theory in crystal chemistry*. Vol. 24. 2024: Oxford University Press.
214. Wells, A.F., *Structural inorganic chemistry*. 2012: Oxford University Press, USA.
215. Tang, Y., G. Dong, and Y.F. Zhao, *A hybrid geometric modeling method for lattice structures fabricated by additive manufacturing.* The International Journal of Advanced Manufacturing Technology, 2019. **102**: p. 4011-4030.
216. Basavaraju, N., et al., *Luminescent and thermal properties of novel orange–red emitting MgNb 2 O 6: Sm 3+ phosphors for displays, photo catalytic and sensor applications.* SN Applied Sciences, 2021. **3**: p. 1-15.
217. Steed, K.M. and J.W. Steed, *Packing problems: high Z' crystal structures and their relationship to cocrystals, inclusion compounds, and polymorphism.* Chemical Reviews, 2015. **115**(8): p. 2895-2933.
218. Holgate, S.A., *Understanding solid state physics*. 2021: cRc Press.
219. Woolman, G., et al., *Structural and electronic properties of the alkali metal incommensurate phases.* Physical Review Materials, 2018. **2**(5): p. 053604.
220. Ariza, M. and M. Ortiz, *Discrete crystal elasticity and discrete dislocations in crystals.* Archive for Rational Mechanics and Analysis, 2005. **178**: p. 149-226.
221. Hicks, D., et al., *The AFLOW library of crystallographic prototypes: part 3.* Computational Materials Science, 2021. **199**: p. 110450.
222. Albrecht, C., et al., *Asymmetric equilibrium core structures of pyramidal-II⟨ c+ a⟩ dislocations in ten hexagonal-close-packed metals.* Physical Review Materials, 2021. **5**(4): p. 043602.
223. Czycholl, G., *Solid State Theory, Volume 1: Basics: Phonons and Electrons in Crystals*. 2023: Springer Nature.
224. Shifler, D.A., *Structural Alloys in Marine Service.* LaQue's Handbook of Marine Corrosion, 2022: p. 453-526.
225. Sun, S., et al., *Identification of the Miller indices of a crystallographic plane: a tutorial and a comprehensive review on fundamental theory, universal methods based on different case studies and matters needing attention.* Nanoscale, 2020. **12**(32): p. 16657-16677.
226. Callister Jr, W.D. and D.G. Rethwisch, *Materials science and engineering: an introduction*. 2020: John wiley & sons.
227. Sholl, D.S. and J.A. Steckel, *Density functional theory: a practical introduction*. 2022: John Wiley & Sons.

228. Chen, H., J.L. Muros-Cobos, and A. Amirfazli, *Contact angle measurement with a smartphone.* Review of Scientific Instruments, 2018. **89**(3).
229. Williams, D., et al., *Contact angle measurements using cellphone cameras to implement the Bikerman method.* Galvanotechnik, 2011. **102**(8): p. 1718.
230. Hsissou, R., et al., *Evaluation of corrosion inhibition performance of phosphorus polymer for carbon steel in [1 M] HCl: Computational studies (DFT, MC and MD simulations).* Journal of Materials Research and Technology, 2020. **9**(3): p. 2691-2703.
231. El-Haitout, B., et al., *Exploring the feasibility of new eco-friendly heterocyclic compounds for establishing efficient corrosion protection for N80 steel in a simulated oil well acidizing environment: From molecular-level prediction to experimental validation.* Colloids and Surfaces A: Physicochemical and Engineering Aspects, 2023. **656**: p. 130372.
232. Kumar, R., et al., *Corrosion inhibition performance of chromone-3-acrylic acid derivatives for low alloy steel with theoretical modeling and experimental aspects*. Journal of Molecular Liquids, 2017. **243**: p. 439-450.
233. Dehri, İ. and M. Özcan, *The effect of temperature on the corrosion of mild steel in acidic media in the presence of some sulphur-containing organic compounds.* Materials Chemistry and Physics, 2006. **98**(2-3): p. 316-323.
234. Nesane, T., S.S. Mnyakeni-Moleele, and L.C. Murulana, *Exploration of synthesized quaternary ammonium ionic liquids as unharmful anti-corrosives for aluminium utilizing hydrochloric acid medium.* Heliyon, 2020. **6**(6).
235. Popova, A., M. Christov, and A. Vasilev, *Mono-and dicationic benzothiazolic quaternary ammonium bromides as mild steel corrosion inhibitors. Part III: influence of the temperature on the inhibition process.* Corrosion science, 2015. **94**: p. 70-78.
236. Popova, A., et al., *AC and DC study of the temperature effect on mild steel corrosion in acid media in the presence of benzimidazole derivatives.* Corrosion science, 2003. **45**(1): p. 33-58.
237. Laabaissi, T., et al., *Coupling of chemical, electrochemical and theoretical approach to study the corrosion inhibition of mild steel by new quinoxaline compounds in 1 M HCl.* Heliyon, 2020. **6**(5).
238. Korde, R., et al., *Electrochemical and Thermo Dynamical Investigation of 5-ethyl 4-(4-methoxyphenyl)-6-methyl-2-thioxo-1, 2, 3, 4 tetrahydropyrimidine-5-carboxylate on Corrosion Inhibition Behavior of Aluminium in 1M Hydrochloric Acid Medium.* International Journal of Electrochemical Science, 2015. **10**(2): p. 1081-1093.
239. Obot, I., N. Obi-Egbedi, and S. Umoren, *The synergistic inhibitive effect and some quantum chemical parameters of 2, 3-diaminonaphthalene and iodide ions on the hydrochloric acid corrosion of aluminium.* Corrosion Science, 2009. **51**(2): p. 276-282.

240. Solomon, M., et al., *Inhibitive and adsorption behaviour of carboxymethyl cellulose on mild steel corrosion in sulphuric acid solution.* Corrosion science, 2010. **52**(4): p. 1317-1325.
241. Poornima, T., J. Nayak, and A. Shetty, *Corrosion inhibition of the annealed 18 Ni 250 grade maraging steel in 0.67 m phosphoric acid by 3, 4-dimethoxybenzaldehydethiosemicarbazone.* Chemical Sciences Journal, 2012.
242. Korde, R., et al., *Electrochemical and Thermo Dynamical Investigation of 5-ethyl 4-(4-methoxyphenyl)-6-methyl-2-thioxo-1, 2, 3, 4 tetrahydropyrimidine-5-carboxylate on Corrosion Inhibition Behavior of Aluminium in 1M Hydrochloric Acid Medium.* International Journal of Electrochemical Science, 2015. **10**(2): p. 1081-1093.
243. Mu, G.N., X. Li, and F. Li, *Synergistic inhibition between o-phenanthroline and chloride ion on cold rolled steel corrosion in phosphoric acid.* Materials Chemistry and Physics, 2004. **86**(1): p. 59-68.
244. Zarrouk, A., et al., *New 1H-pyrrole-2, 5-dione derivatives as efficient organic inhibitors of carbon steel corrosion in hydrochloric acid medium: electrochemical, XPS and DFT studies.* Corrosion Science, 2015. **90**: p. 572-584.
245. Gomma, G.K. and M.H. Wahdan, *Schiff bases as corrosion inhibitors for aluminium in hydrochloric acid solution.* Materials chemistry and physics, 1995. **39**(3): p. 209-213.
246. Tang, L., et al., *The effect of 1-(2-pyridylazo)-2-naphthol on the corrosion of cold rolled steel in acid media: Part 1: Inhibitive action in 1.0 M hydrochloric acid.* Materials Chemistry and Physics, 2005. **94**(2-3): p. 353-359.
247. Ghasemi, O., et al., *Inhibition effect of a synthesized N, N'-bis (2-hydroxybenzaldehyde)-1, 3-propandiimine on corrosion of mild steel in HCl.* Journal of Central South University, 2013. **20**: p. 301-311.
248. Eddy, N.O., et al., *A brief review on fruit and vegetable extracts as corrosion inhibitors in acidic environments.* Molecules, 2022. **27**(9): p. 2991.
249. Yadav, M., et al., *New pyrimidine derivatives as efficient organic inhibitors on mild steel corrosion in acidic medium: electrochemical, SEM, EDX, AFM and DFT studies.* Journal of Molecular Liquids, 2015. **211**: p. 135-145.
250. Kraš, A. and I. Milošev, *Comparative electrochemical and thermodynamic study of cold-rolled steel, Al alloy AA5754, and Zn corrosion in fluoride and chloride solutions*. Electrochimica Acta, 2024. **502**: p. 144819.
251. Ahanotu, C., V. Ezigbo, and S. Okonkwo, *Electrochemical insights into the inhibitory efficiency of crude leaf extract of Datura discolor against corrosion of low-carbon steel in loe pH media–EIS and PDP approaches.* J. Mater. Environ. Sci., 15 (2), 251, 2024. **267**.
252. Fernine, Y., et al., *Anti-corrosion performance of Ocimum basilicum seed extract as environmental friendly inhibitors for mild steel in HCl solution: evaluations of electrochemical, EDX, DFT and Monte Carlo.* Journal of Molecular Liquids, 2022. **355**: p. 118867.

253. Natarajan, K., *Principles of corrosion processes.* Corrosion Processes: Sensing, Monitoring, Data Analytics, Prevention/Protection, Diagnosis/Prognosis and Maintenance Strategies, 2020: p. 27-82.
254. Ferreira, E., et al., *Evaluation of the inhibitor effect of L-ascorbic acid on the corrosion of mild steel.* Materials Chemistry and Physics, 2004. **83**(1): p. 129-134.
255. Mashuga, M.E., et al., *Adsorption, thermodynamic and quantum chemical studies of 1-hexyl-3-methylimidazolium based ionic liquids as corrosion inhibitors for mild steel in HCl.* Materials, 2015. **8**(6): p. 3607-3632.
256. Tan, J., et al., *Electrochemical and computational studies on the corrosion inhibition of mild steel by 1-hexadecyl-3-methylimidazolium bromide in HCl medium.* International Journal of Electrochemical Science, 2020. **15**(3): p. 1893-1903.
257. Yilmaz, N., A. Fitoz, and K.C. Emregül, *A combined electrochemical and theoretical study into the effect of 2-((thiazole-2-ylimino) methyl) phenol as a corrosion inhibitor for mild steel in a highly acidic environment.* Corrosion Science, 2016. **111**: p. 110-120.
258. Mashuga, M.E., et al., *Experimental and computational mediated illustration of effect of different substituents on adsorption tendency of phthalazinone derivatives on mild steel surface in acidic medium.* Journal of Molecular Liquids, 2020. **305**: p. 112844.
259. Li, H., J. Duan, and D. Wei, *Comparison on corrosion behaviour of arc sprayed and zinc-rich coatings.* Surface and Coatings Technology, 2013. **235**: p. 259-266.
260. Singh, M.B., et al., *Theory of impedance for initial corrosion of metals under a thin electrolyte layer: a coupled charge transfer-diffusion model.* Journal of Chemical Sciences, 2022. **134**(1): p. 32.
261. Kotteeswaran, P., et al., *Influence of zinc additive and pH on the electrochemical activities of β-nickel hydroxide materials and its applications in secondary batteries.* Journal of Energy Storage, 2017. **9**: p. 12-24.
262. El-Sayed, A.-R., et al., *The inhibitive action of 2-mercaptobenzothiazole on the porosity of corrosion film formed on aluminum and aluminum–titanium alloys in hydrochloric acid solution.* Scientific Reports, 2023. **13**(1): p. 4812.
263. Lahmady, S., et al., *Electrochemical Examination of an Eco-friendly Corrosion Inhibitor.* Analytical and Bioanalytical Electrochemistry, 2022. **14**(3): p. 303-318.
264. Czech, E. and T. Troczynski, *Hydrogen generation through massive corrosion of deformed aluminum in water.* International journal of hydrogen energy, 2010. **35**(3): p. 1029-1037.
265. Sharma, G. and R.P. Singh. *Corrosive behaviour of friction stir Al alloy welding technique: a review*. in *IOP Conference Series: Materials Science and Engineering*. 2021. IOP Publishing.

266. Khaled, K., *Experimental, density function theory calculations and molecular dynamics simulations to investigate the adsorption of some thiourea derivatives on iron surface in nitric acid solutions.* Applied Surface Science, 2010. **256**(22): p. 6753-6763.
267. Kaya, F., R. Solmaz, and I.H. Gecibesler, *Adsorption and corrosion inhibition capability of Rheum ribes root extract (Işgın) for mild steel protection in acidic medium: A comprehensive electrochemical, surface characterization, synergistic inhibition effect, and stability study.* Journal of Molecular Liquids, 2023. **372**: p. 121219.
268. Zargouni, Y., W. Sassi, and K. Alouani, *Corrosion Inhibition of AISI 316L and Modified-AISI 630 Stainless Steel by the New Organic Inhibitor [(CH3) 2N] 3PSe in Chloride Media: Electrochemical and Physical Study.* Mediterranean Journal of Chemistry, 2015. **4**(2): p. 105-110.
269. Ouakki, M., et al., *A detailed investigation on the corrosion inhibition effect of by newly synthesized pyran derivative on mild steel in 1.0 M HCl: Experimental, surface morphological (SEM-EDS, DRX& AFM) and computational analysis (DFT & MD simulation).* Journal of Molecular Liquids, 2021. **344**: p. 117777.
270. Abdel-Karim, A.M. and A.M. El-Shamy, *A review on green corrosion inhibitors for protection of archeological metal artifacts.* Journal of Bio-and Tribo-Corrosion, 2022. **8**(2): p. 35.
271. Ismail, M.F., et al., *Surface characterization of thin-film composite membranes using contact angle technique: Review of quantification strategies and applications.* Advances in Colloid and Interface Science, 2022. **299**: p. 102524.
272. Rasouli, S., et al., *Superhydrophobic and superoleophilic membranes for oil-water separation application: A comprehensive review.* Materials & Design, 2021. **204**: p. 109599.
273. Kuznetsov, Y.I. and G.V. Redkina, *Thin protective coatings on metals formed by organic corrosion inhibitors in neutral media.* Coatings, 2022. **12**(2): p. 149.
274. Rocca, M., T. Rahman, and L. Vattuone, *Springer handbook of surface science*. 2021: Springer Nature.
275. van Bokhoven, J.A., et al., *Al K-edge near-edge X-ray absorption fine structure (NEXAFS) study on the coordination structure of aluminum in minerals and Y zeolites.* The Journal of Physical Chemistry B, 1999. **103**(36): p. 7557-7564.
276. Chandanabodhi, D. and T. Nanok, *A DFT study of the ring-opening polymerization mechanism of l-lactide and ε-caprolactone using aluminium salen-type initiators: Towards an understanding of their reactivities in homo-and copolymerization.* Molecular Catalysis, 2017. **436**: p. 145-156.

277. Beltrán, H.I., et al., *Nanocap-Shaped Tin Phthalocyanines: Synthesis, Characterization, and Corrosion Inhibition Activity.* Chemistry–A European Journal, 2005. **11**(9): p. 2705-2715.
278. Daoudi, W., et al., *Synthesis, characterization, and corrosion inhibition activity of new imidazo [1.2-a] pyridine chalcones.* Materials Science and Engineering: B, 2023. **290**: p. 116287.
279. Beltrán, H.I., et al., *Nanocap-Shaped Tin Phthalocyanines: Synthesis, Characterization, and Corrosion Inhibition Activity.* Chemistry–A European Journal, 2005. **11**(9): p. 2705-2715.
280. Manganyi, L.E., *Synthetic studies of novel chromone-2-carboxylate derivatives and their biological evaluations*. 2021.
281. Cagide, F., et al., *Optimizing the synthetic route of chromone-2-carboxylic acids: A step forward to speed-up the discovery of chromone-based multitarget-directed ligands.* Molecules, 2019. **24**(23): p. 4214.

Appendix

1. ^{1}H AND ^{13}C NMR Spectra of synthesized compounds

1.2. ^{1}H AND ^{13}C NMR Spectra of 6-substitutedchromone-2-carboxylate

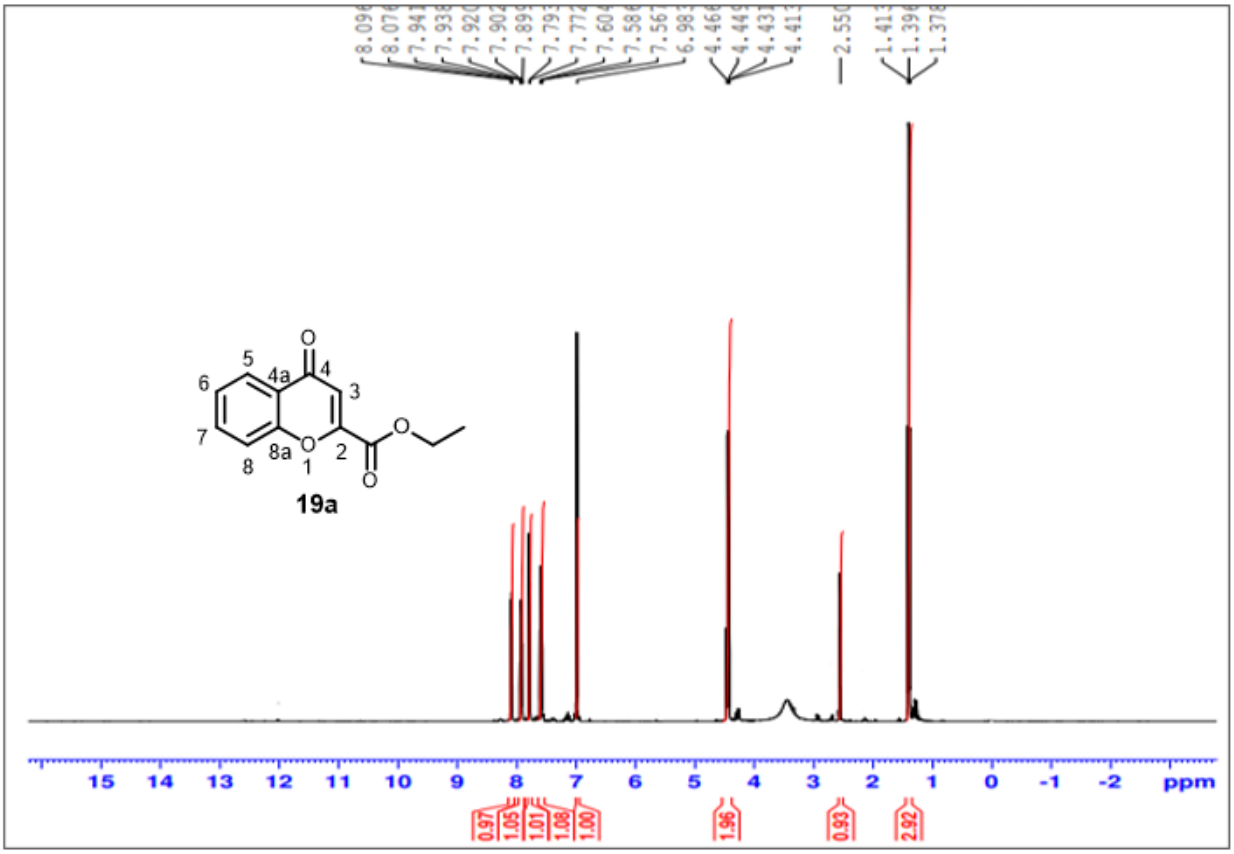

Appendix 1: ^{1}H NMR spectrum of ethyl Chromone-2-carboxylate **19a** in DMSO-d_6 (at 400 MHz).

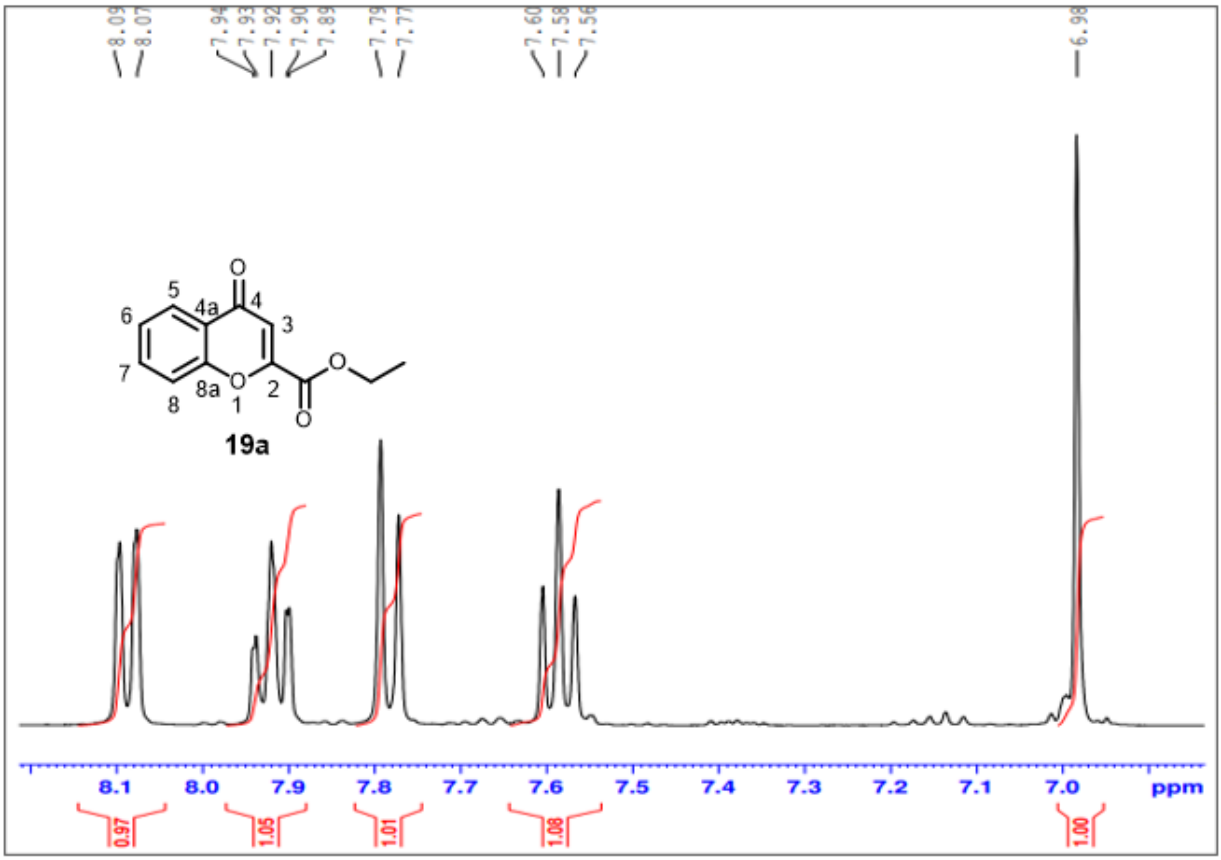

Appendix 2: ^{1}H NMR expansion spectrum of ethyl Chromone-2-carboxylate **19a** in DMSO-d_6 (at 400 MHz)

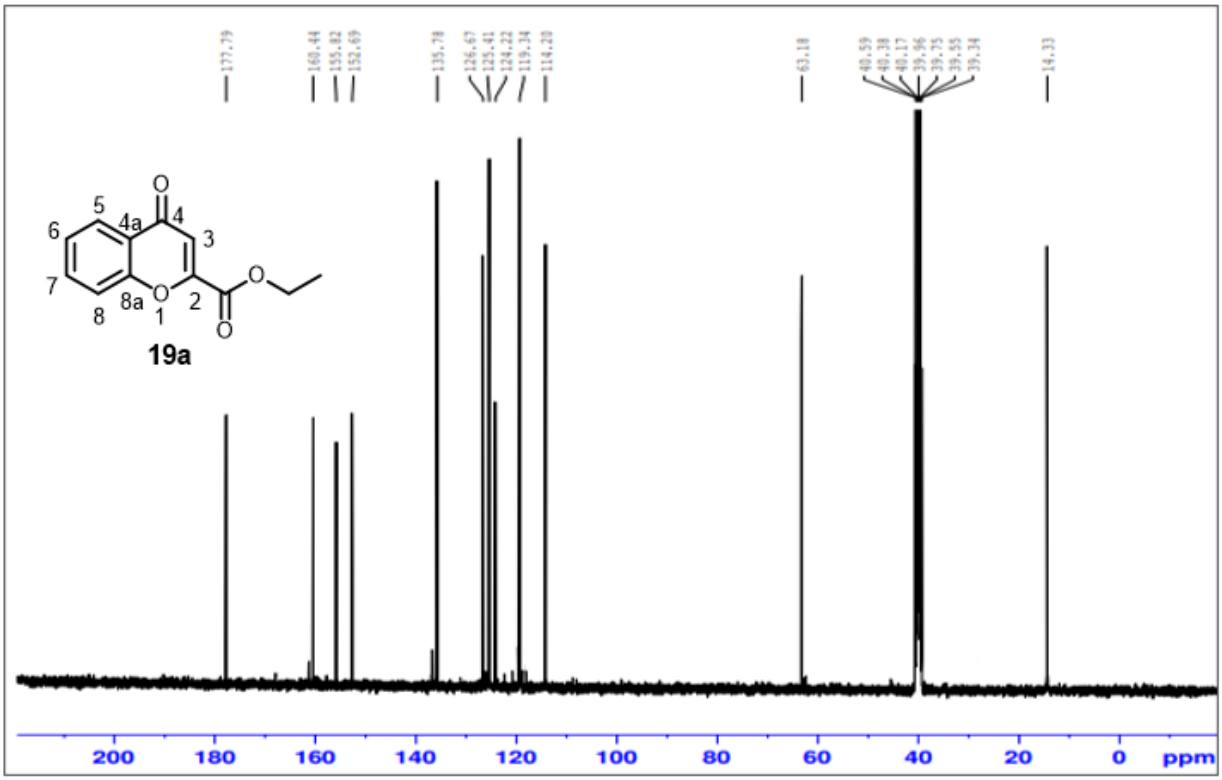

Appendix 3: ^{13}C NMR spectrum of ethyl Chromone-2-carboxylate **19a** in DMSO-d_6 (at 100 MHz)

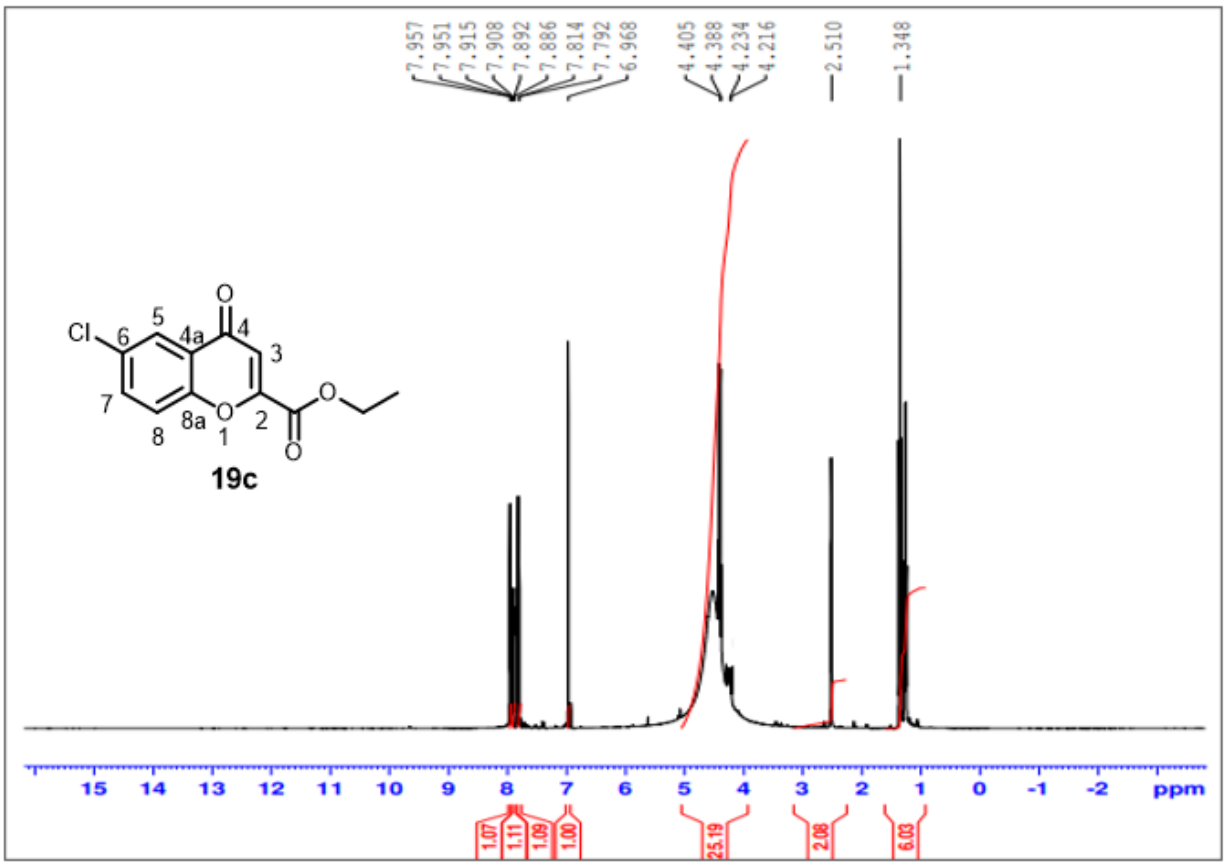

Appendix 4: ^{1}H NMR spectrum of ethyl 6-Chloro-chromone-2-carboxylate **19c** in DMSO-d_6 (at 400 MHz)

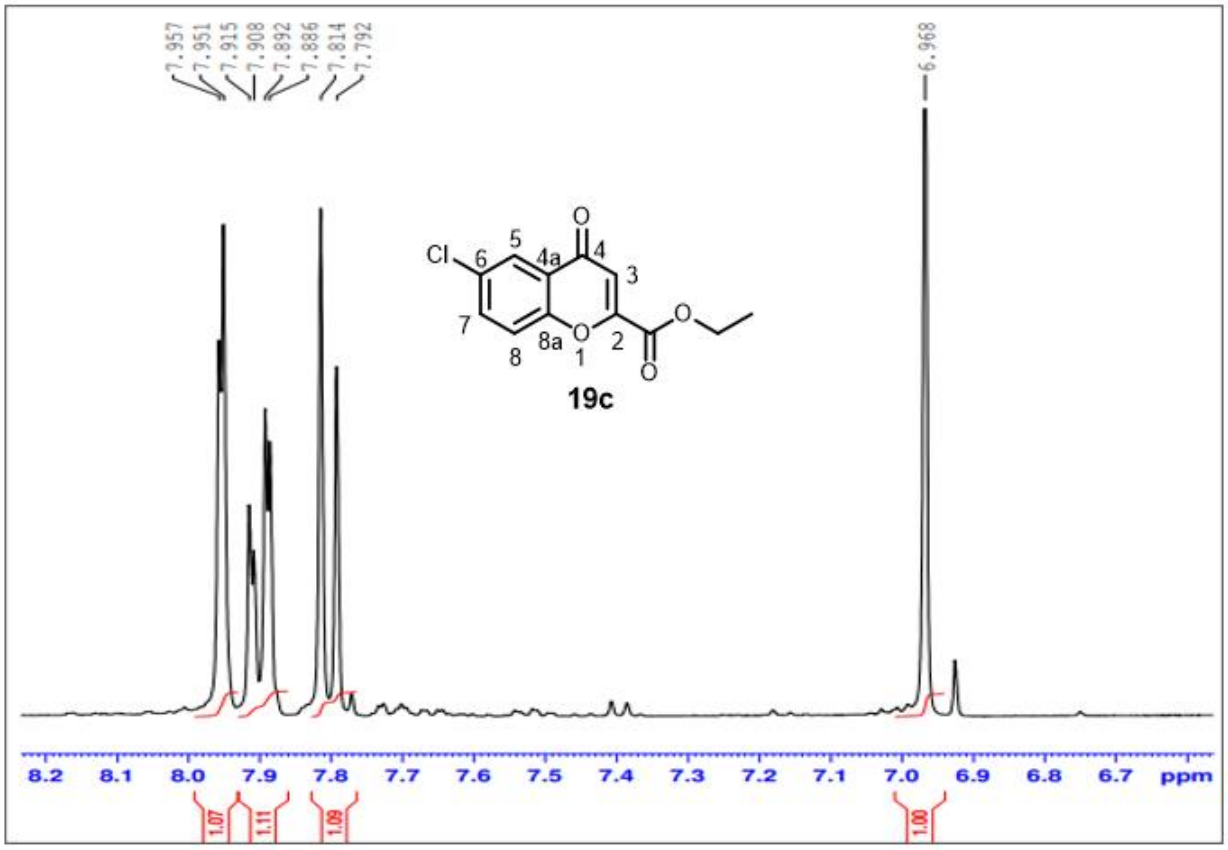

Appendix 5: ^{1}H NMR expansion spectrum of ethyl 6-chlorochromone-2-carboxylate **19c** in DMSO-d_6 (at 400 MHz)

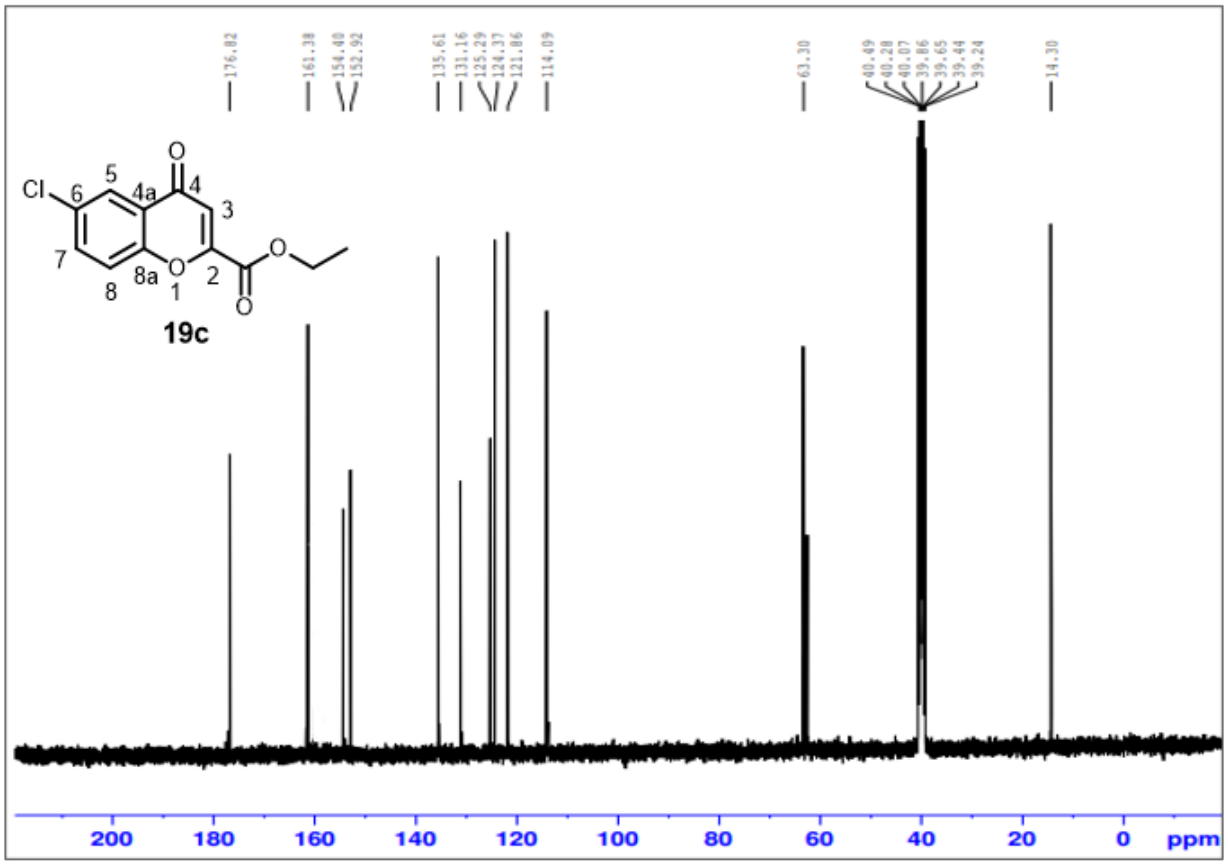

Appendix 6: ^{13}C NMR spectrum of ethyl 6-chlorochromone-2-carboxylate **19c** in DMSO-d_6 (at 100 MHz).

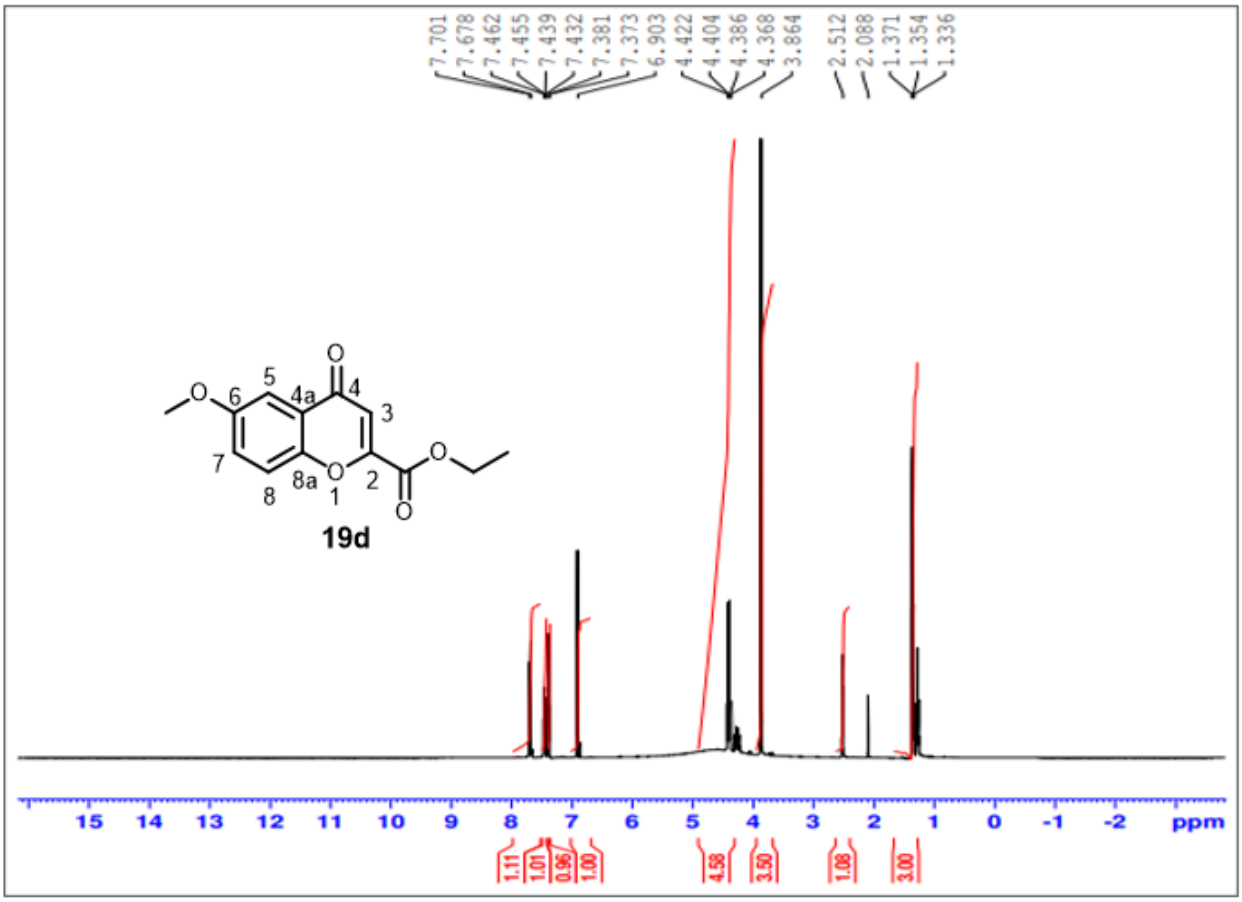

Appendix 7: ^{1}H NMR spectrum of ethyl 6-methoxychromone-2-carboxylate **19d** in DMSO-d_6 (at 400 MHz)

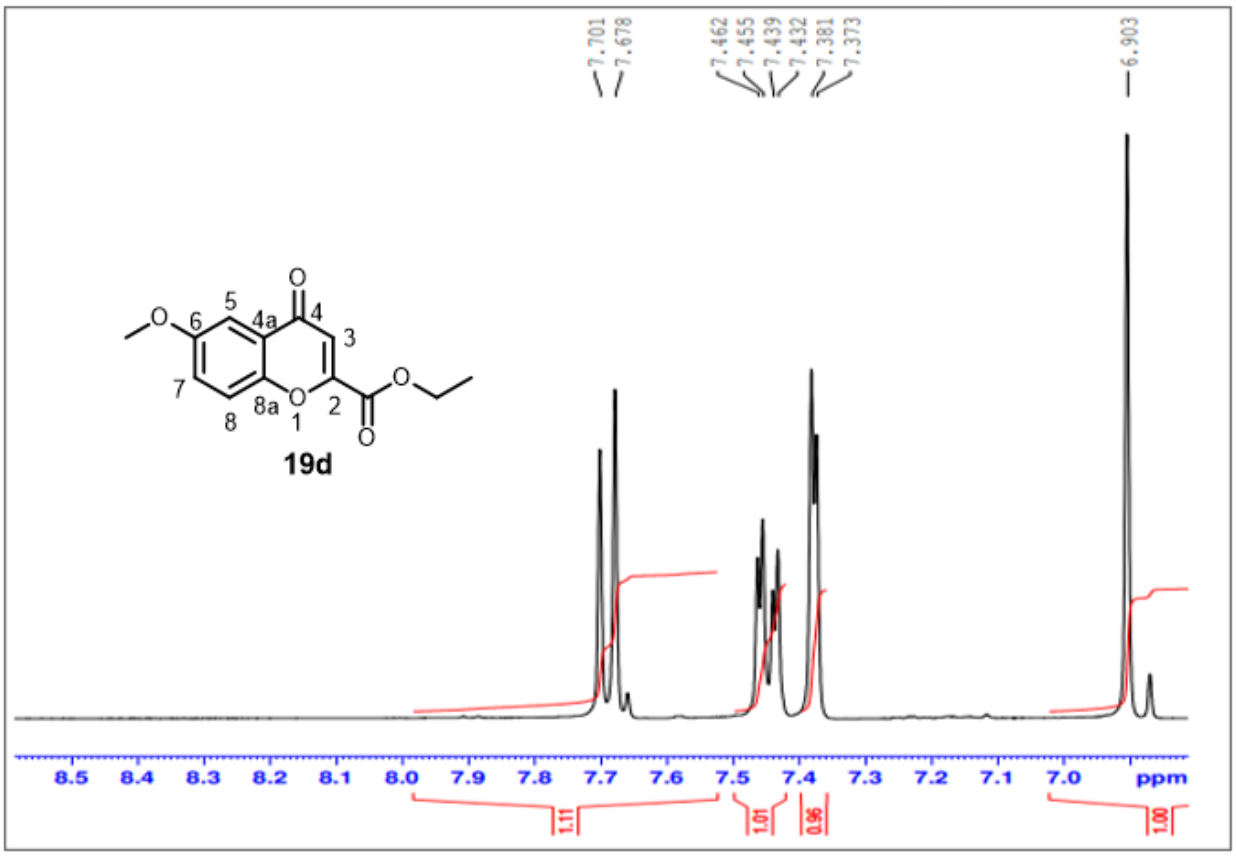

Appendix 8: ^{1}H NMR expansion spectrum of ethyl 6-methoxychromone-2-carboxylate **16d** in DMSO-d_6 (at 400 MHz)

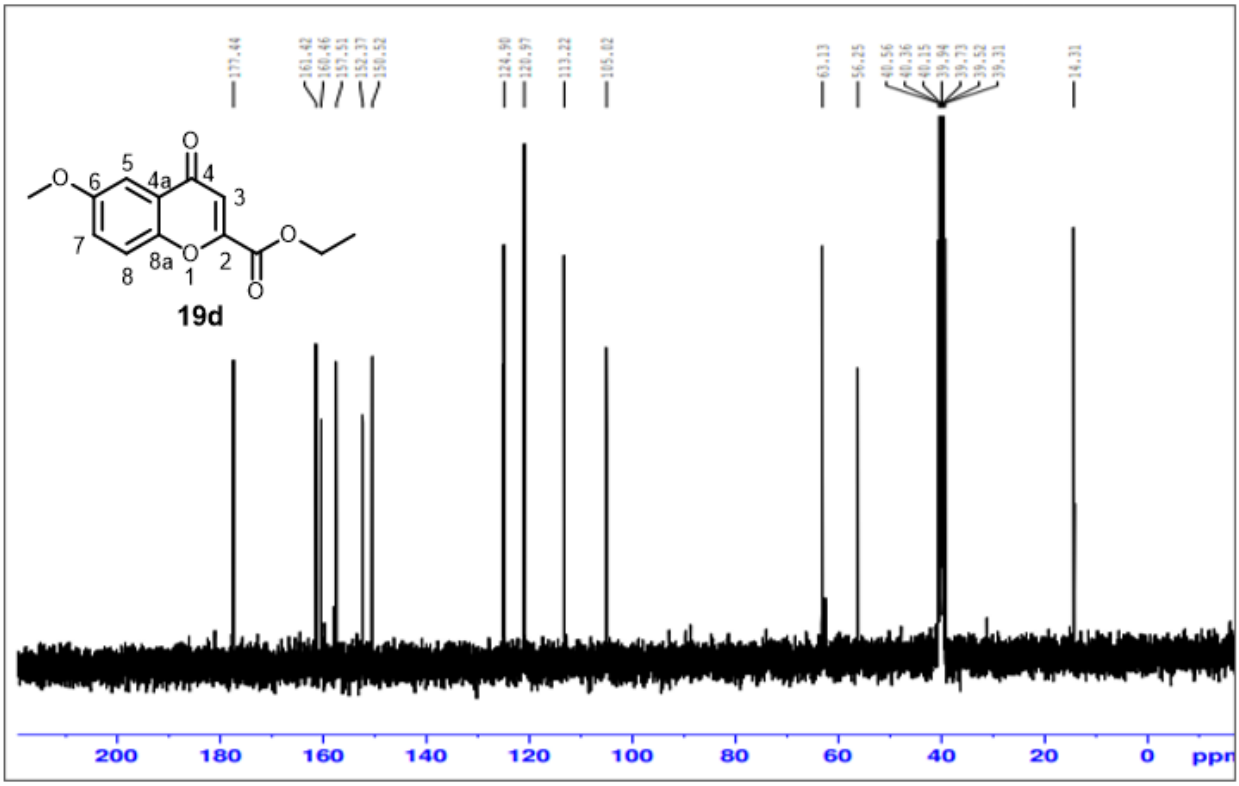

Appendix 9: ^{13}C NMR spectrum of ethyl 6-methoxychromone-2-carboxylate **19d** in DMSO-d_6 (at 100 MHz)

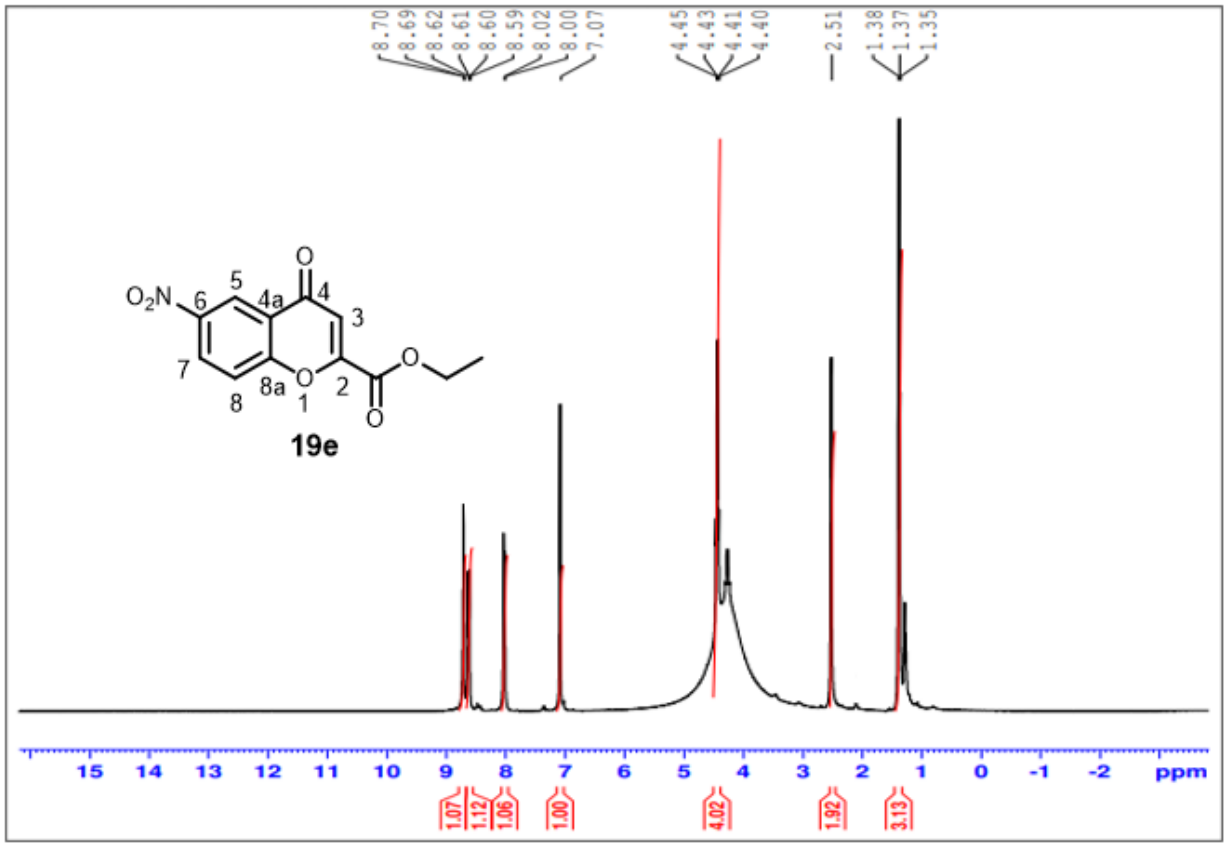

Appendix 10: ^{1}H NMR spectrum of ethyl 6-nitrochromone-2-carboxylate **19e** in DMSO-d_6 (at 400 MHz)

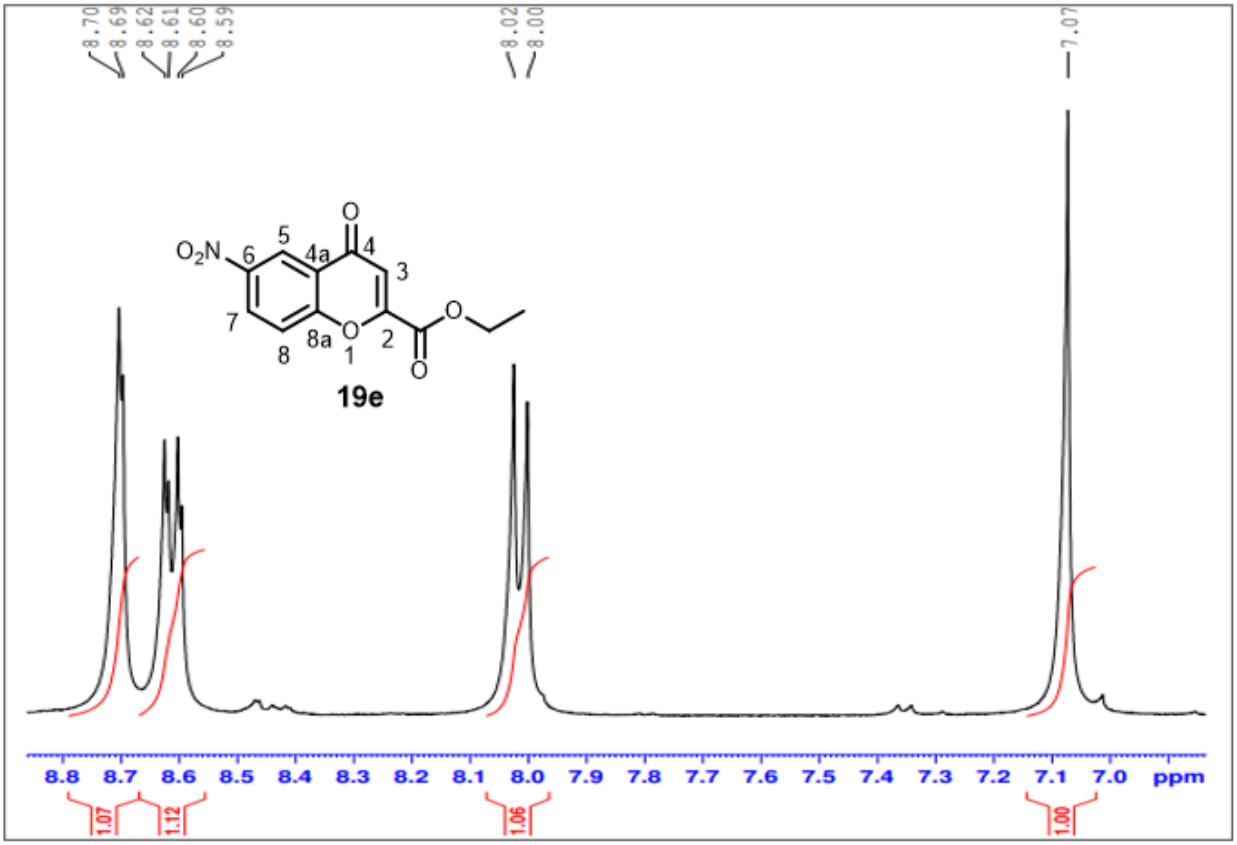

Appendix 11: ^{1}H NMR expansion spectrum of ethyl 6-nitrochromone-2-carboxylate **19e** in DMSO-d_6 (at 400 MHz)

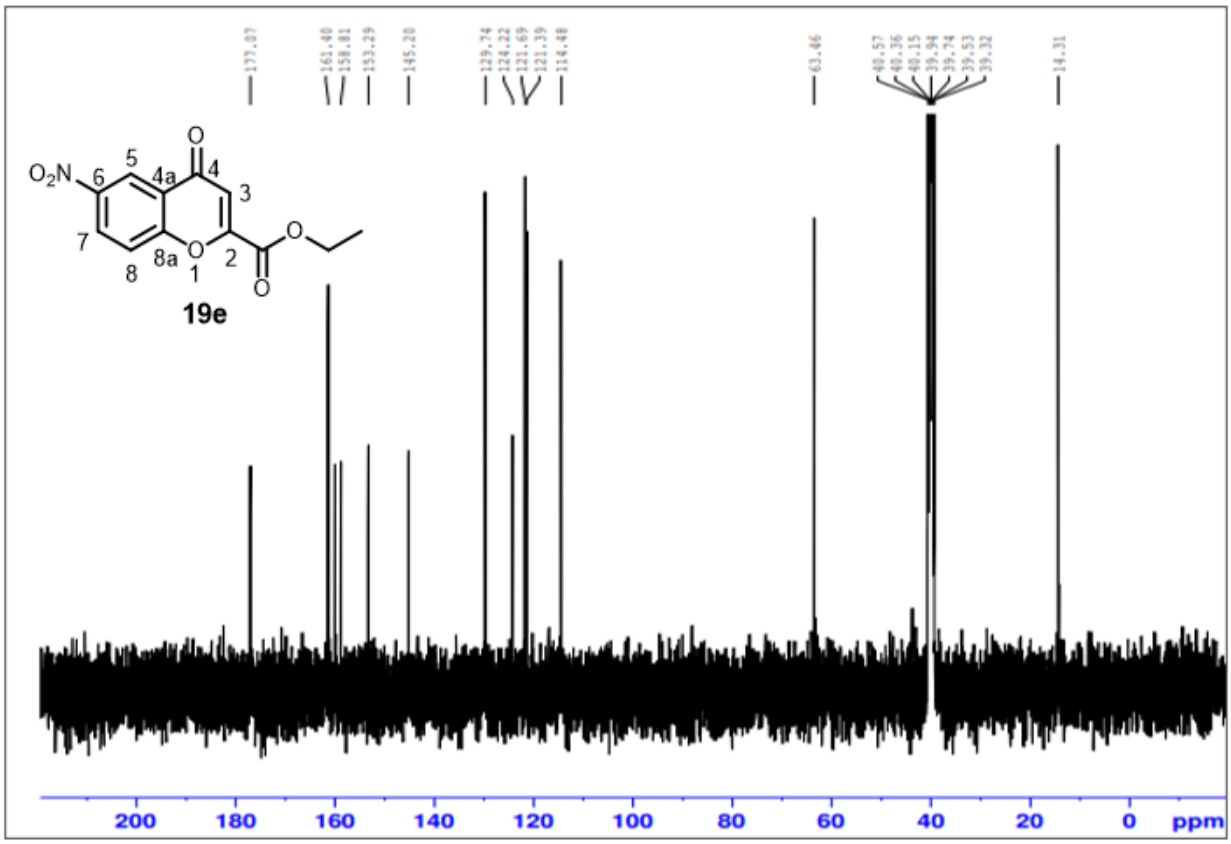

Appendix 12: ^{13}C NMR spectrum of ethyl 6-nitrochromone-2-carboxylate **19e** in DMSO-d_6 (at 100 MHz)

1.2. ^{1}H AND ^{13}C NMR Spectra of 6-substitutedchromone-2-carboxylic acids

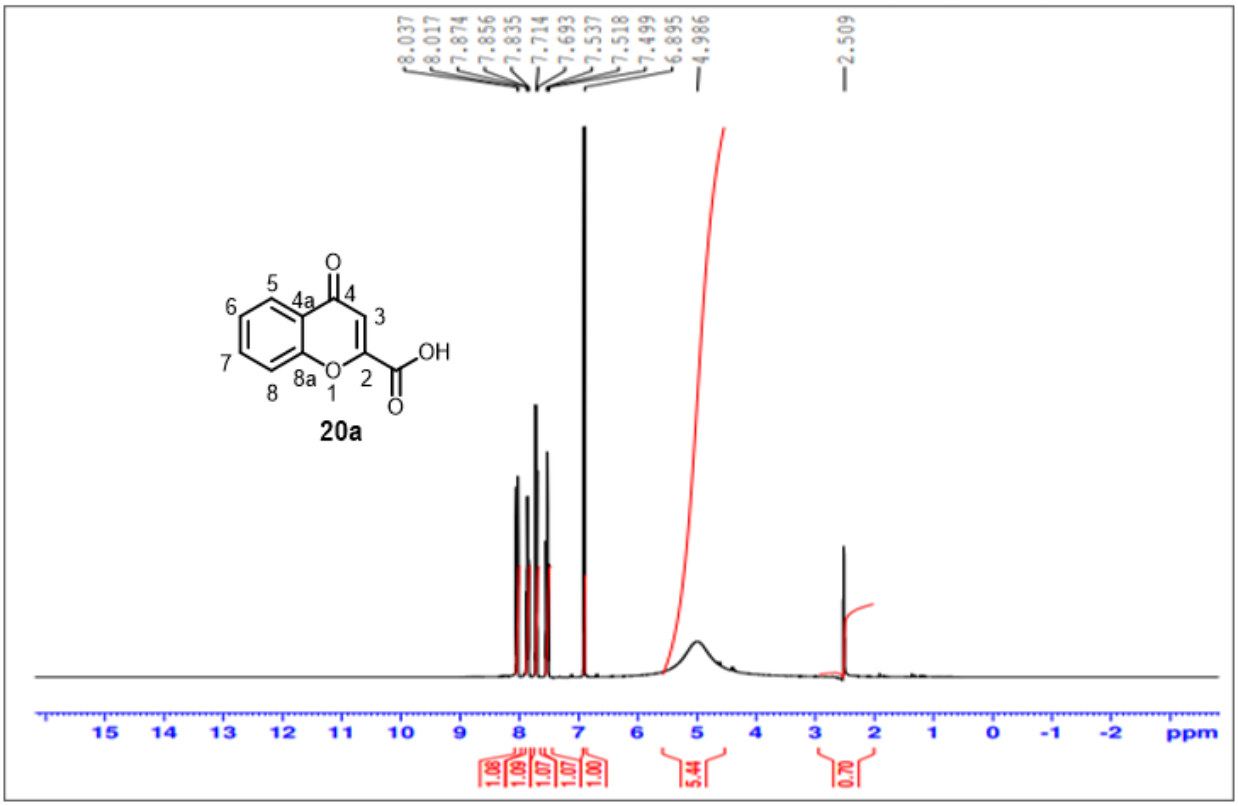

Appendix 13: ^{1}H NMR spectrum of Chromone-2-carboxylic **20a** acid in DMSO-d_6 (at 400 MHz).

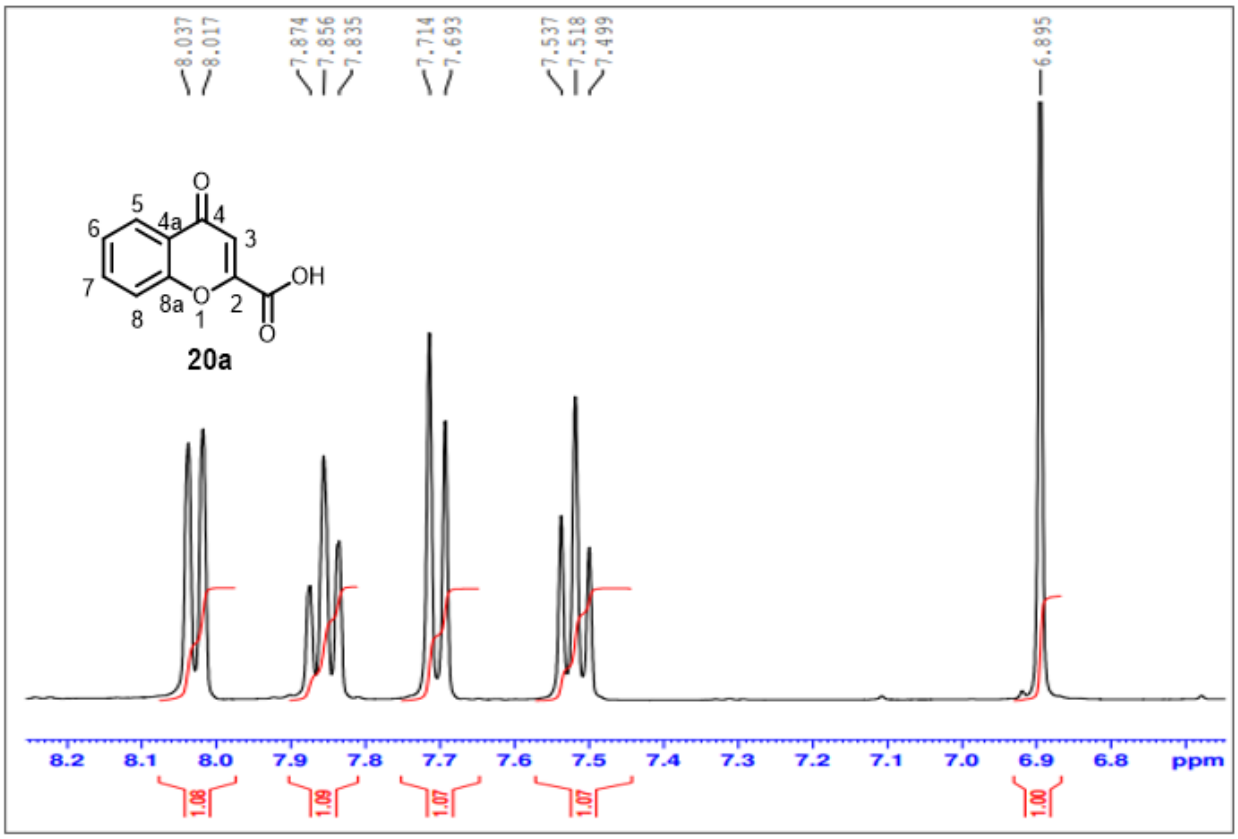

Appendix 14: ^{1}H NMR spectrum expansion of Chromone-2-carboxylic acid **20a** in DMSO-d_6 (at 400 MHz)

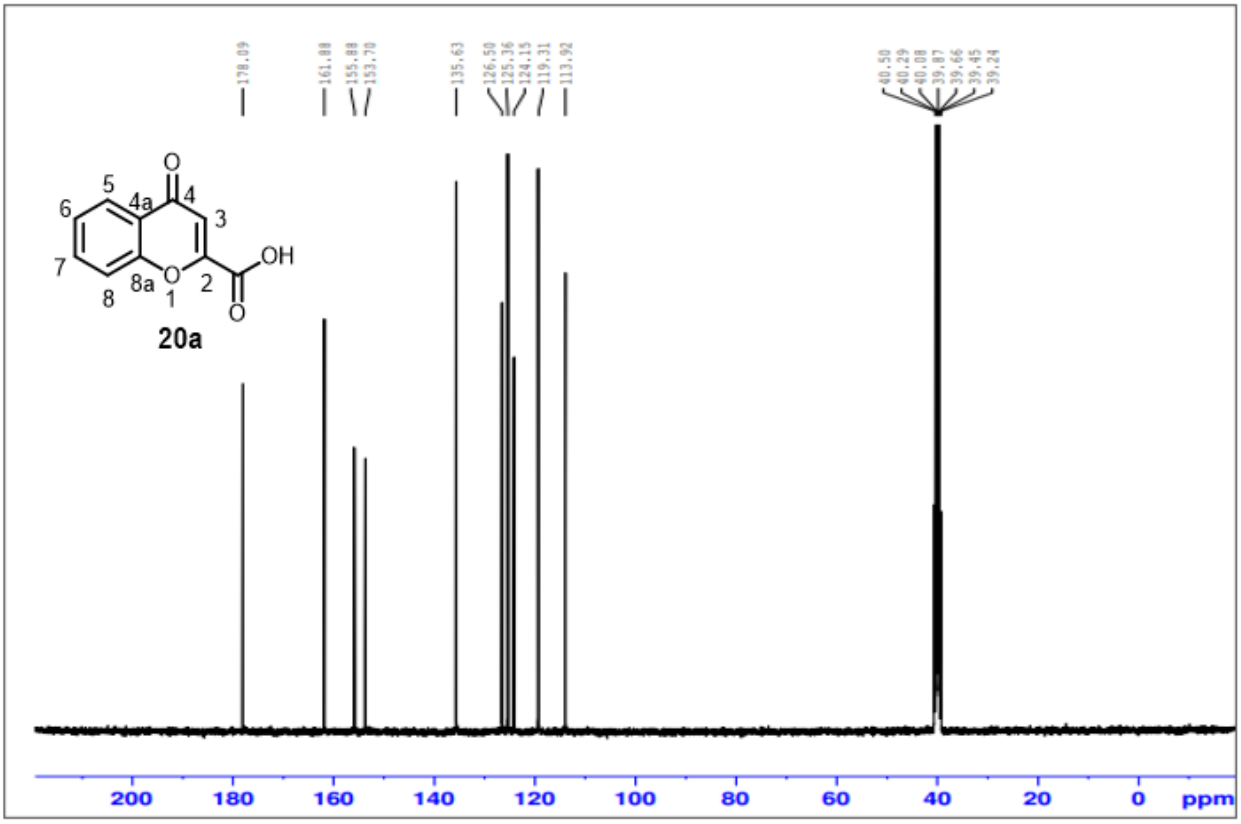

Appendix 15: ^{13}C NMR spectrum of Chromone-2-carboxylic acid **20a** in DMSO-d_6 (at 100 MHz).

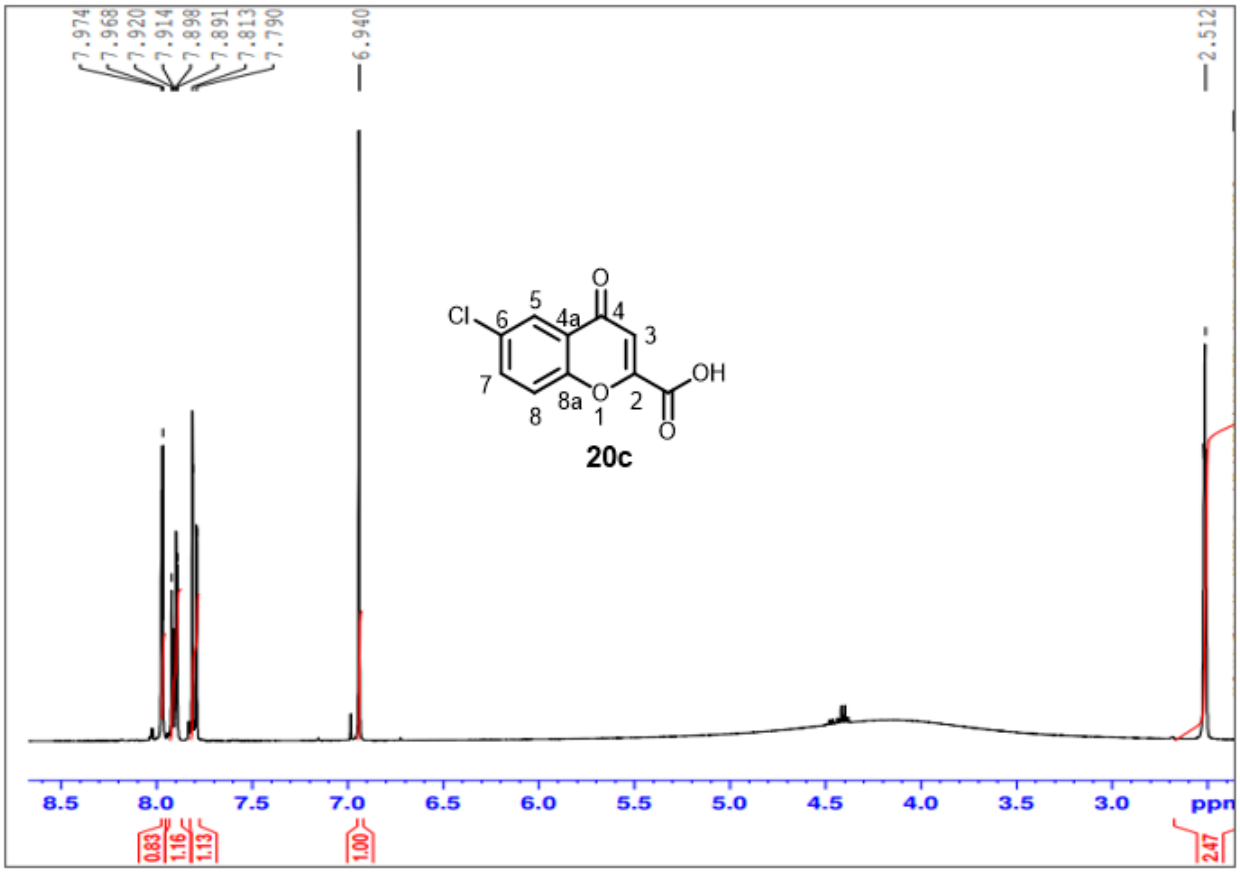

Appendix 16: ^{1}H NMR spectrum of 6-chlorochromone-2-carboxylic **20c** acid in DMSO-d_6 (at 400 MHz).

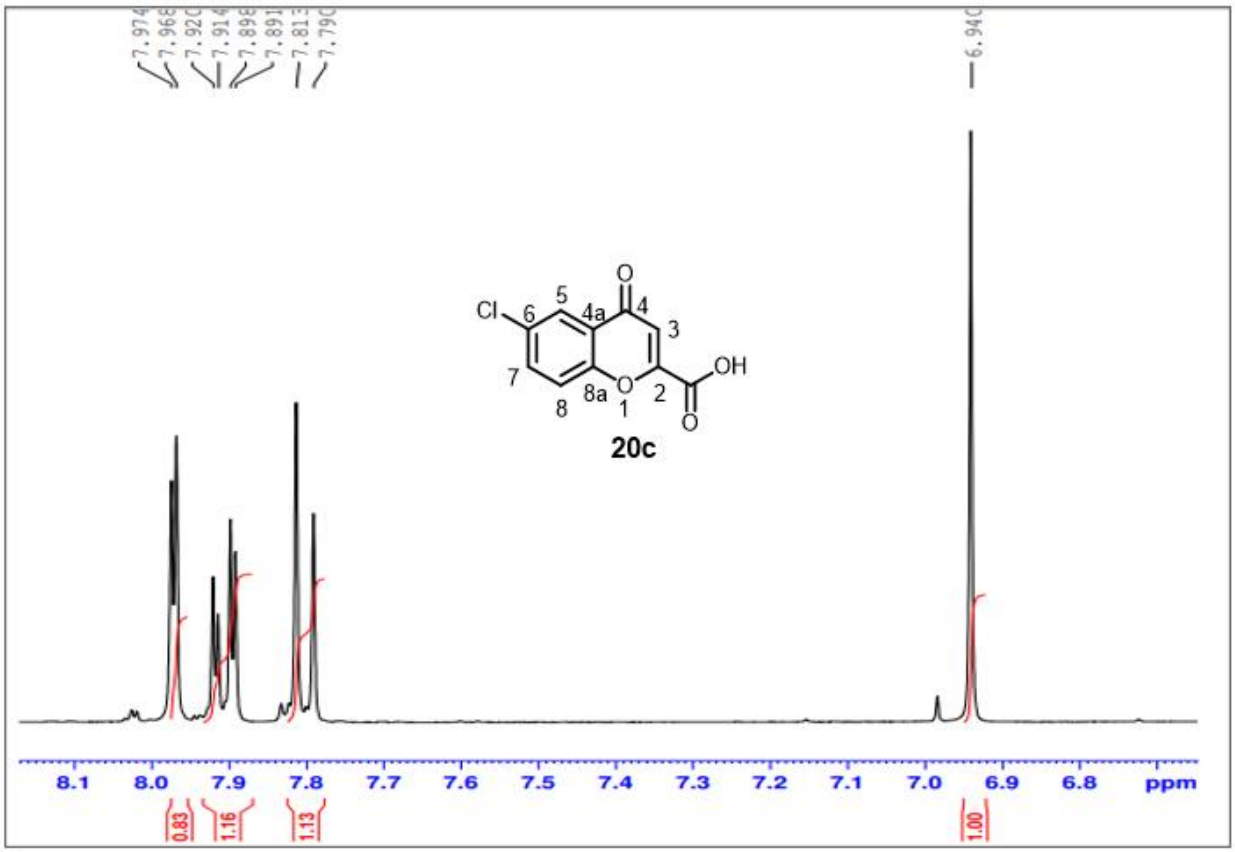

Appendix 17: ^{1}H NMR spectrum expansion of 6-Chlorochromone-2-carboxylic acid **20c** in DMSO-d_6 (at 400 MHz).

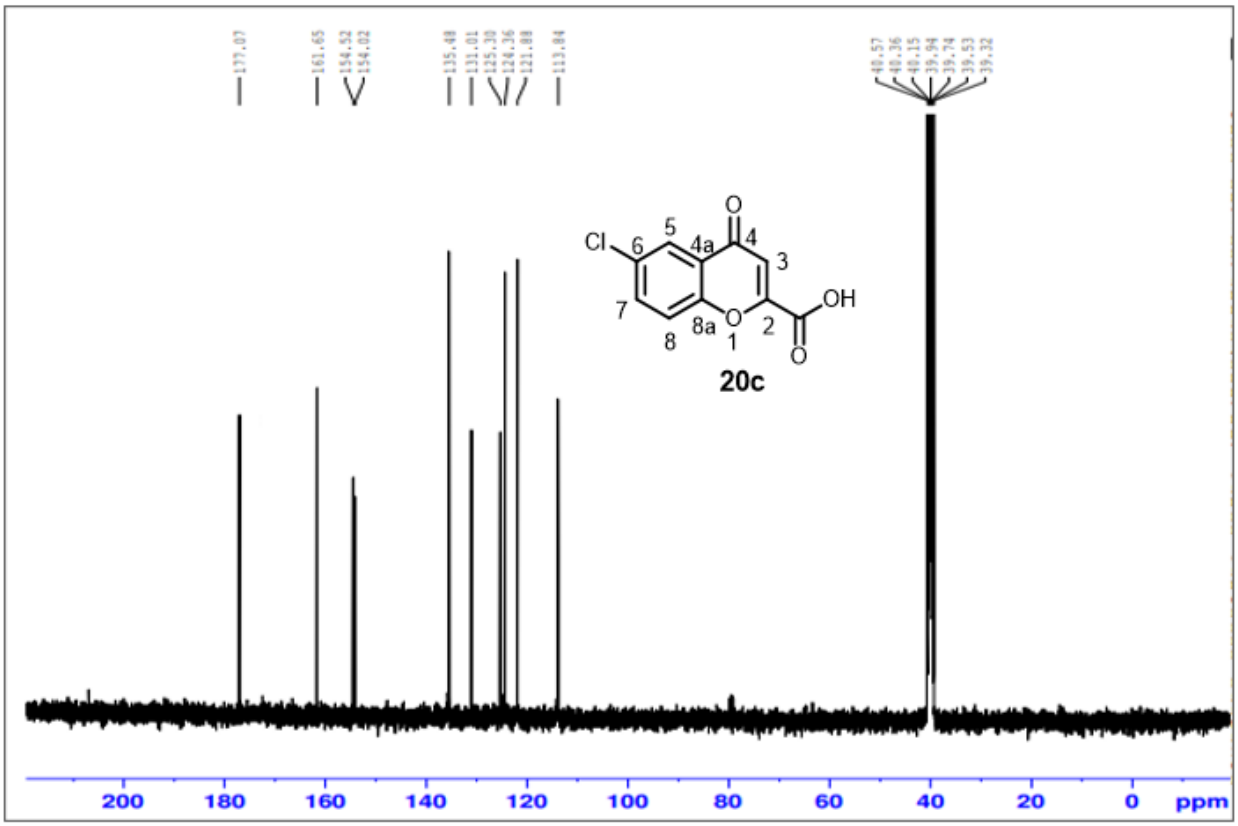

Appendix 18: ^{13}C NMR spectrum of 6-chlorochromone-2-carboxylic acid 20c in DMSO-d_6 (at 100 MHz)

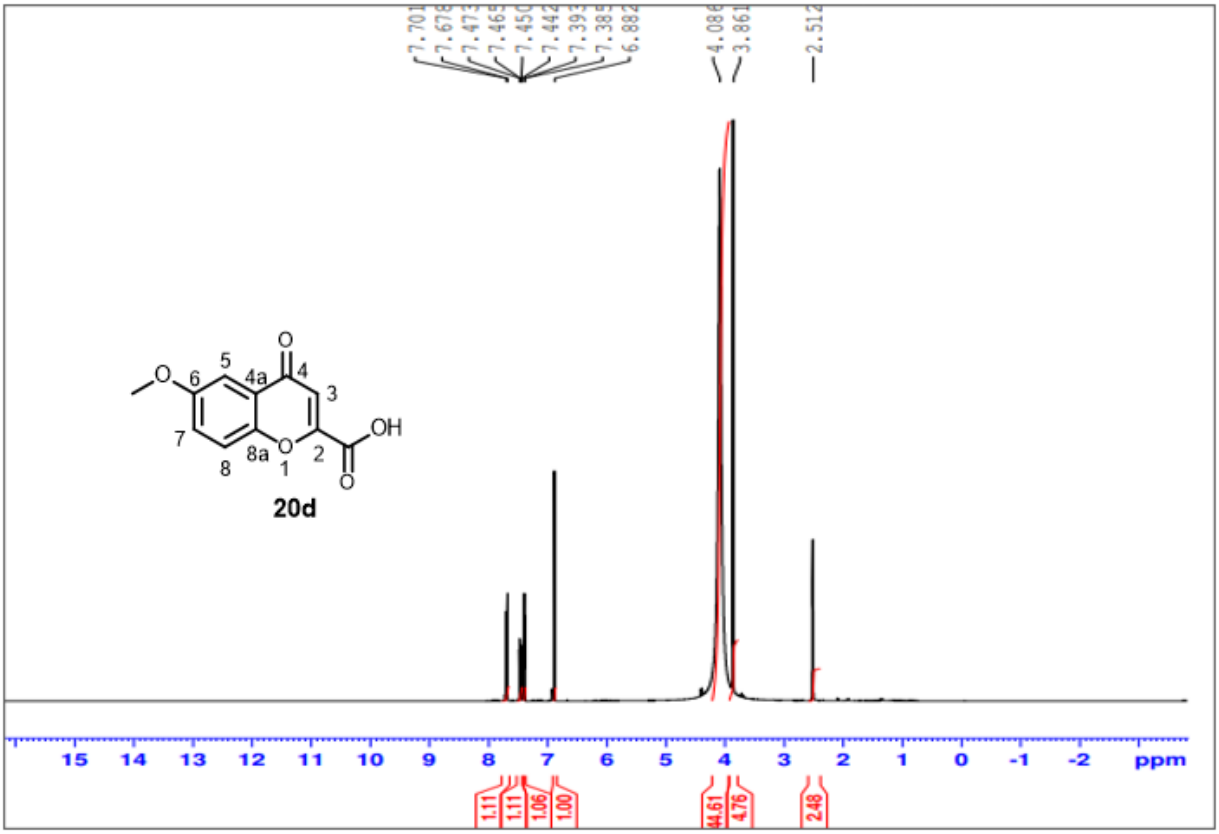

Appendix 19: ^{1}H NMR spectrum of 6-methoxychromone-2-carboxylic acid **20d** in DMSO-d_6 (at 400 MHz).

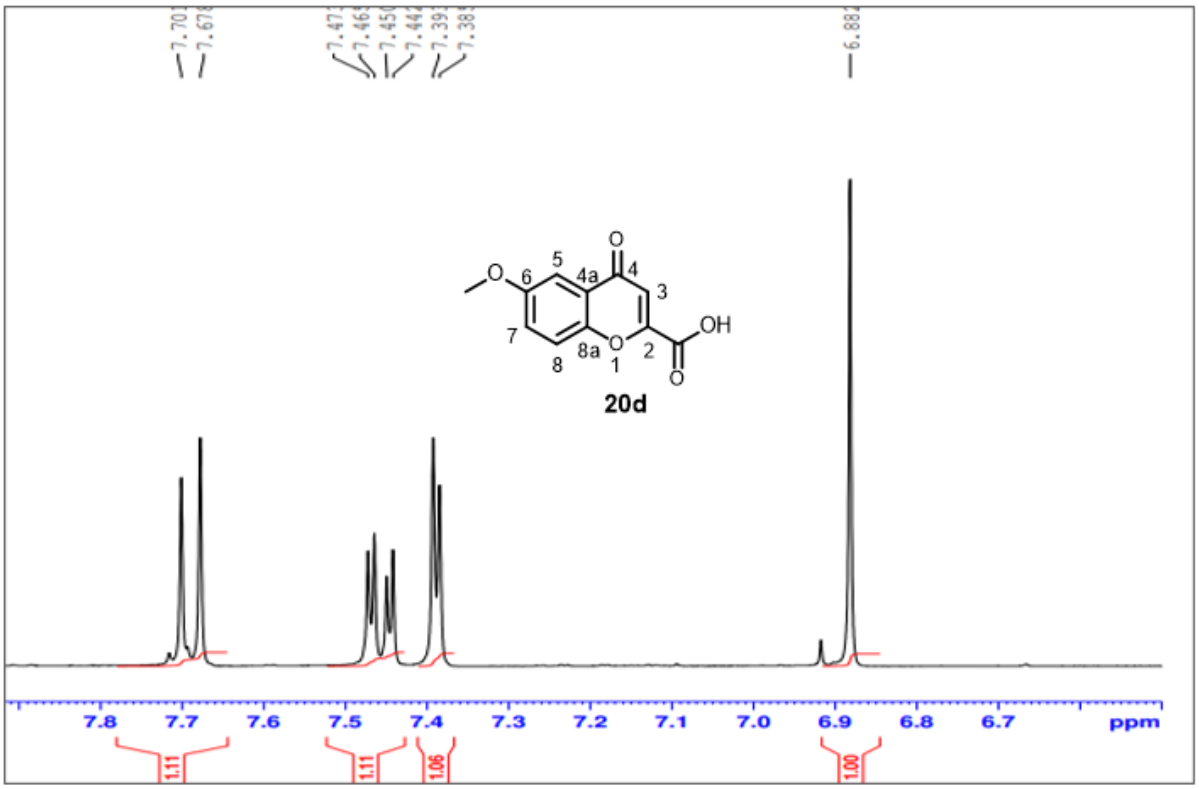

Appendix 20: ^{1}H expansion NMR spectrum of 6-methoxychromone-2-carboxylic acid **20d** in DMSO-d_6 (at 400 MHz).

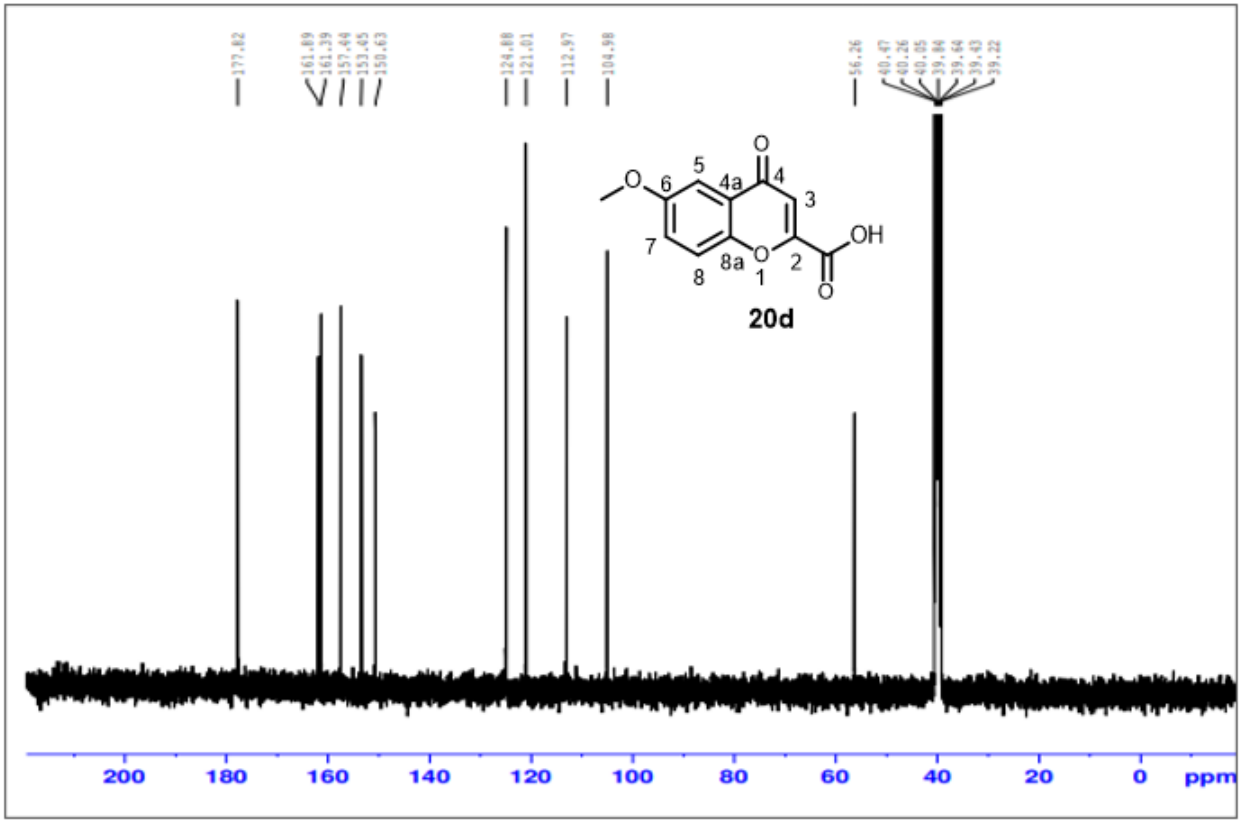

Appendix 21: ^{13}C NMR spectrum of 6-methoxychromone-2-carboxylic acid **20d** in DMSO-d_6 (at 100 MHz).

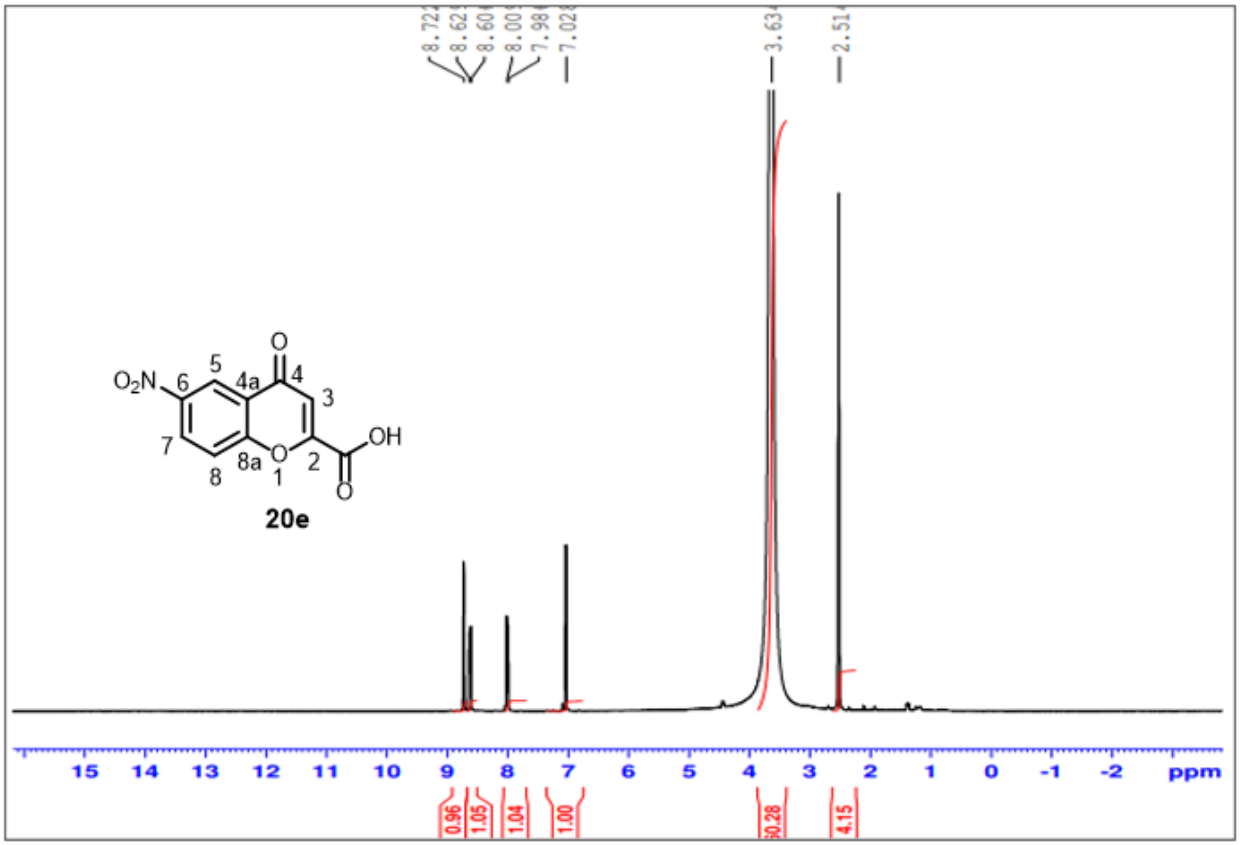

Appendix 22: ^{1}H NMR spectrum of 6-nitrochromone-2-carboxylic acid **20e** in DMSO-d_6 (at 400 MHz).

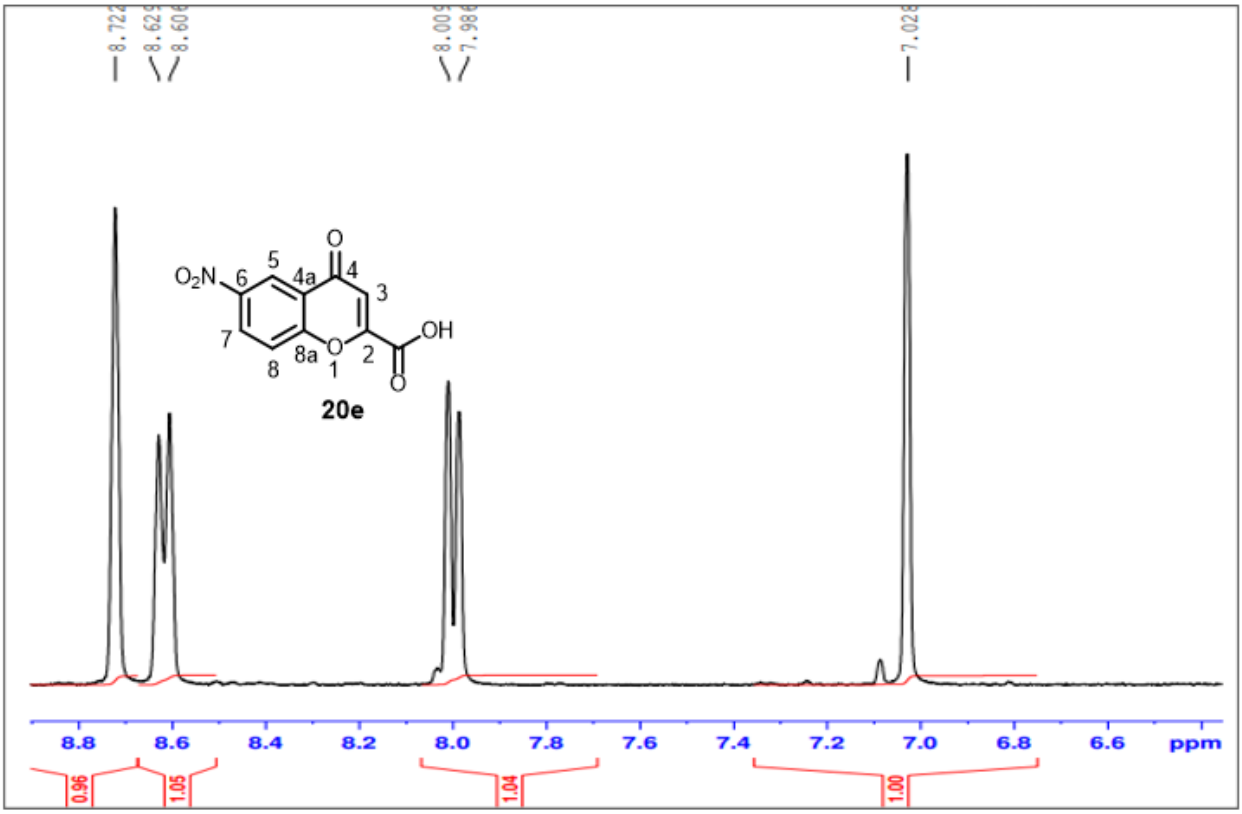

Appendix 23: ^{1}H expansion NMR spectrum of 6-nitrochromone-2-carboxylic acid **20e** in DMSO-d_6 (at 400 MHz).

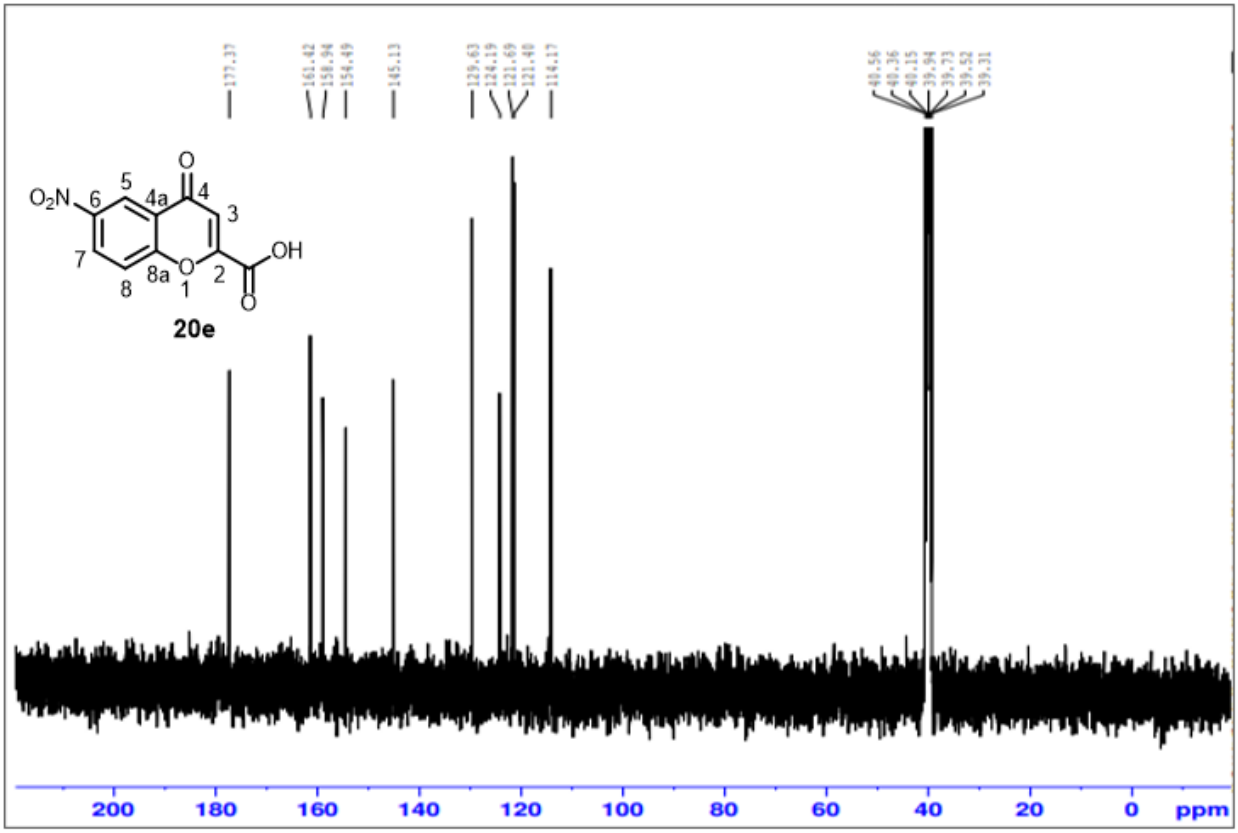

Appendix 24: ^{13}C NMR spectrum of 6-nitrochromone-2-carboxylic acid **17e** in DMSO-d_6 (at 100 MHz).

2. Quantum chemical studies on the interaction between the 6-substituted-chromone-2-carboxamide derivatives and the metal surfaces of aluminium, mild steel (Iron), and zinc

2.1. Interaction of different inhibitors with the Al surface.

structure	Isolated molecule (Ha)	Metal isolated (Ha)	Chr-2-Carb +metal isolated (Ha)	Chr-2-Carb +metal (Ha)	Interaction energy (kcal/mol)
(Al··· Chr-2-Carb)	-665.194081	-18176.5925233	-18841.7866043	-18841.847897	-38.461
(Al··· Chr-2-Carb)	-665.194081	-18176.5925233	-18841.7866043	-18841.808407	-13.681
(Al··· Chr-2-Carb)	-665.194081	-18176.5925233	-18841.7866043	-18841.875015	-55.477
(Al··· Chr-2-Carb)	-665.194081	-18176.5925233	-18841.7866043	-18841.824209	-23.597
(Al··· Chr-2-Carb)	-665.194081	-18176.5925233	-18841.7866043	-18841.862307	-47.503
(Al··· Chr-2-Carb)	-665.194081	-18176.5925233	-18841.7866043	-18841.844534	-36.351
(Al··· Chr-2-Carb)	-665.194081	-18176.5925233	-18841.7866043	-18841.825539	-24.432
(Al··· Chr-2-Carb)	-665.194081	-18176.5925233	-18841.7866043	-18841.826034	-24.742
(Al··· Chr-2-Carb)	-665.194081	-18176.5925233	-18841.7866043	-18841.849240	-39.304
(Al··· Chr-2-Carb)	-665.194081	-18176.5925233	-18841.7866043	-18841.845251	-36.801
(Al··· Chr-2-Carb)	-665.194081	-18176.5925233	-18841.7866043	-18841.826478	-25.021

Appendix 25: Table of the Interaction energies between the Al surface and Chromone-2-carboxamide inhibitor

structure	Isolated molecule (Ha)	Metal isolated (Ha)	Br-Chr-2-Carb +metal isolated (Ha)	Br-Chr-2-Carb +metal (Ha)	Interaction energy (kcal/mol)
(Al···Br-Chr-2-Carb)	-677.980083	-18176.592662	-18854.572745	-18854.645923	-45.920
(Al···Br-Chr-2-Carb)	-677.980083	-18176.592662	-18854.572745	-18854.675783	-64.657

Appendix 26: Table of the Interaction energies between the Al surface and 6-bromochromone-2-carboxamide inhibitor.

structure	Isolated molecule (Ha)	Metal isolated (Ha)	Cl-Chr-2-Carb +metal isolated (Ha)	Cl-Chr-2-Carb +metal (Ha)	Interaction energy (kcal/mol)
(Al···Cl-Chr-2-Carb)	-1124.611446	-18176.592662	-19301.204108	-19301.297490	-58.598
(Al···Cl-Chr-2-Carb)	-1124.611446	-18176.592662	-19301.204108	-19301.288840	-53.170
(Al···Cl-Chr-2-Carb)	-1124.611446	-18176.592662	-19301.204108	-19301.257966	-33.796

Appendix 27: Table of the Interaction energies between the Al surface and 6-chlorochromone-2-carboxamide inhibitor.

structure	Isolated molecule (Ha)	Metal isolated (Ha)	CH_3O-Chr-2-Carb +metal isolated (Ha)	CH_3O-Chr-2-Carb +metal (Ha)	Interaction energy (kcal/mol)
(Al···CH_3O-Chr-2-Carb)	-779.674874	-18176.592525	-18956.267399	-18956.279775	-7.766
(Al···CH_3O-Chr-2-Carb)	-779.674874	-18176.592525	-18956.267399	-18956.288902	-13.493
(Al···CH_3O-Chr-2-Carb)	-779.674874	-18176.592525	-18956.267399	-18956.313222	-28.754
(Al···CH_3O-Chr-2-Carb)	-779.674874	-18176.592525	-18956.267399	-18956.287514	-12.622
(Al···CH_3O-Chr-2-Carb)	-779.674874	-18176.592525	-18956.267399	-18956.276412	-5.656

Appendix 28: Table of the Interaction energies between the Al surface and 6-methoxychromone-2-carboxamide inhibitor.

structure	Isolated molecule (Ha)	Metal isolated (Ha)	NO_2-Chr-2-Carb +metal isolated (Ha)	NO_2-Chr-2-Carb +metal (Ha)	Interaction energy (kcal/mol)
(Al···NO_2-Chr-2-Carb)	-869.607155	-18176.592525	-19046.19968	-19046.298176	-61.806
(Al···NO_2-Chr-2-Carb)	-869.607155	-18176.592525	-19046.19968	-19046.319848	-75.405
(Al···NO_2-Chr-2-Carb)	-869.607155	-18176.592525	-19046.19968	-19046.2767694	-48.374
(Al···NO_2-Chr-2-Carb)	-869.607155	-18176.592525	-19046.19968	-19046.3177617	-74.096
(Al···NO_2-Chr-2-Carb)	-869.607155	-18176.592525	-19046.19968	-19046.2996600	-62.737
(Al···NO_2-Chr-2-Carb)	-869.607155	-18176.592525	-19046.19968	-19046.268335	-43.081
(Al···NO_2-Chr-2-Carb)	-869.607155	-18176.592525	-19046.19968	-19046.296264	-60.606
(Al···NO_2-Chr-2-Carb)	-869.607155	-18176.592525	-19046.19968	-19046.260768	-38.333
(Al···NO_2-Chr-2-Carb)	-869.607155	-18176.592525	-19046.19968	-19046.309655	-69.009
(Al···NO_2-Chr-2-Carb)	-869.607155	-18176.592525	-19046.19968	-19046.289059	-56.085
(Al···NO_2-Chr-2-Carb)	-869.607155	-18176.592525	-19046.19968	-19046.308928	-68.553

Appendix 29: Table of the Interaction energies between the Al surface and 6-nitrochromone-2-carboxamide inhibitor.

2.2. Interaction of different inhibitors with the Fe(111) surface.

structure	Isolated molecule (Ha)	Metal isolated (Ha)	Chr-2-Carb +metal isolated (Ha)	Chr-2-Carb +metal (Ha)	Interaction energy (kcal/mol)
(Fe···Chr-2-Carb)	-665.194081	-2979.6046053	-3644.7986863	-3645.1279040	-206.584
(Fe···Chr-2-Carb)	-665.194081	-2979.6046053	-3644.7986863	-3645.2585290	-288.551
(Fe···Chr-2-Carb)	-665.194081	-2979.6046053	-3644.7986863	-3645.1247888	-204.629
(Fe···Chr-2-Carb)	-665.194081	-2979.6046053	-3644.7986863	-3645.1059589	-192.814
(Fe···Chr-2-Carb)	-665.194081	-2979.6046053	-3644.7986863	-3645.1216083	-202.634
(Fe···Chr-2-Carb)	-665.194081	-2979.6046053	-3644.7986863	-3645.1248980	-204.698

Appendix 30: Table of the Interaction energies between the Fe(111) surface and Chromone-2-carboxamide inhibitor.

structure	Isolated molecule (Ha)	Metal isolated (Ha)	Br-Chr-2-Carb +metal isolated (Ha)	Br-Chr-2-Carb +metal (Ha)	Interaction energy (kcal/mol)
(Fe··· Br-Chr-2-Carb)	-677.980083	-2979.6046053	-3657.5846883	-3657.9671501	-239.995
(Fe··· Br-Chr-2-Carb)	-677.980083	-2979.6046053	-3657.5846883	-3657.9580012	-234.254
(Fe··· Br-Chr-2-Carb)	-677.980083	-2979.6046053	-3657.5846883	-3657.9577149	-234.074
(Fe··· Br-Chr-2-Carb)	-677.980083	-2979.6046053	-3657.5846883	-3657.9581106	-234.322
(Fe··· Br-Chr-2-Carb)	-677.980083	-2979.6046053	-3657.5846883	-3657.9491906	-228.725
(Fe··· Br-Chr-2-Carb)	-677.980083	-2979.6046053	-3657.5846883	-3657.9569421	-233.589

Appendix 31: Table of the Interaction energies between the Fe(111) surface and 6-bromochromone-2-carboxamide inhibitor.

structure	Isolated molecule (Ha)	Metal isolated (Ha)	Cl-Chr-2-Carb +metal isolated (Ha)	Cl-Chr-2-Carb +metal (Ha)	Interaction energy (kcal/mol)
(Fe···Cl-Chr-2-Carb)	-1124.611446	-2979.6046053	-4104.2160513	-4104.5750350	-225.262
(Fe···Cl-Chr-2-Carb)	-1124.611446	-2979.6046053	-4104.2160513	-4104.6026843	-242.612
(Fe···Cl-Chr-2-Carb)	-1124.611446	-2979.6046053	-4104.2160513	-4104.6079438	-245.913
(Fe···Cl-Chr-2-Carb)	-1124.611446	-2979.6046053	-4104.2160513	-4104.5738346	-224.509
(Fe···Cl-Chr-2-Carb)	-1124.611446	-2979.6046053	-4104.2160513	-4104.5820791	-229.682

Appendix 32: Table of the Interaction energies between the Fe(111) surface and 6-chlorochromone-2-carboxamide inhibitor.

structure	Isolated molecule (Ha)	Metal isolated (Ha)	CH_3O-Chr-2-Carb +metal isolated (Ha)	CH_3O-Chr-2-Carb +metal (Ha)	Interaction energy (kcal/mol)
(Fe···CH_3O-Chr-2-Carb)	-779.674874	-2979.6046053	-3759.2794793	-3759.6725655	-246.662
(Fe···CH_3O-Chr-2-Carb)	-779.674874	-2979.6046053	-3759.2794793	-3759.7070012	-268.269
(Fe···CH_3O-Chr-2-Carb)	-779.674874	-2979.6046053	-3759.2794793	-3759.5572862	-174.324
(Fe···CH_3O-Chr-2-Carb)	-779.674874	-2979.6046053	-3759.2794793	-3759.6975219	-262.322
(Fe···CH_3O-Chr-2-Carb)	-779.674874	-2979.6046053	-3759.2794793	-3759.6473141	-230.816
(Fe···CH_3O-Chr-2-Carb)	-779.674874	-2979.6046053	-3759.2794793	-3759.6975937	262.367

Appendix 33: Table of the Interaction energies between the Fe(111) surface and 6-methoxychromone-2-carboxamide inhibitor.

structure	Isolated molecule (Ha)	Metal isolated (Ha)	NO_2-Chr-2-Carb +metal isolated (Ha)	NO_2-Chr-2-Carb +metal (Ha)	Interaction energy (kcal/mol)
(Fe···NO_2-Chr-2-Carb)	-869.607155	-2979.6046053	-3849.2117603	-3849.7079342	-311.349
(Fe···NO_2-Chr-2-Carb)	-869.607155	-2979.6046053	-3849.2117603	-3849.6305919	-262.817
(Fe···NO_2-Chr-2-Carb)	-869.607155	-2979.6046053	-3849.2117603	-3849.5962941	-241.294
(Fe···NO_2-Chr-2-Carb)	-869.607155	-2979.6046053	-3849.2117603	-3849.5985996	-242.742
(Fe···NO_2-Chr-2-Carb)	-869.607155	-2979.6046053	-3849.2117603	-3849.6069171	-247.961
(Fe···NO_2-Chr-2-Carb)	-869.607155	-2979.6046053	-3849.2117603	-3849.6078181	-248.526
(Fe···NO_2-Chr-2-Carb)	-869.607155	-2979.6046053	-3849.2117603	-3849.6699303	-287.501

Appendix 34: Table of the Interaction energies between the Fe(111) surface and 6-nitrochromone-2-carboxamide inhibitor.

2.3. Interaction of different inhibitors with the Zn(111) surface.

Structure	Isolated molecule (Ha)	Metal isolated (Ha)	inhibitor +metal isolated (Ha)	inhibitor +metal (Ha)	Interaction energy (kcal/mol)
(Zn···Chr-2-Carb)	-665.194081	-39760.180957	-40425.375038	-40425.387429	-7.775
(Zn···Br-Chr-2-Carb)	-677.980084	-39760.180957	-40438.161041	-40438.1774349	-10.287
(Zn···Br-Chr-2-Carb)	-677.980084	-39760.180957	-40438.161041	-40438.1752535	-8.918
(Zn···Cl-Chr-2-Carb)	-1124.611446	-39760.180957	-40884.792403	-40884.826494	-21.392
(Zn···Cl-Chr-2-Carb)	-1124.611446	-39760.180957	-40884.792403	-40884.8354584	-27.017

(Zn···CH_3O-Chr-2-Carb)	-779.674874	-39760.180957	-40539.855831	-40547.8031708	-4986.955
(Zn···NO_2-Chr-2-Carb)	-869.607155	-39760.180957	-40629.788112	-40629.794993	-4.318

Appendix 35: Table of the Interaction energies between the Fe(111) surface and Chr-2-Carb, Br-Chr-2-Carb, Cl-Chr-2-Carb, CH_3O-Chr-2-Carb and NO_2-Chr-2-Carb inhibitors.

3. Bode plot of the three metals in HCl in the presence of five various concentrations of the Chr-2-Carb, Br-Chr-2-Carb, Cl-Chr-2-Carb, CH3O-Chr-2-Carb and NO2-Chr-2-Carb inhibitors.

3.1. Bode plot of mild steel metal in 5 M HCl in the presence of five various concentrations of the Chr-2-Carb, Br-Chr-2-Carb, Cl-Chr-2-Carb, CH_3O-Chr-2-Carb and NO_2-Chr-2-Carb inhibitors

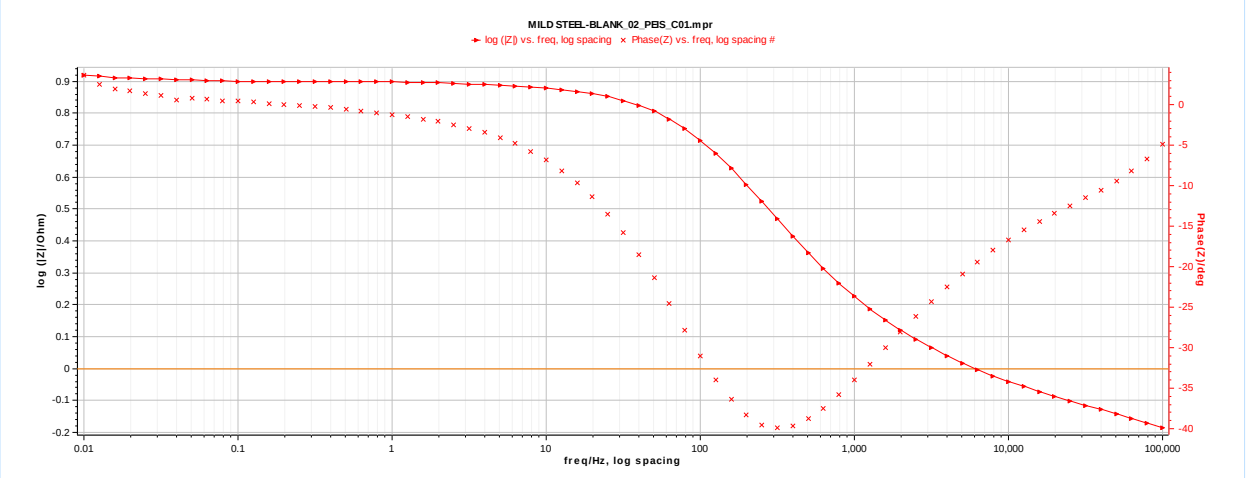

Appendix 36: Bode plot of mild steel in 1.5 M HCl in the absence of various concentrations of 6-substituted chromone-2-carboxamides.

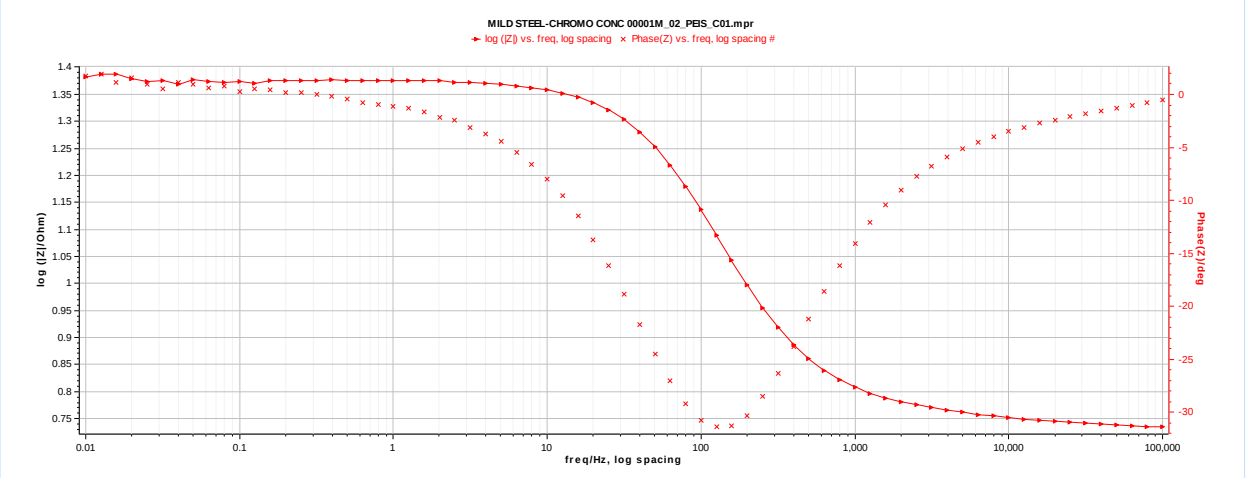

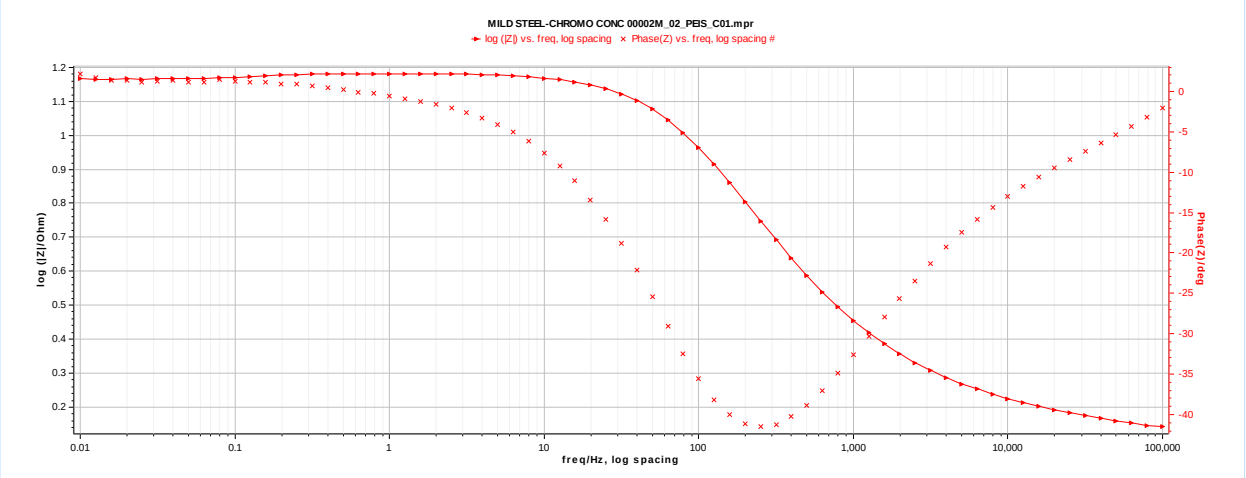

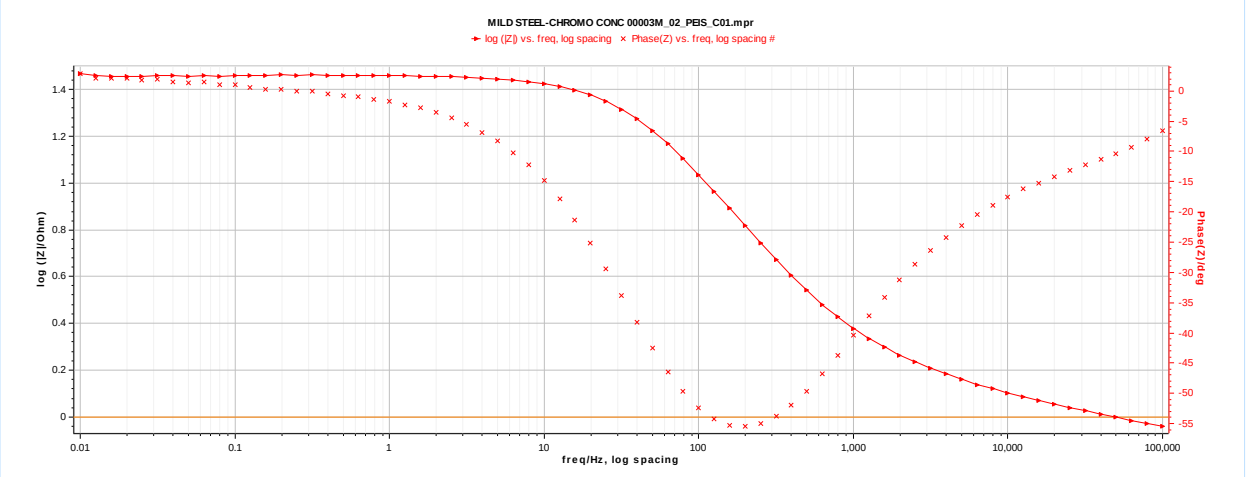

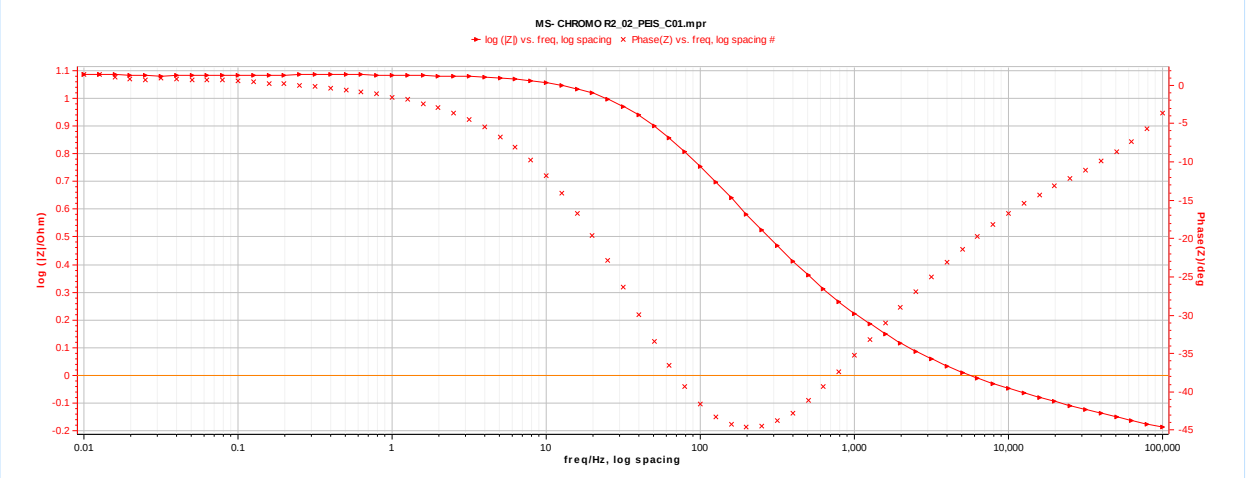

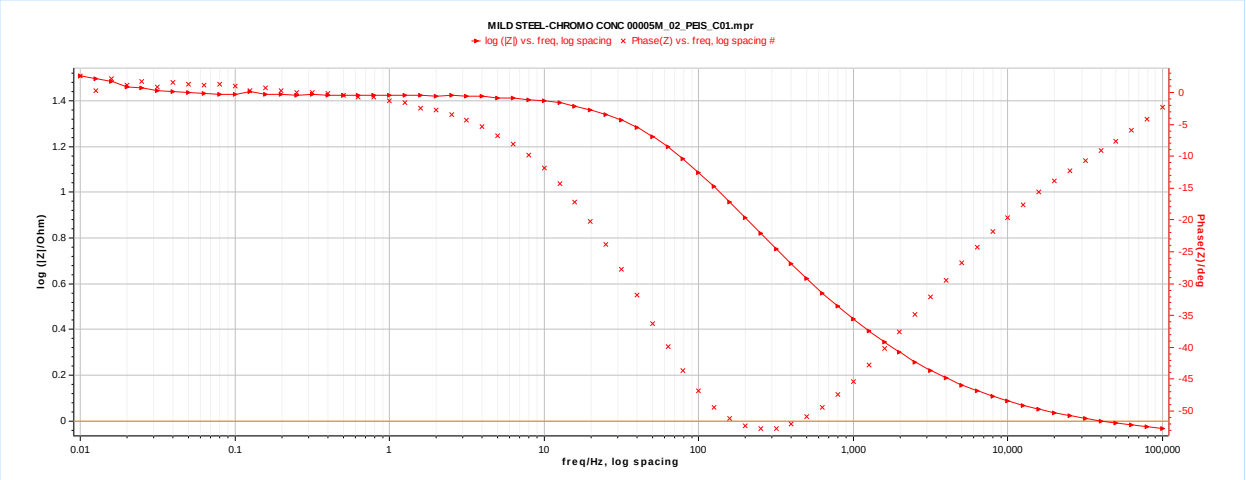

Appendix 37: Bode plot of mild steel in 1.5 M HCl in the presence of five various concentrations of Chr-2-Carb.

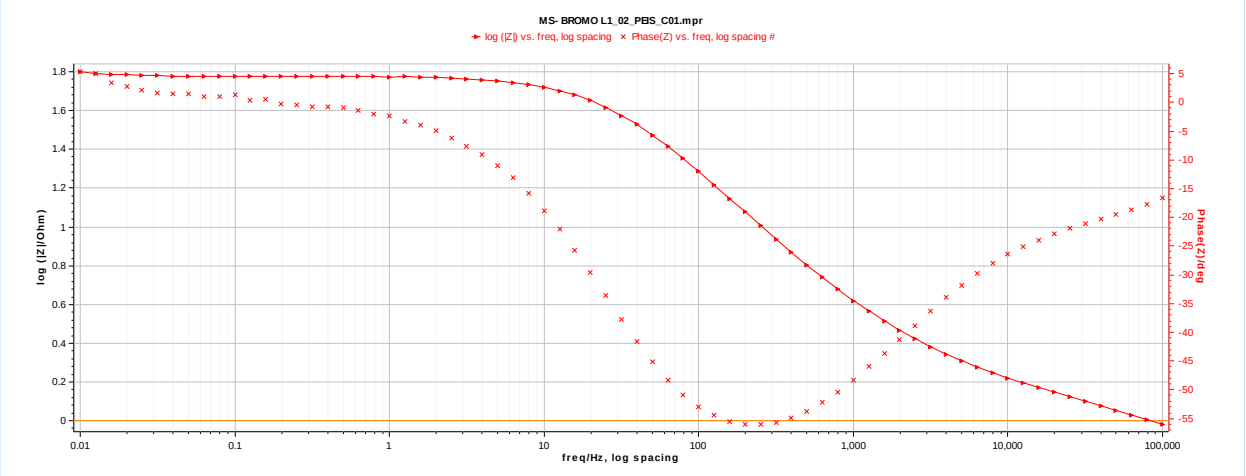

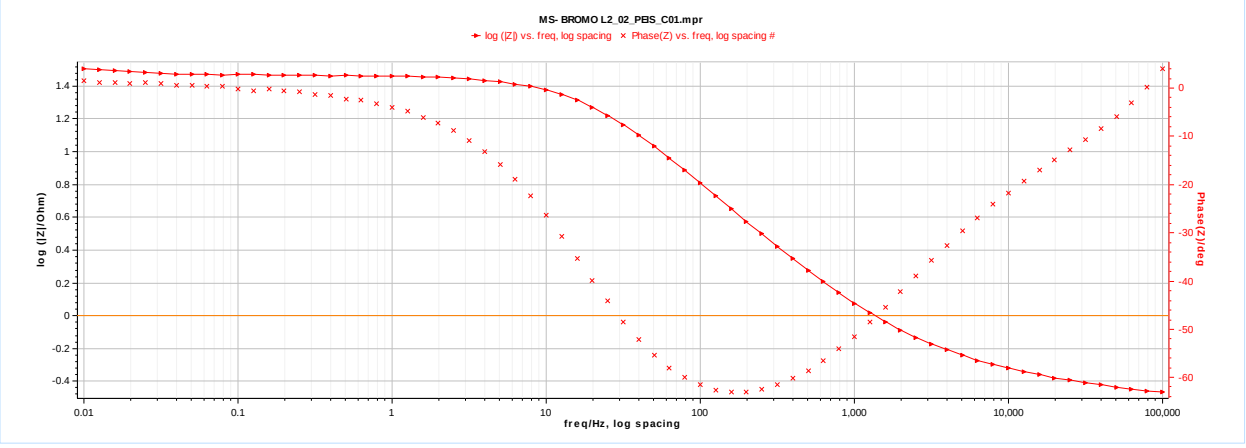

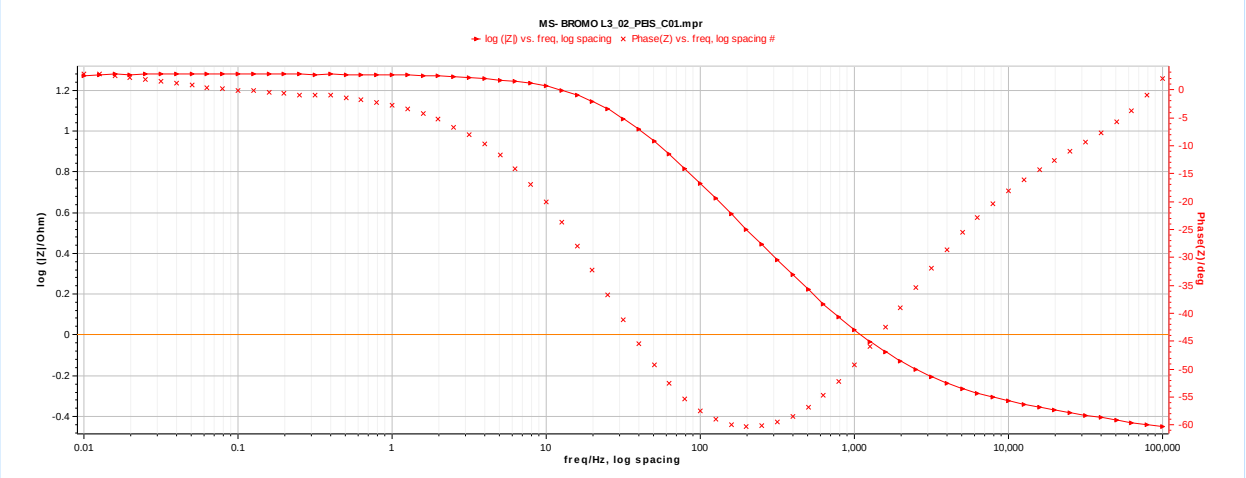

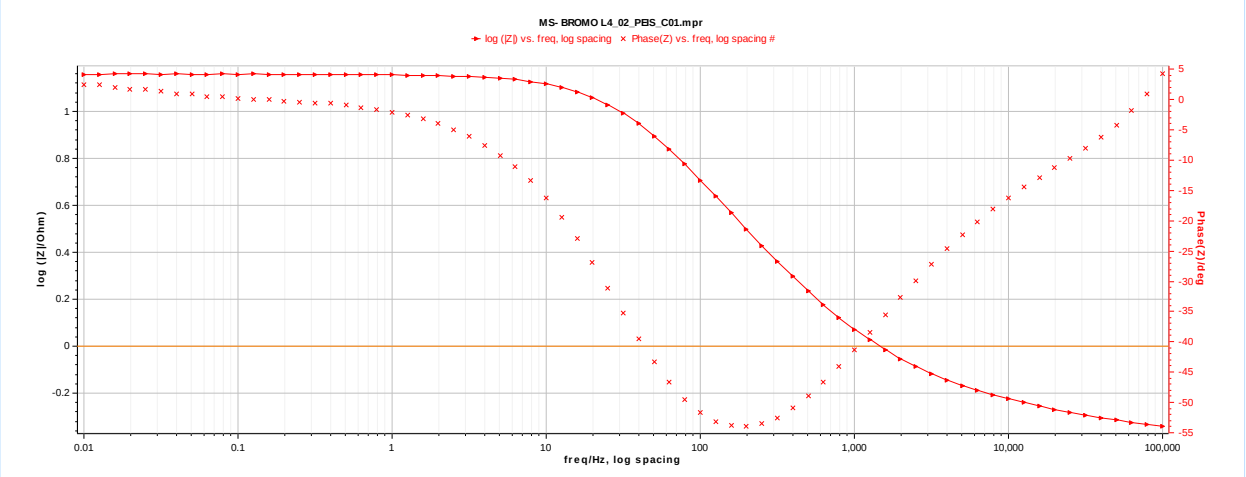

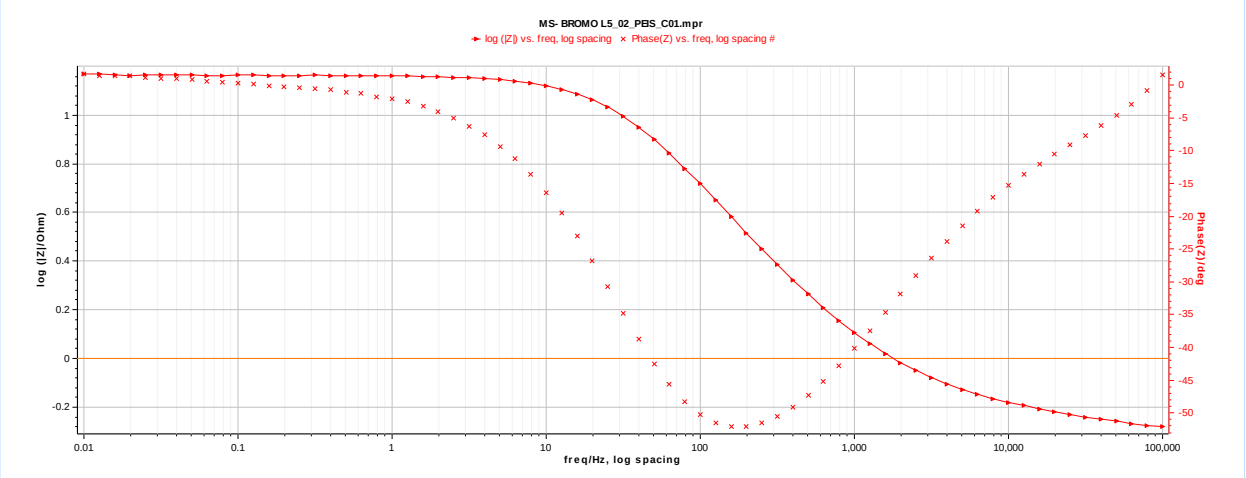

Appendix 38: Bode plot of mild steel in 1.5 M HCl in the presence of five various concentrations of Br-Chr-2-carb.

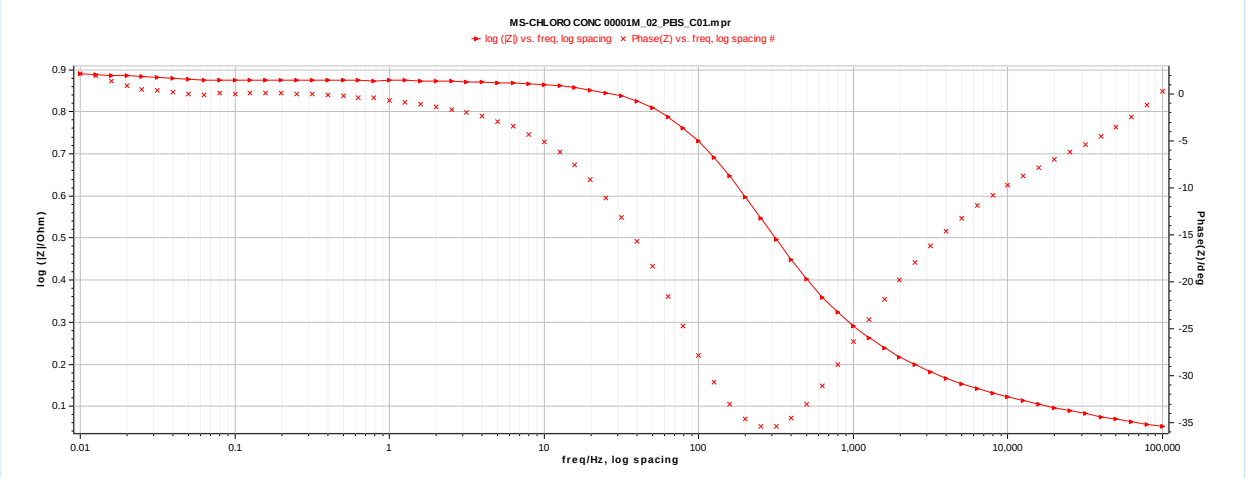

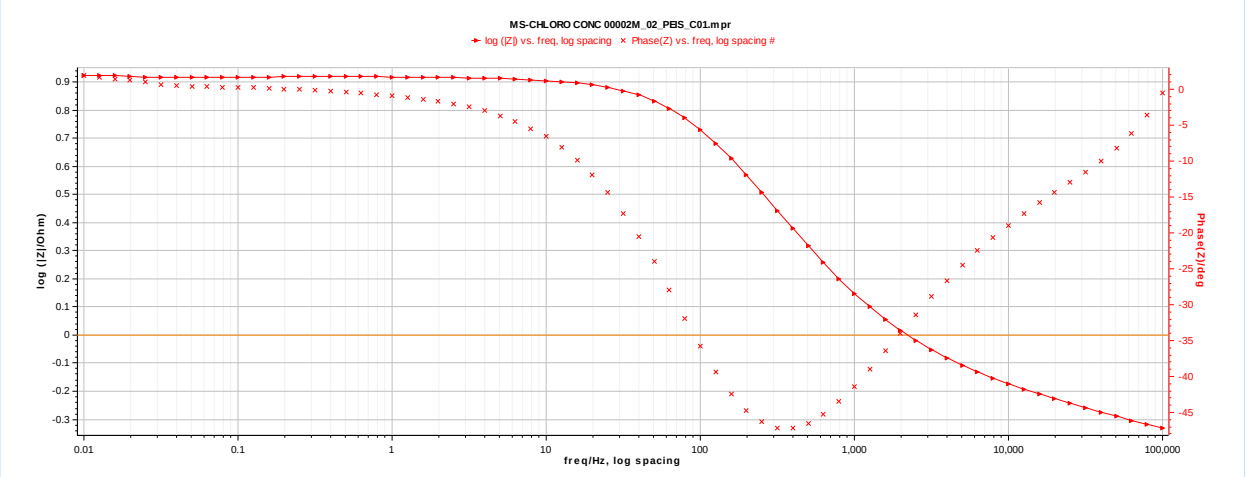

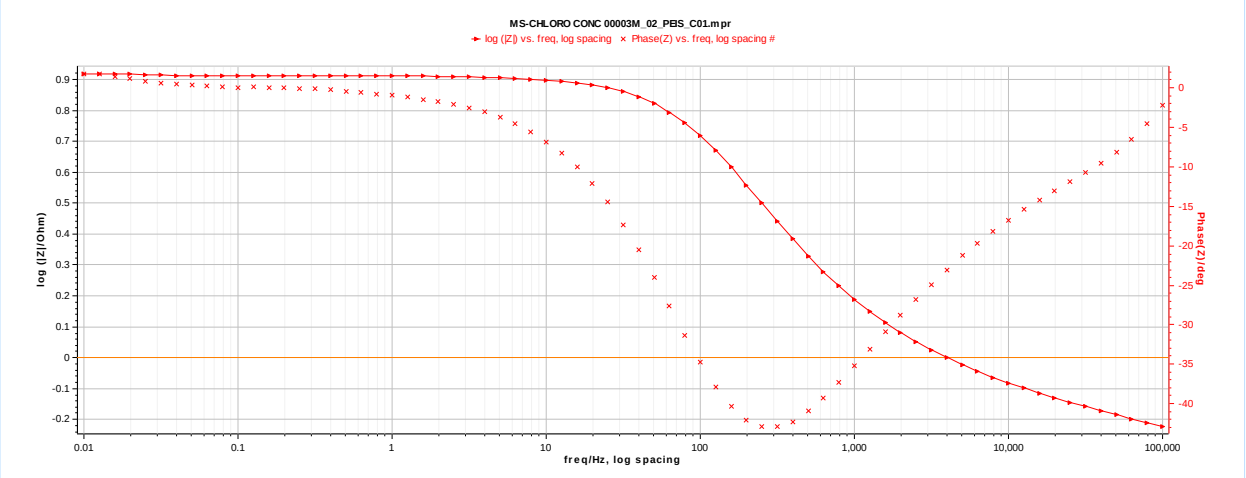

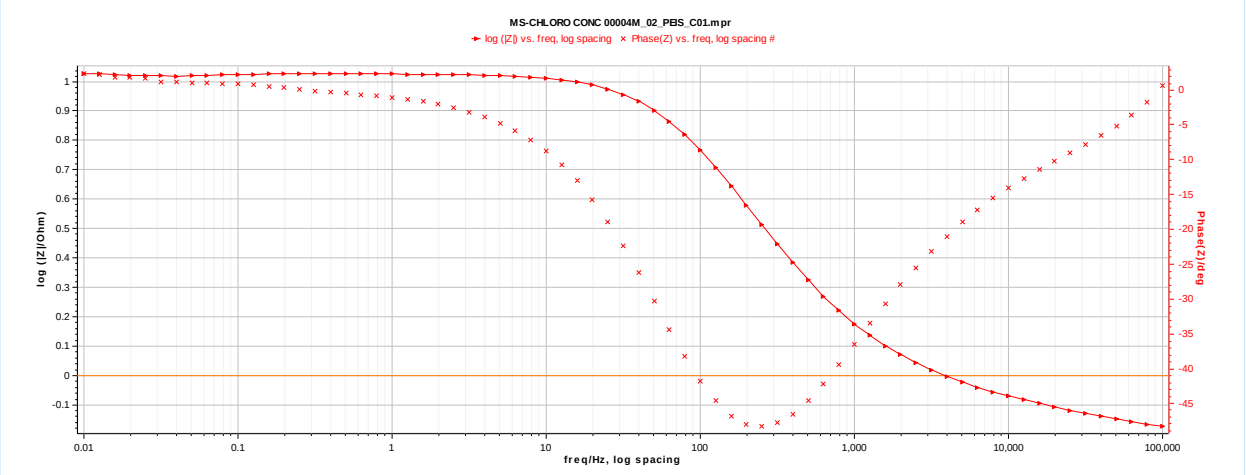

Appendix 39: Bode plots of mild steel in 1.5 M HCl in the presence of five various concentrations of Cl-Chr-2-Carb.

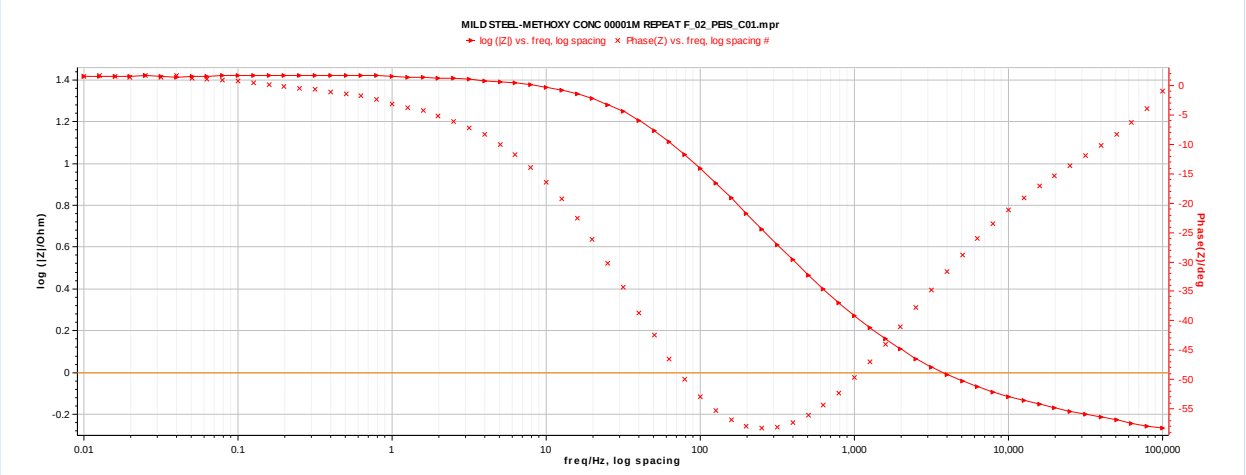

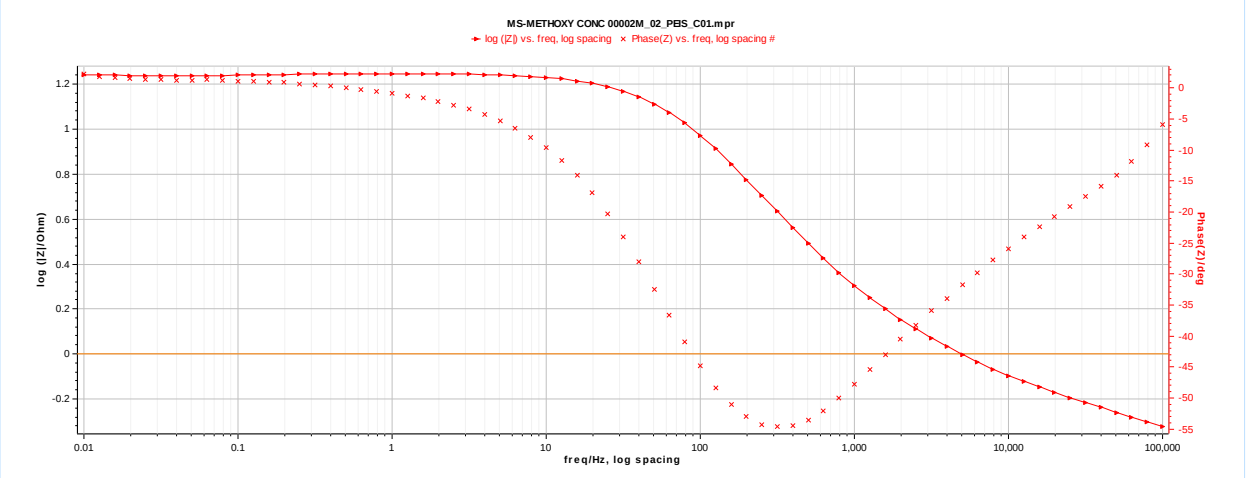

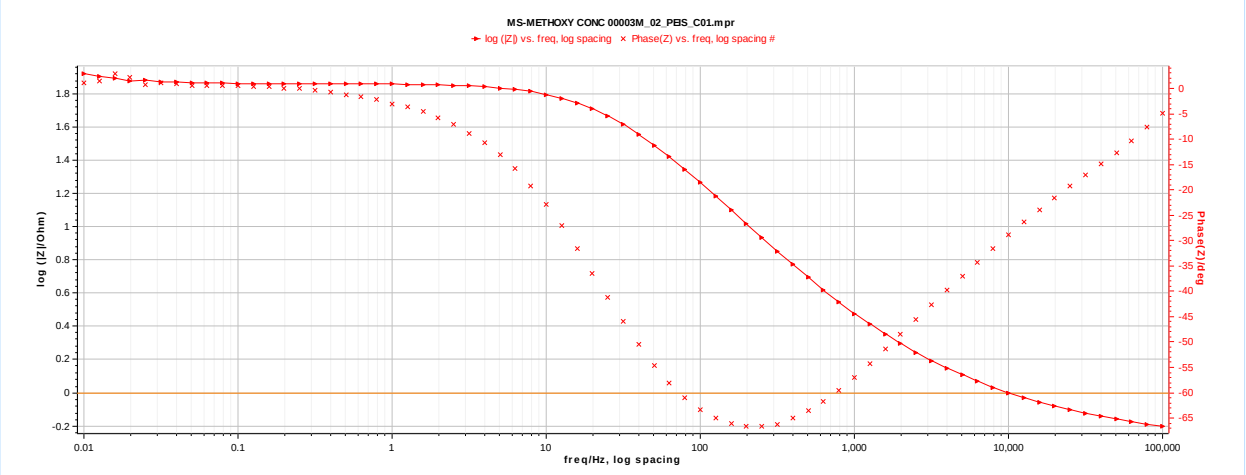

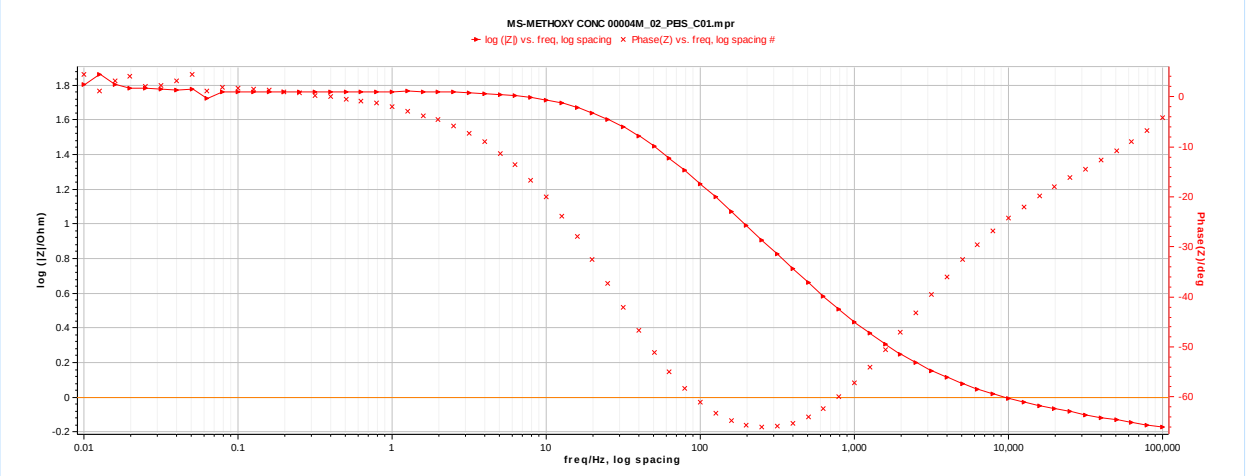

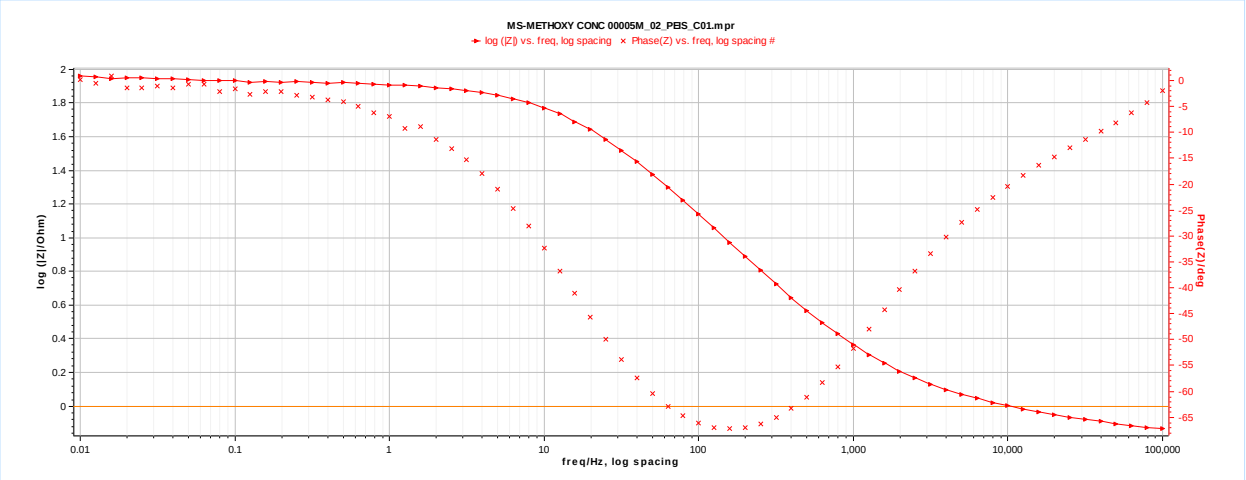

Appendix 40: Bode plots of mild steel in 1.5 M HCl in the presence of five various concentrations of CH_3O-Chr-2-Carb.

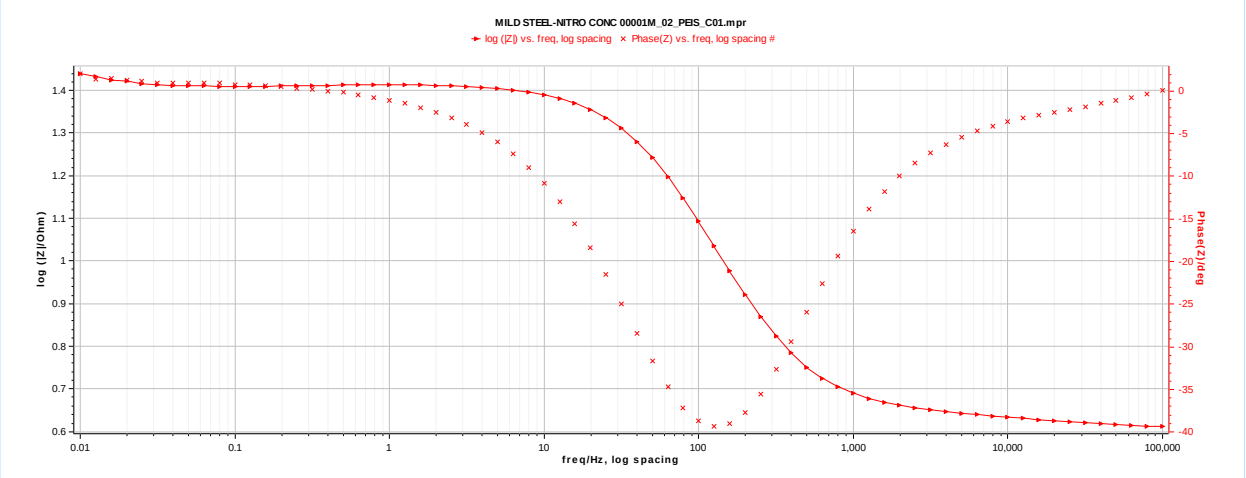

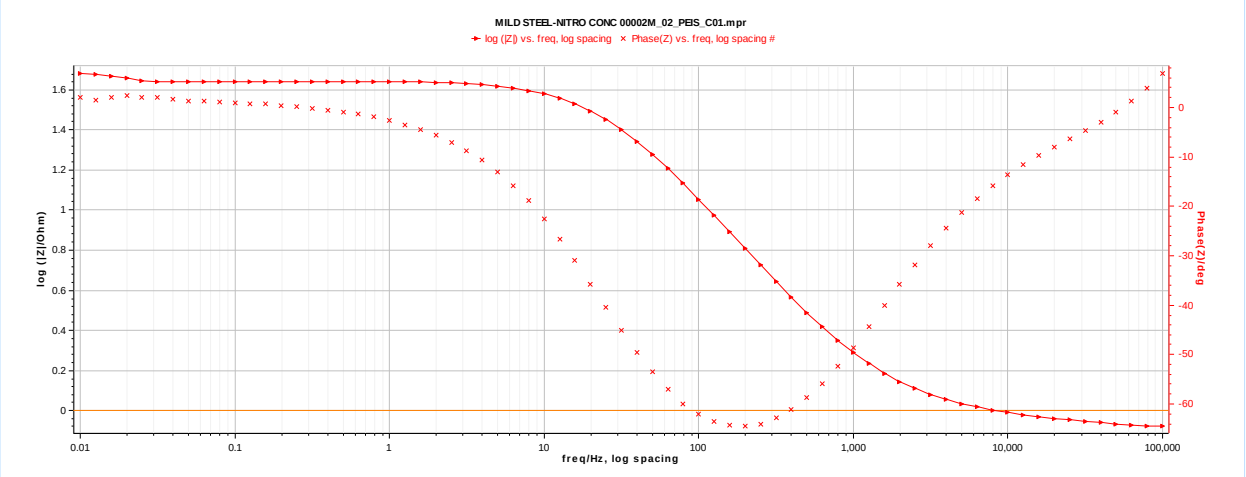

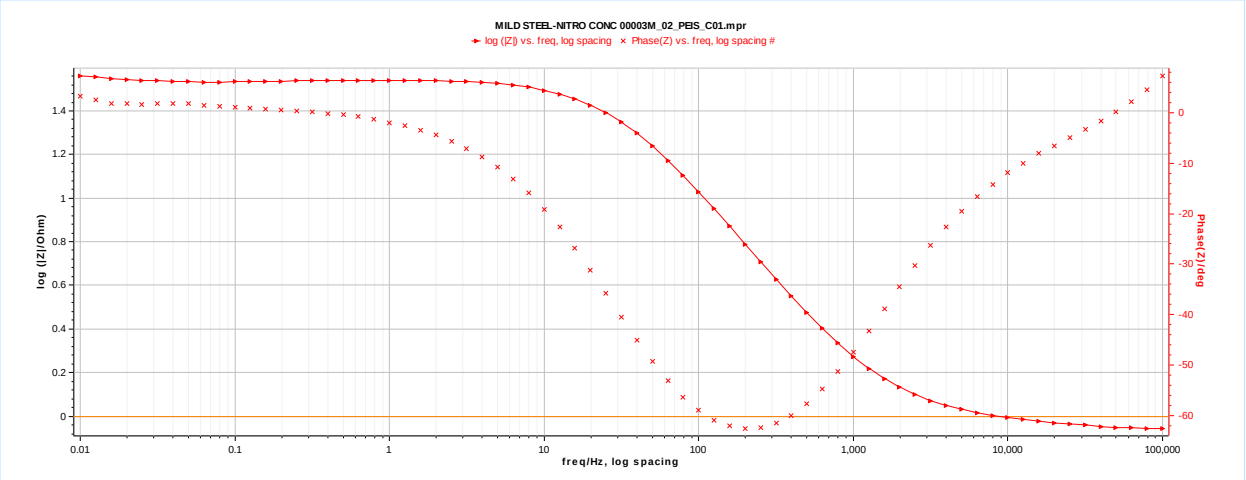

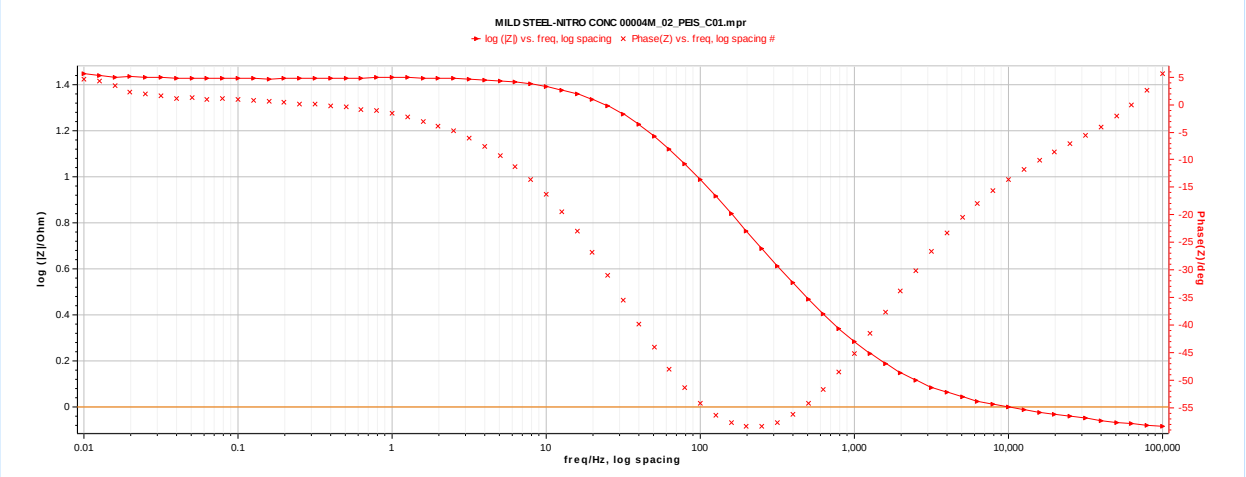

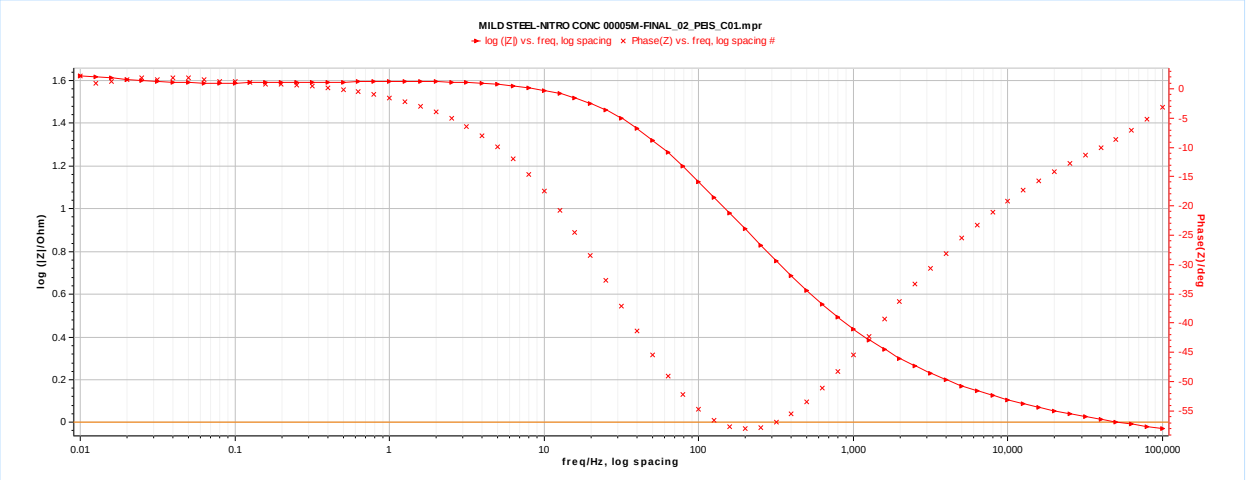

Appendix 41: Bode plots of mild steel in 1.5 M HCl in the presence of five various concentrations of NO_2-Chr-2-Carb.

3.2. Bode plot of Zinc metal in 5 M HCl in the presence of five various concentrations of the Chr-2-Carb, Br-Chr-2-Carb, Cl-Chr-2-Carb, CH_3O-Chr-2-Carb and NO_2-Chr-2-Carb inhibitors.

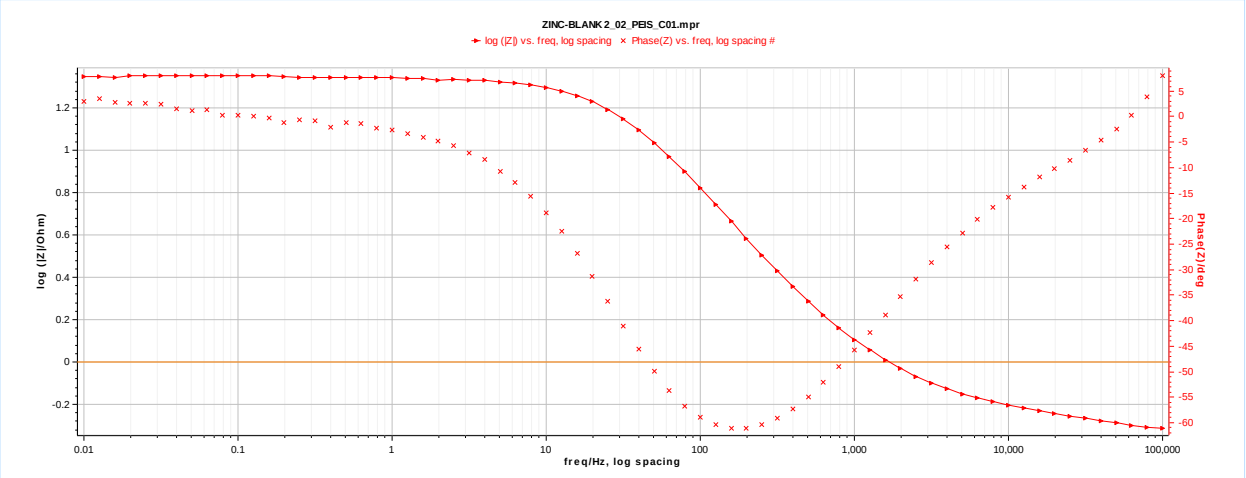

Appendix 42: Bode plot of zinc in 1.5 M HCl in the absence of various concentrations of 6-substitutedchromone-2-carboxamides.

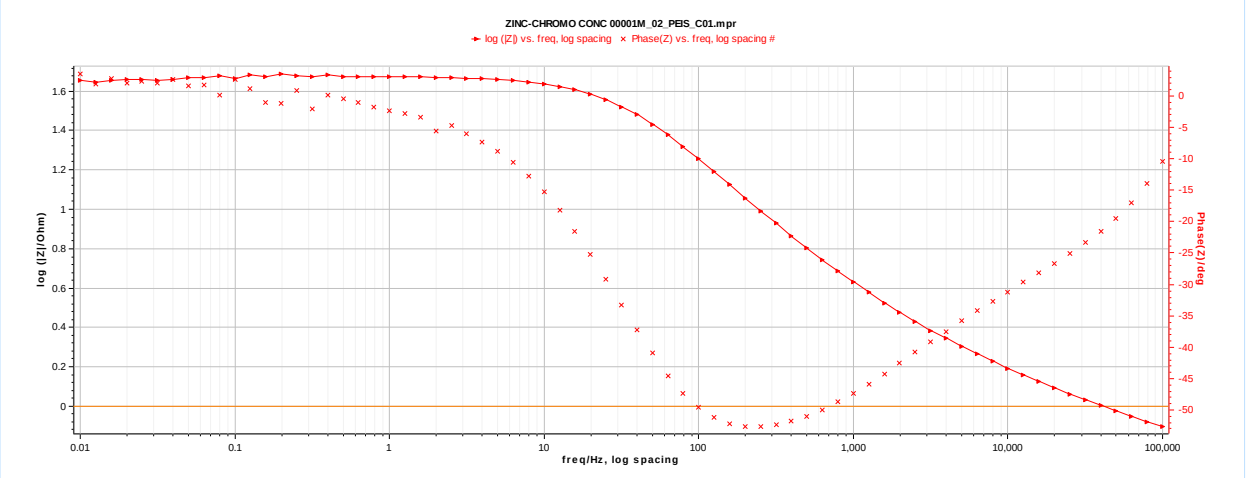

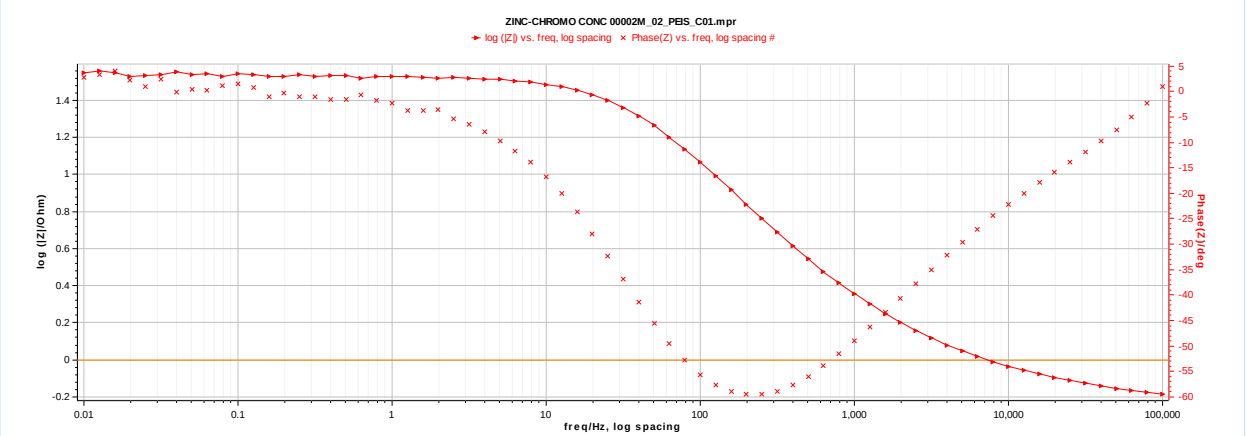

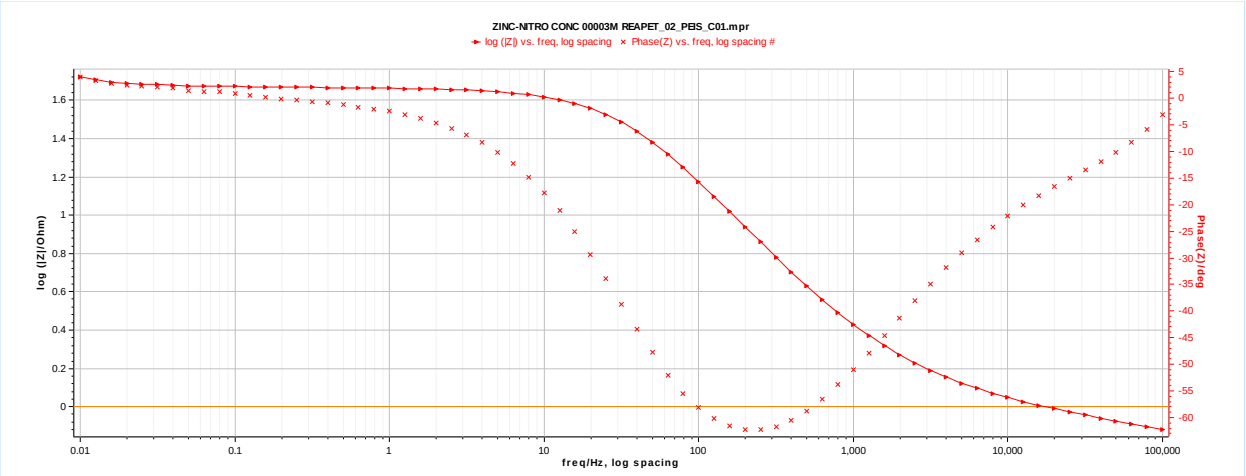

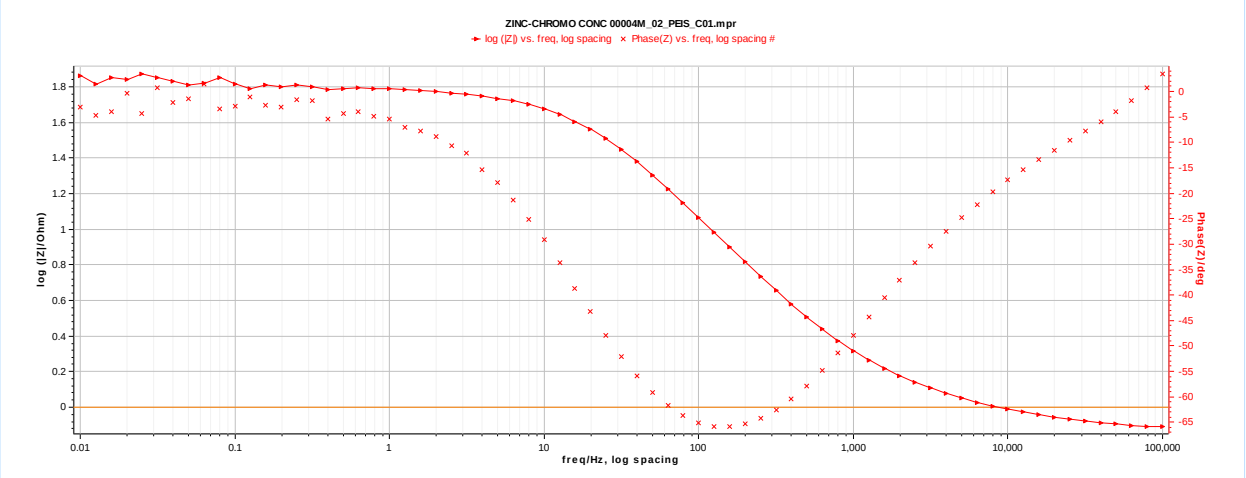

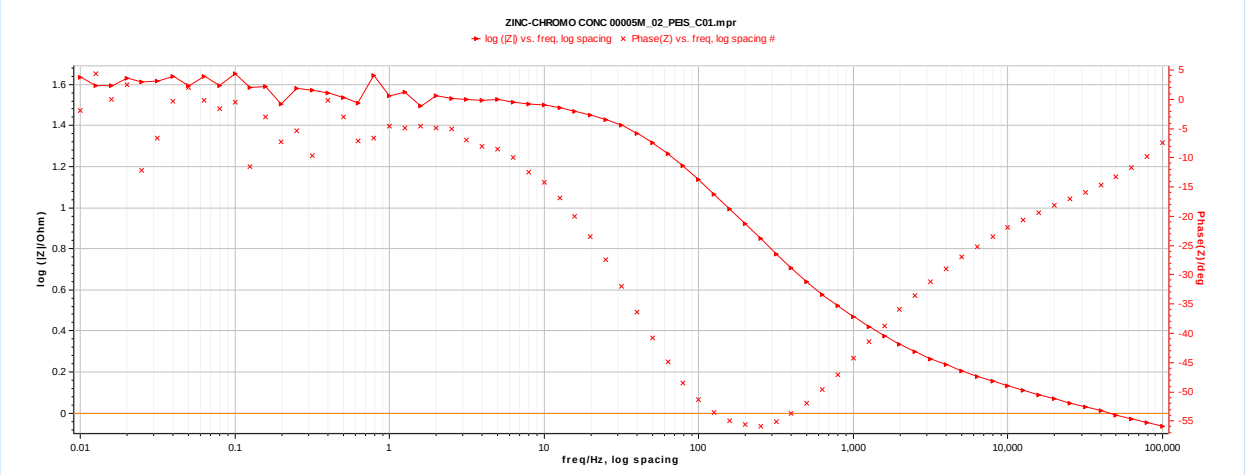

Appendix 43: Bode plot of zinc in 1.5 M HCl in the presence of five various concentrations of Chr-2-Carb.

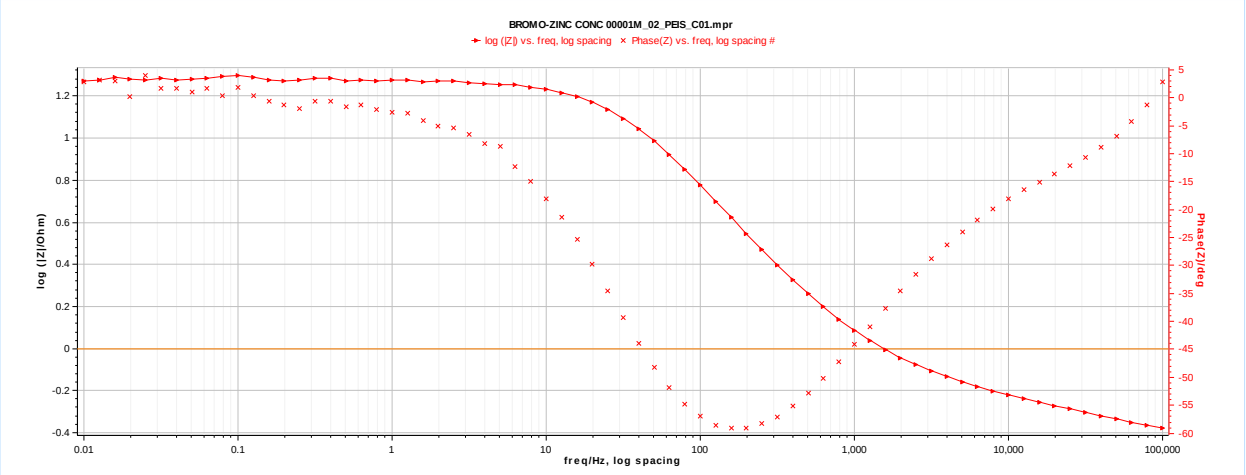

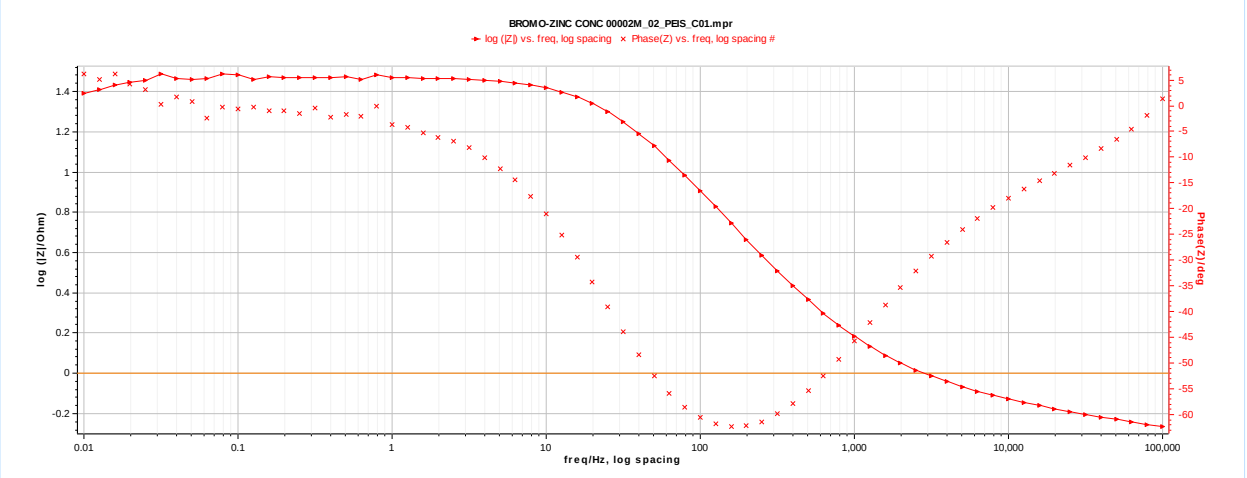

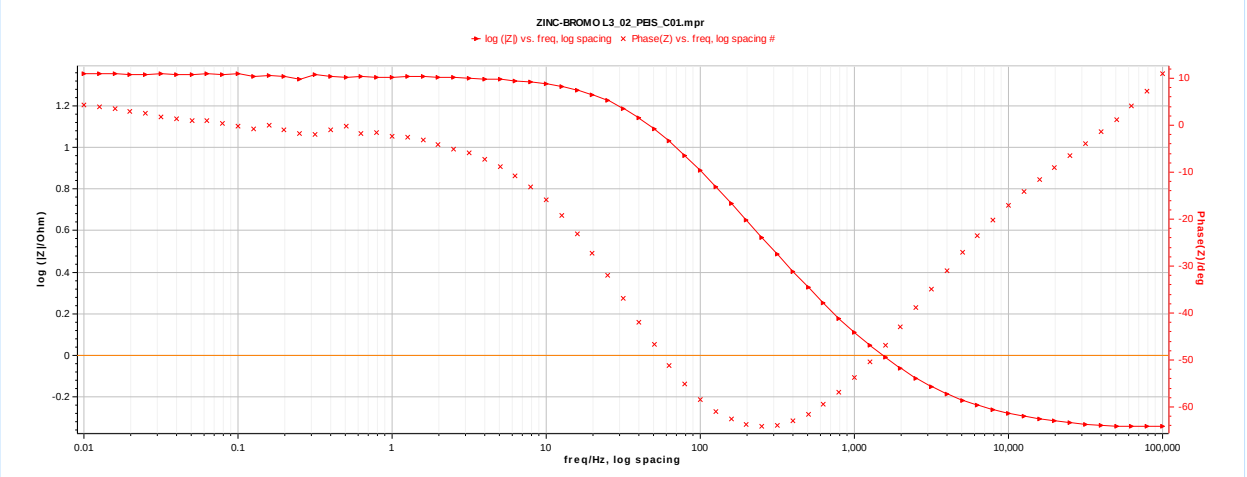

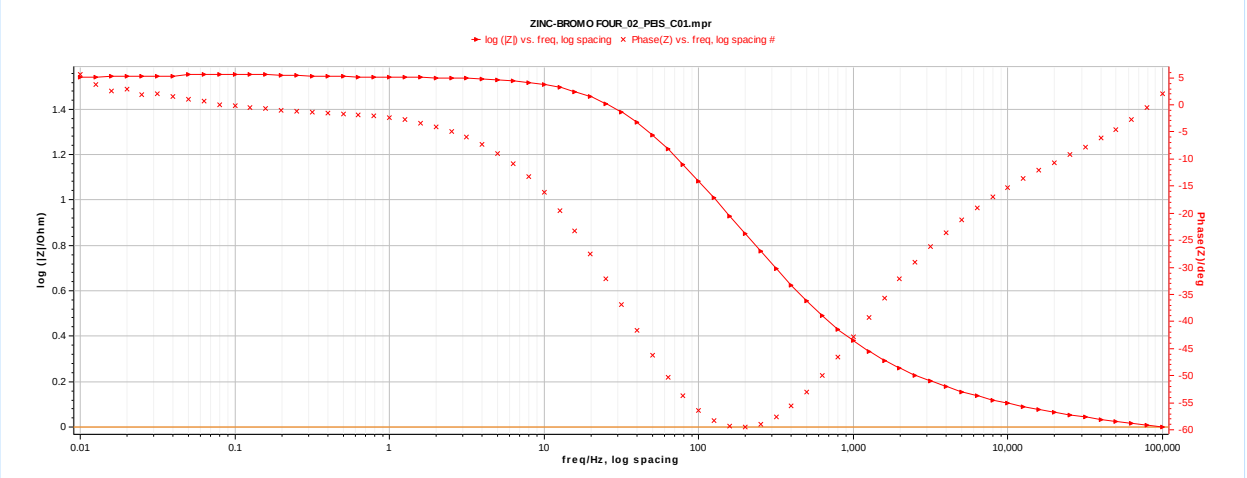

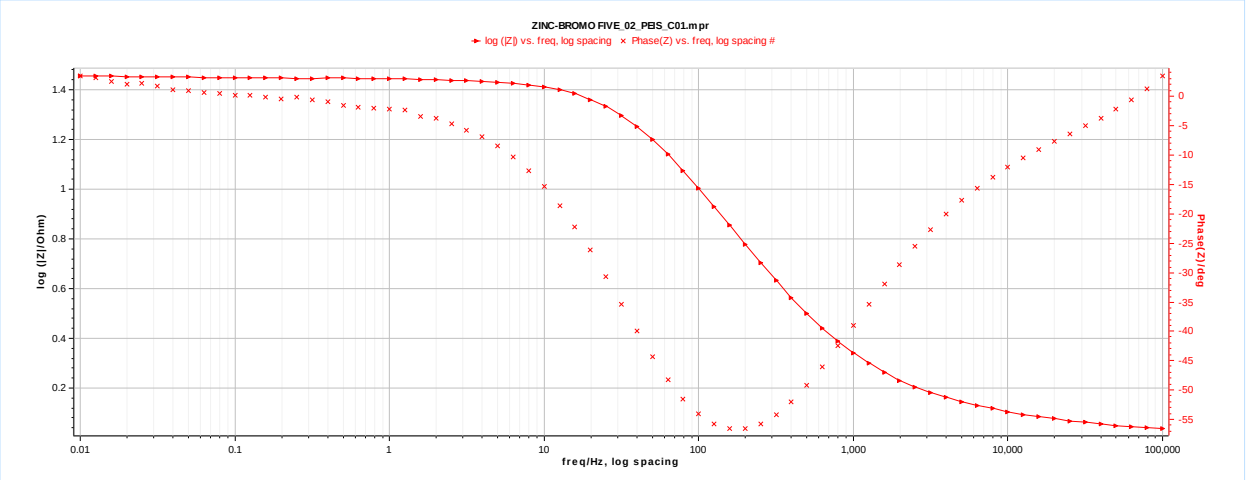

Appendix 44: Bode plot of zinc in 1.5 M HCl in the presence of five various concentrations of Br-Chr-2-carb.

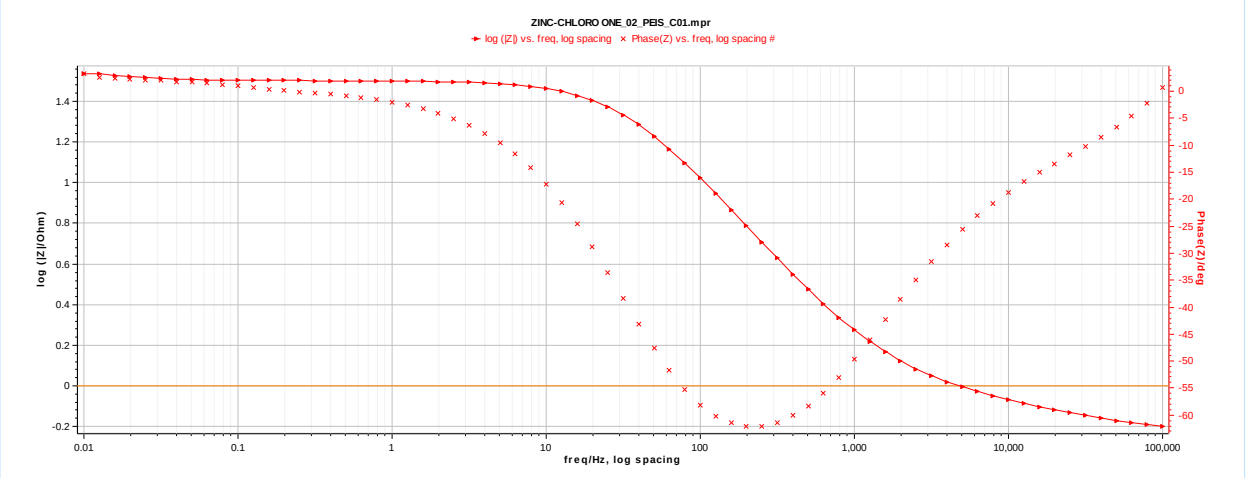

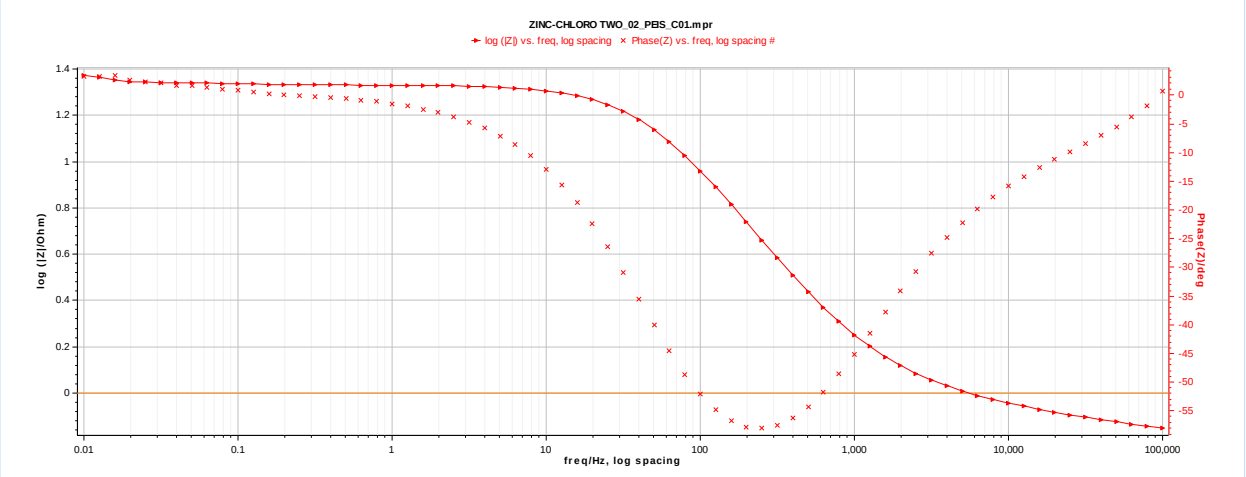

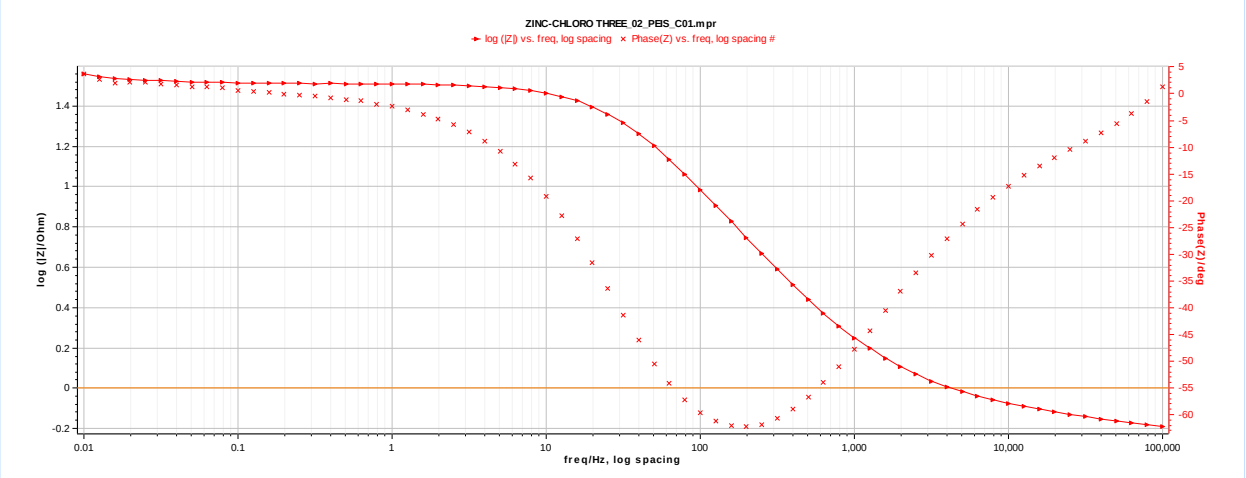

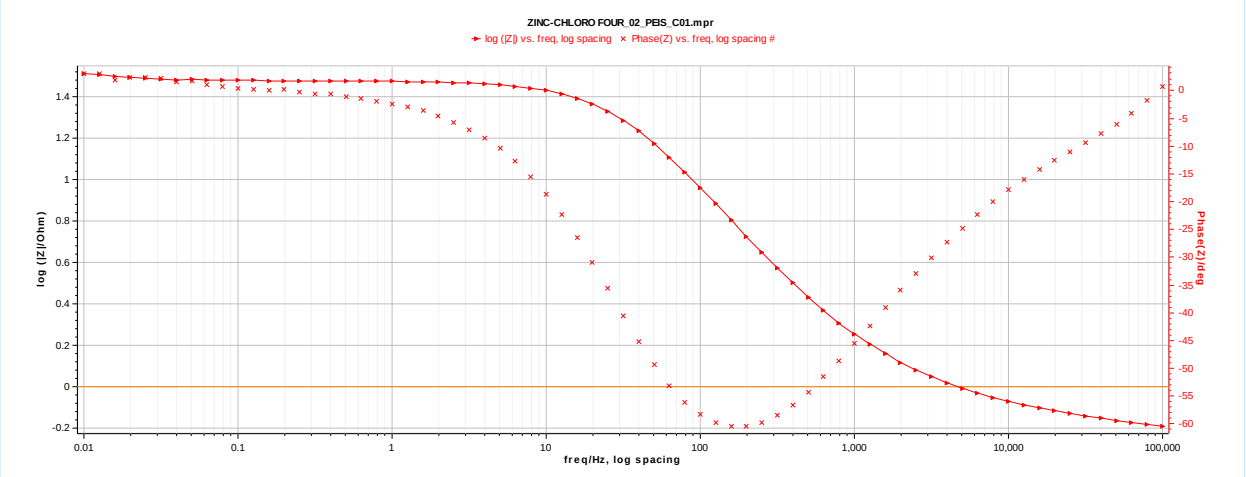

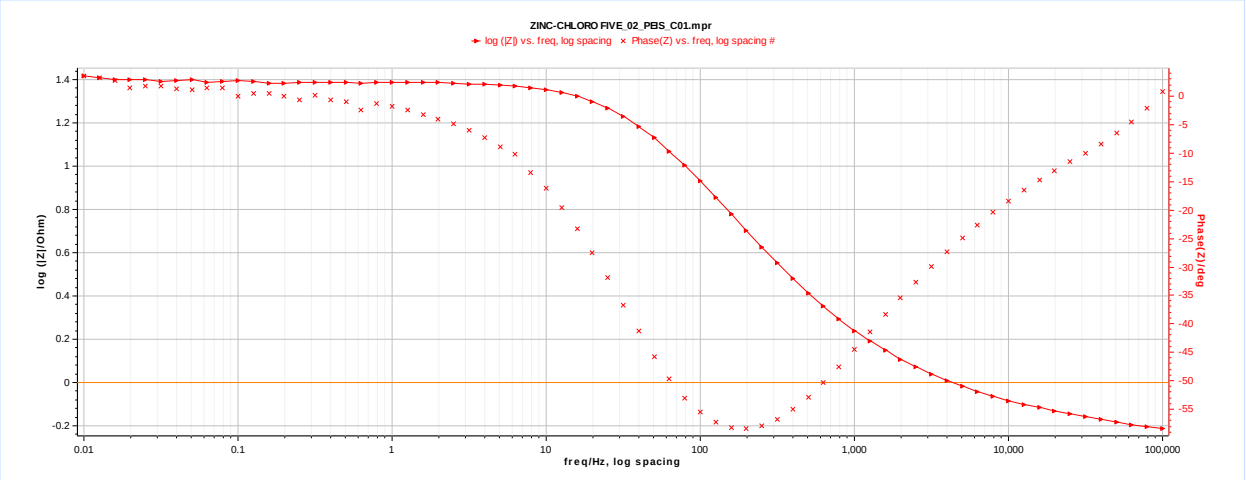

Appendix 45: Bode plots of zinc in 1.5 M HCl in the presence of five various concentrations of Cl-Chr-2-Carb.

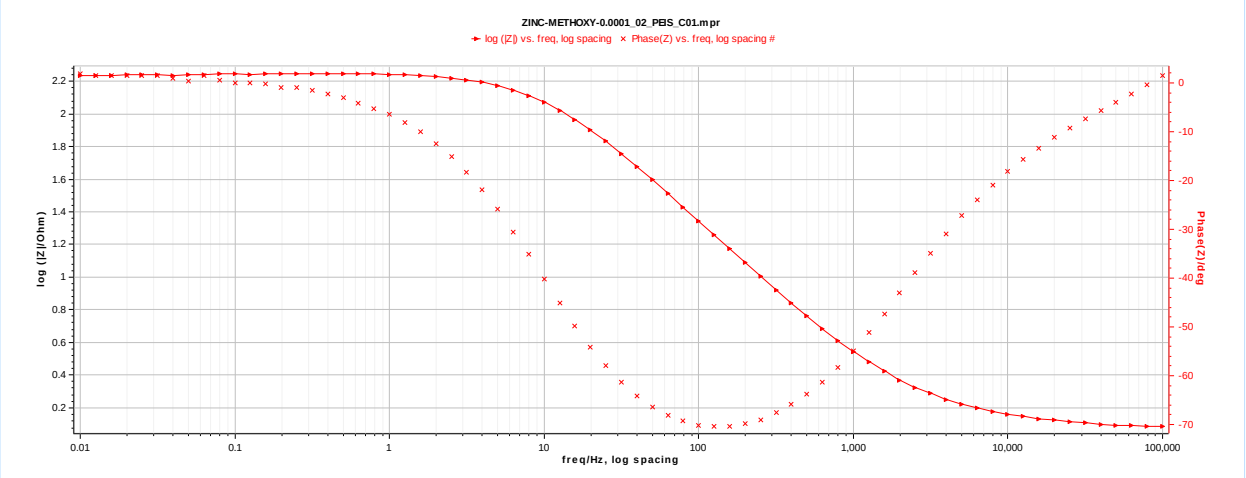

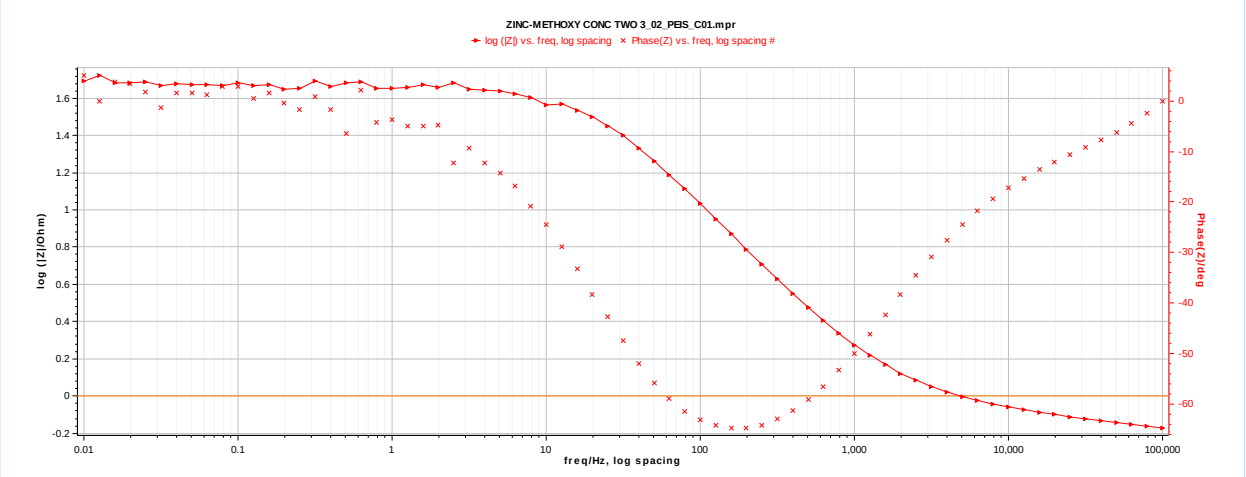

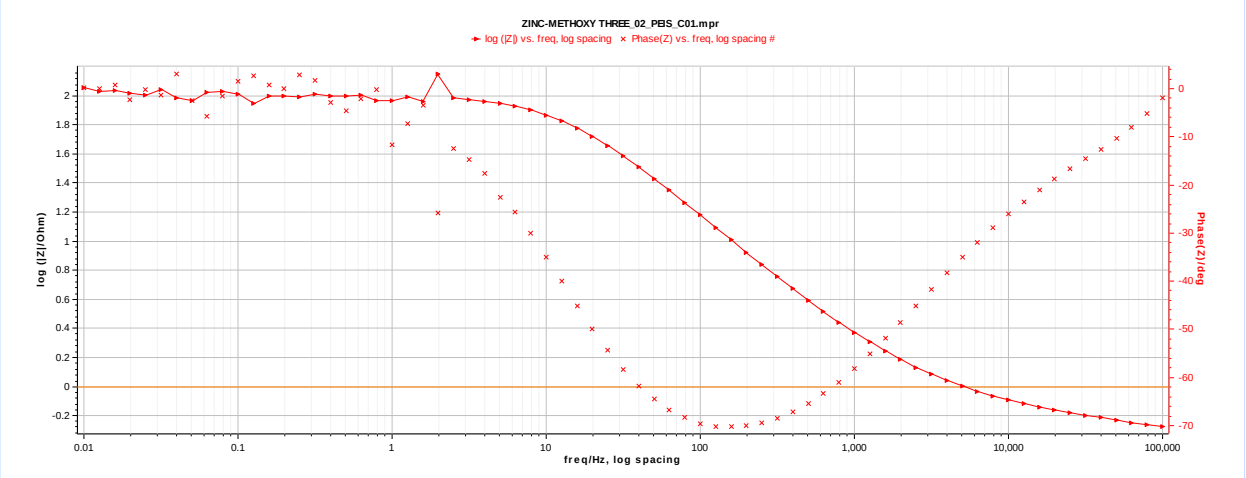

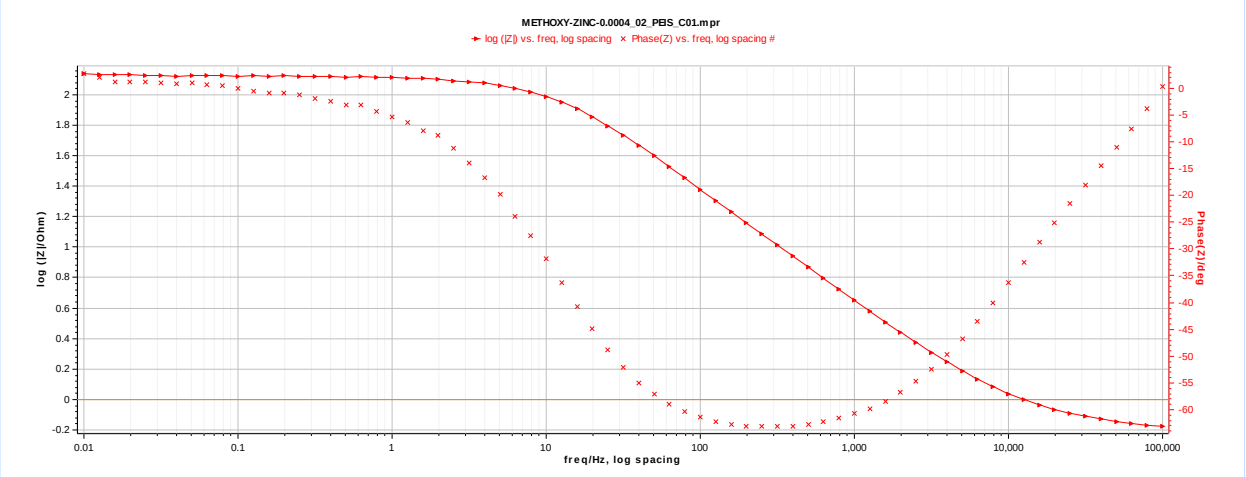

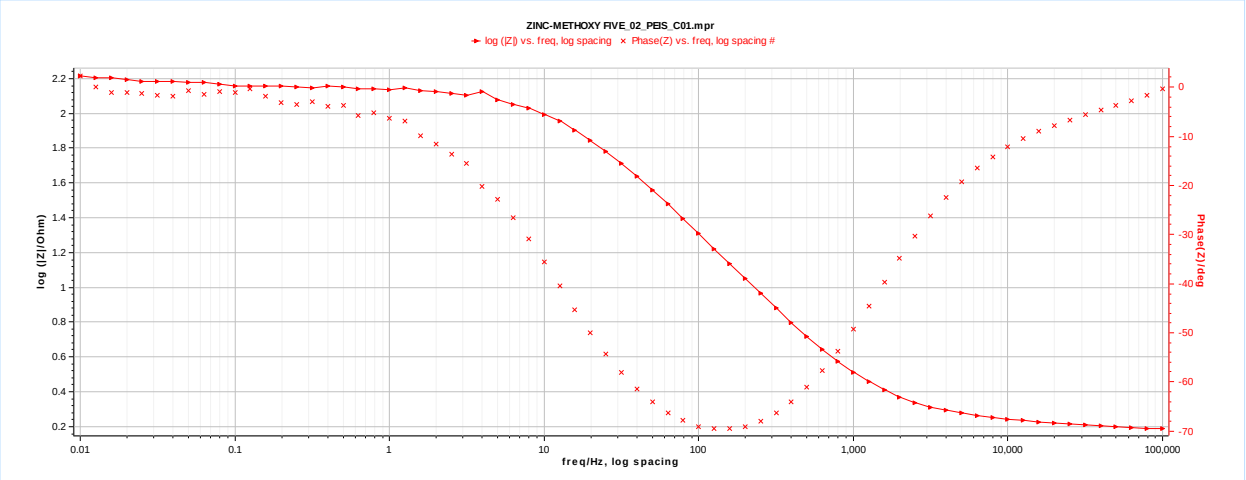

Appendix 46: Bode plots of zinc in 1.5 M HCl in the presence of five various concentrations of CH_3O-Chr-2-Carb.

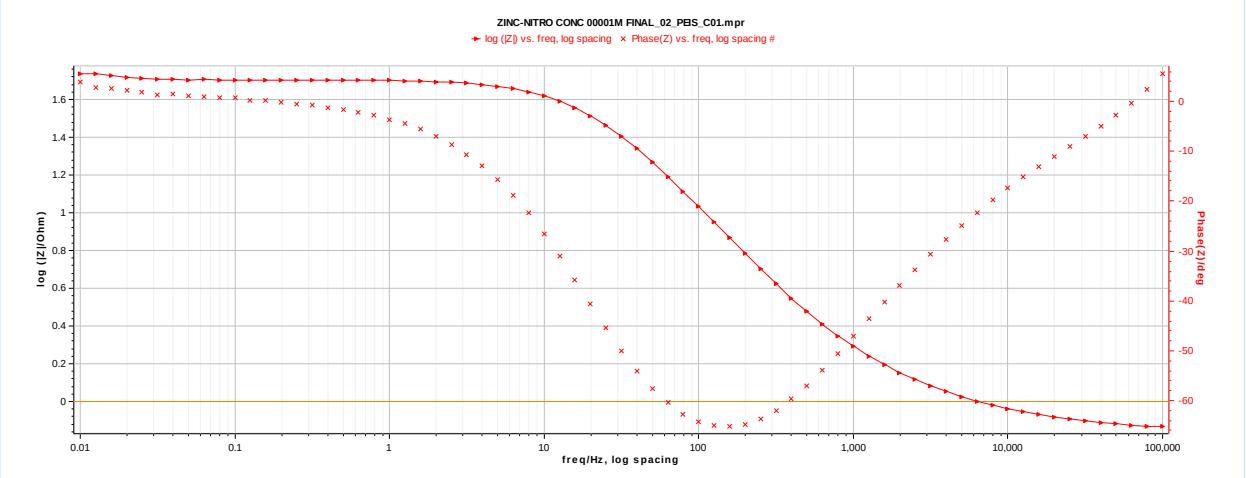

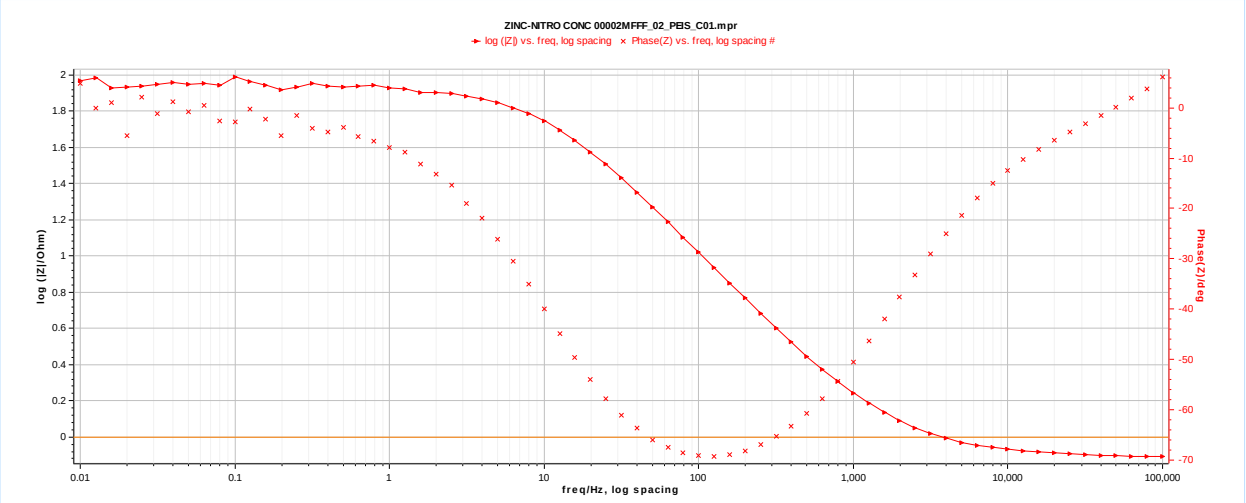

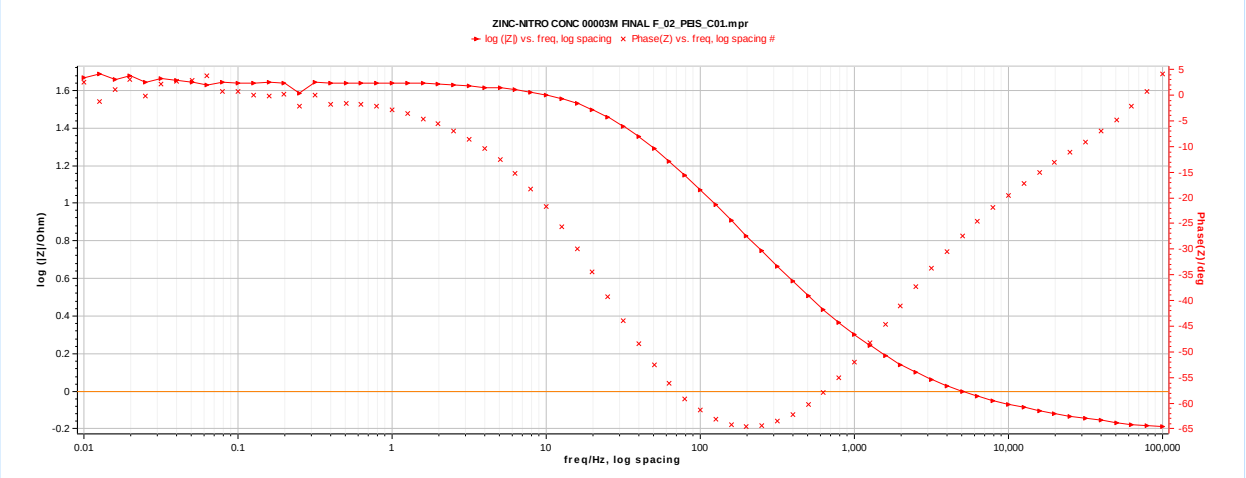

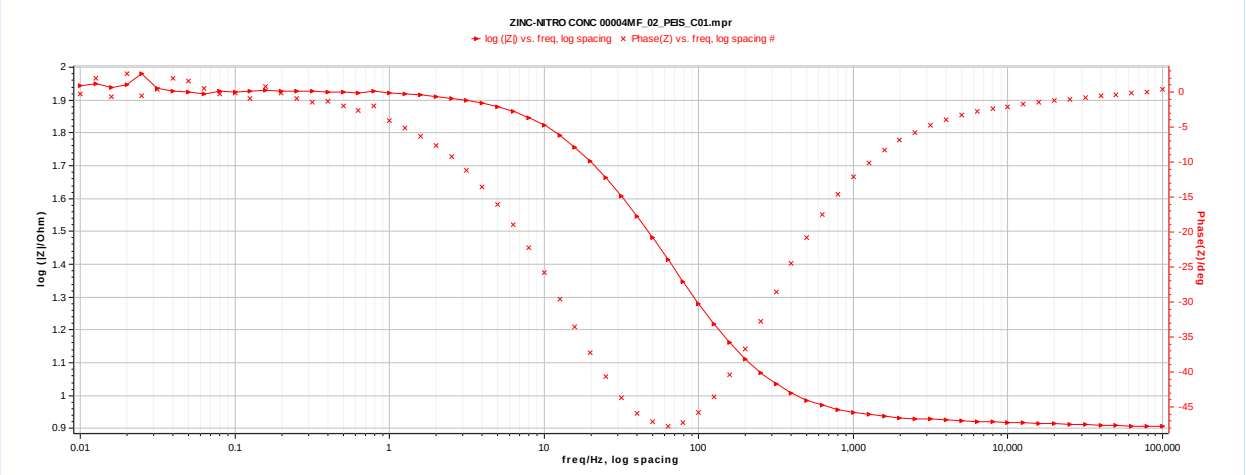

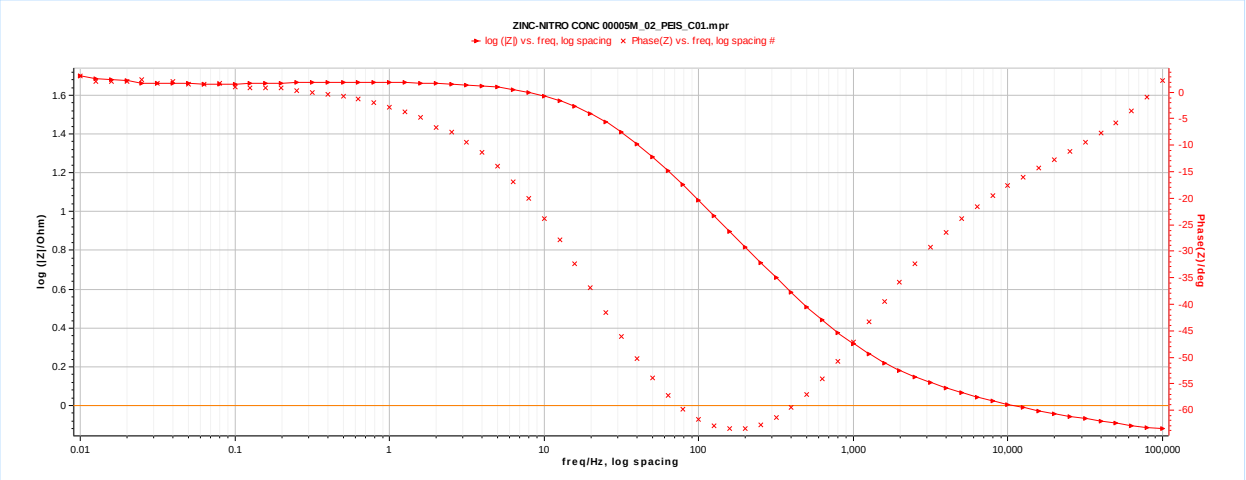

Appendix 47: Bode plots of zinc in 1.5 M HCl in the presence of five various concentrations of NO_2-Chr-2-Carb.

3.3. Bode plot of Aluminium metal in 1 M HCl in the presence of five various concentrations of the Chr-2-Carb, Br-Chr-2-Carb, Cl-Chr-2-Carb, CH_3O-Chr-2-Carb and NO_2-Chr-2-Carb inhibitors.

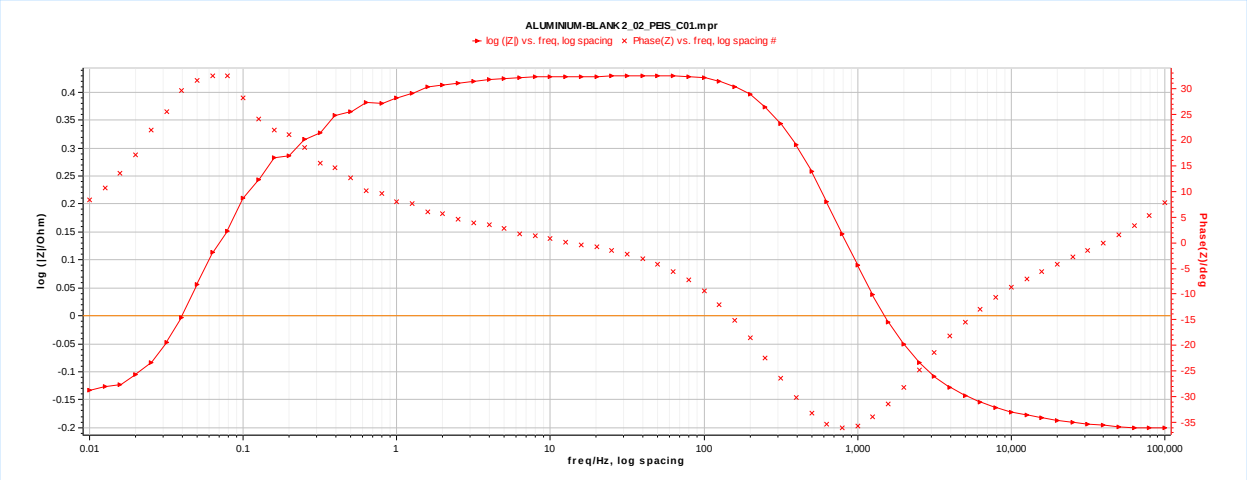

Appendix 48: Bode plot of aluminium in 1.0 M HCl in the absence of various concentrations of 6-substitutedchromone-2-carboxamides.

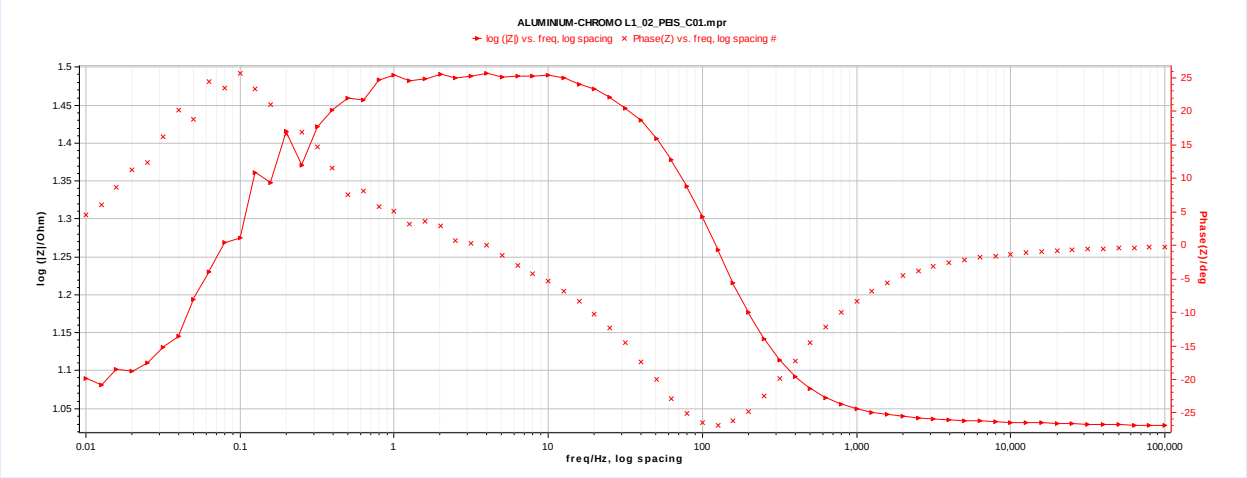

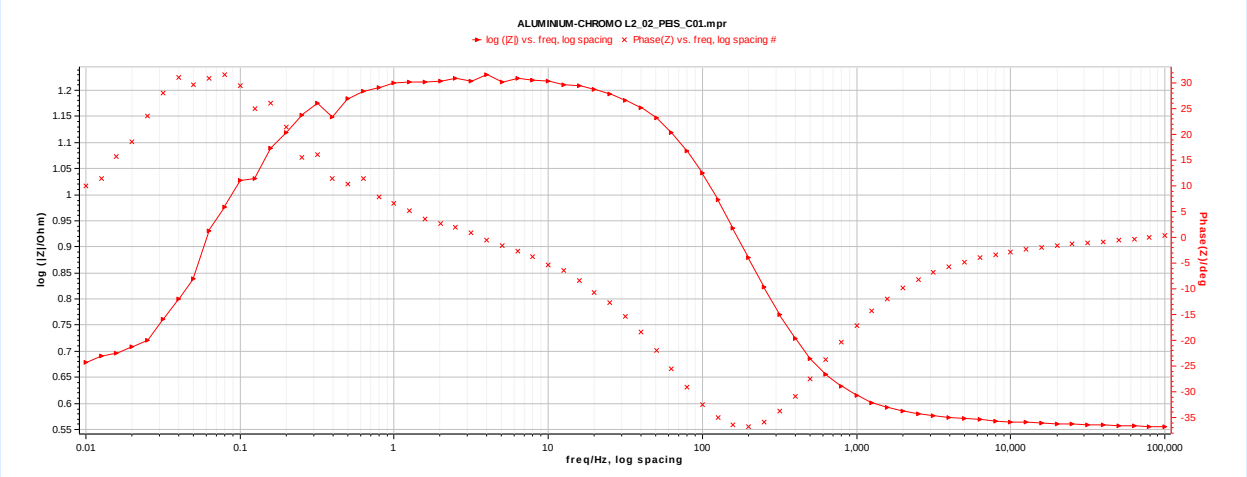

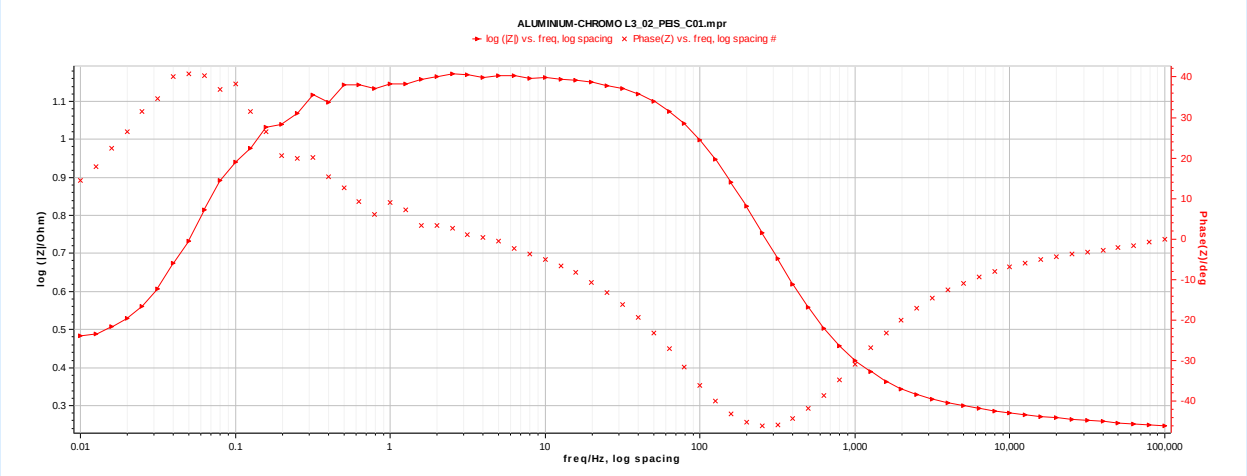

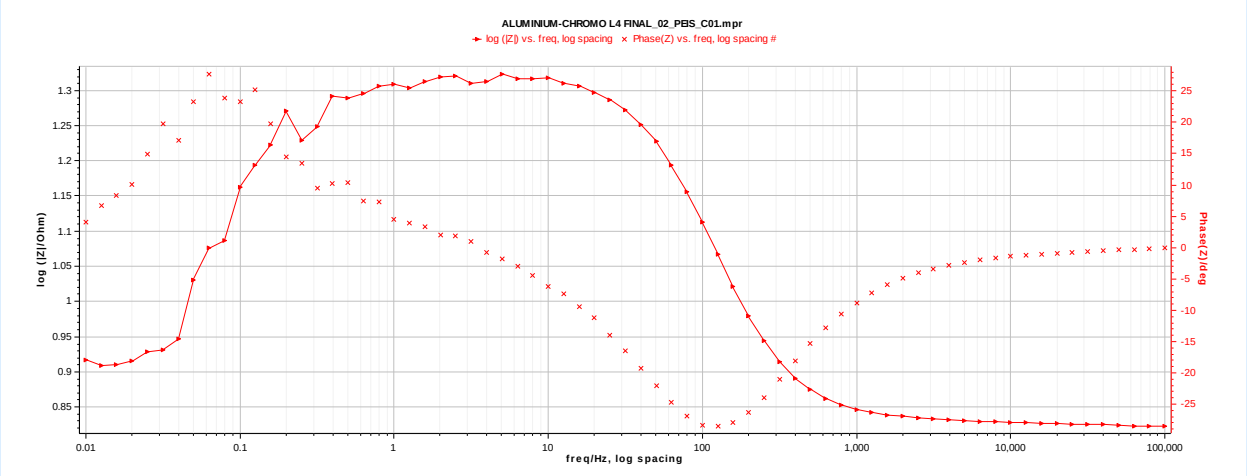

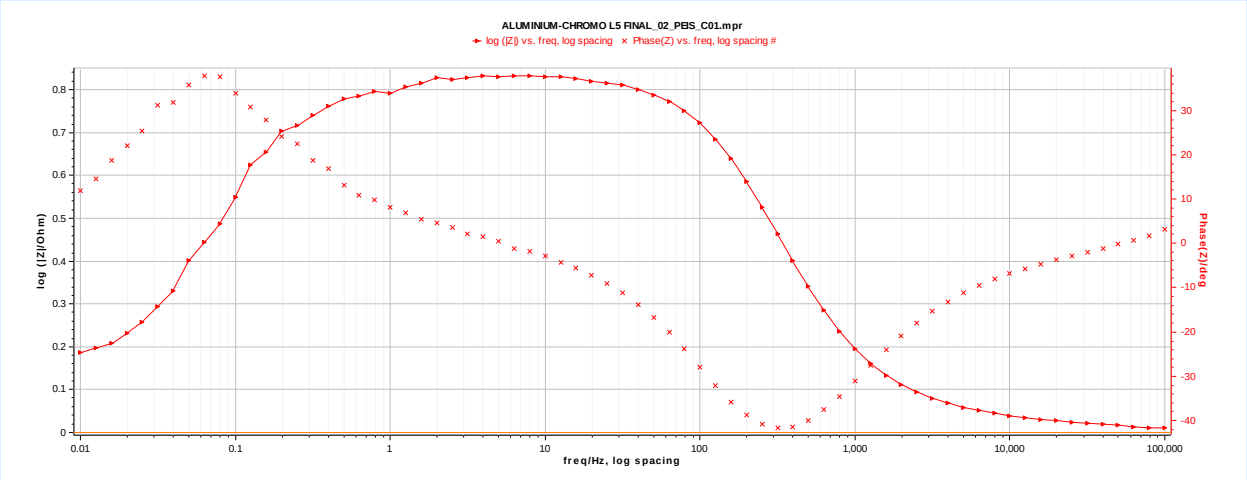

Appendix 49: Bode plot of aluminium in 1.0 M HCl in the presence of five various concentrations of Chr-2-Carb.

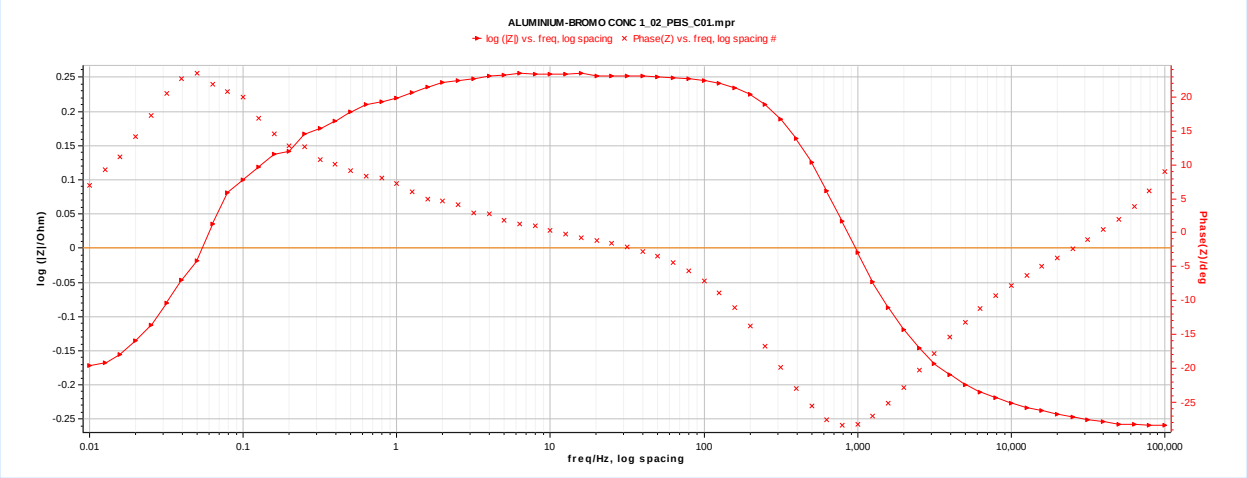

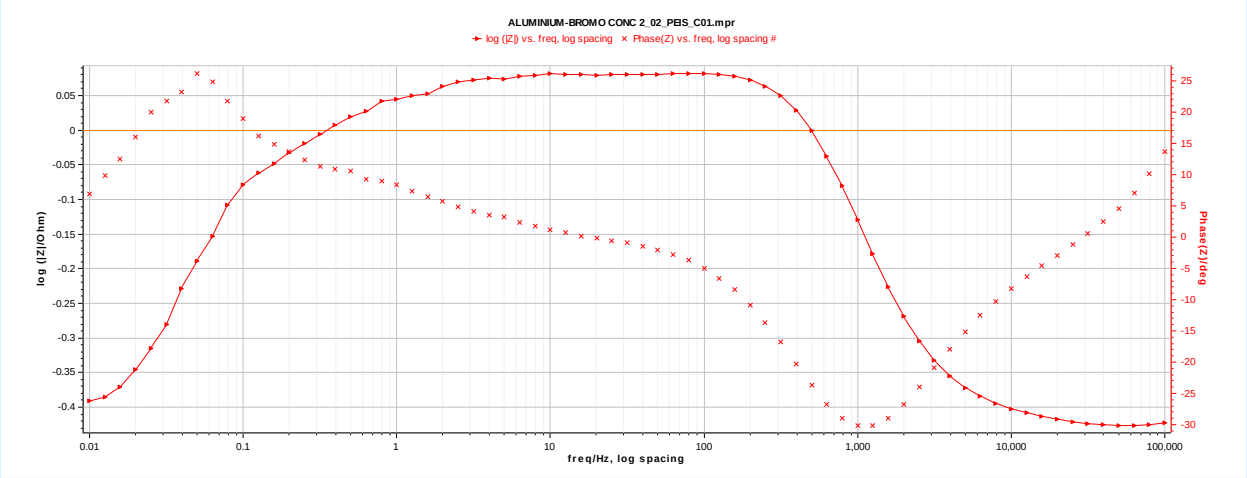

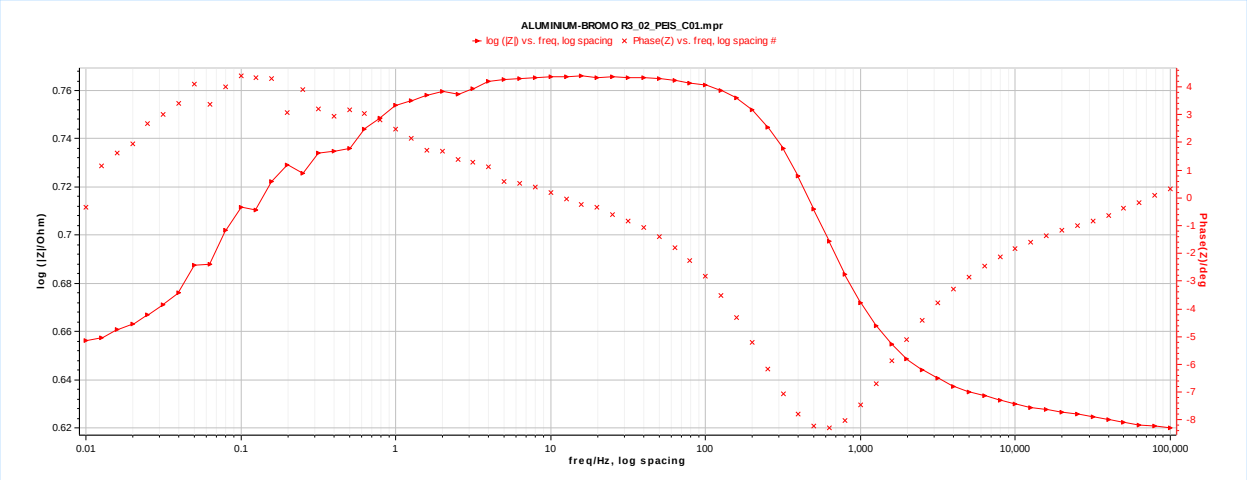

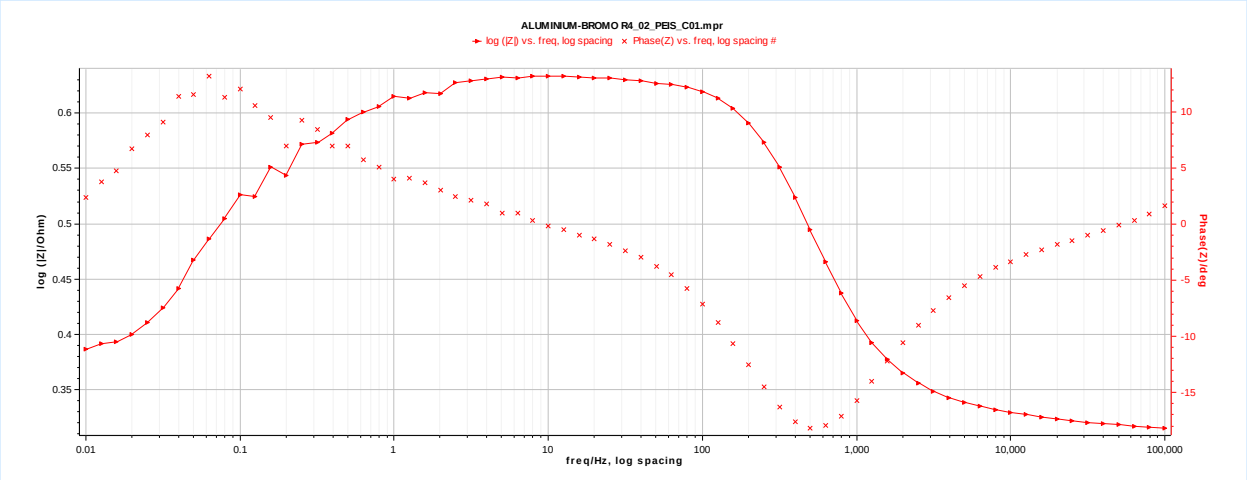

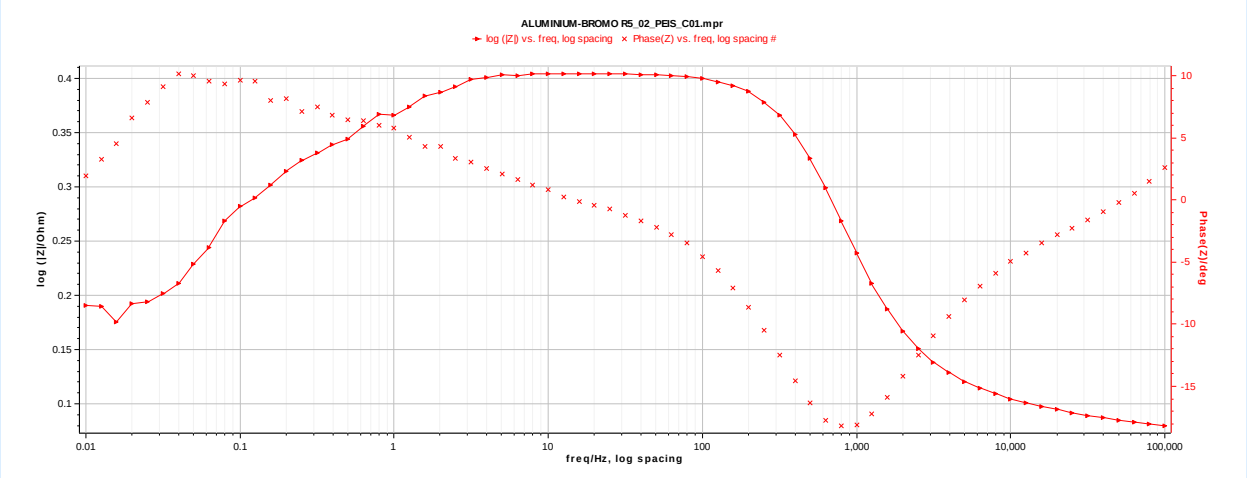

Appendix 50: Bode plot of aluminium in 1.0 M HCl in the presence of five various concentrations of Br-Chr-2-carb.

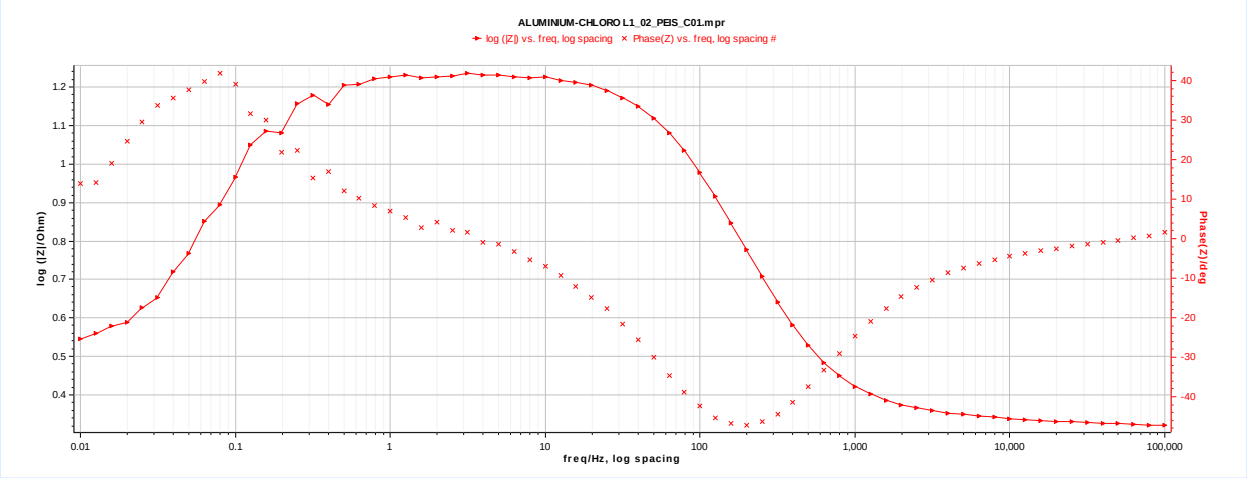

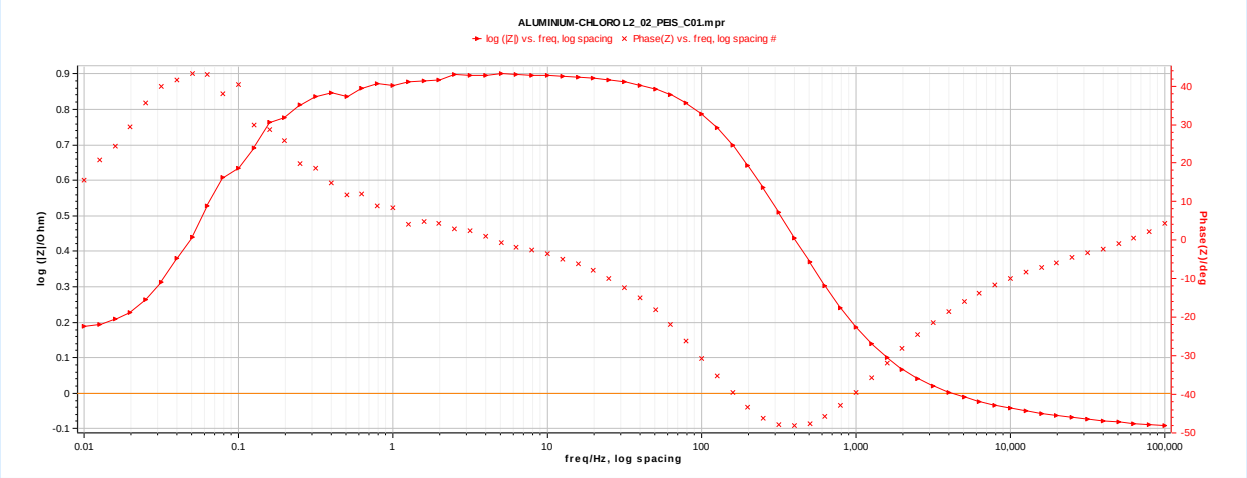

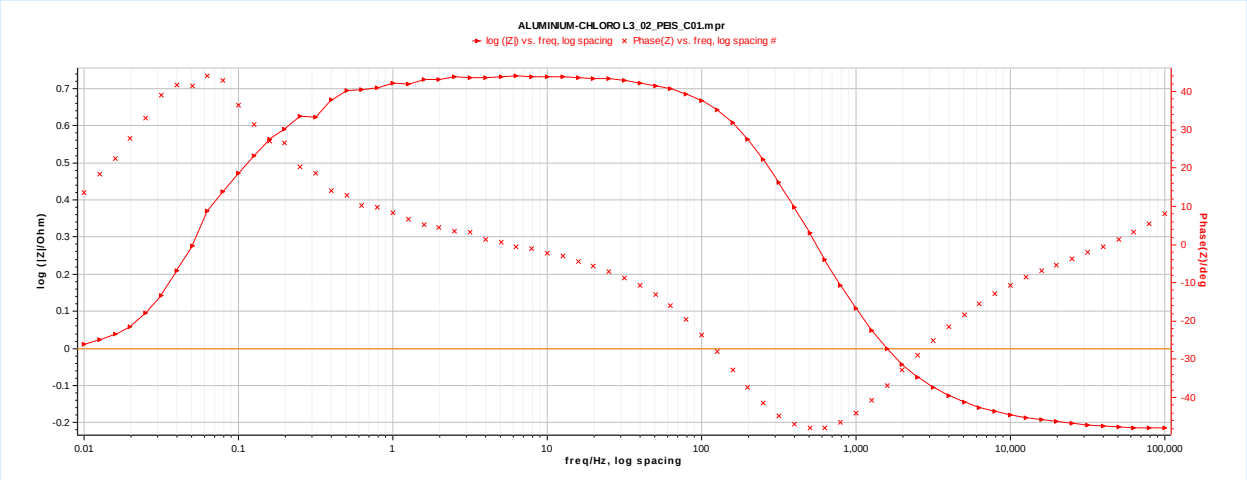

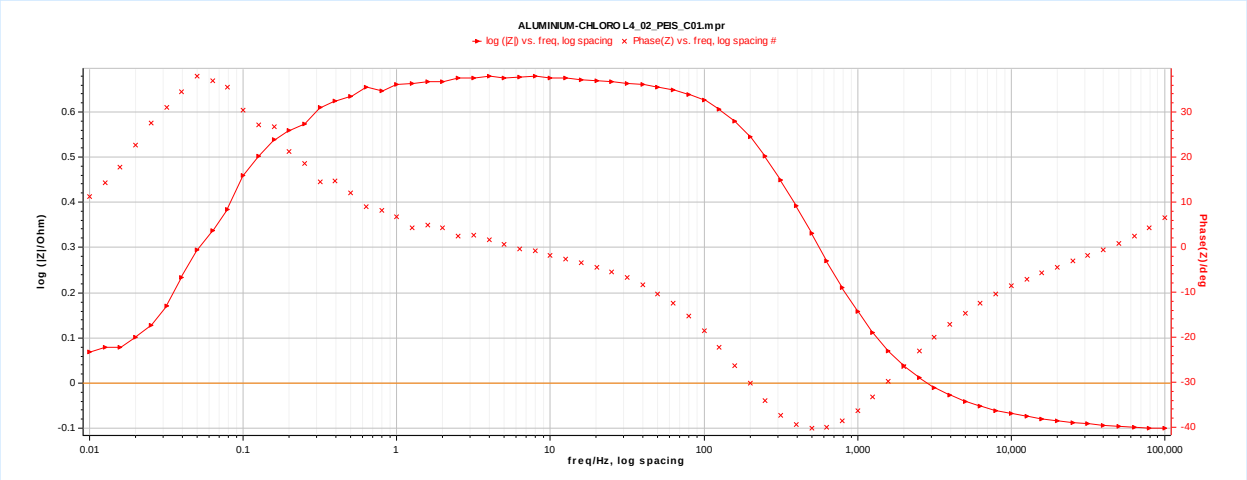

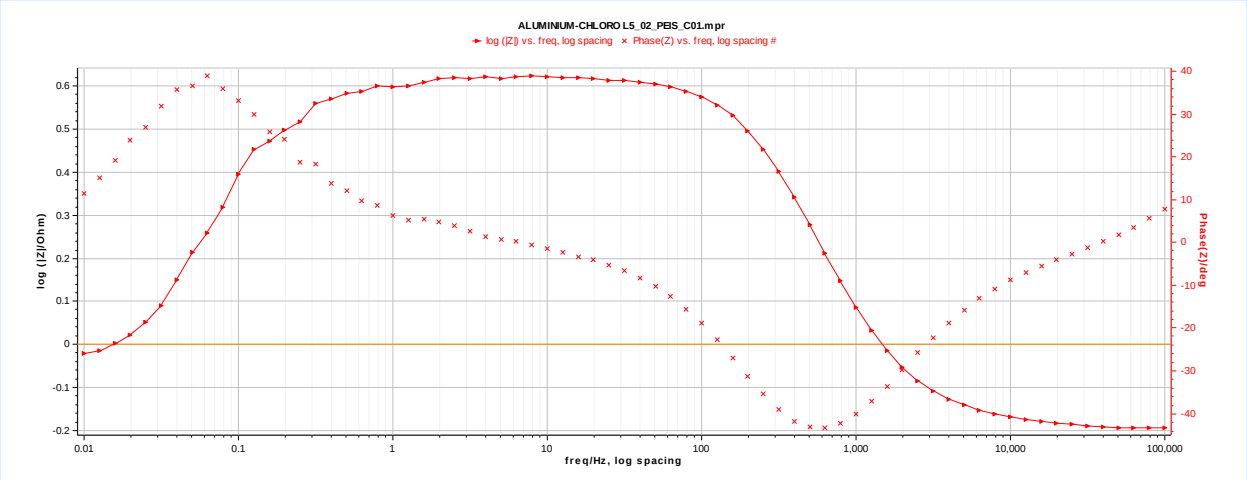

Appendix 51: Bode plots of aluminium in 1.0 M HCl in the presence of five various concentrations of Cl-Chr-2-Carb.

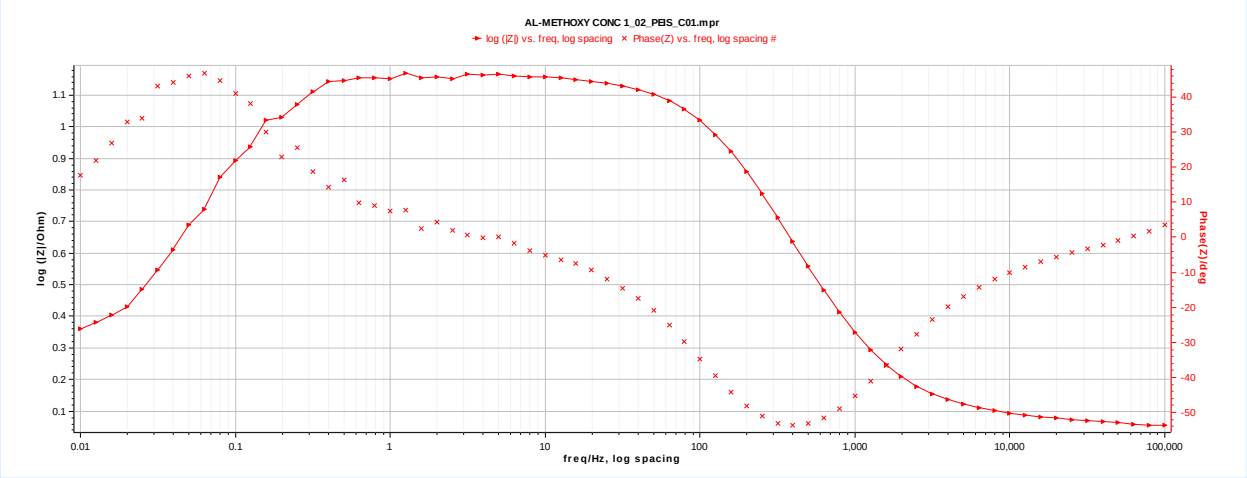

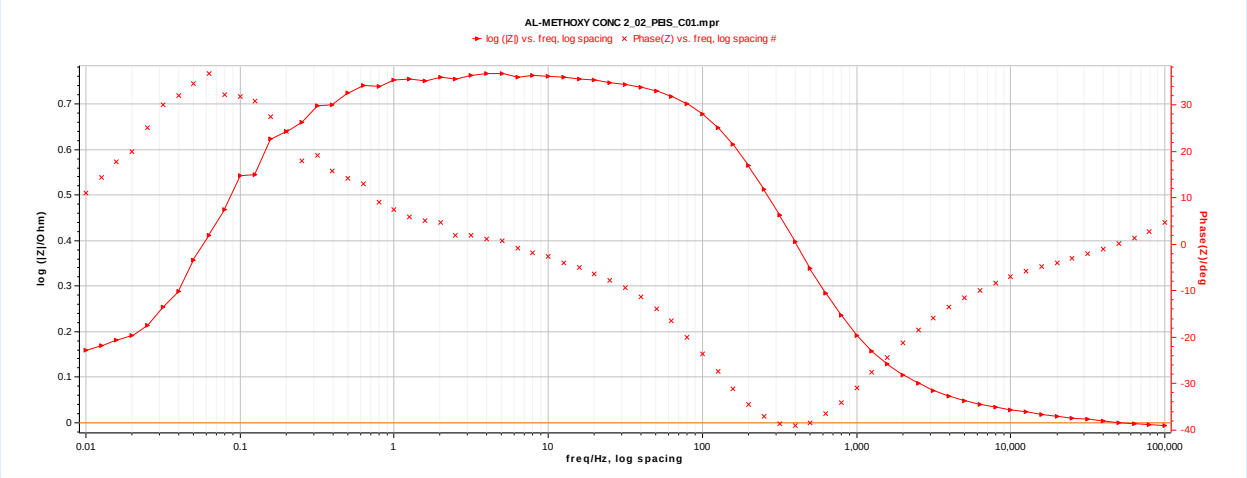

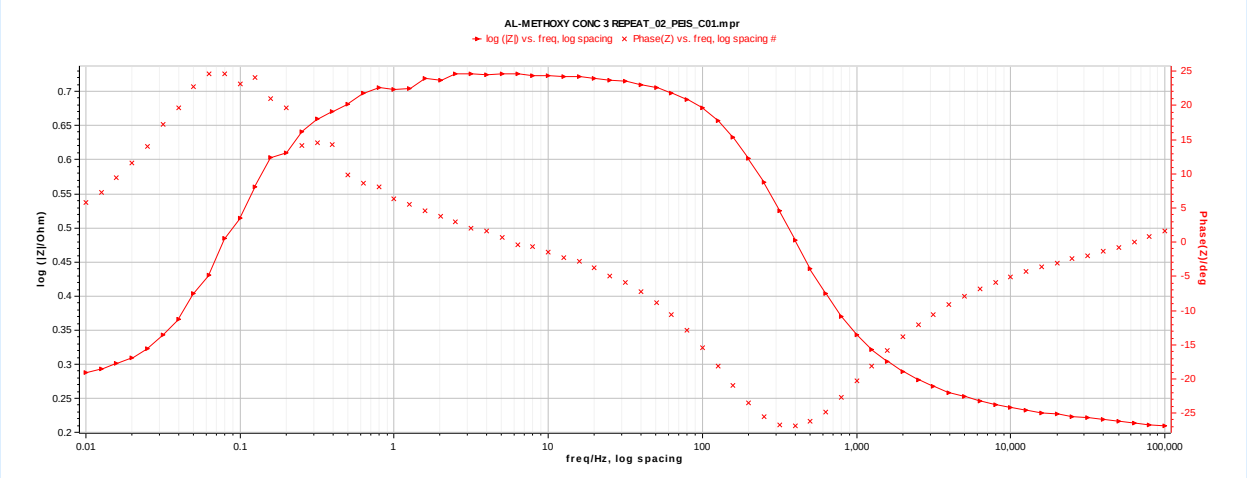

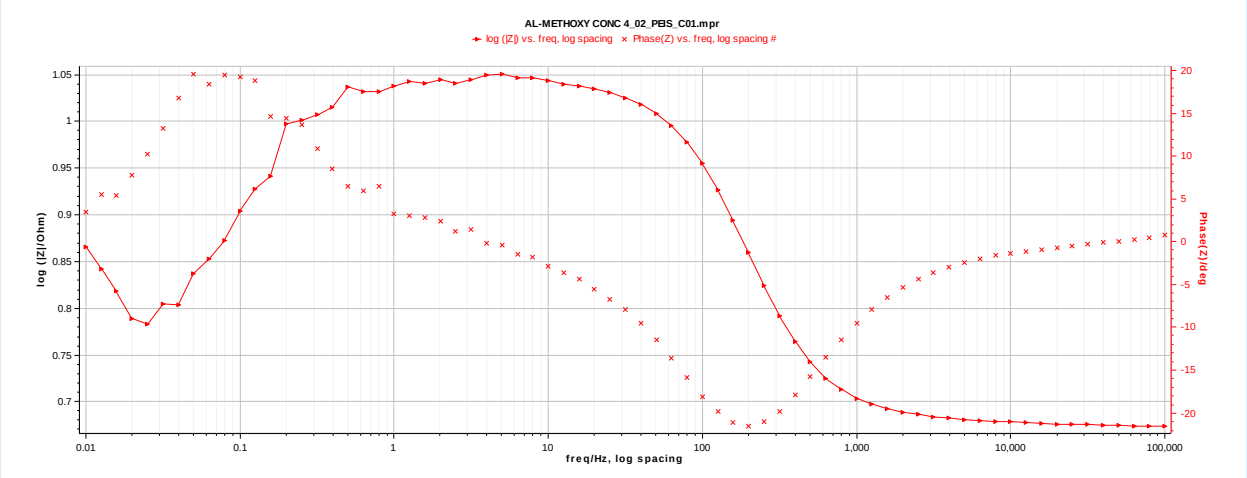

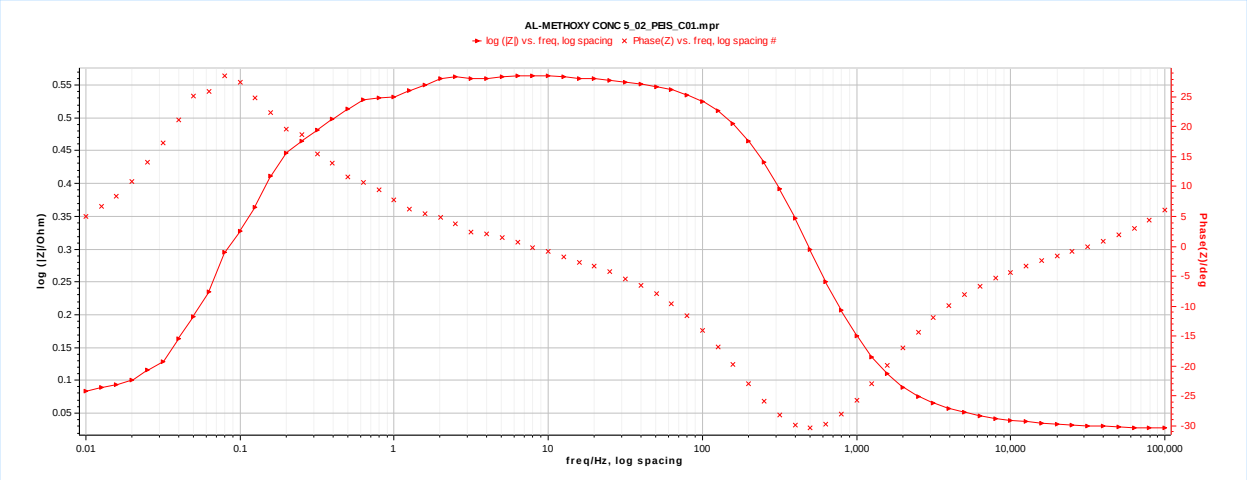

Appendix 52: Bode plots of aluminium in 1.0 M HCl in the presence of five various concentrations of CH_3O-Chr-2-Carb.

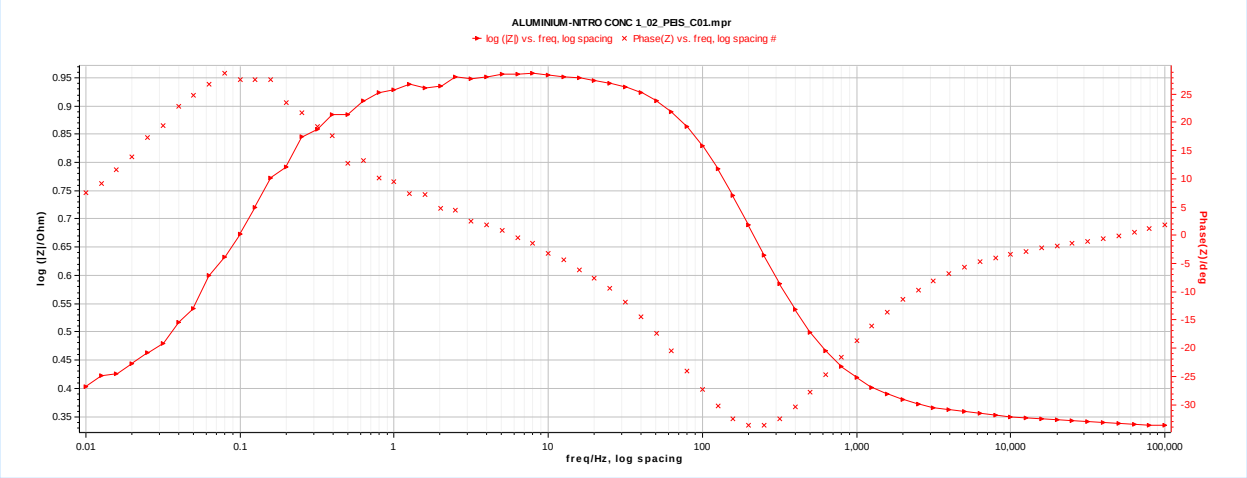

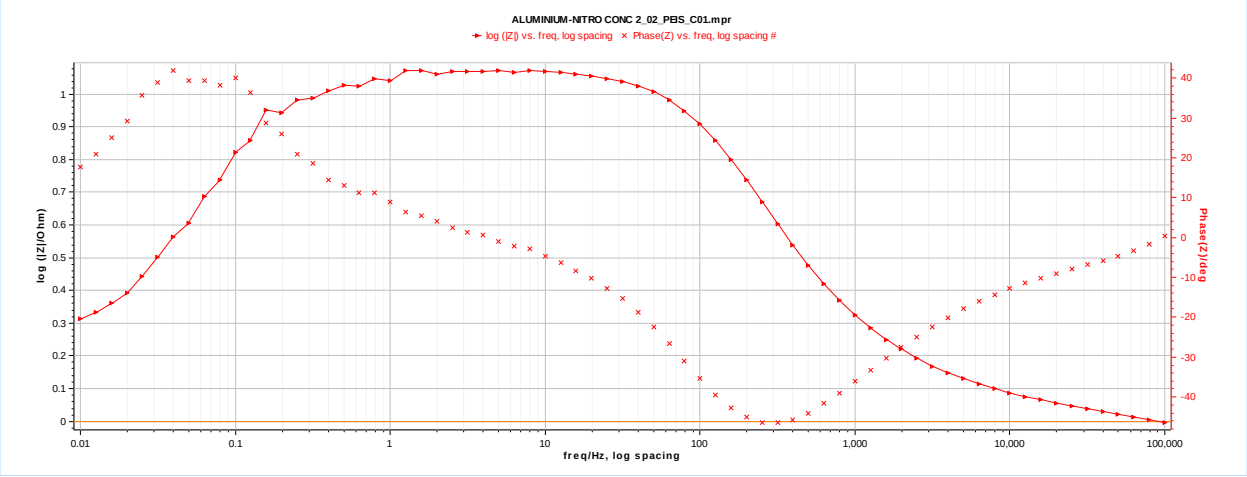

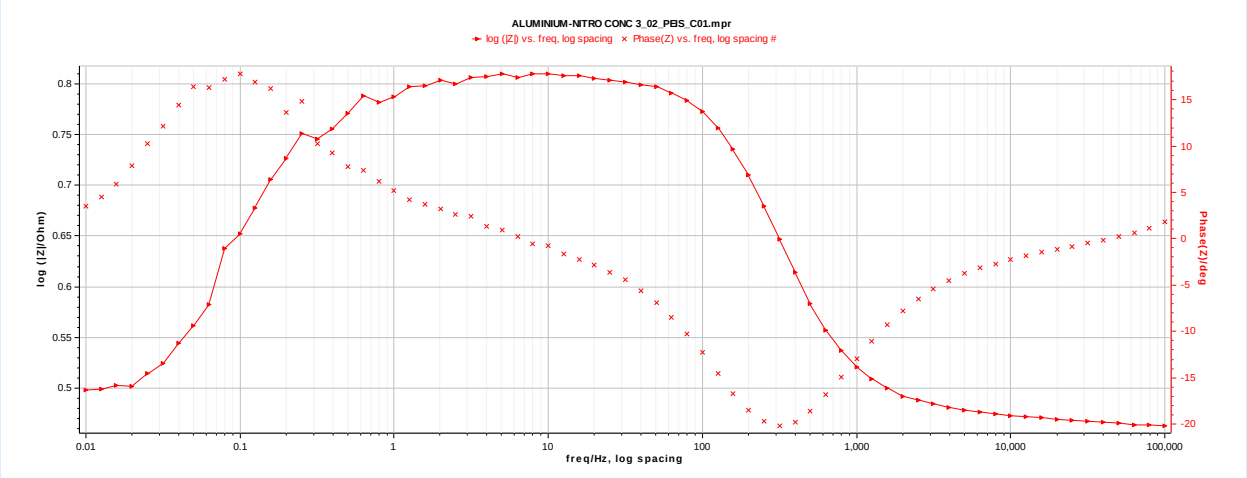

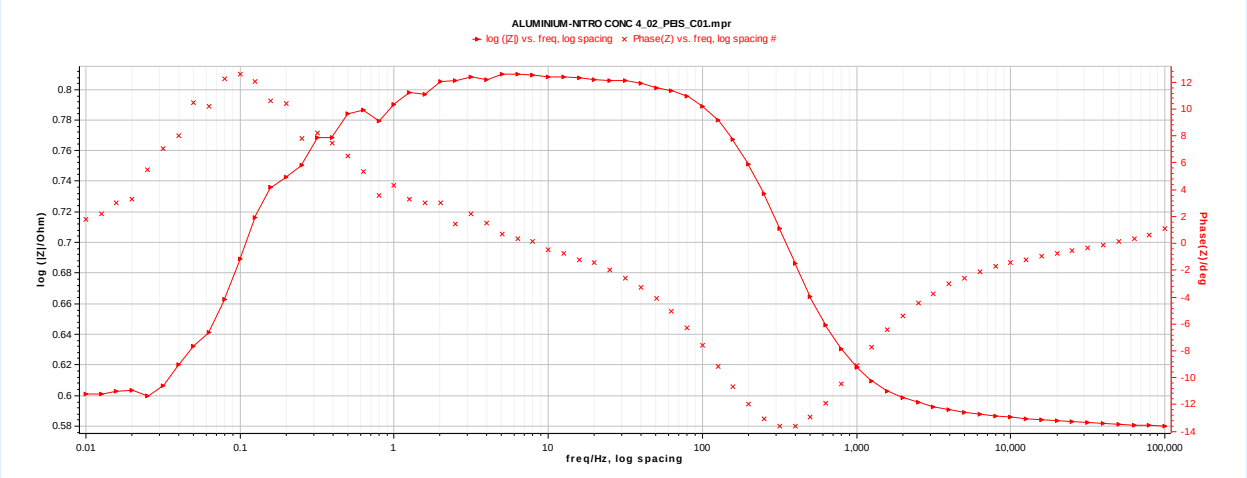

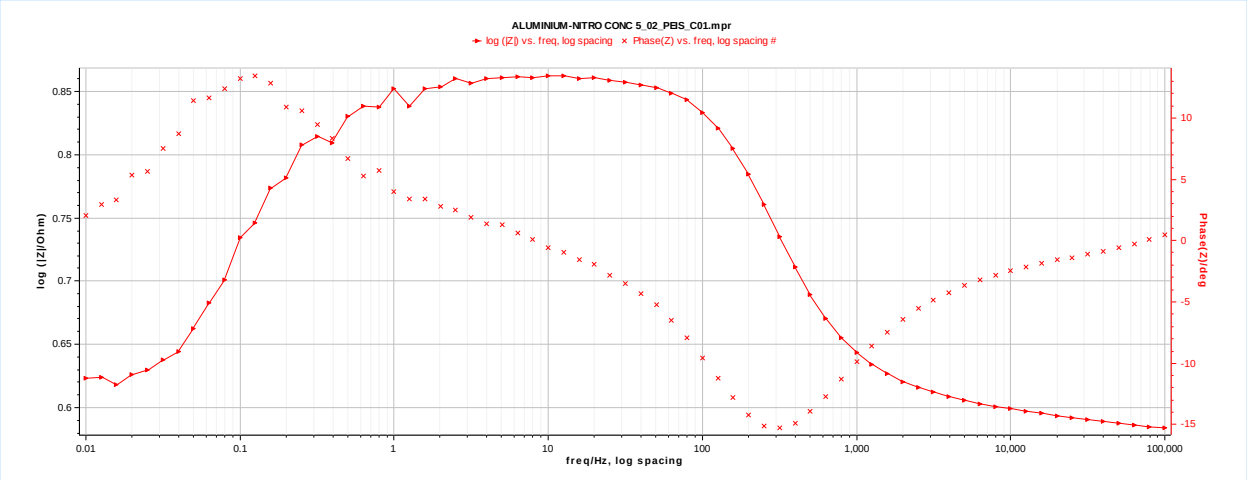

Appendix 53: Bode plots of aluminium in 1.0 M HCl in the presence of five various concentrations of NO_2-Chr-2-Carb.